Plasma Flow Control in an S-shaped Intake: Measurement and Computation

Fan Jiang

Submitted in fulfilment of the requirements for the
Degree of Doctor of Philosophy

Aerospace Science
James Watt School of Engineering
College of Science & Engineering
University of Glasgow

July 2024

Abstract

In modern aerospace engineering, flow control is an engineering technique that regulates fluid motion through active or passive methods to achieve specific performance objectives or optimise flow characteristics. The primary objectives typically include reducing drag, enhancing lift, suppressing flow separation, mitigating turbulence, and improving overall efficiency.

In recent years, a novel active flow control approach, known as dielectric barrier discharge (DBD) plasma flow control technology, has garnered significant attention. The DBD plasma actuator typically consists of two electrodes, with one electrode covered by a dielectric layer to limit current and prevent the occurrence of arc discharge. During operation, a high-frequency, high-voltage alternating current is applied between the two electrodes, ionising the surrounding air and generating plasma. In this process, charged particles within the plasma are accelerated under the influence of the electric field, colliding with neutral particles in the vicinity to produce a volumetric force (electrohydrodynamic force). This force enables control of the flow field. Due to its advantages, including the absence of mechanical components, rapid response, low energy consumption, and suitability for large-area deployment, DBD plasma flow control demonstrates immense potential for applications.

The relatively small magnitude of the volumetric force generated by dielectric barrier discharge significantly limits its practical applications in flow control. According to existing literature, there is a lack of theoretical foundation supporting DBD plasma actuator performance enhancement through a substantial increase in induced velocity. Therefore, this study aims to explore the potential of DBD plasma technology in broader application domains, building upon the currently known physical characteristics of DBD plasma.

Previous studies have been constrained by the limited magnitude of the volumetric force induced by DBD, leading to the selection of relatively small-scale models with simple geometries as experimental subjects. Moreover, the effectiveness of DBD actuators diminishes significantly with increasing freestream velocity, restricting their application primarily to low-speed environments. These limitations have resulted in a predominant focus on low-Reynolds-number scenarios in prior research. Under such conditions, the applicability of DBD plasma flow control in more complex flow fields remains unexplored mainly, leaving significant gaps in the existing body of research.

To address the challenges above, this study employs an S-duct model developed by NASA as

the experimental subject. This duct features a complex geometric configuration and is relatively large. These characteristics enable the test model to achieve higher Reynolds numbers even in low-speed environments, providing more practical and challenging conditions for investigating the application of DBD plasma flow control in complex flow fields.

This study aims to optimise the internal flow field of an S-duct using DBD plasma flow control technology, thereby improving the airflow quality at the duct's outlet. The research methodology integrates experimental investigations and numerical simulations. The results demonstrate that this approach offers a novel perspective for performance optimisation of S-ducts and provides valuable references for future studies on DBD plasma flow control and its applications in complex flow fields.

Contents

List of Tables

List of Figures

Nomenclature

Latin Symbols

A	any of flow properties, such as α_T, β_T, C_O and C_q
a	overheat ratio
C_p	static pressure coefficient
C_{0-4}	voltage to velocity transfer function constants
C_{α_T}	angle of attack coefficient:low angles
C_α	intermediate angle pressure coefficient
C_{β_T}	angle of side-slip coefficient:low angles
C_M	compressibility coefficient
C_O	total pressure coefficient
$C_{p,loss}$	total pressure loss coefficient
C_q	approximate dynamic pressure coefficient
C_w	heat capacity of wire
CV	coefficient of variation
DC_θ	pressure distortion coefficient at the θ sector
h	heat transfer coefficient
I	current, A
K	kurtosis

k_f	heat conductivity of fluid
K_s	calibration curve constants
Max	maximum value
Min	minimum value
n	sample number
Nu	dimensionless heat transfer coefficient
p_s	static pressure, pa
P_{∞_L}	local static pressure, pa
P_n	pressure at probe port n,pa
P_{OL}	local total pressure, pa
$P_{s,AIP}$	average static pressure at the AIP, pa
$p_{s,ref}$	static pressure at the reference point, pa
$P_{t,\theta,min}$	minimal total pressure at the θ sector, pa
$P_{t,AIP}$	average total pressure at the AIP, pa
$P_{t,o}$	freestream total pressure, pa
$P_{t,reference}$	total pressure at the reference point, pa
PR_s	static pressure recovery coefficient
PR_t	total pressure recovery coefficient
Q	heat transfer to surroundings
Q_i	thermal energy stored in wire,Q_i=$C_w T_w$
$q_{reference}$	dynamic pressure at the reference point, pa
R	Range
R_0	resistance of the ambient environment, Ω
R_w	wire resistance, Ω
S	skewness

SC_θ	swirl distortion coefficient at the θ sector
T_0	ambient environment temperature, K
T_w	wire temperature, K
Tu	turbulence intensity
U	velocity magnitude,m/s
u	streamwise velocity component
U_r	relative uncertainty
$U_{crossflow,\theta,max}$	maximal crossflow velocity at the θ sector, m/s
$U_{reference}$	velocity at the reference point, m/s
v	horizontal velocity component at the cross-section
W	power generated by Joule heating, W
w	vertical velocity component at the cross-section
Z_{value}	confidence level

Greek Symbols

α	angle of attack, $^\circ$
α_0	resistance temperature coefficient
β	angle of side-slip, $^\circ$
σ	standard deviation
τ	time constant

Superscripts

T	Transpose

Subscripts

∞	static pressure
L	local
max, exp	estimated maximum velocity in the experiment
$mean$	mean
min, exp	estimated minimum velocity in the experiment
O	total pressure
rms	root-mean-square value
T	tangential reference system

Acronyms

AC	alternating current
AIP	aerodynamic interface plane
AVG	sample averaging
CI	confidence interval
DBD	dielectric barrier discharge
FPS	frame per second

Acknowledgements

As I am about to complete my thesis, I am filled with profound emotions while writing the acknowledgements. Looking back, I realise there are so many people I need to thank.

First and foremost, I would like to express my sincere gratitude to my primary supervisor, Professor Konstantinos Kontis. This PhD journey has been exceptionally challenging due to COVID-19 and personal family reasons. I am thankful for your support and understanding throughout this educational journey. At the same time, I would like to sincerely apologise for constantly troubling you. I also thank my second supervisor, Dr Craig White, for supporting and guiding my studies. Here, I offer my best wishes to both of my supervisors.

I want to extend special thanks to Dr Richard Green for all the assistance provided in my experiments. Your exceptional demeanour and dedicated work ethic have continuously inspired and motivated me.

I would also like to thank my family. My parents, thank you for encouraging me to embark on this learning journey. Your unwavering belief in me has been my greatest strength. To my wife, words cannot express my gratitude. Not only do you understand and support my research, but you have also been raising our daughter alone in Japan. Your selflessness and love have been my anchor. I am sincerely grateful for your love.

Lastly, I would like to thank all the friends who have supported, helped, criticised, encouraged, and understood me along this journey.

Declaration

I declare that the submitted thesis is the result of my independent research conducted under the guidance of my supervisor. Except for the content explicitly cited in the text, this thesis does not contain any other research achievements previously published or written by individuals or groups. Individuals and groups who have made significant contributions to this research have been clearly acknowledged in the thesis.

Chapter 1

Introduction

1.1 Background

As a critical component of high-speed aircraft engines, the intake system is designed to decelerate the incoming airflow, thereby enhancing the performance of both the engine and the compressor. In designing the intake system, meeting deceleration requirements while maintaining the intake duct as short as possible is essential. This is because a shorter intake duct translates to a shorter fuselage, which contributes to the aircraft's overall weight reduction [1, 2]. It is estimated that if the aircraft can reduce its fuselage length by one diameter of its intake duct, the net weight would decrease by 15% [3]. Compared to traditional straight ducts, diffusive S-shaped intake ducts, due to their curvature, can reduce the velocity of the incoming flow more rapidly. This results in shorter intake ducts and significantly reduced weight. Presently, diffusive S-shaped intake ducts have been widely adopted in high-speed aircraft propulsion systems.

However, the use of S-shaped ducts is not without its challenges. While these ducts effectively decelerate airflow, they also introduce pressure losses and flow instability [4, 5]. Unlike conventional straight intake ducts, the pronounced curvature of S-shaped ducts makes flow separation nearly unavoidable. Moreover, the uneven wall pressure distribution within S-shaped ducts exacerbates flow instability by inducing strong secondary flows. These adverse factors significantly degrade the airflow quality at the aerodynamic interface plane (AIP) before it reaches the engine. Once a critical threshold is reached, the engine may experience stall flutter or rotational instability [6].

There are two commonly used methods to address this deficiency: one approach is to optimise the geometry of the S-duct itself, while another is to employ flow control techniques to improve the internal flow field. Flow control methods can be categorised into active flow control and passive flow control based on the presence of external energy input. Passive flow control primarily relies on the object's geometry to influence the flow field, offering high reliability and simplicity in overall design. However, it typically only satisfies specific operating conditions and may even induce additional drag under off-design conditions. In contrast, despite facing

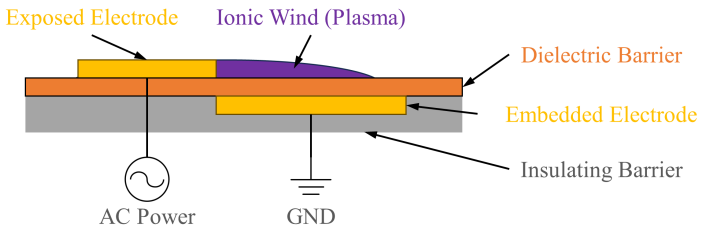

Figure 1.1: The schematic of the surface dielectric barrier discharge (SDBD) actuator.

challenges such as system complexity and high maintenance costs, active flow control allows for more flexible and precise manipulation of the flow field. Common active flow control methods include suction and blow, mechanical oscillation, and temperature control. The utilisation of plasma to achieve effects akin to suction and blowing represents a burgeoning area of research.

Plasma, the fourth state of matter beyond solid, liquid, and gas, is typically generated by applying strong electric or magnetic fields to neutral fluids. When a strong electric field is applied to air, it ionises the gas, forming charged particles. These particles move under the electric field's influence and collide with neutral particles, creating the gas flow. Utilising electricity to generate plasma for flow control falls under the electro-hydrodynamics (EHD) category, which is characterised by its adjustability and rapid responsiveness. A prominent research direction currently is Surface Dielectric Barrier Discharge (SDBD). This method has successfully achieved large-scale, uniform discharge plasma at atmospheric pressure, initially proposed by Professor Roth's team [7, 8]. SDBD has garnered widespread attention due to its simplicity, reliability, ease of large-scale deployment, and lack of additional components since its inception.

A typical SDBD actuator consists of an exposed electrode, a covered electrode, and an insulating layer, as depicted in Figure 1.1. The exposed electrode is connected to a high voltage (AC power source), while the covered electrode is typically grounded. The average velocity field is unaffected by the polarity switching of the AC voltage and is directed from the exposed electrode towards the covered electrode. Although the underlying mechanisms of plasma discharge have not been fully established, extensive experimental and simulation studies have provided insights into some characteristics of plasma-induced airflow.

1.2 Research Problem & Objective

Despite their significant potential in flow control, DBD plasma actuators' practical applications remain constrained by the relatively low thrust they generate. Existing studies suggest that substantially increasing the induced thrust of DBD plasma actuators remains a significant technical challenge. Achieving significant breakthroughs remains impractical without new discoveries or theoretical advancements. Therefore, this study aims to extend the application scope of DBD plasma flow control. The research focuses on an S-shaped duct configuration proposed

by NASA, reproduced at a full 1:1 scale without any geometric scaling. The larger model size ensures that the test object maintains a high Reynolds number even under relatively low test flow velocities, providing conditions more representative of real-world applications for investigating flow control mechanisms.

In optimising S-shaped ducts using DBD plasma flow control, Wojewodka [9] conducted pioneering research, addressing the gap in simulation studies for this application. However, due to the selection of a high test flow velocity, reaching 0.6 Mach, the actual flow control effects of the DBD plasma actuator were not observed. Inspired by this prior research, the present study focuses on low-speed flow scenarios and aims to investigate further the potential applications of DBD plasma actuators in S-shaped ducts through experimentation and computational modelling. Several key objectives of this thesis include:

(1) Study the influence of different extension section lengths on the flow field within the S-duct. Although numerous studies have incorporated extension sections, the existing literature has yet to give their specific role.

(2) Investigate the flow field structure and turbulent characteristics within the S-duct at various velocities. The current body of research in this field has yet to explore this aspect.

(3) Establish and validate simulations of the S-duct. This part of the work includes setting up and running experiments due to the lack of existing experimental data. The verified simulation setup can provide references for future studies.

(4) The comprehensive analysis of the DBD plasma flow control using experiment and simulation. The experiments provide qualitative results, while the simulations offer quantitative analysis. Integrating experiments with simulations not only ensures the reliability of the research but also enhances the accuracy of the results.

The experimental techniques involve pressure measurements and constant-temperature anemometry, and the simulation software utilised is OpenFOAM, an open-source software.

1.3 Thesis Outline

This thesis begins with a comprehensive literature review of prior research on S-shaped ducts and AC-DBD plasma actuators (Chapter 2). The study of S-shaped ducts encompasses both experimental investigations and numerical simulations. Chapter 3 describes the experimental methodologies, numerical computation techniques, and data analysis methods employed in this research.

This research focuses on the pressure measurement of S-shaped ducts as the entry point of the study. Chapter 4 investigates the flow characteristics within an S-shaped duct at low speeds and examines the impact of varying lengths of upstream and downstream extensions on

the internal flow field. The experimental setup includes an S-shaped duct model and an axial fan, with the fan positioned downstream to regulate flow velocity within the duct. Take the S-duct throat as the reference point; the velocity range under investigation spans from 0.06 to 0.15 Mach. Measurements are taken in a region between the S-shaped duct and the fan, using a traverse system to capture aerodynamic interface plane (AIP) flow parameters. Additionally, wall static pressure measurements are utilized to characterize the flow field within the duct.

Subsequently, in Chapter 5, an in-depth investigation of the turbulent characteristics at the AIP interface was conducted using a constant temperature anemometer. Fourier analysis determined the frequency and sampling period for data acquisition, providing precise data recording intervals for subsequent transient simulations.

Chapter 6 establishes and validates the numerical simulation model of the S-shaped duct. The numerical simulations employ the Reynolds-Averaged Navier-Stokes (RANS) approach. To ensure the accuracy of the simulations, a mesh independence study was conducted, and the results were compared with experimental data. Additionally, three common turbulence models—$k-\varepsilon$, $k-\omega$, and the shear stress transport (SST)—were tested. Moreover, the duct radius growth rate was studied further. After comparing the two configurations, the configuration with superior performance was selected for further unsteady simulations. Subsequently, modal analysis was performed using Proper Orthogonal Decomposition (POD), Dynamic Mode Decomposition (DMD), and Spectral Proper Orthogonal Decomposition (SPOD).

Chapter 7 uses experimental and numerical methods to investigate the application of plasma flow control in a low-speed S-duct. Due to the limited velocity generated by the plasma, the Mach number in the duct's throat region is approximately 0.06. Aerodynamic interface plane (AIP) measurements were conducted using a seven-hole probe, and wall pressure coefficients characterized the internal flow field. However, due to the limitations of experimental techniques, direct observation of the internal flow within the duct was not possible, making numerical simulations necessary to visualize the flow. The numerical study employed a low-order body force model to simulate the plasma.

1.4 Originality & Contributions

This study aims to investigate the application of AC-DBD plasma actuators in S-shaped ducts. To achieve this goal, extensive experiments, numerical simulations, and validation efforts were conducted. The insights gained from this work can offer valuable references and guidance for future research on plasma flow control and S-shaped duct dynamics.

This study has identified several key aspects: the influence of upstream and downstream extensions on the flow field within the S-shaped duct, the measurement parameters for turbulence in the duct at low flow velocities, the parameters for numerical simulations, the functionality of modal analysis methods, and both the experimental and simulated application of plasma actua-

tors within the S-shaped duct.

1.5 Research Outcomes

The following list presents a selection of research outcomes achieved during the doctoral program:

Journal Articles:

1. Jiang, F., Kontis, K., & White, C. (2024). Experimental analysis of flow characteristics in S-shaped ducts at low speeds. *Physics of Fluids*, 36(10).

2. Jiang, F., Kontis, K., & White, C. (2024). Numerical Investigation and Mode Analysis of the S-duct. *Physics of Fluids*, 36(11).

3. Jiang, F., Kontis, K., & White, C. (2024). Plasma flow control inside the S-duct. *(Submitted)*

Conference:

1. The 9th European Conference for Aeronautics and Space Sciences; EUCASS-3AF 2022.

2. The UK Fluids Conference 2023.

3. International Conference on Flow Dynamics (ICFD); Sendai, 2023.

Chapter 2

Literature Review

2.1 Introduction

Active flow control, through the manipulation of airflow to achieve desired performance changes, holds significant technical and economic importance in sectors such as the aviation industry. Effective flow control involves the adjustment of three phenomena: the transition from laminar to turbulent flow, flow separation, and turbulence characteristics. Delaying the transition from laminar to turbulent flow can significantly reduce surface friction drag, leading to lower fuel consumption, extended range, and increased speed for aircraft. Moreover, preventing flow separation can enhance wing lift and control stall characteristics, optimising aircraft takeoff and landing performance. Effective management of turbulence, on the other hand, aids in improving flow mixing or reducing aerodynamic noise [10, 11].

Plasma flow control is undergoing extensive development as an emerging method of active flow manipulation. Flow control devices based on surface dielectric barrier discharge are DBD plasma actuators [12–15]. Unlike conventional mechanical devices, plasma actuators are entirely driven by electrical energy, eliminating the need for additional moving parts. Due to the potential for plasma actuators to be fabricated with relatively thin thickness, they can be conveniently adhered to the surface of the control body. Additionally, they offer the advantages of being lightweight and exhibiting rapid response characteristics, circumventing the drawbacks of traditional mechanical systems such as complexity, increased weight, and volume. To a certain extent, plasma flow control represents an ideal methodology for active flow manipulation [11, 15–19].

Plasma actuators, by design, comprise a few components, typically consisting of three main parts: an anode, a cathode, and a dielectric material. The anode is connected to a power source, while the cathode is usually grounded. During operation, a sufficient voltage is applied to the anode to ionise the surrounding air and generate plasma, which then diffuses from the anode towards the cathode. However, this discharge process is self-limiting, as the charge emitted from the anode accumulates on the surface of the dielectric, thereby reducing the potential difference

and suppressing further plasma formation unless the voltage applied to the anode is continuously increased [19]. To address this and form a relatively continuous plasma, the connected power source typically utilises alternating current to achieve a periodically varying voltage, thereby facilitating the plasma's periodic and continuous generation. Actuators operating in the manner above are also referred to as AC-DBD (Alternating Current-Dielectric Barrier Discharge) plasma actuators.

Based on DBD plasma actuator configuration, they can be further categorised into symmetric and asymmetric actuators. Upon activation of the actuator, starting vortices are generated. During operation, the plasma transfers momentum from the discharge phenomenon to the surrounding air through inter-ionic collisions, generating a net body force and accelerating the air. Plasma actuators can generate wall-bound vectored airflow or vortices without needing an air source, a unique method of air acceleration that enables numerous innovative aerodynamic applications. However, much like a coin has two sides, the development of AC-DBD plasma actuators has been constrained despite their numerous advantages due to their low energy conversion efficiency.

This chapter primarily reviews the physical characteristics of AC-DBD plasma and its applications in aerodynamics from an experimental perspective. Furthermore, it consolidates numerical modelling efforts of AC-DBD plasma by researchers in the simulation domain. In this thesis, the S-shaped inlet duct is the application subject of the plasma actuator. This chapter also reviews the flow mechanisms within the S-shaped inlet duct. A better understanding of the performance characteristics of AC-DBD plasma actuators and the flow mechanisms in S-shaped ducts is helpful for the next step: applying AC-DBD plasma actuators in S-shaped inlet ducts.

2.2 The Physical Characteristics of AC-DBD Plasma

2.2.1 Electrical Properties

Within a single cycle of the alternating voltage, the dielectric discharge undergoes a total of six phases as illustrated in Figure 2.1: initiation, expansion, electron migration from the anode to the dielectric surface (forward stroke), re-initiation, expansion, and electron migration from the dielectric surface back to the anode (reverse stroke). The deposition of electrons will decrease the potential difference across the actuator, diminishing its ability to ionise air until it ceases. Therefore, dielectric discharge is self-limiting and requires continuous voltage modulation to sustain plasma generation [20–22]. After the initiation of dielectric discharge, if the voltage waveform applied to the anode is sinusoidal, the resulting current signal comprises three distinct components [23, 24]. Component (1) is attributed to the capacitive effects between the two electrodes, manifesting as sinusoidal waveforms phase-orthogonal to the voltage signal and unrelated to the discharge phenomena. Component (2) consists of a series of pulses with am-

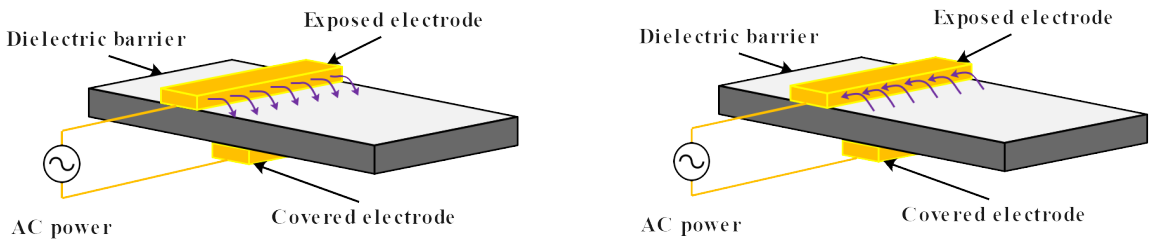

Figure 2.1: Dielectric barrier discharge phases [22].

plitudes reaching up to 20 milliamperes and durations of a few microseconds, which collapse shortly after the voltage achieves its maximum absolute value. In some instances, the amplitude of these pulse signals can reach several amperes [25]. Component (3) involves a series of persistent pulses with amplitudes of only a few milliamperes, representing another manifestation of the capacitive effects.

When both electrodes of the plasma actuator are left unencapsulated (shown in Figure 2.2 (a)), the relationship between voltage and current under atmospheric pressure conditions is illustrated in Figure 2.2 (b); in the experiment here, the electrodes utilised are aluminium foils measuring 20 cm in length and 1 cm in width, with a separation of 5 mm between them. The dielectric material employed is glass with a 2 to 3 mm thickness. The voltage signal is a sinusoidal waveform at 300 Hz with a peak value of 20 kV.

When the cathode of the plasma actuator is encapsulated, allowing discharge only on the anode side, as illustrated in Figure 2.2 (c), the relationship between voltage and current is depicted in Figure 2.2 (d). It can be observed that the pulse signals in Component (2) predominantly occur within the positive voltage half-cycle, and in the negative voltage half-cycle, only a few peaks of similar intensity can be observed.

If the voltage waveform applied to the anode is of a sawtooth configuration, the resultant current-voltage signal profile, as depicted in Figure 2.3, exhibits a pronounced discrepancy between the forward and backward strokes' current signals.

2.2.2 Actuator Parameters

2.2.2.1 Voltage

Pons et al. [23] investigated the relationship between maximum induced velocities and the applied voltage amplitude within the range of 10kV to 20kV, as illustrated in Figure 2.4. Experimental data demonstrated a positive correlation between maximum induced velocities and applied voltage amplitude. A plethora of studies have arrived at similar conclusions. However, some research [21, 22, 27–29] also highlighted that the maximum induced velocity does not keep increasing with the augmentation of voltage amplitude, constrained by the plasma expan-

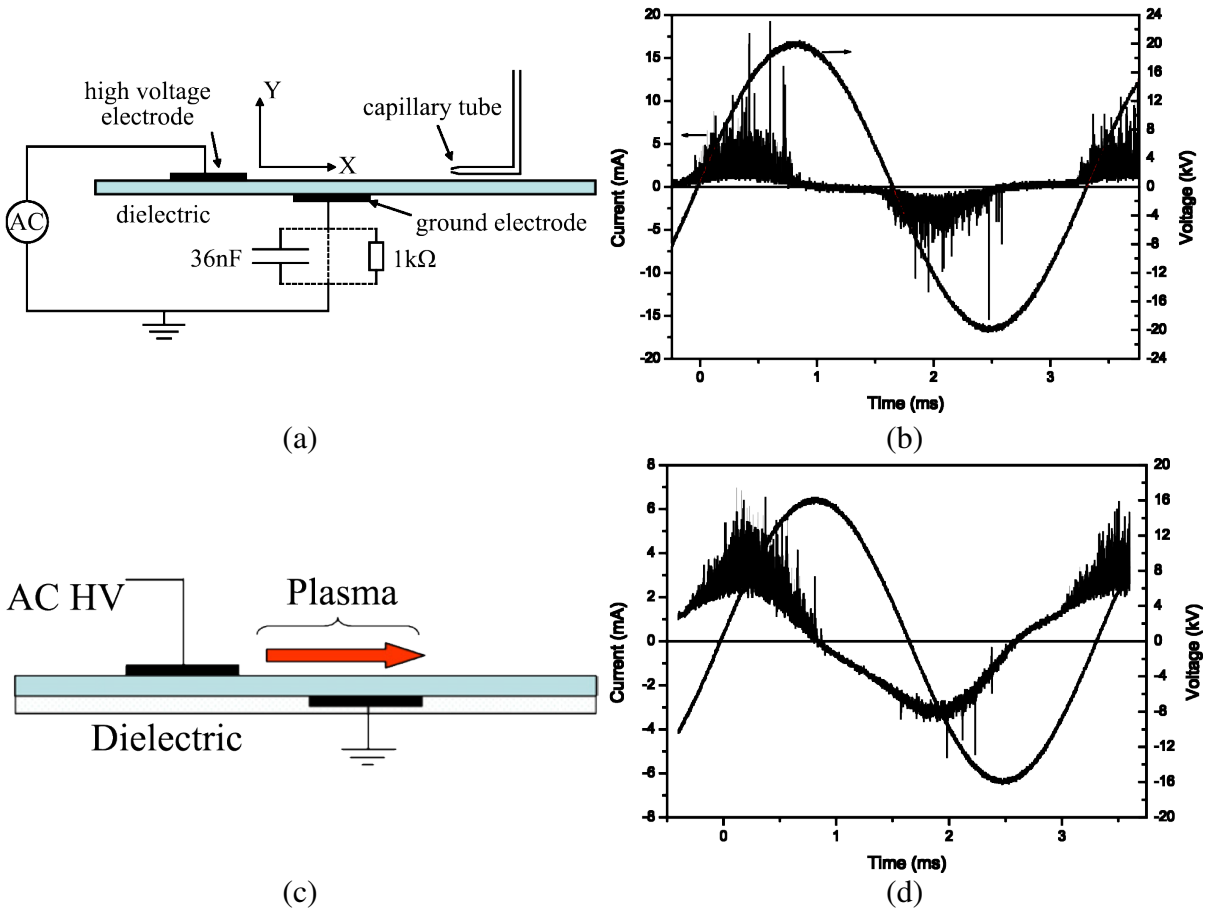

Figure 2.2: The voltage and current versus time of asymmetric AC-DBD plasma actuator; (a-b) with both exposed electrodes; (c-d) with encapsulated cathode [11, 23].

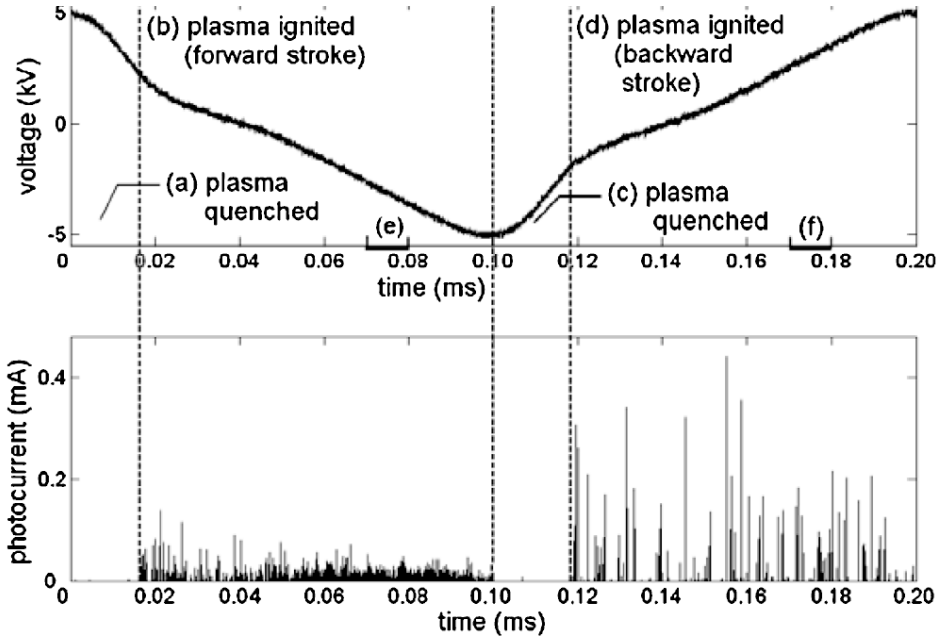

Figure 2.3: The voltage and current versus time of asymmetric AC-DBD plasma actuator (saw-tooth waveform) [26].

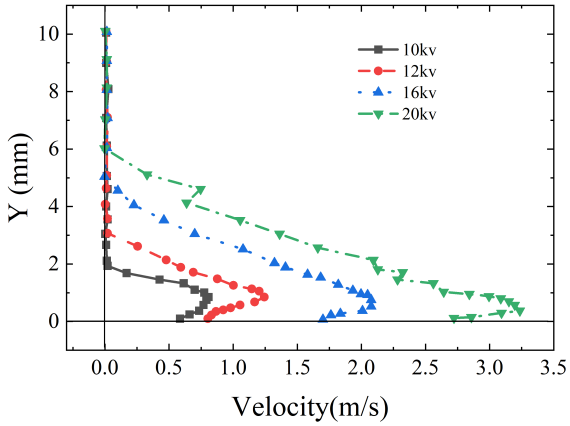

Figure 2.4: The influence of the voltage on the induced velocity [23].

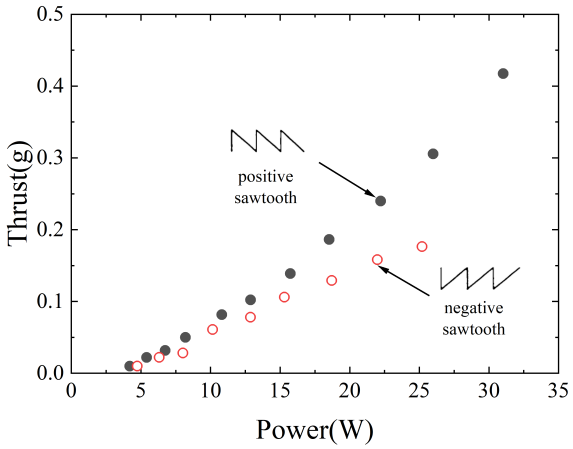

Figure 2.5: The thrust difference between the positive sawtooth and the negative sawtooth waveform [21, 26].

sion region. Within the extant literature, the highest known induced velocity to date is only around 10 m/s [30].

In the preceding section on electrical performance, it is established that in alternating current (AC), based on the voltage waveform, plasma discharge can be categorised into forward stroke and backward stroke. The forward stroke exhibits enhanced macroscopic diffusivity within each cycle period compared to the reverse stroke [26]. This augmented diffusivity allows the plasma to interact with a broader air region, achieving a higher net thrust output during the forward stroke. Consequently, when considering a sawtooth waveform voltage, as illustrated in Figure 2.5, configuring the voltage waveform as a positive sawtooth wave, as opposed to a negative sawtooth wave, facilitates a higher net thrust output.

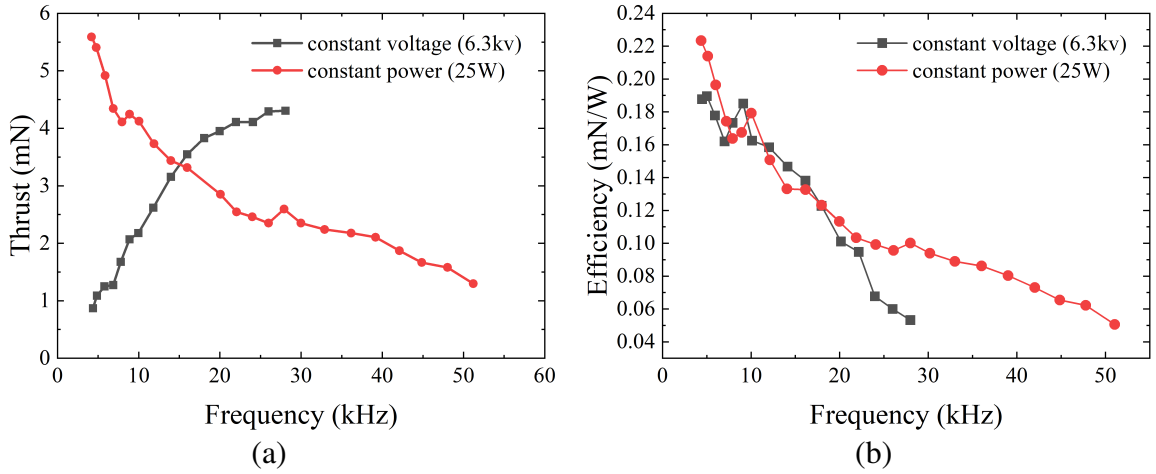

Figure 2.6: The influence of the frequency on the generated thrust and efficiency [26].

2.2.2.2 Frequency

The impact of frequency on induced velocity has been extensively investigated. Under conditions of fixed amplitude, it has been observed that the maximum induced velocity increases with frequency elevation [31, 32]. However, Enloe et al. [26] noted that, to a certain extent, achieving enhanced maximum induced velocity by increasing frequency is merely superficial. Elevating the frequency at a fixed voltage amplitude essentially equates to inputting higher power into the system, and this increase in power is the real reason for the augmentation of thrust or induced velocity.

As illustrated in Figure 2.6, the thrust progressively increases with the rise in frequency under the condition of fixed voltage amplitude. However, an increase in frequency may even reduce the generated thrust under constant actuator power. Regarding the efficiency of thrust generation, there is a continuous downward trend in efficiency with the increase in frequency, indicating that an increase in frequency leads to a decrease in effective power.

Additionally, exceeding high voltage and frequency in plasma propulsion systems can lead to filamentation or arcing on the dielectric surface. This increases the risk of dielectric damage and threatens the overall system operation. Therefore, it is crucial to operate plasma propulsion systems within safe voltage and frequency limits [33, 34].

2.2.2.3 Electrode and Dielectric Barrier

The extent of plasma expansion, characterised by the uniform glow within the ionised region, is constrained by the cathode width. This expansion distance significantly affects the thrust generated by the plasma, as illustrated in Figure 2.7. It is evident that when the lower edge of the cathode limits the plasma expansion, further increases in input power only result in a saturation of net thrust. However, the inherent plasma expansion capacity is physically constrained [33] and does not continue to increase indefinitely with cathode width. Therefore, optimising

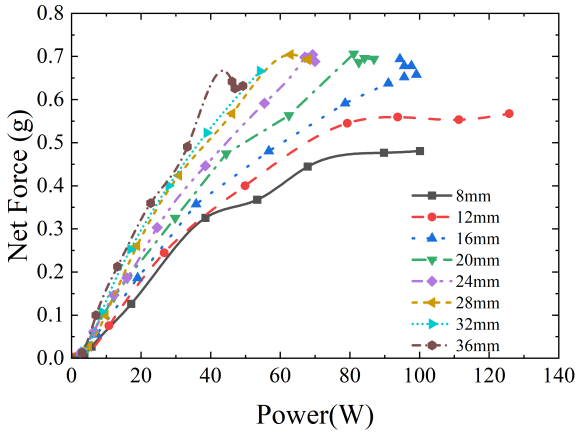

Figure 2.7: The influences of the cathode width on the thrust [26, 35].

the cathode dimensions to facilitate sufficient plasma expansion emerges as a critical design consideration for enhancing the overall performance of plasma propulsion systems.

Pons et al. [23] reported (as indicated by the red line in Figure 2.8(a)) that the maximum induced velocity has a positive correlation with electrode spacing when set to -5, 2, and 5 mm. However, this conclusion is not entirely accurate. Subsequent experiments by Forte et al. [33] provided a more comprehensive investigation into the relationship between electrode spacing and maximum induced velocity. Their findings confirmed the existence of optimal electrode spacing under specific voltage and frequency conditions, as illustrated by the blue line in Figure 2.8(a).

In addition to electrode spacing, the thickness of the dielectric layer also significantly affects the maximum induced velocity [23, 33]. Figure 2.8 (b) illustrates the variation of maximum induced velocity with different dielectric thicknesses, where the glass was used as the dielectric material. The figure shows that the maximum induced velocity decreases progressively with increasing dielectric thickness. Moreover, under fixed electrode geometry, a higher dielectric constant of the dielectric material will result in greater thrust generation, and higher induced velocity, and correspondingly higher power dissipation [23, 32–34, 36–38].

The maximum induced velocity typically does not occur at the dielectric surface but reaches its peak at a certain distance from it. Specifically, when employing a thicker dielectric medium, the peak of the maximum induced velocity is observed at approximately 0.5 millimetres from the surface of the dielectric [23]. However, the peak of this maximum induced velocity is about 2 millimetres from the dielectric surface under a thinner dielectric medium [34, 39].

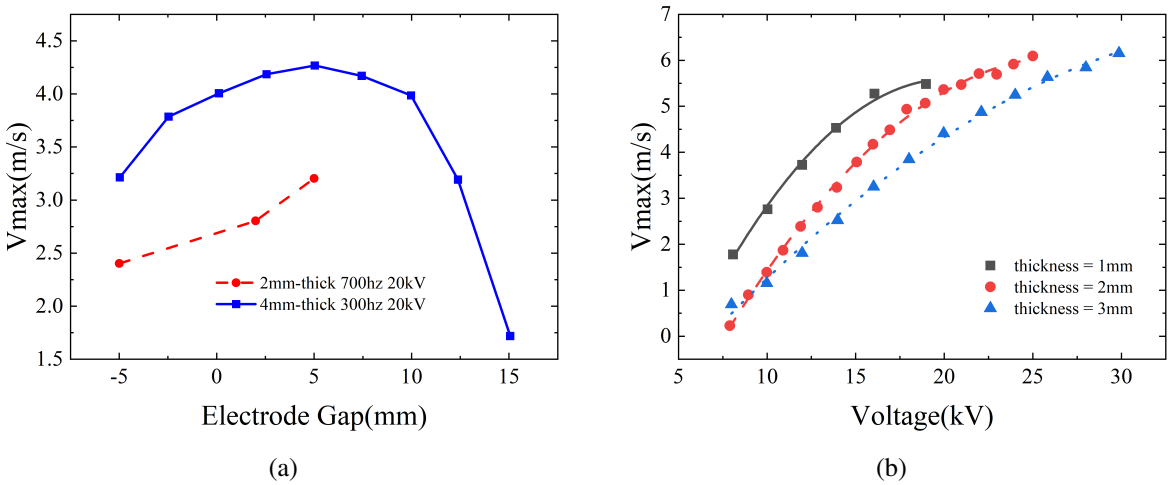

Figure 2.8: The influences of the dielectric barrier properties on the induced velocity [23, 33].

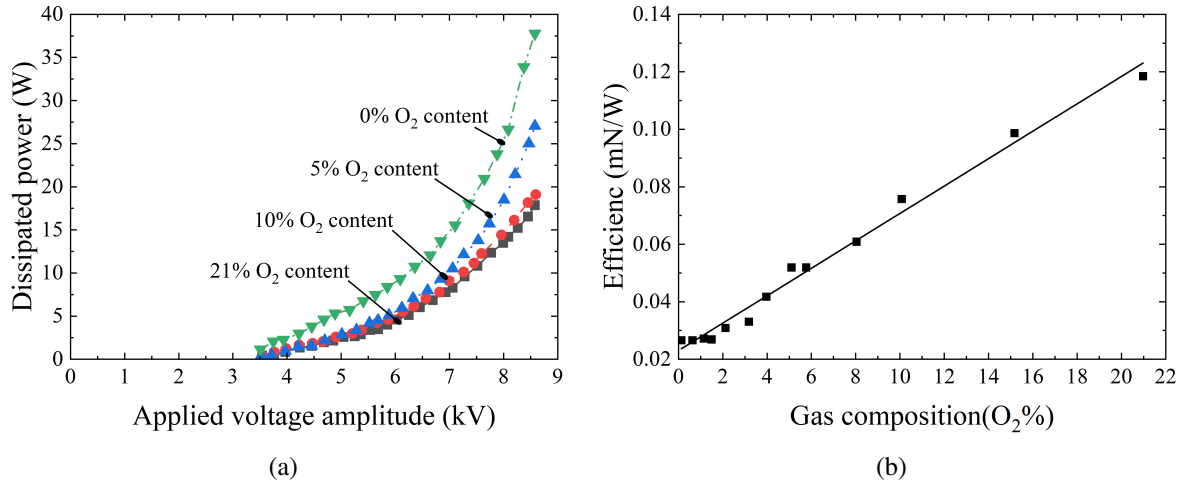

Figure 2.9: The influences of the oxygen content on the plasma [26].

2.2.3 Environment Parameters

2.2.3.1 Oxygen Content

The study on the impact of atmospheric oxygen content on plasma discharge performance demonstrates that when the oxygen concentration exceeds 10%, the discharge performance of the plasma remains relatively consistent with minimal variation. However, as the oxygen concentration decreases below 10%, there is a significant increase in the dissipative power of the plasma under the same voltage conditions, as shown in Figure 2.9 (a). By evaluating the efficiency of the plasma actuator through the ratio of generated thrust to consumed power, it can be found that an increase in oxygen content positively enhances the efficiency of the plasma actuator, as depicted in Figure 2.9 (b) [26].

2.2.3.2 Humidity

Avino et al. [40] studied the performance of DBD (Dielectric Barrier Discharge) plasma actuators under varying humidity conditions. The research indicates that DBD plasma actuators are well-suited for prolonged operation in environments of low humidity. At moderate humidity levels (50%), chemical reactions between the plasma and water lead to the degradation of DBD materials, with the plasma region gradually disappearing over several hours. At higher humidity levels (70%-85%), the plasma is inhibited during the ignition phase.

2.3 Aerodynamic Application of the AC-DBD Plasma

2.3.1 The Mechanism of the DBD Plasma-Induced Flow

In a quasi-static environment, the activation of a DBD plasma actuator induces the formation of a shear layer above its surface, which gradually rolls up to generate vortex structures. Over time, these initial vortices migrate along the wall and progressively move away from the surface. Eventually, a stable wall jet emerges [27].

Whalley and Choi [41] further proved that the starting vortex manifests as tightly compacted spirals and quantified the vortex's vorticity field using PIV. The corresponding smoke visualisation and vorticity fields are shown in Figure 2.10. The mechanism for the genesis and evolution of the starting vortex demonstrates that the plasma actuator entrains air from directly above, culminating in forming a starting vortex. This nascent starting vortex further induced secondary vortices near the wall surface and propelled the primary vortex away from the wall. The development process of the starting vortex is shown in Figure 2.11. In an asymmetric configuration, the inception vortex is generated on one side only, and a symmetric setup yields a pair of counter-rotating starting vortices on both sides [42]. By operating the plasma actuator on and off regularly, a series of vortices merge to form a vortex flow [43–45].

After achieving a steady state, the DBD plasma actuator generates tangential momentum a few millimetres above the wall surface, which has been corroborated through the use of Pitot tubes [8, 46], hot-wire anemometry [47, 48], and PIV [49, 50]. The tangential jet formed by the DBD plasma actuator is as shown in Figure 2.12, with flow velocities typically ranging between 4-5 m/s and the known maximum velocity reaching up to 10 m/s [11, 51]. Unlike classical wall jets, the DBD plasma actuator serves merely as a momentum source without contributing additional mass to the flow field. However, regarding effects, the two mechanisms are almost similar[52, 53].

Using the above flow phenomena, DBD plasma actuators can function as synthetic jets, wall jets, and vortex generators.

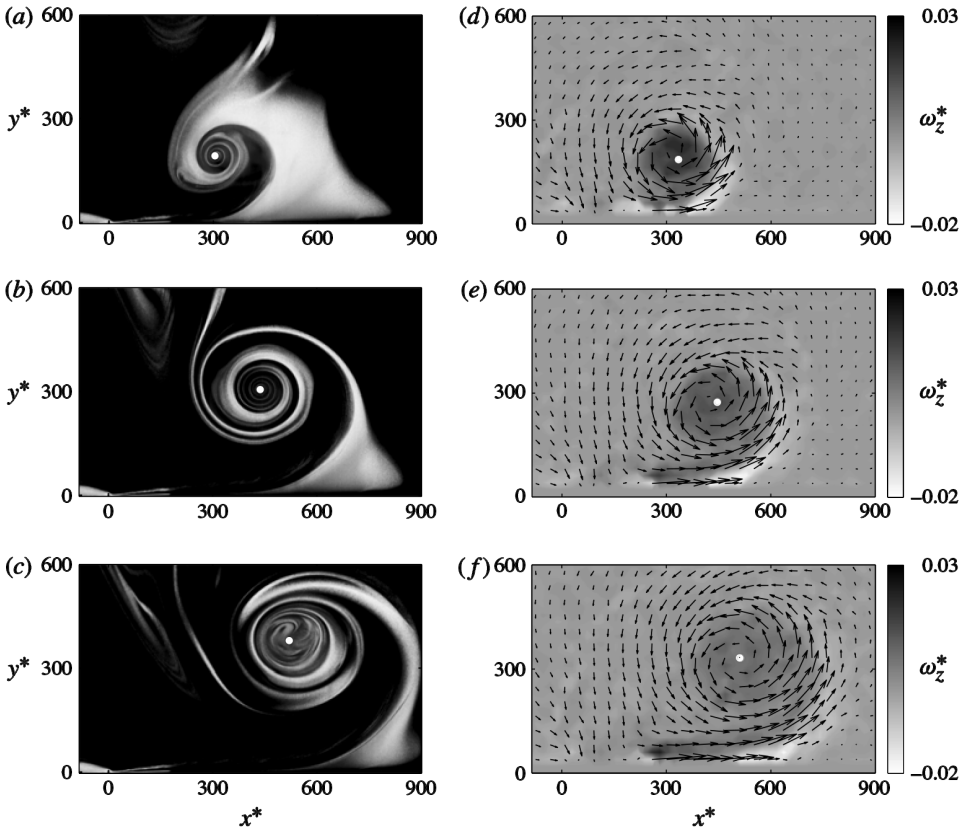

Figure 2.10: Smoke flow visualisation (a-c) and PIV vorticity field of the starting vortex induced by DBD plasma with time development [41].

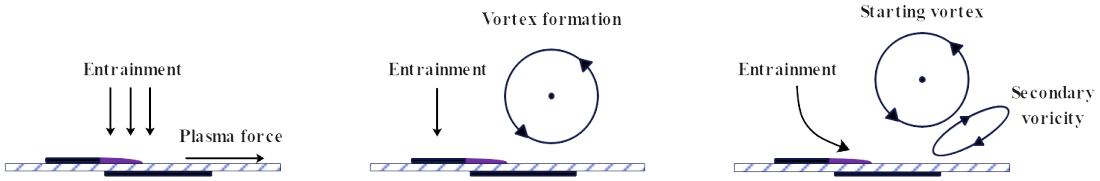

Figure 2.11: The schematic of the development of the starting vortex induced by DBD plasma [41].

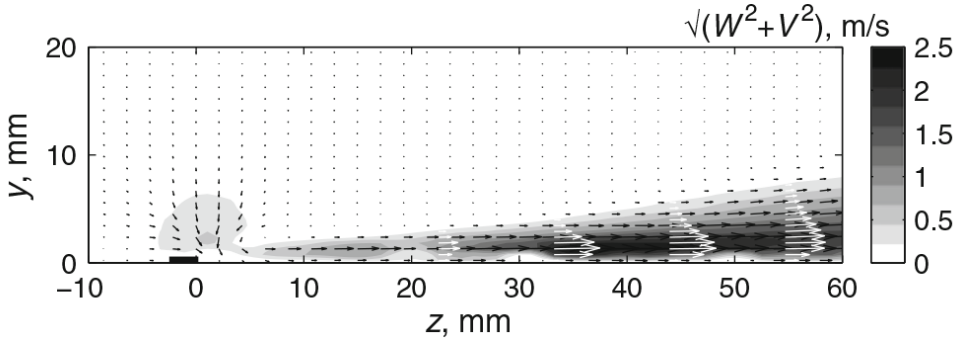

Figure 2.12: The wall jet induced by DBD plasma [54].

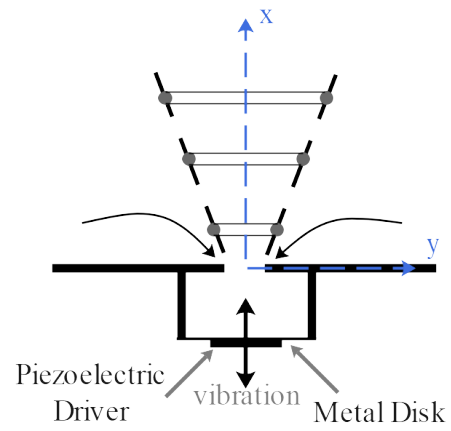

Figure 2.13: The schematic of the conventional mechanical synthetic jets [56].

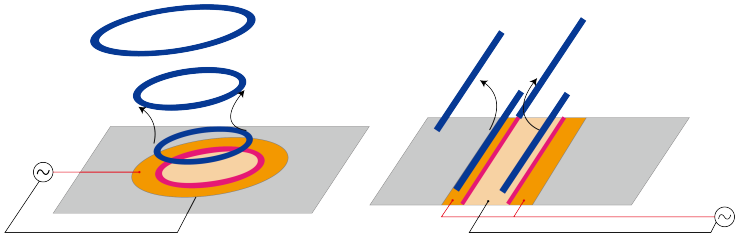

Figure 2.14: The schematic of two basic configurations of DBD plasma synthetic jets [57].

2.3.2 Synthetic Jets

Synthetic jets, a concept initially proposed by Coles in the 1970s and tested by Savas and Coles [55], involve the formation of a turbulent shear layer through synthesising coherent vortex structures. The traditional structure of a synthetic jet actuator is illustrated in Figure 2.13, driven by piezoelectric actuation, which undergoes periodic reciprocating motion within a cavity, thereby periodically drawing in and ejecting airflow at the orifice. A hallmark of synthetic jets is their ability to inject additional momentum into the flow field with a zero mass flux. Hence, they are also referred to as zero-net-mass-flux jets.

DBD plasma synthetic jet technology integrates the characteristics of both plasma actuators and synthetic jets by configuring DBD plasma actuators to embody the properties of synthetic jets. Research into this domain can be traced back to the early works of Santhanakrishnan et al. [57] at the beginning of this century. Based on a similar principle of suction and blowing, many attributes of plasma synthetic jets closely resemble those of traditional synthetic jets ([56, 58–65]). Figure 2.14 displays two fundamental configurations of plasma synthetic jets: a ring configuration and a symmetric linear configuration.

In contrast to traditional synthetic jets, DBD plasma synthetic jets, upon activation, engage in simultaneous suction and blowing of gas, forming a starting vortex. The morphology of the

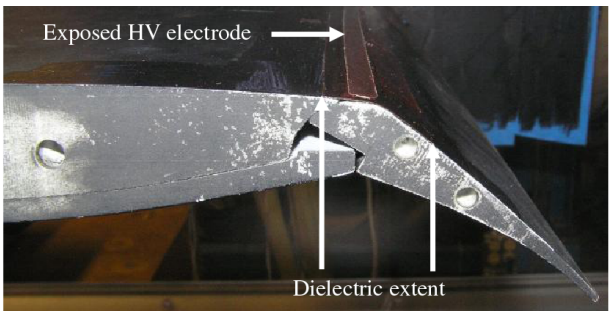

Figure 2.15: The schematic of the high-lift airfoil flap [68].

initiating vortex is contingent upon the anode geometry of the DBD plasma actuator. The anode is analogous to the orifice in conventional synthetic jet generators. As depicted in Figure 2.14, round anodes yield toroidal vortex rings, and symmetric linear anodes generate pairs of symmetric linear vortices, as depicted in Figure 2.14. According to the experiment and numerical simulation studies [60, 64], blowing and suction phenomena can only be observed simultaneously during the discontinuous operation of the actuator. When the DBD plasma actuator continuously operates, there is solely blowing phenomena without the suction. Nonetheless, regardless of whether the operation is continuous or discontinuous, the downstream velocity profiles of plasma synthetic jets demonstrate great self-similarity.

To a certain extent, the inherent ability of DBD plasma actuators to induce air directly dictates the efficacy of plasma synthetic jets. The stronger the air induction capability, the greater the magnitude of flow control achievable by plasma synthetic jets [65, 66]. Furthermore, the performance of plasma synthetic jets can be augmented by deploying arrays, thereby enhancing the jet strength and achieving an elevated level of flow control efficacy [67].

2.3.3 Wall Jet

Little and Samimy [68] employed DBD plasma-induced wall jets to control turbulent boundary-layer separation at the deflected flap of an airfoil, as shown in Figure 2.15. The tests were conducted at inflow velocities reaching up to 45 m/s, corresponding to a Reynolds number of 750,000. Despite the momentum introduced by the plasma being an order of magnitude lower than the incoming flow velocity employed in the experiment, control over vortex shedding at the flap shoulder was still achieved. The findings indicate that plasma control slightly delays flow separation and marginally thins the separation region, yet these alterations have no significant impact on lift. In Little and Samimy [68]'s experiment, the most effective method for increasing lift is modulating the actuator input waveform to improve instability in vortex shedding from the flap shoulder.

In the study by Li et al. [69], a novel structure was designed to integrate plasma actuators on a NACA0025 airfoil. The wing was segmented into an inner and outer section, with a channel between these sections housing eight co-flowing plasma actuators, as depicted in Figure 2.16.

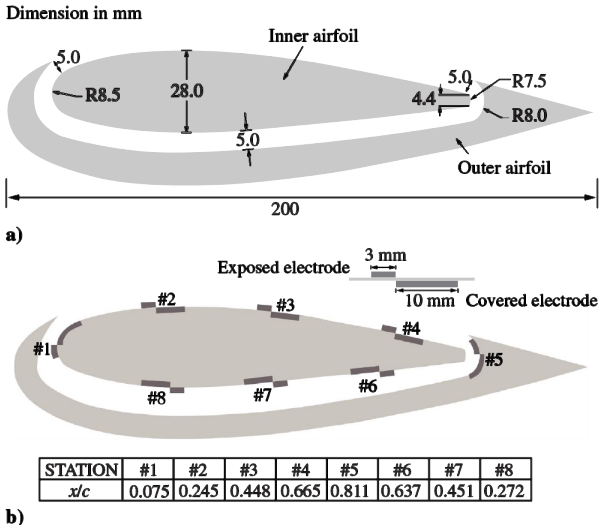

STATION	#1	#2	#3	#4	#5	#6	#7	#8
x/c	0.075	0.245	0.448	0.665	0.811	0.637	0.451	0.272

Figure 2.16: The schematic of the airfoil,(a) with geometric dimensions; (b) with the location of the plasma actuator [69].

The incoming flow velocity in the experiment was set at 5 m/s, and the Reynolds number was 68,000. Wind tunnel experiments subsequently demonstrated that the wall jet produced by the plasma effectively delays flow separation in low-speed airflow. However, regions originally in laminar flow transitioned to turbulent flow due to the introduction of the plasma-induced wall jet.

2.3.4 Vortex Generator

Jukes and Choi [54] explored the application of dielectric barrier discharge (DBD) plasma actuators as vortex generators in flow separation control. A spanwise jet with an angle was generated on the surface by putting the actuators at an angle with the incoming flow direction. This jet interacted with the incoming flow and the boundary layer, forming streamwise longitudinal vortices. The mechanism of vortex formation through this method bears similarities to that of initial vortex generation. Jukes and Choi [54]'s experimental study meticulously investigated the effects of deflection angle, actuator length, and the induced velocity by the plasma on the vortex cycle. The results indicated that the optimal deflection angle occurs when the actuator is perpendicular to the incoming flow. Both plasma-induced velocity magnitude and actuator length have a positive relationship with the strength of the vortex cycle. Ensuring it owns a suitable gap is crucial in determining the spanwise spacing of the actuator. Insufficient spacing may lead to adverse interactions between adjacent vortices, whereas excessive spacing could result in a small coverage area for effective flow control.

Jukes and Choi [54] further validated the effectiveness of DBD vortex generators for flow separation control, accommodating incoming flow velocities up to 14.9m/s, as depicted in Figure 2.17. The investigation indicated that counter-rotating vortex arrays were more efficient in

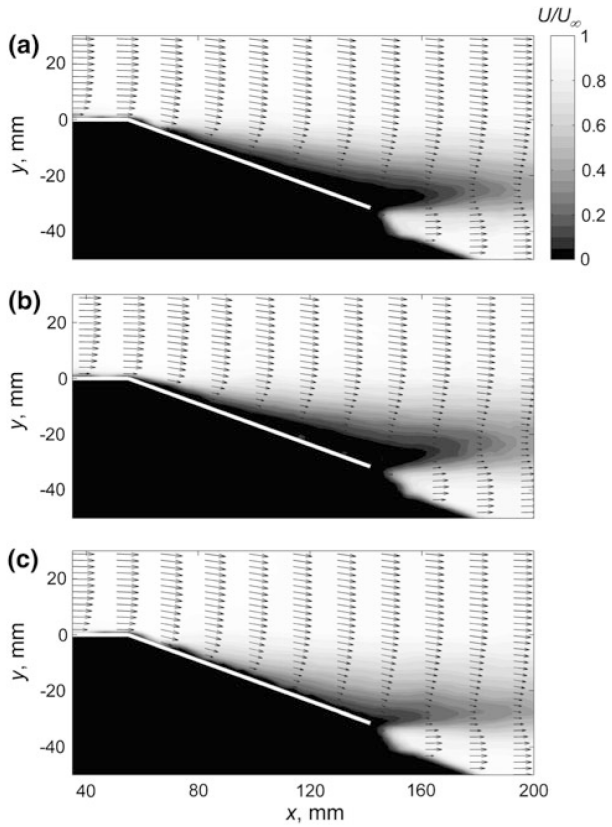

Figure 2.17: Stream-wise velocity magnitude; (a) without plasma, (b) with co-rotating DBD-VGs, (c) with counter-rotating DBD-VGs. Incoming flow velocity U_∞ =14.9m/s [54].

mitigating flow separation, while co-rotating vortex arrays yielded better flow uniformity.

Jukes et al. [70] applied both co-rotating and counter-rotating vortex generators on the NACA 4418 airfoil, a typical airfoil for horizontal axis wind turbines. The plasma vortex generators were installed on the airfoil's leading edge between 5%<x/c<34%, as illustrated in Figure 2.18. Wind tunnel tests were conducted at two free-stream velocities of 5.3m/s and 14.3m/s, corresponding to Reynolds numbers of 35k and 95k, respectively. The study found that DBD vortex generators could effectively control flow. Especially at a flow velocity of 5.3m/s and angles of attack less than 18°, the flow will not occur separation under the plasma flow control. Similarly, the research concluded that counter-rotating vortex generator arrays outperformed co-rotating arrays in effectiveness, although co-rotating arrays exhibited superior flow uniformity.

2.4 Numerical Simulation on AC-DBD Plasma

DBD plasma-induced air flow involves coupling multi-scale physical fields, such as convection, diffusion, and ionisation mechanisms. Direct modelling based on its physical principles results in the derived continuity equations with high stiffness. To reduce the stiffness of the plasma dynamics continuity equations, Jayaraman et al. [71] proposed a sequential finite volume operator splitting algorithm to conserve space charge.

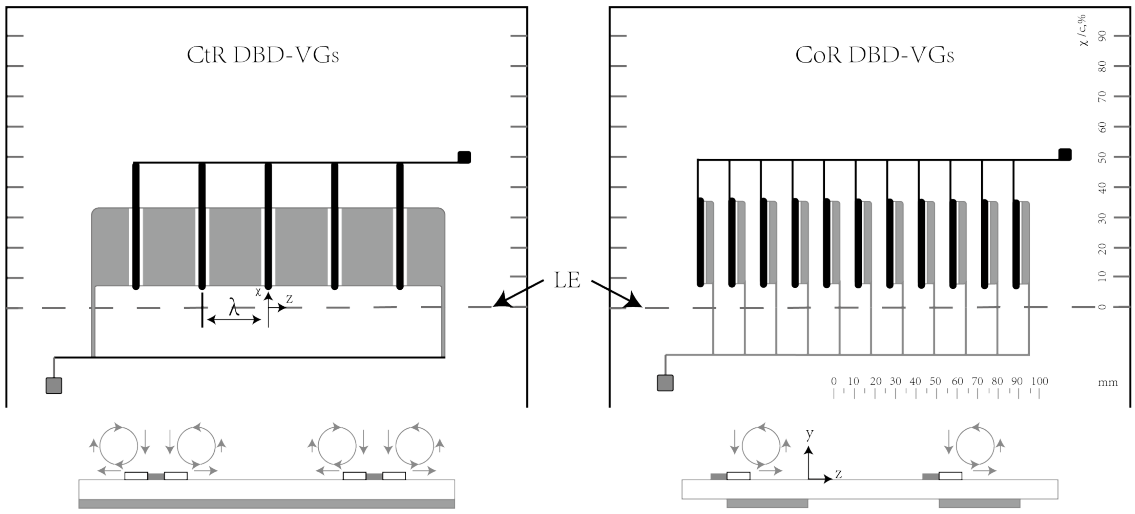

Figure 2.18: DBD plasma configuration: the symmetric configuration is on the left with the counter-rotating plasma vortex, and the asymmetric configuration is on the right with the co-rotating plasma vortex [70].

Despite its high-fidelity discharge model, modelling through first principles presents a significant challenge due to the vast difference in time scales between plasma discharge and the induced neutral flow. Achieving physically meaningful time scales necessitates costly computational resources. Therefore, the challenge in DBD plasma modelling lies in accomplishing simulations at physically meaningful time scales with feasible computational efforts.

At present, high-fidelity discharge models remain impractical for most engineering problems. To significantly reduce computational costs, researchers have proposed simplified reduced-order models [72–75], which incorporate the momentum generated by plasma discharge directly into the Navier-Stokes equations in the form of body forces. This approach adds only an additional source term to the governing equations, substantially reducing computational complexity and the required computational resources.

Singh and Roy [76]'s electromotive model (Equation 2.1) provides the spatial distribution of electromotive forces around an asymmetric DBD plasma actuator. According to simulation results, the simulated electromotive forces distribution yields a relatively accurate spatial velocity distribution. Under this model, voltage amplitude significantly influences the induced velocity, whereas the excitation frequency minimally impacts the induced velocity. Additionally, the authors note that this model only applies to the operational parameters mentioned in the article; employing different DBD plasma actuator configurations necessitates re-calibration of the parameters within the equation. It should be noted that although this model can provide a relatively accurate spatial distribution of plasma-induced electrodynamics, it significantly lacks precision in predicting the magnitude of the electrodynamics. Under this model, a thrust generated by a

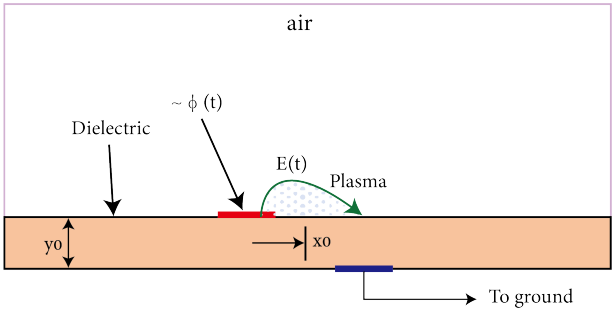

Figure 2.19: Coordinate system of the plasma modelling [76].

voltage of 10kV can induce a velocity exceeding 100m/s.

$$\begin{aligned}\mathbf{F} =& F_{x0}\phi_0^4 exp(-\{[x-x_0-(y-y_0)]/y\}^2-\beta_x(y-y_0)^2)\hat{i} \\ &+F_{y0}\phi_0^4 exp\left\{-[(x-x_0)/y]^2-\beta_y(y-y_0)^2\right\}\hat{j}\end{aligned} \tag{2.1}$$

where values of F_{x0} and F_{y0} represent the average electrodynamic force obtained by solving the air plasma equations. The relationship between the electrodynamic force and the fourth power of the electric potential is derived from plasma simulation data. As illustrated in Figure 2.19, x_0 denotes the midpoint between the anode and cathode, while y_0 represents the surface of the dielectric. β_x and β_y are constants determined based on the dielectric material and used to match the induced velocity.

Soloviev [77] derived the interrelationship between dielectric thickness, voltage amplitude, and excitation frequency with the maximum induced thrust, as presented in Equation 2.2. Due to its direct relation to multiple physical parameters, this model exhibits strong versatility in evaluating the thrust generated by plasma induction.

$$T \approx 2.4\times10^{-10}\alpha_l^4\frac{f_V}{d}\left(\frac{9V_0}{4\triangle V_c}\right)^4\left(1-\frac{7\triangle V_c}{6V_0}\right)^4\times\left(1-exp\left(-\frac{1}{4f_V\triangle\tau_q}\right)\right)Nm^{-1} \tag{2.2}$$

where α_l represents a fitting parameter, f_V is the voltage excitation frequency in kHz, d is the dielectric thickness in centimetres (cm), V_0 is the voltage amplitude in volts (V), Vc is the normal voltage drop across the cathode V, and $\triangle\tau_q$ is the residence time of negative ions in the acceleration region, measured in seconds (s).

Singh and Roy [76]'s research provides the relatively accurate spatial distribution of plasma-induced thrust, while Soloviev [77]'s work offers a relatively accurate prediction of the magnitude of the thrust. These two studies are complementary. Babou et al. [78] proposed a combined model (Equation 2.3) based on these two studies and provided some initial simulation results.

$$\vec{F}_{EHD}(V,f,d,x,y;x_0,y_0) = T_{soloviev}\times\frac{\vec{F}_{Singh}(V,x,y;x_0,y_0)}{\left\|\vec{F}_{Singh}(V,x,y;x_0,y_0)\right\|} \tag{2.3}$$

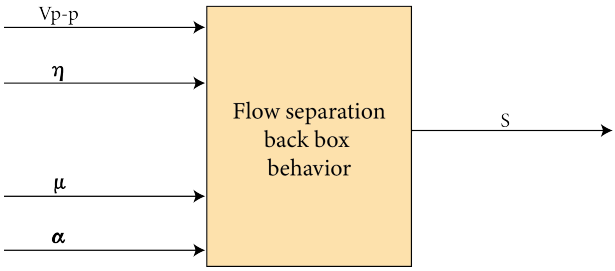

Figure 2.20: Schematic diagram of neuron algorithm applied in AC-DBD plasma actuator [79].

where x_0 and y_0 are still the midpoint between the plasma anode and cathode on the surface of the dielectric.

Moreover, with the rise of artificial intelligence in recent years, researchers have also applied neural algorithm methodologies to predict the performance of AC-DBD plasma actuators. For instance, Barzegaran and Kosari [79] conducted mathematical modelling on the flow control performance of eight asymmetric plasma actuators mounted on a NACA0012 airfoil. The model inputs included the airfoil's angle of attack, flow velocity in the flow field, excitation frequency, and voltage amplitude, and a series of pressure parameters on the airfoil served as the output variables, as shown in Figure 2.20. By continuously feeding data into the neural model, the predicted parameters were in close agreement with experimental outcomes, with discrepancies negligible enough to be considered insignificant.

2.5 Flow in the S-shaped Inlet Duct

2.5.1 Flow Mechanism

As a critical component of high-speed aircraft, the intake system is designed to decelerate the incoming airflow, thereby enhancing the performance of both the engine and the compressor. In designing the intake system, meeting deceleration requirements while maintaining the intake duct as short as possible is essential. This is because a shorter intake duct translates to a shorter fuselage, contributing to the aircraft's overall weight reduction [1, 2]. It is estimated that if the aircraft can reduce its fuselage length by one diameter of its intake duct, the net weight would decrease by 15% [3]. On aircraft, S-shaped ducts are typically located on the fuselage's dorsal side or at the wings' root [80]. Compared to traditional straight ducts, diffusive S-shaped intake ducts, due to their curvature, can reduce the velocity of the incoming flow more rapidly. This results in shorter intake ducts and significantly reduced weight. Presently, diffusive S-shaped intake ducts have been widely adopted in high-speed aircraft propulsion systems.

Research on the flow within S-shaped ducts has been underway since the last century. Figure 2.21 shows a typical S-shaped duct geometry with a diffusing cross-section. D1 gradually increases to D2. The principal geometric parameters of S-shaped ducts include centre line,

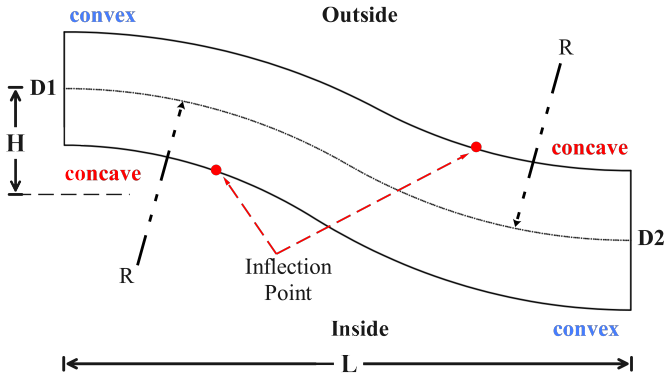

Figure 2.21: A typical S-duct geometry [81].

diffusion ratio, radius ratio, length-to-diameter ratio (LDR), and length-to-offset ratio (LOR) [81, 82]. The centre line of an S-shaped duct is usually composed of two planar circular arcs. The diffusion ratio refers to the ratio of the outlet diameter to the inlet diameter (D2/D1). The radius ratio represents the growth ratio of the cross-sectional circular radius along the centre line, which can be a fixed value or defined by a function. The length-to-diameter ratio (LDR)and the length-to-offset ratio (LOR) are defined as the ratio of the duct length to the inlet diameter (L/D1) and the ratio of the offset distance to the height (L/H), respectively.

After air enters the S-shaped duct, the curvature of the centre line induces a centrifugal pressure gradient relative to the duct walls. The concave surface generates an adverse pressure gradient that decelerates the flow, whereas the convex surface produces a favourable pressure gradient that accelerates the flow. As the airflow advances, the adverse pressure gradient gradually consumes momentum within the boundary layer. When a critical threshold is exceeded, flow separation occurs. As illustrated in Figure 2.21, the separation points in the S-shaped duct are typically located near the two bend inflexion regions. The uneven pressure distribution caused by the centre-line curvature, aided by the duct's diffusion rate, also promotes the formation of secondary flows, thereby further increasing the complexity of the flow within the S-shaped duct. Moreover, there are also strong interactions between different regions inside the S-duct. However, despite the complexity of the flow within S-shaped ducts, the flow patterns still possess some similar regularity. Zachos et al. [83] demonstrated that, within a Mach number range of 0.27 to 0.5, the Mach number only minimally impacts some dimensionless flow parameters.

Moreover, there is a significant discrepancy between the time-averaged flow field and the transient flow field within the S-shaped duct. In the study of time-averaged fields, Taylor et al.[84, 85] conducted experiments at low Reynolds numbers of 790 and 48,000, while Vakili et al. [86] and WELLBORN et al. [81] explored higher Reynolds numbers, specifically 3.25×10^6 and 2.5×10^6. Integrating these studies reveals that the time-averaged aerodynamic data within S-shaped ducts exhibit a symmetrical distribution under a large range of Reynolds numbers. This conclusion can be found in most literature, and based on this finding, researchers

can simulate only half of an S-shaped intake in steady-state modelling, using mirroring to reduce computational load. Notably, this conclusion only represents a tendency and doesn't mean the flow inside the S-duct is perfectly symmetrical. In earlier studies, Bansod and Bradshaw [80] noted that vortices generated by secondary flows could disrupt the axial symmetry at the outlet interface, causing deviations. The flow pattern in the time-averaged field is predominantly characterised by a pair of counter-rotating vortices, which generally form after the second bend [87]. The higher velocity of the flow in the centre of the duct also contributes to vortex formation [88]. The high velocity in the centre of the duct, apart from being attributable to the inherent geometry of the S-shaped duct, the increased central flow velocity is also accelerated by blockages caused by flow separation [81, 89].

Unlike the time-averaged fields, experimental and simulation studies have demonstrated that the transient flow fields exhibit strong asymmetry. Experimentally, Gil-Prieto et al. [90] utilised SPIV to measure a round S-shaped duct at Mach 0.27 and 0.5, discovering significant differences in secondary flow vortices at different moments within the duct. In their subsequent studies, the flow patterns of the transient field were clearly defined, the vertical mode and the switching mode, as illustrated in Figure 2.22. Unsteady numerical simulations also validated these findings. In terms of simulation, MacManus et al. [91] employed the Delayed Detached Eddy Simulation (DDES) method to model the experiments conducted by WELLBORN et al. [81], and Wojewodka et al. [92] further explored the differences between DDES and Unsteady Reynolds-Averaged Navier-Stokes (URANS) simulations. They conducted a Proper Orthogonal Decomposition (POD) of the numerical simulation results to identify the dominant modes of the transient flow field, with simulation outcomes consistent with experimental observations.

2.5.2 Performance Parameters

The performance of S-shaped intakes can be assessed by comparing flow parameters at the Aerodynamic Interface Plane (AIP) with those in the free stream. The AIP refers to a specific plane within an aerodynamic system or device designated for evaluating and analysing the dynamic characteristics of airflow. It is typically positioned at a critical location along the flow path. For S-shaped ducts, the AIP is commonly defined at the duct outlet. There are two crucial parameters: the pressure recovery and distortion coefficients.

The pressure recovery coefficient represents the AIP's pressure ratio to the surrounding environment's freestream pressure. It is commonly used to evaluate pressure losses within the system. Based on the type of pressure considered, the pressure recovery coefficient (PR) can be further classified into total pressure recovery and static pressure recovery coefficients (PR_t and PR_s) [93]. The expression is as follows:

$$PR_s = \frac{P_{s,AIP}}{P_{t,o}} \quad PR_t = \frac{P_{t,AIP}}{P_{t,o}} \tag{2.4}$$

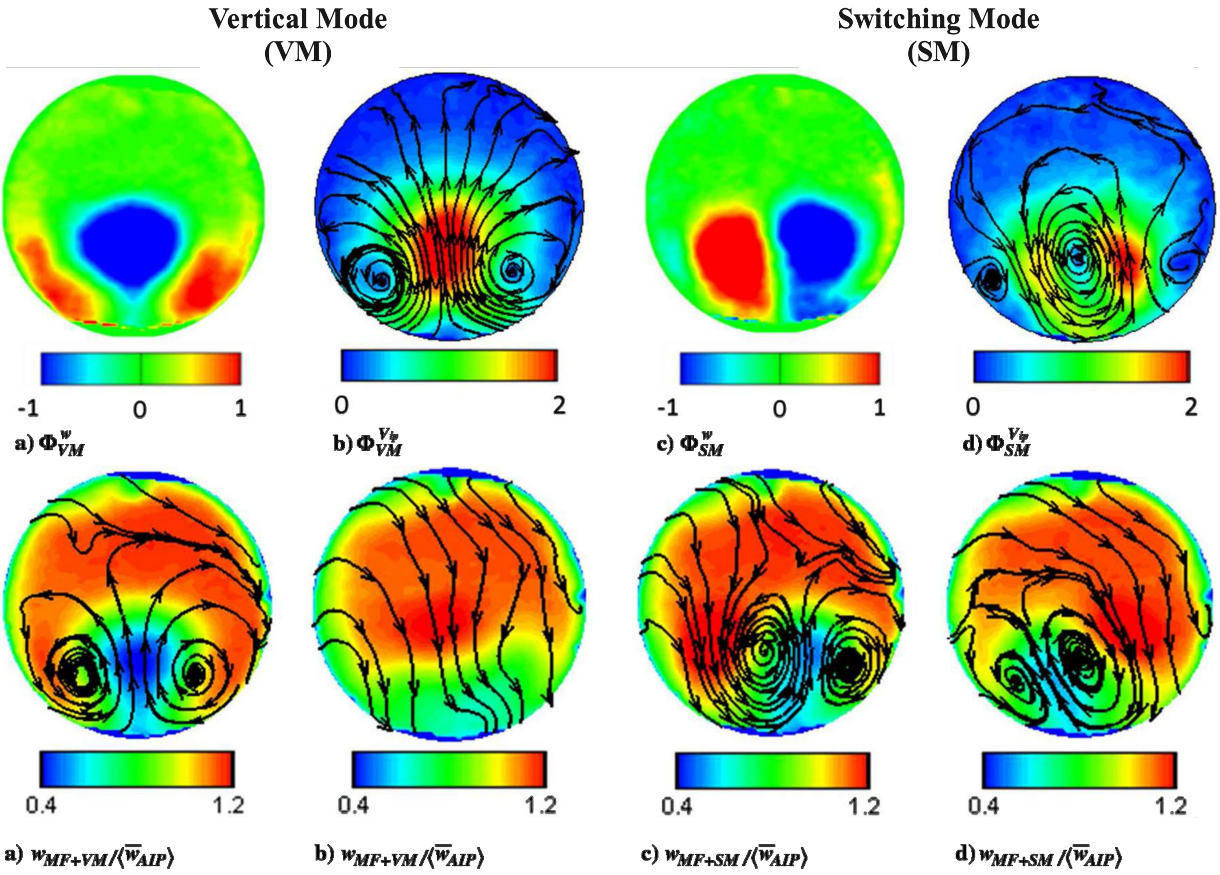

Figure 2.22: The dominant mode of the flow on AIP. The top four pictures, (a) and (b), are the stream-wise velocity and vertical velocity modes, respectively, under VM mode, and (c) and (d) are under SM mode. The bottom four pictures, (a) and (b), are the superposition of the stream-wise mean velocity and the dominant mode with the maximum time coefficient and the minimum time coefficient under VM mode, and (c) & (d) are under SM mode [90].

where PR_s and PR_t represent the static and total pressure recovery coefficients, respectively. $P_{s,AIP}$ and $P_{t,AIP}$ are the mean values of the static and total pressure on AIP. $P_{t,o}$ denotes the total pressure of the free stream.

The distortion coefficient is a metric used to quantify the uniformity of the flow field downstream of an S-shaped duct. Due to the complex geometric configuration of S-shaped ducts, phenomena such as turbulence separation, secondary flows, and pressure losses are often induced, leading to significant non-uniformities in the flow field at the outlet. The distortion coefficient is a crucial parameter for evaluating and characterising these effects. Although the definition of the distortion coefficient varies slightly across different studies, it is generally centred around aspects of pressure and velocity. Equation 2.5 presents the specific definition of the pressure distortion coefficient Standard [94]. It is defined by dividing AIP into several sectors based on the central angle θ. Then, in each sector, the difference between average and minimum total pressure is divided by average dynamic pressure. More definitions can be found in references [82, 93, 95].

$$DC_\theta = \frac{P_{t,AIP} - P_{t,\theta,min}}{q} \tag{2.5}$$

where θ is the central angle corresponding to each sector, typically chosen as 60 degrees. $P_{t,\theta,min}$ is the minimum total pressure within each sector. q denotes the average dynamic pressure on AIP.

The cross-flow velocity can further define the swirl coefficient (SC), namely the velocity distortion coefficient. As shown in Equation 2.6, which computes the ratio of the maximum swirl velocity in each sector on AIP to a reference velocity (commonly selected at the centre of the S-shaped intake inlet, the throat of the S-duct) [96].

$$SC_\theta = \frac{U_{crossflow,\theta,max}}{U_{centreline,throat}} \tag{2.6}$$

Regarding the quantitative analysis of the swirl, Zachos et al. [83] further investigated the swirl intensity (SI), swirl direction (SD), and swirl parameter (SP). These parameters are analysed based on the 'ring and target' method. On AIP, i rings are selected, with n rakes placed on each ring, as illustrated in Figure 2.23 showing an 8x5 ring arrangement. The swirl angle is the angle between the axial and resultant velocities, with a schematic shown in Figure 2.24. Figure 2.25 displays the distribution of the swirl angles at different circumferential positions within a complete ring. Here, the sector swirl (SS) is introduced to quantify the azimuthally averaged extent of positive and negative vortices on a given ring, expressed in degrees, with the Equation as below:

$$\begin{aligned} SS^+_{i,k} &= \frac{1}{\theta^+_{i,k}} \int_{\theta^+_{i,k}} \alpha(\theta)_{i,k} d\theta \\ SS^-_{i,k} &= \frac{1}{\theta^-_{i,k}} \int_{\theta^-_{i,k}} \alpha(\theta)_{i,k} d\theta \end{aligned} \tag{2.7}$$

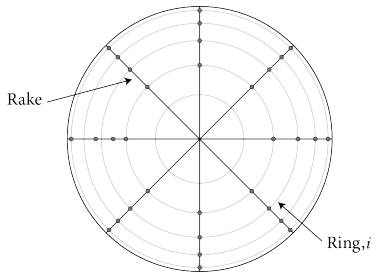

Figure 2.23: 8×5 rings and rakes distribution on AIP [93].

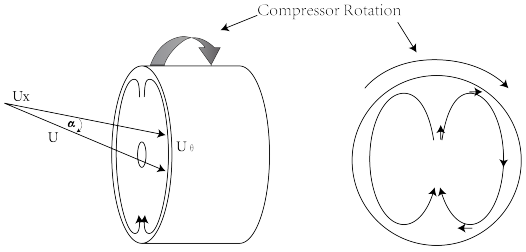

Figure 2.24: The schematic of the swirl angle definition [97].

where the subscript i represents ring i within a specified range, and subscript k is used to identify different pairs of vortices. The superscripts + and - denote the direction of each vortex along the given ring. Typically, the direction of the compressor fan behind the AIP is used as the reference direction, where + indicates rotation in the same direction, and - indicates rotation in the opposite direction.

The absolute values of the vortex angles on the ring are summed and then averaged to characterise the swirl intensity (SI). SI can be approximately calculated by using SS, as indicated below:

$$SI(i) = \frac{\sum_{k=1}^{m} SS_{i,k}^{+} \cdot \theta_{i,k}^{+} + \sum_{k=1}^{m} \left| SS_{i,k}^{-} \right| \cdot \theta_{i,k}^{-}}{360} \tag{2.8}$$

The swirl directivity (SD), which is the overall rotational direction of a selected ring, is

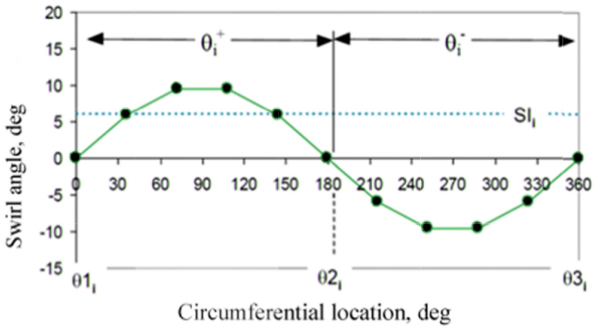

Figure 2.25: The swirl angles at different circumferential locations [98].

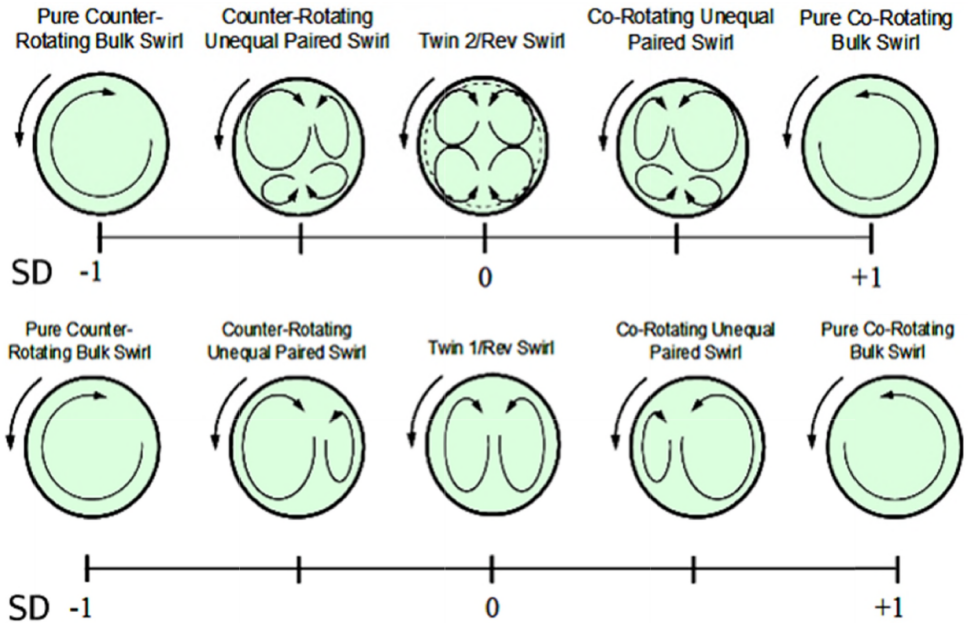

Figure 2.26: Swirl directivity for one-per-revolution and multiple-per-revolution swirl distortion [83, 98].

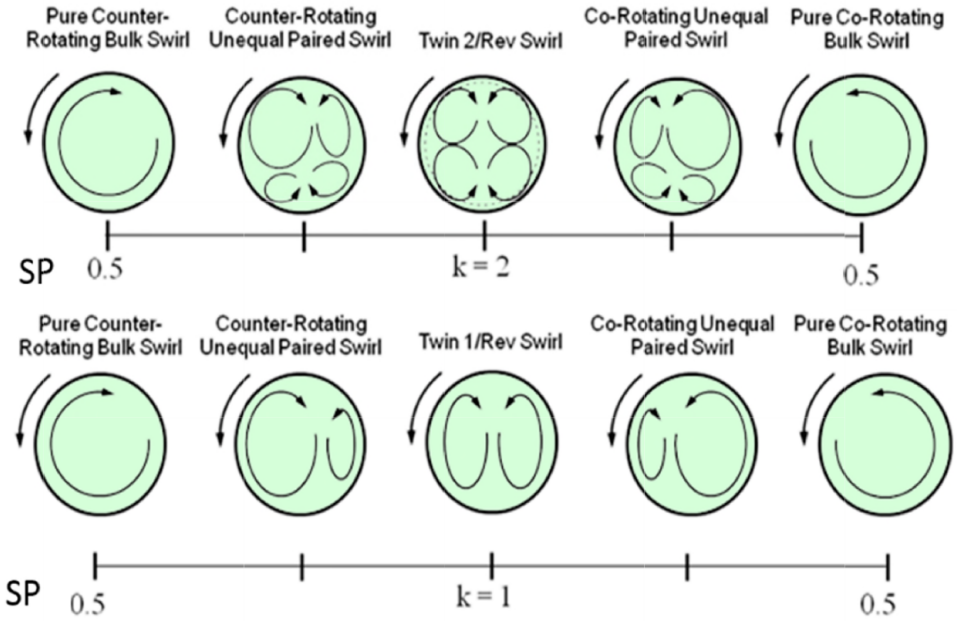

Figure 2.27: Swirl pairs spectrum for one-per-revolution and multiple-per-revolution swirl distortion [83, 98].

defined and illustrated in Equation 2.9 and Figure 2.26, respectively.

$$SD(i) = \frac{\sum_{k=1}^{m} SS_{i,k}^{+} \cdot \theta_{i,k}^{+} + \sum_{k=1}^{m} SS_{i,k}^{-} \cdot \theta_{i,k}^{-}}{\sum_{k=1}^{m} SS_{i,k}^{+} \cdot \theta_{i,k}^{+} + \sum_{k=1}^{m} \left| SS_{i,k}^{-} \right| \cdot \theta_{i,k}^{-}} \tag{2.9}$$

The swirl pair parameter (SP) represents the number of positive and negative vortex pairs along a ring, which considers the vortices' magnitude, as shown in Figure 2.27. The expression is as follows:

$$SP(i) = \frac{\sum_{k=1}^{m} SS_{i,k}^{+} \cdot \theta_{i,k}^{+} + \sum_{k=1}^{m} \left| SS_{i,k}^{-} \right| \cdot \theta_{i,k}^{-}}{2 \cdot Max \left\{ SS_{i,k}^{+} \cdot \theta_{i,k}^{+}, \left| SS_{i,k}^{-} \cdot \theta_{i,k}^{-} \right| \right\}_{k=1,\ldots,m}} \tag{2.10}$$

These parameters allow for a quantitative analysis of an S-shaped intake's performance and flow patterns. Ideally, an aggressive design approach is to achieve as high a PR and as low a DC as possible on AIP while minimising the S-shaped intake's LDR and LOR.

2.6 Chapter Summary

This chapter comprehensively reviews the literature on S-shaped ducts and DBD plasma flow control. While the fundamental physical mechanisms of DBD plasma have yet to be fully elucidated, understanding its physical characteristics has reached a considerable level of maturity. Existing studies have demonstrated the effectiveness of DBD plasma actuators in achieving significant flow control. However, current research and applications of DBD plasma actuators remain predominantly focused on relatively simple geometries. Investigations into their application in S-shaped intakes, particularly those utilising AC-DBD plasma actuators, are still scarce. This study aims to fill this gap to expand the applicability of DBD plasma flow control techniques, providing practical references for future possible applications.

Chapter 3

Methodology

3.1 Experimental Study

3.1.1 Pressure Measurement

3.1.1.1 Wall Pressure Tapping and Pressure Reading

Wall static pressure measurement is one of the most prevalent types of measurement in the duct, fundamentally grounded on the principle of Pascal's Law from fluid mechanics. Pascal's Law posits that the pressure exerted on all walls is uniform within a sealed container. This principle can be construed to mean that when a fluid is at rest, the pressure measured in any direction is representative of its static pressure. Consequently, when conducting measurements in the duct, the pressure hole is perpendicular to the flow velocity. Under these circumstances, the axial velocity approximates stasis, and the pressure measured at this port represents the local static pressure.

According to Bernoulli's principle, it can be known that:

$$\frac{1}{2}\rho v^2 + \rho gh + p = constant \tag{3.1}$$

where ρ, v, g, and h denote density, velocity, gravity, and height respectively. $\frac{1}{2}\rho v^2$ represents the dynamic pressure, ρgh corresponds to the gravitational potential energy, and p signifies the static pressure.

When at the same height and without considering variations in density, by moving the term ρgh to the right side of the equation, $constant - \rho gh$ remains constant. At this point, let total pressure P_t represent $constant - \rho gh$, let $P_d = \frac{1}{2}\rho v^2$ denote the dynamic pressure, and let P signifies the static pressure. Thus, the equation can be expressed as follows:

$$\begin{aligned} \frac{1}{2}\rho v^2 + p &= constant - \rho gh \\ P_d + P &= P_t \end{aligned} \tag{3.2}$$

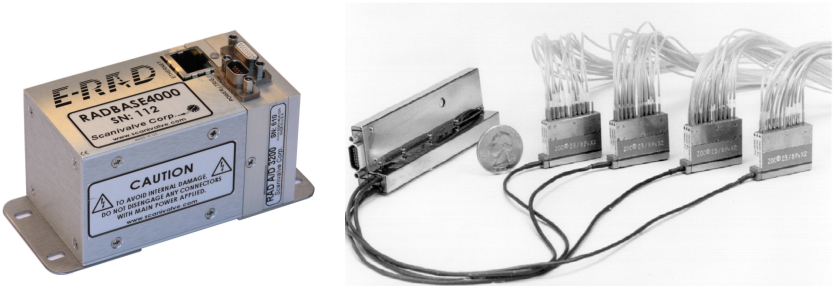

(a) ERAD4000 A/D base (b) ZOC23b pressure scanner

Figure 3.1: The main components of the scanning system [99, 100].

Considering the local atmospheric pressure as the total pressure, it is possible to estimate the local dynamic pressure and velocity after determining the static pressure.

This study employed the pressure scanner manufactured by Scanivalve Corporation. This system comprises an ERAD4000 A/D base and a module connector (the ZOC23b pressure scanner; 32 channels, ± 1 psi range), as shown in Figure 3.1. The connection configuration is as follows: pressure ports on the S-duct are connected to the ZOC23b scanner via flexible hoses; the scanner is linked to the ERAD via a dedicated cable; and the ERAD is connected to the host computer through an Ethernet cable connection.

The data acquisition rate of the ZOC pressure scanner system is determined by three parameters: the period (the duration of a single data collection instance), frames per second (FPS), and sample averaging (AVG). The formula is as follows:

$$DataRate\left[\frac{Hz}{Ch}\right] = \frac{1}{Period\,[s] * FPS * AVG} \tag{3.3}$$

For instance, when the period is set at 0.0001 seconds, the FPS at 10, and the AVG at 10, the data rate at this juncture gives 100 Hz per channel.

3.1.1.2 Seven Hole Probe Measurement

Direct flow measurement, as one of the oldest flow measurement methods, involves inserting probes into the flow field. The five-hole pressure probe and the three-axis hot-wire probe are two commonly used types. However, when the local flow angle exceeds 40°, the results obtained from these probes become less accurate. To address this issue, NASA-Ames and the United States Air Force Academy collaborated to develop the seven-hole cone probe [101, 102]. Through testing, it has been demonstrated that this probe can rapidly provide quantitative flow data at high angles of attack. Under high subsonic conditions, it can handle a maximum angle of attack of 65°, while under low subsonic conditions, the maximum angle of attack can reach 75°.

To minimise flow disturbances, these probes must be tiny, with a diameter of approximately

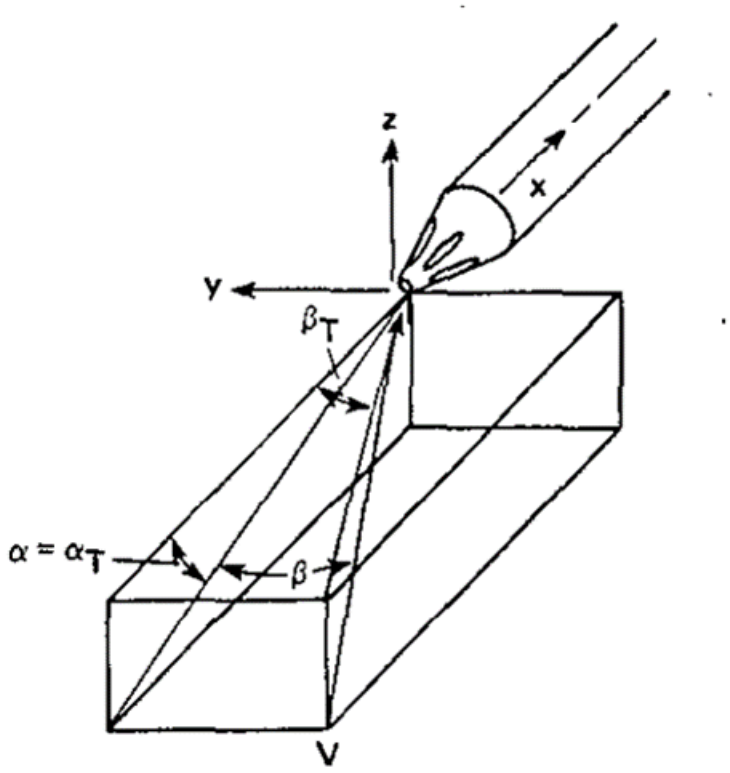

Figure 3.2: Low angles of attack reference system [102].

0.25 cm. Small-sized probes inevitably exhibit dimensional errors during manufacturing, necessitating calibration prior to their use. Polynomial expressions established in calibration theory can represent local angles of attack, side-slip angles, total pressure, and static pressure. When measuring an unknown flow, the parameters can be directly calculated from the corresponding polynomial expressions.

Calibration theory for low angles of attack will be briefly reviewed in the following context, including the seven-hole probe's working principles. For a detailed description of the calibration process, please take a look at the literature[102].

At low angles of attack (typically less than 25°), it is assumed that the flow passing through the seven pressure ports adheres closely to the probe's surface. The reference frame employed here utilises a tangential reference frame, as illustrated in Figure 3.2. α_T represents the angle between the probe's X-axis and the projection of the velocity vector onto the X-Z plane. β_T is the angle between the probe's X-axis and the projection of the velocity vector onto the X-Y plane.

Figure 3.3 illustrates the seven-hole probe employed in this study, with its port numbering convention detailed in Figure 3.4. The central point (pressure port numbered 7) serves as the point of symmetry, while the remaining six pressure ports are symmetrically arranged in pairs. Additionally, these ports define three principal axes. The angular pressure coefficient for each axis is defined as the ratio of the pressure difference between the two ends of the axis to the

(a) Top (b) Side (c) Tail

Figure 3.3: The seven-hole probe employed in this study.

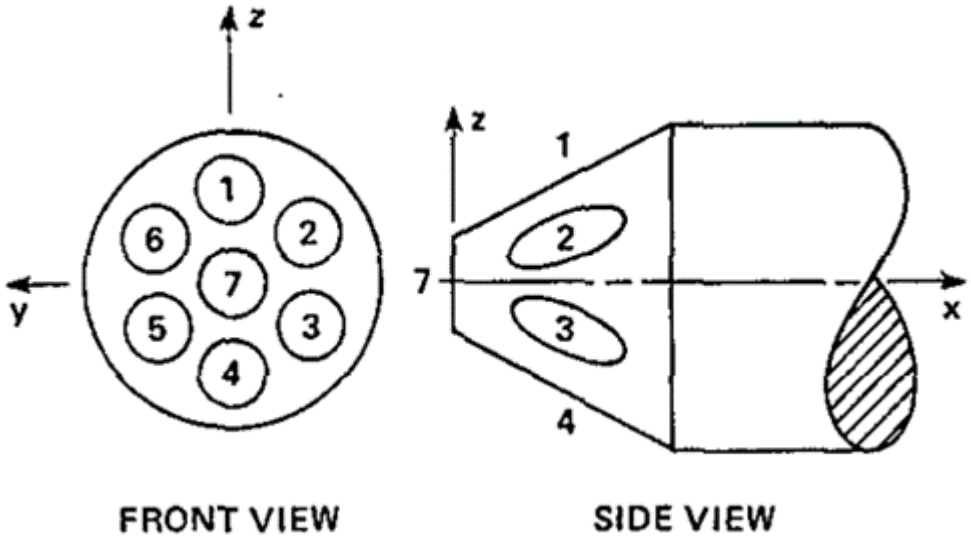

Figure 3.4: The pressure port numbering of the seven-hole probe [102].

dynamic pressure, as expressed by the following equation:

$$C_{\alpha_a} = \frac{P_4 - P_1}{P_7 - \bar{P_{1-6}}}, C_{\alpha_b} = \frac{P_3 - P_6}{P_7 - \bar{P_{1-6}}}, C_{\alpha_c} = \frac{P_2 - P_5}{P_7 - \bar{P_{1-6}}} \tag{3.4}$$

In Equation 3.4, the numerator represents the pressure difference between the respective ports, characterising changes in the angle of attack. The denominator is the dynamic pressure used to non-dimensionalize the equations. P_7 is approximated as the total pressure, while the average pressure of ports 1 to 6 ($\bar{P_{1-6}}$) is approximated as the static pressure. These three coefficients correspond to the reference system in Figure 3.5(a).

When choosing the reference frame as depicted in Figure 3.5 (a), it becomes apparent that only any two of the coefficients are required to determine the direction of the velocity vector. This eliminates the need for the third coefficient, which contains pressure information. To avoid this loss of information, the tangential reference frame shown in Figure 3.5 (b) can be employed. The conversion of the three pressure coefficients in Equation 3.4 into the equivalent coefficients C_{α_T} and C_{β_T} is detailed in the literature[103]. C_{α_T} and C_{β_T} utilise all three coefficients, thereby

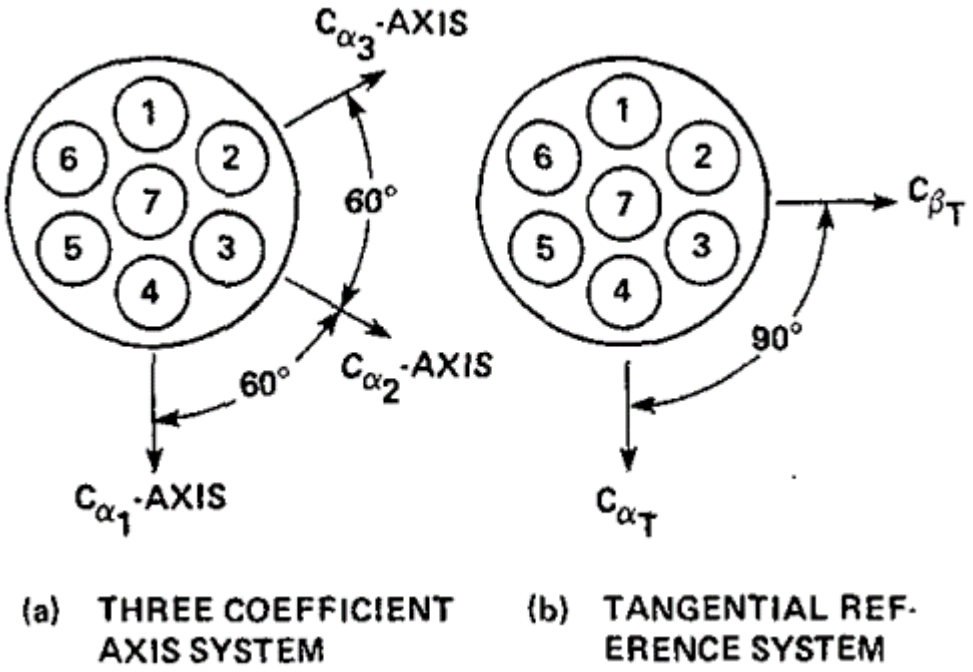

Figure 3.5: Angular coefficient reference systems [102].

preventing the loss of pressure-related information.

$$C_{\alpha_T} = \frac{1}{3}\left(2C_{\alpha_a} + C_{\alpha_b} - C_{\alpha_c}\right), C_{\beta_T} = \frac{1}{\sqrt{3}}\left(C_{\alpha_b} + C_{\alpha_c}\right) \tag{3.5}$$

The compressibility coefficient is given by:

$$C_{M_7} = \frac{P_7 - \bar{P_{1-6}}}{P_7} \tag{3.6}$$

α_T and β_T are used to characterise the deflection angles of the velocity vector, and their values can be directly calculated through polynomials. However, total pressure and static pressure are not provided directly; instead, they are represented by two dimensionless coefficients, C_O and C_q. These two coefficients serve as corrections for total pressure and static pressure.

$$C_O = \frac{P_7 - P_{OL}}{P_7 - \bar{P_{1-6}}} \tag{3.7}$$

$$C_q = \frac{P_7 - \bar{P_{1-6}}}{P_{OL} - P_{\infty_L}} \tag{3.8}$$

where $P_{OL}$is local total pressure and P_{∞_L} is local static pressure.

In the calibration process, α_T, β_T, C_O and C_q are calculated using polynomial expansions,

as follows:

$$
\begin{aligned}
A_i = {} & K_1^A && \text{(0th)} \\
& + K_2^A C_{\alpha_{T_i}} + K_3^A C_{\beta_{T_i}} + K_4^A C_{M_i} && \text{(1st)} \\
& + K_5^A C_{\alpha_{T_i}}^2 + K_6^A C_{\beta_{T_i}}^2 + K_7^A C_{M_i}^2 + K_8^A C_{\alpha_{T_i}} C_{\beta_{T_i}} \\
& + K_9^A C_{\alpha_{T_i}} C_{M_i} + K_{10}^A C_{\beta_{T_i}} C_{M_i} && \text{(2nd)} \\
& + K_{11}^A C_{\alpha_{T_i}}^3 + K_{12}^A C_{\beta_{T_i}}^3 + K_{13}^A C_{M_i}^3 + K_{14}^A C_{\alpha_{T_i}}^2 C_{\beta_{T_i}} \\
& + K_{15}^A C_{\alpha_{T_i}}^2 C_{M_i} + K_{16}^A C_{\alpha_{T_i}} C_{\beta_{T_i}}^2 + K_{17}^A C_{\beta_{T_i}}^2 C_{M_i} \\
& + K_{18}^A C_{\alpha_{T_i}} C_{M_i}^2 + K_{19}^A C_{\beta_{T_i}} C_{M_i}^2 + K_{20}^A C_{\alpha_{T_i}} C_{\beta_{T_i}} C_{M_i} && \text{(3rd)}
\end{aligned}
\tag{3.9}
$$

where A represents a flow property among α_T, β_T, C_O and C_q and K stands for the calibration constants. α_T and β_T are respectively the angle of attack and the sideslip. C_O is the total pressure coefficient, and C_q is the approximate dynamic pressure coefficient. K is the calibration curve constant. The polynomial expansion (Equation 3.9) above is truncated at the third order, requiring a minimum of 20 samples to define the numerical values of 20 K constants. However, C_M approaches zero in low-speed flows, eliminating terms containing C_M from the equation. In this case, the equation on the right-hand side can be simplified to 10 terms. Through data from m points, the system of equations can be obtained in matrix form:

$$
\begin{bmatrix} A_1 \\ A_2 \\ A_3 \\ \vdots \\ A_m \end{bmatrix} = \begin{bmatrix} 1 & C_{\alpha_{T_1}} & C_{\beta_{T_1}} & \cdots \\ 1 & C_{\alpha_{T_2}} & C_{\beta_{T_2}} & \cdots \\ 1 & C_{\alpha_{T_3}} & C_{\beta_{T_3}} & \cdots \\ \vdots & \vdots & \vdots & \vdots \\ 1 & C_{\alpha_{T_m}} & C_{\beta_{T_m}} & \cdots \end{bmatrix} \cdot \begin{bmatrix} K_1 \\ K_2 \\ K_3 \\ \vdots \\ K_{10} \end{bmatrix} \tag{3.10}
$$

Equation 3.10 can be abbreviated as follows:

$$
[A] = [C]\,[K] \tag{3.11}
$$

Transforming Equation 3.11 into the form of Equation 3.12 to calculate the constants Ks.

$$
[K] = \left[C^T C\right]^{-1} [C]^T\,[A] \tag{3.12}
$$

Substituting the constants Ks into the expansion yields:

$$
\begin{aligned}
\alpha_T &= K_1^{\alpha_T} + K_2^{\alpha_T} C_{\alpha_T} + K_3^{\alpha_T} C_{\beta_T} + \cdots \\
\beta_T &= K_1^{\beta_T} + K_2^{\beta_T} C_{\alpha_T} + K_3^{\beta T} C_{\beta_T} + \cdots \\
C_O &= K_1^{C_O} + K_2^{C_O} C_{\alpha_T} + K_3^{C_O} C_{\beta_T} + \cdots \\
C_q &= K_1^{C_q} + K_2^{C_q} C_{\alpha_T} + K_3^{C_q} C_{\beta_T} + \cdots
\end{aligned}
\tag{3.13}
$$

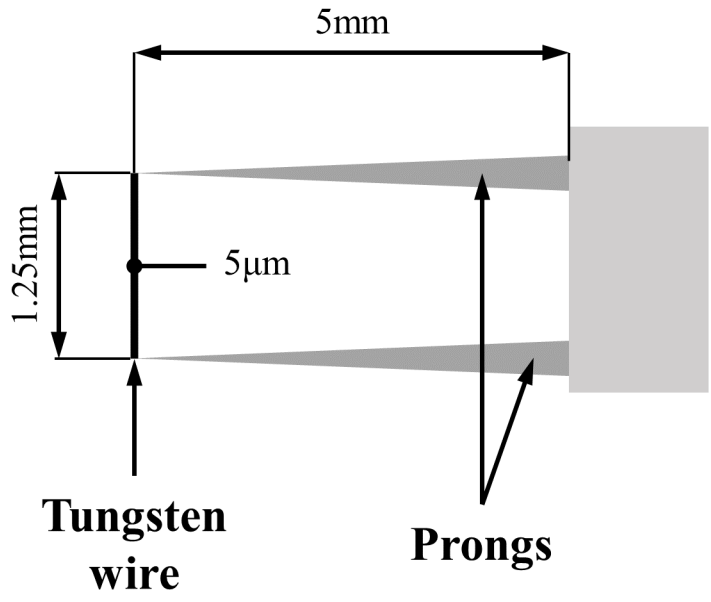

Figure 3.6: The schematic diagram of the Dantec 55P11 miniature wire probe.

Combining the reference system schematic shown in Figure 3.2 with α_T, β_T, C_O and C_q allows for the computation of the three-dimensional velocity components (*uvw*) as well as the local total pressure and static pressure.

The seven-hole probe employed in this thesis underwent calibration within the deHavilland wind tunnel at the University of Glasgow. The associated calibration coefficients and the conversion between pressure and three-dimensional velocity components are explicated in the MATLAB code provided in Appendix A.2.

3.1.2 Constant Temperature Anemometer Measurements

The Constant Temperature Anemometer utilised in the experiments employs the StreamLine Pro system from Dantec Dynamics. This system can acquire real-time velocity signals ranging from 1 to 250 kHz. The probe model used in the experiments is the 55P11, which features a metallic tungsten wire at its tip (as shown in Figure 3.6). During measurements, the metal wire is heated by an electric current. Owing to the convective effect, the velocity determines the strength of the cooling effect, which in turn dictates the changes in the output voltage. Consequently, the voltage signal can infer the flow information at the measurement point.

3.1.2.1 The Principle and Mechanism

The traditional hot-wire anemometer measures flow velocity based on heat conduction and convection principles. As the fluid flows past the hot wire, some heat is dissipated. The rate of heat loss is directly proportional to the flow velocity. However, due to the thermal inertia effects of the wire, the response time and measurement accuracy of the hot wire will be affected. The de-

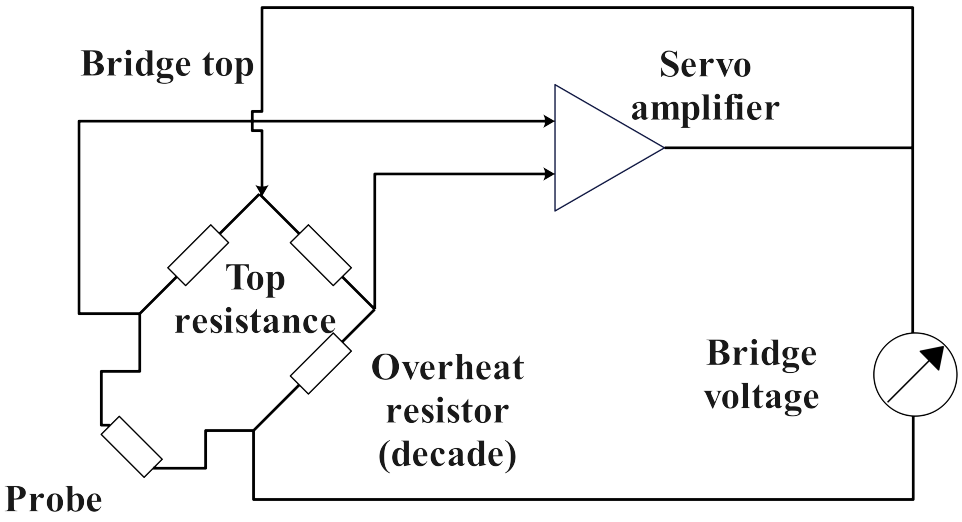

Figure 3.7: The schematic diagram of the CTA principal circuit [104].

sign philosophy of the Constant Temperature Anemometer (CTA) aims to eliminate the thermal inertia effects of the wire during flow measurement, thereby ensuring that the electronic circuitry predominantly determines the output signal. This will significantly improve the hot-wire anemometer's response time and measurement accuracy. The method to achieve this involves supplying the metal wire with electrical energy at the same rate as it transfers heat to the surrounding medium. This approach maintains a constant temperature of the metal wire regardless of the changes in flow velocity, significantly reducing the effects of the thermal inertia (thermal capacity) of the metal wire [104].

Figure 3.7 illustrates the CTA anemometer circuit's operational principle. The circuitry of the CTA primarily consists of a Wheatstone bridge and a feedback loop. The probe is situated in one arm of the Wheatstone bridge, corresponding to a variable resistor. This variable resistor determines the probe's resistance (R_w), thereby setting the operating temperature of the metal wire. Under balanced bridge conditions, there is no voltage difference across its diagonals. However, when the balance is disrupted, such as by an increase in flow velocity, the resistance of the hot wire tends to decrease. This change is detected as a voltage difference at the input of the current regulating amplifier. Triggering this condition, the current applied to the probe is subsequently increased. This elevates the wire's heat generation and resistance, countering the trend of resistance reduction due to the increased flow speed until balance is restored. Owing to the high gain characteristic of the current regulating amplifier and the fact that the voltage balance on the Wheatstone bridge remains essentially unaffected by flow speed, the time constant of the wire can be reduced to a few microseconds.

The relationship between the fluid velocity and the thermal loss of the metal wire is predicated on the assumption that the fluid is incompressible and the flow around the metal wire is

non-compressible [105]. The energy balance equation can be expressed as Equation 3.14.

$$W = Q + \frac{dQ_i}{dt} \tag{3.14}$$

where W is the power generated by joule heating. Q is the heat transferred to surroundings, and $Q_i = C_w T_w$ is the thermal energy stored in the wire. C_w is the heat capacity of the wire and T_w is the wire temperature.

Neglecting the thermal energy stored in the wire and assuming it to be zero, Equation 3.14 can be transformed into Equation 3.15, representing the metal wire's steady-state heat transfer process.

$$W = Q = I^2 R_w = hA\left(T_w - T_0\right) \tag{3.15}$$

where h is the heat transfer coefficient. A is the heat transfer area. T_0 is the ambient environment temperature.

By normalising the convective heat transfer coefficient h with the wire diameter d and the thermal conductivity coefficient k_f, the Nusselt number $Nu = hd/k_f$ is obtained. Subsequently, express h with the Nusselt number Nu and get Equation 3.16.

$$I^2 R_w = \frac{A}{d} Nu k_f \left(T_w - T_0\right) \tag{3.16}$$

The Nusselt number is a function of the Reynolds number for the wire and the fluid velocity [106], which can be represented as follows:

$$Nu = A_1 + B_1 \cdot Re^n = A_2 + B_2 \cdot U^n \tag{3.17}$$

where A1, B1, A2 and B2, respectively, represent specific constants. n denotes a certain exponent. Equation 3.17 can be transformed as:

$$I^2 R_w = \left(R_w - R_0\right)\left(A + BU^n\right) \tag{3.18}$$

No longer neglecting the thermal energy stored in the metal wire, the equation above is modified to include a thermal storage term.

$$I^2 R_w = \left(R_w - R_0\right)\left(A + BU^n\right) + C_w \frac{dT_w}{dt} \tag{3.19}$$

In Equation 3.19, A and B represent specific constants. R_0 is the resistance of the ambient environment temperature. Representing T_w using the resistance R_w and the resistance temperature

coefficient α_0, the equation above becomes:

$$I^2 R_w = (R_w - R_0)(A + BU^n) + \frac{C_w}{\alpha_0 R_0}\frac{dR_w}{dt} \tag{3.20}$$

This differential equation has a time constant τ. A_1 and B_1 also denote specific constants, but to distinguish from Equation 3.20, here they are represented as A_1 and B_1.

$$\tau = \frac{C_w}{\alpha_0 R_0 (A_1 + B_1 U^n - I^2)} \tag{3.21}$$

The limit frequency can be calculated using Equation 3.22.

$$f = \frac{1}{2\pi\tau} \tag{3.22}$$

According to the principle of the CTA, R_w is unaffected by changes in U (velocity). The limit frequency can be increased by more than a thousand times, or even more, compared to measurement under thermal inertia conditions [107, 108].

3.1.2.2 Anemometer Setup and Data Processing

The hardware setup of the CTA includes the overheat adjustment (static bridge balancing) and a square wave test (dynamic balancing). Data processing includes the calibration, conversion and analysis of the velocity samples [104].

Overheat adjustment

The overheat adjustment determines the operating temperature of the sensor. By adjusting the variable resistor on the Wheatstone bridge, the desired operating temperature of the sensor during operation can be set. Cold and hot resistance are interrelated through the overheat ratio (a).

$$a = \frac{R_w - R_0}{R_0} \tag{3.23}$$

Overheat temperature T_w-T_0 can be expressed as:

$$T_w - T_0 = \frac{a}{\alpha_0} \tag{3.24}$$

The recommended value of a in air is approximately 0.8, with the overheating temperature being about 220 degrees Celsius. The temperature remains nearly constant throughout the experiment, with fluctuations less than 0.5 degrees Celsius. An overheat adjustment is performed once at the beginning of the experiment and is then maintained unchanged during subsequent calibration and data collection periods.

Square wave test

The square wave test serves two primary purposes: firstly, it is used to optimise the bandwidth

of the anemometer circuit, and secondly, to check if the servo loop can operate stably and has sufficient bandwidth. This is achieved by applying a square wave signal to the top of the bridge. The time taken for the bridge to reach equilibrium is related to the time constant and, hence, the system's bandwidth. Generally, the default settings suffice for most experimental scenarios, eliminating the need for further adjustments by the user.

Velocity calibration and conversion

Calibration establishes the relationship between the output voltage of the CTA and the fluid velocity. This is achieved by placing the probe in a flow with a set of known velocities U and then recording the corresponding voltages E. The transfer function for converting voltage to velocity is derived from the fitting curve through the points (E,U). A polynomial is the most straightforward and most accurate transfer function in dynamic velocities with a wide range. A fourth-order polynomial is used in this context, as indicated in Equation 3.25. The constants C_0 to C_4 are determined through the calibration.

$$U = C_0 + C_1 E_{corr} + C_2 E_{corr}^2 + C_3 E_{corr}^3 + C_4 E_{corr}^4 \tag{3.25}$$

Calibration can be conducted in a specialised calibrator or the wind tunnel. During the calibration process, monitoring temperature changes is crucial. If there are significant temperature variations, it may be necessary to correct the CTA data according to the temperature changes. The range of velocities for calibration must be extended based on the anticipated extreme velocities during the experimental process to ensure the accuracy of converting voltage to velocity. For the calibration of one-dimensional probes, velocities typically range from 0.1 $U_{min,exp}$ as the lower limit to 1.5 $U_{max,exp}$ as the upper limit.

Amplitude domain data analysis

Amplitude domain analysis offers insights into the distribution of signal amplitudes. A single velocity time series can provide information on the mean, variance, and higher-order moments. The primary statistical information includes the following: Mean velocity:

$$U_{mean} = \frac{1}{N} \sum_{1}^{N} U_i \tag{3.26}$$

Standard deviation of velocity:

$$U_{rms} = \left(\frac{1}{N-1} \sum_{1}^{N} (U_i - U_{mean})^2 \right)^{0.5} \tag{3.27}$$

Turbulence intensity:

$$Tu = \frac{U_{rms}}{U_{mean}} \tag{3.28}$$

Skewness:

$$S = \sum_{1}^{N} \frac{(U_i - U_{mean})^3}{N \cdot \sigma^3} \tag{3.29}$$

Kurtosis (or flatness):

$$K = \sum_{1}^{N} \frac{(U_i - U_{mean})^4}{N \cdot \sigma^4} \tag{3.30}$$

Spectral domain data analysis

Sampling following the Nyquist criterion and analysing the original nonlinear signal yields the frequency spectrum and corresponding amplitudes. The accuracy of the frequency spectrum depends on the algorithm used and the number of samples taken. The algorithm typically takes the discrete Fourier Transform; the number of samples should be as large as possible under this condition.

3.1.2.3 Disturbing Effects

Measurements using hot-wire anemometers are subject to numerous interference effects. In fact, during heat transfer from the metal wire to its surroundings, any variation in parameters can create interference effects, thus reducing the accuracy of the measurement results. Both the flowing medium and the sensor conditions could cause disturbances [104].

Temperature

Because the heat transfer is directly proportional to the temperature difference between the sensor and the fluid, temperature variation is typically the most significant source of error in CTA experiments. A one-degree Celsius change in ambient temperature results in a velocity measurement error of approximately 2% for metal wire operating under normal working conditions. The measured velocity decreases as the surrounding environmental temperature rises.

Pressure

Because the probes actually measure mass flux, changes in pressure directly influence the heat transfer equation. However, calibration is typically based solely on velocity, and pressure variations during the experimental process are generally minimal. Therefore, the influence of pressure in CTA measurements is often disregarded.

Humidity

Although the content of water vapour in the air typically undergoes fluctuations, these variations are minimal, less than 1%, and can be considered negligible.

Sensor particle pollute

Particle contamination can reduce thermal conductivity, leading to a downward drift in calibration results. The impact of particle contamination increases as the sensor's surface area decreases. Regular calibration can effectively prevent this issue.

Sensor robustness

Damage to the metal wire typically does not occur during the experimental process. For probes,

the most significant risk of damage occurs during transportation. Therefore, it is essential to have a look at the robustness of the metal wire before the start of the experiment.

Sensor orientation

During the calibration and measurement processes, if the sensor remains in the same position relative to the flow, the influence of the sensor's orientation is typically minimal and can be disregarded.

3.1.2.4 Measurement Uncertainties

There are numerous potential sources of uncertainty affecting velocity measurements, primarily concentrated in instrumentation, calibration equipment, and experimental setup. The context below analyses the uncertainty from these aspects and provides corresponding evaluation equations. It should be noted that the uncertainties presented in the equations are given in terms of relative standard uncertainty [104].

Drift, noise, repeatability, and frequency response

Constant temperature anemometers typically exhibit low drift, low noise, and good repeatability characteristics. Therefore, compared to other sources of error, these factors do not significantly increase uncertainty.

Calibration equipment

Whether calibrated through dedicated calibration equipment or a Pitot tube, this step is a primary source of uncertainty. Errors are typically random and follow a normal distribution. The relative uncertainty in velocity can be expressed as follows:

$$U_{r,cal} = \frac{1}{100} \cdot STDV\left(U_{calibrator}\left(\%\right)\right) \tag{3.31}$$

The uncertainty of the calibration equipment is usually expressed in relative uncertainty, denoted as a_cal in %, plus a constant contribution represented as b_cal in m/s:

$$STDV\left(U_{calibrator}\right) = \pm a + cal\left(\%\right) + b_{cal}\left(m/s\right) \tag{3.32}$$

The constant term b_cal is typically negligible when the velocity exceeds 5 m/s. Good dedicated calibration equipment can maintain a_cal around ±1%, while Pitot tubes with calibrated micro-manometers generally have a_cal around ±2%. $STDV\left(U_{calibrator}\right)$ represents the standard deviation of the fitting error for the calibration points on the fitting curve, measured in percentage units.

Data conversion (linearisation)

Data is conversed through the transfer function of a fitting curve. The fitting error of the curve also affects the uncertainty. Fitting errors are random and follow a normal distribution. The

relative uncertainty due to fitting error can be calculated using the following formula:

$$U_{r,lin} = \frac{1}{100} \cdot STDV\left(\triangle U_{lin}\left(\%\right)\right) \tag{3.33}$$

A/D board resolution

The uncertainty in resolution is random and follows a square wave distribution. The relative uncertainty can be expressed as follows:

$$U_{r,res} = \frac{1}{\sqrt{3}} \cdot \frac{1}{U} \cdot \frac{E_{AD}}{2^n} \cdot \frac{\partial U}{\partial E} \tag{3.34}$$

where E_{AD} is the A/D board input range, n is its resolution in bits, U is the velocity, and $frac\partial U\partial E$ is the slope of the inverse calibration curve.

Probe positioning

The uncertainty in positioning is related to the alignment of the probe during installation. The uncertainty is random, follows a square wave distribution, and can be expressed as follows:

$$U_{r,pos} = \frac{1}{\sqrt{3}} \cdot (1 - \cos\theta) \tag{3.35}$$

where θ is the deflection angle.

Temperature variation

Temperature fluctuations during the experimental process introduce systematic errors and give rise to random uncertainties following a rectangular distribution, which can be expressed as:

$$U_{r,temp} = \frac{1}{\sqrt{3}} \cdot \frac{1}{U} \cdot \frac{1}{T_w - T_0} \cdot \left(\frac{A}{B} \cdot U^{-0.5} + 1\right)^{0.5} \tag{3.36}$$

where T_w is the sensor temperature, T_0 is the ambient reference temperature, and A and B represent a particular constant.

Ambient pressure variations

Environmental pressure can affect density and, consequently, the final measurement velocity obtained. The resulting error forms random uncertainty following a rectangular distribution and can be expressed as:

$$U_{r,P} = \frac{1}{\sqrt{3}} \cdot \left(\frac{P_0}{P_0 + \triangle P}\right) \tag{3.37}$$

where P_0 is the original pressure value and $\triangle P$ is the pressure difference.

Humidity

The uncertainty caused by humidity is random and follows a rectangular distribution, which can be expressed as:

$$U_{r,hum} = \frac{1}{\sqrt{3}} \cdot \frac{1}{U} \frac{\partial U}{\partial P_{wv}} \cdot \triangle P_{wv} \tag{3.38}$$

Table 3.1: Uncertainty from different error sources (^{*1}: only due to change in sensor overheat. ^{*2}: only due to change in air density with temperature. ^{*3}: the uncertainty here takes into account the two factors contributing to temperature fluctuations) [104].

Source of uncertainty	Input variants	Typical value	Relative output variants	Typical value	Coverage factor	Relative standard uncertainty
	$\triangle X_i$	$\triangle X_i$	$\frac{1}{U}\cdot\triangle y_i$	$\frac{1}{U}\cdot\triangle y_i$	k	$\frac{1}{k}\frac{1}{U}\cdot\triangle y_i$
Calibrator	$\triangle U_{cal}$	1%	$2\cdot STDV\left(100\cdot\triangle U_{cal}\right)$	0.02	2	0.01
Linearisation	$\triangle U_{fit}$	0.5%	$2\cdot STDV\left(100\cdot\triangle U_{fit}\right)$	0.01	2	0.005
A/D resolution	E_{AD} n	10volts 12bit	$\frac{1}{U}\cdot\frac{E_{AD}}{2^n}\cdot\frac{\partial U}{\partial E}$	0.0008	$\sqrt{3}$	0.0013
Probe positioning	θ	1°	$1-\cos\theta$	0.00015	$\sqrt{3}$	≈ 0
Temperature variations^{*1}	$\triangle T$	$1^{\circ}C$	$\frac{1}{U}\cdot\frac{\triangle T}{(T_w-T_0)}\cdot\left(\frac{A}{B}\cdot U^{-0.5}+1\right)$	0.013	$\sqrt{3}$	0.008
Temperature variations^{*2}	$\triangle T$	$1^{\circ}C$	$\frac{\triangle T}{273}$	0.004	$\sqrt{3}$	0.002
Ambient pressure	$\triangle P$	10kPa	$\frac{P_0}{P_0+\triangle P}$	0.01	$\sqrt{3}$	0.006
Humidity	$\triangle P_{wv}$	1kPa	$\frac{1}{U}\cdot\frac{\partial U}{\partial P_{wv}}\cdot\triangle P_{wv}$	0.0006	$\sqrt{3}$	≈ 0
$Relative expanded uncertainty^{*3}$: 3%						

where $\triangle P_{wv}$ is the water vapour pressure. However, the influence of the humidity on the heat transfer is tiny, only $\frac{\partial U}{\partial P_{wv}} \sim 0.01$ U per 1kPa change.

Summarising the uncertainties mentioned above, assuming the experimental environment is as follows: in air, T_w-T_0=200 $^\circ C$, U=15 m/s, A=1.396, B=0.895, U/E=46.5 m/s/volt, a relative uncertainty of 3% can be derived. Detailed parameters are provided in Table 3.1.

3.2 Numerical Methods

All simulations in this thesis were conducted using the open-source software OpenFOAM.

3.2.1 Governing Equations

The governing equations of Computational Fluid Dynamics (CFD) represent the mathematical formulation of the fundamental laws governing fluid motion. These equations are derived from three primary conservation laws: the conservation of mass, momentum, and energy. Together, these principles define the physical constraints that fluid flow must satisfy.

1. **Conservation of Mass (Continuity Equation):** This equation ensures that mass is conserved during the fluid flow process.

2. **Conservation of Momentum (Navier-Stokes Equations):** This equation describes the changes in momentum of the fluid under the influence of external forces.

3. **Conservation of Energy (applicable when energy transfer is involved):** This governs the fluid's thermodynamic behaviour, detailing the mechanisms of energy transfer, transformation, and dissipation.

In practical applications, these governing equations are typically employed in combination to comprehensively model and analyse the complex behaviours of fluid flows, as demonstrated in the following system of equations:

$$\begin{cases} \frac{\partial \rho}{\partial t} + \bigtriangledown \cdot (\rho \mathbf{U}) = 0 \\ \frac{\partial \rho \mathbf{U}}{\partial t} + \bigtriangledown \cdot (\rho \mathbf{U}\mathbf{U}) + \bigtriangledown p - \bigtriangledown \cdot \boldsymbol{\tau} = S_i \\ \frac{\partial \rho \mathbf{E}}{\partial t} + \bigtriangledown \cdot (\rho \mathbf{U}\mathbf{E}) + \bigtriangledown \cdot (\mathbf{U}p) + \bigtriangledown \cdot \mathbf{q} - \bigtriangledown \cdot (\boldsymbol{\tau} \cdot \mathbf{U}) = S_e \end{cases} \tag{3.39}$$

where ρ is the density, $\mathbf{U}$ is the velocity vector, p is the pressure, $\boldsymbol{\tau}$ is the viscous stress tensor. E is the total energy per unit mass, S_i and S_e respectively represent the momentum and the energy source, $\mathbf{q}$ is the heat flux vector.

In the above equation, the components of $\boldsymbol{\tau}$ experienced by an infinitesimal fluid element in three dimensions can be written in full as:

$$\begin{bmatrix} \tau_{xx} & \tau_{xy} & \tau_{xz} \\ \tau_{yx} & \tau_{yy} & \tau_{yz} \\ \tau_{zx} & \tau_{zy} & \tau_{zz} \end{bmatrix} \tag{3.40}$$

where

$$\begin{cases} \tau_{xx} = 2\mu \frac{\partial u}{\partial x} - \lambda \bigtriangledown \cdot \mathbf{U} \\ \tau_{yy} = 2\mu \frac{\partial u}{\partial y} - \lambda \bigtriangledown \cdot \mathbf{U} \\ \tau_{zz} = 2\mu \frac{\partial u}{\partial z} - \lambda \bigtriangledown \cdot \mathbf{U} \\ \tau_{xy} = \tau_{yx} = \mu \left(\frac{\partial u}{\partial y} + \frac{\partial v}{\partial x} \right) \\ \tau_{xz} = \tau_{zx} = \mu \left(\frac{\partial u}{\partial z} + \frac{\partial w}{\partial x} \right) \\ \tau_{yz} = \tau_{zy} = \mu \left(\frac{\partial v}{\partial z} + \frac{\partial w}{\partial y} \right) \end{cases} \tag{3.41}$$

Here, λ is the second viscosity. The value can directly take 2/3, and this is derived from a fully expanded stress tensor equation. μ represents the dynamic viscosity, which can be estimated based on Sutherland's law:

$$\mu = \mu_0 \left(\frac{T_0 + T_S}{T + T_S} \right) \left(\frac{T}{T_0} \right)^{3/2} \tag{3.42}$$

where μ_0 is the reference viscosity at the reference temperature T_0, which value is the reciprocal

of the Reynolds number (Re). T_S denotes the Sutherland temperature taken as 110.4K.

The heat flux components in Equation 3.39 can be written as:

$$q_i = -C_p \frac{\mu}{Pr} \frac{\partial T}{\partial x_i} \tag{3.43}$$

where C_p represents the specific heat capacity at constant pressure. Pr = 0.72 is the Prandtl number for laminar flow, and T denotes the fluid temperature.

In Equation 3.39, it can be observed that although the variables within the equation vary, they each reflect the conservation properties of a physical quantity per unit of time and per unit volume. Let **W** denote the conservative variable vector. **F**,**G**,**H** denote the convective flux terms, and $\mathbf{F^v}$, $\mathbf{G^v}$, $\mathbf{H^v}$ denote the viscous flux terms, and **S** represents the source term. The differential form of the Navier-Stokes equation is as follows:

$$\frac{\partial \mathbf{W}}{\partial t} + \frac{\partial (\mathbf{F} - \mathbf{F^v})}{\partial x} + \frac{\partial (\mathbf{G} - \mathbf{F^v})}{\partial y} + \frac{\partial (\mathbf{H} - \mathbf{H^v})}{\partial z} = \mathbf{S} \tag{3.44}$$

Conservative variable vector **W** and convective flux terms **F** are written in full as:

$$\mathbf{W} = \begin{bmatrix} \rho \\ \rho u \\ \rho v \\ \rho w \\ \rho E \end{bmatrix}, \mathbf{F} = \begin{bmatrix} \rho u \\ \rho u^2 + P \\ \rho uv \\ \rho uw \\ \rho uH \end{bmatrix}, \mathbf{G} = \begin{bmatrix} \rho v \\ \rho vu \\ \rho v^2 + P \\ \rho vw \\ \rho vH \end{bmatrix}, \mathbf{H} = \begin{bmatrix} \rho w \\ \rho wv \\ \rho w^2 + P \\ \rho uw \\ \rho wH \end{bmatrix} \tag{3.45}$$

The vicious flux terms are written in full as:

$$\begin{aligned} \mathbf{F^v} &= \begin{bmatrix} 0 & \tau_{xx} & \tau_{xy} & \tau_{xz} & u\tau_{xx} + v\tau_{xy} + w\tau_{xz} - q_x \end{bmatrix}^T \\ \mathbf{G^v} &= \begin{bmatrix} 0 & \tau_{yx} & \tau_{yy} & \tau_{yz} & u\tau_{yx} + v\tau_{yy} + w\tau_{yz} - q_y \end{bmatrix}^T \\ \mathbf{H^v} &= \begin{bmatrix} 0 & \tau_{zx} & \tau_{zy} & \tau_{zz} & u\tau_{zx} + v\tau_{zy} + w\tau_{zz} - q_z \end{bmatrix}^T \end{aligned} \tag{3.46}$$

3.2.2 Spatial Discretisation

It is imperative to discretise the computational domain before conducting Computational Fluid Dynamics (CFD) computations for a specified problem. This involves segmenting the spatially continuous computational region into a series of sub-domains and establishing nodes within each area to generate a mesh. Subsequently, the governing equations are discretised over this mesh, entailing the transformation of the partial differential format of the governing equations into a set of algebraic equations at each mesh node.

The mesh forms the foundation of discretisation, storing discretised physical quantities at the mesh nodes. The mesh plays a pivotal role in the discretisation process. The geometry and

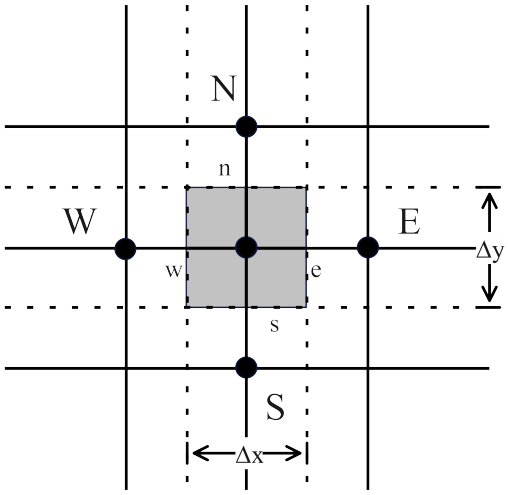

Figure 3.8: The schematic diagram of the discretising mesh.

density of the mesh, as well as the quality of the mesh, have a significant impact on the outcomes of numerical computations.

The finite volume method is a widely utilised discretisation technique in *CFD*. Its fundamental concept involves subdividing the computational region into meshes and forming a unique control volume around each mesh node. The governing equations to be solved are then integrated within each control volume. Equation 3.44 represents the partial differential form of the Navier-Stokes equations, and its integral form is as follows:

$$\frac{d}{dt}\int\int\int_{V(t)}\mathbf{W}+\int\int_{\partial V(t)}(\mathbf{F}-\mathbf{F^v},\mathbf{G}-\mathbf{G^v},\mathbf{H}-\mathbf{H^v})\cdot\mathbf{n}dS=\int\int\int_{V(t)}\mathbf{S}dV \tag{3.47}$$

Taking the computational grid of a two-dimensional problem using the finite volume method as an example, in Figure 3.8, **P** denotes a node, and **E**, **S**, **N**, and **W** represent its adjacent nodes. The shaded area corresponds to the control volume, with **e**, **s**, **n**, and **w** indicating the interfaces. The grid lines are composed of adjacent nodes.

A crucial step in formulating discrete equations using the finite volume method is interpolating physical quantities and their gradients at the control volume interfaces based on nodal physical quantities. This interpolation method, the discretisation scheme, here is exemplified by commonly used low-order schemes: the central differencing scheme and the upwind scheme. ϕ represents a certain physical quantities. In the central differencing scheme:

$$\phi_e=\frac{\phi_P+\phi_E}{2},\phi_w=\frac{\phi_P+\phi_W}{2} \tag{3.48}$$

In the central differencing scheme, the physical quantity ϕ at interface **w** is always influenced by both ϕ_P and ϕ_W. However, this approach is inappropriate in a flow predominantly characterised by convection from west to east, as the value from node **W** should more significantly influence the interface **w**. The first-order upwind scheme accounts for the flow direction when determining

the physical quantities at the interfaces.

$$\phi_w = \phi_W, \phi_e = \phi_P \tag{3.49}$$

There is always an inherent error in any numerical differencing scheme. The low-order discretisation methods mentioned above, due to their truncation errors being less than second order, may lead to false diffusion (numerical viscosity). To mitigate this effect, one can employ higher-order discretisation schemes.

3.2.3 Temporal Discretisation

Compared to spatial discretisation, temporal discretisation is relatively more straightforward. By integrating the Equation 3.47 over the time interval $\triangle t$ (from t to t + $\triangle t$):

$$\int_t^{t+\triangle t} \int\int\int_{V(t)} \mathbf{W} + \int_t^{t+\triangle t} \int\int_{\partial V(t)} (\mathbf{F}-\mathbf{F^v}, \mathbf{G}-\mathbf{G^v}, \mathbf{H}-\mathbf{H^v}) \cdot \mathbf{n} dS = \int_t^{t+\triangle t} \int\int\int_{V(t)} \mathbf{S} dV \tag{3.50}$$

The physical quantity ϕ is initially denoted as ϕ_0 and at the end as ϕ. Introducing a time weighting factor f, over the time interval $\triangle t$:

$$\int_t^{t+\triangle t} \phi dt = \left(f\phi - (1-f)\phi^0\right) \triangle t \tag{3.51}$$

It can be observed that when f=0, the value of the time integral depends on ϕ_0 at the initial moment; when f=1, the value of the time integral depends on ϕ, corresponding to forward and backward time differencing, often referred to as explicit and implicit schemes, respectively. When f=0.5, it represents the Crank-Nicolson time integration scheme. The following study will use an explicit scheme for the steady-state simulation and an implicit scheme for the transient simulation.

3.2.4 Turbulence Modelling

The flow state in turbulence is highly unstable. If velocity data is extracted over a timeline, it will be observed that the velocity is in a state of random fluctuation. Furthermore, turbulence contains numerous vortices, leading to continuous mixing of fluids with different momenta. Simultaneously, due to viscosity, kinetic energy is further converted into internal energy.

The most accurate approach to studying turbulence is Direct Numerical Simulation (DNS), which involves directly solving the Navier-Stokes (NS) equations without adding any turbulence models. Conceptually, DNS is considered one of the simplest methods. However, in practical applications, the grid size must resolve the minor viscous scales, commonly called the Kolmogorov scales. Concurrently, the computational domain size should be several times

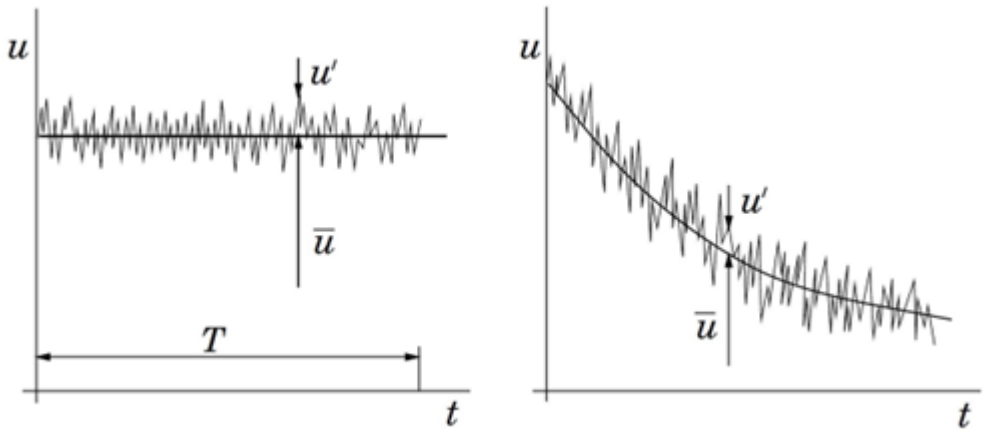

Figure 3.9: The schematic of the principle of Reynolds-Averaged Navier-Stokes (RANS) [111].

larger than the largest eddies that might be present in the flow. Therefore, DNS often demands substantial computational resources.

In turbulence, larger eddies typically contain more energy than smaller ones. Therefore, large eddy simulation (LES) focuses on resolving only the larger eddies while modelling the smaller ones. This method effectively reduces computational resources and was initially employed by Smagorinsky [109] in atmospheric modelling. However, considering the computational resources required for LES, its widespread application in engineering remains impractical.

The Reynolds-Averaged Navier-Stokes (RANS) approach, which arose from Reynolds [110], considers turbulent motion as a superposition of the time-averaged flow (denoted as $\bar{u}$ in Figure 3.9) and the instantaneous fluctuating velocity (denoted as $u^{'}$ in Figure 3.9). Extending this concept to any physical quantity ϕ, its time-averaged value is defined as:

$$\bar{\phi} = \frac{1}{\triangle t}\int_{t}^{t+\triangle t} \phi(t)dt \tag{3.52}$$

The relationship between the instantaneous value of a physical quantity ϕ, its mean value $\bar{\phi}$, and its fluctuating value $\phi^{'}$ is as follows:

$$\phi = \bar{\phi} + \phi^{'} \tag{3.53}$$

Substituting into the momentum equation in Equation 3.39:

$$\frac{\partial \rho \mathbf{U}}{\partial t} + \bigtriangledown \cdot (\rho \mathbf{U}\mathbf{U}) + \bigtriangledown p - \bigtriangledown \cdot \bar{\tau} - \bigtriangledown \cdot \tau^{'} = S_i \tag{3.54}$$

In the momentum equation, an additional term $-\bigtriangledown \cdot \tau^{'}$ appears, which can also expressed as

$\tau - ij$, which is defined as the Reynolds stress term:

$$\tau_{ij} = -\rho\overline{u_i' u_j'} \tag{3.55}$$

The term $\tau - ij$ corresponds to six different stresses: three normal and three shear stresses. The addition of these variables results in the control equations becoming unclosed. To close these equations, the concept of eddy viscosity is introduced. Eddy viscosity originates from the eddy viscosity hypothesis proposed by Boussinesq [112], and the relationship between eddy viscosity and Reynolds stress is as follows:

$$-\rho\overline{u_i' u_j'} = \mu_t \left(\frac{\partial u_i}{\partial x_j} + \frac{\partial u_j}{\partial x_i} \right) - \frac{2}{3} \left(\rho k + \mu_t \frac{\partial u_i}{\partial x_i} \right) \delta_{ij} \tag{3.56}$$

where μ_t is the turbulent viscosity, u_i is the time-averaged velocity, δ_{ij} is the Kronecker delta, k is the turbulent kinetic energy and can be calculated by

$$k = \frac{\overline{u_i' u_i'}}{2} \tag{3.57}$$

Following the introduction of the *Boussinesq* assumption, the crux of computing turbulent flow pivots on determining μ_t.

$k - \epsilon$ Model

The k-Epsilon model is a commonly used turbulence model for turbulence simulation, and it is widely applied in CFD. Based on the turbulent kinetic energy k, introducing an equation for the turbulent dissipation rate ε, a two-equation model known as the k-Epsilon model is formulated, termed the standard $k - \varepsilon$ model. Turbulent viscosity ν_t can be expressed as a function of k and ε:

$$\mu_t = \rho C_\mu \frac{k^2}{\varepsilon} \tag{3.58}$$

where C_μ is an empirical constant. The k-Epsilon model in OpenFOAM corresponds to the k-Epsilon model proposed by Launder and Spalding [113].

$k - \omega$ Model

The $k - \varepsilon$ model exhibits significant computational errors when dealing with adverse pressure gradients, secondary flows, and flows with higher curvature. This has led researchers to shift their focus to the $k - \omega$ model. In the $k - \omega$ model, ω represents the specific turbulence dissipation rate. Compared to the $k - \varepsilon$ model, the $k - \omega$ model is more suitable for wall-bounded flows with adverse pressure gradients. In OpenFOAM, the version used is the model proposed by Wilcox [114] in 1988.

$k - \omega$ SST (Shear Stress Transport) Model

The $k - \omega$ SST model is a hybrid of the $k - \varepsilon$ and $k - \omega$ models. The $k - \omega$ SST model aims to

amalgamate the advantages of both the $k-\varepsilon$ and $k-\omega$ models while mitigating their respective drawbacks, such as the underprediction of adverse pressure gradient regions by the $k-\varepsilon$ model and the excessive sensitivity to inlet conditions of the $k-\omega$ model. Through a blending function, the *SST* model activates the $k-\omega$ model in the near-wall regions and employs the $k-\varepsilon$ model in the free-stream and core flow areas [115]. The version used in OpenFOAM is the model proposed by Menter et al. [116] in 2003.

3.3 Flow Analysis Methods

Modal analysis is a technique used in flow field research to identify and describe flow structures. The mathematical principles behind various modal decomposition methods have been established in the last century. However, due to limited computational resources and experimental techniques at the time, their practical applications were restricted, and research on modal decomposition remained primarily theoretical. With advancements in computer technology, modal analysis has found widespread applications today [117–119].

3.3.1 Proper Orthogonal Decomposition (POD)

The technique known as Proper Orthogonal Decomposition (POD) goes by various names in different fields, such as Principal Component Analysis or Karhunen-Loeve expansion. It was initially comprehensively elucidated by Lumley in 1970 in his work "Stochastic Tools in Turbulence [120]." The POD method demonstrates a relatively low sensitivity to data quality. It can still extract reasonably accurate spatial modes even in substantial spatial errors, provided the data volume is sufficiently large.

The method introduced in the following text was introduced by Sirovich [121] in 1987, a computer-applied snapshot approach. It begins with a dataset of snapshots, where the flow field is sampled at various time points to obtain $u(x_m,t_i)$, where x represents spatial coordinates, subscript m denotes the number of spatial discrete points, t indicates the time, and subscript $i$represents the number of snapshots (1<i<N). The information of $u(x_m,t_i)$ is recorded in a matrix as follows:

$$U(x,t) = \begin{bmatrix} u(x_1,t_1) & u(x_1,t_2) & \cdots & u(x_1,t_N) \\ u(x_2,t_1) & u(x_2,t_2) & \cdots & u(x_2,t_N) \\ \vdots & \vdots & \ddots & \vdots \\ u(x_m,t_1) & u(x_m,t_N) & \cdots & u(x_m,t_N) \end{bmatrix} \tag{3.59}$$

The construction of the covariance matrix is as follows:

$$C = (U(x,t) \cdot U(x,t)') \tag{3.60}$$

Solve the matrix's characteristic eigenvalue matrix, denoted as D, and the corresponding eigen-

vector matrix, represented by Au. The magnitudes of the eigenvalues indicate the magnitudes of the respective modal energies. The matrix V, representing the Proper Orthogonal Decomposition (POD) modes, is calculated by

$$V = U(x,t) \cdot Au/\sqrt{D} \tag{3.61}$$

Each column of the modal matrix V corresponds to a distinct mode:

$$V = \begin{bmatrix} \phi_1 & \phi_2 & \cdots & \phi_m \end{bmatrix} \tag{3.62}$$

The temporal coefficient associated with each mode is denoted as An:

$$An = U(x,t) \cdot V \tag{3.63}$$

Each column of the matrix An corresponds to the temporal coefficients of different modes. Consequently, $U(x,t)$ can be expressed using two independent temporal and spatial signals:

$$U(x,t) = \sum_{i=1}^{N} A_i(t) \cdot \phi_i(x) \tag{3.64}$$

The advent of Snapshot POD is predominantly attributed to the nature of real-world data, wherein the quantity of spatial discretisation points considerably surpasses that of temporal discretisation points. This discrepancy substantially increases the computational time when spatial discretisation points are used as the number of columns in a matrix. Apart from Snapshot POD, Singular Value Decomposition (SVD) is another technique that can facilitate expedited computations. SVD, a widely utilised algorithm for data compression, enables the reduction of a large matrix into the product of several smaller matrices. The decomposition process via SVD is as follows:

$$[U,S,V] = svd(U(t,x)) \tag{3.65}$$

It is necessary to note the order of t and x in $U(t,x)$, where the temporal discretisation points are designated as the matrix's rows and the spatial discretisation points as its columns. V represents the eigenvector matrix, the modal matrix in POD. The computation of the temporal coefficient matrix An and the eigenvalues D proceeds as follows:

$$An = U * S \tag{3.66}$$

$$D = S^2 \tag{3.67}$$

Furthermore, it can be inferred that:

$$U \cdot S \cdot V^{'} = An \cdot V^{'} = U(t,x) = \sum A_i(t) \cdot \phi_i(x) \tag{3.68}$$

The POD method based on SVD exhibits good stability and a higher error tolerance. Moreover, employing the 'econ' mode of SVD typically only needs almost the same computational time as Snapshot POD.

3.3.2 Dynamic Mode Decomposition (DMD)

DMD treats a system's time evolution as a linear transformation, aiming to decompose observed data into a set of characteristic modes along with their associated growth/decay rates, frequencies, and other dynamic features. At the time t_1 in Equation 3.59, the spatial information is represented as a column vector denoted as U_{t_1}.

$$U_{t_1} = \begin{bmatrix} u(x_1,t_1) \\ u(x_2,t_1) \\ \vdots \\ u(x_m,t_1) \end{bmatrix} \tag{3.69}$$

The DMD method posits that if the system is linear, it is possible to find a matrix A such that:

$$\begin{aligned} U_{t_2} &= A * U_{t_1} \\ U_{t_3} &= A * U_{t_2} = A^2 * U_{t_1} \\ U_{t_4} &= A * U_{t_3} = A^3 * U_{t_2} \\ \mathbf{Y}^\sharp &= A * \mathbf{Y}, A = \mathbf{Y}^\sharp * \mathbf{Y}^+ \end{aligned} \tag{3.70}$$

where Y^+ represents the generalized inverse of Y. $Y^\sharp$ is the next state of Y. Consequently, by knowing the initial state U_{t_1} and the system's transformation matrix A, one can determine U_{t_N} at any subsequent time point in the system. The procedural steps for DMD are as follows:
Step1: Define Y and $Y^\sharp$:

$$\mathbf{Y} = U(x, t_1^{N-1}) = \begin{bmatrix} u(x_1,t_1) & u(x_1,t_2) & \cdots & u(x_1,t_{N-1}) \\ u(x_2,t_1) & u(x_2,t_2) & \cdots & u(x_2,t_{N-1}) \\ \vdots & \vdots & \ddots & \vdots \\ u(x_m,t_1) & u(x_m,t_N) & \cdots & u(x_m,t_{N-1}) \end{bmatrix} \tag{3.71}$$

$$\mathbf{Y}^\sharp = U(x, t_2^N) = \begin{bmatrix} u(x_1,t_2) & u(x_1,t_2) & \cdots & u(x_1,t_N) \\ u(x_2,t_2) & u(x_2,t_2) & \cdots & u(x_2,t_N) \\ \vdots & \vdots & \ddots & \vdots \\ u(x_m,t_2) & u(x_m,t_N) & \cdots & u(x_m,t_N) \end{bmatrix} \tag{3.72}$$

Step 2: Perform SVD on matrix Y

$$[U,S,V] = svd(Y) \tag{3.73}$$

Step 3: Calculate matrix A

$$A = U^{'} * Y^{\sharp} * V * S^{-1} \tag{3.74}$$

Step 4: Solve the matrix A's characteristic eigenvector ω and eigenvalue λ

$$[\omega, \lambda] = eig(A) \tag{3.75}$$

Step 5: Calculate DMD modes ϕ

$$\phi = Y^{\sharp} * V * S^{-1} * \omega \tag{3.76}$$

Step 6: Calculate the initial value b

$$\phi * b = U_{t_1} \tag{3.77}$$

3.3.3 Spectral Proper Orthogonal Decomposition (SPOD)

Spectral Proper Orthogonal Decomposition (SPOD) is a numerical analysis method to extract dominant modes at different frequencies from time-series data [122]. Its primary steps include data collection, Fourier transformation, and performing POD decomposition at each frequency. Consequently, SPOD can be considered an extension of the traditional POD method.

The distinguishing feature of SPOD lies in its ability to achieve temporal decoupling of modes. In conventional POD analysis, temporal evolution coefficients often exhibit periodic behaviour but cannot be explicitly represented by specific functions. The most straightforward approach to decouple time is to apply a Fourier transform, converting the time-domain data into the frequency domain to separate frequency-dependent modes. Based on this concept, the SPOD method emerged accordingly.

The algorithm begins by utilising vector q_k to represent a specific physical quantity, $q(x,t)$, at the k moment within a discrete domain Ω, denoting its instantaneous state. q vector at any given moment is a snapshot of the dynamic process. Assuming a total of M such snapshots are captured over a time interval of $\triangle t$, these individual snapshots are amalgamated into a data matrix $\mathbf{Q}$ for further analysis.

$$\mathbf{Q} = [\mathbf{q}_1, \mathbf{q}_2, \cdots, \mathbf{q}_M] \tag{3.78}$$

When directly decoupling the temporal aspects of the data matrix Q (using DFT), it is observed that the obtained spectral estimates do not converge as the number of snapshots increases [122–124]. Therefore, leveraging a method proposed by Welch [125] in 1967, the schematic diagram of which is depicted in Figure 3.10. All snapshots are divided into multiple sub-blocks, which can overlap with each other. The data matrix for each sub-block can be expressed as follows:

$$\mathbf{Q}^{(n)} = [\mathbf{q}_1^{(n)}, \mathbf{q}_2^{(n)}, \cdots, \mathbf{q}_{N_f}^{(n)}] \tag{3.79}$$

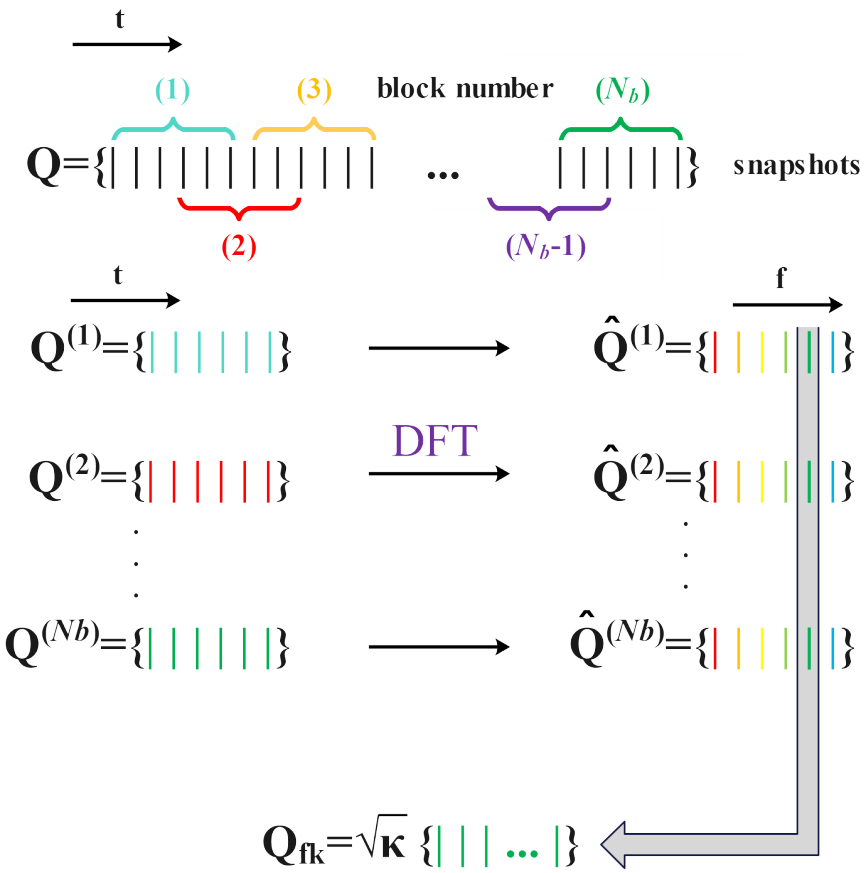

Figure 3.10: The schematic diagram of Welch's method for SPOD method [122].

where, n represents the sub-block index, and the subscript N_f indicates the number of snapshots within each sub-block. Subsequently, a DFT is applied to each of the sub-blocks for further analysis.

$$\hat{\mathbf{Q}}^{(n)} = [\hat{\mathbf{q}}_1^{(n)}, \hat{\mathbf{q}}_2^{(n)}, \cdots, \hat{\mathbf{q}}_{N_f}^{(n)}] \tag{3.80}$$

For each $\hat{\mathbf{Q}}$, the Fourier components at identical frequencies are extracted and assembled to form a new data matrix $\hat{\mathbf{Q}}_{f_k}$.

$$\hat{\mathbf{Q}}_{f_k} = \sqrt{\kappa}[\hat{\mathbf{q}}_k^{(1)}, \hat{\mathbf{q}}_k^{(2)}, \cdots, \hat{\mathbf{q}}_k^{(N_b)}] \tag{3.81}$$

where $\kappa = \triangle t/sN_b$, N_b is the number of blocks. Construct the covariance matrix, denoted here by the symbol S_{f_k}.

$$\mathbf{S}_{f_k} = \hat{\mathbf{Q}}_{f_k} \cdot \hat{\mathbf{Q}}_{f_k}^{'} \tag{3.82}$$

Finally, solve the eigenvalue problem for the covariance matrix of each frequency to obtain the SPOD modes. This step is the same as the POD method.

3.4 Chapter Summary

This chapter introduced the experimental methods, numerical simulation techniques, and analytical approaches employed in this thesis. The subsequent chapter will thoroughly investigate and discuss the effects of flow velocity and extension section length on the flow mechanisms within the S-shaped duct by the pressure experiment.

Chapter 4

Measurement and Analysis of the S-duct

As a critical component of high-speed aircraft engines, the intake system is designed to decelerate the incoming airflow, thereby enhancing the performance of both the engine and the compressor. In designing the intake system, meeting deceleration requirements while maintaining the intake duct as short as possible is essential. This is because a shorter intake duct translates to a shorter fuselage, contributing to the aircraft's overall weight reduction [1, 2]. It is estimated that if the aircraft can reduce its fuselage length by one diameter of its intake duct, the net weight would decrease by 15% [3]. On aircraft, S-shaped ducts are typically located on the fuselage's dorsal side or at the wings' root [80]. Compared to traditional straight ducts, diffusive S-shaped intake ducts, due to their curvature, can reduce the velocity of the incoming flow more rapidly. This allows a shorter intake duct and significantly reduced weight. Presently, diffusive S-shaped intake ducts have been widely adopted in high-speed aircraft propulsion systems.

Research on the flow within S-shaped ducts has been underway since the last century. Figure 4.1 shows a typical S-shaped duct geometry with a diffusing cross-section. D1 gradually increases to D2. The principal geometric parameters of S-shaped ducts include the center line, diffusion ratio, radius ratio, length-to-diameter ratio (LDR), and length-to-offset ratio (LOR) [81, 82, 126]. The center line of an S-shaped duct is usually composed of two planar circular arcs. The diffusion ratio refers to the ratio of the outlet diameter to the inlet diameter (D2/D1). The radius ratio represents the growth ratio of the cross-sectional circular radius along the center line, which can be a fixed value or defined by a function. The length-to-diameter ratio (LDR)and the length-to-offset ratio (LOR) are defined as the ratio of the duct length to the inlet diameter (L/D1) and the ratio of the offset distance to the height (L/H), respectively.

After air enters the S-shaped duct, the curvature of the center line induces a centrifugal pressure gradient relative to the duct walls. The concave surface generates an adverse pressure gradient that decelerates the flow, whereas the convex surface produces a favorable pressure gradient that accelerates the flow. As the center-line curvature increases, once the influence of the centrifugal pressure gradient on the flow velocity exceeds a critical value, flow separation occurs within the S-shaped intake, expected near the two inflection points shown in Figure 4.1. The un-

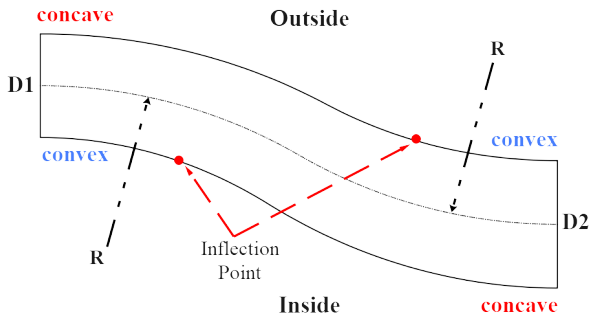

Figure 4.1: The S-duct geometry.

even pressure distribution caused by the center-line curvature, aided by the duct's diffusion rate, also promotes the formation of secondary flows, thereby further increasing the complexity of the flow within the S-shaped duct [4, 5], mainly represented in the pressure distortion [127–131] and the swirl distortion [90, 132, 133]. Non-uniform flow conditions within the duct can significantly increase the likelihood of engine surge and stall [6].

Therefore, although S-shaped intake ducts should avoid large centerline curvatures theoretically, size and weight considerations necessitate inevitable trade-offs. Additionally, to enhance engine performance, a well-designed S-shaped intake duct should not only effectively reduce the airspeed but also minimize flow separation and suppress the development of secondary flows [81].

However, it is not easy to study the S-duct. Its complex geometry also makes the measurement of the experiment difficult. Commonly employed intrusive measurement techniques, such as pressure probes and constant-temperature anemometers, make it almost impossible to collect data without interfering with the flow field. While an ideal method, Stereoscopic Particle Image Velocimetry (SPIV) places high demands on the model itself and may also suffer from insufficient temporal resolution [83].

Although the challenges mentioned above, some initial findings have been concluded after decades of research. First, in the S-duct time-averaged fields, Taylor et al. [84, 85] studied the S-duct at low Reynolds numbers of 790 and 48,000, and Vakili et al. [86] and WELLBORN et al. [81] further explored the scenes under higher Reynolds numbers of 3.25×10^6 and 2.6×10^6. Integrating these studies reveals that the aerodynamic data within S-shaped ducts in the time-average field exhibit a symmetrical distribution in an extensive range of Reynolds numbers. This conclusion can be found in most literature, and based on this finding, researchers can simulate only half of an S-shaped intake in steady-state modeling, using mirroring to reduce computational load. However, this symmetrical distribution is not absolute, though it can be observed in most cases. In earlier studies, Bansod and Bradshaw [80] noted that vortices generated by secondary flows could disrupt the axial symmetry at the outlet interface, causing deviations.

The flow pattern in the time-averaged field is predominantly characterized by one or two pairs of counter-rotating vortices, which generally form after the second bend [87]. The higher

velocity of the flow in the center of the duct also contributes to vortex formation [88]. The high velocity in the center of the duct, apart from being attributable to the inherent geometry of the S-shaped duct, the increased central flow velocity is also accelerated by blockages caused by flow separation [81, 89].

Unlike the symmetry in the time-averaged fields, transient flow fields exhibit strong asymmetry. Experimentally, Gil-Prieto et al. [90] utilized SPIV to perform unsteady measurements of a circular S-shaped duct at Mach 0.27 and 0.6, discovering significant variations in secondary flow vortices at different moments within the duct. In their subsequent studies, the flow patterns of the transient field were clearly defined, predominantly consisting of two modes: a vertical mode and a switching mode [133]. They also pointed out it is essential to understand unsteady characteristics inside the S-duct for stable running of the engine [134]. Unsteady numerical simulations also validated these findings. In terms of simulation, MacManus et al. [91] employed the Delayed Detached Eddy Simulation (DDES) method to model the experiments conducted by Wellborn *et al.* [81], and Wojewodka et al. [92] further explored the differences between DDES and Unsteady Reynolds-Averaged Navier-Stokes (URANS) simulations, they conducted a Proper Orthogonal Decomposition (POD) of the numerical simulation results to identify the principal modes of the transient flow field, with simulation outcomes consistent with experimental observations.

Moreover, the inlet boundary layer thickness and asymmetry inlet conditions also significantly influence the unsteady characteristics of the flow inside the S-duct. McLelland et al. [135] presents the first quantitative analysis of the impact of inlet boundary layer conditions on the swirl distortion at the S-duct exit. They found the peak swirl intensity will significantly increase when the boundary layer becomes thicker. Although the original unsteady modes remain, the dominant frequency of the fluctuation will dramatically decrease. In their subsequent studies, Migliorini et al. [136] further proposed a new method based on SPIV to evaluate the unsteady flow distortion of the S-duct.

Here is a brief overview of the optimization methods applied to the S-duct. Based on different flow control approaches, the optimization methods can be categorized into two main types: passive and active. Common passive flow controls are geometry optimization and vortex generators. In recent studies, Chiang et al. [137] studied geometry optimization by the simulation and verified that rationally optimized S-duct can significantly decrease flow distortion and improve the total pressure recovery coefficient. Also, based on the simulation, the vortex generator scheme proposed by Tanguy et al. [138] matches the experiment and proves vortex generators can efficiently decrease the flow distortion inside the S-duct. Additionally, the performance of the S-duct can be further improved by optimizing the design and configuration of the vortex generators. Regarding active flow control, common methods include the wall jet, active vortex generator, and synthetic jets. Take synthetic jets as an example; a novel optimization scheme is to do the optimization based on plasma synthetic jets Liu et al. [139]. However, this method is

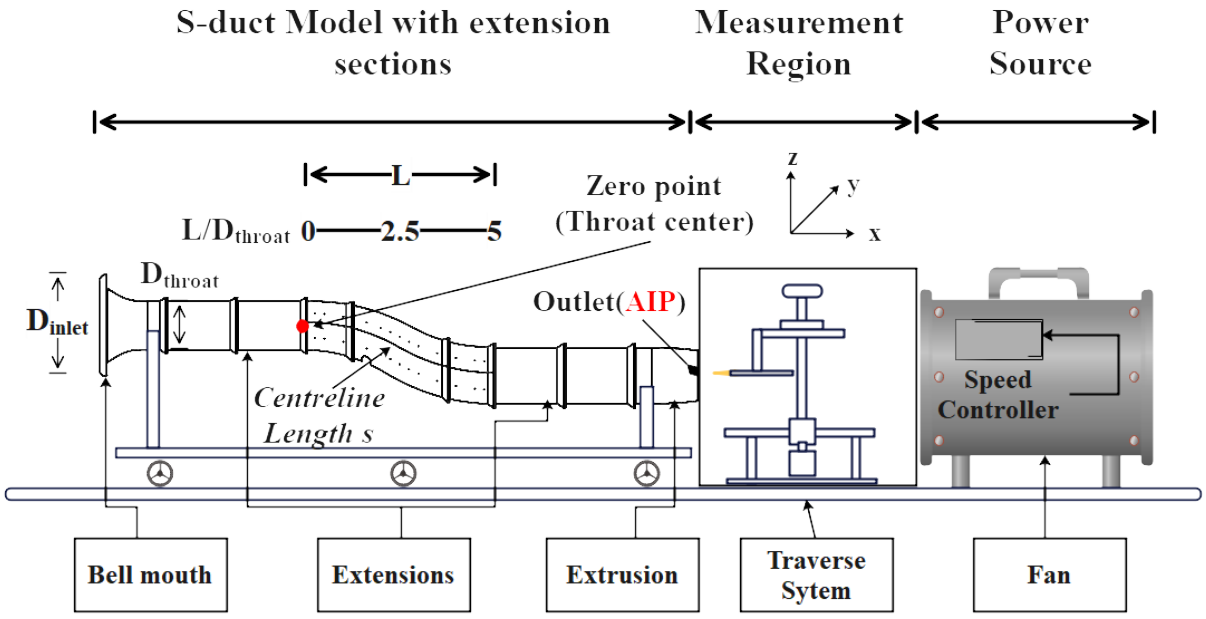

Figure 4.2: The schematic of the experimental setup.

limited by the magnitude of the plasma-induced thrust, and at present, it can only be valid under a low-speed range.

Despite the flow complexity within S-shaped ducts, the pattern still exhibits some regularities. Zachos et al. [83] found that within the Mach number range of 0.27 to 0.6, the influence of the Mach number on dimensionless flow parameters is negligible. However, further verification is still required to determine whether this conclusion applies to the Mach numbers outside the range above. Additionally, in WELLBORN et al. [81]'s experiment, two extensions were upstream and downstream of the S-duct; however, their function was not explained in their article. The relevant research was also not found. However, during the measurement of the S-duct, it was found that the presence or absence of the extensions dramatically influences the flow pattern inside the S-duct.

This chapter aims to fill the research gap of these two issues mentioned above. However, due to the limitation of the experiment conditions, this study only focuses on the low-mach numbers field.

4.1 Experimental Setup

The experimental system consists of an S-shaped duct, a traverse system, an acrylic enclosure, and a fan (as shown in Figure 4.2). The traverse system is installed within the acrylic enclosure, which connects the S-shaped duct to the fan. The enclosure is made of transparent acrylic panels; its internal dimensions are 1 meter in length, width, and height.

4.1.1 Experiment Facilities

The geometry of the S-duct employed in the experiment is similar to that described in the 1992 publication by WELLBORN et al. [81] (as illustrated in Figure 4.3). The distinction between the two lies solely in the growth rate of the duct's radius. The centre lines of both S-shaped ducts are defined by two planar arcs with radii of 102.1 centimetres, where each arc corresponds to a central angle of 30° ($\theta_{max/2}$). The coordinate system for the centre line is defined by Equation 4.1. The radius of each cross-section is perpendicular to the centre line and is determined by Equations 4.2 and 4.3. Here, r_1 represents the duct entrance radius, 102.1 millimetres, and r_2 represents the duct exit radius, 125.7 millimetres. $\triangle x$ is the horizontal length of the S-shaped duct section. The variable r represents the cross-section radius at the angle θ. Equation 4.2 is the S-duct geometry proposed by Wellborn et al. [81], and Equation 4.3 is the geometry adopted in this experiment. The variation in the radius is depicted in Figure 4.4. As can be observed from Figure 4.4, the radius of the duct described by Wellborn et al. [81] still forms an S-shaped curve, and in the actual model employed in this experiment, the radius growth rate is a fixed value.

The duct entrance is connected to a bell mouth in the experiment, and an extrusion section is attached to the exit. The bell mouth serves as the contraction section, with an entrance diameter of 435 millimetres and a throat diameter of 204.2 millimetres (connecting to either the entrance of the S-shaped duct or the extension section). The internal portion of the extrusion section remains cylindrical without the contraction, and external contraction is employed for ease of connection to the measurement region. Both the bell mouth and extrusion section have a length of 350 millimetres. Apart from the extension sections, all other parts of the model are fabricated using 3D printing. The extension section is made of nylon six material and fabricated using conventional mechanical machining techniques.

$$
\begin{aligned}
&0 \leq \theta \leq \theta_{max/2}: \\
&x_{cl} = R\sin\theta \\
&y_{cl} = 0 \\
&z_{cl} = R\cos\theta - R \\
&\\
&\theta_{max/2} \leq \theta \leq \theta_{max}: \\
&x_{cl} = 2R\sin(\theta_{max/2}) - R\sin(\sin\theta_{max}) \\
&y_{cl} = 0 \\
&z_{cl} = 2R\cos(\theta_{max/2}) - R - R\cos(\theta_{max} - \theta)
\end{aligned}
\tag{4.1}
$$

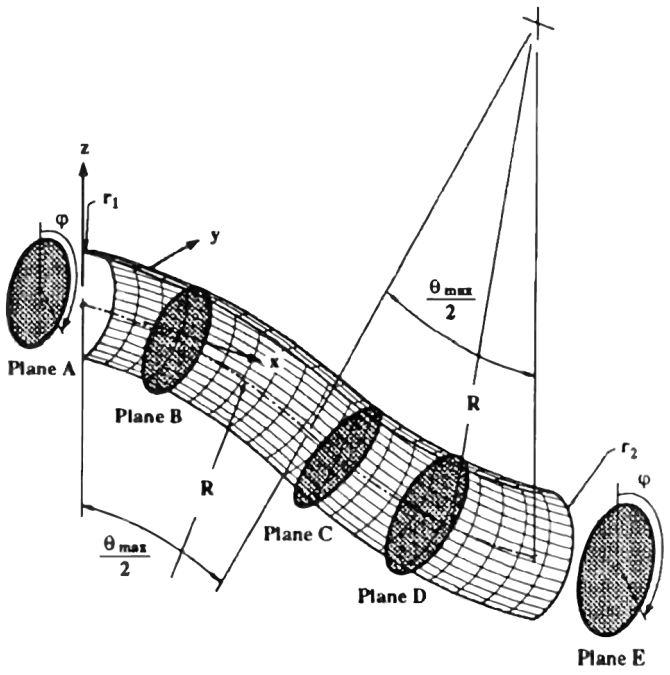

Figure 4.3: Half shell of the circular diffusing S-duct.“Reproduced from S. Wellborn, B.Reichert, and T.Okiisho, “An experimental investigation of the flow in a diffusing s-duct," in *28th joint propulsion conference and exhibit* (1992) p. 3622; with the permission of the American Institute of Aeronautics and Astronautics, Inc."

$$\frac{r}{r_1} = 1 + 3\left(\frac{r_2}{r_1} - 1\right)\left(\frac{\theta}{\theta_{max}}\right)^2 - 2\left(\frac{r_2}{r_1} - 1\right)\left(\frac{\theta}{\theta_{max}}\right)^3 \tag{4.2}$$

$$\frac{r}{r_1} = 1 + \frac{r_2 - r_1}{R} \cdot \frac{\triangle x}{r_1} \tag{4.3}$$

The shape of the contracting section, namely the bell mouth, also significantly impacts the flow inside the duct. Porro [140] proposed a complex polynomial model in 1991 to determine the design of such contraction curves. Their basic design idea is to ensure each section’s curvature or slope will not cause flow separation. For further insights into the optimisation of bell mouth design, one can refer to the research conducted by Blair and Cahoon [141]. In the experiment of this chapter, the bell mouth’s contraction section takes a contraction curve as a circular arc with a radius of 328.5 millimetres (as shown in Figure 4.5).

The experimental setup includes a two-dimensional traverse system controlled by two stepper motors. The motion commands are executed through MATLAB scripts. The stepper motors are MS200HT2 models manufactured by Schrittmotormodul, with a rated current of I = 3.0 A and equipped with M23 12-pol connectors. Detailed technical specifications are as follows:

For the horizontal direction motor:

- 400 steps per millimetre
- Maximum moving speed of 25 millimetres per second

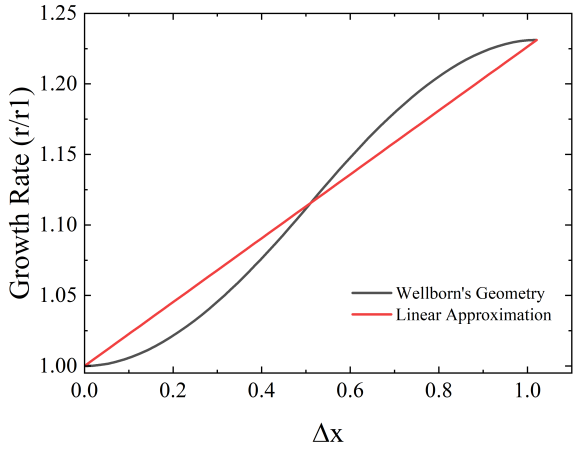

Figure 4.4: Radius growth rate of the S-duct. Wellborn's geometry is from Equation 4.2, and the linear approximation is from Equation 4.3.

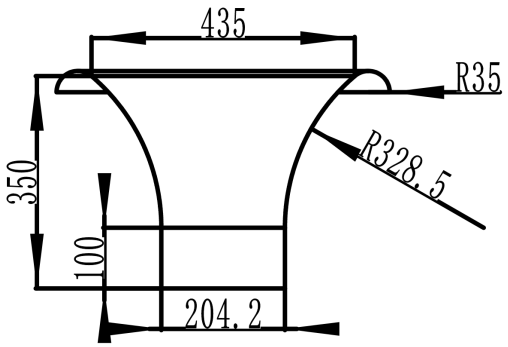

Figure 4.5: Bell mouth geometry.

- Corresponding lead screw travel distance of 64 centimetres

For the vertical direction motor:

- 410 steps per millimetre
- Maximum moving speed of 15 millimetres per second
- Corresponding lead screw travel distance of 64 centimetres

The pressure measurement system comprises a 7-hole probe and a ZOC pressure scanning device. The 7-hole probe, developed as a collaborative research effort between NASA-Ames and the U.S. Air Force Academy, can handle more complex flow conditions, with the highest achievable angle of attack reaching up to 75 degrees [102]. The ZOC pressure scanning system comprises an ERAD4000 A/D base and one module connected, requiring an external power supply. The pressure scanning device has a total of 32 channels. The ERAD base connects to the host via Ethernet. The three critical parameters of the ZOC system are period (PERIOD), frames per second (FPS), and sample averaging (AVG). These three parameters define the data sampling rate according to Equation 4.4. In this experiment, the period, frames per second, and sample averaging are all set to 50. Here, period 50 means 50 milliseconds.

$$DataRate\left[\frac{Hz}{Ch}\right] = \frac{1}{Period\,[s] * FPS * AVG} \tag{4.4}$$

A Flakt Woods EQ511467 fan provides aerodynamic power. The fan has a diameter of 500 millimeters and is equipped with five blades. It can reach a maximum speed of 1380 rpm (12.3 m/s) and is powered by a 220V-240V power source. The fan comes with a speed controller, the ME1.12 model produced by Flakt Woods. The speed controller has a range of settings from 1 to 10, with 10 being the maximum speed setting. In the following text, the notation "Speed X" refers to the specific setting on the speed controller, with "X" representing the numerical value of the setting.

4.1.2 Experimental Description

A stand with a mesh sieve is positioned in front of the bell mouth of the S-duct to own a more uniform incoming flow. The fan is connected to the S-duct through a sealed acrylic box, and the entire traverse system is contained within the acrylic box. To ensure the safety of the equipment, during the experiments, there is a 3–5-millimeter gap between the tip of the 7-hole probe and the outlet. Hence, the measurement interface, the selected aerodynamic intake plane (AIP), is slightly behind the outlet. Additionally, there is a frame between the vertical axis of the traverse system and the 7-hole probe, as shown in Figure 4.6, to keep the vertical axis away from the measurement position, reducing the impact of the vertical support on the flow field, as shown

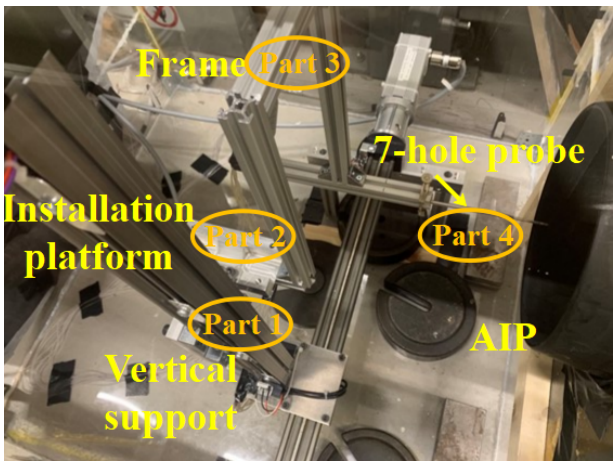

Figure 4.6: The schematic of the 7-hole probe installation.

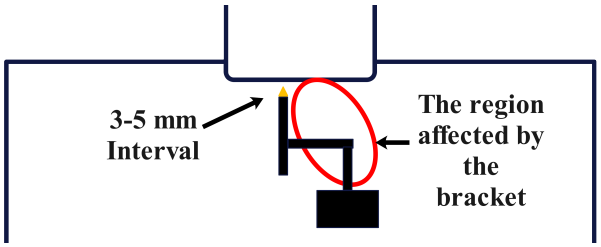

Figure 4.7: The schematic of the interference area.

in Figure 4.7. To guarantee air tightness, all connections and the measurement areas are sealed with tape.

To guarantee the flow symmetry as much as possible, the S-duct, the measurement region, and the fan are symmetrically distributed along the same line. The air source is behind the traverse system, and any obstacles between the fan and the AIP can introduce extra energy losses, thereby interfering with pressure measurements. However, due to space constraints, in this experiment, the traverse system's support structure can only ensure that the vertical axis is not located between the AIP interface and the fan when measuring the left half of the AIP interface (the left side facing the 7-hole probe head). According to extensive research [82, 90, 133, 142], the pressure distribution on the AIP interface should be roughly symmetrical. Furthermore, the experiments were conducted within a relatively low-speed range, where the influence of secondary flows is relatively small. However, some literature also reports the flow asymmetry on AIP [143]. Therefore, this chapter will first verify the flow symmetry. After validation, the selected measurement scheme is that the AIP interface is divided horizontally into two halves, and only the half with less disruption was measured and then mirrored for analysis.

Figure 4.8 shows the various S-duct geometries tested during the experimental investigation. There are totally five configurations. The offset, the ratio of the height difference between the centres of the inlet and outlet interfaces to the horizontal length of the duct, is used to characterise the various configuration geometries in this study.

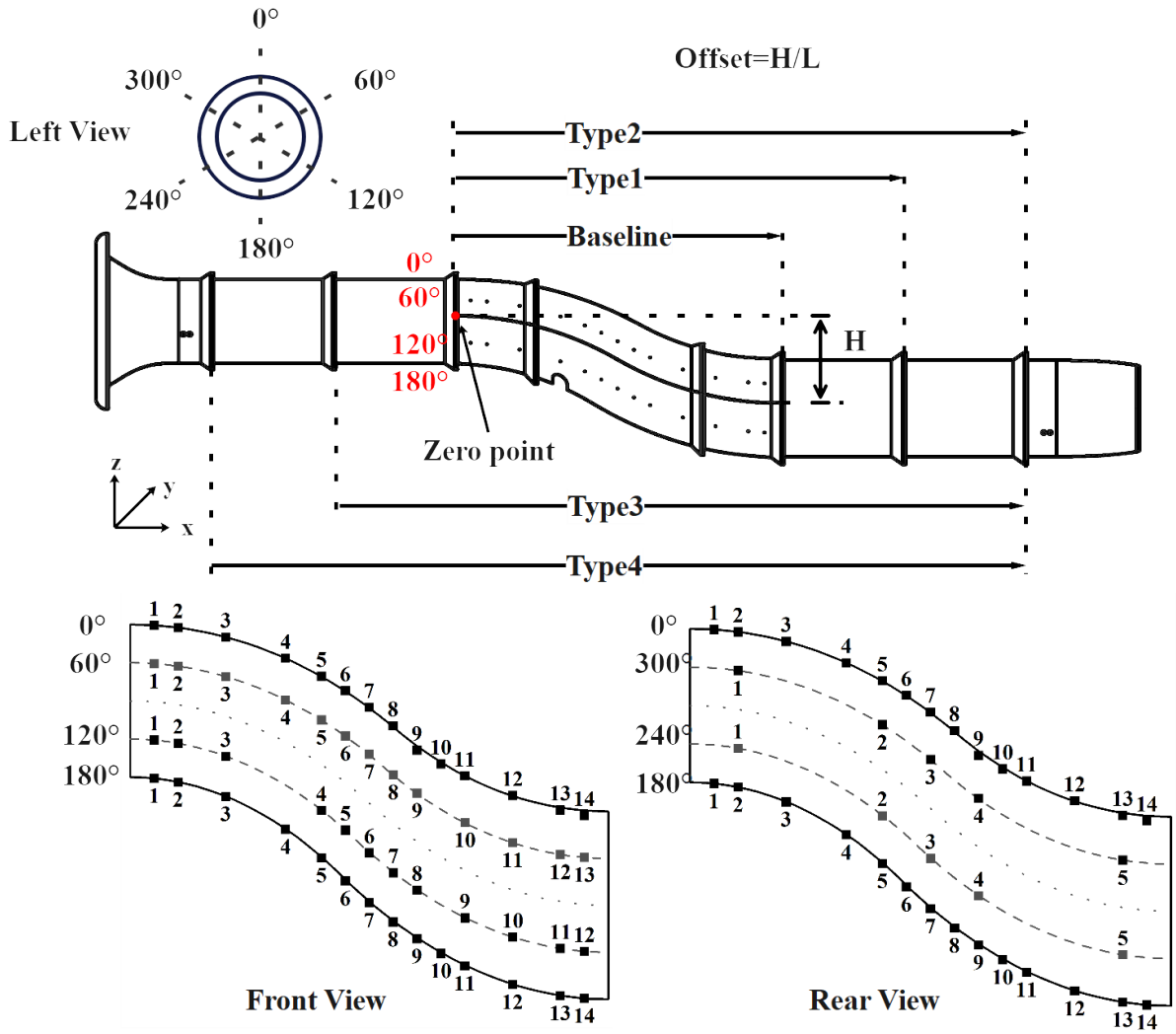

Figure 4.8: The wall pressure taps distribution.

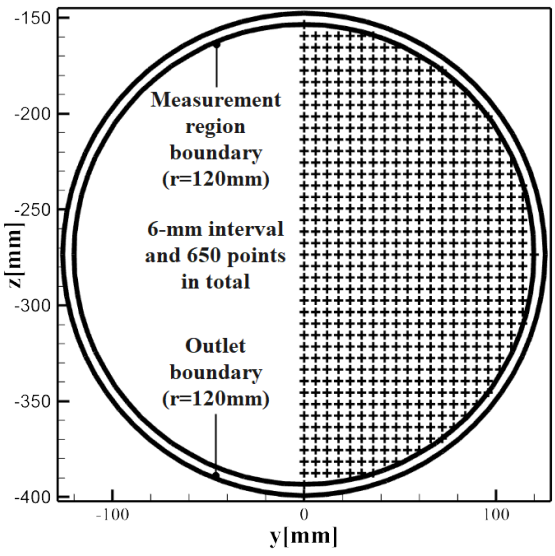

Figure 4.9: Pressure measurement points distribution at the AIP.

Table 4.1: Wall pressure ports distribution.

L/D_{inlet}	0.25	0.5	1	1.625	2	2.25	2.5	2.75	3	3.25	3.5	4	4.5	4.75	Number
0°	x	x	x	x	x	x	x	x	x	x	x	x	x	x	14
60°	x	x	x	x	x	x	x	x	x		x	x	x	x	13
120°	x	x	x		x	x	x	x	x		x	x	x	x	12
180°	x	x	x	x	x	x	x	x	x	x	x	x	x	x	14
240°		x			x		x		x				x		5
300°		x			x		x		x				x		5
Total Number															63

Table 4.2: Flow and experimental environment parameters. P_{env} represents the environment pressure; T denotes the temperature; ρ is the air density; P_{ref} and M_{ref} are the dynamic pressure and the Mach number at the reference point (L/D=0.25); P_{out} and M_{out} are the average static pressure (the value is the difference with the environment pressure) and the Mach number at the AIP; $\dot{m}$ represents the mass flow rate.

Velocity (Geometry)	P_{env}(Pa)	T (°C)	ρ (kg/m3)	P_{ref}(Pa)/M_{ref}	P_{out}(Pa)/M_{out}	$\dot{m}$ (kg/s)
Speed2 (Baseline)	101689	20.14	1.209	314.72/0.06639	-171.19/0.041002	0.845
Speed4(Baseline)	100319	20.75	1.1899	564.621/0.08954	-319.9/0.0059954	1.218
Speed6(Baseline)	99988	20.5	1.1873	946.901/0.116137	-504.04/0.077278	1.566
Speed8(Baseline)	101605	21.51	1.2021	1240.12/0.13185	-681.72/0.08916	1.833
Speed10(Baseline)	101731	21.39	1.2041	1379.67/0.138984	-756.01/0.094574	1.947
Speed2(1 rear)	101016	20.5	1.1996	330.217/0.068231	-163.84/0.039987	0.819
Speed4(1 rear)	99930	20.68	1.1856	598.621/0.092375	-294.47/0.056004	1.134
Speed6(1 rear)	101424	19.87	1.2067	1006.04/0.118869	-511.9/0.075983	1.563
Speed8(1 rear)	101444	19.77	1.2073	1307.33/0.135494	-663.8/0.088581	1.823
Speed10(1 rear)	101351	20.02	1.2052	1451.77/0.142845	-741.56/0.09334	1.919
Speed2(2 rear)	102063	21.28	1.2084	247.51/0.05877	-189.83/0.042758	0.883
Speed4(2 rear)	102241	20.72	1.2186	486.102/0.082101	-332.69/0.060447	1.258
Speed6(2 rear)	102448	20.79	1.215	874.917/0.110296	-549.13/0.07953	1.650
Speed8(2 rear)	102319	20.02	1.2167	1177.38/0.12803	-717.18/0.092257	1.915
Speed10(2 rear)	102530	20.18	1.2185	1325.7/0.135717	-804.98/0.097362	2.024
Speed2(2 rear + 1 front)	100856	19.43	1.2017	240.453/0.058279	-167.96/0.042363	0.867
Speed4(2 rear + 1 front)	101422	19.31	1.2089	470.551/0.081301	-333.06/0.059932	1.234
Speed6(2 rear + 1 front)	101364	19.58	1.2071	817.73/0.107205	-555.19/0.078764	1.620
Speed8(2 rear + 1 front)	101533	19.54	1.2093	1104.13/0.124467	-707.31/0.090125	1.857
Speed10(2 rear + 1 front)	102350	19.43	1.2195	1231/0.130898	-790.44/0.094552	1.965
Speed2(2 rear + 2 front)	100669	21.35	1.1917	245.352/0.058918	-160.29/0.041711	0.850
Speed4(2 rear + 2 front)	100401	20.26	1.1929	469.996/0.08166	-265.8/0.0567	1.044
Speed6(2 rear + 2 front)	100291	20.43	1.1909	785.658/0.105637	-523.05/0.074157	1.507
Speed8(2 rear + 2 front)	100499	20.04	1.195	1029.19/0.12078	-678.98/0.085786	1.749
Speed10(2 rear + 2 front)	100474	20.27	1.1937	1157.34/0.128097	-759/0.090868	1.851

Figures 4.8 and Table 4.1 describe the layout of wall static pressure ports, totalling 63 pressure measurement points. The measurement points at the AIP are placed in a mesh pattern (shown in Figure 4.9), originating from the circle centre and extending within a boundary as a radius of 120-millimetre (inclusive of the boundary), as depicted in the Figure 4.9. The spacing between adjacent points in vertical and horizontal directions is precisely 6 millimetres. There are 650 sampling points in total on AIP.

In previous literature [81, 86, 144–147], researchers commonly adopted a concentric circle distribution of pressure measurement points at the AIP interface. Although the concentric circle distributions can effectively analyse aerodynamic data at the AIP, they are constrained by their distribution pattern, with the highest resolution at the circle centre and gradually diminishing as radial distance increases. In this experiment, pressure measurement point distribution takes a mesh pattern. The aim was to provide a uniform resolution across the AIP, addressing some of the limitations of the concentric circle approach.

The experiment divided the flow velocities into five levels, corresponding to the settings on

the speed controller, denoted as Speed2-10. Table 4.2 provided the flow parameters for each speed level and the experimental environment conditions. The speed of sound used to calculate the Mach number takes the empirical Equation 4.5. Here, c and T are the speed of sound and temperature, and units are, respectively, m/s and °C.

$$c = 331.6 + 0.6T \tag{4.5}$$

Here, it should be noted that the total pressure at the outlet will be lower than the environment due to flow loss. Although Table 4.2 doesn't directly provide the total and dynamic pressures, they can be deduced by other parameters. The S-duct configurations were categorized based on the extension segments. The baseline experiment had no extension segments added, and other configurations gradually increased the number of extensions added from rear to front. Each extension segment had a length of 381 millimeters. The inner radius of the front extension segment matched the inlet radius of the S-duct, 102.1 millimeters, and the inner radius of the rear extension segment matched the outlet radius of the S-duct, 125.7 millimeters. The S-duct with all extensions is the same configuration as that used in WELLBORN et al. [81]'s experiment. The experimental configurations, in the order of experimentation, were as follows: no extension segments(Baseline), one rear extension segment (Type1), two rear extension segments (Type2), two rear extension segments plus one front extension segment (Type3), and two rear extension segments plus two front extension segments (Type4). The experiment's variables are the flow velocity and the extension segment number.

4.1.3 Flow Symmetry Validation

As mentioned in Section Experimental Description, the experiment measures half of the AIP interface and then mirrors data to obtain the complete data on the AIP plane. This approach is based on a flow symmetry analysis before the formal experiment commences. Figure 4.10 shows aerodynamic data on AIP under different measurement schemes under Speed6. Schemes 1-3 take concentric circular distribution, and Scheme 4 takes mesh distribution and mirroring. The measurement point distribution of Schemes 1&2 is relatively sparse, with a 9.8-mm gap in the radial distance (13 points including circle center) and 36° interval in the circumferential direction (10 points on each circle), 121 points in total. The measurement point distributions of Schemes 1&2 are the same, and the difference is if the frame was used when measuring. The frame is as Part 3 in Figure 4.6 shows. The frame acts as a connection to keep the vertical support away from the measurement location, thus reducing the interference of the vertical support and installation platform. Before installing the frame, the seven-hole probe was directly installed on Part 2. But as Figure 4.7 shows, at this moment, vertical support (Part 1) will interfere with the measurement of the seven-hole probe, as Figures 4.10 (e) (i) (m) (q) shows, the uvw and PRt distributions have strong asymmetry. By further comparing Schemes 1 and 2, this asymmetry

is not inherent. After adding the frame, the asymmetry of three velocity components and PRt is improved. Additionally, by comparing Schemes 1 and 2, the high-velocity (u) and high-PRt regions significantly expand. Therefore, it can be deduced that the vertical support and installation platform will affect the measured magnitude of streamwise velocity.

Scheme 3 also uses the frame but uses more measurement points. It has 25 points in the radial distance, a 4.9-mm gap, 40 points on each circle, and a 9° interval, for a total of 961 points. With more measurement points, the symmetry of uvw and PRt is further improved. An apparent symmetry can be observed using Scheme 3, especially for the vw velocity components and PRt distributions. By observing the changing trend from Scheme 1 to Scheme 3, it can be concluded that although it cannot prove that the aerodynamic data on AIP is strictly symmetrical, reducing the traverse system's interference improves the symmetry. However, the frame can only reduce the interference when measuring the right half due to the measurement space limitation. When measuring the left half, the vertical support will move behind the AIP again. Based on the literature mentioned in Section Introduction, the time-average field on AIP of the S-duct is usually symmetrical, and this trend can also be found in the trend from Scheme 1 to Scheme 3; this chapter assumes that the aerodynamic data on AIP is symmetrical. Therefore, the following experiments only measure half of AIP and get the complete plane by mirroring. On the one hand, this saves experiment time. On the other hand, this allows for further increasing measurement points. By comparing Scheme 2 and Scheme 3, it can be found that the aerodynamic data's symmetry on AIP is also enhanced when more data points are used. Therefore, Scheme 4 was introduced, with a higher density of the measurement points and a more uniform distribution. Scheme 4 takes a mesh distribution and mirroring; its detailed information is shown in Figure 4.9. Comparing the right half of AIP (measurement region in Scheme 4), it can be found that measurement points that take mesh distribution show more flow characteristics than those that take concentric circle distribution.

4.2 Simulation Analysis

Building a simulation can help understand the flow inside the S-duct before further analyzing experimental data. All cases were conducted using the open-source software OpenFOAM and the structure mesh. Boundary conditions are set based on the experimental data, taking the 'pressureDirectedInletVelocity' inlet and static pressure outlet. Because the primary aim is to help analyze experimental data, all cases are only conducted with steady-state simulation. The simulation took the Reynolds-averaged Navier-Stokes (RANs) method. The turbulence model took the $k-\omega$ SST model.

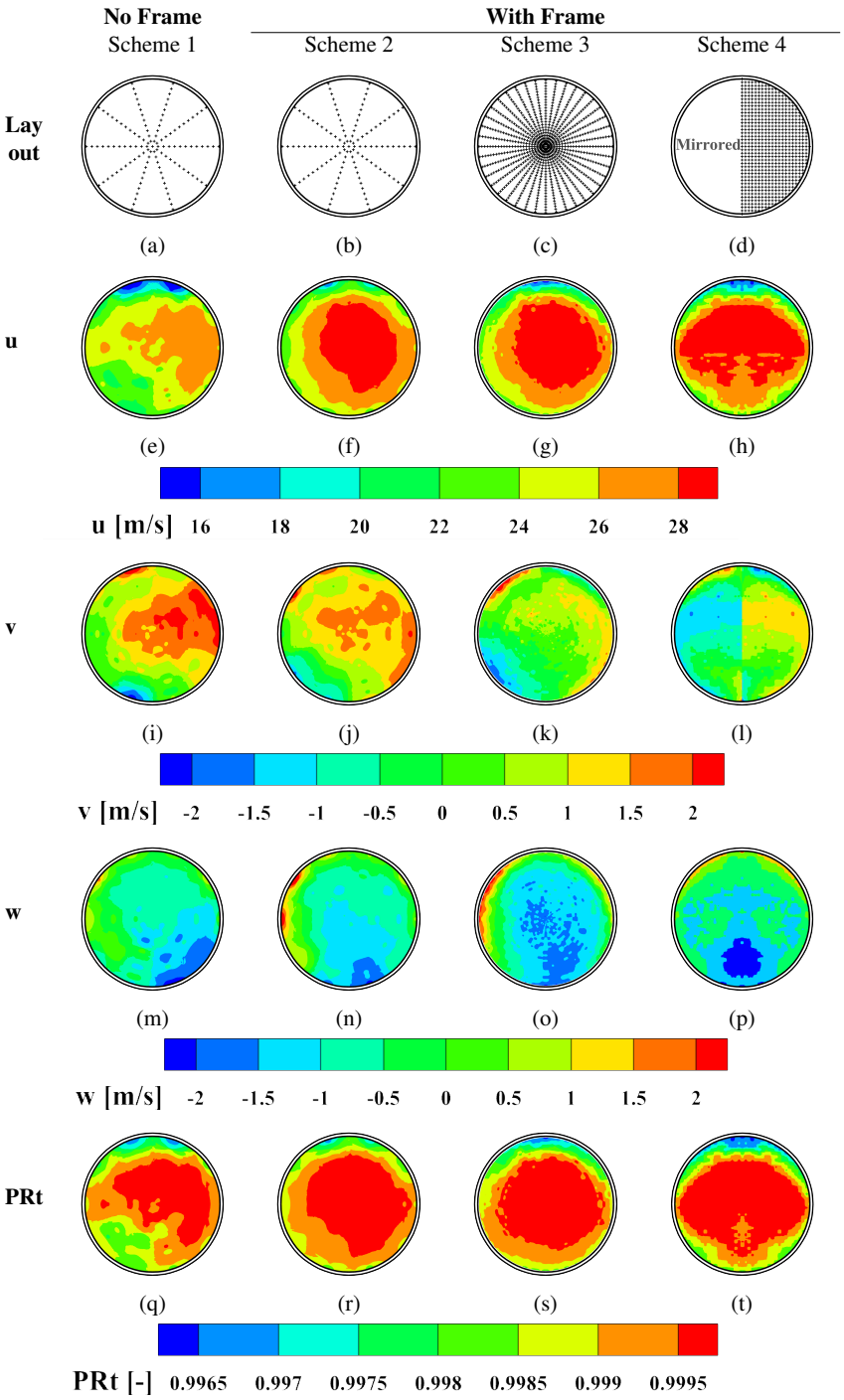

Figure 4.10: Aerodynamic data on AIP under different measurement schemes. Measurement schemes 1-3 take the concentric circular distribution, and scheme 4 takes mesh distribution and mirroring. (a)-(d) are the layouts of the measurement points. (e)-(h) is the velocity distribution along the x direction (u). (i)-(l) and (m)-(p) are, respectively, along the y (v) and z (w) axes. (q)-(t) are AIP's total pressure recovery distributions. The number of measurement points is 121 points for schemes 1 & 2, 961 points for scheme 3, and 650 points for scheme 4.

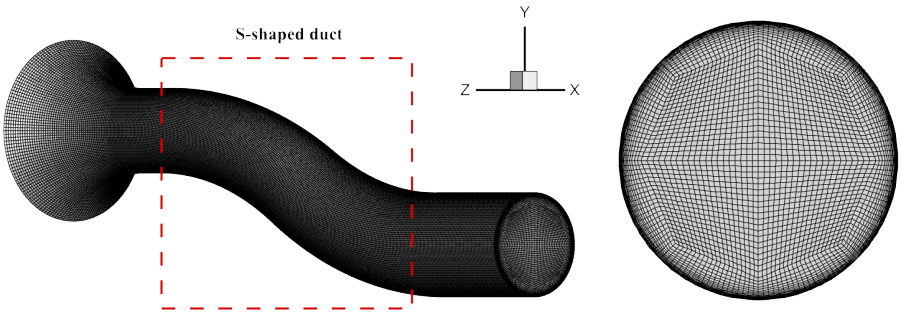

Figure 4.11: Computational mesh: structured and multi-blocks.

Table 4.3: Mesh information. r represents the growth rate. ρ denotes the axial density, the number of divisions along the X-direction for the S-shaped segment. n is the number of meshes, and the unit is million. PRt is the total pressure recovery coefficient at the outlet.

	Coarse	**Medium**	**Fine**
y^+	1	0.8	0.8
r	1.3	1.2	1.15
ρ	100	200	300
n(M)	0.68	2.5	5.8
PRt	0.9995811	0.9998184	0.9998985

4.2.1 Numerical Validation

Select the Baseline configuration for numerical validation. The speed level takes Speed 10. The computational domain includes the bell mouth and the extrusion section. It should be noted that the simulated bellmouth doesn't include the outward-facing rim at the inlet, and the actual simulated length is 350mm, as shown in Figure 4.5. Figure 4.11 shows the distribution of the mesh blocks. Twelve blocks are inside the duct, four for the central part and eight for the boundary layer.

Three meshes corresponding to coarse, medium, and fine resolutions were used for the mesh independence validation. Table 4.3 shows detailed information about the three meshes and includes the outlet's total pressure recovery coefficient (PRt). It can be observed that although the highest speed level, Speed 10, was selected, all PRts are still close to one, which means a tiny flow loss. Additionally, there is no apparent difference among different mesh numbers' PRts. Therefore, this chapter introduces the velocity profiles at the inlet and the central slices to validate the mesh independence further, as shown in Figure 4.12. u is the velocity along the X direction, and the inlet denotes the inlet of the S-shaped duct segment. It can be found that no matter at the inlet or the central slice, the difference between the medium and fine meshes' velocity distribution is almost neglected, which means the simulated flow inside the S-duct is nearly consistent under these two meshes. Considering saving time, other geometries will use the medium mesh size of this case. The mesh of the extension parts is the same size as the S-shaped segment.

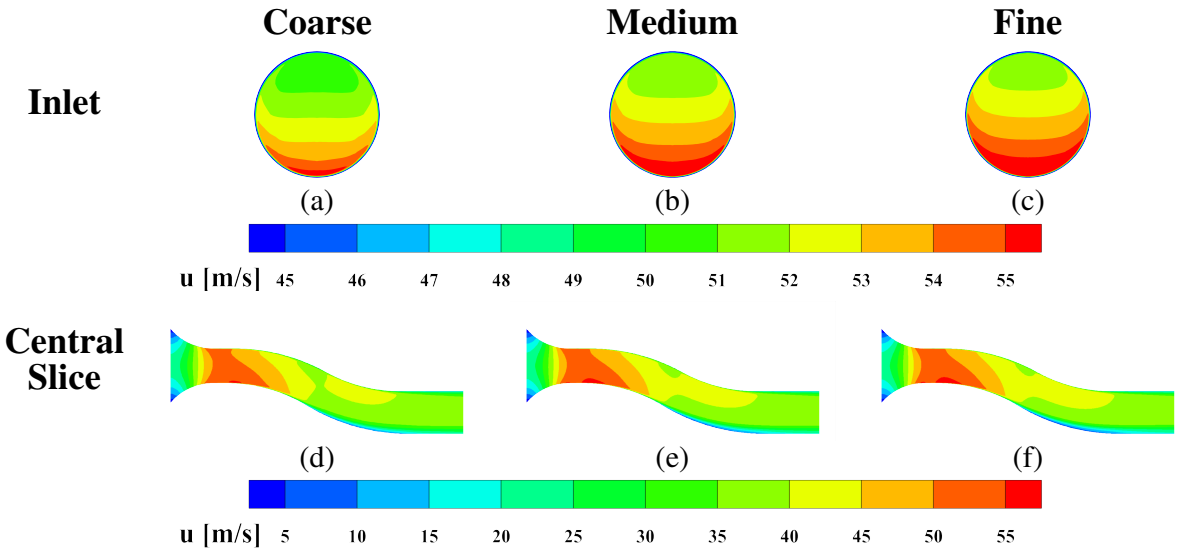

Figure 4.12: The velocity profiles at the inlet and the central slices.

4.2.2 Flow Analysis

Based on the setup in Section Numerical Validation, the simulations of all configurations are conducted under the speed level, 'Speed10'. In general, the boundary layer thickness will significantly influence the position of the flow separation. Therefore, this section first studies the boundary layer thickness of each configuration at the inlet. The boundary layer thickness (δ) takes the definition of Equation 4.6. Here, u_0 is the velocity of the mainstream, so δ is the location where the velocity reaches 99% of the mainstream. However, no fixed mainstream velocity exists because the experiment uses a suction intake system. Thus, ten diameters are taken at the inlet of the S-shaped segment, and each diameter owns 1000 uniformly distributed points. The first diameter starts from 0° and the last starts from 90°, with 10° interval between each diameter. The circumferential angle (θ)distribution is shown in Figure 4.8. Extract each point's velocity and the distance to the circle center (r). If the point is located at the lower part of the inlet, use the sign '-' to mark the distance to the circle center. Take Baseline as the example; Figure 4.13 shows the axial velocity distribution (the X direction) u along r. The maximum velocity that starts from both sides and continues to increase is defined as the mainstream velocity and then takes the location where it reaches 99% of the mainstream as the boundary layer thickness.

$$u(\delta) = 0.99 \times u_0 \tag{4.6}$$

Figure 4.14 shows δ distribution of every configuration. Before adding the front extension, the boundary layer thicknesses at the inlet are relatively uniform, basically around 3-4 mm. Two downstream extension sections do not generate apparent fluctuation on δ. With the addition of the first front extension section, the boundary layer thicknesses become thicker; however, at this moment, δs at different circumferential angles are still relatively uniform. Significant

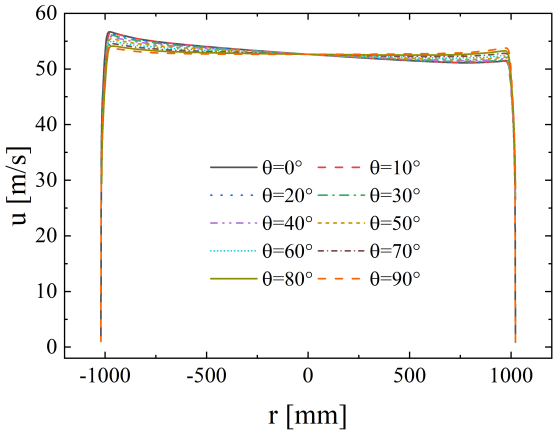

Figure 4.13: The axial velocity profile along the diameters of the inlet.

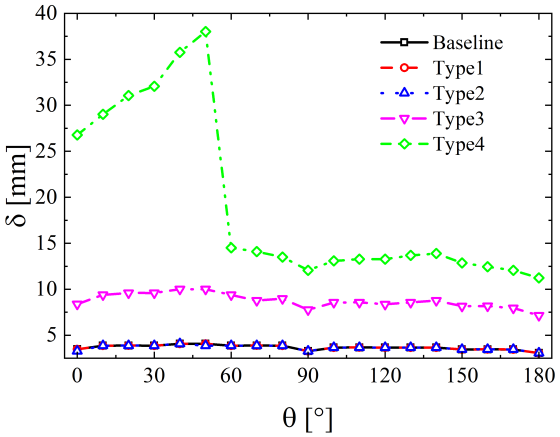

Figure 4.14: The thickness of the boundary layer at the inlet for five configurations under Speed10.

changes occur after the addition of the second forward extension. At this time, the boundary layer becomes thicker and exhibits two distinctly different regions of behavior. The boundary layer at the top becomes very thick and has an increasing trend from the top to the sides. Near the θ=50°, the boundary layer thickness experiences a sharp decrease. To further understand the flow at the inlet of the S-shaped segment, the velocity profiles at different locations for every configuration are introduced, as shown in Figure 4.15. At this moment, it can be intuitively observed that the addition of the rear extension will not significantly increase the thickness of the low-speed region near the inlet boundary, but the front extensions do. Type4 has a significant low-speed region at the inlet top, corresponding to a thicker boundary layer in Figure 4.14. Therefore, it can be found that as the front extension's length increases, the inlet boundary layer thickness becomes thicker. Once the front extension reaches a certain length, the boundary layer thickness will not be uniform anymore. The top will have a significant low-speed region and a thicker boundary layer thickness.

Generally, the thicker the boundary layer, the earlier the flow separation. Here, judge the

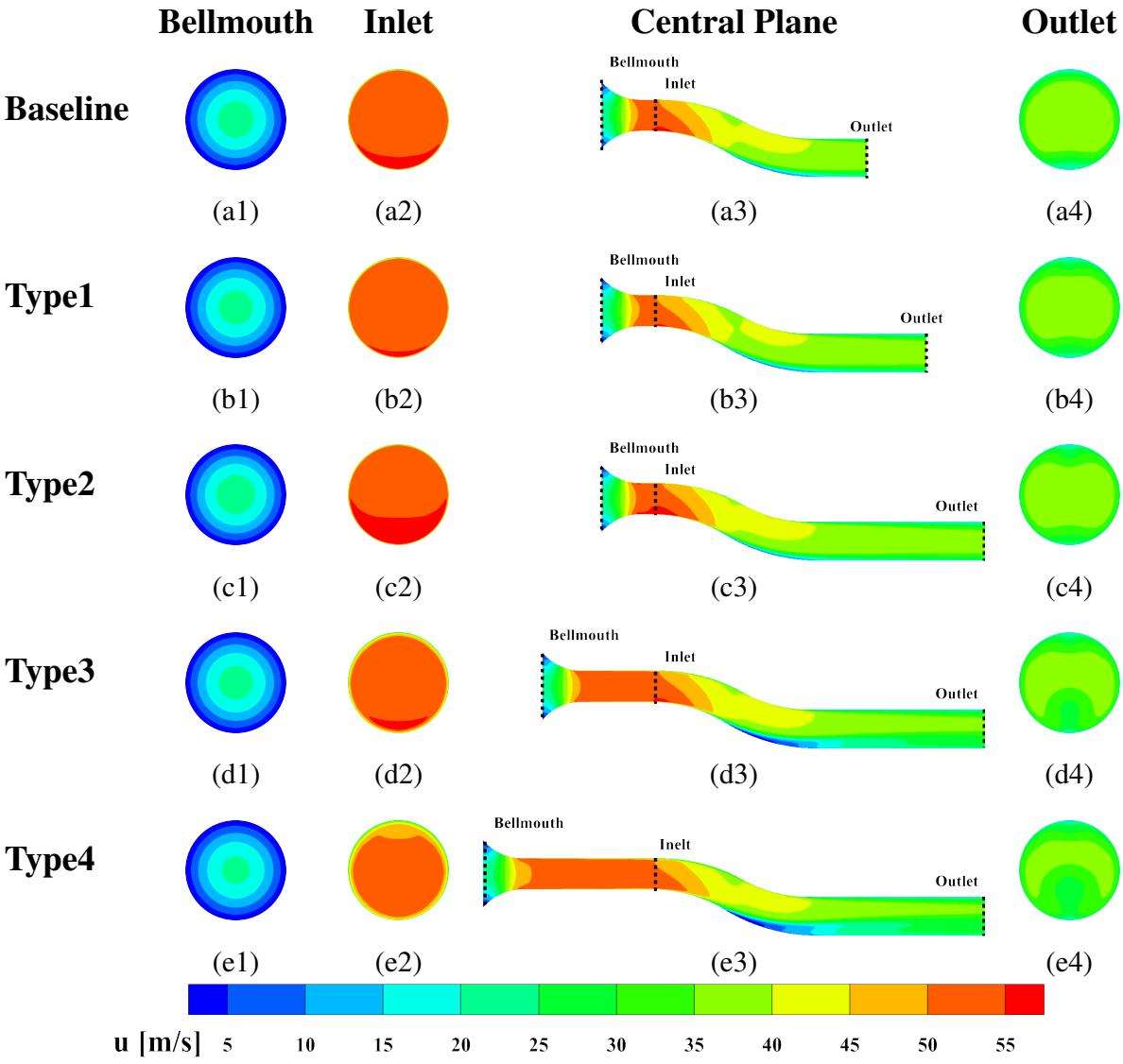

Figure 4.15: The velocity profiles at different locations inside the S-duct. (a) represents Baseline, (b) represents Type1, (c) represents Type2, (d) represents Type3, and (e) represents Type4.

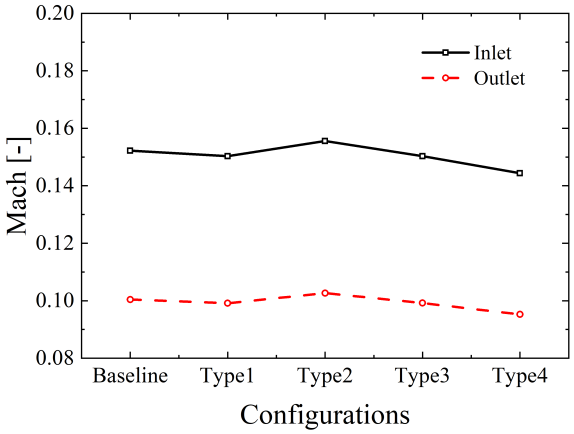

Figure 4.16: The average Mach numbers at the inlet and the outlet for each configuration under Speed 10.

flow separation based on the appearance of the backflow at the central slice. Before adding the front extension, there is no backflow in Baseline, Type 1, and Type 2. The backflow of Type 3 appears at location X=460.7mm, and Type 4 is at location X=439.97mm. This aligns with general expectations; Type 4, with a thicker boundary layer, has an earlier flow separation point. Additionally, according to Figure 4.15, it can be found that the velocity profile at the bellmouth for each configuration is almost consistent but has significant differences at the outlet. A clear trend is that the longer the rear extension, the more pronounced the affected area at the top becomes, with the 35 to 40 m/s contour curving inward from the top toward the center. Similarly, the longer the front extension, the more pronounced the affected area at the bottom becomes, with the 35 to 40 m/s contour curving inward from the bottom toward the center.

Figure 4.16 shows each configuration's average Mach number at the inlet and outlet. It can be seen that the trends at the inlet and the outlet are consistent. Except for Type 2, the configurations with the Mach numbers in descending order are Baseline, Type 1, Type 3, and Type 4, which follow the longer the extension, the lower the Mach number. Generally, Type 2 should also follow this rule, but it doesn't now. Considering Type 2 doesn't appear to have significant extra flow loss compared to Baseline and Type 1, the velocity boundary conditions in the simulation are also set based on the pressure derivation. Therefore, the pressure should be the leading cause for the exception of Type 2. Data in Table 4.2 shows that the environment pressure is significantly higher when measuring Type 2. Higher environmental pressure usually means higher air density; the recorded data in Table 4.2 also proves this. If the fan's rotating speed remains the same, the fan will move more air quality, thus generating a higher pressure difference, as seen in Table 4.2.

4.3 Wall Static Pressure

Wall static pressure is influenced by dynamic and total pressure, where total pressure can be approximated as the local atmospheric pressure, and dynamic pressure depends on the flow velocity at the measurement point. Due to the influence of environmental factors, changes in atmospheric pressure will affect the magnitude of static pressure. Therefore, in the experiment, the difference between the static pressure at the measurement point and the environmental pressure was used to record static pressure. This value can be approximated as the local dynamic pressure (q).

In this experiment, the flow rate was regulated directly through the speed controller on the fan. However, even though the speed controller is set in the same position, differences may exist for each run, thus generating experimental errors. Consequently, this study first investigates the error in flow rate from speed controller performance. Using the Baseline configuration as the test subject, the procedure was initiated three times at each flow rate, with forty data samplings conducted following each initiation.

Next, calculate the uncertainty of the pressure data at a 95% confidence level. The confidence interval (CI) is determined by Equation 4.7, where the confidence level determines the Z_{value}. When the confidence level is 95%, Z_{value} is 1.96. σ represents the sample standard deviation, and n is the number of samples. Then, the uncertainty is normalized with the mean of the dynamic pressure as the baseline. Take the top and bottom of the S-duct as the reference region because the fluctuation of these two regions is more pronounced than that of other locations. Figure 4.17 shows q uncertainties at the Baseline configuration's 0° and 180° positions. It can be seen from the figure that the uncertainty of most 95% confidence intervals is less than 0.3% of the local dynamic pressure, with the highest value reaching only 0.674% of the local dynamic pressure. A low uncertainty indicates that the sample mean represents the population mean well. Based on the uncertainty calculation, the maximum standard deviation is derived to be 3.5% of the mean local dynamic pressure, which still falls within a relatively low range.

$$CI = \frac{Z_{value} * \sigma}{\sqrt{n}} \tag{4.7}$$

4.3.1 Wall Flow Characteristics

The static pressure coefficient, defined by Equation 4.8, characterizes the wall pressure distribution along the S-duct horizontal length. In Equation 4.8, p_s and $p_{s,ref}$ represent the static pressure at the measurement and reference points. q_{ref} is the dynamic pressure at the reference point. The reference point is the center of the inlet (throat), with its value determined by averaging the values at 60° and 120° at $L/D_{inlet} = 0.25$. The change in the C_p has a negative relationship with the flow velocities. The higher C_p, the lower the flow velocity, and vice versa.

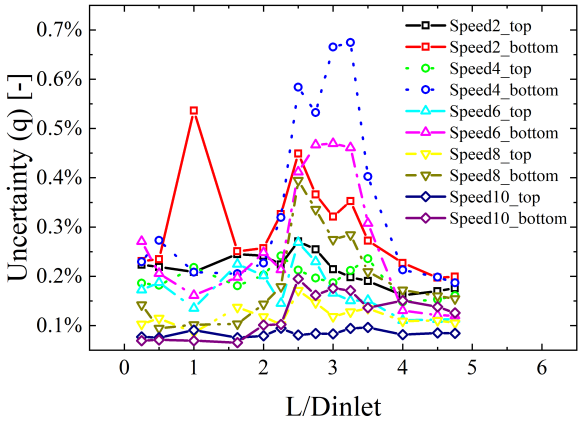

Figure 4.17: The uncertainties of dynamic pressure q at the top and bottom of the S-duct under different flow rates, normalized by the dynamic pressure at the reference point.

If under different flow rates, the smaller the fluctuation range of C_p, the more similar the flow patterns within the S-shaped duct.

$$C_p = \frac{p_s - p_{s,ref}}{q_{ref}} \tag{4.8}$$

Before analyzing the C_p, it is essential to specify the influences of the S-duct geometry. Differing from the general straight duct, the S-duct geometry brings the centerline curvature as well as the diffusion of the cross-section. These two geometry characteristics can significantly influence the flow within the duct. The diffusing cross-section consistently exerts an adverse effect on the flow velocity, while the influence of centerline curvature is more complicated. The curvature of the centerline induces the formation of concave and convex surfaces on the duct walls, with convex surfaces being favorable to flow velocity and concave surfaces being unfavorable. As Figure 4.1 shows, the top initially encounters a convex surface followed by a concave surface, whereas the bottom section first experiences a concave surface followed by a convex surface. Consequently, a significant difference exists in the flow characteristics between the top and bottom of the S-shaped duct. Moreover, the flow interactions between different regions within the duct can not be negligible. Suppose the flow separation or a substantial reduction in velocity occurs at the S-duct's bottom. In that case, it acts like an obstruction, consequently leading to a marked increase in flow velocity at the upper regions.

After airflow entrances the S-duct, the C_p at the top of the S-shaped duct (as illustrated in Figure 4.18 (a)) exhibits a continuous upward trend near the inlet (L/D_{inlet}<1.625). Although the curvature has a beneficial influence on the airflow at the top at this juncture, the persistent rise in C_p indicates that the negative impact of the diffusing cross-section on flow velocity is more significant. Subsequently, in the midsection of the duct (1.625<L/D_{inlet}<3.5), C_p first becomes flat and then declines rapidly. The sharp decline in C_p denotes a substantial increase in flow velocity. In this region, the sole favorable geometric factor contributing to velocity gain at this stage is the centerline curvature. However, the center curvature is not always favorable, even in

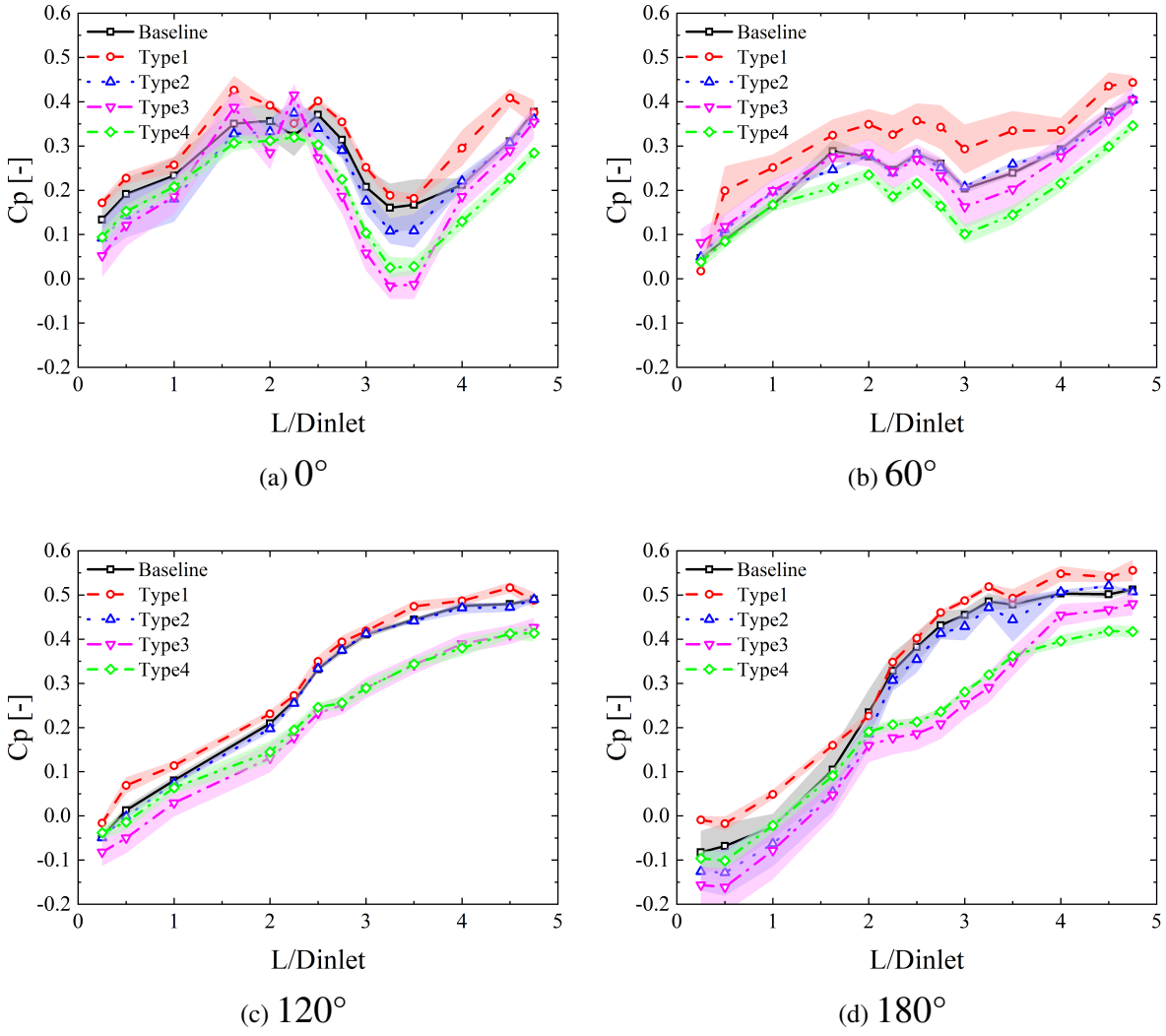

Figure 4.18: Distribution of C_p at different circumferential angles.

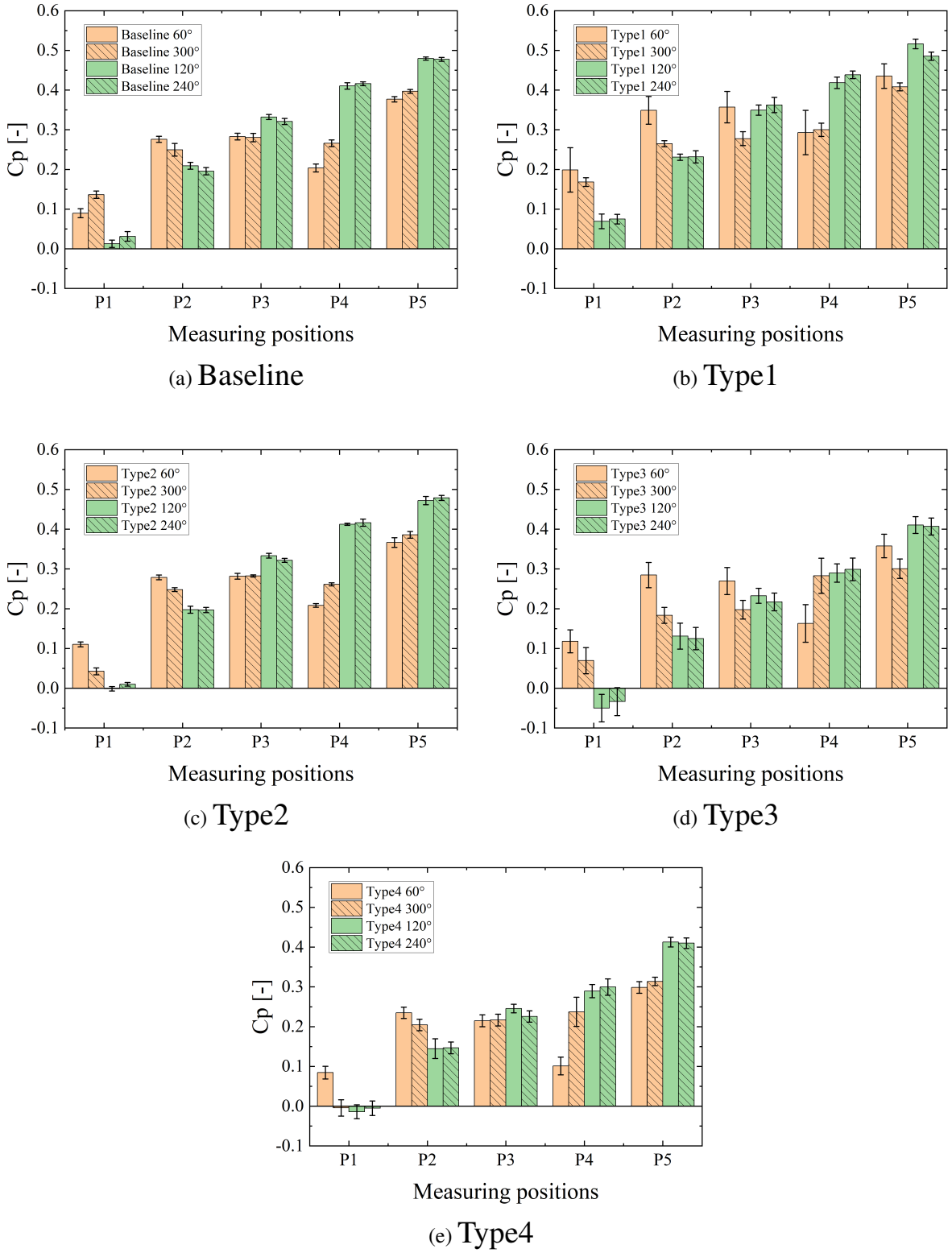

(a) Baseline

(b) Type1

(c) Type2

(d) Type3

(e) Type4

Figure 4.19: C_p at the symmetrical positions on both sides of the S-duct.

this region. After traversing half of the centerline, the influence of curvature on flow velocity becomes adverse. Thus, centerline curvature alone cannot account for the changes in C_p in the top mid-section. At this moment, changing the view to the C_p curve at the bottom, a sharp C_p increase is evident. The rapid increase of C_p means a sharp decrease in the flow velocity. The blockage forming at the bottom is beneficial to the top flow velocity. Therefore, it can be deduced that the blockage forming at the bottom is the primary reason for the acceleration in the top mid-section. After the airflow goes into the end of the S-duct, as the bottom's C_p at this moment levels off ($3.5<L/D_{inlet}<4.75$), the favorable conditions of the bottom to the top disappear. Combined with the effect of the diffusing cross-section and unfavorable center line curvature, the C_p at the top rises again.

At the 60° position, the development trend of C_p curves is similar to that at 0°, exhibiting an initial rise, followed by a plateau, oscillations, a decline, and ultimately, a rise again. A relatively significant change is that, compared to the 0° position, the amplitude of C_p variations at 60° is smaller.

At the 120° position, C_p curves consistently exhibit an upward trend, but there are two different trends. One group contains Baseline, Type1, and Type2; the other combines Type3 and Type4. The primary distinction between these two groups of configurations is the inclusion or exclusion of the upstream extension segment. For configurations with front extensions, C_p at the 120° are relatively smaller, which means higher relative flow velocity at the bottom sides.

At the 180° position, C_p curves also contain two different trends, still corresponding with or without the front extension. However, the differences between bottom's C_p trends are more pronounced, especially in the region of $2 <L/D_{inlet} <3.5$. In the area of $2 <L/D_{inlet} <2.5$, the C_p for Type3 and Type4 configurations approaches a constant value. Considering this region has a diffusing cross-section and unfavorable curvature, C_p should exhibit a noticeable increase. C_p approximating a constant value illustrates flow separation at this location, consistent with the findings of WELLBORN et al. [81]. The bottom blockage formed by flow separation and stall benefits the flow above. As shown in Figure 4.18 (a-c), C_ps of configurations with front extensions (Type3 and Type4) are lower than configurations without extensions (Baseline, Type1, and Type2) at 0° to 120°, which matches the prediction.

Figure 4.19 compares the C_p values at five symmetrically distributed pressure points on both sides of the S-shaped duct to observe the flow symmetry under time-averaged fields. The C_p values in the figure are the average C_p under all flow rates; error bars using the standard deviation are employed to reflect the discretization of C_p values at different flow rates. Across all configurations, the degree of coincidence of C_p values at the bottom (120° and 240°) is notably higher than at the top (60° and 300°), indicating that the flow symmetry at the bottom is significantly superior to that at the top in the time-averaged flow field. Furthermore, the standard deviations for Type 1 and Type 2 are substantially more significant than those of other configurations. Both of these two configurations have only one upstream or downstream extension. Therefore, re-

gardless of whether it is the upstream or downstream extension, if the length of the extension is not sufficiently long, variations in flow velocity can cause pronounced fluctuations in the C_p on the wall surface of the S-shaped duct.

4.3.2 Effects of the Extension Section and the Flow Velocity

As Figure 4.18 shows, the addition of the rear extension section (Baseline, Type1, Type2) will not significantly change C_p tendency, although C_p fluctuates, the tendencies are still quite similar. The main changes occur after adding upstream extensions (Type3, Type4). At this moment, a region where a constant C_p appears at the bottom. Based on the analysis in the last section, this is a flow separation characteristic. Figure 4.20 further demonstrates the change in C_p with the flow velocity. The C_p values in the figures are the mean values of multiple measurements, accompanied by a 95% confidence interval. However, due to tiny confidence intervals, they are almost invisible. It is observable that the flow velocity does not alter the C_p developmental trend within the same configuration, and it only causes C_p to move up or down. The downward shift of the C_p curve indicates the mainstream shifts towards this location, and this location obtains more dynamic energy from the mainstream; conversely, an upward shift in the C_p curve indicates a deviation of the mainstream away from this location.

There are apparent differences between C_p curves of different configurations, and the C_p change tendencies of various configurations with the flow velocity are also different. In the Baseline configuration (Figure 4.20 a-d, without the extensions), an increase in flow rate results in a downward shift of the C_p curves at locations of 0° and 180°, and remain essentially unchanged at 60° and 120°. This change represents the increase in velocity proportion at the top and bottom, and the mainstream shifts towards both the top and bottom, illustrating an expansion in the overall influence range of the mainstream with the flow velocity increases.

With the addition of the first downstream extension segment (Type 1, Figure 4.20 e-h), the impact of flow rate on C_p begins to diminish, and significant changes in C_p are observed only at the upper of the S-duct (at 0° and 60°). The effects of the mainstream weaken at the top and strengthen at the top sides. After adding the second downstream extension segment (Type 2, Figure 4.20 i-l), the influences of flow velocity return to the top and bottom positions again. However, opposite to Baseline, the C_p curves exhibit an upward trend with increasing flow velocity, which means the flow velocities at the bottom and top decrease relative to the mainstream, a tendency for the mainstream influence range to decrease.

In the Type 3 configuration (Figure 4.20 m-p), which adds a front-side extension segment to the Type 2 base, an increase in flow rate results in an upward shift of the C_p curves at 0°, 120°, and 180° within the S-duct, while only a downward shift occurs at 60°. This indicates that as the flow rate increases, the mainstream only strengthens at the upper-middle positions, while the cost is a weakening of influence in other regions.

In the Type 4 configuration (Figure 4.20 q-t), which incorporates all extension segments,

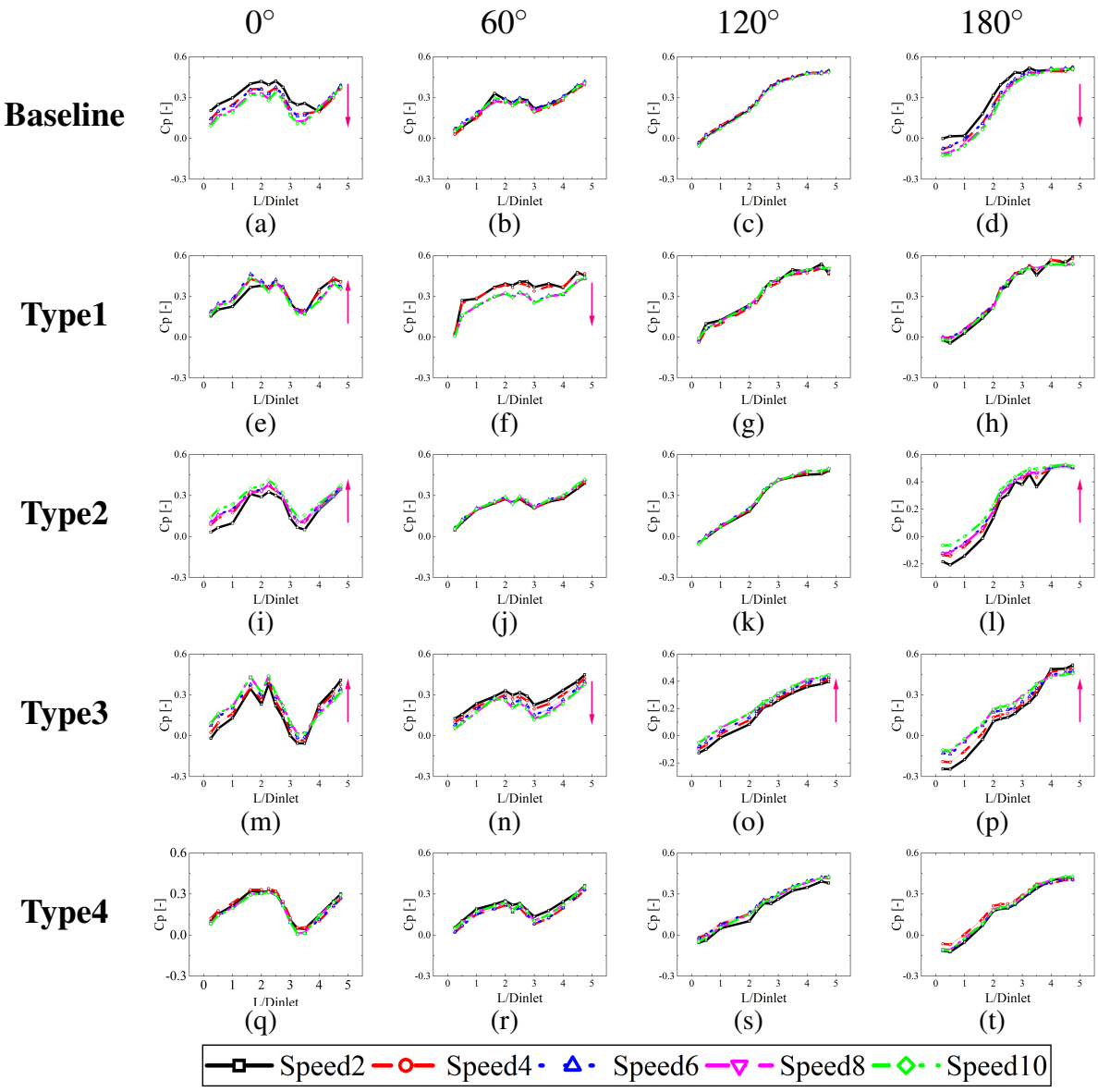

Figure 4.20: C_p distribution of the S-duct with different extension lengths under different flow rates. (a) through (d) represent the Baseline, (e) through (h) represent Type 1, (i) through (l) represent Type 2, (m) through (p) represent Type 3, and (q) through (t) represent Type 4.

the C_p curves at various positions within the S-duct almost completely overlap regardless of changes in flow rate. This indicates that, at this moment, the flow pattern inside the S-duct is highly stable and nearly unaffected by variations in flow rate.

In summary, when the upstream and downstream extensions are not long enough, although the flow velocity does not change the flow pattern within the S-shaped duct, the mainstream's influence range and changing tendency will change with the flow velocity. However, when the S-shaped duct is installed with sufficiently long extension sections both upstream and downstream, the flow pattern within the duct will become very stable, and the flow velocity can almost not even cause the fluctuations of C_p curves.

4.4 Aerodynamic Data at the AIP

4.4.1 Flow Velocity Errors

A higher fan power will generate a faster flow velocity in the S-duct under the same configuration. However, the same fan power for different S-duct configurations does not necessarily mean the same volumetric or mass flow rate. This is because of the differences in aerodynamic resistance for each configuration and the variation in the experiment environment conditions. Here, the coefficient of variation (CV) is introduced to analyze the flow rate error.

$$CV = \frac{\sigma}{mean} \tag{4.9}$$

Coefficient of Variation (CV) is a metric used to measure the relative dispersion of data. The formula for computing the coefficient of variation is presented in Equation 4.9. In this equation, the σ represents the data's standard deviation, and the mean is the dataset's average value. A higher coefficient of variation suggests more significant data dispersion, while a lower coefficient of variation indicates data concentration. Calculating CV helps better understand data dispersion, allowing a more intuitive observation of the flow volume error.

The environmental parameters are presented in Table 4.2. It is observed that the pressure fluctuation range is 2600 Pa, the temperature fluctuation range is 2.2 degrees Celsius, and the density fluctuation range is 0.0339 kg/m3 in the experiment. Variations in environmental conditions lead to differences in air density. Therefore, the effect of the variations in environmental conditions on the fans' performance needs to be identified first.

It is essential to determine whether the measured flow velocity accurately represents the mass flow rate tendency. The average flow velocity takes the mean of 650 measurement points on AIP, multiplied by the air density of the day and AIP's area, which can give the average mass flow rate. Figure 4.21 (a) shows different configurations' mass flow rates on AIP, and their trends are almost identical with the flow velocities (as demonstrated in Figure 4.21 (c)). So, the flow velocity strongly correlates with the mass flow, and the effects of the air density can almost

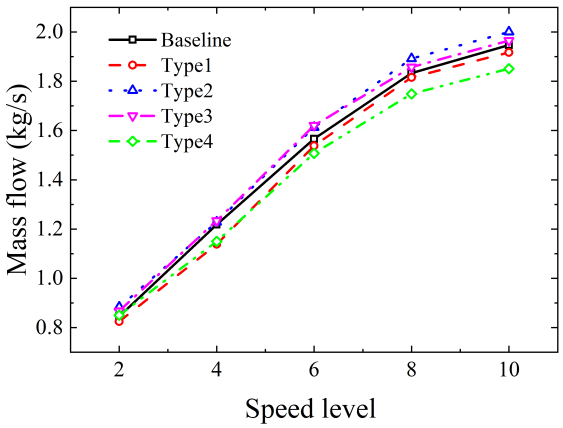

(a) Mass flow for different configurations

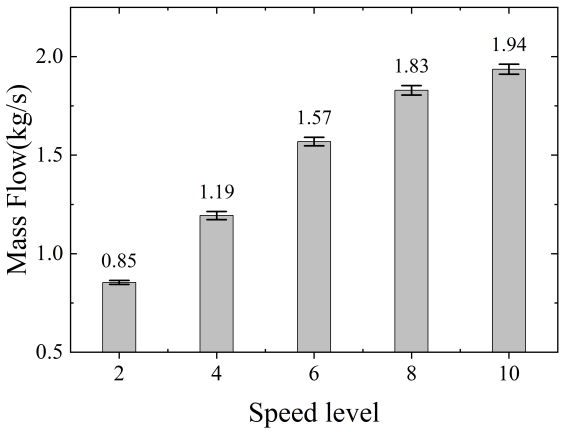

(b) Average mass flow

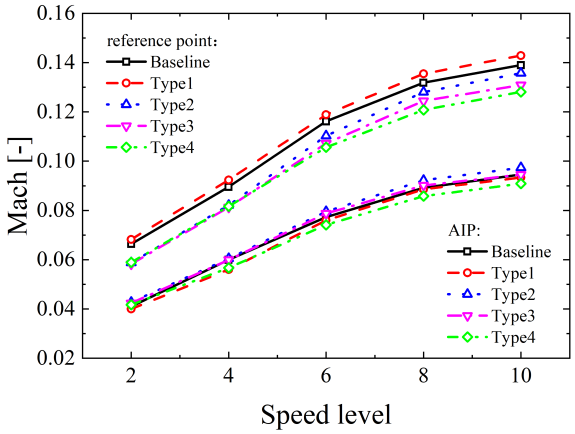

(c) Velocities of AIP and the reference point

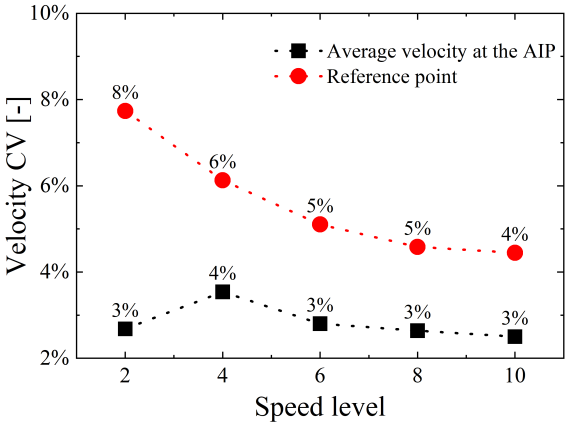

(d) Velocity CV of AIP and the reference point

Figure 4.21: Flow parameters on AIP.

be negligible.

Figure 4.21 (b) shows the average and standard deviation of the mass flow of five configurations under the same fan power. With fan power increases, the standard deviation also clearly becomes greater, apart from the rising mass flow, indicating more significant flow volume differences between different configurations when the flow velocity increases.

Figure 4.21 (c) shows the Mach numbers at the reference point and on AIP, providing a visual representation of the deceleration effect of the diffusing S-duct. Due to apparent geometry differences, there are notable speed differences at the reference point among different extension configurations. Generally, the reference point velocity for the longer duct is lower. This is because longer ducts usually mean higher flow loss. Although most velocity curves of the reference point in Figure 4.21 (c) follow this rule, an exception exists, Type 2. Referring to the content in Section Flow Analysis, this is caused by a higher pressure difference. Also, the interpolation calculates the reference point's value, which has errors. The trends of the outlet velocity are more complicated. However, it can be found that the speed trends of all configurations under Speed10 are entirely consistent with the simulation predictions, which illustrates the experimental data is consistent with the simulation prediction. This further verifies the accuracy of the experimental data from a different perspective. In Figure 4.21 (c) from Speed2 to Speed 8, a more general trend is Type 2 >Type 3 >Baseline >Type 1 >Type 4. (descending Mach numbers), which is increasingly divergent from the general prediction Baseline >Type 1 >Type2 >Type 3 >Type 4. However, by analyzing the trend of environmental pressure variations during the measurement, the average Mach number at the outlet shows a strong correlation with the trend of environmental pressure changes, as illustrated in Figure 4.22. The only exception to this correlation is the Baseline under Speed 6.

Figure 4.21 (d) shows the CV trend with the flow velocity. As the flow velocity increases, the CV trend at the reference point decreases from 8% to 4%, indicating that the higher the flow velocity, the lower the reference point velocity differences between different configurations. The velocity CV consistently ranges between 3% and 4% on AIP, which means that the flow volume differences brought by different configurations are similar under different flow velocities.

Therefore, due to the intrinsic design of the experiment, even though the fan serving as the air source is set to the same power, the flow rate conditions corresponding to each configuration are different. The influence of the experimental environment cannot be negligible, with the primary variations arising from the environmental pressure. The impact of the extension segment length on air intake volume is similar across different flow rates but significantly disrupts the velocity magnitude at the reference points, particularly at lower flow rates.

4.4.2 Velocity Components at the AIP

Figures 4.23-4.25 show the velocity component coefficient distribution at the AIP in the time-averaged field. u represents the axial velocity coefficient (x direction), v represents the horizontal

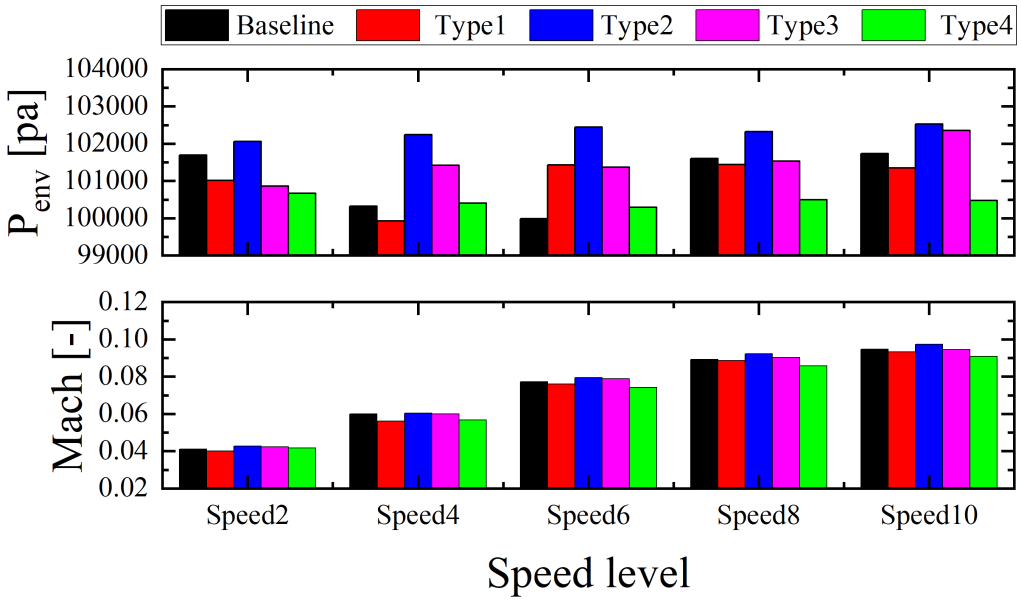

Figure 4.22: The trends of the environment pressure and the Mach number for each configuration under different speeds.

velocity coefficient at the AIP (y direction), and *w* denotes the vertical velocity coefficient (z direction). The axial velocity coefficient, *u*, shows the overall outline of the mainstream flow at the outlet interface, while *v* and *w*, representing the traverse velocity coefficients, are primarily used to assess the magnitude of secondary flows at the AIP. The experimental data were processed using Tecplot software. Data from 650 measurement points were interpolated in a semicircle region and subsequently mirrored to obtain a complete distribution of *uvw* over the AIP.

In terms of the streamwise velocity, it can be found that the flow velocity has a relatively small influence on the velocity profile at the AIP based on Figures 4.23. The axial velocity contours for the same configuration are slightly different under various flow velocities. The extension segment length primarily brings the change in the velocity profiles. Regarding the value magnitude, at the same speed level, Type 3 > Type2 > Type 4 > Baseline > Type 1. However, this cannot obtain some practical conclusions due to the unstable reference point velocity. Regarding the profile shape, the regions of significant changes are located at the top and bottom. At the top, with the addition of the downstream extension section, the top affected region becomes more significant. The single upstream extension section slightly expands the top affected area; however, with the second upstream extension section, the original top affected region changes its tendency to develop to the circle center and exhibits stratified features instead. At the bottom, the affected area will not be apparent until all upstream extension sections are added. This characteristic corresponds to the C_p curve in Figures 4.18 (d) and 4.20 (t), a flow separation characteristic (constant C_p) appears on the bottom C_p curve only after two upstream extension sections are installed.

In terms of the cross-flow, it can be found that flow velocity has a small influence on the

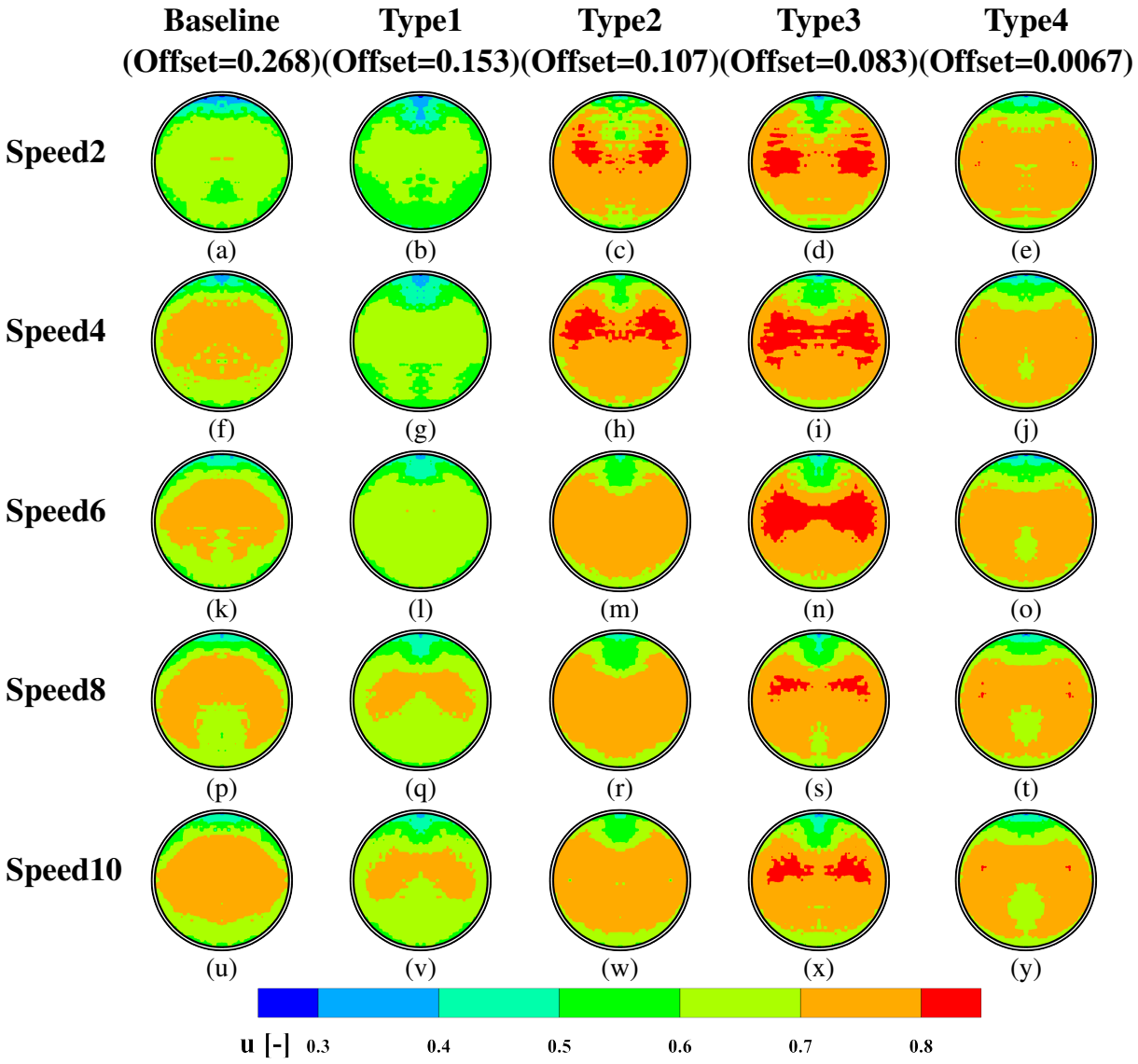

Figure 4.23: Time-averaged axial velocity component u at the AIP, normalized by the velocity at the reference point. 650 measurement points are in the left half, and the right half is the mirroring data. (a) through (e) represent Speed2, (f) through (j) represent Speed4, (k) through (o) represent Speed6, (p) through (t) represent Speed8, and (u) through (y) represent Speed10. The vertical axis is for each configuration.

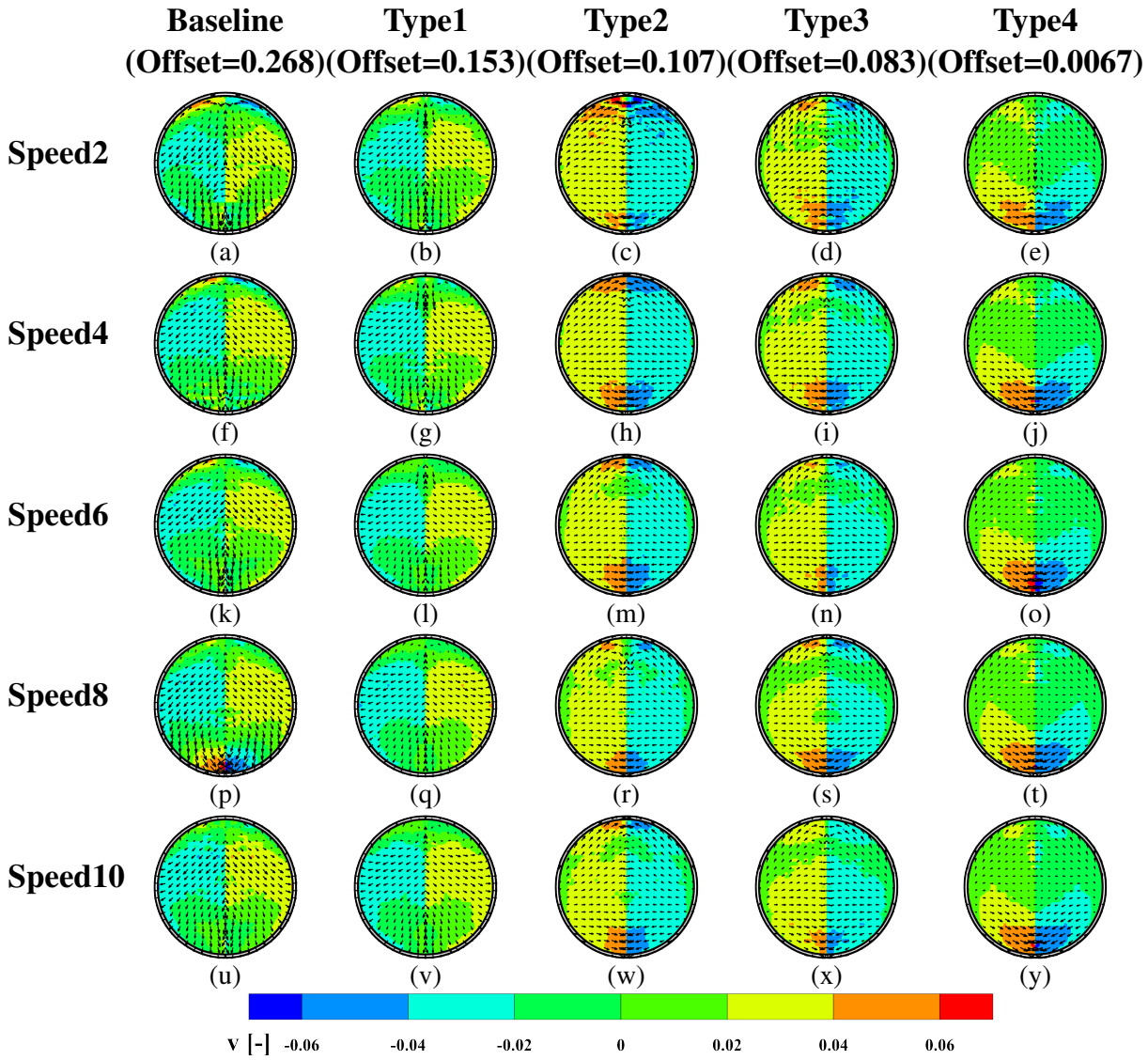

Figure 4.24: Time-averaged horizontal velocity component v at the AIP, normalized by the velocity at the reference point. 650 measurement points are in the left half, and the right half is the mirroring data. (a) through (e) represent Speed2, (f) through (j) represent Speed4, (k) through (o) represent Speed6, (p) through (t) represent Speed8, and (u) through (y) represent Speed10. The vertical axis is for each configuration.

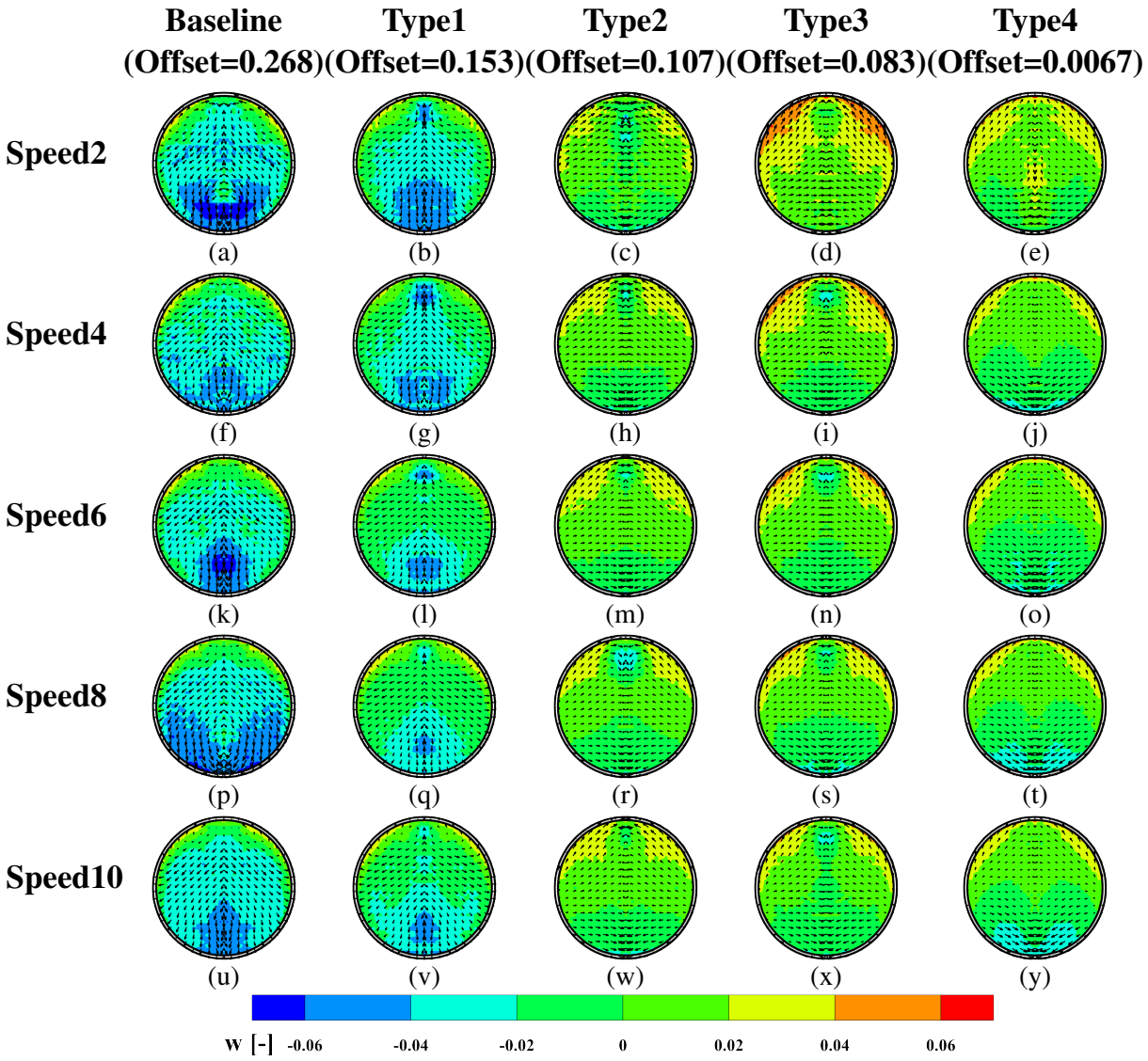

Figure 4.25: Time-averaged vertical velocity component w at the AIP, normalized by the velocity at the reference point. 650 measurement points are in the left half, and the right half is the mirroring data. (a) through (e) represent Speed2, (f) through (j) represent Speed4, (k) through (o) represent Speed6, (p) through (t) represent Speed8, and (u) through (y) represent Speed10. The vertical axis is for each configuration.

horizontal velocity component but a significant influence on the vertical velocity component based on Figures 4.24-4.25. However, the influences of the flow velocity on the vertical velocity component are not fixed. Three motion patterns in Figure 4.25 are delineated by configurations Type1 and Type3, respectively. In configurations with no extension and shorter rear extension segments (Baseline and Type1), the area of high w values expands with increasing flow velocity. However, after the addition of the second rear extension segment, the area of high w values begins to contract with increasing flow velocity (Types 2&3), and the cross-flow direction is opposite to that of Baseline & Type1. The increase in the downstream extension length changes the cross-flow directions. Combined with the flow direction, it can be deduced that airflow bounces down and up after it leaves the S-shaped duct section and will change the direction of rotation of the vortex on the AIP. When both the forward and rear extension segments (Type4) are sufficiently long, the magnitude and distribution of w almost don't change with variations in flow velocity, which also exists in the u and v distributions.

4.4.3 Pressure and Swirl Distortion

The total pressure distortion coefficient (DC) and swirl distortion coefficient (SC) for each sector of the AIP are presented in Figures 4.10 and 4.11. Each sector spans 30 degrees. DC and SC are defined by Equations 4.10 and 4.11. In Equation 4.10 [92, 93], DC_θ represents the total pressure distortion coefficient of the sector corresponding to angle θ. $P_{t,AIP}$ is the average total pressure at the AIP interface. $P_{t,\theta,min}$ represents the minimum total pressure in the sector where the angle is θ. q is the average dynamic pressure at the AIP. In Equation 4.11 [96], SC_θ is the swirl distortion coefficient of the sector corresponding to angle θ. $U_{crossflow,\theta,max}$ represents the maximum crossflow velocity at the sector where the angle is θ. $U_{centerline,throat}$ is the velocity at the reference point. The values of DC and SC take the average across five different velocities. The error bars represent the DC and SC standard deviation at these five velocities, indicating the variability of distortion coefficients under different flow rates.

$$DC_\theta = \frac{P_{t,AIP} - P_{t,\theta,min}}{q_{AIP}} \tag{4.10}$$

$$SC_\theta = \frac{U_{cf,\theta,max}}{U_{ref}} \tag{4.11}$$

DC demonstrates a consistent trend on AIP across all configurations. Initially, there is a decline starting from the top (30° sector), stabilizing in the middle region (90° to 150°), and culminating with a slight increase at the bottom (180°). The incorporation of extension sections does not significantly impact the tendency of DC; it merely causes localized fluctuations. DC maintains a dynamic equilibrium on AIP, exhibiting a compensatory behavior as depicted in Figure 4.26; an increase in one area corresponds to a decrease in another. For instance, with the addition of a downstream extension section (Type1), DC rises in the upper section of the

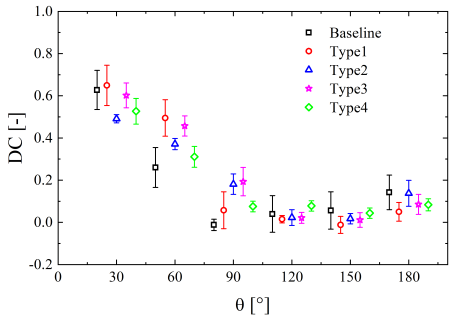

Figure 4.26: Pressure distortion coefficient *DC* at the AIP.

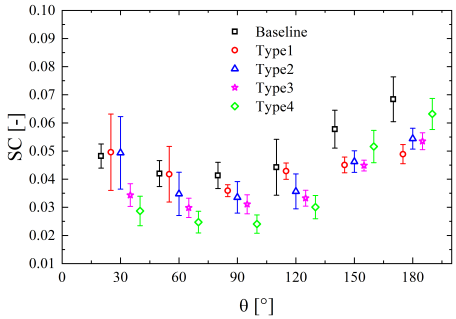

Figure 4.27: Swirl distortion coefficient *SC* at the AIP.

AIP (30° to 90°) but declines in the lower section (120° to 180°). Analysis of the DC standard deviation reveals that in the absence of rear extension sections, or when the rear extension is short, the changes in flow velocity can significantly influence DC's size in every sector region without changing its tendency. When both the front and rear extension segments of the S-shaped duct are sufficiently long, the influence of the flow velocity on DC value is only in the upper region of the AIP (30° to 60°).

Similar to the DC, in all configurations, the SC demonstrates a comparable trend on AIP, with a decrease from the top (30° to 90°) and an increase from the middle region (90°), reaching maximum values at the bottom (180°). There is a discernible trend in the upper and middle regions of the AIP (30° to 120°), where SC keeps decreasing as the extension length increases. This indicates that adding the extension section diminishes the secondary flow in these regions. Although the bottom's SC doesn't show a clear trend, if excluding the Baseline, it can be found that there is a slightly increasing trend from Type 1 to Type 4, suggesting that with the increase in extension length, the intensity of the secondary flow at the bottom also increases.

By examining the SC standard deviation, it can be observed that flow velocity significantly influences SC. However, the regions affected considerably vary with different extension lengths. For the Baseline, the region with the most significant influence is located at the sector of 120°, the lower middle region on AIP. For configurations with rear extension sections (Types 1 and 2), the most pronounced fluctuations occur at the top (sectors of 30° and 60°). With the addition of the front extension, the influence of flow velocity becomes relatively uniform across each sector

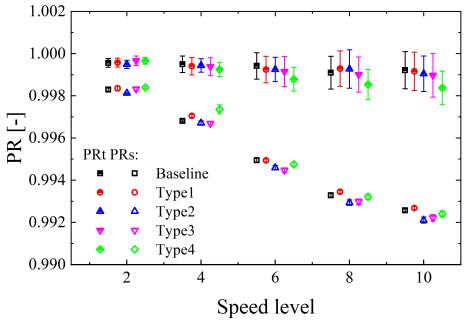

Figure 4.28: PR_t and PR_s at the AIP under different flow rates.

(Types 3 and 4).

4.4.4 Pressure Recovery

The total pressure recovery coefficient (PR_t) and the static pressure recovery coefficient (PR_s) are defined by the Equation 4.12. Figure 4.28 shows the PR_t and PR_s for various configurations of S-shaped ducts at different flow rates, as measured at the AIP. The values of PR_t and PR_s are obtained by averaging the measurements from 650 points on the AIP. Error bars are the standard deviation, characterising the discretisation of pressure data within the AIP.

$$\begin{aligned} PR_t &= \frac{P_{t,AIP}}{P_{t,o}} \\ PR_s &= \frac{P_{s,AIP}}{P_{t,o}} \end{aligned} \tag{4.12}$$

where $P_{t,AIP}$ and $P_{s,AIP}$ are respectively the total and static pressure at the pressure measurement point of the outlet.$P_{t,o}$ is the total pressure of the free stream.

In Figure 4.28, it is observed that with increasing flow velocity, there is a pronounced decline in the PR_s on the AIP, whereas the PR_t exhibits only a slight decrease, which aligns with general expectations. As the flow velocity increases, the dynamic pressure rises, and the static pressure decreases, resulting in a decline in PR_s. Additionally, flow losses increase with rising flow velocity, leading to a modest downward trend in PR_t. The range of standard deviations further indicates that the discretisation of PR_t on the AIP is high, whereas that of PR_s is low, suggesting a uniform distribution of static pressure and a non-uniform distribution of total pressure on the AIP. Figure 4.29 illustrates the distribution of the *PRt* on the AIP. The static pressure distribution on the AIP is relatively uniform, so the variations in total pressure distribution primarily depend on dynamic pressure distribution. Consequently, the distribution of PRt closely resembles that of the axial velocity u.

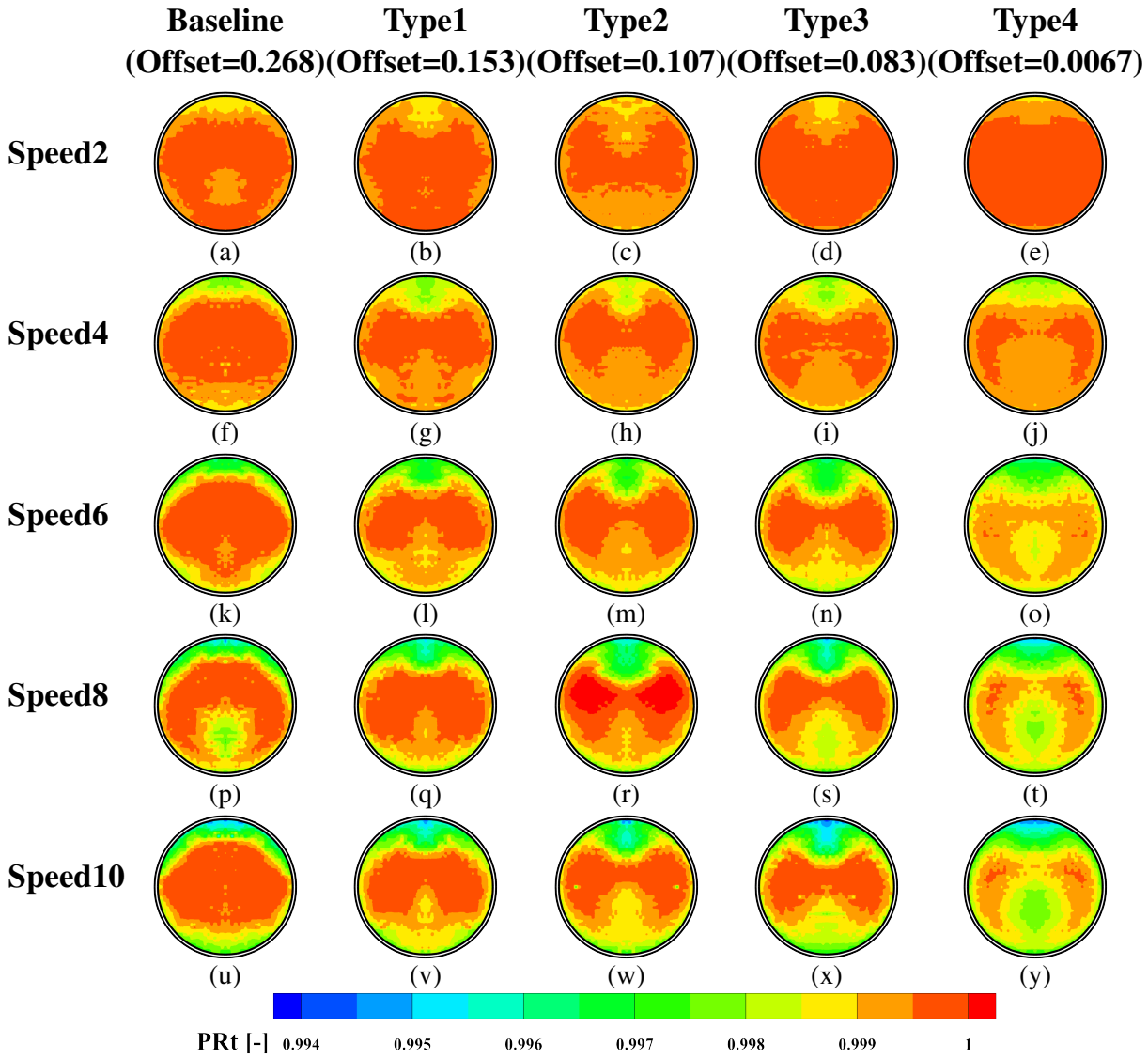

Figure 4.29: Total pressure recovery coefficient (PR_t) distribution at the outlet plane. 650 measurement points are in the left half, and the right half is the mirroring data. (a) through (e) represent Speed2, (f) through (j) represent Speed4, (k) through (o) represent Speed6, (p) through (t) represent Speed8, and (u) through (y) represent Speed10. The vertical axis is for each configuration.

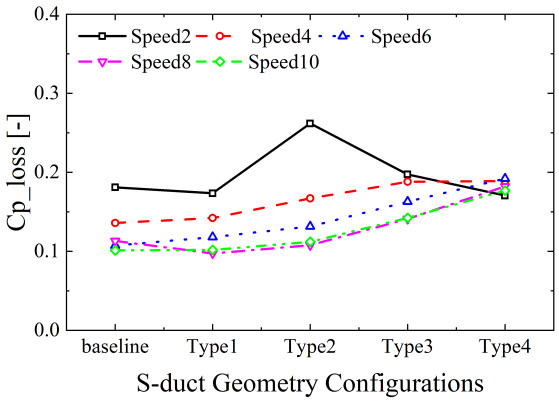

Figure 4.30: Total pressure loss coefficient distribution at the outlet plane.

4.4.5 Pressure Loss

Flow losses are related to dynamic pressure, and at meager Mach numbers, dynamic pressure constitutes only a tiny portion of the total pressure. This results in minimal flow losses, causing PR_t to approach 1 in Figure 4.29. Despite the observable PR_t distribution in the figures, the proximity of all PR_t values to 1 makes quantitative analysis challenging. Additionally, the influence of ambient pressure cannot be overlooked. As indicated in Section Flow Velocity Error, the ambient pressure exhibits up to 2600 Pa fluctuations, and the dynamic pressure corresponding to the highest flow velocity in this experiment is just over 1000 Pa. Therefore, introducing a new dimensionless parameter, the total pressure loss coefficient $C_{p,loss}$, is necessary to quantify total pressure recovery performance and mitigate the effects of low total pressure loss and low dynamic pressure, especially in scenarios with low Mach numbers. Equation4.13 defines $C_{p,loss}$ [148]:

$$C_{p,loss} = \frac{P_{t,ref} - P_{t,AIP}}{q_{ref}} \tag{4.13}$$

where $P_{t,ref}$ represents the total pressure at the reference point, and here directly uses the value of the freestream total pressure. $P_{t,AIP}$ denotes the average total pressure at the AIP. q_{ref} is the dynamic pressure at the throat.

As shown in Figure 4.30, the general tendency is $C_{p,loss}$ increases with the addition of the extension section but decreases with the increasing flow velocity. The decrease of $C_{p,loss}$ as the flow velocity increases means the proportion of the flow loss to the reference point dynamic pressure decreases. Based on Figure 4.28, it can be known that flow losses will slightly increase with the rise in flow velocity. Therefore, it can be deduced that as the flow velocity increases, the magnitude of the dynamic pressure rising at the reference point is higher than that of the flow losses increasing inside the duct.

At extremely low flow velocities, the $C_{p,loss}$ for various configurations clearly shows a different tendency than higher flow velocities. When the flow velocity is at Speed 2, the $C_{p,loss}$ for various configurations almost falls within the same range except for Type 2. According to

Section Flow Velocity Errors, it is known that the Type 2 configuration can have the maximum pressure difference and air intake under the same fan power. Therefore, one possible reason for the higher $C_{p,loss}$ for Type 2 observed at Speed 2 is that although the increased air intake increases dynamic pressure at the reference point, the corresponding increased pressure loss is more significant under the extremely low flow velocity.

4.5 Conclusion

This chapter investigated and discussed the physical characteristics of the S-shaped ducts, focusing on flow velocities within the low Mach number range, with reference point velocities ranging from 0.06 Mach to 0.15 Mach. The effects of flow velocity and the influence of extension sections on both the upstream and downstream sides of the S-duct were extensively analyzed. The principal conclusions drawn are as follows:

(1) The flow symmetry of the suction-type S-duct at the bottom is superior to that of the top. The addition of the rear extension will not significantly change the flow pattern inside the S-duct, but the front extensions will, especially at the duct bottom. After the airflow exits the S-shaped segment, it initially maintains a downward motion trend due to inertia. After encountering the lower wall surface, it is deflected upward. Meanwhile, the direction of the vortices on the cross-section changed. Consequently, the length of the downstream extension section determines the direction of the secondary flow at the AIP.

(2) Although each S-duct configuration exhibited similar flow patterns under different flow velocities, variations in the wall C_p indicated that the mainstream's influence on different regions within the duct changed with velocity. However, changes in flow velocity could no longer affect the flow pattern within the duct, and the mainstream's shape and size could remain stable when the upstream and downstream ends of the S-shaped duct were equipped with sufficiently long extension sections.

(3) On the AIP, the areas with the most severe pressure and swirl distortion were different; the maximum values of *DC* were located at the top, while the maximum values of *SC* were found at the bottom. Flow velocity did not significantly affect pressure distortion but significantly influenced swirl distortion. Regarding the pressure distribution, the trend in total pressure distribution essentially depended on the dynamic pressure distribution. Static pressure distribution on the AIP doesn't change as the flow rate increases and remains uniformly distributed. Additionally, as flow velocity increased, although flow losses within the duct gradually increased, the proportion of these losses relative to the dynamic pressure at the reference point progressively decreased.

The conclusions above have significant reference values for designing and optimising subsequent S-shaped air intakes. The relevant experiment design can also reference the findings in

this chapter. Additionally, the data obtained in the experiments served as boundary conditions for numerical simulations and aided in further validation and optimisation.

However, the limitations of this experiment cannot be ignored. First, it used a square measurement region rather than a conventional circular tube. Although this approach facilitates a more diverse method of pressure measurement, it is evident that the crossflow system used in this experiment induces significant flow asymmetry. While some optimisations were made during the experiment, they came at the cost of data completeness, as only half of the AIP was measured. Additionally, the measurement area, which is significantly larger than the duct itself, also adversely affects the symmetry of the flow. Second, this experiment used an axial flow fan as the power source. As a result, any errors introduced by the experimental environment, as well as the inherent errors of the fan itself, are accumulated in the experiment. Last, due to the segmented design of the S-shaped duct model, the likelihood of air leakage is increased. Although all connections and measurement areas were sealed with tape, the possibility of leakage still exists due to the lack of detection methods. Air leakage could reduce the airflow provided by the fan to the S-duct, thereby introducing additional errors. The limitations mentioned above should be addressed in future work.

In the next chapter, an in-depth study will be conducted on the turbulent characteristics of the Type 4 configuration under different flow velocities.

Chapter 5

Turbulence Study of the S-duct

The previous Chapter investigated the impact of flow velocity and extended length within an S-shaped duct. In subsequent research, numerical simulations will be employed to visualize the duct's internal flow field, complemented by various modal analysis methods for data analysis. Before conducting these numerical simulations, it is crucial to determine an appropriate time recording interval. The time step for unsteady simulations is typically tiny to ensure computational stability and avoid divergence. Recording data at every time step may not only be unnecessary but could also significantly increase the data processing time. In this chapter, a constant-temperature anemometer will be employed to investigate the turbulence characteristics at the AIP interface of the S-duct and determine a suitable time scale for analysis. The experimental model utilizes the Type 4 configuration detailed in the preceding section, encompassing all extensions.

5.1 Experiment Setup

As depicted in Figure 5.1, the experimental schematic primarily consists of an S-duct model, a measurement area, and a power source. In this experiment, an axial fan served as the air source.

5.1.1 Measurement Instruments

Measurement instruments contain a pressure measurement kit and a CTA experiment kit. The measurement probes of both setups are mounted on a traverse system during the experiment. The traverse system consists of two stepper motors(MS200HT2, manufactured by Schrittmotor-modul Company, lead screws, and linear rails. It can move on a two-dimensional plane. The control of the traverse system can be carried out via Matlab or CTA software.

The pressure measurement kit contains a seven-hole probe, a pressure reading system, and a connecting hose. The supporting software is Matlab, which reads and saves pressure data. The

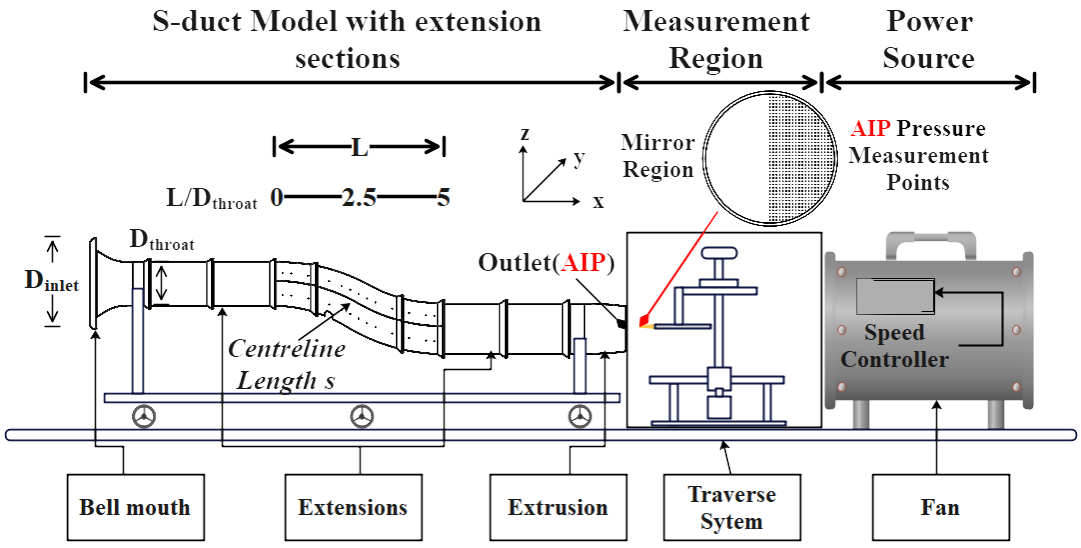

Figure 5.1: The schematic of the experimental setup. "Reproduced from Jiang, F., Kontis, K., and White, C. (2024). Experimental analysis of flow characteristics in S-shaped ducts at low speeds. Physics of Fluids, 36(10), with the permission of AIP Publishing."

seven-hole probe, just like its name, has seven holes on its probe head. It is the result of a joint research effort between NASA-Ames and the U.S. Air Force Academy. Through more measurement holes, it can handle more complex flow fields and has a maximum angle of attack of up to 70*circ*. For detailed principle and calibration methods of the seven-hole probe, please refer to Everett and Durston [102]'s study. The pressure reading system is a ZOC series manufactured by Scanivalve, containing an ERAD4000 A/D base and one module with 32 channels.

The CTA experiment kit took the StreamLine Pro CTA system manufactured by Dantec. It primarily consists of a frame controller, the CTA anemometer modules, an automatic calibrator, and accompanying software. The hot-wire probe used is of model 55P11, with its core component being a tungsten wire measuring 5 micrometers in diameter and 1.25 millimeters in length. This probe is suitable for one-dimensional flow measurements in low-turbulence intensity conditions. The traditional hot-wire anemometer measures flow velocity based on heat conduction and convection principles. As the fluid flows past the hot wire, some heat is dissipated. The rate of heat loss is directly proportional to the flow velocity. However, due to the thermal inertia effects of the wire, the response time and measurement accuracy of the hot wire will be affected. The design philosophy of the Constant Temperature Anemometer (CTA) aims to eliminate the thermal inertia effects of the wire during flow measurement, thereby ensuring that the electronic circuitry predominantly determines the output signal. This will significantly improve the hot-wire anemometer's response time and measurement accuracy. The method to achieve this involves supplying the metal wire with electrical energy at the same rate as it transfers heat to the surrounding medium. This approach maintains a constant temperature of the metal wire regardless of the changes in flow velocity, significantly reducing the effects of the thermal inertia

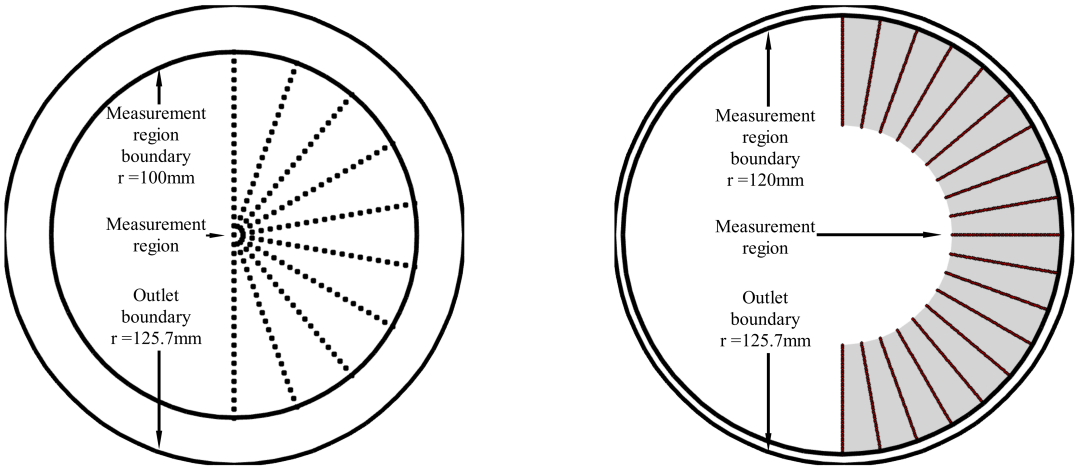

(a) (b)

Figure 5.2: The measurement points distributions in CTA experiments. (a) is used to determine the sampling period and frequency. (b) is for further turbulence study.

(thermal capacity) of the metal wire.

5.1.2 Experiment Description

During the experiment, a support with a sieve was placed in front of the bell mouth to make the incoming flow more uniform. The S-duct was supported by an aluminum alloy shelf. As the power source, the fan (the EQ511467 model manufactured by Flakt Woods Ltd) was equipped with a speed controller (the ME1.12 model produced by Flakt Woods) to control flow velocities inside the S-duct. The scales on the speed controller range from 1 to 10, and 'Speed X' below represents the different speed scales on the speed controller.

In the pressure measurement experiments, the measurement plane, namely the aerodynamic interaction plane (AIP), is the plane at the rear of the outlet with a 5mm gap to avoid potential collisions. During the experiment, it was discovered that the traverse system would move to the middle of the fan and the S-duct outlet, thus interfering with the measurement. To reduce this influence, a frame was designed to connect the pressure probe to the traverse support to prevent the support from being located in the middle of the fan and the outlet. However, due to the limitation of the space of the measurement region, the frame can only guarantee that the measurement in half the area of the outlet will not be affected. Based on a lot of prior research [81, 84–86], it can be found that aerodynamic data at AIP is usually centrally symmetrical. Therefore, only half of AIP was measured, and then the data was mirrored to obtain the whole plane data. The measurement point distribution is shown in Figure 5.1. There is a 6-mm spacing between every point

in horizontal and vertical directions starting from the circle center. The boundary is the circle, which has the AIP's circle center and a radius of 120 mm, including the boundary. There are 650 pressure measurement points in total. Measurements are conducted under five flow velocities: Speed 2, 4, 6, 8, and 10. The S-duct's diffusion rate takes the linear growth. The detailed results and analysis of the pressure measurement experiments (including the experiment errors) can reference the author's prior publication [149], and this chapter only involves some pressure data, which can provide the boundary conditions and validate the simulations.

The setup of the CTA experiment is quite similar to that of the pressure measurement experiment. The main difference is that a hot-wire probe replaces the seven-hole probe. The corresponding accessories and supporting software have also been replaced. To select an appropriate sampling period and frequency, under the Speed10 condition, the sampling period was fixed at 1 second, with sampling conducted at 1 kHz, 10 kHz, 60 kHz, and 100 kHz. Similarly, under the Speed10 condition, with a fixed sampling frequency, the sampling periods of 1s, 2s, and 4s were tested at sampling frequencies of 1 kHz and 60 kHz. Figure 5.2 (a) illustrates the measurement points on the AIP. The measurement area is also the right half of the outlet (from the perspective of an observer standing behind the outlet, facing it), with the center of the outlet interface serving as the starting point. The points are arranged at 20° intervals in the circumferential direction and include 21 points in the radial direction (including the center point). The right half of the AIP is exclusively measured because when measuring the left half, the vertical axis of the traverse system would be positioned between the outlet interface and the suction fan, significantly influencing the flow field.

Ultimately, measurements were taken at a sampling frequency of 1 kHz and a sampling period of 1 second across five different speeds. The center point of the outlet was selected as the observation point to evaluate the measurement error in the CTA experiment. Data were intermittently collected three times at the center point with a sampling frequency of 1 kHz and a sampling period of 1 second. The test velocity was set to Speed2. The fan was turned off between measurements, and the speed controller was reset to zero. Before the subsequent measurement, the speed controller was adjusted back to Speed2, and the fan was turned on. This approach is used to evaluate the system error. The results indicated that the turbulence intensity error was less than 3% (the difference between the maximum and minimum values of the three measurements, divided by the mean value). However, due to the design of this experiment, experimental errors caused by environmental factors are unavoidable. For instance, changes in atmospheric pressure can significantly affect the fan's performance (this was discussed in detail in the author's previous research [149]), and temperature variations can influence the measurements of the CTA. Nonetheless, considering the significant differences in flow rates across the five test velocities, this portion of experimental error should be acceptable in the context of this study. A quantitative analysis of these experimental errors will be addressed in future work. At the final measurement scheme, the total number of measurement points on AIP was 589. The

Table 5.1: Flow and experimental environment parameters. P_{env} represents the environment pressure; T denotes the temperature; ρ is the air density; P_{ref} is the dynamic pressure at the reference point (L/D=0.25); P_{avg} is the average static pressure at the AIP (the value is the difference with the environment pressure); $\dot{m}$ represents the mass flow rate.

Velocity Level	P_{env} (Pa)	T (°C)	ρ (kg/m3)	P_{ref} (Pa)	P_{avg} (Pa)	M_{out}	$\dot{m}$ (kg/s)
Speed2	100669	21.35	1.1917	245.352	-160.29	0.041711	0.850
Speed4	100401	20.26	1.1929	469.996	-265.8	0.0567	1.044
Speed6	100291	20.43	1.1909	785.658	-523.05	0.074157	1.507
Speed8	100499	20.04	1.195	1029.19	-678.98	0.085786	1.749
Speed10	100474	20.27	1.1937	1157.34	-759.32	0.090868	1.851

points were arranged with a circumferential interval of 10°. They included 31 points in the radial direction, each separated by a radial distance of 2mm, as depicted in Figure 5.2 (b). The inner boundary is the circle with AIP's circle center and a radius of 60 mm. The outer boundary's radius is 120 mm. The central area was omitted primarily to keep CTA measurement accuracy (environment temperature would usually fluctuate under long time measurement, which will affect the measurement's accuracy) and also based on the findings in the pressure measurement [149], the region where velocity is most affected is located at the top and bottom of the outlet. Moreover, for unknown reasons, the dominant frequencies measured in the central area show apparent deviation in each measurement (a possible reason is that the traverse system's support is located behind the outlet when measuring the central region; however, the traverse system's stiffness is insufficient and generates the vibration). Therefore, the decision was made to disregard the central area. The results were then mirrored to represent the complete outlet interface. The actual measurement time was approximately 90 minutes. Maintaining a constant environmental temperature at this timescale is still challenging, often fluctuating by one to two degrees Celsius, potentially leading to measurement errors.

5.2 Experiment Analysis

5.2.1 Flow Field Basic Information

The experiment flow volume data and environment information are shown in Table 4.2. The reference dynamic pressure is the average value of the dynamic pressures at the circumferential locations of 60° and 120° at the axial position of L/d =0.25, where L and d represent the axial length and the inlet diameter, as shown in Figure 6.3.

Before further analysis, the data from the pressure measurement and CTA experiment is compared. The center of the AIP was designated as the reference point, and three measurements were taken to calculate the average value. These measurements were conducted consecutively, with re-calibration performed between each CTA experiment to mitigate the impact of temperature

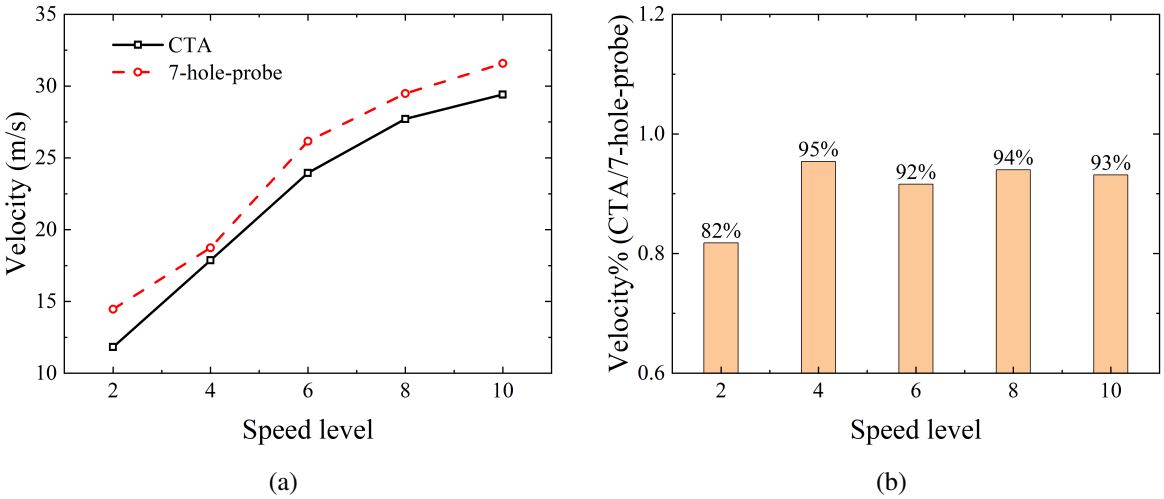

Figure 5.3: Velocity comparison between the CTA and the pressure probe experiments at the reference point.(a) describes the velocity magnitudes measured by two experiment methods, and (b) illustrates the velocity ratio.

fluctuations. During these three measurements, the maximum change in ambient temperature was 0.2 degrees Celsius. The velocity data obtained from the CTA were compared with those obtained from a seven-hole probe, and the results of both measurement techniques are depicted in Figure 5.3. It was observed that the velocities measured by the CTA were relatively lower than those measured by the pressure probe. The differences between the two measurement methods significantly exist. There are many possible reasons, such as calibration error, environmental factors, installation location, etc. However, the most probable cause is atmospheric pressure. As Table 5.1 shows, the environmental pressures are all beyond 10^5 Pa when measuring the pressure, while the environmental pressures are all below 10^5 Pa. This is due to the extended time interval between the two groups of experiments. The pressure measurement was made in summer, while the CTA experiments were conducted in winter. The variations in environmental pressure will influence the fan's performance, thus influencing flow velocities. Regarding this part of the content, the author discussed it in another article in detail [149]. Additionally, because experiment measurement accuracy is not the focus of this study, this chapter doesn't analyze this measurement error.

Figure 5.4 shows the velocity profiles measured by the CTA and the seven-hole probe. It can be found that the velocity profiles obtained by the two measurement methods are very similar in the area extending from a radius of 60 millimeters to 120 millimeters at the outlet. They both exhibit relatively slow flow velocities at the top and the bottom and high at the sides. However, the highest velocity measured by the CTA was still noticeably lower than the seven-hole probe.

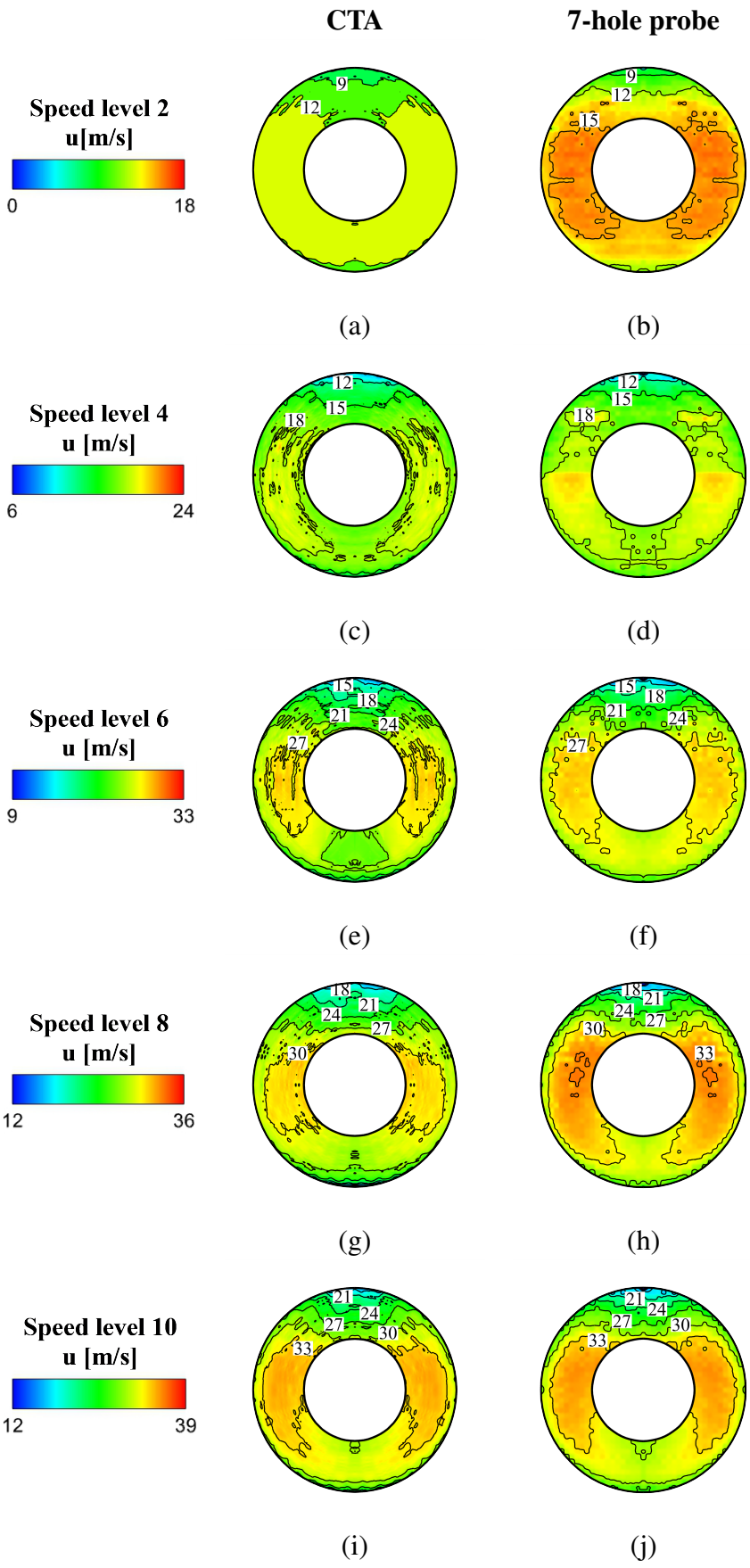

Figure 5.4: Velocity profile (m/s) obtained from the CTA and pressure probe experiments at the area spanning from the radius of 60mm to 120mm at the outlet. (a, b) represent Speed 2; (c, d) represent Speed 4; (e, f) represent Speed 6; (g, h) represent Speed 8; (i, j) represent Speed 10.

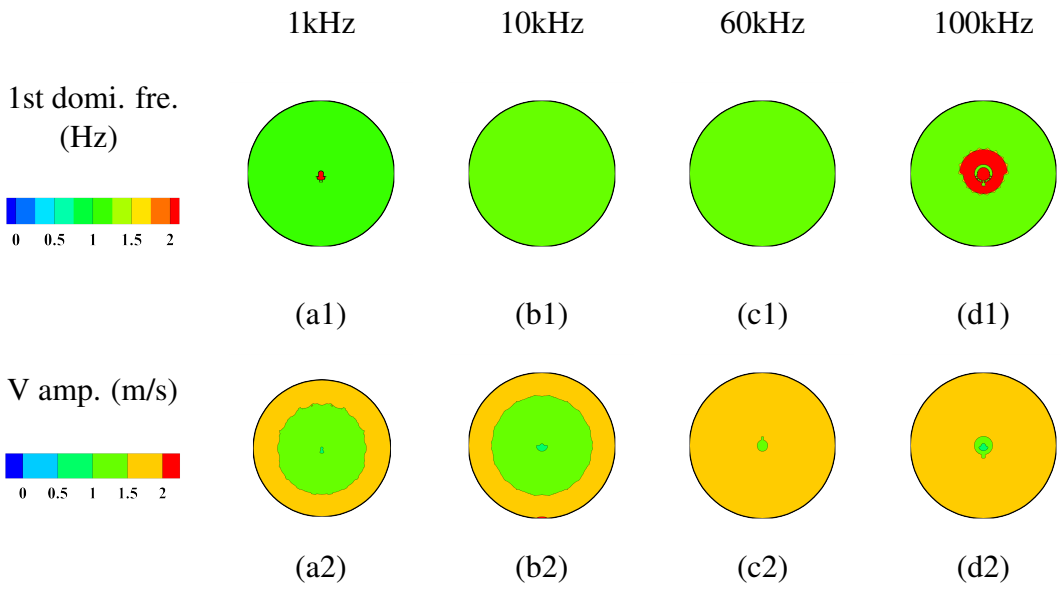

Figure 5.5: The first-order dominant frequency (Hz) and corresponding velocity amplitude (m/s) maps of the AIP under the same sampling period and different sampling frequencies (1s;1khz,10khz,60khz).

5.2.2 Frequency Spectral Analysis

The flow velocity was set to Speed10. Using Tecplot software, Fourier transforms were performed on the velocity signals at each measurement location. A Python script extracted the first-order dominant frequency and corresponding amplitude. The amplitudes were then normalized using Equation 5.1 to determine the amplitude of velocity fluctuations. N is the number of samples. In Figure 5.5, the sampling period is consistently 1 second. According to Equation 5.2, the frequency resolution is 1 Hz. f_0 is the frequency resolution, and T is the period. Per the Nyquist–Shannon sampling theorem (Equation 5.3), the higher the sampling frequency, the greater the maximum resolvable frequency. In Equation 5.3, B represents the resolvable frequency, and f_s is the sampling frequency. Sampling frequencies of 1 kHz, 10 kHz, 60 kHz, and 100 kHz correspond to maximum resolvable frequencies of 500 Hz, 5 kHz, 30 kHz, and 50 kHz, respectively.

$$Amplitude = \frac{Current\_value}{\frac{N}{2}} \tag{5.1}$$

$$f_0 = \frac{1}{T} \tag{5.2}$$

$$B < f_s/2 \tag{5.3}$$

Figure 5.5 observed that the first-order dominant frequency measured is slightly higher at the AIP center. However, this phenomenon may not be because of the turbulence characteristic

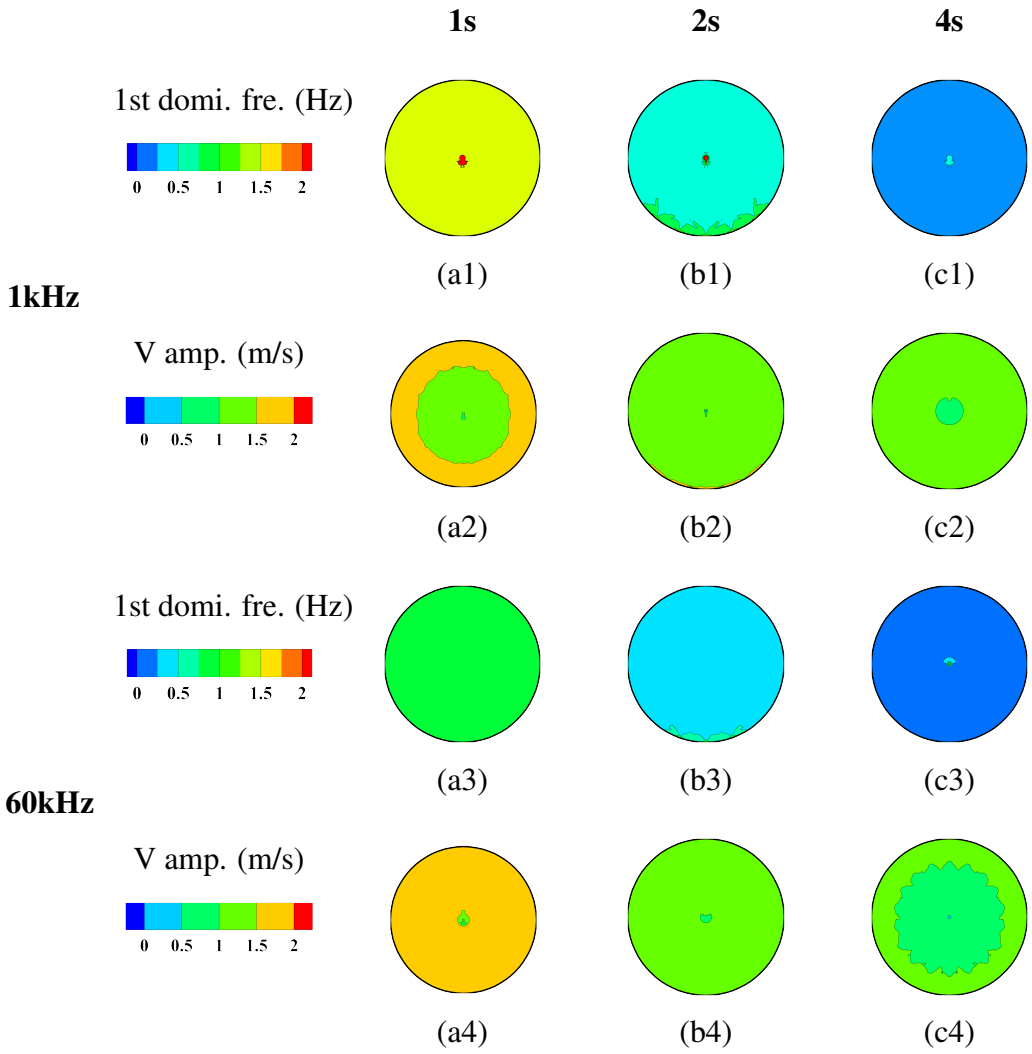

Figure 5.6: The first-order dominant frequency (Hz) and corresponding velocity amplitude (m/s) maps of the AIP under the same sampling frequency and different sampling periods (1kHz/60kHz;1s,2s,4s).

of the AIP. First of all, after multiple measurements, it is found that the area of the central high-frequency region is not fixed and sometimes even disappears. A possible reason is that when measuring the central region, the support of the traverse system is located behind the AIP, namely the outlet; due to insufficient rigidity, the support generated a certain frequency vibration. As for other locations, the measured dominant frequencies are all the minimum frequency resolution. The amplitude of the velocity fluctuation exhibited a trend of being smaller at the center and increasing along the radial direction. This trend indicates that the closer to the duct wall, the larger the dominant signal's velocity fluctuation amplitude. Even though the amplitude of the dominant frequency measured at different sampling frequencies was not precisely the same, the variation was minimal; the difference in magnitude is only zero point several meters per second.

To further investigate the effect of the sampling period on the dominant frequency, measurements were conducted using sampling periods of 1s, 2s, and 4s, as well as sampling frequencies of 1 kHz and 60 kHz. There is a high similarity between 1 kHz and 60 kHz sampling frequency, as shown in Figure 5.6, with similar first-order frequency distribution and velocity amplitude distribution. The difference between different sampling periods mainly focuses on the dominant frequency magnitude. This is because the sampling period can determine the minimum frequency resolution. With the sampling period increasing from 1s to 4s, the primary dominant frequency magnitudes on AIP are all the minimum resolution frequencies, decreasing from 1hz to 0.25hz and gradually trending to zero. 1s corresponds to 1hz, 2s to 0.5hz, and 4s to 0.25hz. So, it can be found that a low-frequency signal dominates the AIP interface under a low Mach number. Meanwhile, this also means flow inside the S-duct trends to a steady state at low speeds. Additionally, it can also be found that the velocity amplitude has a negative correlation with the period from Figures 5.6. The longer the sampling period, the smaller the velocity amplitude. However, no matter the dominant frequency or the corresponding velocity amplitude, different sampling periods and sampling frequencies only brought tiny changes. Therefore, a sampling frequency of 1 kHz and a sampling period of 1s will be adopted to study the turbulence further. Meanwhile, the study of sampling period and frequency can also be the reference for the time analysis scale of the following unsteady simulation.

5.2.3 Turbulence Data Basic Statistics

Figure 5.7 displays turbulence data distribution on AIP. Here, take 10% as the evaluation benchmark of the turbulence intensity, namely 0.1 in the figure, to judge whether the turbulence is strong or weak. It can be found that regardless of velocity variations, regions of high turbulence intensity are consistently located at the top of the AIP. There is a notable similarity between the distribution of turbulence intensity and the velocity profile shown in Figure 5.4, where areas where the velocity is affected (low-speed region) correspond to regions of high turbulence, and the unaffected areas (high-speed region) correspond to low turbulence regions. This illustrates that the region where flow separation occurs will significantly increase turbulence intensity.

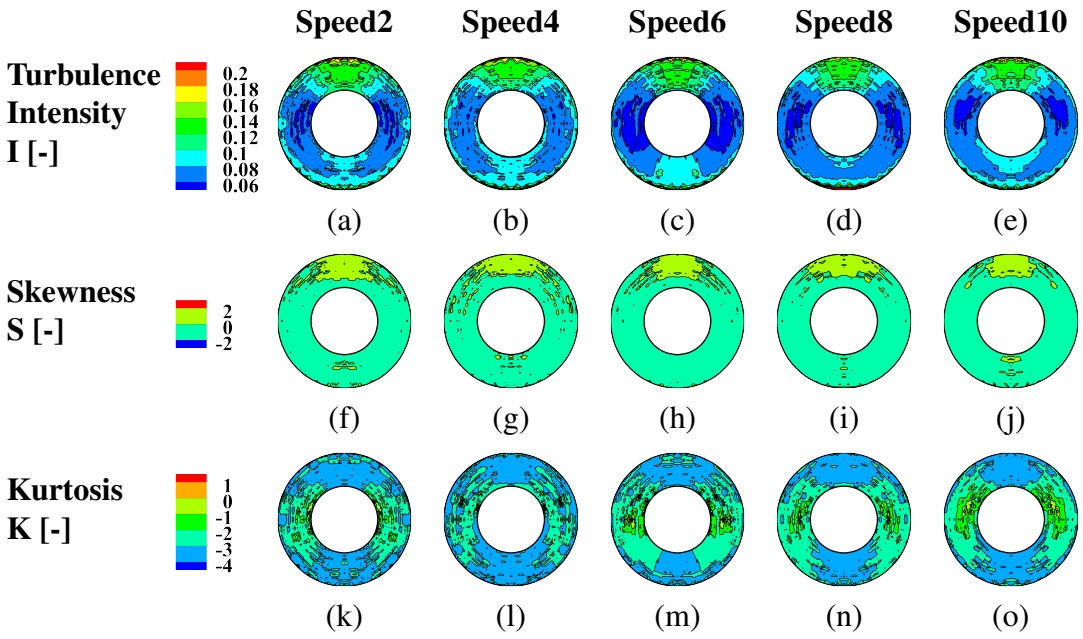

Figure 5.7: Turbulence data distribution (Intensity, Skewness, Kurtosis) at the area spanning from the radius of 60mm to 120mm on AIP. (a-e) represent the turbulence intensity (I); (f-j) represent skewness (S); (k-o) represent kurtosis (k).

Equation 5.4 shows the definition of the turbulence intensity. Both skewness and kurtosis in Figure 5.7 are concepts from statistics, defined by Equations 5.5 and 5.6. U is the velocity, and σ is the standard deviation. N represents the number of the samples.

$$I = \frac{\sigma}{U_{mean}} \tag{5.4}$$

$$S = \sum_{1}^{N} \frac{(U_i - U_{mean})^3}{N \cdot \sigma^3} \tag{5.5}$$

$$K = \sum_{1}^{N} \frac{(U_i - U_{mean})^4}{N \cdot \sigma^4} \tag{5.6}$$

Skewness (S) is a measure of the symmetry of data, divided into negative and positive skewness based on a threshold of 0. When skewness is less than 0, it indicates a likelihood that the velocity in the flow field will more frequently occur below the mean velocity. If skewness equals 0, it signifies that the velocities in the flow field are evenly distributed on both sides of the mean velocity. A skewness greater than 0 suggests that velocities in the flow field are more likely to occur above the mean velocity. Conversely, a skewness smaller than 0 indicates that velocities in the flow field are more likely to occur below the mean velocity. In Figure 5.7, it can be observed that a large area at the AIP top exhibits positive skewness. At the same time, the bottom, although more dispersed, also shows scattered areas of positive skewness. Both these two regions have strong or relatively strong turbulence intensity. Therefore, it can be concluded that

regions of strong turbulence correspond to positive skewness, and weak turbulence corresponds to negative skewness. The stronger the turbulence intensity, the more likely the velocities will exceed the local average speed. Additionally, with the addition of the flow velocity, the high skewness region at the top tends to become smaller.

Kurtosis (K) characterises the amplitude of the data distribution, typically using three as the threshold. In Figure 5.7, K values have been normalised by subtracting 3, establishing 0 as the new benchmark. When K is greater than 0, it means larger amplitudes, suggesting a prevalence of extraordinarily high or low velocities in the flow field. Conversely, when K is less than 0, it implies fewer unusually high and low velocities in the flow field. In the kurtosis distribution figure, it can be observed that the K values are predominantly negative across most positions on the AIP. The regions with the lowest K values are found at the top and bottom, with areas of positive K values located at the central region of the AIP. As the flow velocity increases, the K values on the AIP tend to rise, which means the higher the flow velocity, the larger the amplitude of the velocity fluctuation. Furthermore, in conjunction with the turbulence intensity distribution, it can be seen that regions with weak K values correspond to areas with strong turbulence. This means that in regions of strong turbulence, the occurrence of relatively extraordinarily high or low flow velocities tends to be reduced instead.

5.3 Chapter Summary

This chapter investigated and discussed the turbulent characteristics of an S-duct at the AIP, comparing the obtained data with the pressure measurement experiment. The primary conclusions drawn were as follows:

(1) A low-frequency signal dominated the turbulent variations at the outlet interface at low Mach numbers, suggesting that the flow at the exit of the S duct is relatively steady at low speeds. The sampling period and frequency had minimal impact on the measurement results, so lower sampling frequencies and periods are sufficient for experimental requirements under low Mach numbers.

(2) Although the time-averaged velocity field measured by the CTA experiments has a trend similar to that of the seven-hole probe experiments, the velocities measured at the same locations were noticeably lower than those measured by the seven-hole probe. This phenomenon persisted at reference points even after the potential influences of ambient temperature variations were minimised as much as possible. Through investigation, it was found that the error arises from changes in ambient pressure. Variations in ambient pressure can significantly influence the fan's performance, thus affecting the flow velocity.

(3) Areas where the velocity was reduced due to flow separation also showed high turbulence. The varying turbulence intensity levels also meant different skewness and kurtosis inten-

sities. The high turbulence regions corresponded to small kurtosis and positive skewness, while the low turbulence regions corresponded to relatively high kurtosis and negative skewness. As the flow velocity increased, the areas with high skewness became smaller and the regions with high kurtosis became more significant.

The next chapter will commence with numerical simulations and employ modal analysis to evaluate three commonly used turbulence models ($k-\varepsilon$, $k-\omega$, and SST).

Chapter 6

Simulation of the S-duct

Embedded propulsion systems are widely utilized in the contemporary aviation industry [150, 151] due to their numerous advantages, including smaller drag, noise, installation length, and diminished radar and infrared signatures [1, 3, 152–154]. The diffuser-type S-shaped intake, as a principal component of embedded propulsion systems, also has its inherent challenges. Due to its large curvature of the centreline and diffusing geometry, flow separation within the S-duct is virtually inevitable, accompanied by pronounced secondary flows, as a result, leads to substantial disturbances and distortions to the incoming airstream [90, 155, 156]. The final result is that the air at the aerodynamic interface plane (AIP) (the interface before the engine or compressor) is notably non-uniform, characterised by significant pressure and swirl distortions [134, 157].

The airflow quality on AIP directly influences the efficiency of the compressor, thereby further impacting engine performance [156]. Severe flow distortions can precipitate engine surge and stall, jeopardizing the integrity of the entire aircraft [157–161]. Consequently, a well-designed S-shaped intake should not only effectively reduce air velocity but also minimize flow separation and suppress the development of secondary flows, enabling the engine to operate with high stability [145].

In actuality, research and optimization focusing on the S-ducts have been started since the last century [80]. Researchers have conducted numerous experiments and simulations. During the literature review, it was found that one configuration proposed by NASA was widely studied [81]. Even to this day, research related to this particular configuration has not ceased [149, 162]. This configuration does not adopt a fixed duct diffusion rate but is defined by an S-shaped curve function. However, the principles and advantages of this design were not found in the literature, but this issue will be solved in this chapter. This chapter will compare the configuration with the fixed duct diffusion rate and that proposed by NASA. In the beginning, this study selected the experiment to do the research; however, during the experimental process, it was found that studying this issue only through experiments has its limitations. Although the experiment can provide the most accurate data, limited by the complicated geometry of the S-duct and the

limitation of the experiment methods, they are challenging to offer intuitive flow field data within the S-shaped duct. Relevant experiment literatures [81, 96, 145, 146, 163–165] also have this issue. To address this issue, numerical simulations are necessary, namely, showing the internal flow field through computational fluid dynamics (CFD).

Although theoretically, direct numerical simulation (DNS) has the highest accuracy, directly solving the Navier-Stokes (NS) equations in this problem will cost an unquantifiable amount of computational resources and time. To reduce computational demands, researchers proposed a method that only analyzes the large eddies while using the model to substitute the small ones. This approach, known as Large Eddy Simulation (LES), was initially proposed by Smagorinsky [109] and applied to simulate atmospheric airflow. However, after the author's assessment, even the computational resources required for LES are still impractical in this study. After ruling out the above two options, the Reynolds-Averaged Navier-Stokes (RANS) method was chosen to do this time's simulation. This method was first applied to fluid dynamics by Reynolds [110].

Compared with DNS and LES, the most important feature of the RANS is low computational cost. This feature makes it widely used in engineering applications, although the RANS method sacrifices some accuracy. However, with a deeper understanding of the RANS method's algorithm, it was found that it may not be particularly effective in addressing turbulence-related issues. The RANS approach decomposes all fluid variables into mean and fluctuating components. This decomposition divides the NS equation into two parts: one representing the mean flow field and the other describing turbulence fluctuations. In practical computations, the fluctuating part is typically defined as zero, meaning that the solutions obtained by RANS are time-averaged values over some time or time step, which will introduce temporal averaging errors. When the turbulence intensity of the flow field is low, this characteristic of RANS is disadvantageous for transient flow field analysis. Furthermore, to solve the turbulence fluctuation equations in RANS, additional variables, namely Reynolds stresses, must be introduced to close the equations. Calculating Reynolds stresses requires using turbulence models, making RANS solutions highly dependent on the chosen turbulence model. These turbulence models are based on certain assumptions and empirical formulas, and their capability of accurately capturing turbulence is highly questionable. Driven by this curiosity, the author conducted a literature review, which revealed that no systematic studies have been conducted to compare the capabilities of different turbulence models in capturing turbulent characteristics. To address this gap, a comparative analysis of two S-shaped ducts with different expansion ratios mentioned above will be conducted, after which the configuration with superior performance will be selected for further investigation in this part of the study. Selected turbulence models are $k-\varepsilon$, $k-\omega$ models, and their hybrid model $k-\omega$ SST model (The $k-\omega$ SST model uses $k-\varepsilon$ model in the free-flow region and $k-\omega$ model in near-wall regions and switches between them through a specific blending function. SST model combines the advantages of $k-\varepsilon$ and $k-\omega$ models.). They are the current three most commonly used turbulence models.

In this study of turbulence, in addition to numerical simulations, experiments will be conducted using a constant temperature anemometer (CTA) to obtain some practical data. However, the measurement method is constrained by the capabilities of the CTA. Each measurement only yields point data, making obtaining the spatial structure on the AIP impossible. However, this issue can be addressed by applying modal decomposition to the simulation data. Therefore, although both experiments and simulations have their respective limitations, a comprehensive analysis of turbulence can be effectively achieved by integrating experiment and simulation. Here is a brief introduction of the modal decomposition methods used in this study.

Proper Orthogonal Decomposition (POD) is the earliest proposed modal decomposition method [120, 121], known by various names in different fields, such as Principal Component Analysis (PCA) or Karhunen-Loeve expansion. It was elaborated in detail by Berkooz et al. [166]. POD is a method to reduce dimensionality. It projects the flow field onto mutually orthogonal subspaces and then ranks the modes according to their energy content. Typically, a few high-order modes can retain the majority of the energy. The second method is the Dynamic Mode Decomposition (DMD) method, which fundamentally treats the flow field as a linear system. DMD extracts dynamic features from flow field snapshots. A specific growth/decay rate and frequency characterize each extracted mode. Detailed algorithms of DMD were provided in Schmid [167]'s published articles. Given their long-established history, both POD and DMD methods have already had extensive applications in fluid dynamics [168–171]. The third method, Spectral Proper Orthogonal Decomposition (SPOD), is a recently developed modal analysis technique. Detailed algorithms of SPOD were provided in Towne et al. [122]'s published articles. The SPOD method essentially extends the POD approach. In POD, data is decomposed into eigenmodes, eigenvalues, and temporal evolution coefficients. While the modes in POD are orthogonal to each other, the temporal evolution coefficients cannot be expressed with a specific function. To address this limitation, SPOD achieves temporal and spatial decoupling by transforming the time domain into the frequency domain (discrete Fourier transform, DFT), thus obtaining different modes at different frequencies.

Overall, this study will conduct pressure measurement experiments on the S-duct to obtain the most real boundary conditions for the simulation. A further comparison between the two S-shaped duct geometries is conducted with the aid of simulations. Subsequently, the three modal analysis methods are employed to evaluate the capability of different turbulence models in the RANS approach to capture the coherent structures of the flow field. Before the modal analysis, CTA experiments measured turbulence data at the S-duct's AIP under various velocities. The time record interval in the subsequent transient simulation was determined by analyzing the data of different sampling frequencies and periods. This chapter will also present and demonstrate the features and applications of each modal analysis technique.

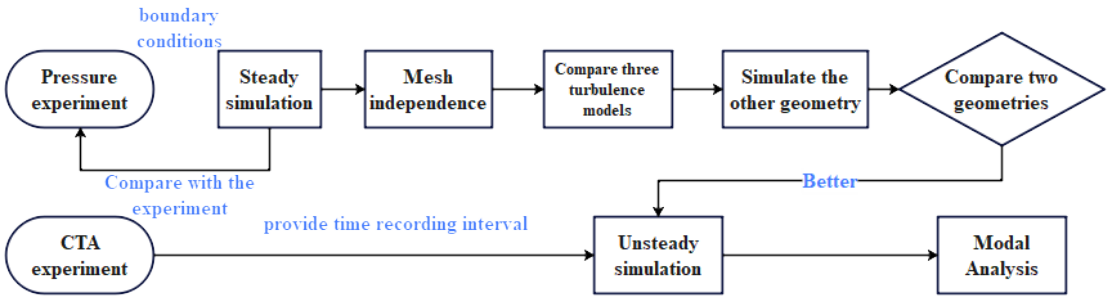

Figure 6.1: The numerical simulation research flow chart.

6.1 Simulation Setup

The simulation research process is illustrated in Figure 6.1. The simulation software used is the open-source software OpenFOAM. The simulation of the S-shaped intake duct took the RANS and URANS (Unsteady Reynolds-Averaged Navier-Stokes, URANS) methods. RANS and URANS methods correspond to *simpleFoam* and *pimpleFoam* solvers in OpenFOAM, respectively. Three common turbulence models are all used and tested in this study. The k-Epsilon model is based on the version proposed by Launder and Spalding [113]; the k-Omega model takes Wilcox [114] 1988 version, and the k-OmegaSST model adheres to the version developed by Menter et al. [116] in 2003.

All boundary conditions are derived from the pressure measurement experiments. Before comparing with the experimental results, mesh independence validation was conducted in this research. This part of the study was conducted by steady simulation. The steady simulation solvers used in OpenFOAM are *simpleFoam* and *rhosimpleFoam*. This part of the content will be detailed in the subsequent Section, Computational Mesh. After validating the simulation setup, the same setups are used to calculate the NASA configuration. Simulation results compared the two geometries, and the better-performing configuration was chosen for further transient analysis. In the transient simulations, the time step is set to 50 microseconds, with a maximum Courant number of approximately 0.73. The simulations were conducted over a physical time scale of 3.024 seconds. According to the turbulence experiments, a sampling frequency of 1kHz suffices to meet the analytical requirements. Hence, the time record interval is 1 millisecond in the simulations. The simulation runtime is referenced from the research of Gil-Prieto et al. [90], who found that the flow properties within the duct would stabilize after 20 convective time scales, with only a 1% change in flow properties between 20 and 50 convective time scales. The total length of the duct in this simulation is 3.245 meters, and based on experimental data, the velocity at the throat of the S-shaped intake duct is approximately 44m/s, making a single time scale of about 0.07375 seconds. 20 convective time is around 1.5 seconds. In the final modal analysis, data from the first two seconds are not analysed; only data from the last 1.024 seconds, equating to 1024 snapshots, are considered. The snapshot number selects

Table 6.1: Numerical parameters used in the simulation.$P_{t,o}$ is the total pressure at the inlet, and P_s is the static pressure at the outlet.

$P_{t,o}$ [Pa]	P_s [Pa]	I_{turb}	k_{turb}	ε	ω
100474	99714.67	0.03	3.04	25.07	222.81

the power of two, which can facilitate SPOD computational efficiency.

6.1.1 Numerical Parameters

The inlet is configured as the 'pressureDirectedInletVelocity.' The outlet is defined as a static pressure outlet with a static pressure value of 99714.67 Pa. The boundary is set as a no-slip boundary. The ambient pressure and temperature are 100474 Pa and 20.27 degrees Celsius, respectively.

Turbulence models require the specification of initial values for epsilon and omega, which can be estimated using Equations 6.1 to 6.4:

$$I_{turb} = 0.16 Re_{in}^{-\frac{1}{8}} \tag{6.1}$$

$$k_{turb} = 1.5(I_{turb} U_{in})^2 \tag{6.2}$$

$$\varepsilon = C_{\mu}^{\frac{3}{4}} k_{turb}^{\frac{3}{2}} l_{mix}^{-1} \tag{6.3}$$

$$\omega = \frac{\varepsilon}{k_{turb} C_{\mu}} = \frac{C_{\mu}^{-\frac{1}{4}} k_{turb}^{\frac{1}{2}}}{l_{mix}} \tag{6.4}$$

where I_{turb} is the turbulence intensity and Re_{in} is the Reynolds number inside the duct. k_{turb} is the turbulence kinetic energy, ε and ω are respectively dissipation rate and specific dissipation rate. C_{μ} is constant 0.09. l_{mix} is the mixing length calculated based on the inlet diameter ($0.07 r_1$). Table 6.1 shows the numerical parameters used in the simulations in detail.

The time discretization scheme in the transient simulation is second-order accurate using the backward scheme. The corrected scheme is employed to discretize face normal gradients (snGradSchemes). The convection scheme utilizes the Gauss Lust, comprising 25% of the linear Upwind scheme and 75% of the linear scheme. The gradient scheme is formulated as Gauss Linear.

6.1.2 Computational Mesh

The computational domain corresponds to the region enclosed by the inner surface of the S-shaped intake duct depicted in Figure 6.3, including both the leading bell mouth and the extrusion discharge section. Figure 6.3 shows the distribution of monitoring faces, which has the same layout as that in WELLBORN et al. [81]'s study. In Figure 6.3, s and d, respectively, rep-

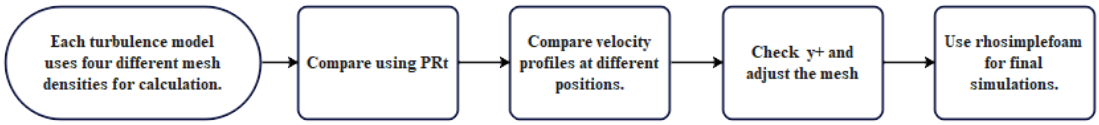

Figure 6.2: The mesh validation flow chart.

Table 6.2: Environment parameters and estimated wall distance (y^+ = 1). T is the environment temperature; ρ and ν are corresponding air density and kinematic viscosity. The experiment obtained the local velocity at the position s/d = 0.25 (the bottom of the S-duct), derived from the wall static pressure measurements; here, this velocity is used to calculate y^+. The characteristic length takes the diameter of the S-duct's inlet, 204.2mm. d is the wall distance of the first layer.

T [°C]	ρ [kg/m^3]	ν [m^2/s]	u_τ [m/s]	d [mm](y^+=1)
20.27	1.1937	15.09e-6	47.349	7e-3

resent the length of the centre line of the S-shaped duct segment and the diameter at the entrance. The mesh uses an O-type structured mesh, with the mesh topology illustrated in Figure 6.4. 4 blocks are located at the duct central, and eight blocks are in the boundary layer. The research approach for mesh quality and independence verification is illustrated in Figure 6.2. First, each turbulence model is calculated using four sets of meshes with different mesh densities. The mesh setups are based on the wall y^+ requirements for each turbulence model. The definition of y^+ is as follows:

$$y^+ = \frac{yu_\tau}{\nu} \tag{6.5}$$

where y is the first layer's distance to the wall,u_τ is the local velocity at the wall, and ν is the local kinematic viscosity. Tabel 6.2 shows relevant environment parameters and the estimated wall distance when y^+ = 1.

According to findings from several studies [113, 172–174], for the standard $k-\varepsilon$ model, the optimal y^+ range is between 30 and 300, while for the $k-\omega$ and SST models, the y^+ is recommended to be less than 1. Since the $k-\omega$ and SST models have the same y^+ requirements, the same four sets of meshes are employed for calculating these two turbulence models. The four mesh sets for the $k-\varepsilon$ model must be configured separately. Table 6.3 provides detailed information on these mesh configurations.

Here, PR_t is used as the evaluation standard. The definition of PR_t is provided in Equation 6.6. Figure 6.5 shows different meshes' PR_t. It can be found that at low Mach numbers, the effect of mesh density on PR_t is minimal, and the influence is merely at a magnitude of one thousandth. Therefore, more than relying solely on PRt to assess mesh independence is required for a convincing evaluation. The mesh independence is further validated by comparing the

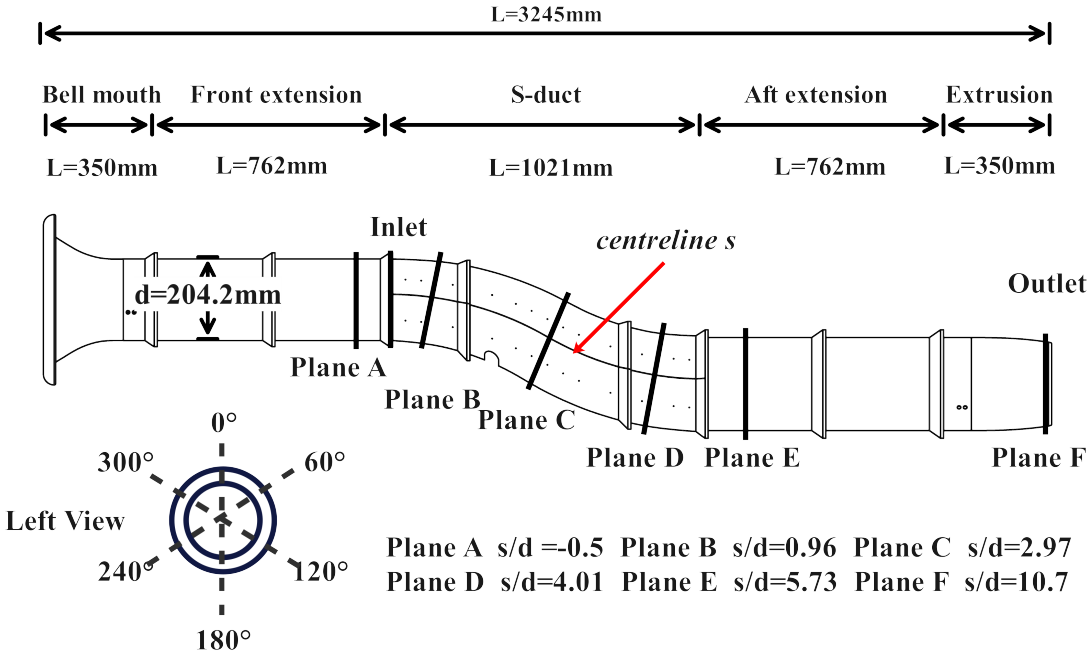

Figure 6.3: The geometry of the simulated S-duct, s and d, respectively, represent the length of the centre-line of the S-shaped duct segment and the diameter at the entrance.

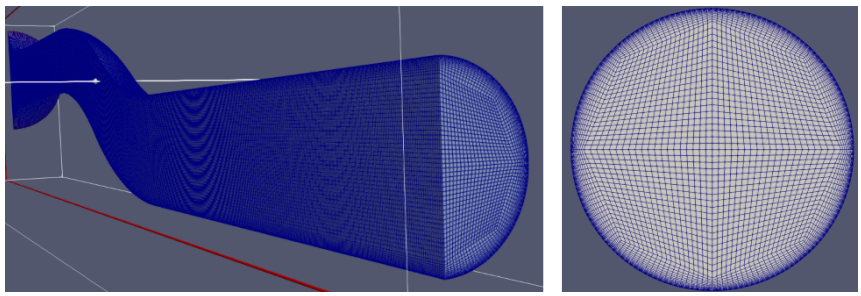

Figure 6.4: Mesh topology.

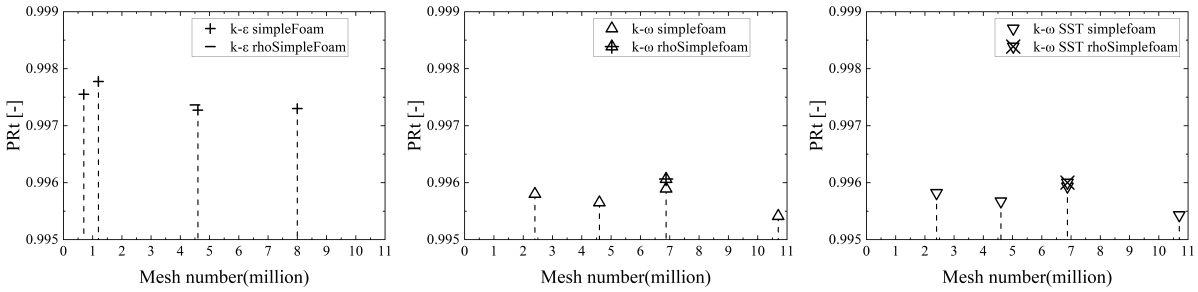

(a) $k-\varepsilon$ (b) $k-\omega$ (c) $k-\omega$ SST

Figure 6.5: Mesh independence validation. (a-c) correspond to $k-\varepsilon$, $k-\omega$ and SST models, respctively.

Table 6.3: Mesh information for mesh independence verification. Cells denote the number of the mesh, and the unit is a million. Est. y^+ is the estimated y^+ based on the data in Table 6.2. AR represents aspect ratio, and N-O represents non-orthogonality. S is the abbreviation of the skewness.

	$k-\varepsilon$					$k-\omega$ & SST				
No.	Cells [M]	Est. y^+	AR	N-O (Max/Avg.)	S	Cells [M]	Est. y^+	AR	N-O	S
1.	0.7	120	12.90	58.23/15.35	2.82	2.4	1	964.42	58.42/12.47	2.85
2.	1.2	50	24.53	58.42/14.52	2.85	4.6	0.8	1124.70	58.61/11.76	2.86
3.	4.6	40	25.08	59.25/14.27	2.89	6.9	0.6	1349.05	59.13/12.01	2.87
4.	8.0	35	23.97	59.71/14.51	2.89	10.7	0.6	1046.69	59.25/12.00	2.89

velocity distributions at various positions within the S-shaped duct.

$$PR_t = \frac{P_{t,AIP}}{P_{t,o}} \tag{6.6}$$

where $P_{t,AIP}$ is the average total pressure on AIP and $P_{t,o}$ represents the total pressure of the free stream.

Using the $k-\varepsilon$ model as an example, the results for different mesh densities are presented in Figure 6.6. It can be observed that once the mesh reaches 4.6 million cells, the velocity profile in the S-shaped duct no longer shows significant changes. Although more cells would undoubtedly capture more flow details, considering the computational cost, the mesh size for the $k-\varepsilon$ model is set at 4.6 million cells in the subsequent simulations. Similarly, the mesh sizes for the $k-\omega$ and SST models were determined using the same approach, with a final mesh count of 6.9 million cells.

As mentioned earlier, each turbulence model has an optimal range of y^+ values. Although the initial y^+ values were set based on recommendations from the literature [113, 172–174], these values were estimated using experimental data. To ensure the accuracy of the simulation, the y^+ values need to be further checked after selecting the mesh size. The y^+ values for the three turbulence models are shown in Figure 6.7. It can be observed that the actual y^+ values in the simulations are significantly lower than the estimated values. This is likely because the minimum diameter of the duct was chosen as the characteristic length, which reduced the y^+ values. For the $k-\omega$ and SST models, smaller y^+ values benefit the computation. However, the $k-\varepsilon$ model's optimal y^+ range should be between 30 and 300. Therefore, the mesh for the $k-\varepsilon$ model needs to be adjusted. The results of the adjusted mesh and the y^+ distribution are shown in Figures 6.6 (e) and 6.7 (b). The mesh adjustment mainly involves increasing the boundary layer thickness, reducing the number of boundary layers, and increasing the mesh density at the centre of the duct while maintaining the total grid count at 4.6 million.

After checking the y^+ values, the solver was switched from the incompressible solver, *simpleFoam*, to the compressible solver, *rhoSimpleFoam*. This change was made to account for the effects of air compressibility, aiming to enhance the simulations' accuracy further, al-

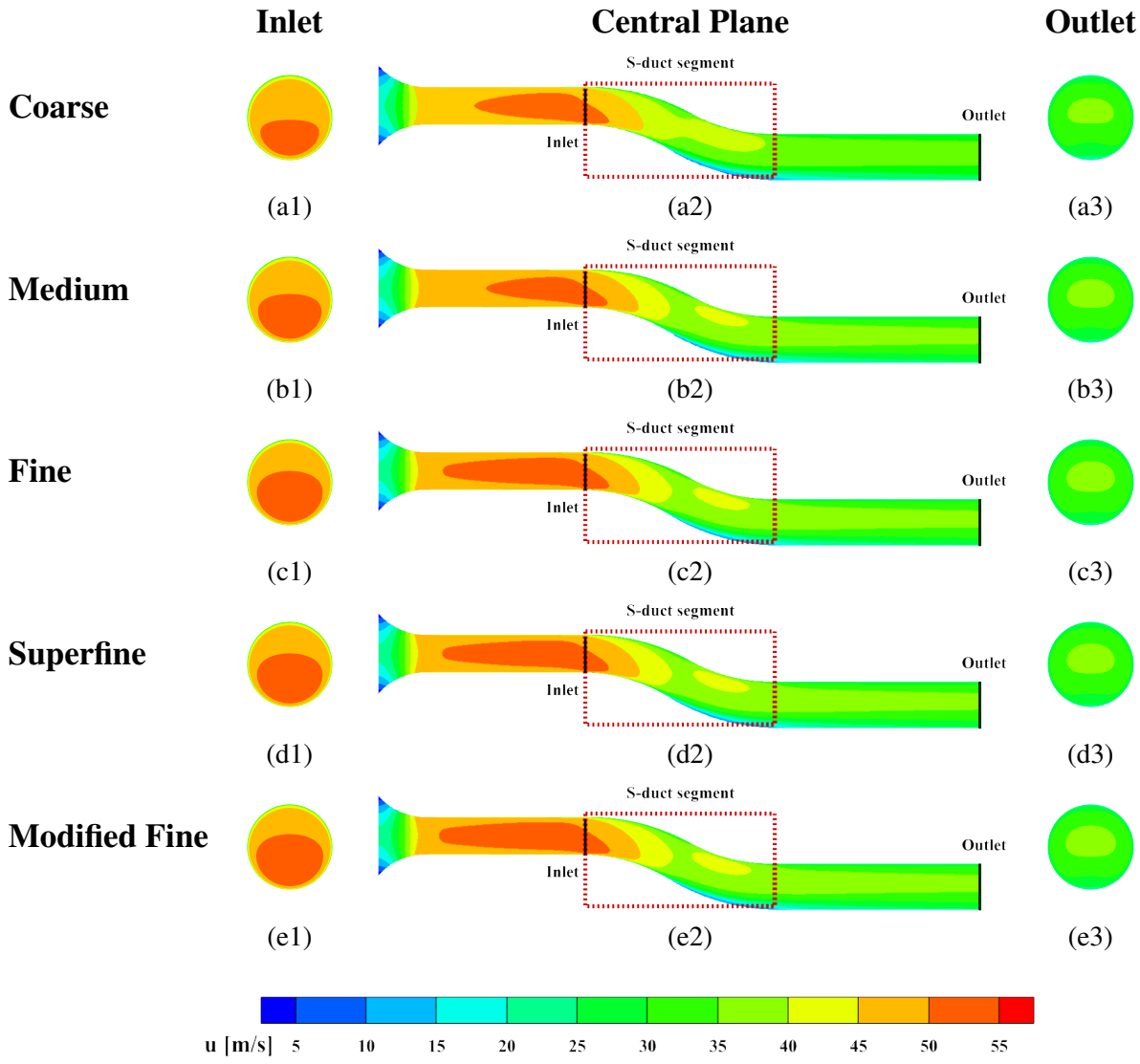

Figure 6.6: The velocity distribution slices at different locations inside the S-duct. (a) denotes coarse mesh, corresponding to the first set of mesh in Table 6.3, the cases (b-d) correspond to the second to fourth mesh in Table 6.3, representing medium, fine, and super-fine meshes, respectively. (e) corresponds to the adjusted fine mesh, in which the total mesh number is the same as the fine mesh.

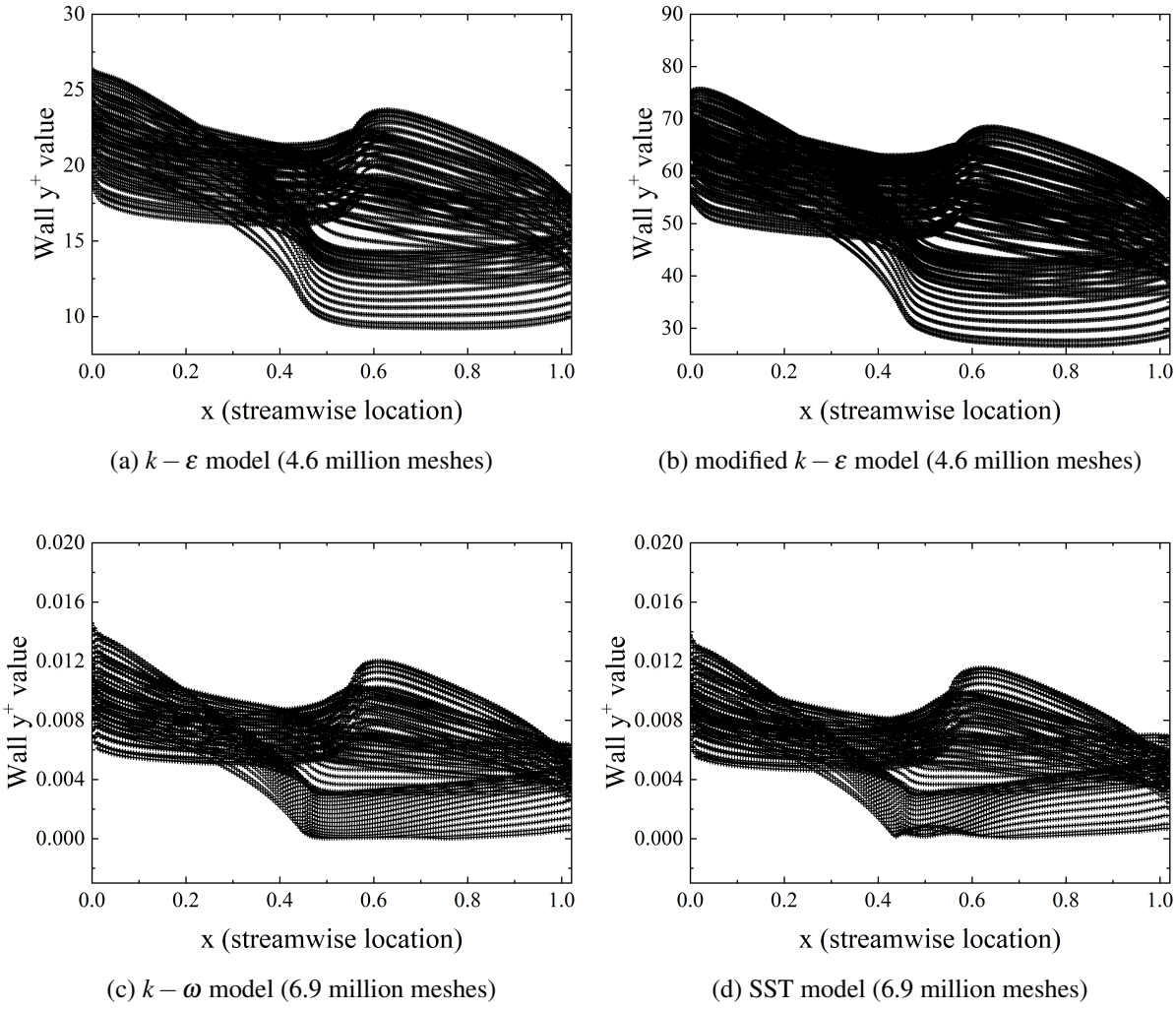

(a) $k-\varepsilon$ model (4.6 million meshes)

(b) modified $k-\varepsilon$ model (4.6 million meshes)

(c) $k-\omega$ model (6.9 million meshes)

(d) SST model (6.9 million meshes)

Figure 6.7: Three turbulence models' near-wall y^+ distributions along the streamwise direction. (a) and (b) represent the y^+ distribution for the $k-\varepsilon$ model and y^+ distribution after mesh corrections, respectively. (c) and (d) represent y^+ distributions for the $k-\omega$ and SST models.

though low-speed flows are generally approximated as incompressible. As shown in Figure 6.5, it can be observed that the total pressure for all turbulence models slightly increased after switching the solver.

6.2 Results and Discussion

6.2.1 Simulation Analysis

6.2.1.1 Numerical Validation

Figure 6.8 compares the static pressure coefficient C_p curves between the experiment and simulation at various circumferential positions, with the definition of C_p shown in Equation 6.7

$$C_p = \frac{p_s - p_{s,ref}}{q_{ref}} \tag{6.7}$$

where p_s and $p_{s,ref}$ represent the static pressure at the measurement and reference points. q_{ref} is the dynamic pressure at the reference point.

In Figure 6.8, s represents the length of the centre line of the S-shaped duct segment, and d refers to the diameter at the entrance of the S-shaped duct segment (204.2mm). The reference point in the simulation directly takes the data at the centre of the entrance to the S-shaped duct segment. It can be found that the wall C_p curves for the different turbulence models are similar, almost overlapping. Although there is no complete overlap between the simulation and experiment data, the trends are identical. At the top of the S-duct (Figure 6.8 (a)), for the first half of the duct (0<s/d<2.5), the simulation and experiment match relatively well, with the curves almost coinciding. However, after s/d>2.5, the simulation underestimates the acceleration region at the top, C_p rising in advance. Meanwhile, changing the view to the bottom of the S-duct (Figure 6.8 (d)), the bottom C_p curve has a faster upward trend but lacks a stagnant region in the middle of the duct in the simulation compared to the experiment. Theoretically, a faster C_p upward trend means the velocity at the bottom decreases faster, which should also benefit the flow above. Still, it can be seen from Figure 6.8 that the acceleration it induces at the top is less significant than that caused by the stall region observed in the experiment. Therefore, the C_p at the top rises in advance should arise from the lack of the stagnant region, which appears in the experiment. A stagnant region of C_p curves means a flow separation; however, the simulation didn't capture this feature. The insufficient prediction of flow separation at the bottom will decrease the blockage at the bottom, leading to the reduced acceleration region at the top. As for C_p curves on both sides match the experiment relatively well. To some extent, C_p curves on both sides continue the top and bottom flow characteristics.

The flow properties on AIP of both simulation and experiment are presented in Figure 6.9. The PR_t distribution shown in Figure 6.9 (a) shows that the PR_t value obtained from the $k-\varepsilon$

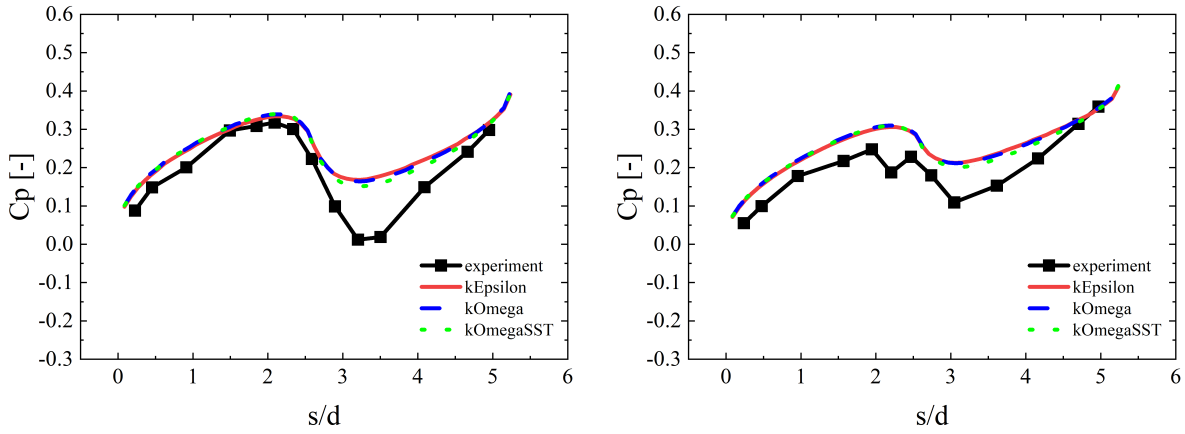

(a) 0°

(b) 60°&300°

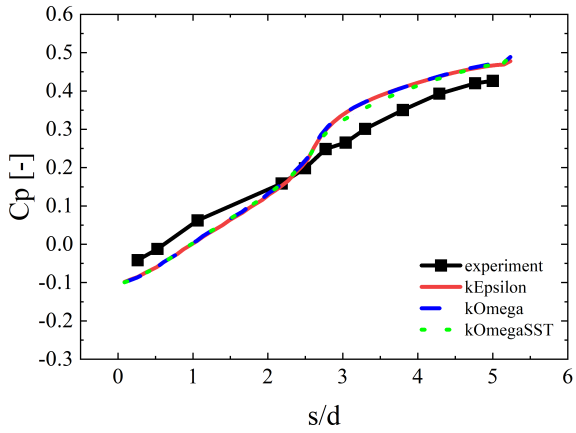

(c) 120°&240°

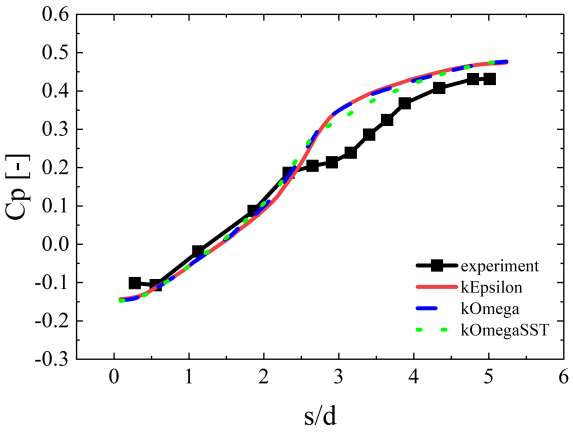

(d) 180°

Figure 6.8: Wall static pressure coefficients C_p at different circumferential angles. (a) corresponds to 0°; (b) corresponds to 60°&300°; (c) corresponds to 120°&240°; (d) corresponds to 180°

.

model is the highest among the three turbulence models, which means that the flow loss of the duct internal flow simulated by the $k-\varepsilon$ model is the minimal. If compared with the experiment directly, the PR_t value of $k-\varepsilon$ is the closest to the experiment, and PR_t values of $k-\omega$ and SST models are significantly lower than the experiment. However, this doesn't necessarily mean the simulation of the $k-\varepsilon$ matches the experiment the best. During the experiment, the boundary radius of sampling points on AIP, 120mm, is smaller than the outlet radius of 125.7mm. The region close to the duct wall wasn't collected. Given the effect of the wall viscosity, the dynamic pressure there is usually smaller than the central region. Meanwhile, the static pressure on AIP can be found in the simulation to be almost constant. This phenomenon is also found in the experiment. The changes in the static pressure of all sampling points are tiny. Therefore, it can be deduced that the total pressure of the outer uncollected region should be lower than the central collected region. If considering the outer area, PR_t of the experiment should be lower. Here, the experimental PR_t only acts as a reference value. However, all PR_t values are close to 1, and this is unfavorable to do analysis, so introduce total pressure loss coefficient $C_{p,loss}$, shown in Figure 6.9 (b), which is used to more intuitively quantify the average total pressure loss magnitude at the AIP. The definition for $C_{p,loss}$ is provided in Equation 6.8, which is the ratio of the average total pressure at the AIP to the dynamic pressure at the reference point.

$$C_{p,loss} = \frac{P_{t,ref} - P_{t,AIP}}{q_{ref}} \tag{6.8}$$

where $P_{t,ref}$ represents the total pressure at the reference point, and here directly uses the value of the freestream total pressure. $P_{t,AIP}$ denotes the average total pressure at the AIP. q_{ref} is the dynamic pressure at the throat.

As shown in Figure 6.9 (b), experimentally, the total pressure loss at the AIP is about 18% of the dynamic pressure at the reference point, whereas, in the simulation, $C_{p,loss}$ of $k-\varepsilon$ turbulence model is about 16% and $C_{p,loss}$s of $k-\omega$ and SST models are about 22%. Based solely on the magnitude, $k-\varepsilon$ still best matches the experiment. The dynamic pressures are almost the same at the reference point among the three turbulence models, so the $C_{p,loss}$ value depends on the total pressure loss on AIP. Here, it can be seen that the total pressure loss of $k-\omega$ and SST models on AIP are 6% larger than the $k-\varepsilon$ model.

DC and SC represent the pressure distortion and swirl distribution coefficients, respectively. Definitions for DC and SC are as follows:

$$DC_\theta = \frac{P_{t,AIP} - P_{t,\theta,min}}{q_{AIP}} \tag{6.9}$$

where DC_θ represents the total pressure distortion coefficient of the sector corresponding to angle θ. $P_{t,AIP}$ is the average total pressure at the AIP interface. $P_{t,\theta,min}$ represents the minimum total pressure in the sector where the angle is θ. q is the average dynamic pressure at the AIP.

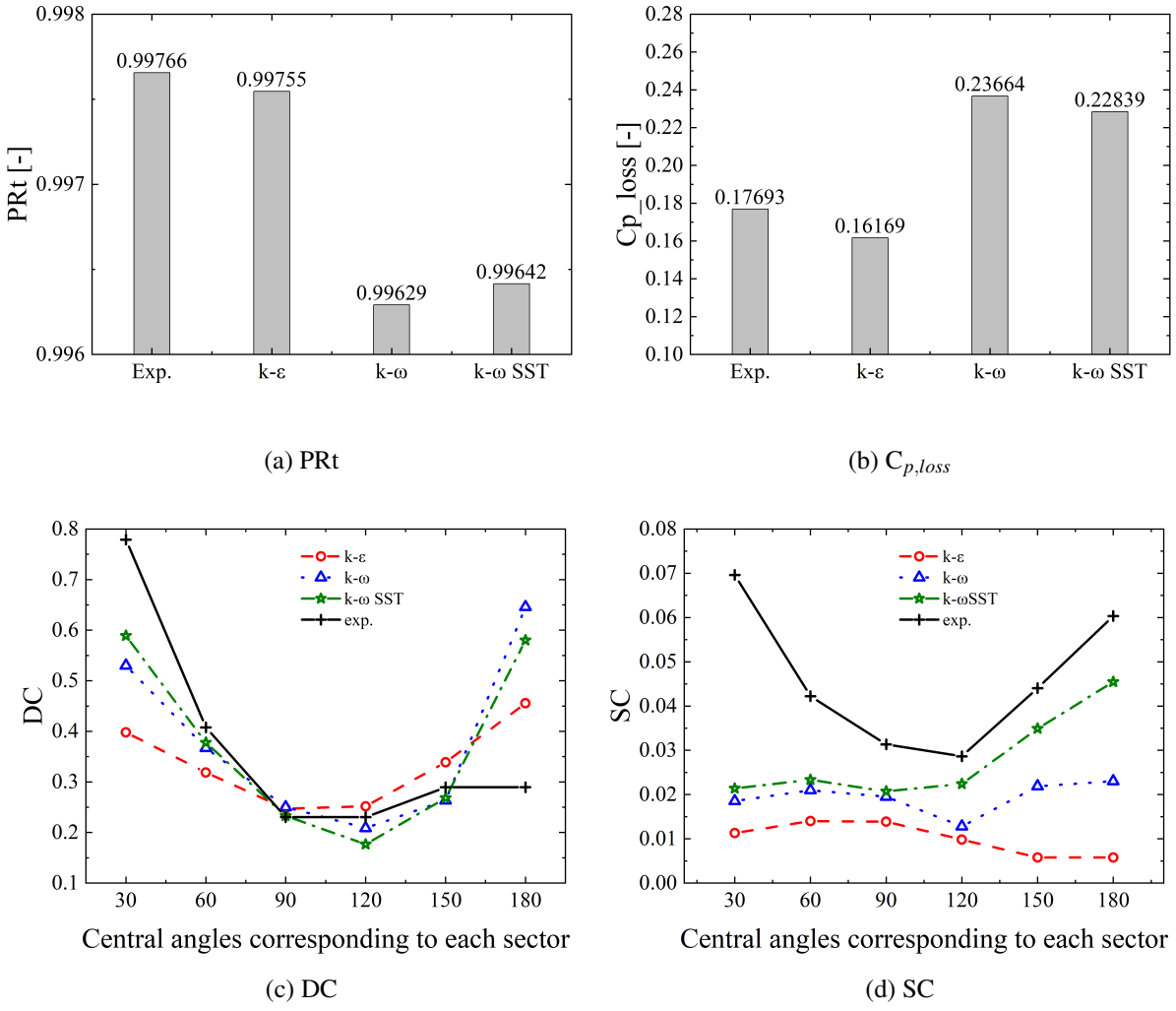

(a) PRt

(b) $C_{p,loss}$

(c) DC

(d) SC

Figure 6.9: Flow properties at the outlet cross-section: (a) is total pressure recovery coefficient; (b) is pressure loss coefficient (pressure loss at the outlet compared to the reference dynamic pressure); (c) is pressure distortion coefficient; (d) is the swirl distortion.

$$SC_\theta = \frac{U_{cf,\theta,max}}{U_{ref}} \tag{6.10}$$

where SC_θ is the swirl distortion coefficient of the sector corresponding to angle θ. $U_{crossflow,\theta,max}$ represents the maximum crossflow velocity at the sector where the angle is θ. U_{ref} is the axial velocity at the reference point.

The experiment measurement boundary radius is 120 mm, and to maintain consistency with the experiment, the simulation's DC and SC are calculated in the same region on the outlet. It can be seen in Figure 6.9 (c) that the tendencies of the three turbulence models' DCs are similar. Compared with the experiment, the SST model's DC matches the experiment the best from $30^c irc$ to $90^c irc$, but all turbulence models underestimate DC. Between $90^c irc$ and $150^c irc$ sector regions, in the strictest sense, $k-\varepsilon$ matches the experiment the best; however, the differences between the three turbulence models are slight. All turbulence models significantly overestimate the DC in the last sector region ($180^c irc$). The size of DC is dependent on the minimal pressure in each sector. The higher the DC value, the smaller the minimal total pressure in the sector. Therefore, the minimal pressure at the top is larger and minor at the bottom in the simulation. Considering the uniform static pressure distribution on Plane F (as Figure 6.14 shows), the simulation overestimated the top velocity while underpredicting the bottom.

The overestimation of the velocity at the outlet top means an underestimation of the separation effect at the top, and its impact is also reflected in the swirl distortion coefficient. The underestimation of the top flow separation leads to a smaller swirl velocity at the top in the simulation, as illustrated in Figure 6.9 (d), the simulation' SCs are not high at the top sectors, which is high in the experiment's top. Among the turbulence models tested, the SST model matches the experimental trend in a few sectors at the bottom more. The reference velocity, U_{ref}, used in the experiment is the average of the three simulations. Therefore, it can be deduced that the swirl velocity predicted by the simulation is overall lower than the experiment measurement.

Figure 6.10 compares the aerodynamic data of the three turbulence models on Plane F with the experimental data on AIP. The location of Plane F slightly differs from the AIP in the experiment. There is a 4-mm gap between the two planes. The direct calculations of coefficients *uvw* and PR_t from experimental data are presented in Figures 6.10 (a), (f), (k), and (p). The reference point data of the experiment is interpolated by the wall static pressure. The selected static pressure ports are located at L/d = 0.25, and the corresponding circumferential angles are respectively 60° and 120°. L represents the axial distance of the S-shaped duct segment, and d is the inlet diameter. Here, a correction is made to the reference point velocity, substituting it with reference point data in simulations. The differences in reference point velocity obtained from the different turbulence models are minimal, being 50.54 m/s ($k-\varepsilon$), 51.36 m/s ($k-\omega$), and 51.4 m/s (SST), respectively. Here, the average of three models of 51.1 m/s is used. The corrected *uvw* is shown in Figures 6.10 (b), (g), and (l).

Figure 6.10 shows that the SST model can closely match experimental data regarding axial

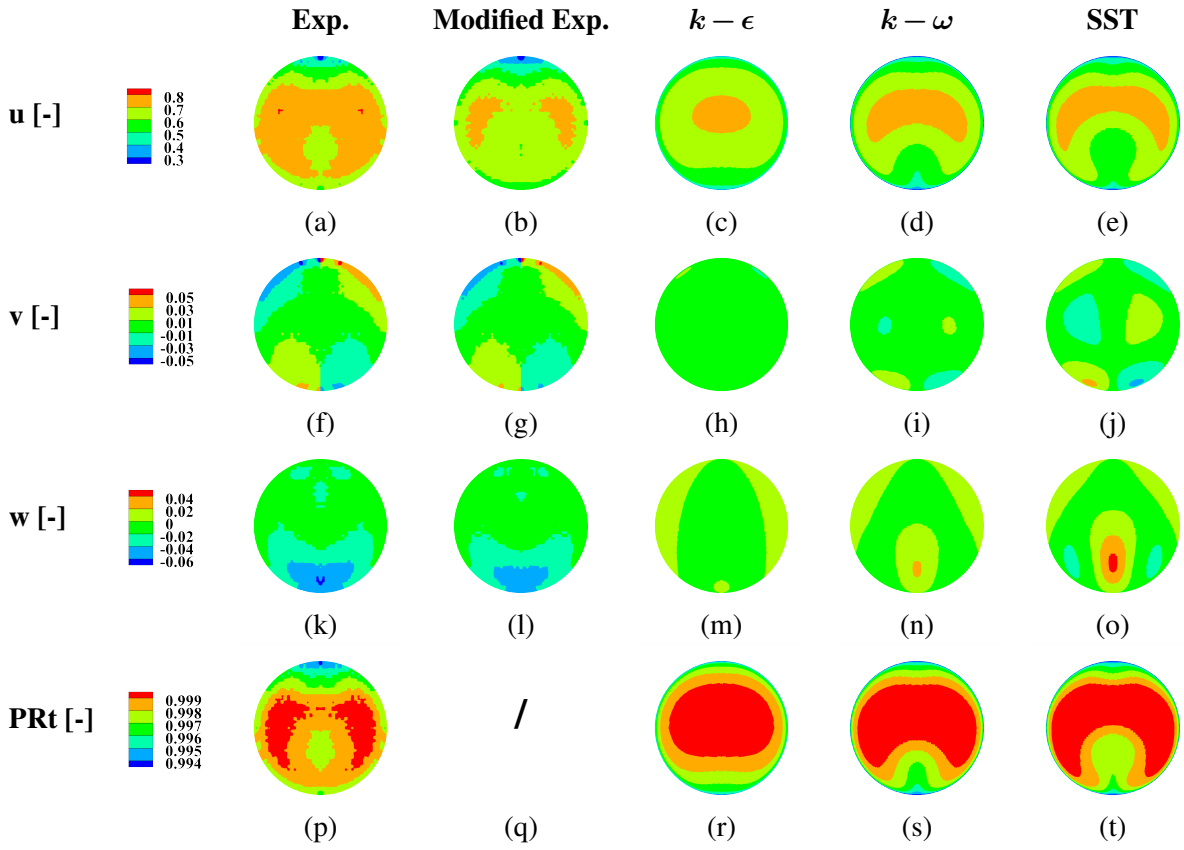

Figure 6.10: Cloud maps of time-averaged aerodynamic data at the outlet cross-section. Modified Exp. represents the velocity coefficients normalised by the velocity at the reference point in the simulation. (a-e) represent streamwise (x-axis) velocity component (u); (f-j) represent the horizontal (y-axis) velocity component (v) on cross-section; (p-t) represent the vertical (z-axis) velocity component (w) on cross-section.

velocity u and total pressure recovery coefficient PR_t. For the horizontal velocity component v on the cross-section, the predicted values from all three turbulence models are lower than those observed experimentally, especially at the top. However, the SST model still yields the highest horizontal velocity component among the models. For the vertical velocity component w on the cross-section, the differences between the simulation and the experiment are apparent and primarily located at the bottom and both sides. In the experiment, the whole interface has a downward velocity component, and the downward velocity component is more robust at the bottom. In contrast, in the simulation, besides the downward velocity component, there are also upward velocity components at the bottom and both sides of Plane F.

6.2.1.2 Comparisons between Two Geometries

Based on the results of numerical validation, it can be found that the SST model demonstrates the best overall performance in simulating the geometry in this experiment. Therefore, the SST turbulence model was chosen to simulate the geometry from NASA. The two geometries are highly similar, with the only difference being the variation in duct radius. The simulations for both geometries utilise the same mesh layout and mesh density.

In the following content, the geometry used in this chapter's experiment will be referred to as Geometry 1, while the geometry proposed by Wellborn et al. [81] will be referred to as Geometry 2. Geometry 1 features a constant radius expansion ratio in the S-shaped duct segment. In contrast, Geometry 2 has a variable radius expansion, with the expansion rate following an S-shaped curve [149]. Figure 6.11 shows wall C_p curves of two geometries; it can be observed that compared with Geometry 1, Geometry 2 has more straight C_p curves at the duct upper regions (0° and 60°/300°). The C_p for Geometry 2 exhibits an almost linear increase, whereas the C_p increase for Geometry 1 shows a pronounced curvature. However, the situation is reversed in the lower regions (180° and 120°/240°). The curve formed by the C_p increase in Geometry 2 is significantly more curved than that of Geometry 1. In magnitude, the C_p values in Geometry 2 are lower than those in Geometry 1 in the first half (s/d <2.5) but higher in the second half across all positions. It can be found from Figure 6.11 that the initial points of the C_p curves for the two geometries at various circumferential positions are almost identical. So, it can be concluded that their initial states are nearly identical. Based on the trend of C_p curves, it can be found that although the flow velocity of Geometry 2 decreases relatively slower after entering the S-duct, near the axial midpoint of the S-duct, Geometry 2's deceleration effect starts beyond Geometry 1 and remains until the exit. The deceleration performance of Geometry 2 is superior to that of Geometry 1 from C_p's point of view.

However, it is challenging to intuitively understand the internal flow inside the S-duct only from the C_p curves. Therefore, Figure 6.12 shows the distribution of the streamwise velocity components at the central planes and its distribution of the velocity coefficient after normalisation to help understand the flow inside the duct. Comparisons and analysis start from the

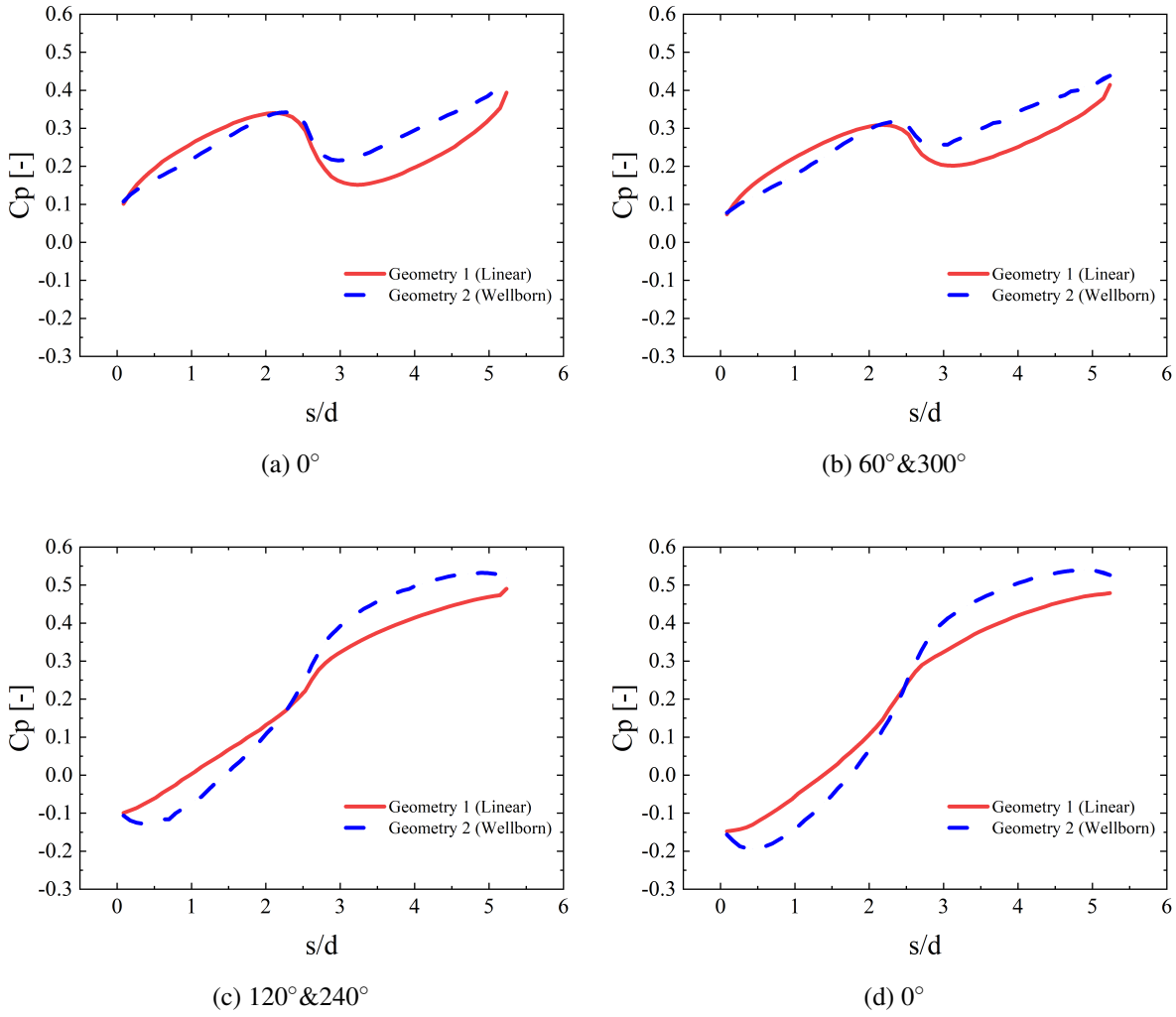

Figure 6.11: Comparisons of wall static pressure coefficients C_p. SST (Linear) denotes the linear growth of the S-shaped segment, corresponding to Equation 4.3. SST (Wellborn) represents the geometry designed by Wellborn *et al. (a) corresponds to 0°; (b) corresponds to 60°&300°; (c) corresponds to 120°&240°; (d) corresponds to 180°.*

[81], corresponding to Equation 4.2

bellmouth. At the bellmouth, it can be found that Geometry 2 has a better velocity uniformity than Geometry 1. Geometry 2's flow velocity has a smooth transition from the front edge of the bellmouth to the front extension. In contrast, Geometry 1 has an apparent low-speed region at the front edge of the bellmouth. At the front extension, in Figure 6.12 (a) and (c), in terms of the velocity distribution inside the front extension section, Geometry 1's distribution is more uniform. Geometry 2 exhibits the characteristic of being high around the boundary and low in the centre. However, after normalisation, it was observed that the airflow in Geometry 1 had a distinct acceleration region before entering the S-shaped duct section, and Geometry 2 had no apparent changes (Figure 6.12 (b) and (d)). After entering the S-shaped segment, Geometry 2's velocity distribution and transition are more uniform and smooth. In contrast, Geometry 1's high-velocity region is still concentrated, as shown in the orange velocity region in Figure 6.12. After normalisation, A discontinuous high-speed region at the middle's top appears in Geometry 1. The previously continuous high-speed area at the top (orange region) has been interrupted and divided into two sections. Also, it can be intuitively found that the stall region in Geometry 1 is more significant than that in Geometry 2 in Figure 6.12. At the rear extension, both geometries keep the trend at the exit of the S-shaped segment.

The difference in duct radius has led to the distinction above. The duct radius at the inlet of Geometry 2 increases more gradually than that of Geometry 1. This allows the airflow to remain relatively uniform after entering the S-shaped duct segment of Geometry 2. Although there are signs of acceleration at the bottom of the throat in Geometry 2, they are much less pronounced than in Geometry 1. Considering the geometry at the bottom of the duct, the acceleration at the bottom of the throat may expedite stall or flow separation in this region, which explains why the stall region at the bottom of Geometry 1 is significantly larger than that of Geometry 2.

Figures 6.13 and 6.14 show the distributions of the velocity component and pressure recovery coefficients at six different slices. It can be seen that the overall trends are similar, but there are apparent differences existing in the details.

For the streamwise velocity u, before the S-shaped duct segment's inlet (Plane A), Geometry 1 exhibits higher velocity at the bottom and lower velocity at the top. Geometry 2 has higher velocities around the boundary and lower in the centre. After the air enters the S-shaped duct segment, Geometry 1 almost keeps the trend in Plane A (higher velocities at the bottom and lower at the top) at the location near the inlet (Plane B), and only magnitudes decrease. By contrast, apparent trend changes occur in Geometry 2; the velocities at the top and centre significantly decrease; however, the bottom velocity is unchanged. The original low-speed region located in the centre moved toward the top. When the air arrives at the middle of the S-shaped duct segment, the trend in Geometry 1 has reversed, and the flow velocities become higher at the top and lower at the bottom. Also, a stall region has appeared at the bottom. Similar trends also exist in Geometry 2, but the top high-speed region is smoother, and the stall region is tiny. Additionally, there is a low-speed region at the centre of Geometry 2. After the airflow moves

for a certain distance again, the trends on Plane D nearly continue that of Plane C, although differences also exist. In Geometry 1, the high-speed region at the top and the bottom stall areas expand. In Geometry 2, the top high-speed region contracts, but the central low-speed expands. The bottom stall regions only slightly increase. When the airflow leaves the S-shaped duct segment and arrives at Plane E, the velocity differences on the whole plane become smaller for both configurations. A relatively big difference exists in the location of the two configurations' low-speed regions. Geometry 1's low-speed region is mainly located at the bottom. Combined with Planes C and D, It can be found that Geometry 1's low-speed region develops from the bottom. In comparison, Geometry 2 has two primary low-speed regions, one at the centre and the other at the bottom. Combined with Planes C and D again, it can be found that Geometry 2's low-speed regions develop from the centre and the bottom, respectively. On Plane E, Geometry 2's two low-speed regions start to connect each other. However, at this moment, the flow at the top for both geometries has no apparent stall phenomenon. Until Plane F, the top velocity is significantly affected. Combined with Figure 6.12, it can be observed that flow separation has not yet occurred at the top, but due to the inertia of the velocity and the geometric gradient of the duct, the high-speed region on plane F is recessed towards the centre. Additionally, the effects of the bottom's stall nearly completely disappear on Plane F.

In terms of crossflow, although both configurations exhibit consistency in overall trends, the differences in details are equally significant. It can be found that the secondary flow in Geometry 1 is noticeably stronger, according to the magnitude of the *vw* coefficients. Stronger secondary flows tend to decrease flow uniformity, making Geometry 2 superior to Geometry 1 in reducing flow distortion. Figure 6.13 shows that the horizontal velocity (v) coefficient distribution overlaps secondary flow vectors. The streamline diagram provides a more intuitive visualization of the characteristics of the secondary flow. It can be observed that Geometry 1 develops two pairs of counter-rotating vortices on plane E, whereas Geometry 2 exhibits only one pair at this stage; on plane F, Geometry 1 and 2 both display two pairs of counter-rotating vortices. However, the secondary flow in Geometry 1 is still stronger and more complex.

Regarding pressure recovery, the two configurations only exhibit tiny differences in the distributions of the static pressure recovery coefficients. Additionally, the static pressure has been almost uniformly distributed on the plane from Plane C. By contrast, there are significant differences between the distributions of the total pressure recovery coefficients. Due to the uniform static pressure distributions, the dynamic pressure distribution determines the total pressure distribution. It can be found that the PRt distribution in Figure 6.14 has a high similarity with the axial flow velocity coefficient (u) distribution in Figure 6.13. The low-speed region also corresponds to the lower total pressure recovery coefficient. From the change trends, Geometry 1 and 2's total pressure weakening regions both start at the bottom and develop toward the duct centre; however, Geometry 2 bottom's total pressure weakening region is smaller and limited at the bottom. When airflow arrives in Plane E, it can be found that Geometry 2 bottom's total

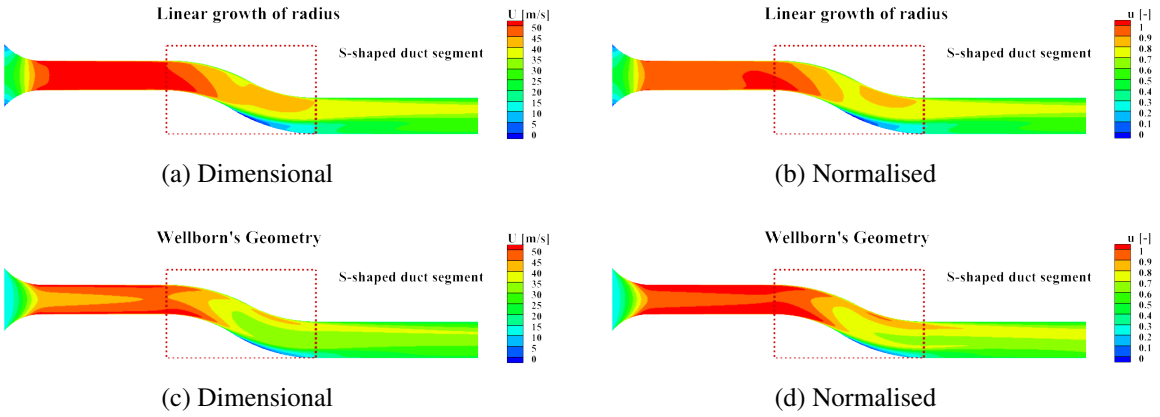

(a) Dimensional (b) Normalised

(c) Dimensional (d) Normalised

Figure 6.12: Comparisons of the central slices. The linear growth of the S-shaped segment corresponds to Equation 4.3. Wellborn *et al.*'s geometry [81] corresponds to Equation 4.2. (a,c) have velocity magnitudes, and (b, d) are after normalization.

pressure weakening region started to merge with the central low-PRt region, and the uniformity is higher than Geometry 1. In comparison, the boundary of the area affected by total pressure in Geometry 1 remains distinctly well-defined. As the airflow continues to move forward, two configurations exhibit the sign of merge, but Geometry 2 still compasses Geometry 1 regarding integration.

6.2.2 Modal Analysis

Based on the above analysis, it can be observed that, compared to Geometry 1, Geometry 2 not only decelerates the airflow more effectively but also maintains better flow uniformity. Therefore, Geometry 2 is selected for further modal analysis. However, a flow property analysis of the transient fields obtained from the three turbulence models will be conducted before the modal analysis.

6.2.2.1 Flow Properties

Details on computation time and time steps can be found in Section Simulation Setup. The velocity and total pressure standard deviation cloud maps at the AIP (Plane F) are presented in Figure 6.15. It can be observed that the standard deviations obtained from the three turbulence models are all relatively small. $k-\varepsilon$ can still have a discernible trend, whereas the $k-\omega$ and SST models essentially fail to provide meaningful information. The standard deviations for the $k-\omega$ and SST models are almost close to 0 on the order of magnitude. There are two leading causes for this phenomenon. On the one hand, the flow on Plane F tends to be steady. On the other hand, limited by the RANS algorithm, the time average error decreases the fluctuation magnitude of the turbulence. Additionally, it can also be found from Figure 6.15 that the velocity fluctuations obtained from $k-\varepsilon$ are significantly greater than those from $k-\omega$ and SST turbulence models.

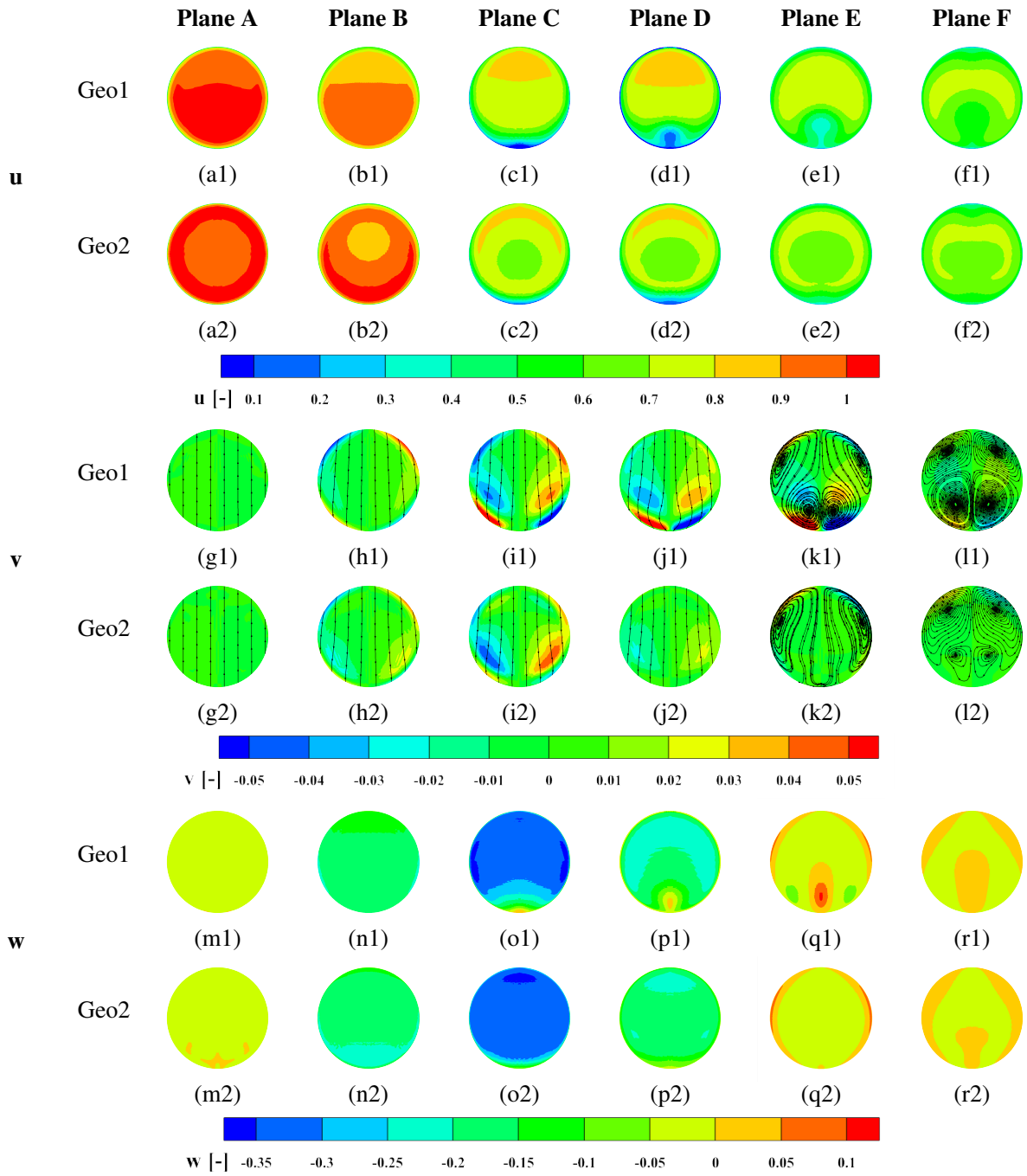

Figure 6.13: Comparisons between two geometries' velocity coefficients at six different slices (normalized by the S-duct throat's resultant velocity). Geo1 represents the linear growth of the S-shaped segment, corresponding to Equation 4.3. Geo2 is the geometry designed by Wellborn *et al.* [81], corresponding to Equation 4.2. (a-f) represent streamwise velocity (u); (g-l) represent the horizontal velocity (v) on cross-section; (m-r) represent the vertical velocity (w) on cross-section.

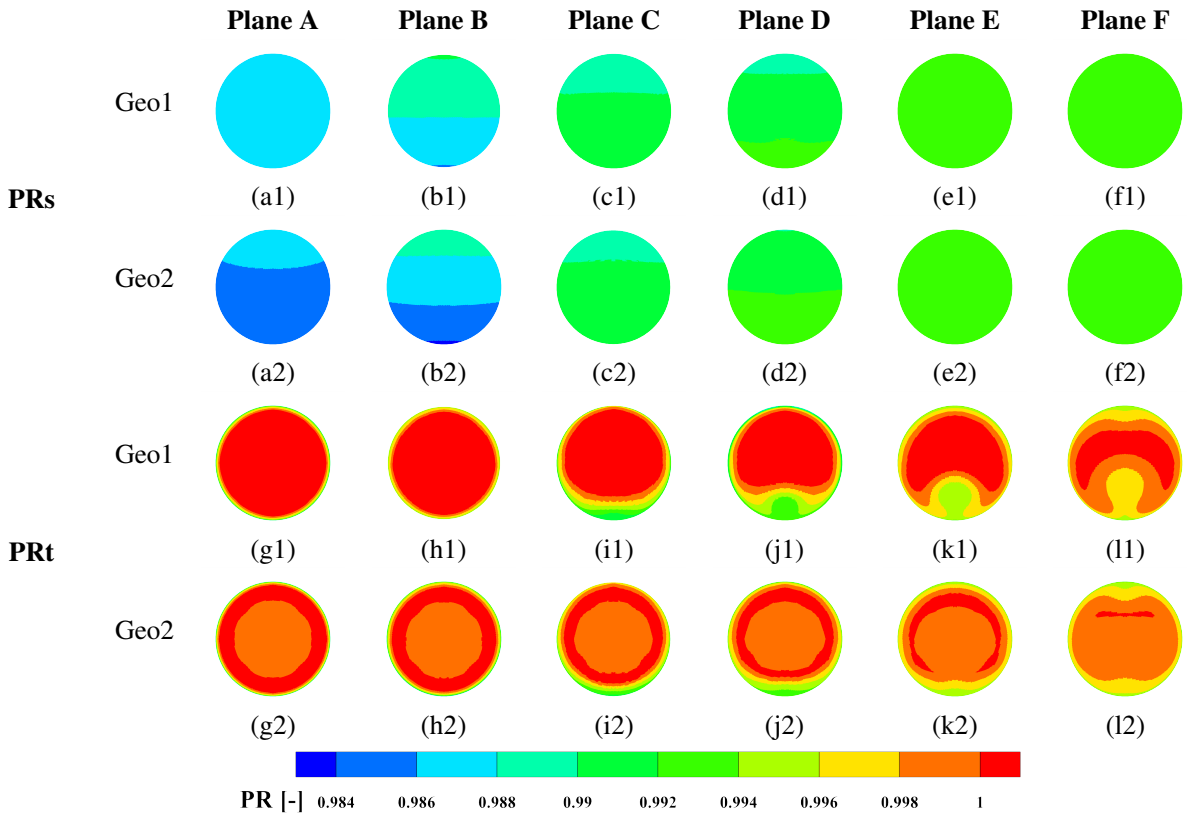

Figure 6.14: Comparisons between two geometries' pressure recovery coefficients at six different slices (normalized by the environmental pressure). Geo1 represents the linear growth of the S-shaped segment, corresponding to Equation 4.3. Geo2 is the geometry designed by Wellborn *et al.* [81], corresponding to Equation 4.2. (a-f) represent the static pressure coefficients (PRs), and (g-l) represent the total pressure coefficients (PRt).

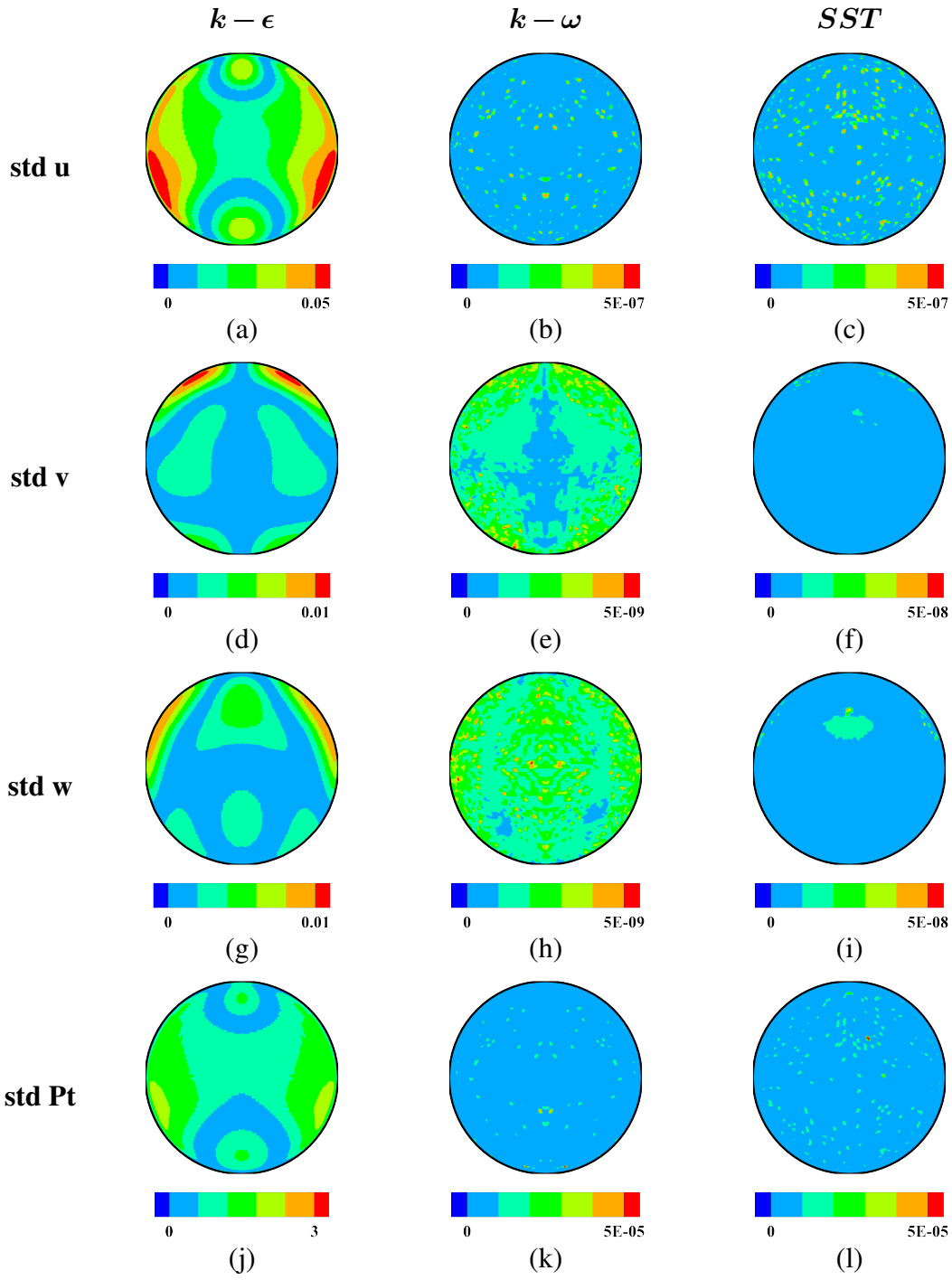

Figure 6.15: Standard deviation cloud maps of aerodynamic data on Plane F. (a), (d), (g), and (j) correspond to $k-\varepsilon$ model; (b), (e), (h), and (k) correspond to $k-\omega$ model; (c), (f), (i) and (l) correspond to SST model.

6.2.2.2 POD

A Proper Orthogonal Decomposition (POD) analysis was conducted on the three-dimensional velocity components of Plane F. Figure 6.16 shows the modal energy distribution for the stream-wise velocity and the cross-flow vector, respectively. The vector mode is computed by combining the velocity data in two dimensions into one dimension. The first-order mode of POD represents the most dominant flow structure, possessing the highest energy contribution. It can be found that regarding the energy proportion of the first-order mode, the $k-\varepsilon$, $k-\omega$, and SST models exhibit energy proportions in the stream-wise velocity field of 47%, 37%, and 33%, respectively. The difference is significant; however, in contrast, the difference is more pronounced in the cross-flow field, at 38%, 22%, and 8%, respectively. If, in terms of flow field reconstruction, to achieve a criterion of 99% of the flow field energy, the $k-\varepsilon$ model requires 14 and 12 modes for stream-wise velocity field and cross-flow field, respectively, the $k-\omega$ model necessitates 176 and 330 modes. The SST model demands more, reaching 377 and 570, for stream-wise velocity and cross-flow field reconstruction, respectively. The number of modes required for the rebuilding stream-wise velocity field is less than that for the cross-flow field. Evidently, one more dimension will significantly increase the flow complexity. Within the turbulence models, the SST model manifests the lowest energy proportion in its first-order mode, accompanied by minor energy discrepancies among its initial modes. It necessitates the maximal number of modes for effective flow field reconstruction. However, this characteristic also represents the SST model, which can characterize more intricate details of the flow field, showing its superiority in capturing complex flow dynamics.

The temporal evolution coefficients of the first-order mode and their predominant frequencies are depicted in Figure 6.17. The dominant frequencies are calculated by the Fast Fourier Transform (FFT). It is easy to observe that the temporal coefficients of the $k-\varepsilon$ model exhibit periodic variations from Figures 6.17 (a) and (c). But when compared against the fluctuation range of the $k-\varepsilon$ model's temporal evolution coefficients, the magnitudes of the $k-\omega$ and SST models' temporal coefficients are much smaller, nearly approaching zero in figures. However, the truth is that they are non-zero and also demonstrate periodic variations. The time coefficients of the $k-\omega$ and SST models are significantly smaller than that of the $k-\varepsilon$ model, which is consistent with the findings shown in Figure 6.15. Figure 6.15 presents the standard deviation cloud maps of three turbulence models on plane F. The standard deviations of velocity and pressure in the $k-\omega$ and SST models are considerably lower than those in the $k-\varepsilon$ model. Considering that the $k-\varepsilon$ model has advantages in handling fully developed turbulent flows far from the wall but may encounter accuracy issues in near-wall regions and low Reynolds number flows, leading to an overestimation of velocity fluctuations, it is possible that the algorithms of the three turbulence models are the reason why the velocity fluctuations of the $k-\omega$ and SST models are much lower than those of the $k-\varepsilon$ model. However, as observed in Figure 6.15, the $k-\varepsilon$ model overestimates velocity fluctuations not only near the wall but also across the entire plane. The

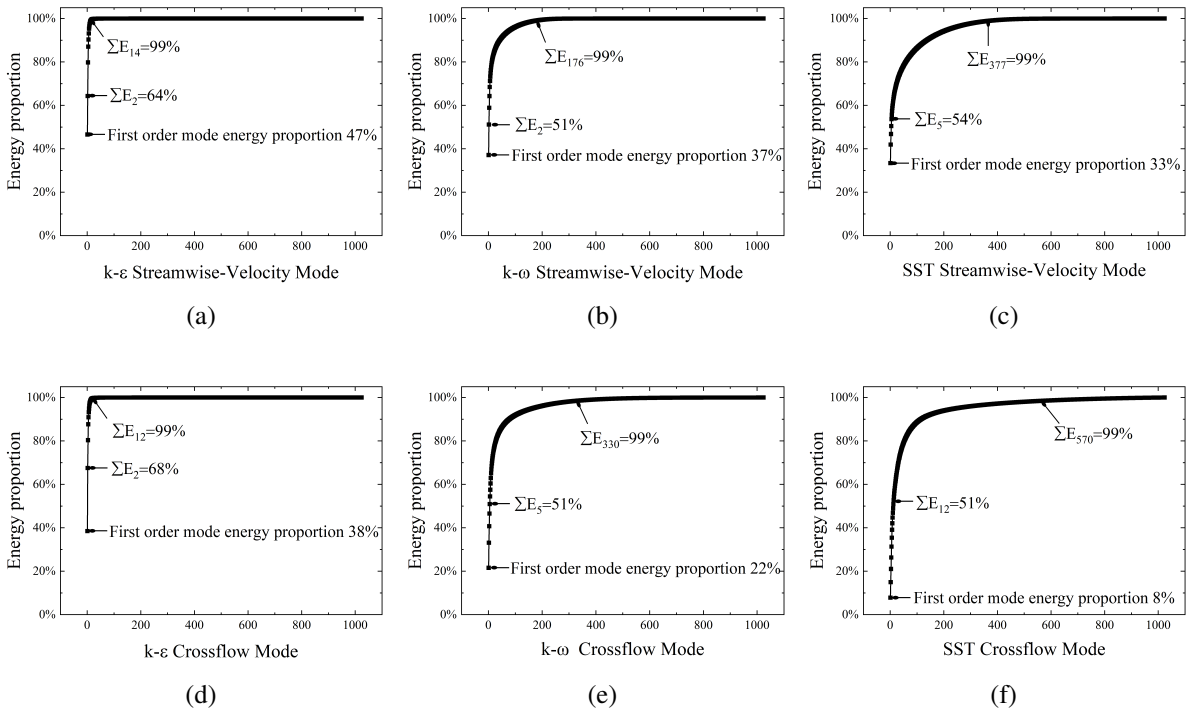

Figure 6.16: Stream-wise (a-c) and cross-flow (d-f) mode energy proportions under three turbulence models.

transient results of the $k-\omega$ and SST models on Plane F approach a quasi-steady state. This is likely because the $k-\omega$ and SST models have more refined treatments of turbulence, allowing for more accurate predictions of velocity fluctuations, but they also have higher time-step requirements. If the time step is too large, the time-averaging effect could reduce the amount of velocity fluctuation. In this study, the same time step was used for all three turbulence models, which may explain the near-steady-state behavior in the $k-\omega$ and SST models. However, this conclusion is speculative and requires further validation in future research.

Through FFT, the first-order mode's frequency characteristics were analysed in Figures 6.17 (b) and (d). Regarding the stream-wise velocity and cross-flow vector, the $k-\varepsilon$ model exhibits dominant frequencies at 16Hz and 15Hz, respectively. The $k-\omega$ model demonstrates dominant frequencies at 124Hz and 2Hz, and the SST model shows dominant frequencies at 28Hz and 205Hz. It can be found that the variance in the dominant frequencies of the first-order mode is significant; for stream-wise dominant frequency, the $k-\varepsilon$ and SST models are predominantly governed by low-frequency components, while a high-frequency component governs the $k-\omega$ model. Regarding the dominant frequency of the cross-flow vector, both the $k-\varepsilon$ and $k-\omega$ models are dominated by low-frequency components, but a high frequency governs the dominant frequency of the SST model. However, the amplitude in Figure 6.17 is not normalized. To intuitively show periodic variations more, Figures 6.18 and 6.19 show the first-order mode extreme cases of three turbulence models and their centreing magnitude after centralization (ac-

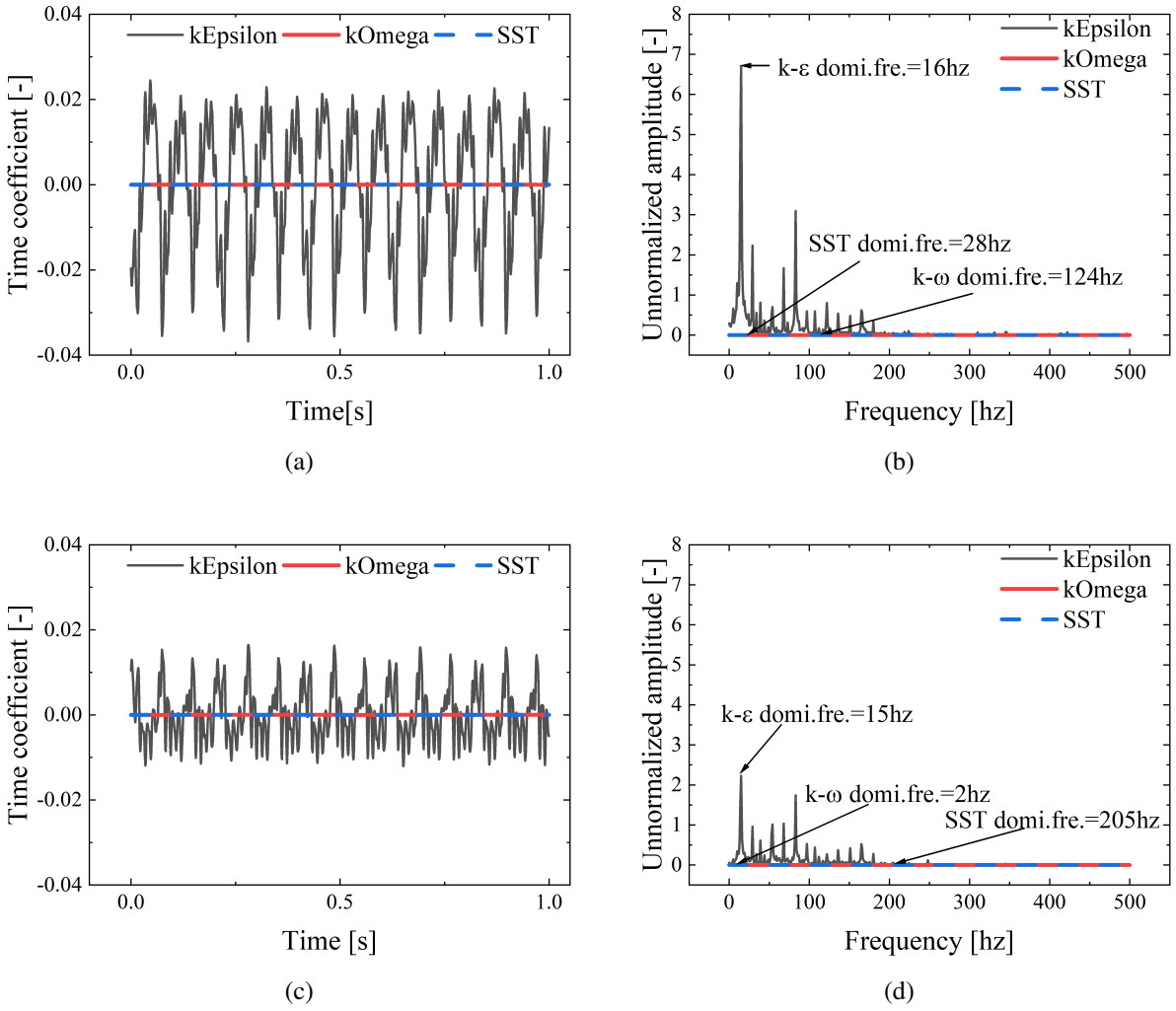

Figure 6.17: POD time evolution coefficients and corresponding frequency spectral analysis (FFT); (a) and (b) are for the stream-wise velocity; (c) and (d) are for the cross-flow vector.

tual velocity fluctuation magnitude). The extreme case refers to the state where the temporal coefficients reach their maximum and minimum values. Unnormalized amplitude is normalized by dividing half of the sampling number, namely 512. For the stream-wise velocity (Figure 6.18), it is evident that the $k-\varepsilon$ model exhibits periodic inverse change trends. Although the $k-\omega$ and SST models also show this trend, the mode's distribution has no apparent rule and only indicates a dotted extreme value distribution. This should be because the flow at Plane F is too close to a steady state under $k-\omega$ and SST models. In addition to the physical phenomena, the flow proximity to a steady state is also attributed to the time-averaging error inherent in the URANS method. It should be noted that the fluctuation range in stream-wise velocity under all three models is tiny. Among turbulence models, the $k-\varepsilon$ model demonstrates the most extensive fluctuation range, yet the magnitude of these fluctuations is confined to approximately $\pm$ 0.0008 m/s. The fluctuation ranges for the $k-\omega$ and SST models are further reduced to the order of magnitude of 10^{-7} m/s. When superimposed upon the average velocity, such minute fluctuations have an insubstantial impact on the overall mean velocity.

Similarly, the fluctuation ranges for the cross-flow magnitude are exceedingly small in Figure 6.19. The fluctuation magnitudes of the $k-\varepsilon$ model are only approximately $\pm$ 0.0004 m/s. The fluctuation ranges of the $k-\omega$ and SST models even descend to the order of magnitude of 10^{-8} m/s. According to vector plots, it can be observed that the $k-\varepsilon$ model has distinct periodic and regular movement patterns. But like the streamwise flow, the $k-\omega$ and SST models don't exhibit regular apparent law of motion. However, it is worth noting that the SST model is not completely irregular across the whole plane. Similar vertical movement can also be found at the SST model's plane top. As for Plane F's bottom under the SST model and the entire Plane F under the $k-\omega$ model, there is no apparent cross-flow movement pattern.

Through the analysis above, it can be found different turbulence models show significant differences in mode decomposition. Although the SST model needs more modes to reconstruct the flow field, more modes also illustrate that the SST model can elucidate more details of the flow field. Meanwhile, this also means the SST model has certain advantages in characterising the flow field. However, the next analysis found that only the $k-\varepsilon$ model exhibits apparent motion patterns. The first mode of the $k-\omega$ and the SST models nearly cannot provide meaningful information. In addition to the fact that the flow on the plane tends to a stable state under low Mach number conditions, the inherent time-averaging error in the URANS method further increases the difficulty of resolving turbulence. Among the three models, the flow field obtained with the $k-\varepsilon$ model has the highest level of instability.

6.2.2.3 DMD

The essence of the Dynamic Mode Decomposition (DMD) method is approximating the flow system to a linear system, with its solution encompassing initial values, eigenvalues, and corresponding modes. The eigenvalues derived encapsulate information on growth rates and frequen-

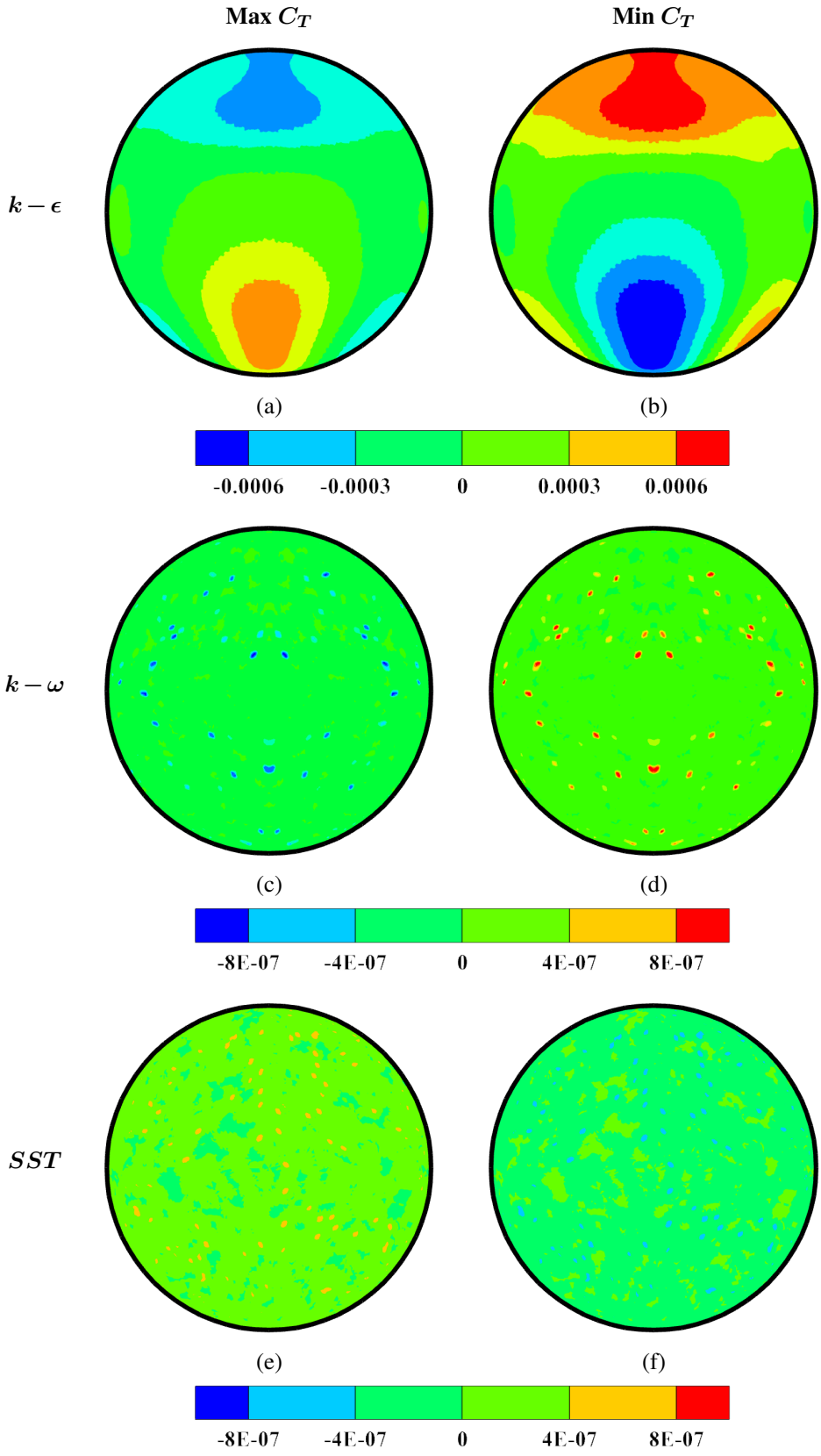

Figure 6.18: Stream-wise velocity first-order mode (m/s); C_T represents the time coefficient. (a) and (b) are $k-\varepsilon$ model, (c) and (d) are $k-\omega$ model, (e) and (f) are SST model.

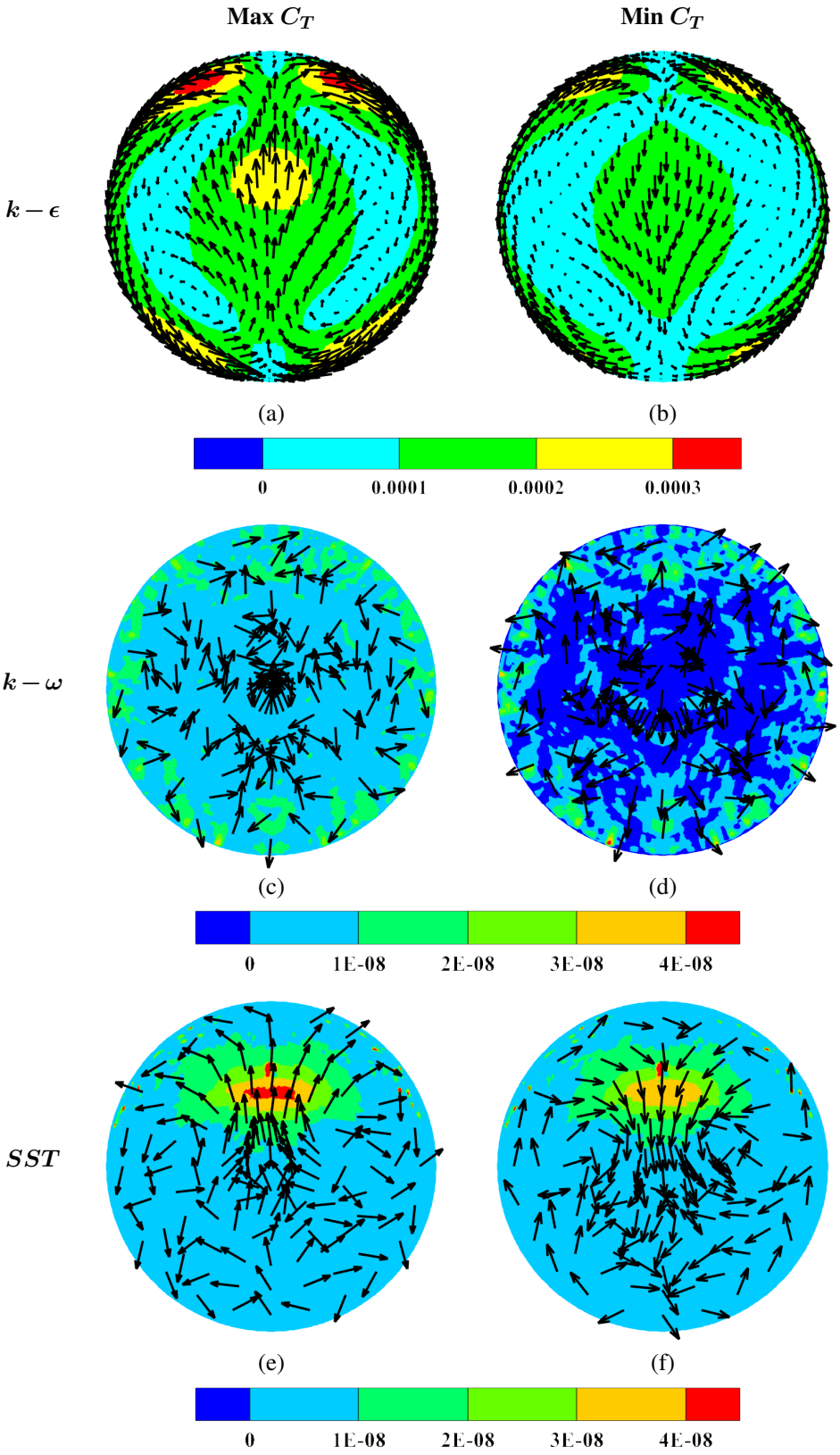

Figure 6.19: Cross-flow velocity vector first-order mode (m/s); C_T represents the time coefficient. Legend bar is the velocity magnitude. (a) and (b) are $k-\varepsilon$ model, (c) and (d) are $k-\omega$ model, (e) and (f) are SST model.

cies. During the calculation, set a benchmark at 10^{-6} to eliminate modes whose eigenvalues are approximately equal to zero to prevent computational divergence. The calculated results are as follows. The $k-\varepsilon$, $k-\omega$, and SST models retained a total of 1023, 283, and 578 modes in the stream-wise velocity, respectively, while 751, 17, and 79 modes were preserved in the cross-flow vector, respectively. The distribution of modal eigenvalues obtained from DMD analysis is depicted in Figure 6.20.

The magnitude of the absolute of the eigenvalue determines whether the overall mode grows or decays (stable or unstable), and the metric is whether it is greater than 1. The unit circle in Figure 6.20 shows the criterion for determining the stability of modes more intuitively. If the eigenvalues are located within the unit circle, the mode decays as time and this mode is viewed as a state of stability; if they are on or near the boundary of the unit circle, the mode is considered neutrally stable because this mode is located at the critical state of growth nor decay. If they are distinctly outside the circle, the mode is unstable [175, 176]. In Figure 6.20, it is observed that only the $k-\varepsilon$ model contains lots of eigenvalues predominantly in or near the boundary after DMD analysis. In contrast, most modes of the $k-\omega$ and the SST models are in the unit circle. This indicates only the $k-\varepsilon$ model is neutrally stable, and the $k-\omega$ and the SST models are solid stable. Moreover, all first-order modes are located on the unit circle, with the real part being 1, signifying neither growth nor decay; zero frequency implies that the mode does not vary over time. As a stationary mode, its value is similar to the mean, allowing it to characterize the average flow field.

Moreover, the eigenvalues, serving as the solutions for the spatiotemporal coherent structures in DMD, can be transformed into a form with a natural number exponent. This form can then characterize the growth rate and frequency. The real part of these values corresponds to the growth rate. In some literature, the growth rate is also called the decay rate; fundamentally, they convey the same meaning. If the real part is greater than 0, it indicates that the amplitude of the mode increases over time; if it is less than 0, the amplitude decreases; and if it equals 0, the amplitude remains constant. The imaginary part corresponds to the oscillation frequency; if it is zero, it indicates that the mode does not oscillate. However, the frequency values are not directly provided but require conversion by dividing the imaginary part by 2π [177], as delineated in Equation 6.11

$$f_i = \frac{imag(\omega_i)}{2\pi} \tag{6.11}$$

where ω_i denotes the imaginary part of the eigenvalue after being transformed into an exponential form with a natural number base, with the subscript i representing the mode number.

Herein, a loss function (Equation 6.12) [175] is introduced to assess the error generated in the reconstruction of unsteady flow fields by DMD

$$\Pi = 100\sqrt{\frac{||\Psi_0 - \Phi D_\alpha V_{and}||_F}{||\Psi_0||_F}} \tag{6.12}$$

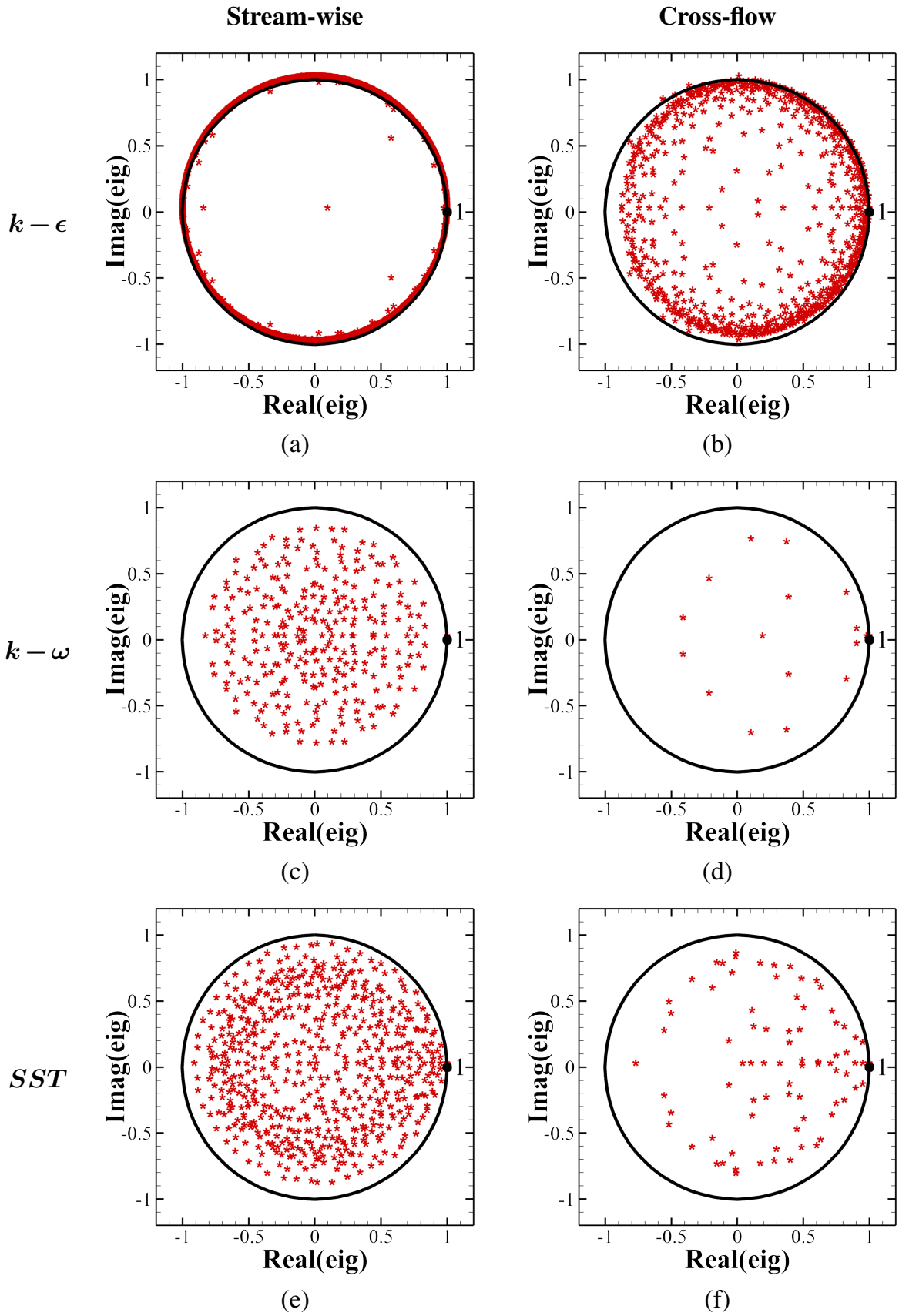

Figure 6.20: Eigenvalue unit circle plot for dynamic mode decomposition of stream-wise velocity and cross-flow vector. (a) and (b) are $k-\varepsilon$ model, (c) and (d) are $k-\omega$ model, (e) and (f) are SST model.

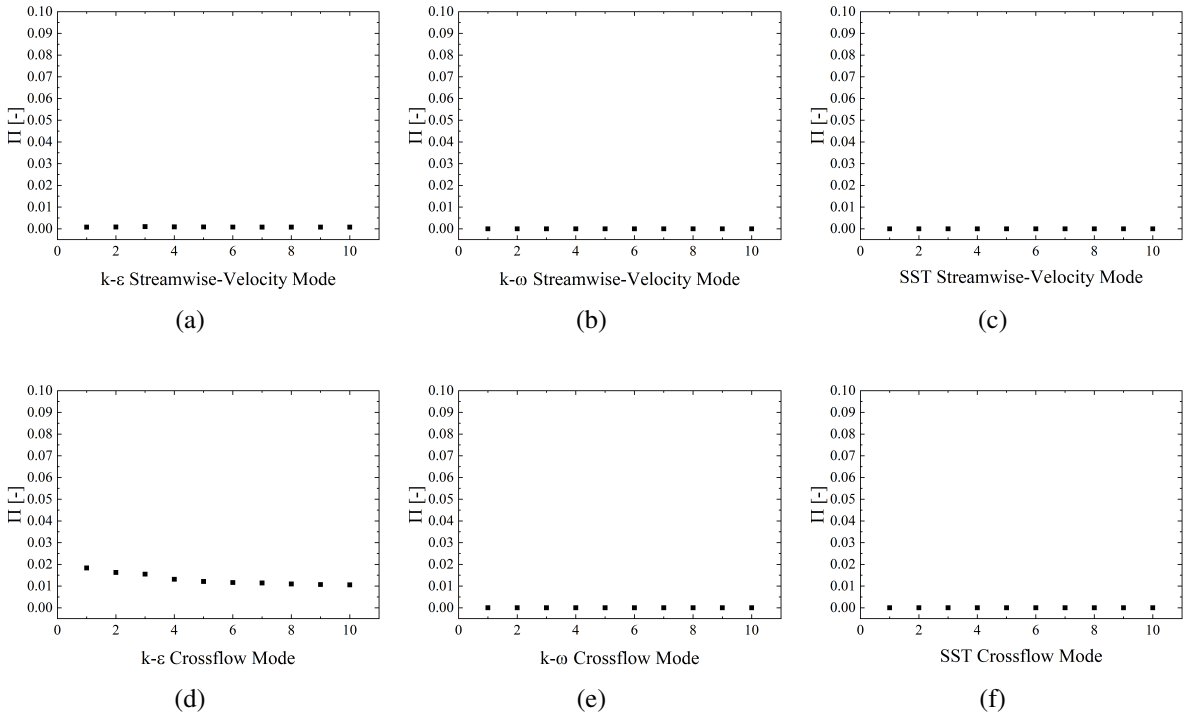

Figure 6.21: The loss coefficient for dynamic mode decomposition of stream-wise velocity (a-c) and cross-flow vector (d-f).

where Ψ_0 represents the original flow field data, Φ denotes the modal matrix, D_α is the modal amplitude matrix, and V_{and} stands for the Vandermonde determinant of eigenvalues. $||||_F$ signifies the computation of the Frobenius norm of a matrix. Figure 6.21 shows three turbulence models' loss coefficient changes with the mode numbers; it can be found that even though only using the first mode to reconstruct the flow field, the difference between the reconstructed flow field and the real flow field is tiny. However, this is not because the first mode has many flow field characteristics but because the divergence between the mean flow field and the instantaneous flow field data is tiny, especially when using $k-\omega$ and SST models. Here, it should be noted that POD has centralized the flow field, whereas DMD has not.

In the analysis conducted through DMD, the frequencies and growth rates of the first five modes are presented in Table 6.4. The growth rate and the frequency can be divided into three modal forms. First, modes characterised by both a zero growth rate and a zero frequency are considered stationary modes, closely resembling the mean flow field. Second, modes appear in conjugate pairs with nonzero growth rates and frequencies, characterising the flow field's main structures. Lastly, modes with a nonzero growth rate but a zero frequency are denoted as drift modes, reflecting the evolution of the flow field's mean value over time within a linearized process [178]. In Table 6.4, the SST model's eighth cross-flow mode is a drift mode, while the ninth and tenth modes are conjugate modes. Due to a mismatch with the stream-wise velocity mode, they are denoted with a slash.

Table 6.4: DMD mode growth rate (r) and frequency (f).

		$k-\varepsilon$		
	Stream-wise		Cross-flow	
	Growth rate	Frequency(Hz)	Growth rate	Frequency(Hz)
1	0	0	0	0
2-3	0.0038	156	-0.0001	83
4-5	0.0004	15	-0.0002	15
6-7	0.0003	83	-0.0008	68
8-9	0.0008	53	-0.0011	54
		$k-\omega$		
	Stream-wise		Cross-flow	
	Growth rate	Frequency(Hz)	Growth rate	Frequency(Hz)
1	0	0	0	0
2	-0.2639	0	-1.6524	0
3-4	-0.3234	135	-0.8376	448
5-6	-0.3217	12	-0.7208	103
7-8	-0.2946	129	-0.7254	322
		SST		
	Stream-wise		Cross-flow	
	Growth rate	Frequency(HzHz)	Growth rate	Frequency(hz)
1	0	0	0	0
2-3	-0.2893	188	-0.038277751	26
4-5	-0.7945	168	-0.087736422	33
6-7	-0.5089	146	-0.216040104	252
8-9	-0.6319	135	\	\

According to the data presented in Table 6.4, it is observed that in terms of frequency analysis, the frequencies of the fourth and fifth modes of $k-\varepsilon$ are consistent with the first-order mode frequency obtained through POD analysis. However, this consistency is not found in $k-\omega$ and SST models. This could be attributed to the transient flow fields of both models being excessively close to a steady state, thereby introducing numerical errors into the analysis.

6.2.2.4 SPOD

In POD analysis, only the $k-\varepsilon$ model exhibits a distinct motion pattern in the modal decomposition, while the $k-\omega$ and SST models don't. Furthermore, since SPOD decouples time-based on the POD framework, in this case, only the $k-\varepsilon$ model was analysed using SPOD.

In total, 1024 snapshots were used in this analysis. Each block contains 64 snapshots, with a 50% overlap between adjacent blocks. Figure 6.22 is the SPOD eigenvalue spectrum of streamwise velocity under the $k-\varepsilon$ model. Modes at each frequency are organised in a descending sequence based on their eigenvalue magnitudes. The modes of the same order are connected. Eigenvalues represent the energy magnitude. The first-order mode at 15.625 Hz has the maximum energy in Figure 6.22. This frequency almost aligns with the first-order mode's dominant

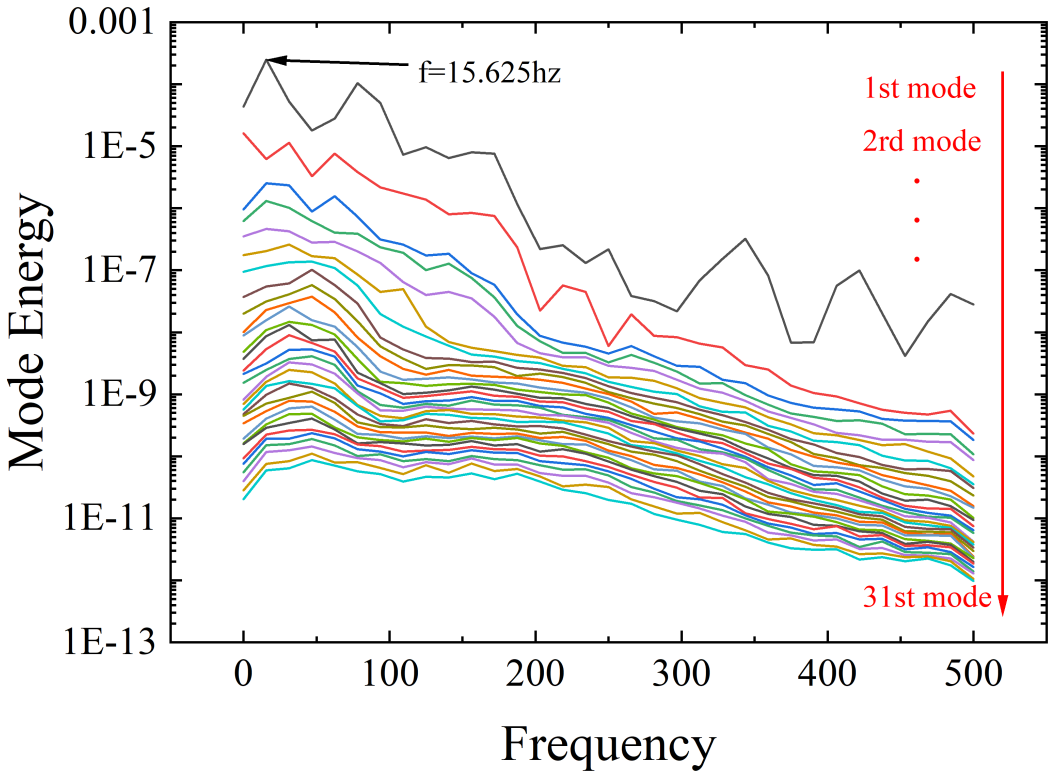

Figure 6.22: SPOD eigenvalue map of the stream-wise velocity under the k-Epsilon model.

frequency (16Hz) determined through POD (as shown in Figure 6.17 (b)).

Figure 6.23 further compares the POD's first-order mode (dominant frequency is 16 Hz) and SPOD's first-order mode at 15.625 Hz. It can be found that the first-order mode of SPOD is consistent with POD in fluctuation magnitude, exhibiting partially similar traits of variation. However, compared to POD, SPOD's first-order mode includes a richer dynamic structure and a larger magnitude. This is because the SPOD method achieves frequency decoupling, filtering out all flow features at frequencies other than 15.624 Hz, thus avoiding interference from other frequencies.

6.3 Chapter Summary

This chapter compared the performance of two different S-shaped duct geometries through numerical approaches and studied the turbulence characteristics within the S-shaped ducts. RANS and URANS methods were employed in the simulation, and three turbulence models were tested. Furthermore, this study also demonstrates the features and functions of various modal decomposition methods. This study addresses a gap in the existing research regarding the ability of different turbulence models to capture the intricate characteristics of turbulence. The findings presented in this chapter hold significant value for future numerical investigations and the design

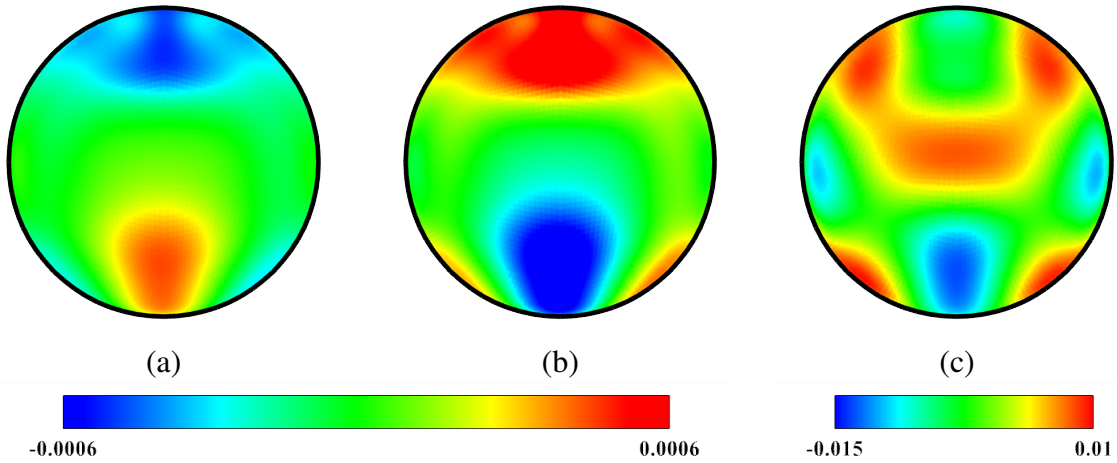

Figure 6.23: The stream-wise velocity modes (m/s) obtained from the $k-\varepsilon$ model. The POD's dominant frequency is 16 Hz, and SPOD selected the first-order mode at 15.625 Hz. (a) with the maximum time coefficient (POD); (b) with the minimum time coefficient (POD); (c) is SPOD first-order mode under frequency = 15.625Hz.

of S-ducts. The main conclusions are as follows:

(1) At low Mach numbers, despite some discrepancies with the experimental results, the wall pressure coefficient (C_p) curves of the S-shaped diffuser obtained from the three turbulence models show no significant differences and almost overlap entirely. The primary deviation from the experimental data lies in the underprediction of the flow separation at the bottom. Furthermore, in terms of pressure loss, the results from all three turbulence models are close to the experimental data, with the $k-\varepsilon$ model providing the closest match. However, regarding flow characteristics and trends, the SST model demonstrates a clear advantage.

(2) The diffusion rate with an S-shaped growth profile demonstrates superior performance compared to a constant diffusion rate. It allows for a more uniform deceleration of the flow within the duct, delaying the onset of flow separation at the bottom and reducing the extent of the affected region. However, when transient simulations of this configuration are conducted using URANS based on the conclusions drawn from experiments, it was found that the transient results of all three turbulence models converged towards a steady state, with the flow fluctuations for the k-Omega and SST models even approaching zero, several orders of magnitude lower than those predicted by the k-Epsilon model. However, even the k-Epsilon model was still lower than the measured value of the experiment. The corresponding influence is also reflected in the modal analysis. For the $k-\omega$ and SST models, the first mode extracted by POD even lacks clear dynamic patterns.

(3) Different modal analysis methods exhibit different characteristics. The POD method could efficiently extract the main spatial structures within the flow field, yet it encountered issues

with multi-frequency coupling, necessitating using FFT to obtain the dominant frequency. To some extent, DMD addressed the issue of multiple-frequency coupling found in POD, allowing for the acquisition of dynamic coherent structures at a single frequency. Furthermore, DMD also has other functions, such as using the eigenvalue circle to assess the stability of modes and predicting future flow fields based on the linearisation of the flow field. For SPOD, this method can also avoid the multiple-frequency coupling inherent to the POD method by decoupling the flow-field data in the temporal and spatial fields. Its single-frequency modes provided more spatial structural details than POD, which gives the SPOD method more advantages in analysing the unsteady flow field.

However, the limitations of this study must be acknowledged. Due to the inherent constraints of the Reynolds-Averaged Navier-Stokes (RANS) methodology, the time-averaging errors in the Unsteady RANS (URANS) approach render it intrinsically inadequate for detailed turbulence analysis. This limitation consequently narrows the findings of turbulence in the present study. While reducing the time-averaging errors within the URANS framework can be partially achieved by employing smaller time steps, a more suitable approach would be the direct application of Large Eddy Simulation (LES) or Direct Numerical Simulation (DNS).

The next chapter will further examine the performance of the plasma flow control inside the S-duct through the experiment and simulation.

Chapter 7

Plasma Flow Control inside the S-duct

Plasma is the fourth state of matter, after solids, liquids, and gases. It is typically accompanied by extremely high temperatures, which makes it challenging to probe its physical properties in depth. However, although the deep physical mechanism is unclear, researchers have mastered its physical phenomenon and rules to some extent through extensive experiments and applied it to the fluid field. A regular method to obtain plasma in the fluid field is to exert a solid electrical/magnetic field on a neutral fluid. When a solid electrical field is exerted on air, the strong electrical field can induce the ionization of gases; at this time, the charged particles collide with other neutral particles, further generating more charged particles. This phenomenon is called avalanche Ionization and Townsend Avalanche, which was first imposed by Townsend [179]. During the collision, influenced by the electrical field, negative ions move toward the positive electrode, and positive ions move toward the negative electrode. Meanwhile, many neutral particles get momentum from the movement of positive and negative ions through the collision, thus forming ion wind. Using this characterization rationally can achieve flow control. Based on this principle, generated fluid movement is also called electrohydrodynamic (EHD); its notable characteristics are rapid response and adjustability [180, 181]. The surface dielectric barrier discharge(SDBD), as one of the branches of EHD, is a hot study direction. This scheme was first officially proposed by Professor Roth's team [7, 8]; it first successfully realised the large-scale plasma discharge uniformly under constant pressure conditions. Because of the advantages of easy structure, reliable performance, easy-to-large-scale deployment, and no extra moving parts needed, it has received widespread attention since it was proposed.

A typical SDBD actuator consists of an exposed electrode, a covered electrode, and the dielectric layer, as Fig. 7.1 shows. The anode (exposed electrode) is connected to a power source, while the cathode is usually grounded. During operation, a sufficient voltage is applied to the anode to ionize the surrounding air and generate plasma, which then diffuses from the anode towards the cathode. However, this discharge process is self-limiting, as the charge emitted from the anode accumulates on the surface of the dielectric, thereby reducing the potential difference around the anode and suppressing plasma further formation unless the voltage applied to the

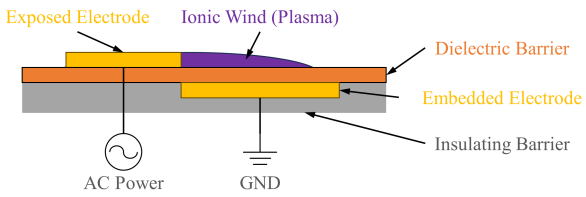

Figure 7.1: The schematic of the surface dielectric barrier discharge (SDBD) actuator.

anode is continuously increased [19]. To address this limitation, the connected power source typically takes alternating current (AC power) to achieve a periodically varying voltage, generating a relatively continuous plasma. Due to the covered cathode, there is no airflow movement on the side of the cathode; thereby, the direction of the time-average velocity field induced by the plasma actuator is always from the anode to the cathode.

The SDBD plasma's jet characterization can function as the wall jet to induce extra momentum into the boundary layer. This enhances the boundary layer's ability to overcome adverse pressure gradients and thus delay or avoid possible flow separation. This chapter aims to use the SDBD plasma actuator to optimize the flow field inside the S-shaped duct. Here is a brief introduction to the S-shaped duct.

The S-shaped ducts are widely used for the current high-speed aircraft intake. When a high-speed aircraft is flying at high speed, the speed of the incoming flow is always too high for the engine or the compressor ahead of the engine. Thus, engines cannot perform at their best. Intakes are induced to slow the airspeed to improve the engine's performance. However, the intake was not initially S-shaped but straight. The conventional intake is usually a straight diffusing duct. However, as the modern aviation industry develops, many new demands, such as stealth and weight loss, make conventional straight ducts no longer suitable. Compared with traditional straight ducts, the S-shaped duct can better hide the engine due to its convoluted geometry, thus reducing infrared reflection signals. In addition, the complicated geometry of the S-shaped duct can more efficiently and quickly slow the incoming air speed. For the same deceleration need, the S-shaped duct can usually reach it in a shorter length than straight ducts. A shorter intake length benefits the weight reduction of the whole aircraft [1, 2]. According to Chen and Wang [3]'s study, the aircraft weight can be reduced by 15%, which only requires shortening the fuselage by one intake diameter. However, like a coin has two sides, the S-shaped intake also has disadvantages.

The traditional straight intake geometry is simple, making manufacturing and maintenance easy and cheap. Due to its simple geometry, there are usually no complicated flow mechanisms inside the duct, and the flow loss is also relatively low. However, the advantages of the straight duct become the disadvantages of the S-shaped duct. The complicated geometries of the S-shaped conduit brought complex flow mechanisms and higher flow loss. Additionally, because of the large curvature of the centre line, flow separation inside the S-duct can nearly not be

avoided in high-speed situations. When slowing down the airflow, a well-designed S-shaped intake should also decrease the pressure loss and instability and make the pressure distribution on the aerodynamic intake plane (AIP) uniform as much as possible [81]. However, flow control is another optimization direction besides optimizing the geometry itself. Therefore, this chapter chose the DBD plasma actuator, an active flow control, to optimize the flow field inside the S-duct.

S-shaped ducts are usually used in the high-speed field. The speed tested extensively is 0.6 Mach [81]. However, the velocity induced by the plasma actuator is still low; the highest known induced velocity to date is only around 10 m/s [30]. Therefore, using current DBD plasma actuators to optimize the S-shaped duct in real application scenarios is impractical. Due to this limitation, the speed range of this study is restricted to between 0.05 and 0.15 Mach (the S-duct throat). The reasons why the S-shaped duct was still chosen as the subject of the experiment are: on the one hand, the S-shaped duct model used this time is large, and although the flow rate is low, the minimum Reynolds number is still over 2.7×10^{-6}. At this Reynolds number, studies of the performance of the DBD plasma actuator are relatively few. This study can fill this gap nicely. On the other hand, S-shaped ducts have complicated flow mechanisms. Through this study, the application areas of DBD plasma have been further expanded, and new optimized schemes have also been provided for the potential applications of S-shaped ducts. Additionally, once the issue of plasma-induced velocity magnitude is resolved, this research will serve as a significant reference for future studies in this field.

In the beginning, this study used an experiment to investigate the performance of the plasma actuator. The experiment method is pressure measurement. However, the plasma actuator generates a lot of heat during the running period, which prevents the experiment from lasting too long, so it is not feasible to deploy many measurement points on the aerodynamic interface plane (AIP, observation interface). Sparse measurement points are not conducive to quantitative analysis, especially in this study, which used a suction-type intake system. The experiment error cannot be ignored relative to the effect of the plasma actuator. Additionally, limited by the experiment method, although the wall static pressure coefficients are used to characterize the flow inside the S-duct, it is not intuitive and not easy to understand. This study incorporates computational fluid dynamics (CFD) to address this problem.

However, DBD plasma-induced air flow involves coupling multi-scale physical fields, such as convection, diffusion, and ionization mechanisms. Direct modelling based on its physical principles results in the derived continuity equations with high stiffness. The high stiffness arises from the significant time-scale disparity among different physical mechanisms, such as plasma discharge and induced neutral flow. To reduce the stiffness of the plasma dynamics continuity equations, Jayaraman et al. [71] proposed a sequential finite-volume operator splitting algorithm to conserve space charge. Despite the efforts made by researchers, modelling plasma using first principles currently requires costly computational resources to solve within a

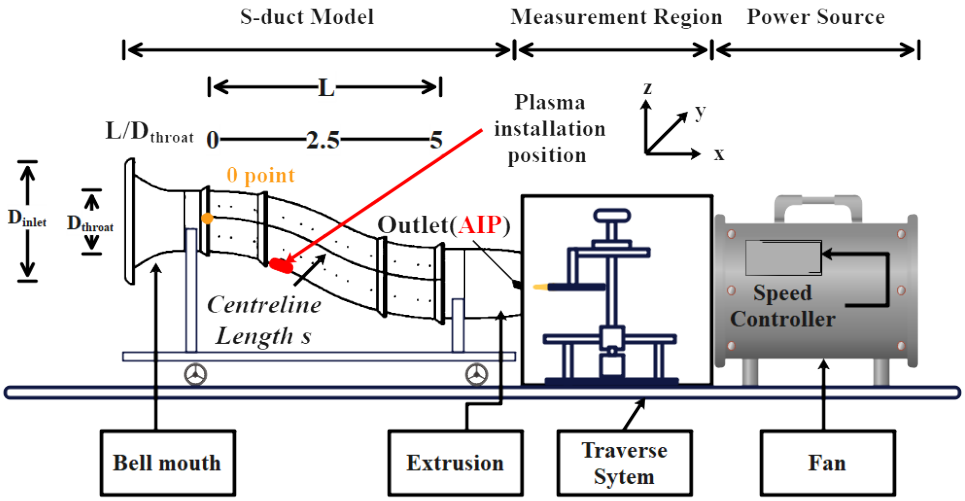

Figure 7.2: The schematic of the experiment setup.

time scale that all physical mechanisms are meaningful. Therefore, although modelling based on the first principle has high fidelity, high-fidelity discharge models remain impractical for most engineering problems. To significantly reduce computational costs, researchers have proposed simplified reduced-order models [72–75], which incorporate the momentum generated by plasma discharge directly into the Navier-Stokes equations in the form of body forces. This approach adds only an additional source term to the governing equations, substantially reducing computational complexity and the required computational resources. The plasma used in this model is a hybrid model based on Singh and Roy [76] and Soloviev [77]'s studies. Babou et al. [78] presented the preliminary analysis of this hybrid model.

This chapter presents a comprehensive study of plasma flow control within an S-shaped duct, employing experimental and numerical simulation methods. The primary focus is on regulating complex flow fields through plasma technology, to explore the underlying mechanisms and effects of this control approach.

7.1 Experiment Setup

The experimental system consists of an S-shaped duct, a traverse system, an acrylic enclosure, and a fan (as shown in Figure 7.2). The traverse system is installed within the acrylic enclosure, which connects the S-shaped duct to the fan. The enclosure is constructed from transparent acrylic panels and its internal dimensions measure 1 meter in length, width, and height.

7.1.1 Experimental Facilities

The S-shaped duct section has the same geometry as used in Chapter 4. However, extension segments are not installed for this experiment due to some limitations. The pressure measurement

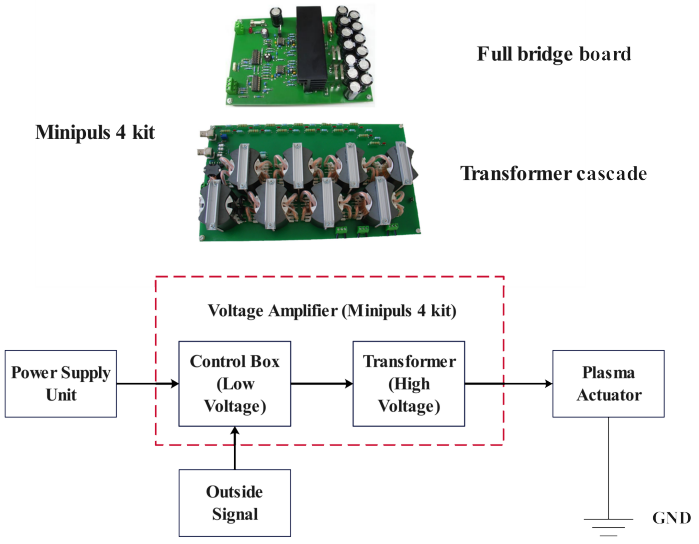

Figure 7.3: The schematic of the plasma system.

system and other equipment remain the same as in Chapter 4.

A plasma kit is used to generate plasma. The whole plasma system consists of a power supply, a voltage amplifier, and plasma actuators; the schematic of the system is shown in Figure 7.3. The power supply used in this setup is the VSP2410, manufactured by Voltcraft. A variable DC power supply delivers a stable 30V voltage throughout the experiment. The voltage amplification apparatus is the Minipuls4, manufactured by GBS Elektronik. Minipuls kit mainly includes two principal components. The first component is a comprehensive bridge board engineered for low-voltage applications equipped to interface with external signals. The second component is a cascading board designed specifically for the conversion to high voltage. This assembly is interfaced with a computer and is governed by a LabVIEW software program, which enables control and surveillance throughout the experimental procedures.

7.1.2 Experimental Description

During the experiment, a grid mesh was positioned in front of the bell mouth of the S-duct to improve the uniformity of the incoming flow. Subsequently, upon starting the fan, the velocity controller was set to a minimum scale of 1, and then the wall and the AIP were measured. A total of 40 sets of wall pressure data were collected during the data acquisition process to analyze experimental errors and uncertainties. For data collection at the outlet interface (AIP), data points were spaced 36 degrees in the circumferential direction, with a radial separation of 9.8 millimetres, as shown in Figure 7.4. The centre of the outlet interface was considered the reference point (zero point) and a total of 121 points were sampled along the concentric circles. The complete data acquisition process for an entire AIP interface typically requires approximately 20 to 30 minutes.

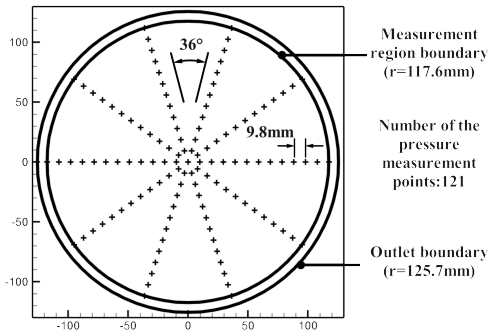

Figure 7.4: The schematic of the outlet (AIP) pressure measurement points distribution.

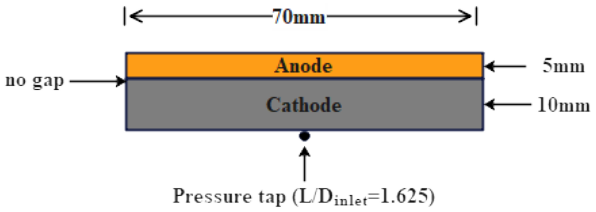

Figure 7.5: The schematic of a single actuator.

The design of the plasma actuator is shown in Figure 7.5. The single-layer electrode's length and thickness are 70mm and 0.1mm, respectively. The width of the anode is 5 mm, and the cathode is 10mm, with no gap between the two electrodes. The dielectric material used is Kapton tape. The installation position is also shown in Figure 7.5, with the lower edge of the cathode close to the pressure sensing port at L/D_{inlet} = 1.625. Here, L is the length of the S-shaped duct segment, and D_{inlet} is the diameter of the inlet, 204.2 mm.

Before initiating flow control, it is essential to perform parameter tuning for the plasma actuator, including voltage, frequency, waveform, dielectric thickness, modulation frequency, and duty cycle. The modulation frequency can be understood as the number of consecutive pulse signals transmitted per second. The duty cycle represents the ratio of the active working time during a voltage pulse signal cycle to the total cycle time, as expressed by Equation 7.1 and 7.2, where T_p is the period time of a single pulse. The modulation frequency only holds significance when the duty cycle is not equal to 100%. If the duty cycle is set at 100%, regardless of variations in modulation frequency, the voltage applied to the plasma actuator remains a continuous signal.

$$f_M = \frac{1}{T_p} \tag{7.1}$$

$$Dutycycle = \frac{workingtime}{T_p} \tag{7.2}$$

The induced velocity generated by AC-DBD plasma actuators remains relatively low. Theoretically, the primary goal of tuning these actuators is to maximize this induced velocity. How-

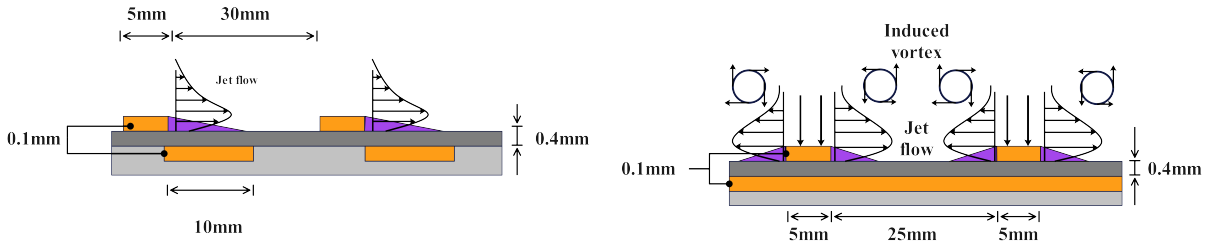

(a) wall jet (b) vortex generators

Figure 7.6: Plasma actuator array schemes. (a) is wall jet scheme, and (b) is vortex generator scheme.

ever, the data acquisition process on the AIP interface, which requires 20 to 30 minutes, imposes requirements on the operating time of the plasma actuator. To achieve the induced velocity as high as possible, the excitation voltage and excitation frequency are set as high as possible, which makes the actuator break easier. Consequently, the tuning strategy must balance the induced velocity and the safe and sustainable operating time of the plasma actuator.

After the configuration for a single plasma actuator is determined, the plasma actuators are arranged into arrays. These arrays are mainly divided into the wall jet scheme and the vortex generator scheme, with their principles illustrated in Figure 7.6. In the experiment, three different configurations of the plasma actuator array were tested, as described in Figure 7.7. Configurations 1 and 2 belong to the jetting scheme; Configuration 3 represents the vortex generator scheme.

In the final selected configuration, the peak voltage is 17 kV, the waveform is sawtooth, the operating frequency is 4 kHz, and the dielectric thickness is 0.4 mm. The duty cycle is set at 100% in the wall jet scheme. A duty cycle of 50% was applied for the vortex generator scheme and modulation frequencies of 50, 200, and 400 were tested, respectively.

7.2 Simulation Setup

The simulation of the S-shaped duct was conducted using the Reynolds-Averaged Navier-Stokes (RANS) method with the $k-\omega$ SST turbulence model. The software used for this simulation is OpenFOAM, with the RANS method implemented through the *simpleFoam* solver. As for plasma simulation, modelling based on first principles currently faces significant challenges and requires vast computational resources. Therefore, a simplified approach is adopted in this study: the plasma discharge process is simplified as a body force and directly incorporated into the momentum equation as a source term. This approach is implemented in OpenFOAM by adding a source term using the fvModel script, with the principle described by Equation 7.3. This method significantly reduces computational demands. In addition, to ensure the accuracy of this simplification, the study validates it in terms of both the magnitude and spatial distribution of

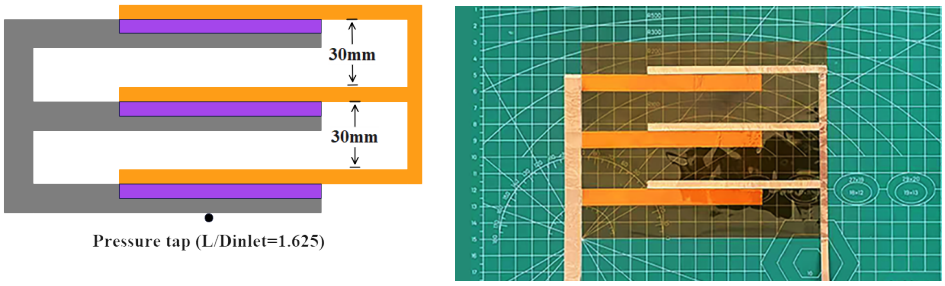

(a) Configuration 1

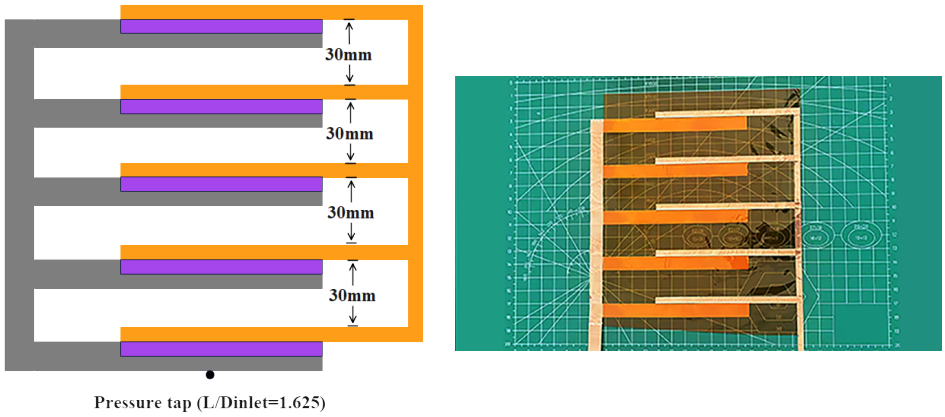

(b) Configuration 2

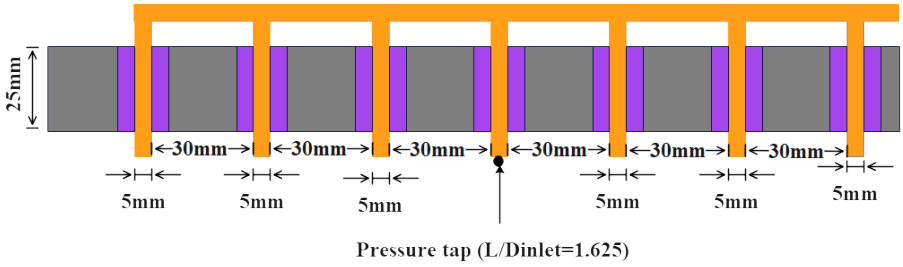

(c) Configuration 3

Figure 7.7: Plasma actuator array configurations tested in the experiment. (a) Configuration 1 and (b) Configuration 2 are the wall jet schemes, and (c) Configuration 3 is the vortex generator scheme.

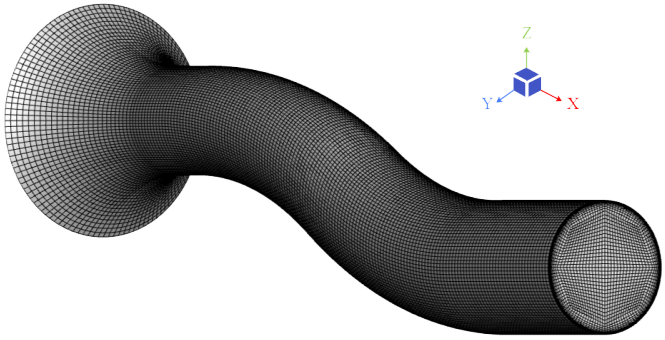

Figure 7.8: The schematic of the computational domain.

	U	P
Inlet	pressureDirected	total pressure (117.9 Pa)
Outlet	zeroGradient	static pressure (0 Pa)
Wall	No-slip	

Table 7.1: The boundary conditions.

the generated thrust.

$$\frac{\partial \mathbf{u}}{\partial t} + \bigtriangledown \cdot (\mathbf{u} \otimes \mathbf{u}) + \bigtriangledown p = S_v \tag{7.3}$$

where S_v represents the source term. As shown in Figure 7.8, the computational domain is divided into 12 mesh blocks, with 4 blocks located in the central region and 8 blocks in the boundary layer. All boundary conditions are from the experiments, and detailed information is shown in Table 7.1.

7.2.1 Plasma Modeling

Soloviev [77] derived the interrelations between parameters, including voltage, frequency, and dielectric thickness, and their influence on plasma-induced thrust, subsequently formulating a predictive model for thrust, shown in Equation 7.4:

$$T \approx 2.4 \times 10^{-10} \alpha_l^4 \frac{f_V}{d} \left(\frac{9V_0}{4 \triangle V_c} \right)^4 \left(1 - \frac{7 \triangle V_c}{6V_0} \right)^4 \times \left(1 - exp\left(-\frac{1}{4 f_V \triangle \tau_q} \right) \right) Nm^{-1} \tag{7.4}$$

where α_l represents a fitting parameter, f_V is the voltage excitation frequency in kHz, d is the dielectric thickness in centimetres (cm), V_0 is the voltage amplitude in volts (V), Vc is the normal voltage drop across the cathode V, and $\triangle \tau_q$ is the residence time of negative ions in the acceleration region, measured in seconds (s).

Although Equation 7.4 describes the interrelation between plasma-induced thrust and physical parameters, the induced thrust is the two-dimensional resultant body force, so at present there is still a lack of the spatial distribution information of the induced thrust. Singh and Roy [76]

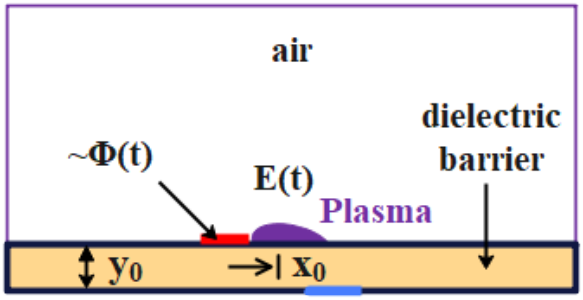

Figure 7.9: Initial coordinate system of the plasma modeling in Singh and Roy [76]'s study.

presented a fitting for the electric potential, spatial distribution, and body force under specific conditions, approximating it to the following Equation:

$$\vec{F}_{EHD} = F_{x0}\phi_0^4 e^{(-\{[x-x_0-(y-y_0)]/y\}^2-\beta_x(y-y_0)^2)}\hat{i} + F_{y0}\phi_0^4 e^{\left\{-[(x-x_0)/y]^2-\beta_y(y-y_0)^2\right\}}\hat{j} \tag{7.5}$$

where values of F_{x0} and F_{y0} represent the average electrodynamic force obtained by solving the air plasma equations. The relationship between the electrodynamic force and the fourth power of the electric potential is derived from plasma simulation data. x_0 and y_0 are the coordinates of the reference point (starting point). As illustrated in Figure 7.9, x_0 is located at the midpoint between the anode and the cathode, while y_0 is the thickness of the dielectric layer. β_x and β_y are constants determined based on the dielectric material and used to match the induced velocity.

Because of the direct measurement, the spatial distribution within Singh and Roy [76]'s model is certainly accurate. However, Singh and Roy [76] normalised the thrust magnitude in their study, so it cannot obtain the actual thrust magnitude. But, Singh and Roy [76] directly points out that this model's prediction of thrust magnitude is not precise; under an excitation voltage of 10 kV, the induced velocities can exceed 100 m/s.

Although the aforementioned models have certain limitations, they can complement each other to some extent. An improved plasma model can be derived by employing the thrust magnitude predicted by Soloviev [77]'s model in conjunction with the spatial distribution determined by Singh and Roy [76]'s model:

$$\vec{F}_{EHD}(V,f,d,x,y;x_0,y_0) = T_{soloviev} \times \frac{\vec{F}_{Singh}(V,x,y;x_0,y_0)}{\left\|\vec{F}_{Singh}(V,x,y;x_0,y_0)\right\|} \tag{7.6}$$

where $\left\|\vec{F}_{Singh}(V,x,y;x_0,y_0)\right\|$ is the area force integral. Some research results on this combined model can be referred to Babou et al. [78]'s study.

Table 7.2: Mesh information. r represents the growth rate. ρ denotes the axial density, the number of divisions along the X-direction for the S-shaped segment. n is the number of meshes, and the unit is million.

	Coarse	Medium	Fine	Superfine
y^+	1	0.8	0.8	0.8
r	1.3	1.2	1.15	1.1
ρ	100	200	300	400
n(M)	0.68	2.5	5.8	11.9

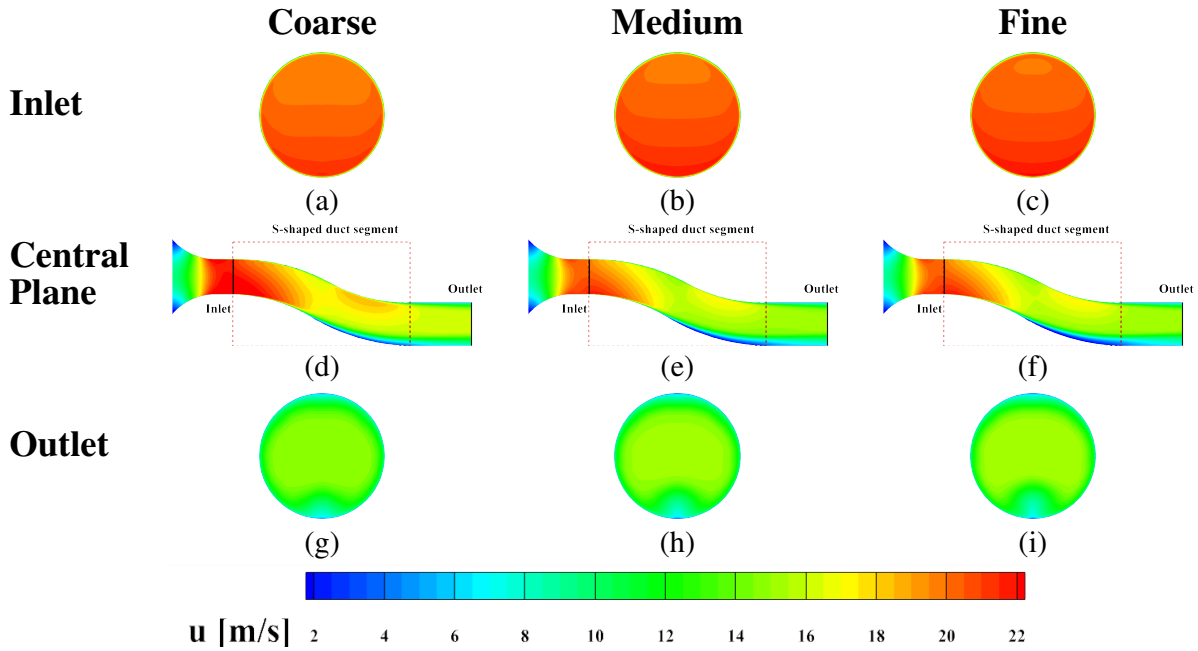

Figure 7.10: The velocity profiles at the inlet, the central slices, and the outlet.

7.2.2 Numerical Validation

A mesh independence study was conducted for the S-shaped duct simulation. The detailed mesh configurations are provided in Table 7.2, with four different mesh resolutions tested. However, it was observed that the simulation results for the fourth configuration, utilising a superfine mesh, failed to converge. This is likely attributed to an increase in flow instability with mesh refinement, which rendered the steady-state solver ineffective. The results for three mesh configurations are illustrated in Figure 7.10, demonstrating that the velocity profiles at various locations within the S-shaped duct exhibit negligible differences when transitioning from medium mesh to fine mesh. Consequently, the fine mesh configuration was adopted for all subsequent analyses in this study.

The validation of the plasma body force model is divided into two main parts: the validation of the induced thrust magnitude and the validation of the spatial distribution of the thrust. Figure 7.11 compares the estimated thrust based on the model of Soloviev [77] and the experimental

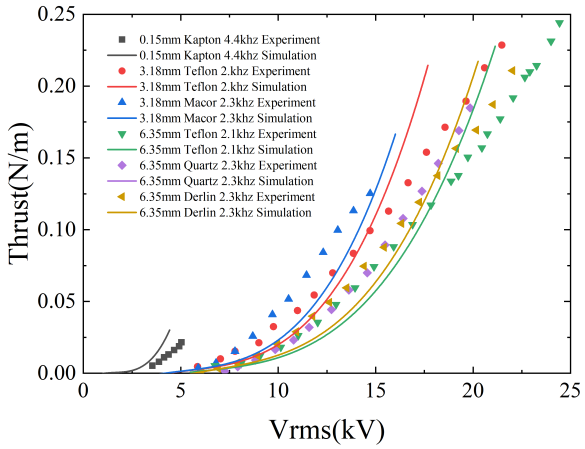

Figure 7.11: Comparison between the estimated thrust based on Equation 7.4 and experimental data. V_{rms} is the equivalent voltage; here, the relationship with the voltage amplitude is $V_0 = 1.7V_{rms}$.

data of Thomas et al. [32]. Here, α_l in Equation 7.4 is set to 1. It can be found that, although Soloviev [77]'s thrust model somewhat reflects the thrust trend, the errors are not negligible. In Figure 7.11, the equivalent voltage is used as the horizontal axis. When the waveform manifests as a sawtooth pattern, the relationship between the equivalent voltage (V_{rms}) and the voltage amplitude (V_0) is $V_0 = 1.7V_{rms}$. If the voltage amplitude was to be used as the horizontal axis, errors in the thrust predictions would become more apparent.

In the study of Thomas et al. [32] and Soloviev [77], some findings can be used to explain these prediction errors. First, according to Thomas et al. [32]'s research, under constant frequency, increasing the voltage, once the plasma reaches saturation state, the induced thrust declines sharply. The appearance of a filamentary plasma marks the saturation of the plasma. The plasma discharge becomes progressively saturated with increased frequency when the voltage remains constant, but Soloviev [77]'s model does not include this mechanism. However, Soloviev [77] also points out that his model can remain accurate when the frequency is below 2.5kHz; once above this frequency, the real thrust is less than the predicted thrust, fundamentally aligning with the physical phenomenon of thrust reduction once the frequency or voltage reaches saturation state. Therefore, high accuracy can only be achieved within a specific range of frequencies and voltages when using this model to predict thrust. This range is where the equivalent voltage is below 15kV, and the frequency is less than 2.5kHz. However, in the experiment, 17 kV and 4 kHz were used, slightly exceeding the range above. As a result, the simulated thrust is expected to be somewhat higher than the actual thrust.

The next step is to validate the spatial distribution of the plasma-induced thrust. The spatial distribution of the body force model is highly dependent on the computational mesh. The mesh suitable for the S-shaped duct may not be appropriate for the plasma model. Therefore, before validating the spatial distribution, the mesh used for the plasma simulation must be verified. The computational domain of Singh and Roy [76] is adopted here, as shown in Figure 7.9, with a

Table 7.3: Area force sum under different mesh sizes.

Mesh size (mm)	$\|F_x\|(\times 10^{-6}$N/m)	$\left\|F_y\right\|(\times 10^{-6}$N/m)	$\left\|\vec{F}_{Singh}(V,x,y;x_0,y_0)\right\|$ $(\times 10^{-6}$N/m)
4	2.10E-12	4.10E-78	2.10352E-12
1	9.3276	3.5456	9.978747473
1E-1	7.6729	1.345	7.789892131
1E-2	7.4694	1.1884	7.563347865
1E-3	7.4481	1.1725	7.539824259
1E-4	7.4466	1.1709	7.538093815
1E-5	7.4464	1.1707	7.537865179

width of 3 cm and a height of 5 mm. In Equation 7.5, x_0 and y_0 are set to 0.015 and 0.001, respectively. The values of Fx_0, Fy_0 and ϕ_0 are 2.6, 2 amd 1, respectively, while β_x and β_y are set to 8×10^5 and 10^7, respectively. substituting the values of Fx_0, Fy_0, β_x, β_y into the Equation 7.5, and conducting an area force integration within the spatial domain of 0 <x <0.03 and 0.001 <y <0.005, the area force integral $\left\|\vec{F}_{Singh}(V,x,y;x_0,y_0)\right\|$ is 7.5359×10^{-6}. However, the spatial domain is discretised in numerical simulations, and the mesh size determines the spatial resolution. In a uniform quadrilateral mesh field, the effects of varying mesh sizes on the area force sum are organised in Table 7.3. Here, $\|F_x\|$ denotes the sum of the area force in the x direction, and $\left\|F_y\right\|$ signifies the sum of the area force in the y direction.

It can be found that when the mesh size is set at 4 mm, namely, the height of a single mesh element equals the height of the computational domain depicted in Figure 7.9, and the area force sum for the entire region is nearly zero. Until the mesh size is reduced to 1 mm, the sum of the area force of the mesh domain begins to approximate the values derived from the theoretical formulations (Equation 7.5). Consequently, the mesh spacing should not be greater than 1 mm when utilising Singh and Roy [76]'s model to make plasma modelling, or the error will not be neglected. As the mesh size decreases, the area force integral of the mesh domain progressively diminishes and converges towards the values obtained from theoretical calculations. When the mesh size reaches 1E-5 mm, the discrepancy between the mesh domain's area force integral and the integral value computed through formulae is less than 1E-5 N/m.

Based on the findings in Table 7.3, three mesh sizes were used to test Singh and Roy [76]'s plasma spatial model: 1, 0.1, and 0.02 mm. Here, the thrust was set at 0.24 N / m. 0.24 N/m was the maximum thrust value in the experiments of Thomas et al. [32]. The reason for selecting a thrust as large as possible is for future potential applications. The greater the thrust, the more potential applications that arise. Figure 7.12 shows the velocity distributions of the computational domain in three mesh sizes. In Figure 7.12, the horizontal and vertical velocities were normalised by the maximal velocity magnitudes obtained in the three simulations (18 m/s and 5 m/s, respectively). It can be found that the velocity distributions under three mesh sizes have significant differences. When the mesh size was refined from 1 to 0.1 mm, an increase in the maximum magnitude of the horizontal velocity and the vertical velocity was observed;

however, the average velocity throughout the spatial domain decreased from 3.05 to 2.33 m/s. This may be because the $\left\|\vec{F}Singh(V,x,y;x0,y_0)\right\|$=7.5359 $\times$ 10-6 N/m was used to normalise area force in all mesh sizes. It can be found in Table 7.3 that when a coarser mesh was used, the actual force integral of the area of the mesh exceeded this value, leading to an overestimation of the overall plasma-induced thrust. Theoretically, this error would be virtually eliminated when the mesh size is reduced to 1E-5 mm. However, achieving such precision would require an exceedingly substantial computational resource, even for the two-dimensional space of 1.2e-4 square meters as in Figure 7.9.

When the mesh size was further reduced from 0.1 mm to 0.02 mm, the average horizontal velocity over the entire spatial domain changed to -1.32 m/s, a counter-intuitive phenomenon. The velocity component induced by the plasma is reversed with the expectations. However, the residual plot (Figure 7.13) reveals that the residuals have significant fluctuations without apparent decreasing signs, indicating an unstable flow field. This phenomenon is related to the finite-volume method algorithm. With larger mesh sizes, the average effect of physical quantities within each mesh cell is more pronounced, increasing the viscosity and facilitating convergence to a steady state. In contrast, this artificial viscosity decreases as the mesh size decreases, making the flow field more unsteady. After the test, it can be found that upon further reducing the mesh size to 0.01 mm, the steady-state solver *simpleFoam* in OpenFOAM can no longer perform the necessary computations. Therefore, when using a steady-state solver to solve the plasma model in this study, it is essential to confine the mesh size within the 0.1 to 1 mm range. If the mesh size is too small, the steady-state solver cannot process an unsteady flow field. Conversely, if the mesh size is too large, the body force model cannot be correctly added to the computational domain.

Lastly, based on the mesh validation, the space distribution of the body force is further validated. Under the 0.1 mm mesh size, $T_{soloviev}$ is set as 0.01, 0.05, 0.1, 0.15, 0.2, 0.24 N/m to perform the simulation to obtain the maximum induced velocity under different thrusts. Figure 7.14 shows the relationship between the thrust and the maximum induced velocity and gives the fitting curve, which can deduce the thrust inversely according to the measured maximum induced velocity. Validation is carried out using experimental data from Wojewodka et al. [38]. In their experiment, the maximum horizontal-induced velocity was approximately 3.23 m/s. According to the formula presented in Figure 7.14, the thrust is estimated to be around 0.01 N/m. A comparison between the corresponding simulation and the experiment data from Wojewodka et al. [38] is shown in Figure 7.15. It can be found that downstream of the anode edge, the velocity profiles obtained from the simulations match the experimental results relatively well, particularly at the two locations, 4 millimetres and 5 millimetres, where the velocity magnitudes reach the maximum.

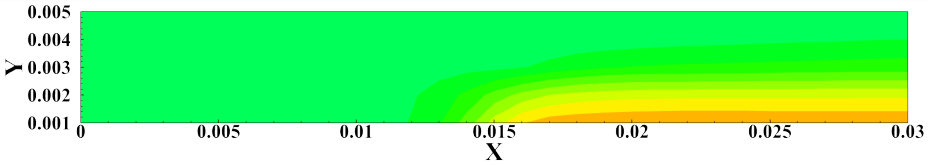

(a) Coarse mesh size 1 mm (horizontal velocity)

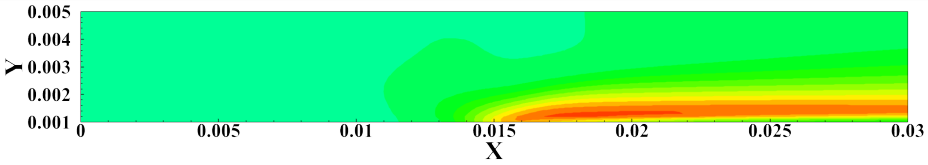

(b) Medium mesh size 0.1 mm (horizontal velocity)

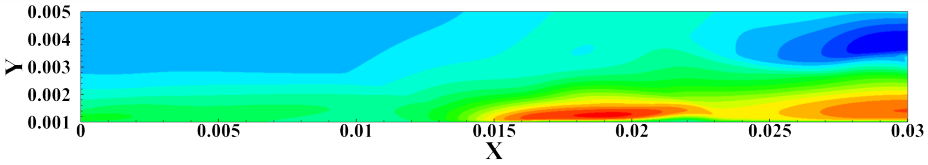

(c) Fine mesh size 0.02 mm (horizontal velocity)

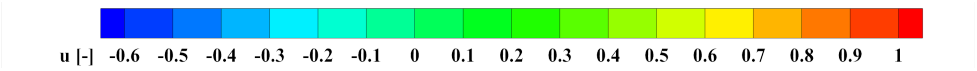

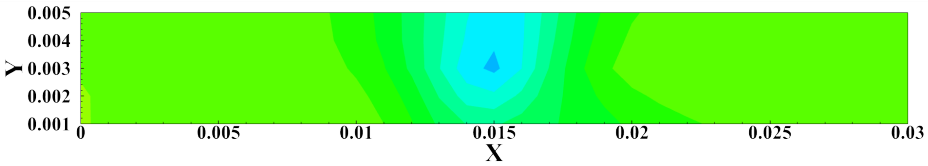

(e) Coarse mesh size 1 mm (vertical velocity)

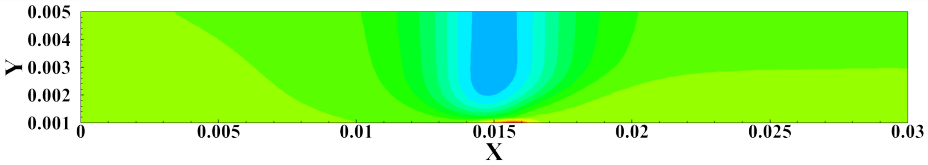

(f) Medium mesh size 0.1 mm (vertical velocity)

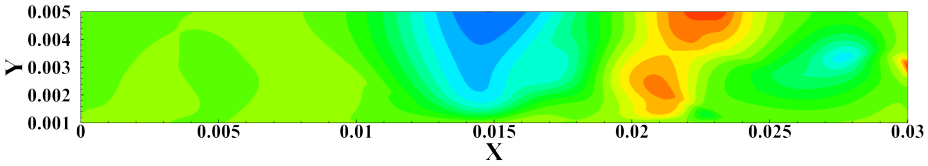

(g) Fine mesh size 0.02 mm (vertical velocity)

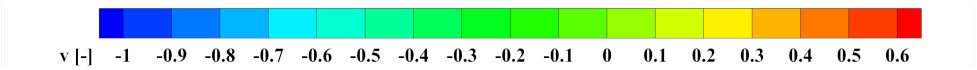

Figure 7.12: The horizontal and vertical velocity components distributions under different mesh sizes; (a,d) mesh side length is 1E-3 m; (b,e) mesh side length is 1E-4 m; (c,f) mesh side length is 2E-5 m. Horizontal and vertical velocities are normalised by 18m/s and 5m/s, respectively.

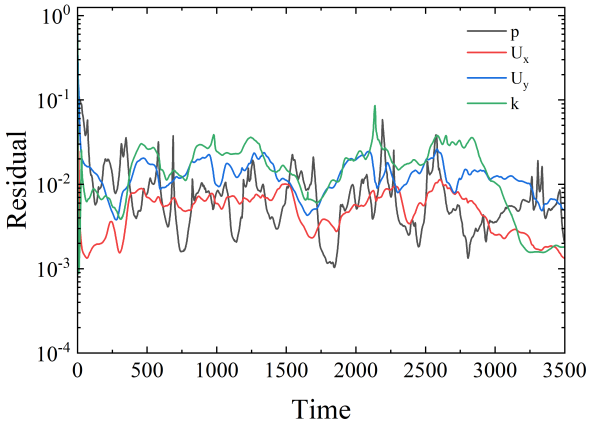

Figure 7.13: The residual curve of the fine mesh. The definition of residual r in OpenFOAM is $r = \frac{1}{n}\sum|b - Ax|$, where $n = \sum(|Ax - A\bar{x}| + |b - A\bar{x}|)$ and $\bar{x}$ is the average of the solution vector. The matrix system is $Ax = b$ and $r = b - Ax$.

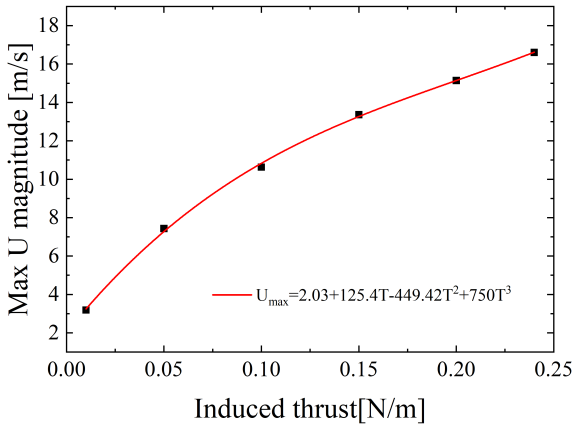

Figure 7.14: The relationship between the maximum induced velocity and the induced thrust.

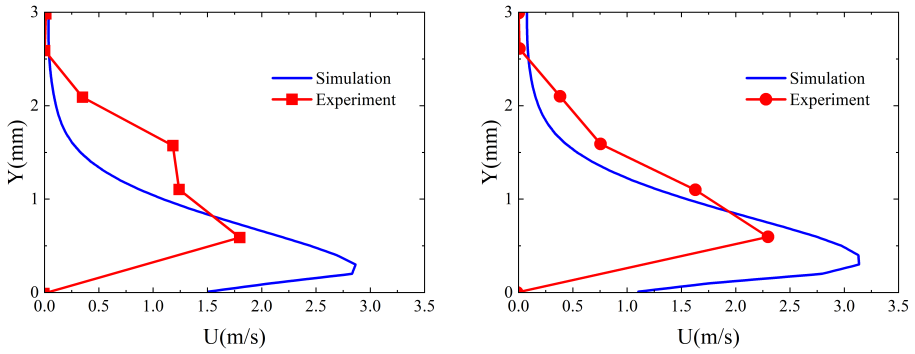

(a) 2mm

(b) 3mm

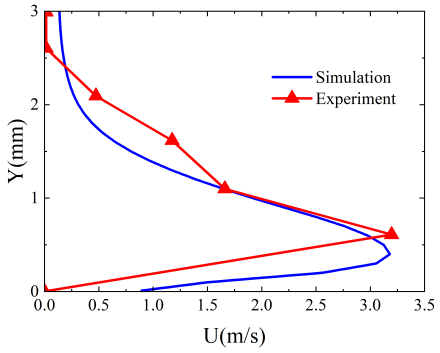

(c) 4mm

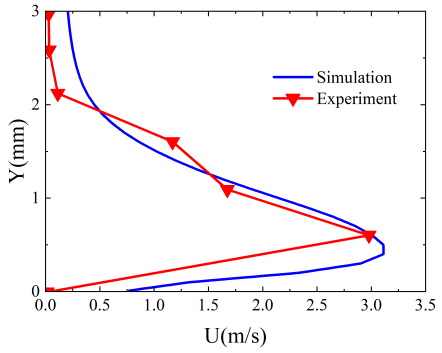

(d) 5mm

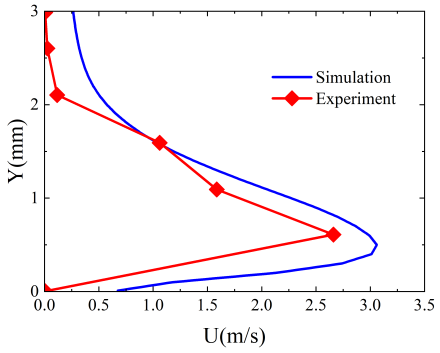

(e) 6mm

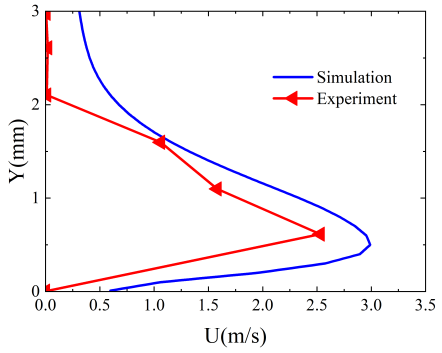

(f) 7mm

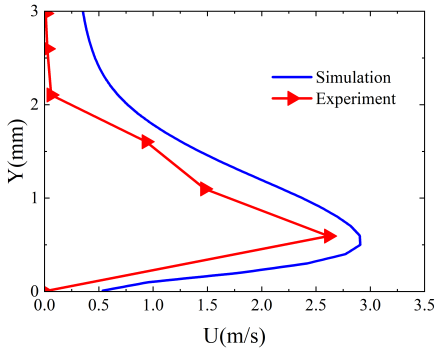

(g) 8mm

Figure 7.15: The horizontal velocity contours at different distances of the plasma jet downstream. Experiment data is re-plotted from Wojewodka et al. [38].

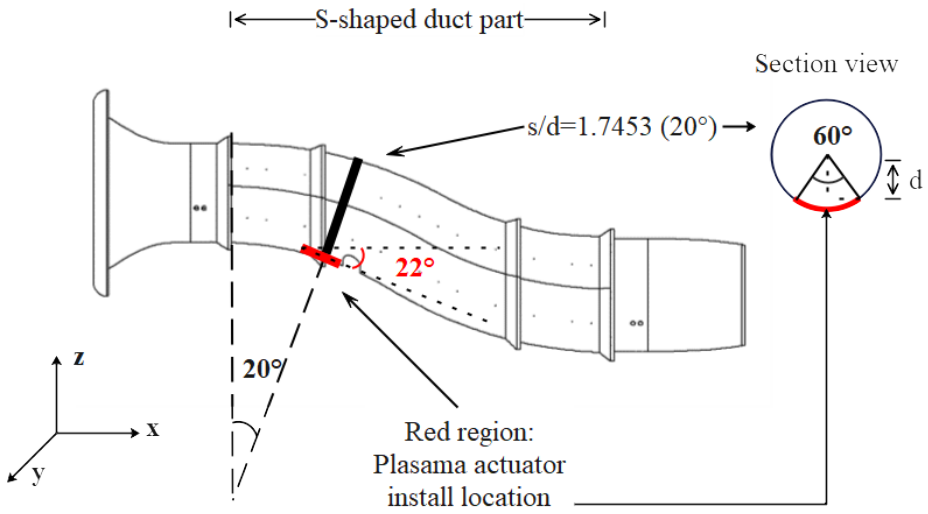

Figure 7.16: The schematic of the plasma actuator installation in the simulation.

7.2.3 Coordinate System Transform

The computational domain of the S-duct is illustrated in Figure 7.8. The axial distance in the S-shaped duct segment is 1.021 m, with an axial mesh number of 300. This results in an approximate axial mesh size of 3.4 mm. Numerical validation has indicated that the mesh size should be between 0.1 mm and 1 mm. Since the $k-\omega$ SST model is employed, the y^+ value needs to be less than 1. Therefore, the mesh size in the growth direction of the boundary layer is less than 0.1 mm. However, this has no impact. Although it may increase flow-field instability, a finer mesh size would be beneficial for capturing the spatial distribution of plasma thrust. Additionally, the jet that the plasma actuator generates primarily propagates in the streamwise direction. As a result, no adjustment will be made to the mesh size in the growth direction of the boundary layer, but the mesh size in the axial direction must be modified accordingly. OpenFOAM can achieve this by using the *topoSet* and *refineMesh* functions. A single execution of *topoSet* and *refineMesh* only doubles the mesh density; hence, multiple executions are required. In this study, by executing the function *refineMesh* four times, the resolution of the mesh was enhanced 16 times, achieving an axial mesh size of approximately 0.2 mm.

The installation location of the plasma actuator is shown in Figure 7.16, positioned at s/d = 1.7453. The centre line comprises two segments of planar circular arcs, and the location s/d = 1.7453 corresponds to the first arc segment's central angle of 20°. The region where the plasma actuator is installed in the simulation is a circular ring, as shown in the section view of Figure 7.16. Its length corresponds to the cross-section's central angle of 60°, and the slice of the arc ring is a box with a height of 1 cm and a width of 4 cm. However, as Figure 7.16 shows, the whole arc has an inclination angle of 22°. This is due to the continuously increasing duct radius.

The S-duct's zero point is at the centre of the S-shaped duct segment's inlet. The horizontal direction is the X axis, the vertical direction is the Z axis, and the Y axis is perpendicular to the plane composed of the X and Z axes. Because of the curvature of the S-shaped duct, there is no fixed coordinate of plasma initiation. Observing each slice on the Y axis, it can be found that every plasma initial coordinate is different. Plasma initial coordinates' XY coordinates (x_0 and y_0) correspond to values on the X and Z axes. New x_0 and y_0 can be calculated based on trigonometric functions, as the following Equation shows:

$$\begin{aligned} x_0 &= X_c - sin(\theta) \cdot d \\ y_0 &= Z_c - cos(\theta) \cdot d \end{aligned} \tag{7.7}$$

where X_c and Z_c are the plasma ring's centre coordinates at the S-duct's centre line. θ is the angle between the tangent of the ring and the horizontal line, as shown in Figure 7.16 (here 22°), and d is the projection of the cross-section of the ring onto the radius. The coordinates of the region where the plasma actuator is located also need to undergo the corresponding transformation, as below:

$$\begin{aligned} x_1 &= x_0 + (x - x_0) \cdot cos(\theta) - (y - y_0) \cdot sin(\theta) \\ y_1 &= y_0 + (z - x_0) \cdot sin(\theta) + (z - y_0) \cdot cos(\theta) \end{aligned} \tag{7.8}$$

where x and z are the original mesh coordinates of the S-duct. In Singh and Roy [76]'s study, y starts from 0.001. Consequently, a modification of Equation 7.6 is necessary. The revised formula is Equation 7.9.

$$\begin{aligned} \vec{F}_{EHD}(V,f,d,x,y;x_0,y_0) =& T_{soloviev} \times \frac{1}{\left\| \vec{F}_{Singh}(V,x,y;x_0,y_0) \right\|} \\ & \times (F_{x0} exp(-\{[x - x_0 - (z - y_0)]/(z - y_0 + 0.001)\}^2 - \beta_x (z - y_0)^2)\hat{i} \\ & + F_{y0} exp\left\{-[(x - x_0)/(z - y_0 + 0.001)]^2 - \beta_y (z - y_0)^2\right\} \hat{j}) \end{aligned} \tag{7.9}$$

$$\begin{aligned} \vec{F}_{EHD}(V,f,d,x,y;x_0,y_0) =& T_{soloviev} \cdot \cancel{length} \times \frac{1}{\cancel{length} \left\| \vec{F}_{Singh}(V,x,y;x_0,y_0) \right\|} \\ & \times (F_{x0} exp(-\{[x - x_0 - (z - y_0)]/(z - y_0 + 0.001)\}^2 - \beta_x (z - y_0)^2)\hat{i} \\ & + F_{y0} exp\left\{-[(x - x_0)/(z - y_0 + 0.001)]^2 - \beta_y (z - y_0)^2\right\} \hat{j}) \end{aligned} \tag{7.10}$$

It should be noted that, after changing from two dimensions to three, the original area force becomes the volume force. Here, the thrust $T_{soloviev}$ requires multiplication by a length to acquire the three-dimensional body force. However, the two-dimensional area force sum (N/m) also needs to be multiplied by a length (m), resulting in a unit of Newtons (N). It can be found in Equation 7.10, the length can be cancelled out, implying that Equation 7.9, in essence, remains unaltered. The derivation process is as Equation 7.10. Moreover, $\hat{i}$ and $\hat{j}$ denote mesh area in

two-dimensional contexts, whereas they represent mesh volume in three-dimensional scenarios.

7.3 Results and Discussion

This study will use the wall static pressure coefficient (C_p), the static pressure recovery coefficient (PR_s), the total pressure recovery coefficient (PR_t), and the total pressure loss coefficient ($C_{p,loss}$). Their definitions are as follows:

$$C_p = \frac{p - p_r}{q_r} \tag{7.11}$$

where p is local static pressure, p_r is the static pressure of the reference point, q_r is the dynamic pressure of the reference point. The reference pressure is determined as the average of the pressures measured at L/D_{inlet}= 0.25 at the circumferential locations of 60° and 120°. The reference dynamic pressure is 234.481 Pa, which corresponds to a flow velocity of 19.16 m/s (0.056 Mach).

$$PR_s = \frac{P_{s,AIP}}{P_{t,o}} \tag{7.12}$$

$$PR_t = \frac{P_{t,AIP}}{P_{t,o}} \tag{7.13}$$

where $P_{s,AIP}$ is the average static pressure on the AIP, $P_{t,AIP}$ is the average total pressure on the AIP, and $P_{t,o}$ is the total pressure of the freestream.

$$C_{p,loss} = \frac{P_{t,o} - P_{t,AIP}}{q_r} \tag{7.14}$$

Equation 7.14 defines the total pressure recovery coefficient. The total pressure loss coefficient is introduced because, at low Mach numbers, the total pressure recovery coefficient tends to approach 1, and its range of variation is exceedingly minimal, posing challenges for flow analysis. The total pressure loss coefficient provides a more informative reference for evaluating pressure losses within the duct than the total pressure recovery coefficient.

7.3.1 Experimental Measurement

Figure 7.17 displays the experimental wall static pressure coefficient (C_p) and the simulation results. s is the length of the centre line. It can be found that C_p curves at the selected four locations have significant differences. However, it can be observed that there is a notable similarity between the top and its adjacent sides (60° and 300°), while a comparable similarity is also evident between the bottom and its corresponding sides (120° and 240°). Therefore, the flow at the top and bottom of the S-shaped duct is the most representative. Before further analysing the wall curvature of the S-shaped duct, it is essential to first clarify the specific effects of its

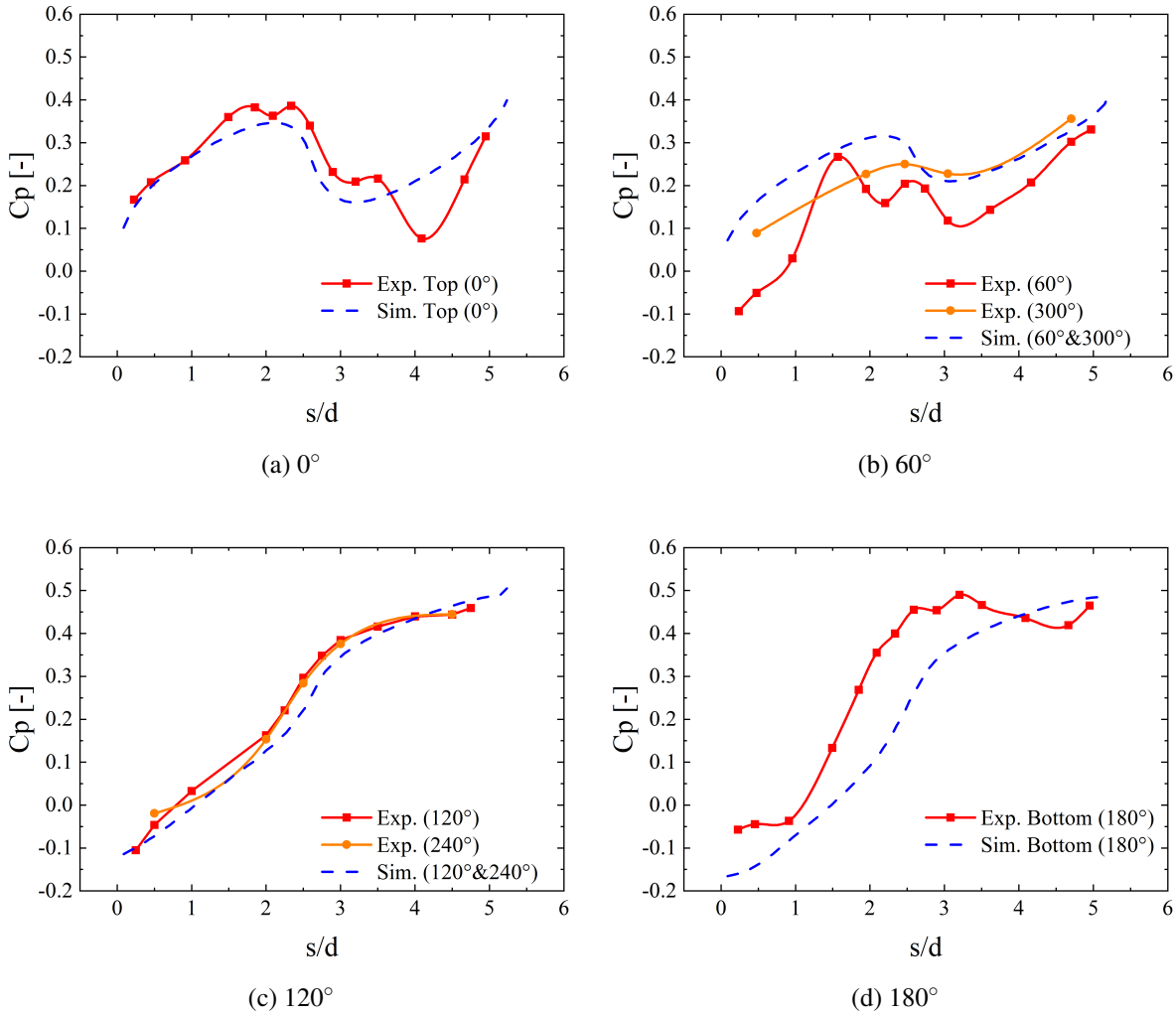

Figure 7.17: Wall static pressure coefficient (Cp) comparisons between the experiments and the simulations.

geometry on the flow velocity. Inside the S-duct, the expanding cross-sectional area consistently will reduce the flow velocity, whereas the impact of the centreline curvature on the flow velocity is comparatively complex. The presence of curvature generates concave and convex surfaces within the duct. The convex surface, analogous to a contraction section, accelerates the fluid, while conversely, the concave surface decelerates the fluid, akin to a diffusion section. Additionally, acceleration or deceleration in a specific region will have corresponding effects on the surrounding areas. For example, a deceleration in one region can create a localised blockage within the duct, which in turn accelerates the flow in adjacent areas.

After airflow enters the S-shaped segment, the airflow at the top first encounters the convex surface and subsequently experiences the concave surface. Theoretically, the flow should first accelerate and then decelerate. However, rising C_p indicates that the top is slowing down. This suggests that despite the centre line curvature creating a convex surface conducive to higher flow velocities, the unfavourable influence of the expanding cross-sectional area still predominates.

As the axial distance progresses, the upward trend of C_p begins to decelerate, followed by a rapid decline in C_p within the region of 2.5 $< s/D_{inlet} <$4. This rapid decrease in C_p indicates a rapid increase in flow velocity in this region. Upon analysis, two factors contribute to the rapid increase in flow velocity: the convex surface created by the duct curvature and the blockage effect caused by the sharp decrease in flow velocity at the bottom. However, most of this region has passed the centreline's midpoint, and most regions are located at the concave, which is an unfavourable curvature for the flow rate. Therefore, the reduction at the bottom should be the main cause of the increase in the flow velocity at the top.

The flow at the bottom undergoes the opposite sequence. In contrast, the C_p at the bottom exhibits a relatively simple trend, basically keeping upward, especially in the region of 1 $< s/D_{inlet} <$3. The adverse curvature causes this primarily. Furthermore, the decline at the top C_p should also be mainly attributed to this. The bottom C_p has a slight downward trend in the region of $L/D_{inlet} >$3. A slight increase in flow velocity is observed near the bottom close to the outlet, indicating that the adverse effects of the diffusing cross-section have started to weaken, while the favourable influence of the curvature on the bottom is becoming more dominant.

The overlap level of the C_p curves in Figures 7.17 (b) and (c) suggests that the flow symmetry is significantly better at the bottom of the S-shaped duct than at the top. However, no significant flow separation signs were observed in Figure 7.17. Based on Jiang et al. [149]'s study, this is because of the lack of extensions at the upstream and downstream. No clear flow separation is observed at the bottom, which complicates the determination of the optimal placement of the plasma actuator. Based on studies by WELLBORN et al. [81] and Jiang et al. [149], the extent of the flow separation region has been determined to be within the range of 2 $< s/D_{inlet} <$3.2. When converted to axial distances, this corresponds to 1.87 $< L/D_{inlet} <$3.08. Before this region, the nearest wall static pressure tap is located at L/D_{inlet} = 1.625, as shown in Figure 7.5. Consequently, this position has been selected as the installation location for the plasma actuator.

The aerodynamic data at the outlet are presented in Figure 7.18, including the three-dimensional velocity components (uvw), dynamic pressure (q), static pressure recovery coefficient (PR_s), and total pressure recovery coefficient (PR_t). To prevent physical collision, a gap of approximately 3 mm is maintained between the AIP plane and the exit plane of the S-shaped duct. The reference point for the experiment is located at the centre of the throat of the S-shaped duct. This value is obtained by averaging the wall static pressures at $L/D_{inlet} = 0.25$ with circumferential positions of 60° and 120°. Based on the distribution of u, q, and PR_t on the AIP, it can be observed that the regions experiencing the most significant flow disturbances are located at the top and bottom of the AIP. v and w represent the horizontal and vertical velocity flow coefficients on the AIP, respectively, normalised by the axial velocity at the reference point. Based on the distribution of vw, it can be inferred that, in the time-averaged field, the crossflow exhibits a downward trend from the centre and an upward trend from the sides, forming a convective structure at the top, characterised by two counter-rotating vortices. In terms of pressure recovery coefficients,

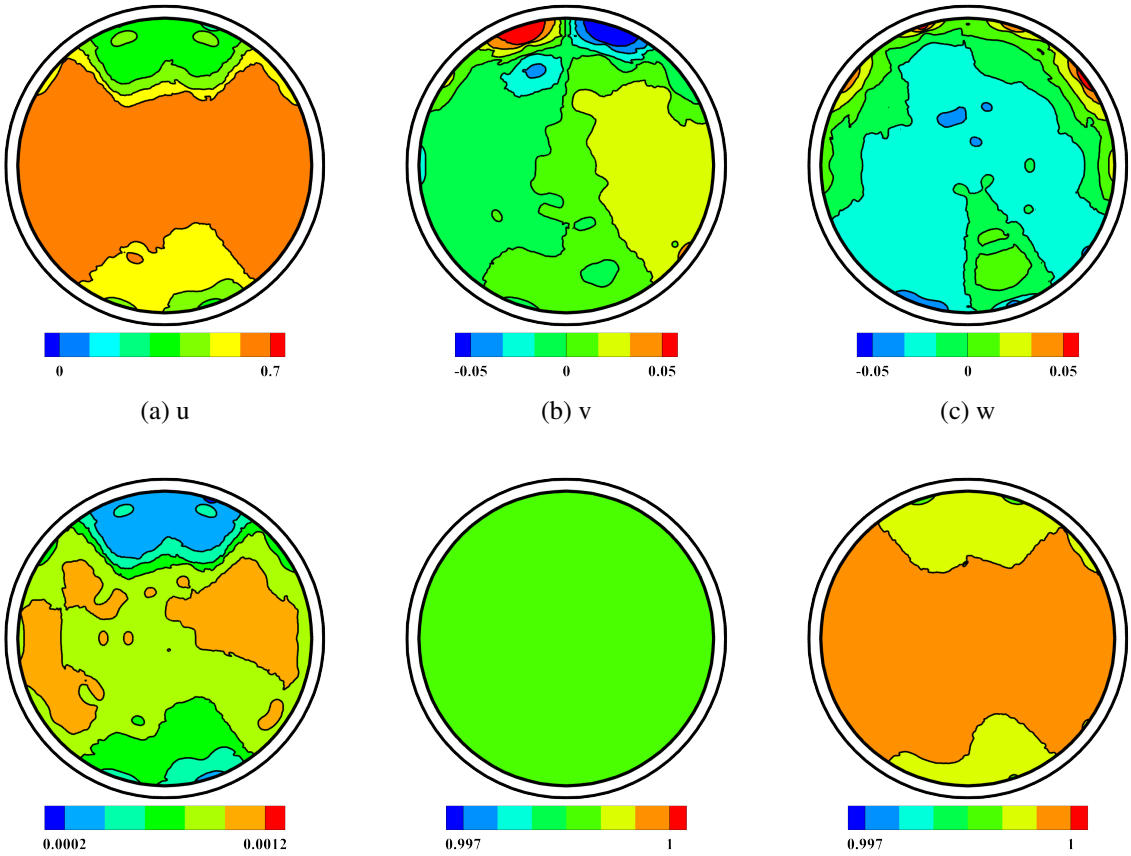

(a) u (b) v (c) w

(d) q (e) PR_s (f) PR_t

Figure 7.18: Aerodynamic data on AIP, uvw (a,b,c) represents the velocity components in three dimensions normalised by the reference point velocity. Dynamic pressure q is shown in (d). (e) and (f)represent the static and total pressure recovery coefficients (PR_s and PR_t).

the distribution of the static pressure recovery coefficient (PR_s) is relatively uniform, resulting in the total pressure recovery coefficient (PR_t) closely resembling the distribution of dynamic pressure (q).

7.3.2 Performance of Single Plasma Actuator and Array

Before employing the plasma actuator array, the performance of a single plasma actuator was experimentally investigated, and its parameters were optimised based on the findings. The comparison of actuator performance was evaluated through the velocity at the installation location, with the velocity calculated from the measured static pressure data (as shown in Equation 7.15). The pressure difference between the measured static and ambient total pressure is considered the dynamic pressure. Each data group was measured 10 times and the average was taken for analysis.

$$q = \frac{1}{2}\rho u^2 \tag{7.15}$$

Figure 7.19 illustrates the effects of dielectric thickness, excitation voltage, frequency, waveform, and modulation frequency on the performance of the plasma actuator. As shown in Figure 7.19 (a), under the conditions of a 20 kV voltage and sinusoidal waveform, the performance of four different material thicknesses was tested at three different frequencies. It is evident that thinner dielectric layers induce higher velocities; however, thinner dielectric layers are also more prone to damage. To ensure the safe operation of the plasma actuator during data collection, a thickness of 0.4 mm (4 layers of Kapton tapes) was selected.

Subsequently, with the dielectric thickness set to 0.4 mm and the sinusoidal waveform maintained, the variation of two different voltages with frequency is presented in Figure 7.19 (b). Higher peak voltages can be observed to result in increased induced velocity. However, the effect of frequency is more complex and does not exhibit a straightforward linear relationship. Similarly, to ensure the safe operation of the plasma actuator during the measurement, the voltage was set to 17 kV, and the frequency was determined to be 4 kHz. Figure 7.19 (c) illustrates the effect of the waveform on performance. It can be observed that the influence of waveform is relatively minor. In the end, a square wave was selected as the driving waveform. This decision was made because plasma actuators that typically induce higher velocities are also more prone to damage. For safety reasons, the square wave was chosen, which induces the lowest velocity. At this point, the operating parameters for the single plasma actuator have been fully determined.

When the duty cycle is set to 100%, a gradual decrease in current through the plasma actuator can be observed over time, likely attributable to electron deposition. This phenomenon hinders the accurate measurement of power consumption. However, when the duty cycle is not 100%, the current stabilises. The modulation frequency significantly influences the plasma actuator, as illustrated in Figure 7.19 (d). Specifically, when the duty cycle is reduced from 100% to 50%, an increase in the modulation frequency results in a corresponding reduction in the in-

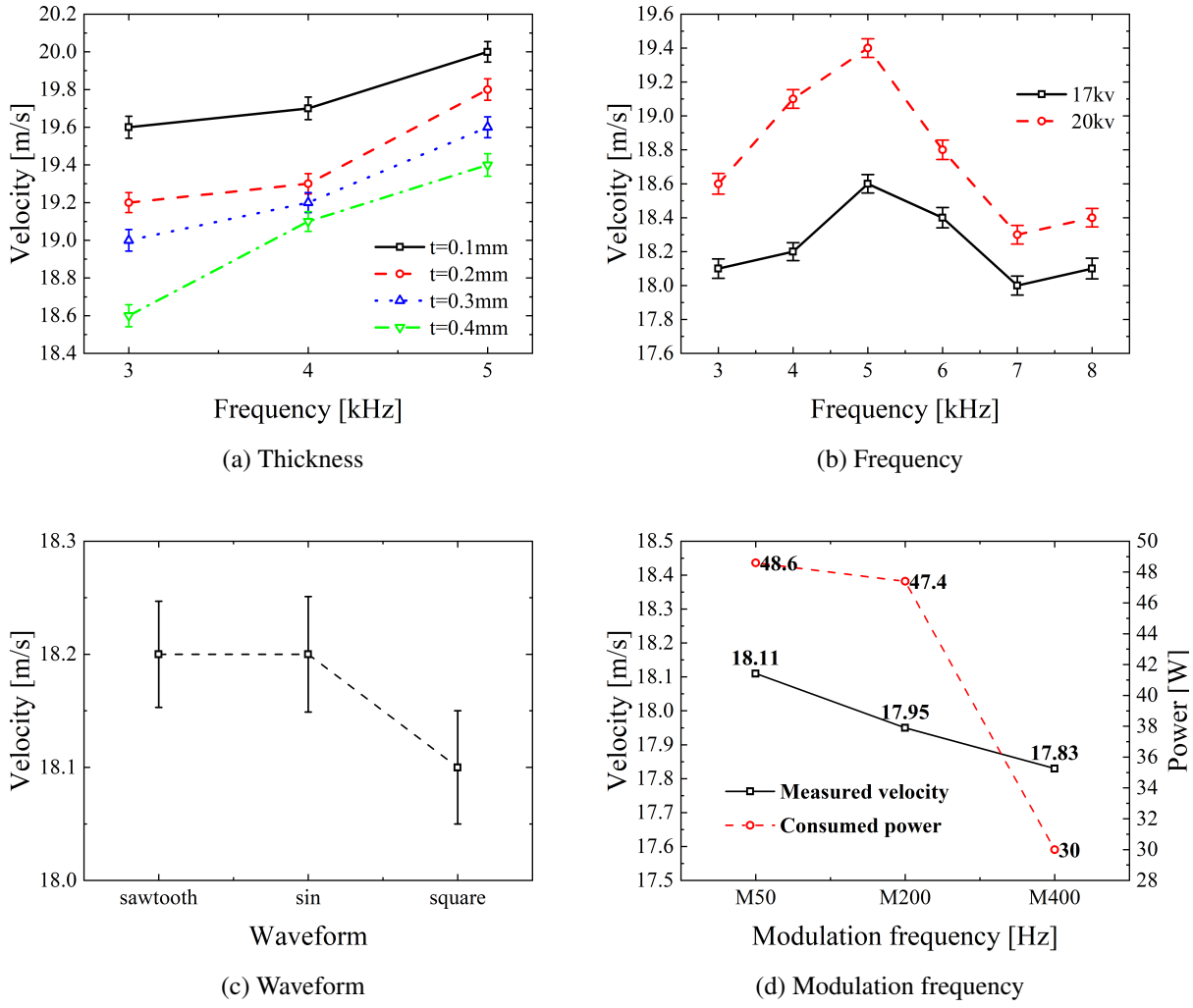

Figure 7.19: The effects of different parameters on the performance of plasma actuators; the influence of the thickness is shown in (a), voltage and frequency is in (b), waveform is in (c), modulation frequency under 50% duty cycle is in (d).

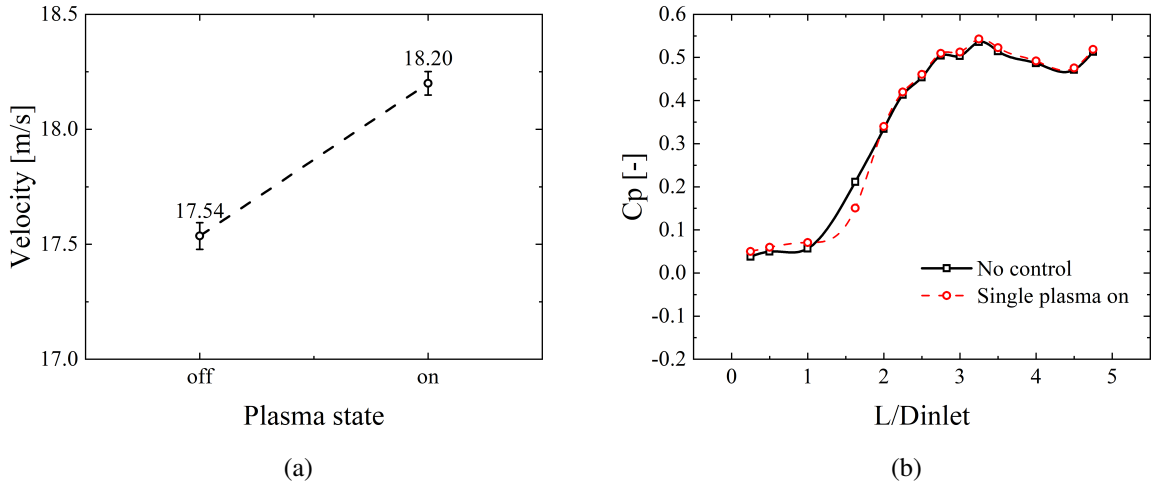

Figure 7.20: The measured velocities comparison at L/D_{inlet} = 1.625 (a), and the bottom C_p variations (b).

duced velocity and power consumption. In the final configuration, the wall jet schemes operate under a duty cycle of 100%, and the effect of the modulation frequency is not tested. Instead, modulation frequency testing is conducted in the vortex generator configuration. At this stage, the operational parameters for the single plasma actuator have been completely determined.

At this point, the operational parameters of the single plasma actuator have been fully determined and its performance is illustrated in Figure 7.20. As shown in Figure 7.20 (a), the velocity increment induced by the plasma actuator is quite limited when applied to a flow with an existing velocity, and it is significantly smaller compared to the velocity increment observed in a quasi-static environment Wojewodka et al. [38]. Figure 7.20 (b) shows the bottom wall static pressure curves before and after the plasma actuator is activated. It can be seen that, although there is a significant drop in the pressure coefficient C_p at L/D_{inlet} = 1.625, the changes at other positions are minimal.

Each array configuration was then performed with four measurements, and the mean value was subsequently calculated for further analysis. Compared with the baseline, the pressure distribution at the outlet interface did not change significantly, regardless of any plasma array configuration used. Consequently, the velocity at the installation location and PR_t and $C_{p,loss}$ on AIP were selected as comparative parameters. The installation locations of the various plasma actuator configurations are illustrated in Figure 7.7.

Figure 7.21 presents the performance of the various plasma array schemes. It can be found that relative to a single plasma actuator, the arrays composed of multiple plasma actuators as wall jets did not yield a significant increase in velocity. In the configuration with three actuators as wall jets, there was only a marginal improvement in velocity, while in the configuration with five actuators as wall jets, the measured velocity at L/D_{inlet}=1.625 even showed a slight decrease. When plasma was used as the vortex generator, the velocities measured in all configurations

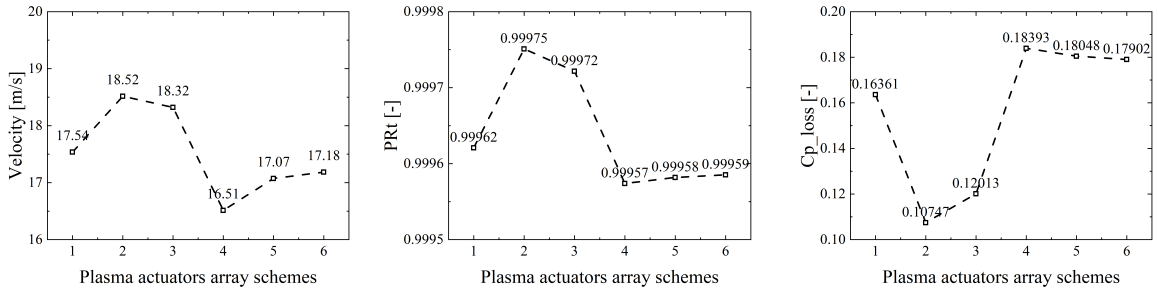

Figure 7.21: Velocities at the installation location (a), average PR_t (b) and average $C_{p,loss}$ (c) on AIP. Schemes 1 has no plasma control (Baseline); Schemes 2-3 are the wall jet with 3 actuators and 5 actuators, respectively; Schemes 4-6 are vortex generators with a modulation frequency of 50 Hz, 200 Hz, and 400 Hz, respectively.

were lower than the baseline, and the lower the modulation frequency, the greater the reduction in velocity.

Based on the trends of PR_t and $C_{p,loss}$ shown in Figures 7.21 (b) and (c), it can be concluded that, overall, the plasma actuator arrays enhance the performance of the jet schemes. However, the effectiveness does not increase proportionally with the number of plasma actuators. The array with three plasma actuators outperforms the array with five. When plasma actuators are used as wall jets, their mechanism involves injecting additional momentum directly into the boundary layer, thereby delaying flow separation. The performance of the five-actuator array, especially in terms of velocity optimisation, should theoretically exceed that of the three-actuator array. However, the observed reduction in effectiveness indicates that the installation of additional plasma actuators likely introduces more flow losses. Considering that the plasma actuators are mounted directly onto the inner wall surface of the S-shaped duct, this hypothesis is highly plausible.

However, when plasma actuators are employed as vortex generators, they do not improve the flow field and instead increase pressure losses, thus reducing the recovery coefficient in the AIP (Figure 7.21 (b) and (c)). When functioning as vortex generators, plasma actuators aim to use induced velocity to create vortices that draw momentum from outside the boundary layer into it, thereby delaying boundary layer separation. Moreover, in a quasi-static environment, the initiation of plasma actuators generates a starting vortex accompanied by an induced vortex[41, 182]. These vortices can work as vortex generators to introduce momentum from the mainstream. Therefore, several potential factors may have contributed to the failure in optimizing the flow field. First, the vortex generators used in this experiment may not have effectively generated vortices but introduced an additional cross-flow velocity component, leading to energy losses. Second, even if the vortices were successfully generated, they may have quickly disintegrated at a high flow speed of approximately 20 m/s, preventing sufficient momentum from being injected into the boundary layer, and the disintegration of the vortices also results in energy losses.

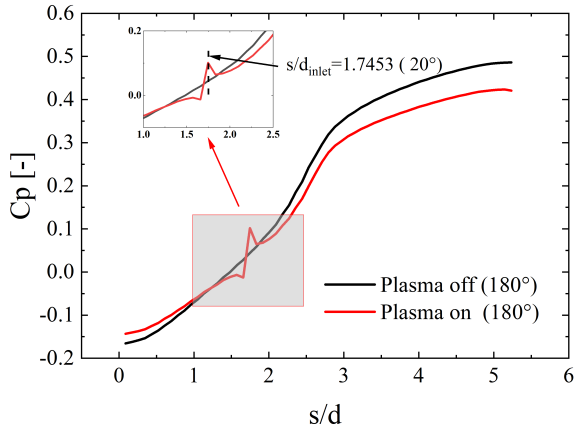

Figure 7.22: Bottom wall C_p before and after activation of the plasma actuator

7.3.3 Simulation Analysis

The experiments demonstrate that the plasma actuator effectively alters the flow field. However, because of experimental uncertainties, it is challenging to perform a quantitative analysis of the actuator's performance, and the experiments do not provide a clear visualization of the flow field within the S-duct. Therefore, this study employs numerical simulations to further investigate the effects of the plasma actuator. Based on the experimental behaviour of the plasma vortex generator, the simulation focuses solely on the plasma wall jet.

The simulation results indicate a negligible impact of the plasma actuator's activation and deactivation on the velocity and pressure at the reference point. In the simulation, interpolation at the reference point is unnecessary, as the values at the centre of the S-duct throat can be directly used. Figure 7.22 shows the C_p distribution at the bottom of the S-shaped duct. The activation of the plasma actuator is observed to induce significant fluctuations in the nearby C_p values. Segmenting based on this fluctuation, upstream C_p shows a slight increase, while downstream C_p shows a significant decrease.

The variation in the C_p curve suggests that upon activation of the plasma actuator, the wall flow velocity downstream of the actuator increases significantly. However, this comes at the expense of a slight reduction in wall flow velocity upstream. Figure 7.23 provides a more intuitive representation of the impact of the plasma actuator on the flow field within the S-duct. After activating the actuator, a reduction in the area of the highest velocity region is observed at the installation location (20°) and the subsequent slice (21°). In the outlet section, the high-speed region area in the central part expands significantly. These phenomena indicate an improvement in the stall region near the lower surface, a change reflected in the velocity distribution at the centre cross-section. However, this improvement is minimal in terms of pressure. The average total pressure in the outlet section increased only by 0.83 Pa. Furthermore, since the actuation voltage is 17 kV and the frequency is 4 kHz, these values exceed the accurate range of the model proposed by Soloviev [77]. In the simulation, the calculated thrust of the plasma actuator

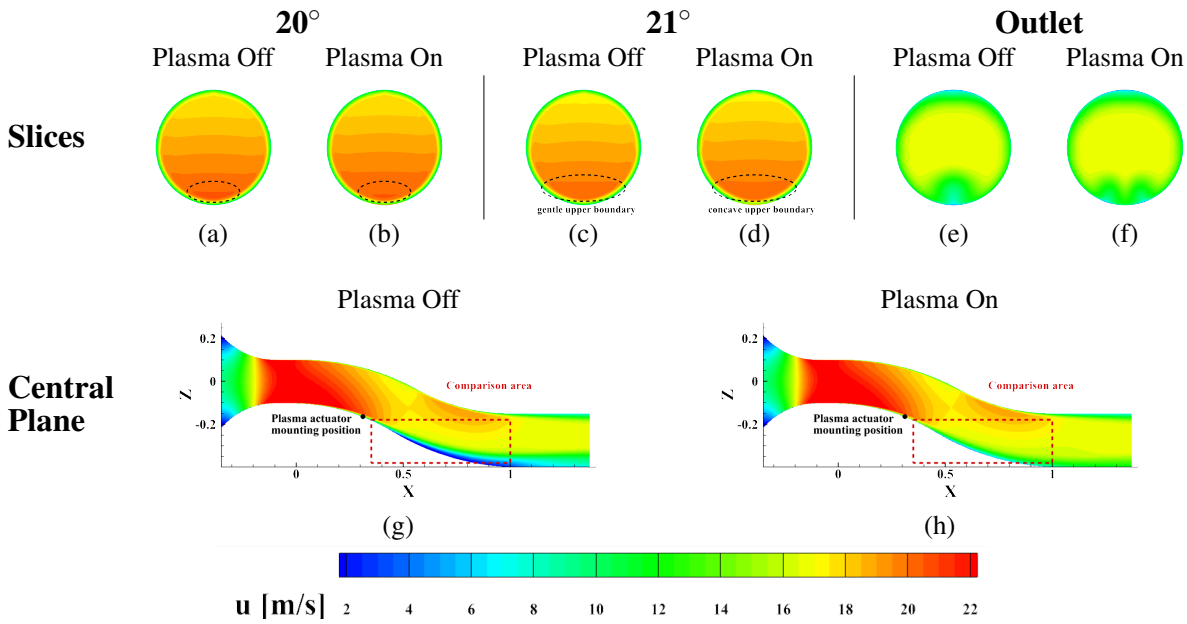

Figure 7.23: The velocity profiles at the inlet, the central slices, and the outlet before and after the plasma actuator are aviated. (a)-(f) are the velocity distributions of different slices. (g) and (h) are the velocity distributions at the central plane.

is 0.335 N/m, whereas in the experiment carried out by Thomas et al. [32], a thrust of 0.24 N/m was achieved using 42 kV and 2.1 kHz. This indicates that the plasma thrust in the simulation is overestimated compared to the actual values.

7.4 Conclusion and Future work

This study investigates plasma flow control in an S-shaped duct through experiments and numerical simulations. In the experimental phase, the plasma actuators generate significant heat during operation, necessitating parameter adjustments for the long run. The adjusted parameters include dielectric thickness, actuation voltage, frequency, waveform, and modulation frequency. After these adjustments, a single plasma actuator and arrays of actuators were installed in the S-shaped duct for testing. Based on the experimental data, numerical simulations of the S-shaped duct were conducted, and the plasma model was validated before its integration. This research can offer valuable references for future experiments and simulations. The main conclusions drawn in this study are as follows:

(1) During the adjustment of plasma actuator parameters, it was observed that as the dielectric thickness decreases and the actuation voltage increases, the induced flow velocity significantly increases. The influences of frequency and waveform do not exhibit a clear pattern. When the duty cycle is less than 100%, the actuator operating in an unsteady mode, the modulation frequency plays a key role in regulating the induced flow velocity. Higher modulation frequencies will result in lower induced velocities and reduced power

consumption.

(2) Although a single plasma actuator can significantly affect local flow velocity, its influence is limited to the immediate vicinity, with downstream changes measured in the experiments nearly negligible. This is because the plasma actuator's influence is smaller than that of experimental errors. Even when multiple plasma actuators are introduced, the changes in the flow field remain relatively limited. Furthermore, the installation of additional plasma actuators itself can introduce additional flow losses, which should be carefully considered in future experimental designs.

(3) The experimental results showed that, although the plasma flow control effect was minor, a slight increase in total pressure was observed at the outlet when the plasma actuator was used as a wall jet, indicating effective flow control. However, when the plasma actuator was used as a vortex generator, the total pressure at the outlet decreased and the flow velocity at the installation site also decreased, suggesting that the plasma vortex generators did not improve the flow field. This difference is mainly attributed to the different mechanisms by which the two control methods affect the flow field. The principle of the wall jet is relatively simple: injecting momentum directly into the boundary layer, so even if effective flow control is not achieved, it generally does not introduce additional flow losses. By contrast, the mechanism of the plasma vortex generator is much more complex. Plasma VGs need to generate the vortices first and use the vortices to induce the momentum into the boundary layer from the mainstream. Given the current limited understanding of plasma dynamics, the wall jet approach is a more robust option for flow control using plasma actuators.

(4) In the simulations, although the model proposed by Soloviev [77] explains the relationship between plasma-induced thrust and physical parameters, it provides relatively accurate results only under specific conditions, namely when the frequency is below 2.5 kHz and the equivalent voltage is less than 15 kV. Consequently, the plasma thrust in this simulation is overestimated, which also explains why the flow control effects are more pronounced in the simulation. Additionally, the average total pressure increase at the outlet is less than 1 Pa, when analysing the simulation results from the pressure perspective. This accounts for the lack of significant changes observed at the outlet in the pressure experiments. Furthermore, the influence of mesh size on plasma modelling cannot be ignored. When using a steady-state solver, the mesh size should be between 0.1 mm and 1 mm to adapt the plasma model used this time.

The limitations of this study also suggest directions for future research. First, in the experimental aspect, the spatial resolution of the pressure measurements is relatively low due to the constraints of measurement methods and time. Future studies could improve this by incorporating PIV

techniques to improve the precision of measurement. In terms of simulations, if computational resources are sufficient, an unsteady analysis of the plasma actuators can be conducted. With an unsteady solver, a grid size smaller than 1 mm would be enough to meet accuracy requirements.

Chapter 8

Conclusion and Future Work

This thesis aimed to optimise the flow field in the S-shaped duct using AC-DBD plasma flow control, and the study included both the experiment and the simulation. The research trajectory of this paper is as follows: firstly, a literature review was conducted on AC-DBD plasma actuators and S-shaped ducts (Chapter 2) to identify the study range. Subsequently, the relevant experimental methods, numerical approaches, and data analysis techniques used in this study were introduced in the methodology section (Chapter 3). The study began with pressure measurements in the S-shaped duct (Chapter 4), thoroughly investigating the flow on the duct wall and the AIP and discussing the effects of flow velocity and the upstream and downstream extension section. Based on pressure experiments, the turbulent characteristics of the AIP were further explored using Constant Temperature Anemometry (CTA) (Chapter 5). The experimental data obtained were used to generate numerical simulations (Chapter 6). Chapter 6 explores the impact of the radius growth rate of the S-shaped duct and performs an in-depth analysis of the spatial structure of the flow field using various modal analysis methods. In the end, Chapter 7 uses experiments and simulations to investigate the plasma flow control inside the S-duct.

8.1 Conclusions

The main findings of this thesis are as follows.

In the pressure measurement experiments:

(1) The flow symmetry of the suction-type S-duct at the bottom is superior to that of the top. The addition of the rear extension will not significantly change the flow pattern inside the S-duct, but the front extensions will, especially at the duct bottom. After the airflow exits the S-shaped segment, it initially maintains a downward motion trend due to inertia. After encountering the lower wall surface, it is deflected upward. Meanwhile, the direction of the vortices on the cross-section changed. Consequently, the length of the downstream extension section determines the direction of the secondary flow at the AIP.

(2) Although each S-duct configuration exhibited similar flow patterns under different flow velocities, variations in the wall C_p indicated that the mainstream's influence on different regions within the duct changed with velocity. However, changes in flow velocity could no longer affect the flow pattern within the duct, and the mainstream's shape and size could remain stable when the upstream and downstream ends of the S-shaped duct were equipped with sufficiently long extension sections.

(3) On the AIP, the areas with the most severe pressure and swirl distortion were different; the maximum values of *DC* were located at the top, while the maximum values of *SC* were found at the bottom. Flow velocity did not significantly affect pressure distortion but significantly influenced swirl distortion. Regarding the pressure distribution, the trend in total pressure distribution essentially depended on the dynamic pressure distribution. Static pressure distribution on the AIP doesn't change as the flow rate increases and remains uniformly distributed. Additionally, as flow velocity increased, although flow losses within the duct gradually increased, the proportion of these losses relative to the dynamic pressure at the reference point progressively decreased.

In the CTA experiments:

(1) A low-frequency signal dominated the turbulent variations at the outlet interface at low Mach numbers, suggesting that the flow at the exit of the S duct is relatively steady at low speeds. The sampling period and frequency had minimal impact on the measurement results, so lower sampling frequencies and periods are sufficient for experimental requirements under low Mach numbers.

(2) Although the time-averaged velocity field measured by the CTA experiments has a trend similar to that of the seven-hole probe experiments, the velocities measured at the same locations were noticeably lower than those measured by the seven-hole probe. This phenomenon persisted at reference points even after the potential influences of ambient temperature variations were minimised as much as possible. Through investigation, it was found that the error arises from changes in ambient pressure. Variations in ambient pressure can significantly influence the fan's performance, thus affecting the flow velocity.

(3) Areas where the velocity was reduced due to flow separation also showed high turbulence. The varying turbulence intensity levels also meant different skewness and kurtosis intensities. The high turbulence regions corresponded to small kurtosis and positive skewness, while the low turbulence regions corresponded to relatively high kurtosis and negative skewness. As the flow velocity increased, the areas with high skewness became smaller and the regions with high kurtosis became more significant.

In the S-duct simulations:

(1) At low Mach numbers, despite some discrepancies with the experimental results, the wall pressure coefficient (C_p) curves of the S-shaped diffuser obtained from the three turbulence models show no significant differences and almost overlap entirely. The primary deviation from the experimental data lies in the underprediction of the flow separation at the bottom. Furthermore, in terms of pressure loss, the results from all three turbulence models are close to the experimental data, with the $k-\varepsilon$ model providing the closest match. However, regarding flow characteristics and trends, the SST model demonstrates a clear advantage.

(2) The diffusion rate with an S-shaped growth profile demonstrates superior performance compared to a constant diffusion rate. It allows for a more uniform deceleration of the flow within the duct, delaying the onset of flow separation at the bottom and reducing the extent of the affected region. However, when transient simulations of this configuration are conducted using URANS based on the conclusions drawn from experiments, it was found that the transient results of all three turbulence models converged towards a steady state, with the flow fluctuations for the k-Omega and SST models even approaching zero, several orders of magnitude lower than those predicted by the k-Epsilon model. However, even the k-Epsilon model was still lower than the measured value of the experiment. The corresponding influence is also reflected in the modal analysis. For the $k-\omega$ and SST models, the first mode extracted by POD even lacks clear dynamic patterns.

(3) Different modal analysis methods exhibit different characteristics. The POD method could efficiently extract the main spatial structures within the flow field, yet it encountered issues with multi-frequency coupling, necessitating using FFT to obtain the dominant frequency. To some extent, DMD addressed the issue of multiple-frequency coupling found in POD, allowing for the acquisition of dynamic coherent structures at a single frequency. Furthermore, DMD also has other functions, such as using the eigenvalue circle to assess the stability of modes and predicting future flow fields based on the linearisation of the flow field. For SPOD, this method can also avoid the multiple-frequency coupling inherent to the POD method by decoupling the flow-field data in the temporal and spatial fields. Its single-frequency modes provided more spatial structural details than POD, which gives the SPOD method more advantages in analysing the unsteady flow field.

In the plasma flow control experiments and simulations:

(1) During the adjustment of plasma actuator parameters, it was observed that as the dielectric thickness decreases and the actuation voltage increases, the induced flow velocity significantly increases. The influences of frequency and waveform do not exhibit a clear pattern. When the duty cycle is less than 100%, the actuator operating in an unsteady mode, the modulation frequency plays a key role in regulating the induced flow velocity.

Higher modulation frequencies will result in lower induced velocities and reduced power consumption.

(2) Although a single plasma actuator can significantly affect local flow velocity, its influence is limited to the immediate vicinity, with downstream changes measured in the experiments nearly negligible. This is because the plasma actuator's influence is smaller than that of experimental errors. Even when multiple plasma actuators are introduced, the changes in the flow field remain relatively limited. Furthermore, the installation of additional plasma actuators itself can introduce additional flow losses, which should be carefully considered in future experimental designs.

(3) The experimental results showed that, although the plasma flow control effect was minor, a slight increase in total pressure was observed at the outlet when the plasma actuator was used as a wall jet, indicating effective flow control. However, when the plasma actuator was used as a vortex generator, the total pressure at the outlet decreased and the flow velocity at the installation site also decreased, suggesting that the plasma vortex generators did not improve the flow field. This difference is mainly attributed to the different mechanisms by which the two control methods affect the flow field. The principle of the wall jet is relatively simple: injecting momentum directly into the boundary layer, so even if effective flow control is not achieved, it generally does not introduce additional flow losses. By contrast, the mechanism of the plasma vortex generator is much more complex. Plasma VGs need to generate the vortices first and use the vortices to induce the momentum into the boundary layer from the mainstream. Given the current limited understanding of plasma dynamics, the wall jet approach is a more robust option for flow control using plasma actuators.

(4) In the simulations, although the model proposed by Soloviev [77] explains the relationship between plasma-induced thrust and physical parameters, it provides relatively accurate results only under specific conditions, namely when the frequency is below 2.5 kHz and the equivalent voltage is less than 15 kV. Consequently, the plasma thrust in this simulation is overestimated, which also explains why the flow control effects are more pronounced in the simulation. Additionally, the average total pressure increase at the outlet is less than 1 Pa, when analysing the simulation results from the pressure perspective. This accounts for the lack of significant changes observed at the outlet in the pressure experiments. Furthermore, the influence of mesh size on plasma modelling cannot be ignored. When using a steady-state solver, the mesh size should be between 0.1 mm and 1 mm to adapt the plasma model used this time.

8.2 Future Work

Based on the findings and limitations of this thesis, future work could focus on exploring the following areas:

(1) The limitations of pressure measurement experiments cannot be ignored. First, it used a square measurement region rather than a conventional circular tube. Although this approach facilitates more layouts of pressure measurement, it is evident that the square measurement region will induce more experimental error. In addition, the traverse system used in this experiment induces significant flow asymmetry. Although some optimizations were made during the experiment, they came at the cost of data completeness, as only half of the AIP was measured. Secondly, this experiment used an axial flow fan as the power source and lacked a feedback control mechanism. The influence of the experimental environment on the fan and the inherent errors of the fan itself will accumulate in the experiment. Lastly, due to the segmented design of the S-shaped duct model, the likelihood of air leakage increases. Although all connections and measurement areas were sealed with tape, the possibility of leakage still exists due to the lack of detection methods. Air leakage could reduce the airflow provided by the fan to the S-duct, thus introducing additional errors. The limitations mentioned above should be addressed in future work.

(2) The limitations of the simulations must be acknowledged. Due to the inherent constraints of the Reynolds-average Navier-Stokes (RANS) methodology, the time-averaging errors in the unsteady RANS (URANS) approach render it intrinsically inadequate for detailed turbulence analysis. This limitation consequently narrows the turbulence findings in the present study. While reducing the time-averaging errors within the URANS method can be achieved by employing smaller time steps to some extent, a more suitable approach would be the direct application of Large Eddy Simulation (LES) or Direct Numerical Simulation (DNS).

(3) The limitations of plasma flow control experiments and simulations also suggest directions for future research. First, in the experimental aspect, the spatial resolution of the pressure measurements is relatively low due to the constraints of measurement methods and time. Future studies could improve this by incorporating PIV techniques to improve the precision of measurement. In terms of simulations, if computational resources are sufficient, an unsteady analysis of the plasma actuators can be conducted. This thesis only investigated the steady-state field of the AC-DBD plasma model; the relevant unsteady simulation should be further studied in future work.

(4) Attempt to increase the induced thrust of AC-DBD plasma actuators. The numerous advantageous characteristics of DBD plasma actuators make them highly effective for flow

control; however, the small magnitude of the induced thrust remains a significant limitation. Increasing the induced thrust would enable flow control over a broader range of velocities and make many innovative flow control methods feasible.

Bibliography

[1] Hui Yang, Feng Li, Yaoying Song, and Baigang Sun. Numerical investigation of electro-hydrodynamic (ehd) flow control in an s-shaped duct. *Plasma Science and Technology*, 14(10):897, 2012.

[2] John C Vaccaro, Yossef Elimelech, Yi Chen, Onkar Sahni, Kenneth E Jansen, and Michael Amitay. Experimental and numerical investigation on steady blowing flow control within a compact inlet duct. *International Journal of Heat and Fluid Flow*, 54:143–152, 2015.

[3] ZhanJun Chen and JinJun Wang. Numerical investigation on synthetic jet flow control inside an s-inlet duct. *Science China Technological Sciences*, 55:2578–2584, 2012.

[4] Eric Garnier. Flow control by pulsed jet in a curved s-duct: a spectral analysis. *AIAA Journal*, 53(10):2813–2827, 2015.

[5] Daniel Miller and G Addington. Aerodynamic flowfield control technologies for highly integrated airframe propulsion flowpaths. In *2nd AIAA Flow Control Conference*, page 2625, 2004.

[6] BRUCEA Reichert and BRUCEJ Wendt. Improving diffusing s-duct performance by secondary flow control. In *32nd Aerospace Sciences Meeting and Exhibit*, page 365, 1994.

[7] Chaoyu Liu and J Reece Roth. An atmospheric glow discharge plasma for aerodynamic boundary layer control. In *Proceedings of 1994 IEEE 21st International Conference on Plasma Sciences (ICOPS)*, pages 97–98. IEEE, 1994.

[8] J Roth, Daniel Sherman, and Stephen Wilkinson. Boundary layer flow control with a one atmosphere uniform glow discharge surface plasma. In *36th AIAA Aerospace Sciences Meeting and Exhibit*, page 328, 1998.

[9] Michael M Wojewodka. *Complex flow physics & active plasma flow control in convoluted ducts*. PhD thesis, University of Glasgow, 2020.

[10] M Gad-el Hak. Flow control cambridge univ, 2000.

[11] Eric Moreau. Airflow control by non-thermal plasma actuators. *Journal of physics D: applied physics*, 40(3):605, 2007.

[12] David A Cavalieri. *On the experimental design for instability analysis on a cone at Mach 3.5 and 6.0 using a corona discharge perturbation method*. PhD thesis, Illinois Institute of Technology, 1995.

[13] Thomas Corke and Eric Matlis. Phased plasma arrays for unsteady flow control. In *Fluids 2000 Conference and Exhibit*, page 2323, 2000.

[14] TC Corke, DA Cavalieri, and E Matlis. Boundary-layer instability on sharp cone at mach 3.5 with controlled input. *AIAA journal*, 40(5):1015–1018, 2002.

[15] Thomas C Corke, Martiqua L Post, and Dmitry M Orlov. Sdbd plasma enhanced aerodynamics: concepts, optimization and applications. *Progress in Aerospace Sciences*, 43 (7-8):193–217, 2007.

[16] Thomas C Corke, C Lon Enloe, and Stephen P Wilkinson. Dielectric barrier discharge plasma actuators for flow control. *Annual review of fluid mechanics*, 42:505–529, 2010.

[17] G Touchard. Plasma actuators for aeronautics applications-state of art review. *International Journal of Plasma Environmental Science and Technology*, 2(1):1–24, 2008.

[18] Young-Chang Cho and Wei Shyy. Adaptive flow control of low-reynolds number aerodynamics using dielectric barrier discharge actuator. *Progress in Aerospace Sciences*, 47 (7):495–521, 2011.

[19] Jin-Jun Wang, Kwing-So Choi, Li-Hao Feng, Timothy N Jukes, and Richard D Whalley. Recent developments in dbd plasma flow control. *Progress in Aerospace Sciences*, 62: 52–78, 2013.

[20] C Enloe, Thomas McLaughlin, Robert Van Dyken, and John Fischer. Plasma structure in the aerodynamic plasma actuator. In *42nd AIAA Aerospace Sciences Meeting and Exhibit*, page 844, 2004.

[21] CL Enloe, Thomas E McLaughlin, Robert D VanDyken, KD Kachner, Eric J Jumper, and Thomas C Corke. Mechanisms and responses of a single dielectric barrier plasma actuator: plasma morphology. *AIAA journal*, 42(3):589–594, 2004.

[22] C Lon Enloe, Thomas E McLaughlin, Robert D VanDyken, KD Kachner, Eric J Jumper, Thomas C Corke, M Post, and O Haddad. Mechanisms and responses of a dielectric barrier plasma actuator: Geometric effects. *AIAA journal*, 42(3):595–604, 2004.

[23] Jerome Pons, Eric Moreau, and Gérard Touchard. Asymmetric surface dielectric barrier discharge in air at atmospheric pressure: electrical properties and induced airflow characteristics. *Journal of physics D: applied physics*, 38(19):3635, 2005.

[24] Antoine Debien, Nicolas Benard, and Eric Moreau. Streamer inhibition for improving force and electric wind produced by dbd actuators. *Journal of Physics D: Applied Physics*, 45(21):215201, 2012.

[25] Alain Seraudie, Eddy Aubert, Nicolas Naudé, and Jean Cambronne. Effect of plasma actuators on a flat plate laminar boundary layer in subsonic conditions. In *3rd AIAA Flow Control Conference*, page 3350, 2006.

[26] CL Enloe, Thomas E McLaughlin, GI Font, and JW Baughn. Parameterization of temporal structure in the single-dielectric-barrier aerodynamic plasma actuator. *AIAA journal*, 44(6):1127–1136, 2006.

[27] Martiqua L Post. *Plasma actuators for separation control on stationary and oscillating airfoils*. University of Notre Dame, 2004.

[28] Binjie Dong, Jean-Marc Bauchire, Jean Michel Pouvesle, Pierre Magnier, and Dunpin Hong. Experimental study of a dbd surface discharge for the active control of subsonic airflow. *Journal of Physics D: Applied Physics*, 41(15):155201, 2008.

[29] Louis N Cattafesta III and Mark Sheplak. Actuators for active flow control. *Annual Review of Fluid Mechanics*, 43:247–272, 2011.

[30] E Moreau, A Debien, N Benard, T Jukes, R Whalley, KS Choi, Artur Berendt, J Podlinski, and J Mizeraczyk. Surface dielectric barrier discharge plasma actuators. *ERCOFTAC Bulletin*, 94(5):5–10, 2013.

[31] Dmitriy M Orlov. *Modelling and simulation of single dielectric barrier discharge plasma actuators*. 2006.

[32] Flint O Thomas, Thomas C Corke, Muhammad Iqbal, Alexey Kozlov, and David Schatzman. Optimization of dielectric barrier discharge plasma actuators for active aerodynamic flow control. *AIAA journal*, 47(9):2169–2178, 2009.

[33] Maxime Forte, Jerome Jolibois, Eric Moreau, Gerard Touchard, and Michel Cazalens. Optimization of a dielectric barrier discharge actuator by stattionary and non-stationary measurements of the induced flow velocity-application to airflow control. In *3rd AIAA Flow Control Conference*, page 2863, 2006.

[34] J Reece Roth and Xin Dai. Optimization of the aerodynamic plasma actuator as an electrohydrodynamic (ehd) electrical device. In *44th AIAA Aerospace Sciences Meeting and Exhibit*, page 1203, 2006.

[35] Robert Van Dyken, Thomas McLaughlin, and CL Enloe. Parametric investigations of a single dielectric barrier plasma actuator. In *42nd AIAA aerospace sciences meeting and exhibit*, page 846, 2004.

[36] Alexey V Kozlov. *Plasma actuators for bluff body flow control*. University of Notre Dame, 2010.

[37] Jérôme Pons, Eric Moreau, Gérard Touchard, et al. Electrohydrodynamic properties of surface dielectric barrier discharges in ambient air for aerodynamic airflow control. *Power*, 140(10):11, 2007.

[38] Michael M Wojewodka, Craig White, and Konstantinos Kontis. Effect of permittivity and frequency on induced velocity in ac-dbd surface and channel plasma actuators. *Sensors and Actuators A: Physical*, 303:111831, 2020.

[39] James Baughn, Christopher Porter, Brent Peterson, Thomas McLaughlin, C Enloe, Gabriel Font, and Corrie Baird. Momentum transfer for an aerodynamic plasma actuator with an imposed boundary layer. In *44th AIAA Aerospace Sciences Meeting and Exhibit*, page 168, 2006.

[40] F Avino, AA Howling, M Von Allmen, A Waskow, L Ibba, J Han, and I Furno. Surface dbd degradation in humid air, and a hybrid surface-volume dbd for robust plasma operation at high humidity. *Journal of Physics D: Applied Physics*, 56(34):345201, 2023.

[41] Richard D Whalley and Kwing-So Choi. The starting vortex in quiescent air induced by dielectric-barrier-discharge plasma. *Journal of Fluid Mechanics*, 703:192–203, 2012.

[42] TN Jukes, KS Choi, T Segawa, and H Yoshida. Jet flow induced by a surface plasma actuator. *Proceedings of the Institution of Mechanical Engineers, Part I: Journal of Systems and Control Engineering*, 222(5):347–356, 2008.

[43] Timothy N Jukes, Kwing-So Choi, Graham A Johnson, and Simon J Scott. Characterization of surface plasma-induced wall flows through velocity and temperature measurements. *AIAA journal*, 44(4):764–771, 2006.

[44] Timothy Jukes, Kwing-So Choi, Graham Johnson, and Simon Scott. Turbulent drag reduction by surface plasma through spanwise flow oscillation. In *3rd AIAA Flow Control Conference*, page 3693, 2006.

[45] Timothy N Jukes. *Turbulent drag reduction using surface plasma*. PhD thesis, University of Nottingham, 2007.

[46] J Reece Roth, Daniel M Sherman, and Stephen P Wilkinson. Electrohydrodynamic flow control with a glow-discharge surface plasma. *AIAA journal*, 38(7):1166–1172, 2000.

[47] G Johnson and S Scott. Plasma-aerodynamic boundary layer interaction studies. In *32nd AIAA Plasmadynamics and Lasers Conference*, page 3052, 2001.

[48] Stephen P Wilkinson. Investigation of an oscillating surface plasma for turbulent drag reduction. In *41st Aerospace Sciences Meeting and Exhibit*, number AIAA Paper 2003-1023, 2003.

[49] Thomas Corke, Eric Jumper, Martiqua Post, Dmitriy Orlov, and Thomas McLaughlin. Application of weakly-ionized plasmas as wing flow-control devices. In *40th AIAA Aerospace Sciences Meeting & Exhibit*, page 350, 2002.

[50] Martiqua L Post and Thomas C Corke. Separation control on high angle of attack airfoil using plasma actuators. *AIAA journal*, 42(11):2177–2184, 2004.

[51] Maxime Forte, Jerome Jolibois, J Pons, Eric Moreau, G Touchard, and Michel Cazalens. Optimization of a dielectric barrier discharge actuator by stationary and non-stationary measurements of the induced flow velocity: application to airflow control. *Experiments in fluids*, 43:917–928, 2007.

[52] J Reece Roth, Raja Chandra Mohan Madhan, Manish Yadav, Jozef Rahel, and Stephen Wilkinson. Flow field measurements of paraelectric, peristaltic, and combined plasma actuators based on the one atmosphere uniform glow discharge plasma (oaugdp). In *42nd AIAA Aerospace Sciences Meeting and Exhibit*, page 845, 2004.

[53] Tim Jukes, Kwing-So Choi, Graham Johnson, and Simon Scott. Turbulent boundary-layer control for drag reduction using surface plasma. In *2nd AIAA flow control conference*, page 2216, 2004.

[54] Timothy N Jukes and Kwing-So Choi. Dielectric-barrier-discharge vortex generators: characterisation and optimisation for flow separation control. *Experiments in fluids*, 52: 329–345, 2012.

[55] Ömer Savas and Donald Coles. Coherence measurements in synthetic turbulent boundary layers. *Journal of Fluid Mechanics*, 160:421–446, 1985.

[56] Barton L Smith and Ari Glezer. The formation and evolution of synthetic jets. *Physics of fluids*, 10(9):2281–2297, 1998.

[57] Arvind Santhanakrishnan, Jamey Jacob, and Yildirim Suzen. Flow control using plasma actuators and linear/annular plasma synthetic jet actuators. In *3rd AIAA Flow Control Conference*, page 3033, 2006.

[58] Arvind Santhanakrishnan and Jamey D Jacob. Flow control with plasma synthetic jet actuators. *Journal of Physics D: Applied Physics*, 40(3):637, 2007.

[59] Arvind Santhanakrishnan, Daniel Reasor, and Raymond LeBeau. Unstructured numerical simulation of experimental linear plasma actuator synthetic jet flows. In *46th AIAA Aerospace Sciences Meeting and Exhibit*, page 541, 2008.

[60] Arvind Santhanakrishnan and Jamey Jacob. Characterization of linear plasma synthetic jet actuators. In *46th AIAA Aerospace Sciences Meeting and Exhibit*, page 538, 2008.

[61] Arvind Santhanakrishnan, Daniel A Reasor, and Raymond P LeBeau. Characterization of linear plasma synthetic jet actuators in an initially quiescent medium. *Physics of Fluids*, 21(4), 2009.

[62] Takehiko Segawa, Hirohide Furutani, Hiro Yoshida, Timothty Jukes, and Kwing-So Choi. Wall normal jet under elevated temperatures produced by surface plasma actuator. In *45th AIAA Aerospace Sciences Meeting and Exhibit*, page 784, 2007.

[63] Takehiko Segawa, Hiro Yoshida, Shinya Takekawa, Timothy Jukes, and Kwing-So Choi. Wall normal jet produced by dbd plasma actuator with doughnut-shaped electrode. In *Fluids Engineering Division Summer Meeting*, volume 48401, pages 465–472, 2008.

[64] AB Liu, PF Zhang, B Yan, CF Dai, and JJ Wang. Flow characteristics of synthetic jet induced by plasma actuator. *AIAA journal*, 49(3):544–553, 2011.

[65] PanFeng Zhang, ChenFeng Dai, AiBing Liu, and JinJun Wang. The effect of actuation frequency on the plasma synthetic jet. *Science China Technological Sciences*, 54:2945–2950, 2011.

[66] Arvind Santhanakrishnan and Jamey Jacob. Effect of plasma morphology on flow control using plasma synthetic jet actuators. In *45th AIAA Aerospace Sciences Meeting and Exhibit*, page 783, 2007.

[67] Michael Bolitho and Jamey Jacob. Use of aggregate plasma synthetic jet actuators for flow control. In *45th AIAA Aerospace Sciences Meeting and Exhibit*, page 637, 2007.

[68] Jesse Little and Mo Samimy. High-lift airfoil separation with dielectric barrier discharge plasma actuation. *AIAA journal*, 48(12):2884–2898, 2010.

[69] Bo Li, Xuanshi Meng, Shiqing Yin, Weiwei Hui, and Huaxing Li. Flow separation control over an airfoil using plasma co-flow jet. *AIAA Journal*, 60(4):2195–2206, 2022.

[70] Timothy N Jukes, Takehiko Segawa, and Hirohide Furutani. Flow control on a naca 4418 using dielectric-barrier-discharge vortex generators. *AIAA journal*, 51(2):452–464, 2013.

[71] Balaji Jayaraman, Yongsheng Lian, and Wei Shyy. Low-reynolds number flow control using dielectric barrier discharge-based actuators. In *37th AIAA Fluid Dynamics Conference and Exhibit*, page 3974, 2007.

[72] Wei Shyy, B Jayaraman, and A Andersson. Modeling of glow discharge-induced fluid dynamics. *Journal of applied physics*, 92(11):6434–6443, 2002.

[73] Kortny Hall, Eric Jumper, Thomas Corke, and Thomas McLaughlin. Potential flow model of a plasma actuator as a lift enhancement device. In *43rd AIAA Aerospace Sciences Meeting and Exhibit*, page 783, 2005.

[74] Yildirim Suzen, George Huang, Jamey Jacob, and David Ashpis. Numerical simulations of plasma based flow control applications. In *35th AIAA Fluid Dynamics Conference and Exhibit*, page 4633, 2005.

[75] Dmitriy Orlov, Thomas Corke, and Mehul Patel. Electric circuit model for aerodynamic plasma actuator. In *44th AIAA Aerospace Sciences Meeting and Exhibit*, page 1206, 2006.

[76] Kunwar Pal Singh and Subrata Roy. Force approximation for a plasma actuator operating in atmospheric air. *Journal of Applied Physics*, 103(1), 2008.

[77] VR Soloviev. Analytical estimation of the thrust generated by a surface dielectric barrier discharge. *Journal of Physics D: Applied Physics*, 45(2):025205, 2011.

[78] Yacine Babou, E Nieto Martin, and P Fajardo Pena. Simple body force model for dielectric barrier discharge plasma actuator. In *Proceedings of the 7th European Conference for Aeronautics and Aerospace Sciences (EUCASS), Milan, Italy*, pages 3–6, 2017.

[79] Mohammadreza Barzegaran and Amirreza Kosari. A model of flow separation controlled by dielectric barrier discharge. *Chinese Journal of Aeronautics*, 30(5):1660–1669, 2017.

[80] P Bansod and P Bradshaw. The flow in s-shaped ducts. *Aeronautical Quarterly*, 23(2): 131–140, 1972.

[81] STEVENR WELLBORN, BRUCEA REICHERT, and THEODOREH OKIISHI. An experimental investigation of the flow in a diffusing s-duct. In *28th joint propulsion conference and exhibit*, page 3622, 1992.

[82] Michael M Wojewodka, Craig White, Shahrokh Shahpar, and Konstantinos Kontis. A review of flow control techniques and optimisation in s-shaped ducts. *International Journal of Heat and Fluid Flow*, 74:223–235, 2018.

[83] Pavlos K Zachos, David G MacManus, Daniel Gil Prieto, and Nicola Chiereghin. Flow distortion measurements in convoluted aeroengine intakes. *AiAA Journal*, 54(9):2819–2832, 2016.

[84] AMKP Taylor, James H Whitelaw, and M Yianneskis. Developing flow in s-shaped ducts. 1: Square cross-section duct. Technical report, 1982.

[85] AMKP Taylor, James H Whitelaw, and M Yianneskis. Developing flow in s-shaped ducts. 2: Circular cross-section duct. Technical report, NASA, 1984.

[86] AD Vakili, JM Wu, P Liver, and MK Bhat. Flow control in a diffusing s-duct. Technical report, 1985.

[87] RW Guo and J Seddon. An investigation of the swirl in an s-duct. *Aeronautical Quarterly*, 33(1):25–58, 1982.

[88] YT Ng, SC Luo, TT Lim, and QW Ho. On the relation between centrifugal force and radial pressure gradient in flow inside curved and s-shaped ducts. *Physics of Fluids*, 20 (5), 2008.

[89] John C Vaccaro, Yossef Elimelech, Yi Chen, Onkar Sahni, Kenneth E Jansen, and Michael Amitay. Experimental and numerical investigation on the flow field within a compact inlet duct. *International journal of heat and fluid flow*, 44:478–488, 2013.

[90] Daniel Gil-Prieto, David G MacManus, Pavlos K Zachos, Geoffrey Tanguy, and Kevin R Menzies. Convoluted intake distortion measurements using stereo particle image velocimetry. *AIAA Journal*, 55(6):1878–1892, 2017.

[91] David G MacManus, Nicola Chiereghin, Daniel Gil Prieto, and Pavlos Zachos. Complex aeroengine intake ducts and dynamic distortion. *Aiaa Journal*, 55(7):2395–2409, 2017.

[92] Michael M Wojewodka, Craig White, Shahrokh Shahpar, and Konstantinos Kontis. Numerical study of complex flow physics and coherent structures of the flow through a convoluted duct. *Aerospace Science and Technology*, 121:107191, 2022.

[93] Norbert C Bissinger and Thomas Breuer. Basic principles–gas turbine compatibility–intake aerodynamic aspects. *Encyclopedia of Aerospace Engineering*, 2010.

[94] SAE Standard. 1419b: Inlet total pressure distortion considerations for gas turbine engines. In *S-16 Turbine Engine Inlet Flow Distortion Committee*. SAE International, p. 279., 2013.

[95] SAE Standard. 1420b: Gas turbine engine inlet flow distortion guidelines. 2011.

[96] RW Guo and J Seddon. The swirl in an s-duct of typical air intake proportions. *Aeronautical quarterly*, 34(2):99–129, 1983.

[97] Alejandro Castillo Pardo, Ahad Mehdi, Vassilios Pachidis, and David G MacManus. Numerical study of the effect of multiple tightly-wound vortices on a transonic fan stage performance. In *Turbo Expo: Power for Land, Sea, and Air*, volume 45578, page V01AT01A033. American Society of Mechanical Engineers, 2014.

[98] SAE S-16 Committee et al. A methodology for assessing inlet swirl distortion.

[99] Scanivalve Corporation. Data systems for zoc scanners, 2024. URL `https://scanivalve.com/products/pressure-measurement/data-systems` Accessed: 2024-12-03.

[100] Scanivalve Corporation. Zoc23b miniature pressure scanner, 2024. URL `https://scanivalve.com/products/pressure-measurement/miniature-an` Accessed: 2024-12-03.

[101] Walter P Nelms and Donald A Durston. Preliminary aerodynamic characteristics of several advanced vstol fighter/attack aircraft concepts. *SAE Transactions*, pages 3531–3551, 1980.

[102] K Everett and D Durston. Theory and calibration of non-nulling seven-hole cone probes for usein complex flow measurement. In *20th Aerospace Sciences Meeting*, page 232, 1982.

[103] RW Gallington. Measurement of very large flow angles with non-niilling seven-hole probes. *04I Force Academy*, page 60, 1980.

[104] Finn E Jorgensen. How to measure turbulence with hot-wire anemometers-a practical guide. *Dantec Dynamics*, 19, 2002.

[105] Louis Vessot King. On the convection of heat from small cylinders in a stream of fluid: Determination of the convection constants of small platinum wires with applications to hot-wire anemometry. *Philosophical Transactions of the Royal Society of London Series A*, 214:373–432, 1914.

[106] C Forbes Dewey Jr. A correlation of convective heat transfer and recovery temperature data for cylinders in compressible flow. *International Journal of Heat and Mass Transfer*, 8(2):245–252, 1965.

[107] Peter Freymuth. Frequency response and electronic testing for constant-temperature hot-wire anemometers. *Journal of Physics E: Scientific Instruments*, 10(7):705, 1977.

[108] Peter Freymuth. Interpretations in the control theory of thermal anemometers. *Measurement Science and Technology*, 8(2):174, 1997.

[109] Joseph Smagorinsky. General circulation experiments with the primitive equations: I. the basic experiment. *Monthly weather review*, 91(3):99–164, 1963.

[110] Osborne Reynolds. Iv. on the dynamical theory of incompressible viscous fluids and the determination of the criterion. *Philosophical transactions of the royal society of london.(a.)*, (186):123–164, 1895.

[111] Joel H Ferziger and Milovan Perić. *Computational methods for fluid dynamics*. Springer, 2002.

[112] François G Schmitt. About boussinesq's turbulent viscosity hypothesis: historical remarks and a direct evaluation of its validity. *Comptes Rendus Mécanique*, 335(9-10): 617–627, 2007.

[113] Brian Edward Launder and Dudley Brian Spalding. The numerical computation of turbulent flows. In *Numerical prediction of flow, heat transfer, turbulence and combustion*, pages 96–116. Elsevier, 1983.

[114] David C Wilcox. Reassessment of the scale-determining equation for advanced turbulence models. *AIAA journal*, 26(11):1299–1310, 1988.

[115] Florianr Menter. Zonal two equation kw turbulence models for aerodynamic flows. In *23rd fluid dynamics, plasmadynamics, and lasers conference*, page 2906, 1993.

[116] Florian R Menter, Martin Kuntz, Robin Langtry, et al. Ten years of industrial experience with the sst turbulence model. *Turbulence, heat and mass transfer*, 4(1):625–632, 2003.

[117] Clarence W Rowley and Scott TM Dawson. Model reduction for flow analysis and control. *Annual Review of Fluid Mechanics*, 49:387–417, 2017.

[118] Kunihiko Taira, Steven L Brunton, Scott TM Dawson, Clarence W Rowley, Tim Colonius, Beverley J McKeon, Oliver T Schmidt, Stanislav Gordeyev, Vassilios Theofilis, and Lawrence S Ukeiley. Modal analysis of fluid flows: An overview. *Aiaa Journal*, 55(12): 4013–4041, 2017.

[119] Kunihiko Taira, Maziar S Hemati, Steven L Brunton, Yiyang Sun, Karthik Duraisamy, Shervin Bagheri, Scott TM Dawson, and Chi-An Yeh. Modal analysis of fluid flows: Applications and outlook. *AIAA journal*, 58(3):998–1022, 2020.

[120] John L Lumley. *Stochastic tools in turbulence*. Courier Corporation, 2007.

[121] L Sirovich. Turbulence and the dynamics of coherent structures, parts i, ii and iii. *Quart. Appl. Math.*, pages 561–590, 1987.

[122] Aaron Towne, Oliver T Schmidt, and Tim Colonius. Spectral proper orthogonal decomposition and its relationship to dynamic mode decomposition and resolvent analysis. *Journal of Fluid Mechanics*, 847:821–867, 2018.

[123] Julius S Bendat and Allan G Piersol. Random data analysis and measurement procedures. *Measurement Science and Technology*, 11(12):1825–1826, 2000.

[124] William K George, Paul D Beuther, and John L Lumley. Processing of random signals. In *Proceedings of the Dynamic Flow Conference 1978 on Dynamic Measurements in Unsteady Flows*, pages 757–800. Springer, 1978.

[125] Peter Welch. The use of fast fourier transform for the estimation of power spectra: a method based on time averaging over short, modified periodograms. *IEEE Transactions on audio and electroacoustics*, 15(2):70–73, 1967.

[126] WH Ball. Tests of wall suction and blowing in highly offset diffusers. *Journal of Aircraft*, 22(3):161–167, 1985.

[127] SAE AIR1419. Inlet total-pressure-distortion considerations for gas-turbine engines. 1999.

[128] DS Kidman, PV Reagan, and DJ Malloy. Comparison of inlet compatibility results from subscale wind tunnel and full-scale flight tests of the f/a-22 aircraft with the f119-pw-100 engine. In *Proceedings of the 17th Symposium on Air Breathing Engines*, pages 1–18. International Soc. of Air Breathing Engines Munich, Germany, 2005.

[129] Leon M Wenzel and Ronald J Blaha. Analysis of dynamic inlet distortion applied to a parallel compressor model. Technical report, 1977.

[130] Rudolf PM Rademakers, Stefan Bindl, and Reinhard Niehuis. Effects of flow distortions as they occur in s-duct inlets on the performance and stability of a jet engine. *Journal of Engineering for Gas Turbines and Power*, 138(2):022605, 2016.

[131] William T Cousins. History, philosophy, physics, and future directions of aircraft propulsion system/inlet integration. In *Turbo Expo: Power for Land, Sea, and Air*, volume 41677, pages 305–320, 2004.

[132] S-16 Turbine Engine Inlet Flow Distortion Committee. *A methodology for assessing inlet swirl distortion*. SAE International, 2022.

[133] Daniel Gil-Prieto, David G MacManus, Pavlos K Zachos, and Abian Bautista. Assessment methods for unsteady flow distortion in aero-engine intakes. *Aerospace Science and Technology*, 72:292–304, 2018.

[134] Daniel Gil-Prieto, Pavlos K Zachos, David G MacManus, and Grant McLelland. Unsteady characteristics of s-duct intake flow distortion. *Aerospace Science and Technology*, 84:938–952, 2019.

[135] Grant McLelland, David G MacManus, Pavlos K Zachos, Daniel Gil-Prieto, and Matteo Migliorini. Influence of upstream total pressure profiles on s-duct intake flow distortion. *Journal of Propulsion and Power*, 36(3):346–356, 2020.

[136] Matteo Migliorini, Pavlos K Zachos, and David G MacManus. Novel method for evaluating intake unsteady flow distortion. *Journal of Propulsion and Power*, 38(1):135–147, 2022.

[137] Christopher Chiang, David Koo, and David W Zingg. Aerodynamic shape optimization of an s-duct intake for a boundary-layer ingesting engine. *Journal of Aircraft*, 59(3): 725–741, 2022.

[138] Geoffrey Tanguy, David G MacManus, and Eric Garnier. Numerical investigation of the unsteady distortion for an s-duct intake with mechanical vortex generators. *International Journal of Heat and Fluid Flow*, 95:108975, 2022.

[139] Ru-bing Liu, Xiao-yin Mei, Sheng-hui Xue, Yu-wen Lu, Zhe-zhe Su, and Qi Lin. Active flow control of s-duct by plasma synthetic jet. *Journal of Zhejiang University-SCIENCE A*, 23(8):652–668, 2022.

[140] AR Porro. *The NASA Lewis Research Center Internal Fluid Mechanics Facility*, volume 105187. Lewis Research Center, 1991.

[141] GP Blair and WM Cahoon. Special investigation: design of an intake bellmouth. *Race Engine Technology*, 17(2006):34–41, 2006.

[142] Nicola Chiereghin, David G MacManus, Mark Savill, and Romain Dupuis. Dynamic distortion simulations for curved aeronautical intakes. 2014.

[143] Courtney Rider, Asad Asghar, William DE Allan, Grant Ingram, Robert Stowe, and Rogerio Pimentel. Investigation of a passive flow control device in an s-duct inlet at high subsonic flow. In *Turbo Expo: Power for Land, Sea, and Air*, volume 84898, page V001T01A018. American Society of Mechanical Engineers, 2021.

[144] AD Vakili, JM Wu, MK Bhat, and P Liver. Compressible flow in a diffusing s-duct with flow separation. *Heat transfer and fluid flow in rotating machinery*, pages 201–211, 1987.

[145] Steven R Wellborn, Theodore H Okiishi, and Bruce A Reichert. A study of the compressible flow through a diffusing s-duct. Technical report, 1993.

[146] Steven R Wellborn, Bruce A Reichert, and Theodore H Okiishi. Study of the compressible flow in a diffusing s-duct. *Journal of Propulsion and Power*, 10(5):668–675, 1994.

[147] JW Hamstra, DN Miller, PP Truax, BA Anderson, and BJ Wendt. Active inlet flow control technology demonstration. *The Aeronautical Journal*, 104(1040):473–479, 2000.

[148] Amer Anabtawi, Ron Blackwelder, Peter Lissaman, and Robert Liebeck. An experimental investigation of boundary layer ingestion in a diffusing s-duct with and without passive flow control. In *37th Aerospace Sciences Meeting and Exhibit*, page 739, 1999.

[149] Fan Jiang, Konstantinos Kontis, and Craig White. Experimental analysis of flow characteristics in s-shaped ducts at low speeds. *Physics of Fluids*, 2024.

[150] James E Giuliani and Jen-Ping Chen. Fan response to boundary-layer ingesting inlet distortions. *AIAA Journal*, 54(10):3232–3243, 2016.

[151] Robert H Liebeck. Design of the blended wing body subsonic transport. *Journal of aircraft*, 41(1):10–25, 2004.

[152] Russell M Cummings, Carsten M Liersch, Andreas Schütte, and Kerstin C Huber. Aerodynamics and conceptual design studies on an unmanned combat aerial vehicle configuration. *Journal of Aircraft*, 55(2):454–474, 2018.

[153] Razvan V Florea, Claude Matalanis, Larry W Hardin, Mark Stucky, and Aamir Shabbir. Parametric analysis and design for embedded engine inlets. *Journal of Propulsion and Power*, 31(3):843–850, 2015.

[154] Stuart S Ochs, Gregory Tillman, Jongwook Joo, and Dmytro M Voytovych. Computational fluid dynamics-based analysis of boundary layer ingesting propulsion. *Journal of Propulsion and Power*, 33(2):522–530, 2017.

[155] Daniel Gil-Prieto, David G MacManus, Pavlos K Zachos, Geoffrey Tanguy, François Wilson, and Nicola Chiereghin. Delayed detached-eddy simulation and particle image velocimetry investigation of s-duct flow distortion. *AIAA Journal*, 55(6):1893–1908, 2017.

[156] S-16 Turbine Engine Inlet Flow Distortion Committee. *Inlet total-pressure-distortion considerations for gas-turbine engines*. SAE International, 2017.

[157] Geoffrey Tanguy, David G MacManus, Eric Garnier, and Peter G Martin. Characteristics of unsteady total pressure distortion for a complex aero-engine intake duct. *Aerospace Science and Technology*, 78:297–311, 2018.

[158] EM Greitzer. Axial compressor stall phenomena. 1980.

[159] AH Stenning. Rotating stall and surge. 1980.

[160] JL Jacocks and KR Kneile. Statistical prediction of maximum time-variant inlet distortion levels. *Arnold Engineering Development Center Technical Report AD/A-004. US Department of Commerce, National Technical Information Service, Washington, DC*, 1975.

[161] Bin Wang and Qiang Wang. Aerodynamic optimization of double s-duct caret intake by self-adapting non-dominated sorting genetic algorithm. *Physics of Fluids*, 36(9), 2024.

[162] Jingtao Ma, Lincheng Xu, Jérôme Jacob, Eric Serre, and Pierre Sagaut. An averaged mass correction scheme for the simulation of high subsonic turbulent internal flows using a lattice boltzmann method. *Physics of Fluids*, 36(3), 2024.

[163] GARY HARLOFF, BRUCE REICHERT, and STEVEN WELLBORN. Navier-stokes analysis and experimental data comparison of compressible flow in a diffusing s-duct. In *10th Applied Aerodynamics Conference*, page 2699, 1992.

[164] CF Smith, JE Bruns, GJ Harloff, and JR DeBonis. Three-dimensional compressible turbulent computations for a diffusing s-duct. Technical report, NASA, 1992.

[165] Michael J Brear, Zachary Warfield, John F Mangus, Steve Braddom, James D Paduano, and Jeffry S Philhower. Flow separation within the engine inlet of an uninhabited combat air vehicle (ucav). *J. Fluids Eng.*, 126(2):266–272, 2004.

[166] Gal Berkooz, Philip Holmes, and John L Lumley. The proper orthogonal decomposition in the analysis of turbulent flows. *Annual review of fluid mechanics*, 25(1):539–575, 1993.

[167] Peter J Schmid. Dynamic mode decomposition of numerical and experimental data. *Journal of fluid mechanics*, 656:5–28, 2010.

[168] Jurgen Seidel, Stefan Siegel, Kelly Cohen, and Thomas McLaughlin. Pod based separation control on the naca0015 airfoil. In *43rd AIAA Aerospace Sciences Meeting and Exhibit*, page 297, 2005.

[169] Wang Yangang, Li Yue, and Chen Junxu. Analysis of the unsteady flow in compressor cascade with pod method. In *Turbo Expo: Power for Land, Sea, and Air*, volume 49729, page V02DT44A033. American Society of Mechanical Engineers, 2016.

[170] Jiaqing Kou, Weiwei Zhang, Yilang Liu, and Xintao Li. The lowest reynolds number of vortex-induced vibrations. *Physics of Fluids*, 29(4), 2017.

[171] Sathesh Mariappan, Anthony Donald Gardner, Kai Richter, and Markus Raffel. Analysis of dynamic stall using dynamic mode decomposition technique. *AIAA journal*, 52(11): 2427–2439, 2014.

[172] DC Wilcox. Turbulence modeling for cfd. *DCW industries, La Canada*, 1998.

[173] Henk Kaarle Versteeg. *An introduction to computational fluid dynamics the finite volume method, 2/E*. Pearson Education India, 2007.

[174] Florian R Menter. Two-equation eddy-viscosity turbulence models for engineering applications. *AIAA journal*, 32(8):1598–1605, 1994.

[175] Mihailo R Jovanović, Peter J Schmid, and Joseph W Nichols. Sparsity-promoting dynamic mode decomposition. *Physics of Fluids*, 26(2), 2014.

[176] Zhe Bai, Eurika Kaiser, Joshua L Proctor, J Nathan Kutz, and Steven L Brunton. Dynamic mode decomposition for compressive system identification. *AIAA Journal*, 58(2):561–574, 2020.

[177] Bingni W Brunton, Lise A Johnson, Jeffrey G Ojemann, and J Nathan Kutz. Extracting spatial–temporal coherent patterns in large-scale neural recordings using dynamic mode decomposition. *Journal of neuroscience methods*, 258:1–15, 2016.

[178] Bernd R Noack, Konstantin Afanasiev, MAREK MORZYŃSKI, Gilead Tadmor, and Frank Thiele. A hierarchy of low-dimensional models for the transient and post-transient cylinder wake. *Journal of Fluid Mechanics*, 497:335–363, 2003.

[179] John Townsend. *The theory of ionization of gases by collision*. Constable, Limited, 1910.

[180] Alekseĭ Ivanovich Morozov. *Introduction to plasma dynamics*. CRC Press, 2012.

[181] Yutaka Kaneko, Hiroyuki Nishida, and Yoshiyuki Tagawa. Visualization of the electrohydrodynamic and thermal effects of ac-dbd plasma actuators of plate-and wire-exposed electrodes. In *Actuators*, volume 11, page 38. MDPI, 2022.

[182] Sohrab Gholamhosein Pouryoussefi and Masoud Mirzaei. Experimental study of the unsteady actuation effect on induced flow characteristics in dbd plasma actuators. *Plasma Science and Technology*, 17(5):415, 2015.

Appendix

A.1 Schematic Diagrams of Experimental Setup

(a) (b)

Figure 1: The CTA experiment components: (a) CTA processing unit, (b) CTA calibrator.

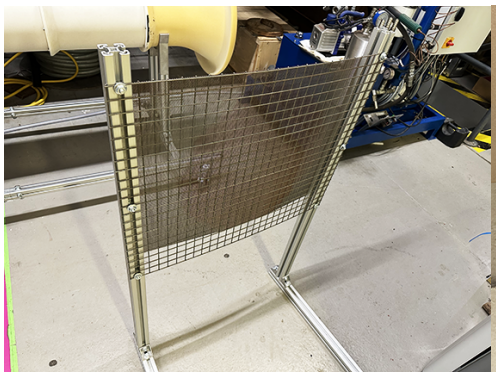

(a) Grid mesh

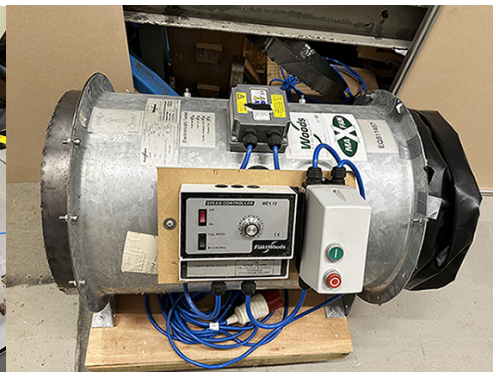

(b) Fan

(c) Traverse system

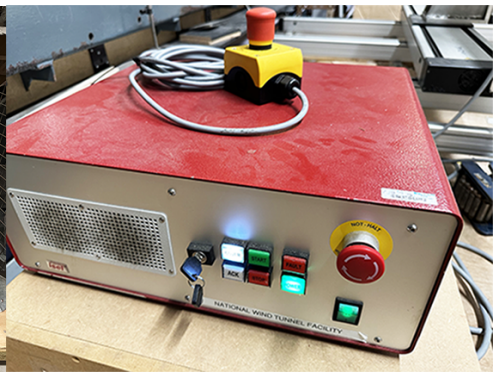

(d) Control unit

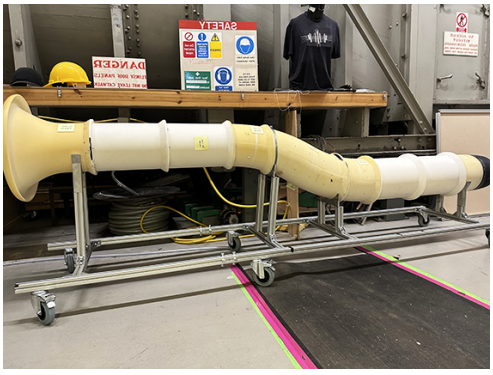

(e) S-duct

Figure 2: The experiment components: (a) grid mesh, (b) fan, (c) traverse system, (d) traverse system control unit, (e) the S-shaped duct with all extensions.

A.2 The Calibration File for 7-hole Probe

```
function [Xpos, Ypos, u,v,w, alpha_fit, beta_fit, pL, poL,q, Co,CaT, ...
    CbT]= process_7hole_testdata_3rdyrlab_v2(fname)

%process 7 hole probe test data
%Usage [Xpos, Ypos, u,v,w, alpha_fit, beta_fit, pL, poL,q, Co,CaT, CbT]=
%process_7hole_testdata_3rdyrlab_v2(fname);
%fname is the absolute file name of the data including its path, this ...
    is a
%matlab -mat file.
%Returned data include: velocity components (u,v,w), pressure pL, ...
    stagnation
%pressure poL, dynamic pressure q, traverse position Xpos and Ypos, ...
    flow angles alpha and beta. Note
%that the senses of the traverse coordinate systems and probe velocities
%are indicated in the laboratory notes.

%calibration data....
%stagnation pressure....

K_Co = [-0.0310
  -0.0271
   0.0694
  -0.0986
  -0.1184
   0.0059
   0.0023
  -0.0068
  -0.0083
   0.0002];

%dynamic pressure....

K_Cq =[ 0.6172
  -0.0106
   0.0275
  -0.0104
  -0.0116
  -0.0001
   0.0004
  -0.0011
  -0.0014
   0.0000];

```

```
40 %probe angle alpha
41
42 K_alpha = [1.4747
43   -0.3123
44   12.5495
45   -0.1037
46    0.6268
47   -0.0709
48   -0.0055
49   -0.0344
50   -0.0944
51   -0.0182];
52
53 %probe angle beta
54
55 K_beta = [-0.6498
56   11.9919
57    0.6286
58   -0.1477
59   -0.1252
60    0.8895
61   -0.1019
62   -0.0192
63   -0.1050
64   -0.0187];
65
66 %load in experimental data
67
68 load(fname,'-mat');
69
70 %extract 7 hole probe data...
71
72 chan7=(probe_module(1)-1)*8+7;
73 chan1=(probe_module(1)-1)*8+1;
74 chan6=(probe_module(1)-1)*8+6;
75
76 p7data(:,1)=data_avg(:,chan7);
77 p16data(:,1:6)=data_avg(:,chan1:chan6);
78
79 pbar=mean(p16data,2);
80
81 %calculate probe orifice pressure coefficients....
82 C_alpha_a=(p16data(:,1)-p16data(:,4))./(p7data-pbar);
83 C_alpha_b=(p16data(:,2)-p16data(:,5))./(p7data-pbar);
84 C_alpha_c=(p16data(:,3)-p16data(:,6))./(p7data-pbar);
85 CaT=(2*C_alpha_a+C_alpha_b-C_alpha_c)/3;
```

```
86 CbT=(C_alpha_b+C_alpha_c)/sqrt(3);
87
88 %calculate stagnation pressure, dynamic pressure, probe angles from probe
89 %pressure coefficients and calibration data....
90
91 Co=K_Co(1)+K_Co(2)*CaT+K_Co(3)*CbT+K_Co(4)*CaT.^2+K_Co(5)*CbT.^2+ ...
       K_Co(6)*CaT.*CbT+K_Co(7)*CaT.^3+K_Co(8)*CbT.^3+ ...
       K_Co(9)*(CaT.^2).*CbT+K_Co(10)*CaT.*(CbT.^2);
92 Cq=K_Cq(1)+K_Cq(2)*CaT+K_Cq(3)*CbT+K_Cq(4)*CaT.^2+K_Cq(5)*CbT.^2+ ...
       K_Cq(6)*CaT.*CbT+K_Cq(7)*CaT.^3+K_Cq(8)*CbT.^3+ ...
       K_Cq(9)*(CaT.^2).*CbT+K_Cq(10)*CaT.*(CbT.^2);
93 alpha_fit=K_alpha(1)+K_alpha(2)*CaT+K_alpha(3)*CbT+K_alpha(4)*CaT.^2+ ...
       K_alpha(5)*CbT.^2+K_alpha(6)*CaT.*CbT+K_alpha(7)*CaT.^3+ ...
       K_alpha(8)*CbT.^3+K_alpha(9)*(CaT.^2).*CbT+K_alpha(10)*CaT.*(CbT.^2);
94 beta_fit=K_beta(1)+K_beta(2)*CaT+K_beta(3)*CbT+K_beta(4)*CaT.^2+ ...
       K_beta(5)*CbT.^2+K_beta(6)*CaT.*CbT+K_beta(7)*CaT.^3+ ...
       K_beta(8)*CbT.^3+K_beta(9)*(CaT.^2).*CbT+K_beta(10)*CaT.*(CbT.^2);
95
96 poL=p7data-Co.*(p7data-pbar);
97 pL=poL-(p7data-pbar)./Cq;
98 q=(p7data-pbar)./Cq;
99
100 U=sqrt(2*q./rho); %this is the velocity magnitude....
101
102 %resolve velocity into (u,v,w) components from compputed probe alpha, ...
       beta angles....
103
104 alphar=pi*alpha_fit/180; betar=pi*beta_fit/180;
105
106 v=U.*sin(betar);
107 u=U.*cos(betar).*cos(alphar);
108 w=U.*cos(betar).*sin(alphar);
```

A.3 Mesh File

```
1 /*---------------------------------*- C++ ...
      -*----------------------------------*\
2 | =========                 | ...
                                                  |
3 | \\      /  F ield         | OpenFOAM: The Open Source CFD Toolbox ...
                |
4 |  \\    /   O peration     | Version:  3.0.1 ...
                                      |
```

```
5  |   \\  /    A nd           | Web:      www.OpenFOAM.org ...
                          |
6  |    \\/     M anipulation  | ...
                                                    |
7  \*---------------------------------------------- ...
     ----------------------------*/
8  FoamFile
9  {
10     version     2.0;
11     format      ascii;
12     class       dictionary;
13     object      blockMeshDict;
14 }
15 // * * * * * * * * * * * * * * * * * * * * * * * * * * * * * * * * * * * * ...
     * * * * //
16
17 convertToMeters 1;
18
19 vertices
20 (
21     //S-duct inlet centre
22     (0 0 0)//0                                  #0
23     //S-dcut inlet outerside
24     (0 0.1021 0)//top            #1
25     (0 0.072195602 0.072195602)//45      #2
26     (0 0 0.1021)//90             #3
27     (0 -0.072195602 0.072195602)//135    #4
28     (0 -0.1021 0)//180           #5
29     (0 -0.072195602 -0.072195602)//225   #6
30     (0 0 -0.1021)//270           #7
31     (0 0.072195602 -0.072195602)//315    #8
32     //S-duct inlet inner
33     (0 0.0821 0)//0              #9
34     (0 0.058053467 0.058053467)//45      #10
35     (0 0 0.0821)//90             #11
36     (0 -0.058053467 0.058053467)//135    #12
37     (0 -0.0821 0)//180           #13
38     (0 -0.058053467 -0.058053467)//225   #14
39     (0 0 -0.0821)//270           #15
40     (0 0.058053467 -0.058053467)//315    #16
41     //S-duct outlet outside
42     (1.021 -0.1478761 0)//0          #17
43     (1.021 -0.184692778 0.088883322)//45     #18
44     (1.021 -0.2735761 0.1257)//90        #19
45     (1.021 -0.362459422 0.088883322)//135    #20
46     (1.021 -0.3992761 0)//180        #21
```

```
47      (1.021 -0.362459422 -0.088883322)//225  #22
48      (1.021 -0.2735761 -0.1257)//270     #23
49      (1.021 -0.184692778 -0.088883322)//315  #24
50      //S-duct outlet inner
51      (1.021 -0.1678761 0)//0         #25
52      (1.021 -0.198834913 0.074741187)//45    #26
53      (1.021 -0.2735761 0.1057)//90       #27
54      (1.021 -0.348317287 0.074741187)//135   #28
55      (1.021 -0.3792761 0)//180       #29
56      (1.021 -0.348317287 -0.074741187)//225  #30
57      (1.021 -0.2735761 -0.1057)//270     #31
58      (1.021 -0.198834913 -0.074741187)//315  #32
59      //bellmouth outside
60      (-1.112 0.2175 0)//0            #33
61      (-1.112 0.153795725 0.153795725)//45    #34
62      (-1.112 0 0.2175)//90           #35
63      (-1.112 -0.153795725 0.153795725)//135  #36
64      (-1.112 -0.2175 0)//180         #37
65      (-1.112 -0.153795725 -0.153795725)//225 #38
66      (-1.112 0 -0.2175)//270         #39
67      (-1.112 0.153795725 -0.153795725)//315  #40
68      //bellmouth inner
69      (-1.112 0.1975  0)//0           #41
70      (-1.112 0.139653589 0.139653589)//45    #42
71      (-1.112 0 0.1975)//90           #43
72      (-1.112 -0.139653589 0.139653589)//135  #44
73      (-1.112 -0.1975 0)//180         #45
74      (-1.112 -0.139653589 -0.139653589)//225 #46
75      (-1.112 0 -0.1975)//270         #47
76      (-1.112 0.139653589 -0.139653589)//315  #48
77      //front extension outside
78      (-0.862 0.1021 0)//top          #49
79      (-0.862 0.072195602 0.072195602)//45    #50
80      (-0.862 0 0.1021)//90           #51
81      (-0.862 -0.072195602 0.072195602)//135  #52
82      (-0.862 -0.1021 0)//180         #53
83      (-0.862 -0.072195602 -0.072195602)//225 #54
84      (-0.862 0 -0.1021)//270         #55
85      (-0.862 0.072195602 -0.072195602)//315  #56
86      //front extension inner
87      (-0.862 0.0821 0)//0            #57
88      (-0.862 0.058053467 0.058053467)//45    #58
89      (-0.862 0 0.0821)//90           #59
90      (-0.862 -0.058053467 0.058053467)//135  #60
91      (-0.862 -0.0821 0)//180         #61
92      (-0.862 -0.058053467 -0.058053467)//225 #62
```

```
93      (-0.862 0 -0.0821)//270          #63
94      (-0.862 0.058053467 -0.058053467)//315  #64
95      //aft extension outside
96      (2.133 -0.1478761 0)//0          #65
97      (2.133 -0.184692778 0.088883322)//45    #66
98      (2.133 -0.2735761 0.1257)//90        #67
99      (2.133 -0.362459422 0.088883322)//135   #68
100     (2.133 -0.3992761 0)//180        #69
101     (2.133 -0.362459422 -0.088883322)//225  #70
102     (2.133 -0.2735761 -0.1257)//270      #71
103     (2.133 -0.184692778 -0.088883322)//315  #72
104     //aft extension inner
105     (2.133 -0.1678761 0)//0          #73
106     (2.133 -0.198834913 0.074741187)//45    #74
107     (2.133 -0.2735761 0.1057)//90        #75
108     (2.133 -0.348317287 0.074741187)//135   #76
109     (2.133 -0.3792761 0)//180        #77
110     (2.133 -0.348317287 -0.074741187)//225  #78
111     (2.133 -0.2735761 -0.1057)//270      #79
112     (2.133 -0.198834913 -0.074741187)//315  #80
113     //bellmouth centre
114     (-1.112 0 0)//               #81
115     //front extension centre
116     (-0.862 0 0)//               #82
117     //s-duct outlet centre
118     (1.021 -0.2735761 0)//           #83
119     //aft extension centre
120     (2.133 -0.2735761 0)//           #84
121 );
122
123 blocks
124 (
125     //s-duct
126     hex (83 27 26 25 0 11 10 9) (15 15 200) simpleGrading (1 1 1)//inner1
127     hex (83 29 28 27 0 13 12 11) (15 15 200) simpleGrading (1 1 ...
            1)//inner2
128     hex (83 31 30 29 0 15 14 13) (15 15 200) simpleGrading (1 1 ...
            1)//inner3
129     hex (83 25 32 31 0 9 16 15) (15 15 200) simpleGrading (1 1 1)//inner4
130     hex (25 26 18 17 9 10 2 1) (15 26 200) simpleGrading (1 0.001417 ...
            1)//outer1
131     hex (26 27 19 18 10 11 3 2) (15 26 200) simpleGrading (1 0.001417 ...
            1)//outer2
132     hex (27 28 20 19 11 12 4 3) (15 26 200) simpleGrading (1 0.001417 ...
            1)//outer3
133     hex (28 29 21 20 12 13 5 4) (15 26 200) simpleGrading (1 0.001417 ...
```

```
        1) //outer4
134     hex (29 30 22 21 13 14 6 5) (15 26 200) simpleGrading (1 0.001417 ...
        1) //outer5
135     hex (30 31 23 22 14 15 7 6) (15 26 200) simpleGrading (1 0.001417 ...
        1) //outer6
136     hex (31 32 24 23 15 16 8 7) (15 26 200) simpleGrading (1 0.001417 ...
        1) //outer7
137     hex (32 25 17 24 16 9 1 8) (15 26 200) simpleGrading (1 0.001417 ...
        1) //outer8
138     //front extension
139     hex (0 11 10 9 82 59 58 57) (15 15 169) simpleGrading (1 1 1) //inner1
140     hex (0 13 12 11 82 61 60 59) (15 15 169) simpleGrading (1 1 ...
        1) //inner2
141     hex (0 15 14 13 82 63 62 61) (15 15 169) simpleGrading (1 1 ...
        1) //inner3
142     hex (0 9 16 15 82 57 64 63) (15 15 169) simpleGrading (1 1 1) //inner4
143     hex (9 10 2 1 57 58 50 49) (15 26 169) simpleGrading (1 0.001417 ...
        1) //outer1
144     hex (10 11 3 2 58 59 51 50) (15 26 169) simpleGrading (1 0.001417 ...
        1) //outer2
145     hex (11 12 4 3 59 60 52 51) (15 26 169) simpleGrading (1 0.001417 ...
        1) //outer3
146     hex (12 13 5 4 60 61 53 52) (15 26 169) simpleGrading (1 0.001417 ...
        1) //outer4
147     hex (13 14 6 5 61 62 54 53) (15 26 169) simpleGrading (1 0.001417 ...
        1) //outer5
148     hex (14 15 7 6 62 63 55 54) (15 26 169) simpleGrading (1 0.001417 ...
        1) //outer6
149     hex (15 16 8 7 63 64 56 55) (15 26 169) simpleGrading (1 0.001417 ...
        1) //outer7
150     hex (16 9 1 8 64 57 49 56) (15 26 169) simpleGrading (1 0.001417 ...
        1) //outer8
151     //aft extension
152     hex (84 75 74 73 83 27 26 25) (15 15  218) simpleGrading (1 1 ...
        1) //inner1
153     hex (84 77 76 75 83 29 28 27) (15 15  218) simpleGrading (1 1 ...
        1) //inner2
154     hex (84 79 78 77 83 31 30 29) (15 15  218) simpleGrading (1 1 ...
        1) //inner3
155     hex (84 73 80 79 83 25 32 31) (15 15  218) simpleGrading (1 1 ...
        1) //inner4
156     hex (73 74 66 65 25 26 18 17) (15 26 218) simpleGrading (1 ...
        0.001417 1) //outer1
157     hex (74 75 67 66 26 27 19 18) (15 26 218) simpleGrading (1 ...
        0.001417 1) //outer2
158     hex (75 76 68 67 27 28 20 19) (15 26 218) simpleGrading (1 ...
```

```
        0.001417 1)//outer3
159     hex (76 77 69 68 28 29 21 20) (15 26 218) simpleGrading (1 ...
        0.001417 1)//outer4
160     hex (77 78 70 69 29 30 22 21) (15 26 218) simpleGrading (1 ...
        0.001417 1)//outer5
161     hex (78 79 71 70 30 31 23 22) (15 26 218) simpleGrading (1 ...
        0.001417 1)//outer6
162     hex (79 80 72 71 31 32 24 23) (15 26 218) simpleGrading (1 ...
        0.001417 1)//outer7
163     hex (80 73 65 72 32 25 17 24) (15 26 218) simpleGrading (1 ...
        0.001417 1)//outer8
164     //bellmouth
165     hex (82 59 58 57 81 43 42 41) (15 15 49) simpleGrading (1 1 ...
        1)//inner1
166     hex (82 61 60 59 81 45 44 43) (15 15 49) simpleGrading (1 1 ...
        1)//inner2
167     hex (82 63 62 61 81 47 46 45) (15 15 49) simpleGrading (1 1 ...
        1)//inner3
168     hex (82 57 64 63 81 41 48 47) (15 15 49) simpleGrading (1 1 ...
        1)//inner4
169     hex (57 58 50 49 41 42 34 33) (15 26 49) simpleGrading (1 ...
        0.001417 1)//outer1
170     hex (58 59 51 50 42 43 35 34) (15 26 49) simpleGrading (1 ...
        0.001417 1)//outer2
171     hex (59 60 52 51 43 44 36 35) (15 26 49) simpleGrading (1 ...
        0.001417 1)//outer3
172     hex (60 61 53 52 44 45 37 36) (15 26 49) simpleGrading (1 ...
        0.001417 1)//outer4
173     hex (61 62 54 53 45 46 38 37) (15 26 49) simpleGrading (1 ...
        0.001417 1)//outer5
174     hex (62 63 55 54 46 47 39 38) (15 26 49) simpleGrading (1 ...
        0.001417 1)//outer6
175     hex (63 64 56 55 47 48 40 39) (15 26 49) simpleGrading (1 ...
        0.001417 1)//outer7
176     hex (64 57 49 56 48 41 33 40) (15 26 49) simpleGrading (1 ...
        0.001417 1)//outer8
177
178 );
179
180 edges
181 (
182     //s-duct inlet inner
183     arc 1 2 (0 0.0943281 0.039071978)//22.5
184     arc 2 3 (0 0.039071978 0.0943281)//67.5
185     arc 3 4 (0 -0.039071978 0.0943281)//112.5
186     arc 4 5 (0 -0.0943281 0.039071978)//157.5
```

```
187     arc 5 6 (0 -0.0943281 -0.039071978)//202.5
188     arc 6 7 (0 -0.039071978 -0.0943281)//247.5
189     arc 7 8 (0 0.039071978 -0.0943281)//292.5
190     arc 8 1 (0 0.0943281 -0.039071978)//337.5
191     //s-duct outlet
192     arc 17 18 (1.021 -0.157444442763331 0.048103307)
193     arc 18 19 (1.021 -0.225472792551708 0.116131657)
194     arc 19 20 (1.021 -0.321679407448292 0.116131657)
195     arc 20 21 (1.021 -0.389707757236669 0.048103307)
196     arc 21 22 (1.021 -0.389707757236669 -0.048103307)
197     arc 22 23 (1.021 -0.321679407448292 -0.116131657)
198     arc 23 24 (1.021 -0.225472792551708 -0.116131657)
199     arc 24 17 (1.021 -0.157444442763331 -0.0481033070)
200     //bell mouth
201     arc 33 34 (-1.112 0.200943798 0.083233647)
202     arc 34 35 (-1.112 0.083233647 0.200943798)
203     arc 35 36 (-1.112 -0.083233647 0.200943798)
204     arc 36 37 (-1.112 -0.200943798 0.083233647)
205     arc 37 38 (-1.112 -0.200943798 -0.083233647)
206     arc 38 39 (-1.112 -0.083233647 -0.200943798)
207     arc 39 40 (-1.112 0.083233647 -0.200943798)
208     arc 40 33 (-1.112 0.200943798 -0.083233647)
209     //front extension
210     arc 49 50 (-0.862 0.0943281 0.039071978)
211     arc 50 51 (-0.862 0.039071978 0.0943281)
212     arc 51 52 (-0.862 -0.039071978 0.0943281)
213     arc 52 53 (-0.862 -0.0943281 0.039071978)
214     arc 53 54 (-0.862 -0.0943281 -0.039071978)
215     arc 54 55 (-0.862 -0.039071978 -0.0943281)
216     arc 55 56 (-0.862 0.039071978 -0.0943281)
217     arc 56 49 (-0.862 0.0943281 -0.039071978)
218     //aft extension
219     arc 65 66 (2.133 -0.157444442763331 0.048103307)
220     arc 66 67 (2.133 -0.225472792551708 0.116131657)
221     arc 67 68 (2.133 -0.321679407448292 0.116131657)
222     arc 68 69 (2.133 -0.389707757236669 0.048103307)
223     arc 69 70 (2.133 -0.389707757236669 -0.048103307)
224     arc 70 71 (2.133 -0.321679407448292 -0.116131657)
225     arc 71 72 (2.133 -0.225472792551708 -0.116131657)
226     arc 72 65 (2.133 -0.157444442763331 -0.0481033070)
227     //bellmouth outer
228     arc 49 33 (-0.994524 0.1300178 0)
229     arc 50 34 (-0.994524 0.091936468 0.091936468)
230     arc 51 35 (-0.994524 0 0.1300178)
231     arc 52 36 (-0.994524 -0.091936468 0.091936468)
232     arc 53 37 (-0.994524 -0.1300178 0)
```

```
    arc 54 38 (-0.994524 -0.091936468 -0.091936468)
    arc 55 39 (-0.994524 0 -0.1300178)
    arc 56 40 (-0.994524 0.091936468 -0.091936468)
    //bellmouth inner
    arc 57 41 (-0.994524 0.1100178 0)
    arc 58 42 (-0.994524 0.077794332 0.077794332)
    arc 59 43 (-0.994524 0 0.1100178)
    arc 60 44 (-0.994524 -0.077794332 0.077794332)
    arc 61 45 (-0.994524 -0.1100178 0)
    arc 62 46 (-0.994524 -0.077794332 -0.077794332)
    arc 63 47 (-0.994524 0 -0.1100178)
    arc 64 48 (-0.994524 0.077794332 -0.077794332)
    //s-duct inner 0
    spline 9 25
    (
        (0.0192520889579534 0.0819514377131162 0)
        (0.0385003192301122 0.0815048929465998 0)
        (0.0577407480137045 0.0807591053011669 0)
        (0.0769693406670129 0.0797128528781169 0)
        (0.0961819707554861 0.0783649563178684 0)
        (0.115374420239076 0.0767142828492016 0)
        (0.134542379801174 0.0747597503448933 0)
        (0.153681449319405 0.0725003313794211 0)
        (0.172787138478407 0.0699350572844077 0)
        (0.191854867524609 0.0670630221974769 0)
        (0.210879968162909 0.0638833871001848 0)
        (0.229857684595013 0.0603953838407022 0)
        (0.248783174699089 0.0565983191369262 0)
        (0.267651511350269 0.0524915785557103 0)
        (0.286457683881406 0.0480746304639122 0)
        (0.305196599683388 0.0433470299469798 0)
        (0.323863085944161 0.0383084226908119 0)
        (0.34245189152553 0.03295854882265 0)
        (0.360957688976677 0.0272972467067915 0)
        (0.37937507668319 0.0213244566909293 0)
        (0.397698581150332 0.0150402247989711 0)
        (0.415922659419121 0.00844470636621062 0)
        (0.434041701613687 0.00153816961277204 0)
        (0.452050033618274 -0.00567900084871842 0)
        (0.469941919882128 -0.013206300575229 0)
        (0.487711566350388 -0.0210431019291439 0)
        (0.50535312351903 -0.0291886507917093 0)
        (0.522860689611745 -0.0376420633579564 0)
        (0.540228313876576 -0.0464023230168972 0)
        (0.55745 -0.0554682773207293 0)
        (0.571818932805686 -0.0629202214545006 0)
```

```
279         (0.586306069879445 -0.0701165041753133 0)
280         (0.600906292332057 -0.0770564494378915 0)
281         (0.615614535016601 -0.0837395016480488 0)
282         (0.630425789672776 -0.0901652224914644 0)
283         (0.645335107951361 -0.0963332876781775 0)
284         (0.660337604316598 -0.10224348360658 0)
285         (0.675428458824387 -0.107895703950744 0)
286         (0.690602919774275 -0.113289946174973 0)
287         (0.705856306233371 -0.118426307979512 0)
288         (0.721184010430377 -0.123304983681416 0)
289         (0.736581500018085 -0.127926260534597 0)
290         (0.752044320202769 -0.13229051499313 0)
291         (0.767568095739044 -0.13639820892194 0)
292         (0.783148532788847 -0.140249885759001 0)
293         (0.798781420643349 -0.143846166633254 0)
294         (0.814462633306688 -0.147187746442435 0)
295         (0.830188130940562 -0.15027538989507 0)
296         (0.845953961168806 -0.15310992752089 0)
297         (0.861756260241241 -0.155692251653961 0)
298         (0.877591254056149 -0.158023312392817 0)
299         (0.893455259040895 -0.16010411354193 0)
300         (0.909344682890312 -0.161935708538829 0)
301         (0.925256025162589 -0.163519196371216 0)
302         (0.941185877732524 -0.164855717488415 0)
303         (0.957130925102134 -0.165946449711498 0)
304         (0.97308794456872 -0.166792604146434 0)
305         (0.989053806250617 -0.16739542110459 0)
306         (1.00502547297097 -0.167756166034922 0)
307     )
308     //s-duct inner 45
309     spline ... # determined by the S-duct geometry
310
311 );
312
313 boundary
314 (
315     INLET
316     {
317         type patch;
318         faces
319         (
320             (81 43 42 41)
321             (81 45 44 43)
322             (81 47 46 45)
323             (81 41 48 47)
324             (41 42 34 33)
```

```
325             (42 43 35 34)
326             (43 44 36 35)
327             (44 45 37 36)
328             (45 46 38 37)
329             (46 47 39 38)
330             (47 48 40 39)
331             (48 41 33 40)
332         );
333     }
334
335     OUTLET
336     {
337         type patch;
338         faces
339         (
340             (84 73 74 75)
341             (84 75 76 77)
342             (84 77 78 79)
343             (84 79 80 73)
344             (73 65 66 74)
345             (74 66 67 75)
346             (75 67 68 76)
347             (76 68 69 77)
348             (77 69 70 78)
349             (78 70 71 79)
350             (79 71 72 80)
351             (80 72 65 73)
352         );
353     }
354
355     WALL
356     {
357         type wall;
358         faces
359         (
360             (1 2 18 17)//s-duct
361             (2 3 19 18)
362             (3 4 20 19)
363             (4 5 21 20)
364             (6 5 21 22)
365             (7 6 22 23)
366             (8 7 23 24)
367             (1 8 24 17)
368             (49 50 2 1)//front extension
369             (50 51 3 2)
370             (51 52 4 3)
```

```
            (52 53 5 4)
            (54 53 5 6)
            (55 54 6 7)
            (56 55 7 8)
            (49 56 8 1)
            (17 18 66 65)//aft extesnion
            (18 19 67 66)
            (19 20 68 67)
            (20 21 69 68)
            (22 21 69 70)
            (23 22 70 71)
            (24 23 71 72)
            (17 24 72 65)
            (33 34 50 49)//bellmouth
            (34 35 51 50)
            (35 36 52 51)
            (36 37 53 52)
            (38 37 53 54)
            (39 38 54 55)
            (40 39 55 56)
            (33 40 56 49)
        );
    }
);

mergePatchPairs
(
);

// ************************************************* ...
    ************************ //
```

A.4 fvModel

```
/*--------------------------------*- C++ ...
    -*---------------------------------*\
  =========                 |
  \\      /  F ield         | OpenFOAM: The Open Source CFD Toolbox
   \\    /   O peration     | Website:  https://openfoam.org
    \\  /    A nd           | Version:  10
     \\/     M anipulation  |
\*-------------------------------------------------------------------------*/
FoamFile
```

```
{
    format      ascii;
    class       dictionary;
    location    "constant";
    object      fvModels;
}
// * * * * * * * * * * * * * * * * * * * * * * * * * * * * * * * * * ...
   * * * * //


momentumSource
{
type            coded;
selectionMode   cellZone;
field U;
redirectType    velocitySource;
active          ture;
cellZone        ionicWindRegion;


codeInclude
#{
#include "fvModel.H"
#include "codedBase.H"
#include "cmath"
#include "OFstream.H"
#};

codeAddSup
#{
Pout<< "**codeAddSup**" << endl;

//Getting Cells in a Specific Area
const cellZone& cz = mesh().cellZones()["ionicWindRegion"];


vectorField& Su = eqn.source();




// Apply thrust only to cells in a specific area
forAll(cz, cellI)
{
const label zoneCellI = cz[cellI];

```

```
54 //Inputs
55 scalar fv= 2; ///frequency of voltage (kHz)
56 scalar d = 0.1; //thickness of dielectric  (cm)
57 scalar V0 = 16000; //V0 the applied voltage peak-to-peak (kV)
58 scalar ▵_vc = 600; //the normal falldown of cathode voltage
59 scalar ▵_tq = 1e-4; //is the residence time of negative ions inside ...
       the acceleration volume
60 scalar Fx_0 = 2.6;
61 scalar Fy_0 = 2.0;
62 scalar beta_x = 8e5;
63 scalar beta_y = 1e7;
64 scalar f_mod = 7.5359e-6;
65 scalar alpha = 1;
66 scalar theta = 22;
67
68
69 scalar yref = 0;
70 scalar r = 0.108219;
71
72 scalar Xc = 0.3492025;
73 scalar Yc = -0.0615738;
74
75
76 scalar cX = mesh().cellCentres()[zoneCellI].x();
77 scalar cY = mesh().cellCentres()[zoneCellI].y();
78 scalar cZ = mesh().cellCentres()[zoneCellI].z();
79 scalar d1 = sqrt(sqr(r)-sqr(cZ));
80
81 scalar y0 = Yc-cos(theta*3.1415926/180)*d1;
82 scalar x0 = Xc-sin(theta*3.1415926/180)*d1;
83
84 scalar X1 = x0 + ...
       (cX-x0)*cos(theta*3.1415926/180)-(cY-y0)*sin(theta*3.1415926/180);
85 scalar Y1 = y0 + ...
       (cX-x0)*sin(theta*3.1415926/180)+(cY-y0)*cos(theta*3.1415926/180);
86
87 //Equations
88 scalar ...
       thrust_soloviev=2.4e-10*pow(alpha,4.0)*(fv/d)*pow(((9.0/4.0)*V0/▵_vc),4.0)*pow
       - exp(-1.0/(4.0*fv*▵_tq)));
89 scalar distribution_singh_x = Fx_0*exp(-1.0*sqr((X1 - x0 - (Y1 - y0) ...
       )/(Y1- y0 + 0.001)) - beta_x*sqr(Y1 - y0))*mesh().V()[zoneCellI];
90 scalar distribution_singh_y = Fy_0*exp(-1.0*(sqr(((X1 - x0)/(Y1- y0 + ...
       0.001)))) - beta_y*sqr((Y1 - y0)))*mesh().V()[zoneCellI];
91
92 myFile<<thrust_soloviev << endl;
```

```
myFile<<mesh().V()[zoneCellI] << endl;
scalar test = test + distribution_singh_x;
vector distribution_singh = vector::zero;
distribution_singh.x() = distribution_singh_x/f_mod;
distribution_singh.y() = distribution_singh_y/f_mod;


vector total_thrust = thrust_soloviev*(distribution_singh);

myFile<<test << endl;
Su[zoneCellI] -= total_thrust;
}

#};
}
```

A.5 TopoSet File

```
/*--------------------------------*- C++ ...
    -*----------------------------------*\
  =========                 |
  \\      /  F ield         | OpenFOAM: The Open Source CFD Toolbox
   \\    /   O peration     | Website:  https://openfoam.org
    \\  /    A nd           | Version:  10
     \\/     M anipulation  |
\*---------------------------------------------- ...
    ---------------------------*/
FoamFile
{
    format      ascii;
    class       dictionary;
    object      topoSetDict;
}
// * * * * * * * * * * * * * * * * * * * * * * * * * * * * * * * * * * * * ...
    * * * * //

actions
(


    {
        name    annulusCells;
        type    cellSet;
```

```
23          source  cylinderAnnulusToCell;
24          action  new;    // create a topoSet
25          sourceInfo
26          {
27              p1          (0.339806 -0.05815 0);  // cylinder bottom ...
                    centre coordinate
28              p2          (0.377393 -0.07183 0);  // cylinder top ...
                    centre coordinate
29              innerRadius 0.098219;          // inner cylinder radius
30              outerRadius 0.108219;          // outer cylinder radius
31          }
32      }
33
34      {
35          action  new;
36          type    cellSet;
37          name    sectorCells;
38          source  rotatedBoxToCell;
39          sourceInfo
40          {
41          origin  (0.302793 -0.15985 -0.0541);
42          i   (0.037588 -0.013681 0);
43          j   (0.004959 0.013625 0);
44          k   (0 0 0.1082);
45          }
46      }
47
48      {
49          action  subset;
50          type    cellSet;
51          name    sectorCells;
52          source  cellToCell;
53          set     annulusCells;
54      }
55
56      {
57          action  new;
58          type    cellZoneSet;
59          name    ionicWindRegion;
60          source  setToCellZone;
61          set sectorCells;
62
63      }
64
65
66
```

```
67
68 );
69
70
71
72 // ************************************************ ...
       *************************** //
```

A.6 refineMesh

```
1  /*--------------------------------*- C++ ...
       -*----------------------------------*\
2    =========                 |
3    \\      /  F ield         | OpenFOAM: The Open Source CFD Toolbox
4     \\    /   O peration     | Website:  https://openfoam.org
5      \\  /    A nd           | Version:  10
6       \\/     M anipulation  |
7  \*---------------------------------------------------------------------------*/
8  FoamFile
9  {
10     format      ascii;
11     class       dictionary;
12     object      refineMeshDict;
13 }
14 // * * * * * * * * * * * * * * * * * * * * * * * * * * * * * * * * * * * * ...
       * * * * //
15
16 // Cells to refine; name of cell set
17 set ionicWindRegion;
18
19 // Type of coordinate system:
20 // - global : coordinate system same for every cell. Usually aligned with
21 //   x,y,z axis. Specify in globalCoeffs section below.
22 // - patchLocal : coordinate system different for every cell. Specify in
23 //   patchLocalCoeffs section below.
24 // - fieldBased : uses the list of field names from the directions ...
       list for
25 //   selecting the directions to cut. Meant to be used with ...
       geometricCut, but
26 //   can also be used with useHexTopology.
27 coordinateSystem global;
28 //coordinateSystem patchLocal;
29 //coordinateSystem fieldBased;
```

```
30
31 // .. and its coefficients. x,y in this case. (normal (e3) direction is
32 // calculated as e1^e2)
33 globalCoeffs
34 {
35     e1      (1 0 0);
36     e2      (0 1 0);
37 }
38
39 patchLocalCoeffs
40 {
41     patch   WALL;  // Normal direction is facenormal of zero'th face ...
           of patch
42     e1      (1 0 0);
43 }
44
45 // List of directions to refine, if global or patchLocal
46 directions
47 (
48     e1
49
50 );
51
52 // List of directions to refine, if "fieldBased". Keep in mind that these
53 // fields must be of type "vectorField", not "volVectorField".
54 //directions
55 //(
56 //    radialDirectionFieldName
57 //    angularDirectionFieldName
58 //    heightDirectionFieldName
59 //);
60
61 // Whether to use hex topology. This will
62 // - if patchLocal: all cells on selected patch should be hex
63 // - split all hexes in 2x2x2 through the middle of edges.
64 useHexTopology  true;
65
66 // Cut purely geometric (will cut hexes through vertices) or take ...
       topology
67 // into account. Incompatible with useHexTopology
68 geometricCut    false;
69
70 // Write meshes from intermediate steps
71 writeMesh       false;
72
73 // ...
```

```
        ********************************************************************** ...
        //
```

A.7 The Experiment Data of the S-duct

Table 1: Statistical Parameters for Baseline C_p Experimental Data at 0°

0°

Speed2

Measured Pressure Value

L/D_{inlet}	0.25	0.5	1	1.625	2	2.25	2.5	2.75	3	3.25	3.5	4	4.5	4.75
Average	-250.3649895	-236.3357575	-221.094044	-188.357071	-183.025445	-190.6298365	-182.216172	-196.27314	-228.60743	-237.0891175	-233.471675	-252.714503	-217.575761	-192.6348855
Standard Deviation	1.805635885	1.670453887	1.489994819	1.490359075	1.426474086	1.378087032	1.593259533	1.612788402	1.58052022	1.516758784	1.434859641	1.318057562	1.193307633	1.094352389
Standard Error	0.285496101	0.26412195	0.235588866	0.23564646	0.225545357	0.217894692	0.251916451	0.255004237	0.249902189	0.239820621	0.226871229	0.208403199	0.188678503	0.173032306
95%CI	0.559572358	0.517679023	0.461754178	0.461867062	0.442068899	0.427073596	0.493756245	0.499808304	0.489808291	0.470048417	0.44466761	0.40847027	0.369809867	0.339143319
95%/Average	0.22%	0.22%	0.21%	0.25%	0.24%	0.22%	0.27%	0.25%	0.21%	0.20%	0.19%	0.16%	0.17%	0.18%

C_p

Average	0.204483384	0.249060252	0.297489692	0.401509052	0.418449908	0.394287505	0.421021314	0.376356317	0.273616453	0.246666505	0.258160667	0.197017975	0.308668782	0.387916607
Standard Deviation	0.005737277	0.005307746	0.004734351	0.004735508	0.004532518	0.004378772	0.005062467	0.005124518	0.005021988	0.004819391	0.004559163	0.004188032	0.003791649	0.003477225
Standard Error	0.000907143	0.000839228	0.000748567	0.00074875	0.000716654	0.000692345	0.000800446	0.000810257	0.000794046	0.000762013	0.000720867	0.000662186	0.000599512	0.000549798
95%CI	0.001778001	0.001644888	0.00146719	0.001467549	0.001404642	0.001356995	0.001568875	0.001588105	0.00155633	0.001493545	0.001412899	0.001297885	0.001175044	0.001077603
95%/Average	0.87%	0.66%	0.49%	0.37%	0.34%	0.34%	0.37%	0.42%	0.57%	0.61%	0.55%	0.66%	0.38%	0.28%

Speed4

Measured Pressure Value

L/D_{inlet}	0.25	0.5	1	1.625	2	2.25	2.5	2.75	3	3.25	3.5	4	4.5	4.75
Average	-483.3877205	-452.1352255	-426.1235045	-360.9788245	-358.5388355	-373.754151	-353.58868	-384.372555	-442.6111985	-465.1358205	-460.7034655	-454.2879295	-397.2788005	-358.221756
Standard Deviation	2.902597678	2.65229786	2.996053443	2.104671881	2.34672535	2.912706855	2.426086495	2.438979472	2.667429609	3.177853299	3.505780799	2.17367472	1.96202282	1.856251098
Standard Error	0.45894099	0.419365114	0.473717644	0.332777844	0.371049858	0.460539391	0.383597956	0.385636515	0.421757653	0.502462725	0.554312615	0.34368815	0.310223047	0.293499069
95%CI	0.89952434	0.821955623	0.928486582	0.652244573	0.727257721	0.902657206	0.751851994	0.755847569	0.826645	0.98482694	1.086452726	0.673628775	0.608037172	0.575258175
95%/Average	0.19%	0.18%	0.22%	0.18%	0.20%	0.24%	0.21%	0.20%	0.19%	0.21%	0.24%	0.15%	0.15%	0.16%

C_p

Average	0.143872225	0.199223505	0.245292852	0.360670566	0.364992029	0.338044191	0.373759247	0.31923794	0.216091505	0.176198157	0.184048299	0.195410852	0.296379695	0.365553609
Standard Deviation	0.005140789	0.004697484	0.005306309	0.003727583	0.004156284	0.005158694	0.004296841	0.004319675	0.004724283	0.005628295	0.006209087	0.003849794	0.003474938	0.003287605
Standard Error	0.00081283	0.000742737	0.000839001	0.000589383	0.000657166	0.000815661	0.00067939	0.000683001	0.000746975	0.000889912	0.000981743	0.000608706	0.000549436	0.000519816
95%CI	0.001593147	0.001455765	0.001644442	0.00115519	0.001288046	0.001598696	0.001331605	0.001338681	0.001464071	0.001744227	0.001924216	0.001193064	0.001076894	0.001018839
95%/Average	1.11%	0.73%	0.67%	0.32%	0.35%	0.47%	0.36%	0.42%	0.68%	0.99%	1.05%	0.61%	0.36%	0.28%

Speed6

Measured Pressure Value

L/D_{inlet}	0.25	0.5	1	1.625	2	2.25	2.5	2.75	3	3.25	3.5	4	4.5	4.75
Average	-828.466926	-771.660189	-733.1802	-621.442609	-618.025979	-650.4493435	-602.053209	-657.842964	-757.6597395	-806.380418	-801.7674065	-737.9988305	-649.195137	-589.855886
Standard Deviation	4.6094596	4.667732436	3.200615147	4.508514912	4.015338807	3.046886372	5.223245362	4.874160654	4.056437651	3.914658105	3.911091342	2.635424289	2.354648901	2.151562413
Standard Error	0.728819556	0.7380333	0.506061689	0.712858799	0.63488081	0.481755035	0.825867606	0.770672467	0.641379108	0.618961794	0.618397839	0.416697168	0.372302681	0.340191888
95%CI	1.42848633	1.446545268	0.99188091	1.397203247	1.244366388	0.944239869	1.618700508	1.510518036	1.257103052	1.213165116	1.212059764	0.816726449	0.729713254	0.6667761
95%CI/Average	0.17%	0.19%	0.14%	0.22%	0.20%	0.15%	0.27%	0.23%	0.17%	0.15%	0.15%	0.11%	0.11%	0.11%

C_p

Average	0.141396966	0.200270091	0.240149818	0.355951948	0.359492861	0.325890072	0.376046652	0.318227503	0.214779817	0.164286887	0.169067701	0.235155907	0.327189901	0.388687662
Standard Deviation	0.004777132	0.004837525	0.00331704	0.004672516	0.0041614	0.003157719	0.005413245	0.005051462	0.004203994	0.004057057	0.00405336	0.00273129	0.002440301	0.002229827
Standard Error	0.000755331	0.00076488	0.00052447	0.00073879	0.000657975	0.000499279	0.000855909	0.000798706	0.00066471	0.000641477	0.000640893	0.000431855	0.000385845	0.000352567
95%CI	0.001480449	0.001499164	0.001027961	0.001448028	0.001289631	0.000978587	0.001677582	0.001565464	0.001302831	0.001257295	0.001256149	0.000846435	0.000756257	0.000691031
95%CI/Average	1.05%	0.75%	0.43%	0.41%	0.36%	0.30%	0.45%	0.49%	0.61%	0.77%	0.74%	0.36%	0.23%	0.18%

Speed8

Measured Pressure Value

L/D_{inlet}	0.25	0.5	1	1.625	2	2.25	2.5	2.75	3	3.25	3.5	4	4.5	4.75
Average	-1110.999775	-1032.381433	-985.556534	-834.8276135	-830.6694395	-878.6958245	-804.6919975	-881.1219245	-1016.308689	-1086.512205	-1080.86604	-960.0519935	-845.6877145	-770.3582485
Standard Deviation	3.690783654	3.821237821	2.73068957	3.690017868	3.164462289	2.886695144	4.445375634	4.160905586	3.884138456	4.482800454	4.703895662	3.384476419	3.010712178	2.620447677
Standard Error	0.583564135	0.60419075	0.431759931	0.583443054	0.50034542	0.456426578	0.702875603	0.657896939	0.614136213	0.708792987	0.743751208	0.535132709	0.476035393	0.414329157
95%CI	1.143785704	1.18421387	0.846249465	1.143548385	0.980677023	0.894596093	1.377636182	1.289478001	1.203706978	1.389234254	1.457752368	1.048860109	0.93302937	0.812085149
95%CI/Average	0.10%	0.11%	0.09%	0.14%	0.12%	0.10%	0.17%	0.15%	0.12%	0.13%	0.13%	0.11%	0.11%	0.11%

C_p

Average	0.104118415	0.16751422	0.205272612	0.326816528	0.330169573	0.291442334	0.351117113	0.289485989	0.180474867	0.123864561	0.128417483	0.225838816	0.318059223	0.378802963
Standard Deviation	0.002976153	0.003081348	0.002201958	0.002975535	0.002551741	0.002327757	0.003584636	0.003355247	0.003132069	0.003614815	0.0037931	0.002729155	0.002427761	0.002113061
Standard Error	0.000470571	0.000487204	0.00034816	0.000470473	0.000403466	0.000368051	0.000566781	0.000530511	0.000495224	0.000571552	0.000599742	0.000431517	0.000383863	0.000334104
95%CI	0.000922319	0.00095492	0.000682394	0.000922128	0.000790793	0.000721379	0.00111089	0.001039802	0.000970638	0.001120243	0.001175494	0.000845774	0.000752371	0.000654845
95%CI/Average	0.89%	0.57%	0.33%	0.28%	0.24%	0.25%	0.32%	0.36%	0.54%	0.90%	0.92%	0.37%	0.24%	0.17%

Speed10

Measured Pressure Value

L/D_{inlet}	0.25	0.5	1	1.625	2	2.25	2.5	2.75	3	3.25	3.5	4	4.5	4.75
Average	-1252.736965	-1163.356995	-1113.75212	-939.5417085	-938.054598	-995.299087	-906.400046	-993.624124	-1147.619855	-1228.93398	-1223.20864	-1071.139355	-943.705253	-860.0848605
Standard Deviation	3.114995989	2.832990275	3.264436998	2.288059985	2.395326731	3.038725099	2.364027453	2.687068249	3.085119365	3.744085878	3.791995776	2.817983878	2.592719561	2.336105027
Standard Error	0.492524111	0.447935093	0.51615281	0.361774049	0.378734411	0.480464625	0.37378556	0.424862795	0.487800202	0.591991957	0.599567177	0.445562373	0.409944957	0.369370637
95%CI	0.965347258	0.877952782	1.011659507	0.709077136	0.742319445	0.941710665	0.732619698	0.832731078	0.956088397	1.160304235	1.175151666	0.873302251	0.803492116	0.723966448
95%CI/Average	0.08%	0.08%	0.09%	0.08%	0.08%	0.09%	0.08%	0.08%	0.08%	0.09%	0.10%	0.08%	0.09%	0.08%

C_p

Average	0.092003777	0.156787269	0.192741376	0.319010817	0.320088689	0.278597314	0.343032224	0.279811344	0.168193705	0.109256417	0.113406201	0.223627532	0.315993038	0.376601931
Standard Deviation	0.00225778	0.00205338	0.002366096	0.001658409	0.001736157	0.002202498	0.001713471	0.001947614	0.002236125	0.002713751	0.002748476	0.002042503	0.001879229	0.001693232
Standard Error	0.000356986	0.000324668	0.000374113	0.000262217	0.00027451	0.000348246	0.000270923	0.000307945	0.000353562	0.000429082	0.000434572	0.000322948	0.000297132	0.000267724
95%CI	0.000699693	0.000636349	0.000733261	0.000513946	0.000538041	0.000682561	0.00053101	0.000603572	0.000692982	0.000841	0.000851762	0.000632978	0.000582379	0.000524738
95%CI/Average	0.76%	0.41%	0.38%	0.16%	0.17%	0.24%	0.15%	0.22%	0.41%	0.77%	0.75%	0.28%	0.18%	0.14%

Table 2: Statistical Parameters for Baseline C_p Experimental Data at 60°

60°
Speed2
Measured Pressure Value

L/D_{inlet}	0.25	0.5	1	1.625	2	2.25	2.5	2.75	3	3.5	4	4.5	4.75
Average	-301.0721055	-288.360371	-265.8860905	-210.8257905	-225.1102745	-232.9543325	-221.9914455	-226.741882	-245.6150585	-237.299458	-220.472293	-194.381438	-186.155713
Standard Deviation	1.72169629	1.608818371	1.474364739	1.341433129	1.204635533	1.411297405	1.202416301	1.346881557	1.5979739	1.543126131	1.406955563	1.041559855	0.950547666
Standard Error	0.272224086	0.25437652	0.233117534	0.212099201	0.190469602	0.223145713	0.19011871	0.212960673	0.252661858	0.243989665	0.222459207	0.164685073	0.150294782
95%CI	0.533559208	0.498577978	0.456910366	0.415714434	0.373320419	0.437365597	0.372632672	0.417402919	0.495217242	0.478219743	0.436020046	0.322782743	0.294577773
95%CI/Average	0.18%	0.17%	0.17%	0.20%	0.17%	0.19%	0.17%	0.18%	0.20%	0.20%	0.20%	0.17%	0.16%

C_p

Average	0.043365196	0.083755812	0.15516621	0.330116324	0.284728411	0.259804485	0.294638264	0.279544096	0.219575945	0.245998163	0.299465261	0.382367063	0.408503708
Standard Deviation	0.005470565	0.005111904	0.004684687	0.004262307	0.003827642	0.004484295	0.003820591	0.004279619	0.005077446	0.004903171	0.004470499	0.003309481	0.003020296
Standard Error	0.000864972	0.000808263	0.000740714	0.00067393	0.000605203	0.000709029	0.000604088	0.000676667	0.000802815	0.000775259	0.000706848	0.000523275	0.000477551
95%CI	0.001695346	0.001584195	0.0014518	0.001320902	0.001186199	0.001389697	0.001184013	0.001326268	0.001573517	0.001519509	0.001385422	0.001025619	0.000936
95%CI/Average	3.91%	1.89%	0.94%	0.40%	0.42%	0.53%	0.40%	0.47%	0.72%	0.62%	0.46%	0.27%	0.23%

Speed4
Measured Pressure Value

L/D_{inlet}	0.25	0.5	1	1.625	2	2.25	2.5	2.75	3	3.5	4	4.5	4.75
Average	-547.9725295	-523.661913	-479.5634425	-409.5816325	-415.731944	-430.103816	-411.5257	-424.446021	-455.534769	-436.0203845	-405.588052	-358.17391	-342.423603
Standard Deviation	2.38924402	2.354408936	2.278622736	2.117245063	2.117573144	2.202585261	2.058357154	2.155686848	2.362407006	2.236863611	2.117799248	1.875391195	1.882951468
Standard Error	0.377772649	0.372264739	0.360281889	0.334765838	0.334817712	0.348259308	0.325454842	0.340844018	0.373529345	0.353679191	0.334853463	0.296525384	0.297720768
95%CI	0.740434393	0.729638889	0.706152502	0.656141043	0.656242716	0.682588244	0.637891491	0.668054276	0.732117516	0.693211215	0.656312787	0.581189753	0.583532705
95%CI/Average	0.14%	0.14%	0.15%	0.16%	0.16%	0.16%	0.16%	0.16%	0.16%	0.16%	0.16%	0.16%	0.17%

C_p

Average	0.029486099	0.072542621	0.150645402	0.274590154	0.26369734	0.238243324	0.271147017	0.248263842	0.193202575	0.227764492	0.281663183	0.365638349	0.39353371
Standard Deviation	0.004231589	0.004169893	0.004035668	0.003749852	0.003750433	0.003900998	0.003645555	0.003817936	0.004184058	0.003961708	0.003750833	0.003321505	0.003334895
Standard Error	0.000669073	0.000659318	0.000638095	0.000592904	0.000592996	0.000616802	0.000576413	0.000603669	0.000661558	0.000626401	0.000593059	0.000525176	0.000527293
95%CI	0.001311383	0.001292263	0.001250666	0.001162091	0.001162271	0.001208932	0.001129769	0.001183191	0.001296653	0.001227746	0.001162395	0.001029345	0.001033495
95%CI/Average	4.45%	1.78%	0.83%	0.42%	0.44%	0.51%	0.42%	0.48%	0.67%	0.54%	0.41%	0.28%	0.26%

Speed6
Measured Pressure Value

L/D_{inlet}	0.25	0.5	1	1.625	2	2.25	2.5	2.75	3	3.5	4	4.5	4.75
Average	-896.8516635	-856.2234025	-782.9563985	-690.406125	-684.651268	-712.554354	-678.3980905	-702.2181985	-753.560085	-717.9534505	-668.189919	-588.72352	-562.579198
Standard Deviation	3.580444558	3.454242594	3.305222285	2.95995288	2.809804978	3.477799355	2.607068522	2.756846404	3.349996346	3.088790638	2.870713064	2.270296912	2.203143608
Standard Error	0.566117992	0.546163709	0.52260153	0.468009643	0.444269176	0.54988836	0.412213727	0.43589569	0.52968093	0.488380682	0.45389959	0.35896546	0.348347591
95%CI	1.109591264	1.07048087	1.024298998	0.917298901	0.870767584	1.077781186	0.807938905	0.854355552	1.038174624	0.957226136	0.889643195	0.703572302	0.682761278
95%CI/Average	0.12%	0.13%	0.13%	0.13%	0.13%	0.15%	0.12%	0.12%	0.14%	0.13%	0.13%	0.12%	0.12%

C_p

Average	0.070524682	0.112630827	0.188562973	0.284479833	0.290444027	0.261525945	0.296924668	0.272238086	0.2190286	0.255930452	0.30750417	0.389861219	0.41695656
Standard Deviation	0.003710686	0.003579893	0.003425452	0.003067623	0.002912014	0.003604307	0.002701903	0.002857129	0.003471855	0.003201148	0.002975137	0.002352881	0.002283285
Standard Error	0.000586711	0.000566031	0.000541612	0.000485034	0.00046043	0.000569891	0.000427208	0.000451752	0.000548948	0.000506146	0.000470411	0.000372023	0.000361019
95%CI	0.001149953	0.00110942	0.001061559	0.000950666	0.000902442	0.001116986	0.000837328	0.000885433	0.001075939	0.000992046	0.000922005	0.000729165	0.000707597
95%CI/Average	1.63%	0.99%	0.56%	0.33%	0.31%	0.43%	0.28%	0.33%	0.49%	0.39%	0.30%	0.19%	0.17%

Speed8
Measured Pressure Value

L/D_{inlet}	0.25	0.5	1	1.625	2	2.25	2.5	2.75	3	3.5	4	4.5	4.75
Average	-1171.120125	-1116.857445	-1020.327297	-906.6358535	-894.7320775	-936.448905	-887.676187	-919.702406	-988.4078735	-939.4882635	-873.4618295	-768.502248	-734.0137645
Standard Deviation	3.22012772	3.046550769	2.644478419	2.329037207	2.751916584	3.671992429	3.314875926	3.815115977	4.47330718	4.225483702	3.989476969	3.078204393	2.71143193
Standard Error	0.509146898	0.481701972	0.418128751	0.368253116	0.435116217	0.580592981	0.524127904	0.603222801	0.707291968	0.668107636	0.630791695	0.486706849	0.428715031
95%CI	0.997927919	0.944135865	0.819532353	0.721776108	0.852827785	1.137962243	1.027290693	1.182316691	1.386292257	1.309490966	1.236351722	0.953945424	0.840281461
95%CI/Average	0.09%	0.08%	0.08%	0.08%	0.10%	0.12%	0.12%	0.13%	0.14%	0.14%	0.14%	0.12%	0.11%

C_p

Average	0.055638914	0.099394941	0.177234365	0.268912214	0.278511113	0.244871738	0.284200801	0.258375683	0.202973365	0.242420878	0.295662892	0.380299594	0.408110218
Standard Deviation	0.002596628	0.00245666	0.002132439	0.001878076	0.002219075	0.002961	0.002673031	0.003076411	0.00360716	0.003407321	0.003217011	0.002482185	0.002186429
Standard Error	0.000410563	0.000388432	0.000337168	0.00029695	0.000350867	0.000468175	0.000422643	0.000486423	0.000570342	0.000538745	0.000508654	0.000392468	0.000345705
95%CI	0.000804703	0.000761327	0.00066085	0.000582022	0.000687698	0.000917623	0.000828381	0.00095339	0.00111787	0.00105594	0.000996962	0.000769237	0.000677581
95%CI/Average	1.45%	0.77%	0.37%	0.22%	0.25%	0.37%	0.29%	0.37%	0.55%	0.44%	0.34%	0.20%	0.17%

Speed8
Measured Pressure Value

L/D_{inlet}	0.25	0.5	1	1.625	2	2.25	2.5	2.75	3	3.5	4	4.5	4.75
Average	-1305.958355	-1244.817215	-1137.03323	-969.205604	-998.561266	-1047.35328	-991.4898465	-1027.509738	-1104.920965	-1049.96132	-976.0156925	-858.1481575	-819.439029
Standard Deviation	3.032825029	2.856063402	2.608211151	3.709895353	2.459077171	4.33904715	2.666623603	3.045981335	4.357014443	3.941634488	3.332275194	2.605420883	2.342672757
Standard Error	0.479531742	0.451583275	0.412394393	0.58658596	0.38881424	0.686063593	0.421630212	0.481611936	0.688904472	0.623227134	0.52687897	0.411953213	0.370409086
95%CI	0.939882214	0.885103218	0.80829301	1.149708481	0.762075911	1.344684643	0.826395216	0.943959395	1.350252765	1.221525183	1.032682782	0.807428297	0.726001809
95%CI/Average	0.07%	0.07%	0.07%	0.12%	0.08%	0.13%	0.08%	0.09%	0.12%	0.12%	0.11%	0.09%	0.09%

C_p

Average	0.053428384	0.097744091	0.175866996	0.29751013	0.276232854	0.240867916	0.281358289	0.255250713	0.199142285	0.238977583	0.29257411	0.378005673	0.406062434
Standard Deviation	0.002198222	0.002070103	0.001890457	0.002688969	0.001782364	0.003144985	0.001932795	0.002207758	0.003158007	0.002856936	0.002415266	0.001888435	0.001697993
Standard Error	0.000347569	0.000327312	0.000298908	0.000425163	0.000281816	0.000497266	0.000305602	0.000349077	0.000499325	0.000451721	0.000381887	0.000298588	0.000268476
95%CI	0.000681236	0.000641532	0.000585859	0.00083332	0.00055236	0.000974641	0.000598979	0.000684191	0.000978677	0.000885374	0.000748499	0.000585232	0.000526213
95%CI/Average	1.28%	0.66%	0.33%	0.28%	0.20%	0.40%	0.21%	0.27%	0.49%	0.37%	0.26%	0.15%	0.13%

Table 3: Statistical Parameters for Baseline C_p Experimental Data at 120°

120°

Speed2

Measured Pressure Value

L/D_{inlet}	0.25	0.5	1	2	2.25	2.5	2.75	3	3.5	4	4.5	4.75
Average	-329.1063095	-311.2505735	-288.5283125	-248.6543575	-232.1670135	-210.0553165	-194.97835	-183.722783	-174.7446915	-165.657425	-164.974527	-159.749839
Standard Deviation	4.82081346	4.550244734	4.19954319	3.706268131	3.412065239	3.094587955	2.889489954	2.707821989	2.586395516	2.579074357	2.6214608	2.465394806
Standard Error	0.762237535	0.719456864	0.664006081	0.586012446	0.539494884	0.489297318	0.456868477	0.428144249	0.408945038	0.407787461	0.414489346	0.389813146
95%CI	1.493985569	1.410135453	1.301451918	1.148584394	1.057409973	0.959022743	0.895462214	0.839162728	0.801532275	0.799263424	0.812399119	0.764033766
95%CI/Average	0.45%	0.45%	0.45%	0.46%	0.46%	0.46%	0.46%	0.46%	0.46%	0.48%	0.49%	0.48%

C_p

Average	-0.045711456	0.011023851	0.08322219	0.209918793	0.262306134	0.332564449	0.380470418	0.416234167	0.444761402	0.473635533	0.475805392	0.49240646
Standard Deviation	0.015317786	0.014458073	0.013343744	0.011776398	0.01084159	0.009832829	0.009181145	0.008603908	0.008218084	0.008194822	0.008329502	0.007833613
Standard Error	0.002421955	0.002286022	0.002109831	0.001862012	0.001714206	0.001554707	0.001451666	0.001360397	0.001299393	0.001295715	0.00131701	0.001238603
95%CI	0.004747031	0.004480603	0.004135269	0.003649544	0.003359844	0.003047225	0.002845266	0.002666379	0.002546811	0.002539602	0.002581339	0.002427662
95%CI/Average	10.38%	40.64%	4.97%	1.74%	1.28%	0.92%	0.75%	0.64%	0.57%	0.54%	0.54%	0.49%

Speed4

Measured Pressure Value

L/D_{inlet}	0.25	0.5	1	2	2.25	2.5	2.75	3	3.5	4	4.5	4.75
Average	-580.4358925	-547.8259105	-510.0970305	-438.1295325	-410.471479	-370.791144	-346.119044	-326.6776765	-308.416481	-291.7398685	-289.5074135	-283.0405675
Standard Deviation	13.46675819	12.57963714	11.74835237	10.18834626	9.579729094	8.54220315	8.115547892	7.538298664	7.171538637	6.595786069	6.53307198	6.569472344
Standard Error	2.129281429	1.989015274	1.857577613	1.610918989	1.514688165	1.350640909	1.28318079	1.191909673	1.133919821	1.042885347	1.032969379	1.038724782
95%CI	4.173391601	3.898469938	3.640852121	3.157401218	2.968788804	2.647256183	2.515034348	2.336142959	2.222482849	2.04405528	2.024619982	2.035900572
95%CI/Average	0.72%	0.71%	0.71%	0.72%	0.72%	0.71%	0.73%	0.72%	0.72%	0.70%	0.70%	0.72%

C_p

Average	-0.028009749	0.029745775	0.096567378	0.224028981	0.273014148	0.343291971	0.386988716	0.421421314	0.453763709	0.48329965	0.48725355	0.498706978
Standard Deviation	0.023850969	0.02227979	0.020807502	0.018044575	0.016966654	0.015129092	0.014373443	0.013351077	0.012701509	0.011681794	0.011570721	0.01163519
Standard Error	0.003771169	0.003522744	0.003289955	0.002853098	0.002682664	0.00239212	0.002272641	0.002110991	0.002008285	0.001847054	0.001829492	0.001839685
95%CI	0.007391492	0.006904578	0.006448312	0.005592072	0.005258021	0.004688554	0.004454376	0.004137542	0.003936238	0.003620225	0.003585804	0.003605783
95%CI/Average	26.39%	23.21%	6.68%	2.50%	1.93%	1.37%	1.15%	0.98%	0.87%	0.75%	0.74%	0.72%

Speed6

Measured Pressure Value

L/D_{inlet}	0.25	0.5	1	2	2.25	2.5	2.75	3	3.5	4	4.5	4.75
Average	-996.773634	-939.5415255	-876.457073	-752.8703485	-705.8590435	-636.043979	-596.398805	-563.1094165	-529.6377185	-499.5692775	-494.5891495	-486.792674
Standard Deviation	2.597138525	2.176059855	2.004087467	1.853712033	1.707639978	1.975171697	1.648545055	1.86479581	1.839957146	2.163832304	1.832329231	1.476296971
Standard Error	0.410643657	0.344065273	0.316874051	0.293097607	0.270001588	0.312302067	0.26065786	0.294850107	0.290922769	0.342131928	0.28971669	0.233423047
95%CI	0.804861568	0.674367936	0.621073141	0.574471311	0.529203112	0.612112051	0.510889406	0.577906209	0.570208627	0.670578578	0.567844712	0.457509171
95%CI/Average	0.08%	0.07%	0.07%	0.08%	0.07%	0.10%	0.09%	0.10%	0.11%	0.13%	0.11%	0.09%

C_p

Average	-0.033032025	0.026281944	0.091661141	0.219743426	0.268464803	0.340819443	0.38190674	0.416407055	0.451096311	0.482258514	0.487419798	0.495499876
Standard Deviation	0.002691611	0.002255216	0.002076988	0.001921142	0.001769757	0.00204702	0.001708512	0.001932629	0.001906887	0.002242543	0.001898982	0.001529998
Standard Error	0.000425581	0.000356581	0.000328401	0.000303759	0.000279823	0.000323662	0.000270139	0.000305576	0.000301505	0.000354577	0.000300255	0.000241914
95%CI	0.000834139	0.000698899	0.000643665	0.000595368	0.000548453	0.000634378	0.000529473	0.000598928	0.00059095	0.000694971	0.0005885	0.000474151
95%CI/Average	2.53%	2.66%	0.70%	0.27%	0.20%	0.19%	0.14%	0.14%	0.13%	0.14%	0.12%	0.10%

Speed8

Measured Pressure Value

L/D_{inlet}	0.25	0.5	1	2	2.25	2.5	2.75	3	3.5	4	4.5	4.75
Average	-1308.80626	-1233.12464	-1150.503275	-988.8613045	-927.40265	-834.0203915	-783.7540565	-738.934151	-694.2114265	-654.020583	-648.5133575	-639.193717
Standard Deviation	2.884554719	2.555064332	2.518830426	2.289700977	2.031708123	2.270293285	1.846234854	2.07313133	2.102666268	2.533361555	2.069963731	1.675284457
Standard Error	0.456088147	0.403991143	0.398262059	0.362033512	0.32124126	0.358964887	0.291915362	0.327790845	0.332460728	0.400559633	0.327290003	0.264885731
95%CI	0.893932769	0.79182264	0.780593636	0.709585684	0.629632871	0.703571178	0.572154109	0.642470056	0.651623028	0.78509688	0.641488406	0.519176032
95%CI/Average	0.07%	0.06%	0.07%	0.07%	0.07%	0.08%	0.07%	0.09%	0.09%	0.12%	0.10%	0.08%

C_p

Average	-0.055387636	0.005640072	0.072263811	0.20260773	0.252166405	0.327467452	0.368000929	0.404142545	0.440205798	0.472614658	0.477055543	0.484570661
Standard Deviation	0.002326031	0.002060338	0.00203112	0.001846356	0.001638317	0.001830706	0.001488756	0.00167172	0.001695536	0.002042837	0.001669165	0.001350906
Standard Error	0.000367778	0.000325768	0.000321148	0.000291934	0.000259041	0.00028946	0.000235393	0.000264322	0.000268088	0.000323001	0.000263918	0.000213597
95%CI	0.000720844	0.000638505	0.000629451	0.000572192	0.00050772	0.000567342	0.00046137	0.000518071	0.000525452	0.000633082	0.00051728	0.00041865
95%CI/Average	1.30%	11.32%	0.87%	0.28%	0.20%	0.17%	0.13%	0.13%	0.12%	0.13%	0.11%	0.09%

Speed10

Measured Pressure Value

L/D_{inlet}	0.25	0.5	1	2	2.25	2.5	2.75	3	3.5	4	4.5	4.75
Average	-1453.11396	-1368.12057	-1278.35014	-1098.32489	-1030.257252	-926.3635855	-870.6731	-820.975215	-770.6354255	-725.7035035	-718.809157	-708.854269
Standard Deviation	2.765838327	2.443633715	2.470575238	2.459410094	2.031704579	2.367545537	1.861082927	2.215565152	2.251332477	2.7859161	2.298952941	1.845865521
Standard Error	0.437317438	0.386372415	0.390632244	0.38886688	0.3212407	0.374341818	0.294263048	0.350311609	0.35596692	0.440492012	0.363496376	0.291856965
95%CI	0.857142178	0.757289934	0.765639199	0.762179084	0.629631772	0.733709963	0.576755574	0.686610754	0.697695163	0.863364344	0.712452898	0.572039651
95%CI/Average	0.06%	0.06%	0.06%	0.07%	0.06%	0.08%	0.07%	0.08%	0.09%	0.12%	0.10%	0.08%

C_p

Average	-0.053231464	0.008372591	0.073439093	0.203923186	0.253259288	0.328562451	0.36892747	0.404948991	0.441435772	0.474002876	0.478999967	0.486215369
Standard Deviation	0.002004707	0.00177117	0.001790698	0.001782605	0.0014726	0.001716021	0.001348931	0.001605864	0.001631788	0.00201926	0.001666304	0.001337902
Standard Error	0.000316972	0.000280047	0.000283134	0.000281855	0.000232838	0.000271327	0.000213285	0.000253909	0.000258008	0.000319273	0.000263466	0.000211541
95%CI	0.000621265	0.000548891	0.000554943	0.000552435	0.000456363	0.0005318	0.000418038	0.000497662	0.000505696	0.000625775	0.000516393	0.00041462
95%CI/Average	1.17%	6.56%	0.76%	0.27%	0.18%	0.16%	0.11%	0.12%	0.11%	0.13%	0.11%	0.09%

Table 4: Statistical Parameters for Baseline C_p Experimental Data at 180°

180°

Speed2

Measured Pressure Value

L/D_{inlet}	0.25	0.5	1	1.625	2	2.25	2.5	2.75	3	3.25	3.5	4	4.5	4.75
Average	-315.086477	-309.8720435	-308.822121	-257.6883485	-215.554694	-190.7648115	-177.256264	-162.2003085	-163.6858305	-151.8560305	-158.986316	-156.1778585	-159.217721	-150.416277
Standard Deviation	2.346159098	2.348949559	5.343818143	2.08550273	1.788366004	2.008005556	2.570203291	1.916924719	1.695856219	1.728236034	1.39739818	1.145059974	1.01443699	0.967757255
Standard Error	0.370960325	0.371401536	0.844931837	0.329746935	0.282765493	0.317493555	0.406384823	0.303092411	0.268138412	0.27325811	0.220948052	0.181049879	0.160396572	0.153015857
95%CI	0.727082237	0.72794701	1.6560664	0.646303992	0.554220366	0.622287369	0.796514252	0.594061125	0.525551287	0.535585896	0.433058183	0.354857762	0.31437728	0.29991108
95%CI/Average	0.23%	0.23%	0.54%	0.25%	0.26%	0.33%	0.45%	0.37%	0.32%	0.35%	0.27%	0.23%	0.20%	0.20%

C_p

Average	-0.001164454	0.015404031	0.018740083	0.181213941	0.315090576	0.393858631	0.436781063	0.48462027	0.479900132	0.517488464	0.494832499	0.503756169	0.494097226	0.522063177
Standard Deviation	0.007454751	0.007463617	0.016979595	0.006626534	0.005682403	0.006380292	0.008166635	0.006090889	0.00538846	0.005491345	0.004440131	0.003638345	0.0032233	0.003074979
Standard Error	0.0011787	0.001180101	0.00268471	0.001047747	0.000898467	0.001008813	0.001291258	0.000963054	0.00085199	0.000868258	0.000702046	0.000575273	0.000509648	0.000486197
95%CI	0.002310251	0.002312999	0.005262031	0.002053584	0.001760995	0.001977273	0.002530866	0.001887586	0.001669901	0.001701785	0.001376011	0.001127535	0.000998911	0.000952946
95%CI/Average	198.40%	15.02%	28.08%	1.13%	0.56%	0.50%	0.58%	0.39%	0.35%	0.33%	0.28%	0.22%	0.20%	0.18%

Speed4

Measured Pressure Value

L/D_{inlet}	0.25	0.5	1	1.625	2	2.25	2.5	2.75	3	3.25	3.5	4	4.5	4.75
Average	-609.0989925	-597.964641	-572.703563	-501.1704605	-423.395541	-376.1110745	-353.3134455	-324.401178	-310.9961395	-290.100599	-295.590103	-285.5809215	-287.2405975	-279.4636945
Standard Deviation	4.515130359	5.270011996	3.853057379	3.323175918	3.097300508	3.879636751	6.656525065	5.571614673	6.677456626	6.313754097	3.838858704	1.963329264	1.838152624	1.687058606
Standard Error	0.713904793	0.83326206	0.609221864	0.525440248	0.48972621	0.613424431	1.052489025	0.880949631	1.055798596	0.998292177	0.606976856	0.310429614	0.290637449	0.266747387
95%CI	1.399253395	1.633193638	1.194074853	1.029862887	0.959863372	1.202311886	2.06287849	1.726661276	2.069365248	1.956652666	1.189674638	0.608442042	0.5696494	0.522824879
95%CI/Average	0.23%	0.27%	0.21%	0.21%	0.23%	0.32%	0.58%	0.53%	0.67%	0.67%	0.40%	0.21%	0.20%	0.19%

C_p

Average	-0.078774953	-0.059054908	-0.014315024	0.112377222	0.250124347	0.333869845	0.374246715	0.425453219	0.449194877	0.486202959	0.476480501	0.494207758	0.491268307	0.505041976
Standard Deviation	0.007996745	0.009333716	0.006824148	0.005885675	0.005485628	0.006871223	0.011789369	0.009867884	0.01182644	0.011182287	0.006799001	0.003477252	0.003255551	0.002987949
Standard Error	0.001264396	0.00147579	0.001078993	0.000930607	0.000867354	0.001086436	0.001864063	0.001560249	0.001869924	0.001768075	0.001075016	0.000549802	0.000514748	0.000472436
95%CI	0.002478217	0.002892549	0.002114825	0.00182399	0.001700014	0.002129414	0.003653563	0.003058089	0.003665052	0.003465427	0.002107032	0.001077611	0.001008906	0.000925975
95%CI/Average	3.15%	4.90%	14.77%	1.62%	0.68%	0.64%	0.98%	0.72%	0.82%	0.71%	0.44%	0.22%	0.21%	0.18%

Speed6

Measured Pressure Value

L/D_{inlet}	0.25	0.5	1	1.625	2	2.25	2.5	2.75	3	3.25	3.5	4	4.5	4.75
Average	-1036.152806	-1020.032388	-968.605153	-858.908519	-736.802904	-643.907153	-588.856172	-543.7942975	-517.334393	-490.6271685	-492.728902	-468.0147665	-467.551706	-461.7988615
Standard Deviation	9.05497232	6.774999614	5.044093496	5.499298457	5.902287581	4.441845086	7.823446896	8.191974619	7.840846692	7.300122054	4.893123363	1.975143112	1.826600105	1.791139475
Standard Error	1.431716834	1.071221496	0.797541209	0.869515433	0.933233608	0.702317374	1.236995567	1.295264917	1.239746717	1.154250644	0.773670735	0.312297547	0.288810835	0.283204017
95%CI	2.806164995	2.099594133	1.563180769	1.704250249	1.829137872	1.376542054	2.424511312	2.538719236	2.429903565	2.262331263	1.516394641	0.612103192	0.566069237	0.555079874
95%CI/Average	0.27%	0.21%	0.16%	0.20%	0.25%	0.21%	0.41%	0.47%	0.47%	0.46%	0.31%	0.13%	0.12%	0.12%

C_p

Average	-0.073843644	-0.057136834	-0.003838894	0.109848037	0.236395336	0.33267024	0.389723742	0.436424776	0.463847179	0.491525899	0.489347713	0.514960844	0.515440749	0.521402857
Standard Deviation	0.009384354	0.007021445	0.005227576	0.00569934	0.006116988	0.004603421	0.008108031	0.008489964	0.008126063	0.007565669	0.005071114	0.00204699	0.001893044	0.001856294
Standard Error	0.001483797	0.001110188	0.000826552	0.000901145	0.000967181	0.000727865	0.001281992	0.001342381	0.001284843	0.001196237	0.000801814	0.000323658	0.000299317	0.000293506
95%CI	0.002908241	0.002175968	0.001620043	0.001766244	0.001895674	0.001426615	0.002512705	0.002631067	0.002518293	0.002344625	0.001571555	0.000634369	0.00058666	0.000575271
95%CI/Average	3.94%	3.81%	42.20%	1.61%	0.80%	0.43%	0.64%	0.60%	0.54%	0.48%	0.32%	0.12%	0.11%	0.11%

Speed8

Measured Pressure Value

L/D_{inlet}	0.25	0.5	1	1.625	2	2.25	2.5	2.75	3	3.25	3.5	4	4.5	4.75
Average	-1378.848905	-1365.334265	-1293.727385	-1148.82459	-992.403821	-865.128726	-786.3077365	-725.844996	-683.432577	-652.0845585	-651.855036	-610.003671	-608.2060425	-603.982072
Standard Deviation	6.325376375	4.169008291	4.254235289	3.824826051	4.599430783	4.993619654	10.0116933	7.867094103	6.05862104	5.986378081	4.405410065	3.385857319	3.145895375	3.006742894
Standard Error	1.00012982	0.659178089	0.672653661	0.604758099	0.727233861	0.789560594	1.582987703	1.243896797	0.957952098	0.946529484	0.696556492	0.535351048	0.497409733	0.475407794
95%CI	1.960254448	1.291989055	1.318401175	1.185325874	1.425378367	1.547538764	3.102655897	2.438037721	1.877586113	1.855197788	1.365250724	1.049288054	0.974923077	0.931799276
95%CI/Average	0.14%	0.09%	0.10%	0.10%	0.14%	0.18%	0.39%	0.34%	0.27%	0.28%	0.21%	0.17%	0.16%	0.15%

C_p

Average	-0.11186822	-0.100970363	-0.04322842	0.073617459	0.199751136	0.302382492	0.365941707	0.414697302	0.448897584	0.474175818	0.474360899	0.508108761	0.509558323	0.512964424
Standard Deviation	0.00510062	0.003361781	0.003430506	0.003084241	0.003708862	0.004026726	0.008073171	0.006343822	0.004885516	0.004827261	0.003552409	0.002730268	0.002536769	0.00242456
Standard Error	0.000806479	0.000531544	0.000542411	0.000487661	0.000586423	0.000636681	0.00127648	0.001003046	0.000772468	0.000763257	0.000561685	0.000431693	0.000401098	0.000383357
95%CI	0.001580699	0.001041827	0.001063125	0.000955816	0.001149388	0.001247895	0.002501902	0.001965971	0.001514037	0.001495984	0.001100903	0.000846119	0.000786153	0.000751379
95%CI/Average	1.41%	1.03%	2.46%	1.30%	0.58%	0.41%	0.68%	0.47%	0.34%	0.32%	0.23%	0.17%	0.15%	0.15%

Speed10

Measured Pressure Value

L/D_{inlet}	0.25	0.5	1	1.625	2	2.25	2.5	2.75	3	3.25	3.5	4	4.5	4.75
Average	-1551.05215	-1541.710015	-1457.902605	-1291.76616	-1125.63281	-978.4541235	-887.6829185	-818.066239	-766.695215	-733.205356	-732.7619615	-682.151024	-679.5392415	-675.478423
Standard Deviation	3.478113436	3.526376508	3.261163478	2.724622278	3.680585359	3.232647355	5.582732209	4.268104704	4.347660468	4.050402377	3.216492697	3.321753074	3.026532291	2.743806364
Standard Error	0.549938021	0.557569083	0.515635221	0.430800608	0.581951643	0.511126426	0.882707467	0.674846608	0.687425479	0.640424848	0.50857215	0.525215277	0.478536773	0.433833878
95%CI	1.077878521	1.092835402	1.010645033	0.844369192	1.14062522	1.001807794	1.730106636	1.322699351	1.347353938	1.255232701	0.996801414	1.029421943	0.937932074	0.850314402
95%CI/Average	0.07%	0.07%	0.07%	0.07%	0.10%	0.10%	0.19%	0.16%	0.18%	0.17%	0.14%	0.15%	0.14%	0.13%

C_p

Average	-0.124218039	-0.117446766	-0.056702321	0.063715028	0.184130134	0.290806711	0.356598584	0.407057446	0.444291676	0.468565459	0.468886836	0.505570147	0.507463193	0.510406515
Standard Deviation	0.002520971	0.002555953	0.002363724	0.001974833	0.002667725	0.002343055	0.00404642	0.003093565	0.003151228	0.002935772	0.002331346	0.00240764	0.002193661	0.001988738
Standard Error	0.000398601	0.000404132	0.000373738	0.000312249	0.000421804	0.00037047	0.000639795	0.000489136	0.000498253	0.000464186	0.000368618	0.000380681	0.000346848	0.000314447
95%CI	0.000781257	0.000792098	0.000732526	0.000612007	0.000826737	0.00072612	0.001253999	0.000958706	0.000976576	0.000909805	0.000722492	0.000746135	0.000679823	0.000616316
95%CI/Average	0.63%	0.67%	1.29%	0.96%	0.45%	0.25%	0.35%	0.24%	0.22%	0.19%	0.15%	0.15%	0.13%	0.12%

Table 5: Statistical Parameters for Type1 C_p Experimental Data at 0°

0°

Speed2

Measured Pressure Value

L/D_{inlet}	0.25	0.5	1	1.625	2	2.25	2.5	2.75	3	3.25	3.5	4	4.5	4.75
Average	-279.9232725	-263.8702085	-256.754296	-209.7552365	-205.6481855	-214.1593805	-199.2994135	-210.0378845	-247.159176	-267.34203	-274.7682425	-215.631173	-189.3763795	-196.2563145
Standard Deviation	1.350894104	1.261475879	1.163670177	2.026050302	1.058756832	1.409954982	1.11688106	1.143661834	1.290314118	1.550624366	1.639942403	3.892857704	2.873446344	2.818546574
Standard Error	0.213595112	0.19945685	0.18399241	0.32034668	0.167404154	0.222933457	0.176594401	0.180828813	0.204016576	0.24517524	0.259297661	0.615514848	0.454331759	0.445651343
95%CI	0.41864642	0.390935425	0.360625124	0.627879494	0.328112142	0.436949576	0.346125026	0.354424474	0.399872488	0.48054347	0.508223416	1.206409101	0.890490248	0.873476633
95%CI/Average	0.15%	0.15%	0.14%	0.30%	0.16%	0.20%	0.17%	0.17%	0.16%	0.18%	0.18%	0.56%	0.47%	0.45%

C_p

Average	0.154726607	0.203201419	0.224689062	0.36661029	0.379012192	0.353311268	0.398183331	0.365756789	0.253663072	0.192717695	0.170293051	0.348866954	0.42814753	0.407372459
Standard Deviation	0.004079242	0.00380923	0.003513889	0.006117985	0.003197087	0.004257586	0.003372602	0.003453471	0.003896311	0.00468236	0.00495207	0.011755111	0.008676834	0.008511055
Standard Error	0.000644985	0.000602292	0.000555595	0.000967338	0.000505504	0.000673183	0.000533255	0.000546042	0.000616061	0.000740346	0.000782991	0.001858646	0.001371928	0.001345716
95%CI	0.00126417	0.001180492	0.001088966	0.001895983	0.000990787	0.00131944	0.00104518	0.001070242	0.001207479	0.001451078	0.001534662	0.003642947	0.002688979	0.002637603
95%CI/Average	0.82%	0.58%	0.48%	0.52%	0.26%	0.37%	0.26%	0.29%	0.48%	0.75%	0.90%	1.04%	0.63%	0.65%

Speed4

Measured Pressure Value

L/D_{inlet}	0.25	0.5	1	1.625	2	2.25	2.5	2.75	3	3.25	3.5	4	4.5	4.75
Average	-492.4513225	-458.5714795	-439.3629025	-341.89273	-359.622693	-380.0821245	-352.945921	-379.5435705	-440.115602	-475.6609765	-481.8470035	-400.7400065	-338.9654305	-355.259567
Standard Deviation	4.525584505	4.287808753	4.010720099	2.161051356	3.526531206	3.780588973	3.556221619	3.863308864	4.345479265	4.883194249	4.979024847	2.54320216	1.88947572	2.098230833
Standard Error	0.715557739	0.677962092	0.634150529	0.341692221	0.557593543	0.597763603	0.562288009	0.610842766	0.6870806	0.772100804	0.787252952	0.402115569	0.298752343	0.331759424
95%CI	1.402493168	1.3288057	1.242935036	0.669716754	1.092883343	1.171616661	1.102084498	1.197251821	1.346677976	1.513317576	1.543015786	0.788146515	0.585554592	0.650248472
95%CI/Average	0.28%	0.29%	0.28%	0.20%	0.30%	0.31%	0.31%	0.32%	0.31%	0.32%	0.32%	0.20%	0.17%	0.18%

C_p

Average	0.17720727	0.23381406	0.265907948	0.428762113	0.399138709	0.364954881	0.410294328	0.365854702	0.264650329	0.205260752	0.194925075	0.330439479	0.433653075	0.406428665
Standard Deviation	0.007561393	0.007164115	0.006701152	0.003610707	0.005892165	0.006316647	0.005941772	0.006454856	0.007260471	0.008158891	0.008319006	0.004249208	0.003156955	0.003505746
Standard Error	0.001195561	0.001132746	0.001059545	0.000570903	0.000931633	0.00099875	0.000939477	0.001020602	0.001147981	0.001290034	0.00131535	0.000671859	0.000499158	0.000554307
95%CI	0.0023433	0.002220182	0.002076709	0.00111897	0.001826001	0.001957549	0.001841374	0.002000381	0.002250043	0.002528467	0.002578087	0.001316843	0.000978351	0.001086442
95%CI/Average	1.32%	0.95%	0.78%	0.26%	0.46%	0.54%	0.45%	0.55%	0.85%	1.23%	1.32%	0.40%	0.23%	0.27%

Speed6

Measured Pressure Value

L/D_{inlet}	0.25	0.5	1	1.625	2	2.25	2.5	2.75	3	3.25	3.5	4	4.5	4.75
Average	-824.196481	-767.459199	-735.3419105	-558.580533	-606.1508895	-649.4318205	-599.0140565	-650.2586735	-749.9131545	-813.736322	-816.9076765	-737.7324145	-611.951783	-649.0497915
Standard Deviation	1.494932574	1.439094913	1.47440483	3.35958717	1.447864456	2.061220384	1.662481295	1.788918154	1.969589375	2.614955696	2.677769931	2.048129834	1.706218434	1.674432151
Standard Error	0.236369594	0.227540885	0.233123873	0.531197373	0.228927471	0.325907559	0.262861373	0.282852796	0.311419424	0.413460799	0.423392602	0.323837761	0.269776822	0.264750969
95%CI	0.463284405	0.445980134	0.456922791	1.041146851	0.448697843	0.638778815	0.515208291	0.55439148	0.610382071	0.810383166	0.829849499	0.634722011	0.528762571	0.5189119
95%CI/Average	0.06%	0.06%	0.06%	0.19%	0.07%	0.10%	0.09%	0.09%	0.08%	0.10%	0.10%	0.09%	0.09%	0.08%

C_p

Average	0.188458214	0.247259357	0.280544936	0.463736142	0.414435378	0.36958007	0.421831818	0.36872314	0.265443652	0.199298869	0.196012154	0.278067476	0.408423472	0.369975996
Standard Deviation	0.00154932	0.001491443	0.001528037	0.003481795	0.001500532	0.002136199	0.001722955	0.001853991	0.002041235	0.002710077	0.002775176	0.002122632	0.001768283	0.001735341
Standard Error	0.000244968	0.000235818	0.000241604	0.00055052	0.000237255	0.000337763	0.000272423	0.000293142	0.000322748	0.000428501	0.000438794	0.000335618	0.00027959	0.000274381
95%CI	0.000480137	0.000462203	0.000473544	0.001079019	0.00046502	0.000662015	0.000533949	0.000574558	0.000632585	0.000839861	0.000860036	0.000657811	0.000547997	0.000537788
95%CI/Average	0.25%	0.19%	0.17%	0.23%	0.11%	0.18%	0.13%	0.16%	0.24%	0.42%	0.44%	0.24%	0.13%	0.15%

Speed8

Measured Pressure Value

L/D_{inlet}	0.25	0.5	1	1.625	2	2.25	2.5	2.75	3	3.25	3.5	4	4.5	4.75
Average	-1076.28069	-1000.616023	-958.5623135	-722.345222	-791.1184	-855.6943295	-783.588843	-853.7107275	-984.250335	-1070.26552	-1069.160395	-961.628805	-793.8845205	-844.590788
Standard Deviation	2.315771663	2.287293459	2.177353021	2.409878082	2.387095974	2.852175928	2.744101736	2.781434723	2.514582415	2.607965384	2.430238632	2.699091253	2.173447132	2.301495732
Standard Error	0.36615565	0.36165285	0.344269741	0.381035181	0.377433014	0.450968611	0.433880581	0.439783444	0.39759039	0.412355534	0.384254467	0.426763799	0.343652165	0.363898427
95%CI	0.717665074	0.708839587	0.674768692	0.746828955	0.739768707	0.883898477	0.850405939	0.861975551	0.779277164	0.808216846	0.753138755	0.836457045	0.673558244	0.713240917
95%CI/Average	0.07%	0.07%	0.07%	0.10%	0.09%	0.10%	0.11%	0.10%	0.08%	0.08%	0.07%	0.09%	0.08%	0.08%

C_p

Average	0.176731843	0.234609227	0.266776932	0.447464007	0.394858058	0.345462666	0.400617563	0.346979962	0.247127662	0.181332964	0.182178296	0.264431313	0.392742198	0.353955982
Standard Deviation	0.001771379	0.001749596	0.0016655	0.001843363	0.001825936	0.002181685	0.002099017	0.002127574	0.001923453	0.001994884	0.001858937	0.002064588	0.001662512	0.001760459
Standard Error	0.00028008	0.000276635	0.000263339	0.000291461	0.000288706	0.000344955	0.000331884	0.000336399	0.000304125	0.000315419	0.000293924	0.00032644	0.000262866	0.000278353
95%CI	0.000548956	0.000542205	0.000516144	0.000571264	0.000565864	0.000676111	0.000650492	0.000659342	0.000596084	0.000618221	0.000576091	0.000639822	0.000515218	0.000545572
95%CI/Average	0.31%	0.23%	0.19%	0.13%	0.14%	0.20%	0.16%	0.19%	0.24%	0.34%	0.32%	0.24%	0.13%	0.15%

Speed10

Measured Pressure Value

L/D_{inlet}	0.25	0.5	1	1.625	2	2.25	2.5	2.75	3	3.25	3.5	4	4.5	4.75
Average	-1207.07863	-1121.693665	-1075.58444	-814.165539	-887.5061195	-964.2858045	-879.6085185	-959.7095865	-1106.701765	-1204.25187	-1200.70826	-1063.412465	-876.468912	-933.9739635
Standard Deviation	2.487617955	2.459867506	2.433039135	2.281761545	2.366512757	3.659751578	2.599202762	2.530925226	2.463286208	2.872949555	2.880088046	4.40177374	3.708856897	3.971517114
Standard Error	0.393326934	0.388939203	0.384697265	0.360778178	0.374178521	0.578657533	0.410970041	0.400174415	0.389479747	0.45425321	0.455381904	0.695981538	0.586421766	0.627951992
95%CI	0.770920791	0.762320838	0.75400664	0.707125229	0.733389902	1.134168764	0.805501281	0.784341854	0.763380305	0.890336291	0.892548533	1.364123815	1.14938666	1.230785905
95%CI/Average	0.06%	0.07%	0.07%	0.09%	0.08%	0.12%	0.09%	0.08%	0.07%	0.07%	0.07%	0.13%	0.13%	0.13%

C_p

Average	0.168548071	0.227362379	0.25912303	0.439191871	0.388673897	0.335787021	0.39411387	0.338939182	0.237689	0.170495181	0.172936067	0.26750725	0.396276473	0.356666223
Standard Deviation	0.001713505	0.00169439	0.00167591	0.001571708	0.001630086	0.002520886	0.001790366	0.001743335	0.001696745	0.001978926	0.001983843	0.003032001	0.00255471	0.002735634
Standard Error	0.000270929	0.000267907	0.000264985	0.000248509	0.000257739	0.000398587	0.000283082	0.000275645	0.000268279	0.000312896	0.000313673	0.000479401	0.000403935	0.000432542
95%CI	0.000531021	0.000525097	0.00051937	0.000487077	0.000505169	0.000781231	0.00055484	0.000540265	0.000525827	0.000613276	0.000614799	0.000939627	0.000791713	0.000847782
95%CI/Average	0.32%	0.23%	0.20%	0.11%	0.13%	0.23%	0.14%	0.16%	0.22%	0.36%	0.36%	0.35%	0.20%	0.24%

Table 6: Statistical Parameters for Type1 C_p Experimental Data at 60°

60°
Speed2
Measured Pressure Value

L/D_{inlet}	0.25	0.5	1	1.625	2	2.25	2.5	2.75	3	3.5	4	4.5	4.75
Average	-323.7915715	-241.8225805	-237.77434	-209.6361175	-201.5860645	-204.842751	-196.387226	-195.620099	-209.172781	-201.0788105	-210.717008	-173.8928435	-180.726162
Standard Deviation	5.759087785	4.350434209	3.889893079	3.18302822	3.168947697	3.346112769	3.07244927	3.122211773	3.52440887	5.222898259	3.201364343	2.75380916	2.534606127
Standard Error	0.910591732	0.687864046	0.615046099	0.503280952	0.501054625	0.529066883	0.485796884	0.493665027	0.557257972	0.825812724	0.506180147	0.435415459	0.400756417
95%CI	1.784759795	1.348213529	1.205490354	0.986430665	0.982067066	1.03697109	0.952161893	0.967583453	1.092225625	1.61859294	0.992113089	0.8534143	0.785482577
95%CI/Average	0.55%	0.56%	0.51%	0.47%	0.49%	0.51%	0.48%	0.49%	0.52%	0.80%	0.47%	0.49%	0.43%

C_p

Average	0.022259215	0.269777782	0.282002096	0.366969989	0.39127842	0.381444331	0.40697715	0.409293614	0.368369108	0.392810155	0.363706066	0.47490256	0.454268255
Standard Deviation	0.017390493	0.013136837	0.011746158	0.009611666	0.009569148	0.010104126	0.009277755	0.009428021	0.01064252	0.015771382	0.009667035	0.00831557	0.007653651
Standard Error	0.002749678	0.002077116	0.001857231	0.001519738	0.001513015	0.001597603	0.001466942	0.001490701	0.00168273	0.002493674	0.001528492	0.001314807	0.001210149
95%CI	0.00538937	0.004071148	0.003640172	0.002978686	0.00296551	0.003131301	0.002875206	0.002921774	0.003298151	0.004887602	0.002995845	0.002577022	0.002371891
95%CI/Average	24.21%	1.51%	1.29%	0.81%	0.76%	0.82%	0.71%	0.71%	0.90%	1.24%	0.82%	0.54%	0.52%

Speed4
Measured Pressure Value

L/D_{inlet}	0.25	0.5	1	1.625	2	2.25	2.5	2.75	3	3.5	4	4.5	4.75
Average	-580.9574265	-448.491181	-427.011151	-382.458865	-368.8668975	-378.9438135	-362.624196	-368.889918	-395.860166	-374.75193	-377.4587015	-320.9111995	-319.380079
Standard Deviation	4.023114387	2.876972567	2.413040195	1.921029223	2.064325432	2.413660109	2.060284115	2.176716301	2.701079609	2.675097521	2.654617672	2.045348737	1.825644062
Standard Error	0.636110237	0.454889304	0.381535155	0.30374139	0.32639851	0.381633172	0.325759522	0.344169067	0.427078185	0.422970056	0.419731908	0.323398031	0.288659672
95%CI	1.246776065	0.891583035	0.747808904	0.595333124	0.639741079	0.748001017	0.638488662	0.674571371	0.837073243	0.829021311	0.82267454	0.63386014	0.565772957
95%CI/Average	0.21%	0.20%	0.18%	0.16%	0.17%	0.20%	0.18%	0.18%	0.21%	0.22%	0.22%	0.20%	0.18%

C_p

Average	0.029330362	0.250656326	0.286545381	0.360983798	0.383693397	0.366856782	0.394123767	0.383654934	0.338592767	0.373860624	0.369338123	0.46381827	0.466376482
Standard Deviation	0.006721861	0.004806875	0.004031732	0.003209675	0.003449096	0.004032768	0.003442344	0.00363688	0.004512992	0.00446958	0.004435362	0.00341739	0.003050305
Standard Error	0.00106282	0.000760034	0.000637473	0.000507494	0.00054535	0.000637637	0.000544282	0.000575041	0.000713567	0.000706703	0.000701292	0.000540337	0.000482296
95%CI	0.002083126	0.001489666	0.001249447	0.000994689	0.001068886	0.001249768	0.001066793	0.001127081	0.001398591	0.001385137	0.001374533	0.00105906	0.000945299
95%CI/Average	7.10%	0.59%	0.44%	0.28%	0.28%	0.34%	0.27%	0.29%	0.41%	0.37%	0.37%	0.23%	0.20%

Speed6
Measured Pressure Value

L/D_{inlet}	0.25	0.5	1	1.625	2	2.25	2.5	2.75	3	3.5	4	4.5	4.75
Average	-983.848316	-846.1432835	-776.5894995	-704.88276	-679.533902	-706.4871635	-673.641079	-693.9854435	-747.104487	-698.5964705	-691.8929855	-590.2192985	-573.3802705
Standard Deviation	4.777719693	2.355252032	2.139034826	1.883161075	1.92281561	3.021858583	1.840835721	1.965159768	2.766459003	2.523547503	2.818458323	2.630426883	1.945715068
Standard Error	0.755423813	0.372398044	0.338211102	0.29775391	0.304023842	0.477797794	0.291061684	0.310719042	0.437415575	0.399007895	0.445637389	0.415907008	0.307644565
95%CI	1.480630673	0.729900167	0.66289376	0.583597663	0.595886731	0.936483677	0.5704809	0.609009322	0.857334527	0.782055474	0.873449283	0.815177736	0.602983347
95%CI/Average	0.15%	0.09%	0.09%	0.08%	0.09%	0.13%	0.08%	0.09%	0.11%	0.11%	0.13%	0.14%	0.11%

C_p

Average	0.022058451	0.158936739	0.22807294	0.299349171	0.324545841	0.2977544	0.330403285	0.310181063	0.257380932	0.305597719	0.312260958	0.413324223	0.430062154
Standard Deviation	0.004749036	0.002341112	0.002126193	0.001871855	0.001911272	0.003003716	0.001829784	0.001953361	0.00274985	0.002508397	0.002801537	0.002614634	0.001934034
Standard Error	0.000750888	0.000370162	0.000336181	0.000295966	0.000302199	0.000474929	0.000289314	0.000308854	0.000434789	0.000396612	0.000442962	0.00041341	0.000305798
95%CI	0.001471741	0.000725518	0.000658914	0.000580094	0.000592309	0.000930861	0.000567056	0.000605353	0.000852187	0.00077736	0.000868205	0.000810284	0.000599363
95%CI/Average	6.67%	0.46%	0.29%	0.19%	0.18%	0.31%	0.17%	0.20%	0.33%	0.25%	0.28%	0.20%	0.14%

Speed8
Measured Pressure Value

L/D_{inlet}	0.25	0.5	1	1.625	2	2.25	2.5	2.75	3	3.5	4	4.5	4.75
Average	-1295.7389	-1102.35705	-1008.245135	-919.5934905	-886.3557705	-926.020758	-880.345124	-908.8026365	-980.1651215	-914.423829	-896.980403	-769.211841	-742.485385
Standard Deviation	7.347795953	2.990040989	2.787669523	2.595895727	2.754049938	4.863818568	2.581112631	2.690112357	4.210753544	3.608561352	4.004378973	2.322112424	1.924237002
Standard Error	1.16178855	0.472766991	0.440769253	0.410447153	0.43545353	0.76903724	0.408109741	0.425344111	0.665778593	0.570563647	0.633147909	0.367158212	0.304248584
95%CI	2.277105557	0.926623302	0.863907736	0.80447642	0.853488918	1.507312991	0.799895092	0.833674457	1.304926043	1.118304749	1.240969901	0.719630096	0.596327225
95%CI/Average	0.18%	0.08%	0.09%	0.09%	0.10%	0.16%	0.09%	0.09%	0.13%	0.12%	0.14%	0.09%	0.08%

C_p

Average	0.008863964	0.156785525	0.22877357	0.296584947	0.32200913	0.291668605	0.326606791	0.304839083	0.250252522	0.300539323	0.31388214	0.411614813	0.432058402
Standard Deviation	0.005620473	0.002287141	0.002132343	0.001985651	0.002106627	0.00372043	0.001974344	0.00205772	0.003220888	0.002760259	0.003063028	0.001776229	0.001471887
Standard Error	0.000888675	0.000361629	0.000337153	0.000313959	0.000333087	0.000588252	0.000312171	0.000325354	0.000509267	0.000436435	0.000484307	0.000280846	0.000232726
95%CI	0.001741803	0.000708792	0.00066082	0.00061536	0.00065285	0.001152973	0.000611855	0.000637694	0.000998163	0.000855413	0.000949242	0.000550459	0.000456142
95%CI/Average	19.65%	0.45%	0.29%	0.21%	0.20%	0.40%	0.19%	0.21%	0.40%	0.28%	0.30%	0.13%	0.11%

Speed10
Measured Pressure Value

L/D_{inlet}	0.25	0.5	1	1.625	2	2.25	2.5	2.75	3	3.5	4	4.5	4.75
Average	-1441.42687	-1218.71534	-1113.696215	-1017.036856	-980.75717	-1027.547429	-974.631636	-1006.437379	-1086.46359	-1013.70809	-989.661055	-850.1998635	-819.089996
Standard Deviation	10.91162626	4.891824764	4.500676532	4.120438658	3.946139581	6.219687992	3.881110621	4.169540379	5.814880475	5.60151467	5.877191939	3.221752791	2.929626248
Standard Error	1.725279597	0.773465408	0.711619443	0.651498556	0.623939452	0.983419019	0.613657471	0.65926222	0.919413331	0.885677235	0.929265639	0.509403844	0.463214582
95%CI	3.381548011	1.5159922	1.394774108	1.27693717	1.222921326	1.927501278	1.202768642	1.292153951	1.802050129	1.735927381	1.821360652	0.998431534	0.90790058
95%CI/Average	0.23%	0.12%	0.13%	0.13%	0.12%	0.19%	0.12%	0.13%	0.17%	0.17%	0.18%	0.12%	0.11%

C_p

Average	0.007125864	0.160532549	0.232871129	0.29945139	0.324441324	0.292211567	0.328660674	0.306752452	0.251629326	0.301744289	0.318308209	0.414370946	0.435799839
Standard Deviation	0.007516074	0.003369554	0.003100126	0.002838213	0.002718154	0.004284204	0.002673361	0.002872035	0.004005368	0.003858398	0.004048289	0.002219186	0.002017966
Standard Error	0.001188396	0.000532773	0.000490173	0.000448761	0.000429778	0.000677392	0.000422695	0.000454109	0.000633304	0.000610066	0.000640091	0.000350884	0.000319068
95%CI	0.002329256	0.001044236	0.000960739	0.000879571	0.000842365	0.001327689	0.000828483	0.000890053	0.001241276	0.00119573	0.001254578	0.000687733	0.000625374
95%CI/Average	32.69%	0.65%	0.41%	0.29%	0.26%	0.45%	0.25%	0.29%	0.49%	0.40%	0.39%	0.17%	0.14%

Table 7: Statistical Parameters for Type1 C_p Experimental Data at 120°

120°

Speed2

Measured Pressure Value

L/D_{inlet}	0.25	0.5	1	2	2.25	2.5	2.75	3	3.5	4	4.5	4.75
Average	-336.0580465	-298.5185025	-289.7798995	-252.541079	-239.9035025	-213.426501	-195.9421195	-193.85692	-167.31195	-171.233104	-153.1069695	-176.973774
Standard Deviation	2.381846196	2.12319605	1.904590624	1.625104976	1.433454036	1.406127683	1.312167544	1.154886112	1.105233658	1.154415325	1.09183029	0.929311971
Standard Error	0.376602951	0.335706772	0.301142219	0.256951658	0.226648984	0.222328308	0.207471906	0.182603528	0.174752785	0.18252909	0.172633527	0.146937124
95%CI	0.738141784	0.657985273	0.590238749	0.50362525	0.444232008	0.435763484	0.406644935	0.357902914	0.342515459	0.357757016	0.338361713	0.287996763
95%CI/Average	0.22%	0.22%	0.20%	0.20%	0.19%	0.20%	0.21%	0.18%	0.20%	0.21%	0.22%	0.16%

C_p

Average	-0.014781381	0.098575316	0.124962935	0.23741155	0.275572747	0.355524316	0.408321221	0.414617817	0.494774628	0.482934072	0.537668853	0.465599194
Standard Deviation	0.007192368	0.006411332	0.005751218	0.004907266	0.004328545	0.004246029	0.003962301	0.003487365	0.003337431	0.003485943	0.003296957	0.002806207
Standard Error	0.001137213	0.001013721	0.000909347	0.000775907	0.000684403	0.000671356	0.000626495	0.000551401	0.000527694	0.000551176	0.000521295	0.0004437
95%CI	0.002228938	0.001986892	0.001782321	0.001520778	0.00134143	0.001315858	0.00122793	0.001080745	0.001034281	0.001080305	0.001021738	0.000869653
95%CI/Average	15.08%	2.02%	1.43%	0.64%	0.49%	0.37%	0.30%	0.26%	0.21%	0.22%	0.19%	0.19%

Speed4

Measured Pressure Value

L/D_{inlet}	0.25	0.5	1	2	2.25	2.5	2.75	3	3.5	4	4.5	4.75
Average	-621.106337	-565.7248195	-540.873784	-469.1123155	-445.431137	-400.3182885	-373.828578	-359.910809	-321.9606825	-315.8494275	-295.6677505	-316.3639315
Standard Deviation	4.046573667	3.063845118	2.573748125	2.168130709	1.882252832	2.23770152	2.73848123	2.334977131	1.493706918	1.237833561	1.1216621	1.098578219
Standard Error	0.639819475	0.484436448	0.40694531	0.342811565	0.297610304	0.353811676	0.432991901	0.369192301	0.236175801	0.195718671	0.17735035	0.173700468
95%CI	1.254046172	0.949495439	0.797612807	0.671910668	0.583316196	0.693470886	0.848664125	0.72361691	0.46290457	0.383608595	0.347606686	0.340452917
95%CI/Average	0.20%	0.17%	0.15%	0.14%	0.13%	0.17%	0.23%	0.20%	0.14%	0.12%	0.12%	0.11%

C_p

Average	-0.03775085	0.054781158	0.096302524	0.216202323	0.255769079	0.33114409	0.37540337	0.398657322	0.462064783	0.472275531	0.505995284	0.471415892
Standard Deviation	0.006761057	0.005119104	0.004300245	0.003622535	0.003144887	0.003738775	0.004575483	0.003901304	0.002495701	0.002068185	0.001874085	0.001835516
Standard Error	0.001069017	0.000809401	0.000679928	0.000572773	0.00049725	0.000591152	0.000723447	0.00061685	0.000394605	0.000327009	0.000296319	0.000290221
95%CI	0.002095273	0.001586427	0.00133266	0.001122635	0.000974611	0.001158658	0.001417957	0.001209027	0.000773426	0.000640937	0.000580785	0.000568832
95%CI/Average	5.55%	2.90%	1.38%	0.52%	0.38%	0.35%	0.38%	0.30%	0.17%	0.14%	0.11%	0.12%

Speed6

Measured Pressure Value

L/D_{inlet}	0.25	0.5	1	2	2.25	2.5	2.75	3	3.5	4	4.5	4.75
Average	3.133376625	2.16631775	2.0954125	1.82840415	1.605632775	2.0528908	2.070804375	2.087295525	1.5977502	1.5349969	1.5086735	1.5365075
Standard Deviation	4.290251333	2.941084018	2.806081375	2.383409018	2.212595882	2.841200284	2.865723105	2.950820261	2.112533071	1.985008391	1.982912576	2.050563238
Standard Error	0.678348297	0.465026214	0.443680422	0.376850055	0.349842126	0.449233209	0.453110608	0.46656565	0.334020807	0.313857385	0.313526007	0.324222516
95%CI	1.329562663	0.91145138	0.869613627	0.738626107	0.685690568	0.88049709	0.888096791	0.914468673	0.654680782	0.615160474	0.614510974	0.635476131
95%CI/Average	42.43%	42.07%	41.50%	40.40%	42.71%	42.89%	42.89%	43.81%	40.98%	40.08%	40.73%	41.36%

C_p

Average	-0.021491375	0.062979459	0.110361973	0.228569702	0.272825946	0.350149708	0.393515037	0.421943461	0.469808314	0.488119122	0.511022514	0.494531515
Standard Deviation	0.004264494	0.002923427	0.002789234	0.0023691	0.002199312	0.002824142	0.002848518	0.002933104	0.00209985	0.001973091	0.001971008	0.002038252
Standard Error	0.000674276	0.000462234	0.000441017	0.000374588	0.000347742	0.000446536	0.00045039	0.000463765	0.000332015	0.000311973	0.000311644	0.000322276
95%CI	0.00132158	0.000905979	0.000864393	0.000734192	0.000681574	0.000875211	0.000882765	0.000908978	0.00065075	0.000611467	0.000610822	0.000631661
95%CI/Average	6.15%	1.44%	0.78%	0.32%	0.25%	0.25%	0.22%	0.22%	0.14%	0.13%	0.12%	0.13%

Speed8

Measured Pressure Value

L/D_{inlet}	0.25	0.5	1	2	2.25	2.5	2.75	3	3.5	4	4.5	4.75
Average	3.4314325	2.138584	1.560663	1.2646024	1.182191075	2.0643705	1.3793313	1.4835382	1.0472425	1.026349	0.921394675	0.9352968
Standard Deviation	4.301378455	2.693266407	1.897277159	1.665249095	1.450535201	2.628930747	1.899904667	2.018196604	1.327871545	1.260096459	1.12205108	1.153603192
Standard Error	0.68010765	0.42584281	0.299985859	0.263299001	0.229349753	0.415670449	0.300401304	0.319104902	0.209954926	0.199238744	0.177411853	0.18240068
95%CI	1.333010994	0.834651907	0.587972283	0.516066041	0.449525516	0.814714079	0.588786556	0.625445607	0.411511655	0.390507938	0.347727232	0.357505333
95%CI/Average	38.85%	39.03%	37.67%	40.81%	38.02%	39.47%	42.69%	42.16%	39.29%	38.05%	37.74%	38.22%

C_p

Average	-0.008711765	0.068464248	0.118943409	0.23567358	0.280370827	0.357367872	0.398770956	0.429865301	0.473637448	0.494924623	0.513920866	0.503611458
Standard Deviation	0.003290209	0.002060132	0.001451264	0.001273782	0.001109543	0.002010921	0.001453274	0.001543758	0.001015715	0.000963872	0.000858279	0.000882414
Standard Error	0.000520228	0.000325735	0.000229465	0.000201403	0.000175434	0.000317954	0.000229783	0.00024409	0.000160599	0.000152402	0.000135706	0.000139522
95%CI	0.001019646	0.000638442	0.000449752	0.000394749	0.000343851	0.000623191	0.000450374	0.000478416	0.000314773	0.000298707	0.000265983	0.000273463
95%CI/Average	11.70%	0.93%	0.38%	0.17%	0.12%	0.17%	0.11%	0.11%	0.07%	0.06%	0.05%	0.05%

Speed10

Measured Pressure Value

L/D_{inlet}	0.25	0.5	1	2	2.25	2.5	2.75	3	3.5	4	4.5	4.75
Average	3.364297	2.304643	2.2904915	2.144578	1.8869285	2.132506	1.6336182	1.5750956	1.308955875	1.284967925	1.3417258	1.419358175
Standard Deviation	4.149610033	2.934235343	2.957674321	2.615790232	2.307898028	2.510160419	2.017912943	1.912845013	1.631678493	1.636513191	1.715210684	1.747458079
Standard Error	0.656110955	0.463943344	0.467649372	0.413592751	0.364910719	0.396891211	0.319060051	0.302447353	0.257991022	0.258755455	0.271198621	0.276297382
95%CI	1.285977472	0.909328954	0.916592768	0.810641791	0.715225009	0.777906773	0.6253577	0.592796811	0.505662404	0.507160692	0.531549298	0.541542869
95%CI/Average	38.22%	39.46%	40.02%	37.80%	37.90%	36.48%	38.28%	37.64%	38.63%	39.47%	39.62%	38.15%

C_p

Average	-0.007336235	0.067687812	0.117183711	0.234708591	0.279876999	0.357339535	0.398001705	0.430154099	0.472690001	0.495153296	0.512841595	0.504457631
Standard Deviation	0.002858307	0.002021141	0.002037286	0.001801791	0.001589711	0.001729032	0.001389965	0.001317593	0.001123922	0.001127252	0.00118146	0.001203673
Standard Error	0.000451938	0.00031957	0.000322123	0.000284888	0.000251355	0.000273384	0.000219773	0.00020833	0.000177708	0.000178234	0.000186805	0.000190317
95%CI	0.000885799	0.000626358	0.000631361	0.000558381	0.000492657	0.000535833	0.000430755	0.000408326	0.000348307	0.000349339	0.000366138	0.000373022
95%CI/Average	12.07%	0.93%	0.54%	0.24%	0.18%	0.15%	0.11%	0.09%	0.07%	0.07%	0.07%	0.07%

Table 8: Statistical Parameters for Type1 C_p Experimental Data at 180°

180°

Speed2

Measured Pressure Value

L/D_{inlet}	0.25	0.5	1	1.625	2	2.25	2.5	2.75	3	3.25	3.5	4	4.5	4.75
Average	-338.18598	-345.6997825	-321.1100075	-284.6354	-257.1581585	-215.8789175	-206.248398	-178.7994705	-174.7181885	-157.487943	-180.2147315	-142.9881625	-149.715842	-136.8765255
Standard Deviation	1.682193288	1.83307929	1.59950022	1.310465029	1.39020038	1.195859538	2.003581741	1.574369286	1.252445402	1.179765314	0.927371867	2.332156984	2.275243874	2.164391466
Standard Error	0.265978113	0.289835284	0.252903191	0.207202714	0.21980998	0.189081995	0.316794089	0.248929641	0.198029006	0.186537275	0.146630367	0.368746397	0.359747644	0.342220339
95%CI	0.521317101	0.568077158	0.495690254	0.40611732	0.430827561	0.370600711	0.620916414	0.487902097	0.388136851	0.365613059	0.287395519	0.722742937	0.705105382	0.670751865
95%CI/Average	0.00154151	0.001643267	0.001543677	0.001426798	0.001675341	0.001716706	0.003010527	0.002728767	0.002221502	0.00232153	0.001594739	0.51%	0.47%	0.49%

C_p

Average	-0.021207019	-0.043896155	0.03035663	0.14049758	0.223469535	0.348118849	0.377199754	0.46008621	0.472410298	0.524439799	0.455812601	0.56822422	0.547908909	0.586679292
Standard Deviation	0.005079653	0.005535278	0.004829948	0.00395716	0.004197934	0.00361109	0.006050138	0.004754062	0.003781961	0.003562491	0.002800349	0.007042324	0.006870465	0.006535729
Standard Error	0.000803164	0.000875204	0.000763682	0.000625682	0.000663752	0.000570964	0.000956611	0.000751683	0.00059798	0.000563279	0.000442774	0.001113489	0.001086316	0.001033389
95%CI	0.001574201	0.0017154	0.001496817	0.001226337	0.001300953	0.001119089	0.001874957	0.001473299	0.001172042	0.001104027	0.000867837	0.002182439	0.002129179	0.002025443
95%CI/Average	0.074230184	0.039078603	0.049307731	0.008728525	0.005821613	0.003214674	0.004970727	0.003202224	0.002480983	0.002105156	0.001903934	0.38%	0.39%	0.35%

Speed4

Measured Pressure Value

L/D_{inlet}	0.25	0.5	1	1.625	2	2.25	2.5	2.75	3	3.25	3.5	4	4.5	4.75
Average	-601.1037725	-600.179632	-563.5162275	-497.1313045	-456.941643	-384.3771085	-354.3621965	-318.5628385	-304.979668	-284.111599	-302.99594	-259.0244915	-264.5373665	-252.7957485
Standard Deviation	5.876958499	5.662102235	5.567126701	4.66972564	4.443306223	3.8847148	4.02668482	3.871218725	3.521007548	3.280849764	2.974674418	2.204945647	2.231361805	1.917847279
Standard Error	0.929228729	0.89525697	0.88024002	0.738348454	0.7025484	0.614227341	0.636674773	0.612093425	0.556720176	0.518747896	0.470337323	0.348632518	0.352809279	0.30323828
95%CI	1.821288308	1.754703662	1.725270439	1.447162969	1.376994865	1.203885589	1.247882554	1.199703112	1.091171544	1.016745876	0.921861153	0.683319736	0.691506188	0.594347029
95%CI/Average	0.30%	0.29%	0.31%	0.29%	0.30%	0.31%	0.35%	0.38%	0.36%	0.36%	0.30%	0.26%	0.26%	0.24%

C_p

Average	-0.00433036	-0.002786297	0.058471296	0.169387908	0.236537207	0.357778777	0.407928001	0.467741936	0.490436837	0.525303421	0.49375127	0.567219218	0.55800825	0.577626266
Standard Deviation	0.009819283	0.009460299	0.009301613	0.007802226	0.007423922	0.006490621	0.006727826	0.006468072	0.005882936	0.005481678	0.004970117	0.003684046	0.003728182	0.003204359
Standard Error	0.001552565	0.001495805	0.001470714	0.00123364	0.001173825	0.001026257	0.001063763	0.001022692	0.000930174	0.000866729	0.000785844	0.000582499	0.000589477	0.000506654
95%CI	0.003043027	0.002931777	0.0028826	0.002417935	0.002300697	0.002011464	0.002084975	0.002004476	0.001823141	0.001698789	0.001540255	0.001141698	0.001155376	0.000993041
95%CI/Average	70.27%	105.22%	4.93%	1.43%	0.97%	0.56%	0.51%	0.43%	0.37%	0.32%	0.31%	0.20%	0.21%	0.17%

Speed6

Measured Pressure Value

L/D_{inlet}	0.25	0.5	1	1.625	2	2.25	2.5	2.75	3	3.25	3.5	4	4.5	4.75
Average	-1005.374856	-1011.736358	-949.035986	-837.043337	-774.432973	-653.815886	-592.8851765	-542.0676325	-511.0043695	-484.876481	-499.6856055	-467.7268425	-471.5165675	-463.428712
Standard Deviation	2.078339927	1.938396226	1.619623598	1.622505161	2.715513529	2.257002169	5.673647178	4.273849611	4.259100937	4.028082587	2.886541658	1.96344318	1.742920027	1.510834313
Standard Error	0.328614396	0.306487354	0.256084976	0.256540591	0.429360389	0.356863377	0.897082386	0.675754957	0.673422987	0.636895779	0.45640231	0.310447625	0.275579853	0.23888388
95%CI	0.644084216	0.600715214	0.501926553	0.502819559	0.841546361	0.699452219	1.758281477	1.324479717	1.319909055	1.248315727	0.894548528	0.608477345	0.540136512	0.468212404
95%CI/Average	0.06%	0.06%	0.05%	0.06%	0.11%	0.11%	0.30%	0.24%	0.26%	0.26%	0.18%	0.13%	0.11%	0.10%

C_p

Average	0.000661151	-0.005662159	0.056661777	0.167982051	0.230216519	0.350109453	0.41067435	0.461186799	0.492063567	0.51803459	0.503314376	0.535081267	0.531314294	0.539353592
Standard Deviation	0.002065862	0.001926759	0.0016099	0.001612764	0.00269921	0.002243452	0.005639584	0.004248191	0.00423353	0.004003899	0.002869212	0.001951655	0.001732456	0.001501764
Standard Error	0.000326641	0.000304647	0.000254548	0.000255	0.000426783	0.000354721	0.000891697	0.000671698	0.00066938	0.000633072	0.000453662	0.000308584	0.000273925	0.00023745
95%CI	0.000640217	0.000597109	0.000498913	0.000499801	0.000836494	0.000695253	0.001747725	0.001316528	0.001311985	0.001240821	0.000889178	0.000604824	0.000536894	0.000465401
95%CI/Average	96.83%	10.55%	0.88%	0.30%	0.36%	0.20%	0.43%	0.29%	0.27%	0.24%	0.18%	0.11%	0.10%	0.09%

Speed8

Measured Pressure Value

L/D_{inlet}	0.25	0.5	1	1.625	2	2.25	2.5	2.75	3	3.25	3.5	4	4.5	4.75
Average	-1312.62853	-1323.890675	-1237.71436	-1092.06455	-1014.429653	-855.7063465	-771.3749555	-707.707619	-663.1136615	-633.6988375	-645.253182	-609.183871	-611.486256	-605.7951235
Standard Deviation	3.352645494	3.281245776	3.314274531	2.419896123	2.59616219	2.12329824	4.420215318	3.772442572	3.122824667	2.729239155	1.951018534	2.720468664	2.232345258	1.953296028
Standard Error	0.530099797	0.518810511	0.524032815	0.382619173	0.410489285	0.33572293	0.698897408	0.596475543	0.493761934	0.4315306	0.308483116	0.430143864	0.352964777	0.30884322
95%CI	1.038995603	1.016868601	1.027104318	0.749933578	0.804558998	0.658016942	1.369838919	1.169092065	0.967773391	0.845799977	0.604626908	0.843081974	0.691810963	0.605332711
95%CI/Average	0.08%	0.08%	0.08%	0.07%	0.08%	0.08%	0.18%	0.17%	0.15%	0.13%	0.09%	0.14%	0.11%	0.10%

C_p

Average	-0.004055244	-0.012669879	0.05324807	0.16465846	0.224042911	0.345453474	0.409960205	0.458660596	0.492771387	0.515271361	0.506433217	0.534023338	0.532262199	0.536615458
Standard Deviation	0.002564504	0.002509889	0.002535153	0.001851026	0.001985855	0.001624152	0.003381109	0.002885615	0.00238871	0.002087648	0.001492372	0.0020804	0.001707565	0.001494114
Standard Error	0.000405484	0.000396848	0.000400843	0.000292673	0.000313991	0.000256801	0.0005346	0.000456256	0.000377688	0.000330086	0.000235965	0.000329025	0.00026999	0.00023624
95%CI	0.000794748	0.000777823	0.000785652	0.000573639	0.000615423	0.00050333	0.001047817	0.000894261	0.000740269	0.000646969	0.000462491	0.00064489	0.00052918	0.000463031
95%CI/Average	19.60%	6.14%	1.48%	0.35%	0.27%	0.15%	0.26%	0.19%	0.15%	0.13%	0.09%	0.12%	0.10%	0.09%

Speed10

Measured Pressure Value

L/D_{inlet}	0.25	0.5	1	1.625	2	2.25	2.5	2.75	3	3.25	3.5	4	4.5	4.75
Average	-1475.963095	-1485.82489	-1387.781945	-1224.438765	-1139.930555	-961.5223055	-864.7637035	-794.462884	-742.3677895	-711.348713	-721.270391	-673.329577	-674.988278	-670.1327655
Standard Deviation	3.227846444	3.206984184	3.223015147	2.88924558	2.851293893	2.284685554	5.129137214	3.704084117	3.038586479	2.733635315	2.201373196	2.993749596	2.992148557	2.834484676
Standard Error	0.510367335	0.507068722	0.50960344	0.456829838	0.450829149	0.361240504	0.810987801	0.585667123	0.480442707	0.432225694	0.348067664	0.473353373	0.473100227	0.448171379
95%CI	1.000319977	0.993854695	0.998822742	0.895386482	0.883625132	0.708031389	1.589536091	1.14790756	0.941667706	0.847162361	0.682212621	0.927772612	0.927276445	0.878415902
95%CI/Average	0.07%	0.07%	0.07%	0.07%	0.08%	0.07%	0.18%	0.14%	0.13%	0.12%	0.09%	0.14%	0.14%	0.13%

C_p

Average	-0.01666315	-0.023456087	0.044077207	0.156590177	0.214800564	0.337690556	0.404339178	0.452763324	0.488647123	0.510013478	0.503179293	0.536201568	0.535059033	0.538403575
Standard Deviation	0.002223384	0.002209014	0.002220056	0.001990151	0.001964009	0.001573722	0.003533018	0.002551423	0.002093019	0.001882965	0.001516335	0.002062135	0.002061032	0.001952431
Standard Error	0.000351548	0.000349276	0.000351022	0.000314671	0.000310537	0.000248827	0.000558619	0.000403415	0.000330935	0.000297723	0.000239754	0.000326052	0.000325878	0.000308706
95%CI	0.000689034	0.00068458	0.000688002	0.000616754	0.000608653	0.000487702	0.001094894	0.000790694	0.000648633	0.000583537	0.000469917	0.000639062	0.00063872	0.000605065
95%CI/Average	4.14%	2.92%	1.56%	0.39%	0.28%	0.14%	0.27%	0.17%	0.13%	0.11%	0.09%	0.12%	0.12%	0.11%

Table 9: Statistical Parameters for Type2 C_p Experimental Data at 0°

0°

Speed2

Measured Pressure Value

L/D_{inlet}	0.25	0.5	1	1.625	2	2.25	2.5	2.75	3	3.25	3.5	4	4.5	4.75
Average	-239.591436	-231.31702	-223.39484	-170.731082	-176.150276	-166.772528	-173.162334	-180.9809	-214.174952	-231.14038	-235.056192	-198.617732	-175.688206	-162.254192
Standard Deviation	1.491072583	1.342403013	1.379270158	0.844130534	0.828080028	0.742000668	0.775099898	0.935404844	1.34504561	1.719552676	1.763246622	1.022121326	0.95684377	0.90117257
Standard Error	0.471518552	0.424505106	0.436163521	0.266937513	0.261861897	0.234641214	0.245108109	0.295800984	0.425340768	0.543770301	0.55758754	0.323223143	0.302580568	0.284975789
95%CI	0.924176361	0.832030007	0.854880501	0.523197526	0.513249319	0.459896779	0.480411894	0.579769929	0.833667906	1.06578979	1.092871579	0.633517361	0.593057913	0.558552546
95%CI/Average	-0.39%	-0.36%	-0.38%	-0.31%	-0.29%	-0.28%	-0.28%	-0.32%	-0.39%	-0.46%	-0.46%	-0.32%	-0.34%	-0.34%

C_p

Average	0.031879474	0.065314024	0.09732529	0.310124486	0.288227072	0.326119872	0.300300492	0.268707901	0.134580222	0.066027776	0.050205099	0.197442503	0.290094165	0.344377176
Standard Deviation	0.006024998	0.005424267	0.005573237	0.00341089	0.003346035	0.002998213	0.003131957	0.003779704	0.005434945	0.006948221	0.007124776	0.0041301	0.003866332	0.003641381
Standard Error	0.001905272	0.001715304	0.001762412	0.001078618	0.001058109	0.000948118	0.000990412	0.001195247	0.00171868	0.00219722	0.002253052	0.001306052	0.001222642	0.001151506
95%CI	0.003734333	0.003361995	0.003454328	0.002114092	0.002073894	0.001858311	0.001941207	0.002342685	0.003368614	0.004306552	0.004415982	0.002559863	0.002396378	0.002256951
95%CI/Average	11.71%	5.15%	3.55%	0.68%	0.72%	0.57%	0.65%	0.87%	2.50%	6.52%	8.80%	1.30%	0.83%	0.66%

Speed4

Measured Pressure Value

L/D_{inlet}	0.25	0.5	1	1.625	2	2.25	2.5	2.75	3	3.25	3.5	4	4.5	4.75
Average	-444.08444	-420.557422	-401.481766	-326.809938	-326.954076	-305.984974	-323.313526	-346.15572	-402.283218	-433.517822	-435.69548	-382.966532	-339.645828	-313.799776
Standard Deviation	2.170341034	1.920137725	2.21126197	1.574500997	1.5424461	1.473120576	1.682953698	1.779657034	2.076983529	2.786759224	3.008050077	2.592759618	2.22646455	2.177465292
Standard Error	0.686322097	0.607200863	0.699262433	0.497900933	0.487764284	0.465841629	0.532196688	0.562776968	0.656799862	0.881250644	0.951228956	0.819902582	0.704069911	0.688574985
95%CI	1.345191309	1.190113692	1.370554368	0.975885829	0.956017998	0.913049593	1.043105509	1.103042857	1.287327729	1.727251262	1.864408753	1.60700906	1.379977025	1.34960697
95%CI/Average	-0.30%	-0.28%	-0.34%	-0.30%	-0.29%	-0.30%	-0.32%	-0.32%	-0.32%	-0.40%	-0.43%	-0.42%	-0.41%	-0.43%

C_p

Average	0.086437744	0.134837088	0.174079173	0.327692669	0.327396151	0.370533398	0.334885423	0.287894886	0.172430441	0.108175194	0.103695356	0.212168368	0.301286915	0.354456933
Standard Deviation	0.004464785	0.003950072	0.004548967	0.003239034	0.003173091	0.003030476	0.003462141	0.003661077	0.004272732	0.005732869	0.006188105	0.005333777	0.004580241	0.004479441
Standard Error	0.001411889	0.001249122	0.00143851	0.001024273	0.00100342	0.000958321	0.001094825	0.001157734	0.001351156	0.001812892	0.001956851	0.001686688	0.0014484	0.001416524
95%CI	0.002767303	0.00244828	0.002819479	0.002007574	0.001966702	0.001878309	0.002145857	0.002269159	0.002648267	0.003553269	0.003835427	0.003305909	0.002838863	0.002776386
95%CI/Average	3.20%	1.82%	1.62%	0.61%	0.60%	0.51%	0.64%	0.79%	1.54%	3.28%	3.70%	1.56%	0.94%	0.78%

Speed6

Measured Pressure Value

L/D_{inlet}	0.25	0.5	1	1.625	2	2.25	2.5	2.75	3	3.25	3.5	4	4.5	4.75
Average	-783.386472	-734.81311	-700.80909	-586.94387	-576.37803	-537.744826	-571.121022	-619.729028	-715.891228	-775.336688	-771.597292	-682.644426	-606.532008	-560.326222
Standard Deviation	2.943333852	2.554381769	2.800768677	2.085334243	2.131410102	2.246766731	2.766235089	3.467715009	4.708894919	5.854986814	5.956491601	42.30814415	37.65861968	34.80704253
Standard Error	0.930763889	0.80776644	0.885680822	0.659440589	0.674011055	0.710490024	0.874760342	1.096587777	1.489083321	1.8515094	1.883608032	13.37900991	11.90870117	11.0069533
95%CI	1.824297222	1.583222223	1.735934411	1.292503555	1.321061668	1.392560447	1.714530271	2.14931203	2.918603308	3.628958425	3.691871743	26.22285942	23.3410543	21.57362847
95%CI/Average	-0.23%	-0.22%	-0.25%	-0.22%	-0.23%	-0.26%	-0.30%	-0.35%	-0.41%	-0.47%	-0.48%	-3.84%	-3.85%	-3.85%

C_p

Average	0.104616241	0.160133921	0.198999345	0.32914337	0.341219761	0.385376183	0.347228341	0.291671064	0.181760981	0.113816867	0.118090868	0.21976093	0.306754803	0.359566425
Standard Deviation	0.003364129	0.00291957	0.003201182	0.002383465	0.002436128	0.002567977	0.003161711	0.003963479	0.005382105	0.006692048	0.006808065	0.048356752	0.043042505	0.039783251
Standard Error	0.001063831	0.000923249	0.001012303	0.000753718	0.000770371	0.000812066	0.000999821	0.001253362	0.001701971	0.002116211	0.002152899	0.015291748	0.013611235	0.012580569
95%CI	0.002085109	0.001809568	0.001984113	0.001477287	0.001509928	0.001591649	0.001959649	0.00245659	0.003335863	0.004147775	0.004219682	0.029971825	0.026678021	0.024657914
95%CI/Average	1.99%	1.13%	1.00%	0.45%	0.44%	0.41%	0.56%	0.84%	1.84%	3.64%	3.57%	13.64%	8.70%	6.86%

Speed8

Measured Pressure Value

L/D_{inlet}	0.25	0.5	1	1.625	2	2.25	2.5	2.75	3	3.25	3.5	4	4.5	4.75
Average	-1063.74402	-994.516416	-948.22565	-802.208552	-782.053214	-730.177594	-775.214756	-843.585664	-972.20732	-1054.08144	-1043.81486	-901.348678	-802.986484	-740.793824
Standard Deviation	1.966456166	1.78894436	1.967720169	1.476594315	1.617928342	1.546924049	1.776285995	1.724204373	1.678800556	2.438786926	2.558102922	3.004628887	2.508739395	2.525953742
Standard Error	0.62184804	0.565713878	0.622247753	0.466940121	0.511633865	0.489180336	0.561710952	0.545241297	0.530883349	0.771212141	0.808943172	0.950147081	0.793333055	0.798776709
95%CI	1.218822159	1.108799202	1.219605596	0.915202638	1.002802376	0.958793459	1.100953466	1.068672942	1.040531365	1.511575797	1.585528618	1.862288278	1.554932787	1.56560235
95%CI/Average	-0.11%	-0.11%	-0.13%	-0.11%	-0.13%	-0.13%	-0.14%	-0.13%	-0.11%	-0.14%	-0.15%	-0.21%	-0.19%	-0.21%

C_p

Average	0.096515976	0.155313989	0.194630748	0.318649415	0.335768219	0.379828438	0.341576419	0.283506035	0.174262073	0.104722825	0.113442678	0.234445397	0.317988683	0.370811612
Standard Deviation	0.001670197	0.001519428	0.00167127	0.001254136	0.001374177	0.00131387	0.001508677	0.001464442	0.001425878	0.002071368	0.002172708	0.002551962	0.002130781	0.002145402
Standard Error	0.000528163	0.000480485	0.000528502	0.000396593	0.000434553	0.000415482	0.000477086	0.000463097	0.000450902	0.000655024	0.000687071	0.000807001	0.000673812	0.000678436
95%CI	0.001035199	0.000941751	0.001035864	0.000777321	0.000851724	0.000814345	0.000935088	0.00090767	0.000883769	0.001283847	0.001346658	0.001581722	0.001320672	0.001329734
95%CI/Average	1.07%	0.61%	0.53%	0.24%	0.25%	0.21%	0.27%	0.32%	0.51%	1.23%	1.19%	0.67%	0.42%	0.36%

Speed10

Measured Pressure Value

L/D_{inlet}	0.25	0.5	1	1.625	2	2.25	2.5	2.75	3	3.25	3.5	4	4.5	4.75
Average	-1138.70678	-1064.01508	-1013.735894	-859.654556	-837.11991	-781.623206	-829.976868	-904.102878	-1042.17628	-1130.68276	-1118.32366	-1007.395284	-901.071148	-829.892744
Standard Deviation	1.897236173	1.898414216	2.008400096	1.656027235	1.671962296	1.618531388	1.739101331	1.523819795	1.890060119	3.041355895	3.1557278	3.881078836	2.810506418	2.989875547
Standard Error	0.599958757	0.600331286	0.635111876	0.523681793	0.528720902	0.511824565	0.549952129	0.481874129	0.597689489	0.96176118	0.997928752	1.22730489	0.888760166	0.945481665
95%CI	1.175919163	1.176649321	1.244819277	1.026416314	1.036292967	1.003176148	1.077906172	0.944473294	1.171471399	1.885051913	1.955940355	2.405517585	1.741969925	1.853144063
95%CI/Average	-0.10%	-0.11%	-0.12%	-0.12%	-0.12%	-0.13%	-0.13%	-0.10%	-0.11%	-0.17%	-0.17%	-0.24%	-0.19%	-0.22%

C_p

Average	0.14105244	0.197393769	0.235320288	0.351546688	0.368544988	0.410407177	0.373933116	0.318018497	0.21386718	0.147105107	0.156427804	0.240103127	0.320305387	0.373996572
Standard Deviation	0.00143112	0.001432009	0.001514973	0.001249172	0.001261192	0.001220888	0.001311836	0.001149445	0.001425707	0.002294151	0.002380424	0.002927569	0.002120017	0.002255318
Standard Error	0.00045256	0.000452841	0.000479077	0.000395023	0.000398824	0.000386079	0.000414839	0.000363487	0.000450848	0.000725474	0.000752756	0.000925779	0.000670408	0.000713194
95%CI	0.000887018	0.000887568	0.00093899	0.000774245	0.000781695	0.000756714	0.000813085	0.000712434	0.000883663	0.001421929	0.001475402	0.001814526	0.001314	0.001397861
95%CI/Average	0.63%	0.45%	0.40%	0.22%	0.21%	0.18%	0.22%	0.22%	0.41%	0.97%	0.94%	0.76%	0.41%	0.37%

Table 10: Statistical Parameters for Type2 C_p Experimental Data at 60°

60°

Speed2

Measured Pressure Value

L/D_{inlet}	0.25	0.5	1	1.625	2	2.25	2.5	2.75	3	3.5	4	4.5	4.75
Average	-235.881106	-221.724308	-199.043684	-187.240342	-179.838026	-186.631822	-179.700138	-188.111	-196.230844	-184.64124	-179.330564	-160.875822	-151.177396
Standard Deviation	1.415468684	1.394545925	1.288176292	1.216590938	1.198842791	1.449791572	1.187288075	1.278071784	1.480025701	1.244118139	1.252632595	1.119123192	1.051244108
Standard Error	0.4476105	0.440994143	0.407357111	0.384719834	0.379107377	0.45846435	0.375453456	0.404161785	0.468025221	0.3934247	0.396117207	0.353897827	0.332432576
95%CI	0.87731658	0.864348519	0.798419938	0.754050875	0.74305046	0.898590126	0.735888773	0.792157099	0.917329434	0.771112412	0.776389726	0.693639741	0.651567848
95%CI/Average	0.37%	0.39%	0.40%	0.40%	0.41%	0.48%	0.41%	0.42%	0.47%	0.42%	0.43%	0.43%	0.43%

C_p

Average	0.046871857	0.104075432	0.195721352	0.243415284	0.273325928	0.24587414	0.273883094	0.239897204	0.207087235	0.253917513	0.275376437	0.349946776	0.389135344
Standard Deviation	0.005719504	0.005634962	0.005205152	0.004915896	0.004844181	0.005858193	0.004797492	0.005164323	0.005980361	0.005027126	0.00506153	0.004522057	0.004247777
Standard Error	0.001808666	0.001781931	0.001646014	0.001554543	0.001531865	0.001852523	0.0015171	0.001633102	0.001891156	0.001589717	0.001600596	0.00143	0.001343265
95%CI	0.003544986	0.003492585	0.003226187	0.003046904	0.003002455	0.003630946	0.002973516	0.00320088	0.003706666	0.003115845	0.003137169	0.0028028	0.002632799
95%CI/Average	7.56%	3.36%	1.65%	1.25%	1.10%	1.48%	1.09%	1.33%	1.79%	1.23%	1.14%	0.80%	0.68%

Speed4

Measured Pressure Value

L/D_{inlet}	0.25	0.5	1	1.625	2	2.25	2.5	2.75	3	3.5	4	4.5	4.75
Average	-462.396952	-433.346372	-390.801626	-367.061626	-351.95454	-368.634174	-350.55241	-366.594184	-385.491792	-361.697568	-349.005248	-310.737314	-292.130654
Standard Deviation	2.856221919	2.609079731	2.283031961	2.206361961	2.064224692	2.438606159	2.050095663	2.19687271	2.530796448	2.47061666	2.43328559	1.812564203	1.58082574
Standard Error	0.903216677	0.825063455	0.721958097	0.697712914	0.652765163	0.771154978	0.648297172	0.694712149	0.800308107	0.781277587	0.769472466	0.573183129	0.499900992
95%CI	1.770304686	1.617124371	1.41503787	1.367517311	1.279419719	1.511463756	1.270662456	1.361635813	1.56860389	1.53130407	1.508166034	1.123438932	0.979805945
95%CI/Average	0.38%	0.37%	0.36%	0.37%	0.36%	0.41%	0.36%	0.37%	0.41%	0.42%	0.43%	0.36%	0.34%

C_p

Average	0.048765584	0.108527897	0.196050158	0.244887645	0.275965662	0.241652628	0.278850097	0.245849258	0.20697345	0.255922485	0.28203289	0.360756973	0.399034248
Standard Deviation	0.005875767	0.00536735	0.004696611	0.004538887	0.004246485	0.005016655	0.004217419	0.004519366	0.005206307	0.005082507	0.00500571	0.003728773	0.003252045
Standard Error	0.001858081	0.001697305	0.001485199	0.001435322	0.001342856	0.001586406	0.001333665	0.001429149	0.001646379	0.00160723	0.001582944	0.001179142	0.001028387
95%CI	0.003641838	0.003326718	0.00291099	0.002813231	0.002631998	0.003109355	0.002613983	0.002801132	0.003226903	0.00315017	0.003102571	0.002311118	0.002015639
95%CI/Average	7.47%	3.07%	1.48%	1.15%	0.95%	1.29%	0.94%	1.14%	1.56%	1.23%	1.10%	0.64%	0.51%

Speed6

Measured Pressure Value

L/D_{inlet}	0.25	0.5	1	1.625	2	2.25	2.5	2.75	3	3.5	4	4.5	4.75
Average	-820.3187956	-767.0610644	-693.6082133	-650.5073089	-622.2070956	-658.3146067	-619.3474644	-646.0298222	-684.0083867	-639.3185889	-613.72974	-544.0329644	-512.3837533
Standard Deviation	3.482501277	3.043752407	2.594654454	2.103344384	2.174644789	1.90236299	2.413031613	2.486528382	2.118347924	2.682527928	3.477040256	3.205683751	2.771425521
Standard Error	1.160833759	1.014584136	0.864884818	0.701114795	0.724881596	0.634120997	0.804343871	0.828842794	0.706115975	0.894175976	1.159013419	1.06856125	0.923808507
95%CI	2.275234167	1.988584906	1.695174243	1.374184998	1.420767929	1.242877153	1.576513987	1.624531876	1.38398731	1.752584913	2.2716663	2.094380051	1.810664673
95%CI/Average	0.28%	0.26%	0.24%	0.21%	0.23%	0.19%	0.25%	0.25%	0.20%	0.27%	0.37%	0.38%	0.35%

C_p

Average	0.062403867	0.12327562	0.207229699	0.256492549	0.288838718	0.247569076	0.292107178	0.261610162	0.21820197	0.26928087	0.298528043	0.378189057	0.414363016
Standard Deviation	0.003980379	0.003478904	0.002965601	0.00240405	0.002485544	0.002174335	0.002758012	0.002842016	0.002421199	0.003066037	0.003974137	0.003663986	0.003167644
Standard Error	0.001326793	0.001159635	0.000988534	0.00080135	0.000828515	0.000724778	0.000919337	0.000947339	0.000807066	0.001022012	0.001324712	0.001221329	0.001055881
95%CI	0.002600514	0.002272884	0.001937526	0.001570646	0.001623889	0.001420566	0.001801901	0.001856784	0.00158185	0.002003144	0.002596436	0.002393804	0.002069527
95%CI/Average	4.17%	1.84%	0.93%	0.61%	0.56%	0.57%	0.62%	0.71%	0.72%	0.74%	0.87%	0.63%	0.50%

Speed8

Measured Pressure Value

L/D_{inlet}	0.25	0.5	1	1.625	2	2.25	2.5	2.75	3	3.5	4	4.5	4.75
Average	-1115.97486	-1042.26968	-943.031446	-883.095582	-844.07266	-898.181284	-839.988392	-875.060264	-929.81542	-867.654764	-831.604538	-735.124928	-691.708556
Standard Deviation	3.582945547	3.632377074	3.22760738	3.12288021	3.397968715	2.811158603	3.224447441	2.883489914	2.548575677	2.45347945	2.366229212	3.068919756	2.965941903
Standard Error	1.133026866	1.148658488	1.020659072	0.987541432	1.074532056	0.888966405	1.019659811	0.911839574	0.805930393	0.775858325	0.748267377	0.970477638	0.937913182
95%CI	2.220732657	2.251370636	2.00049178	1.935581207	2.10608283	1.742374154	1.99853323	1.787205565	1.57962357	1.520682318	1.46660406	1.902136171	1.838309837
95%CI/Average	0.20%	0.22%	0.21%	0.22%	0.25%	0.19%	0.24%	0.20%	0.17%	0.18%	0.18%	0.26%	0.27%

C_p

Average	0.052154054	0.114755066	0.199042411	0.249948545	0.283092409	0.237135603	0.286561355	0.25677329	0.210267356	0.263063103	0.293682126	0.375626452	0.412501863
Standard Deviation	0.003043151	0.003085136	0.002741347	0.002652398	0.002886042	0.002387639	0.002738663	0.002449073	0.002164616	0.002083847	0.002009741	0.002606567	0.002519103
Standard Error	0.000962329	0.000975606	0.00086689	0.000838762	0.000912647	0.000755038	0.000866041	0.000774465	0.000684512	0.00065897	0.000635536	0.000824269	0.00079661
95%CI	0.001886165	0.001912187	0.001699105	0.001643973	0.001788788	0.001479874	0.001697441	0.001517951	0.001341643	0.001291582	0.001245651	0.001615567	0.001561356
95%CI/Average	3.62%	1.67%	0.85%	0.66%	0.63%	0.62%	0.59%	0.59%	0.64%	0.49%	0.42%	0.43%	0.38%

Speed10

Measured Pressure Value

L/D_{inlet}	0.25	0.5	1	1.625	2	2.25	2.5	2.75	3	3.5	4	4.5	4.75
Average	-1251.3118	-1168.77916	-1057.99216	-989.81467	-945.03149	-1008.917198	-938.928962	-977.307644	-1041.37334	-972.615936	-930.877586	-821.30507	-773.32666
Standard Deviation	4.602994846	4.171807186	3.661234842	2.966875512	2.572395441	4.372948241	2.82939553	3.303803349	4.134014317	4.461148882	4.632969793	2.994336135	2.678473384
Standard Error	1.455594777	1.319241267	1.157784115	0.938208415	0.813462864	1.382847653	0.894733428	1.044754352	1.307290112	1.410739145	1.465073688	0.946892227	0.847007655
95%CI	2.852965763	2.585712883	2.269256865	1.838888494	1.594387213	2.7103814	1.753677518	2.047718531	2.56228862	2.765048724	2.871544428	1.855908764	1.660135003
95%CI/Average	0.23%	0.22%	0.21%	0.19%	0.17%	0.27%	0.19%	0.21%	0.25%	0.28%	0.31%	0.23%	0.21%

C_p

Average	0.056112393	0.118368288	0.201936969	0.253364509	0.287145289	0.23895512	0.291748539	0.26279879	0.214472852	0.266337832	0.297821841	0.380474414	0.416665414
Standard Deviation	0.003472124	0.003146871	0.002761737	0.002237969	0.001940405	0.003298596	0.002134265	0.00249212	0.003118363	0.003365127	0.003494735	0.002258683	0.002020422
Standard Error	0.001097982	0.000995128	0.000873338	0.000707708	0.00061361	0.001043108	0.000674914	0.000788078	0.000986113	0.001064147	0.001105132	0.000714258	0.000638914
95%CI	0.002152045	0.001950451	0.001711742	0.001387108	0.001202676	0.002044491	0.001322831	0.001544632	0.001932782	0.002085727	0.002166059	0.001399946	0.001252271
95%CI/Average	3.84%	1.65%	0.85%	0.55%	0.42%	0.86%	0.45%	0.59%	0.90%	0.78%	0.73%	0.37%	0.30%

Table 11: Statistical Parameters for Type2 C_p Experimental Data at 120°

120°

Speed2

Measured Pressure Value

L/D_{inlet}	0.25	0.5	1	2	2.25	2.5	2.75	3	3.5	4	4.5	4.75
Average	-235.881106	-221.724308	-199.043684	-187.240342	-179.838026	-186.631822	-179.700138	-188.111	-196.230844	-184.64124	-179.330564	-160.875822
Standard Deviation	1.415468684	1.394545925	1.288176292	1.216590938	1.198842791	1.449791572	1.187288075	1.278071784	1.480025701	1.244118139	1.252632595	1.119123192
Standard Error	0.4476105	0.440994143	0.407357111	0.384719834	0.379107377	0.45846435	0.375453456	0.404161785	0.468025221	0.3934247	0.396117207	0.353897827
95%CI	0.87731658	0.864348519	0.798419938	0.754050875	0.74305046	0.898590126	0.735888773	0.792157099	0.917329434	0.771112412	0.776389726	0.693639741
95%CI/Average	0.37%	0.39%	0.40%	0.40%	0.41%	0.48%	0.41%	0.42%	0.47%	0.42%	0.43%	0.43%

C_p

Average	-0.046874693	-0.007915969	0.069435884	0.184122248	0.248041579	0.324902833	0.373943244	0.410765618	0.435237606	0.451689261	0.456291691	0.480338596
Standard Deviation	0.011354426	0.011129816	0.010082182	0.008779575	0.00832003	0.007521934	0.007323331	0.006456064	0.006457633	0.005424256	0.005124825	0.004672204
Standard Error	0.003590585	0.003519557	0.003188266	0.002776346	0.002631025	0.002378644	0.002315841	0.002041587	0.002042083	0.0017153	0.001620612	0.001477481
95%CI	0.007037546	0.006898331	0.006249001	0.005441637	0.005156808	0.004662143	0.004539048	0.00400151	0.004002482	0.003361989	0.003176399	0.002895862
95%CI/Average	15.01%	87.14%	9.00%	2.96%	2.08%	1.43%	1.21%	0.97%	0.92%	0.74%	0.70%	0.60%

Speed4

Measured Pressure Value

L/D_{inlet}	0.25	0.5	1	2	2.25	2.5	2.75	3	3.5	4	4.5	4.75
Average	-509.807088	-488.02387	-451.708144	-392.04196	-363.754664	-325.740198	-305.355848	-287.463608	-273.809216	-260.093982	-259.294922	-250.2037
Standard Deviation	3.205962576	3.070432655	2.855582788	2.369295526	2.152904479	1.955001835	1.989556169	1.964523887	1.832791614	1.97542139	1.996009767	2.014848564
Standard Error	1.013814383	0.970956059	0.903014566	0.749237031	0.680808174	0.618225863	0.629152903	0.621237	0.579579598	0.624683093	0.631193709	0.63715106
95%CI	1.987076192	1.903073876	1.769908549	1.468504581	1.334384021	1.211722691	1.233139689	1.21762452	1.135976012	1.224378862	1.237139671	1.248816078
95%CI/Average	0.39%	0.39%	0.39%	0.37%	0.37%	0.37%	0.40%	0.42%	0.41%	0.47%	0.48%	0.50%

C_p

Average	-0.048765666	-0.003953635	0.070754401	0.193498566	0.251690666	0.329893319	0.371827625	0.408635208	0.43672477	0.464939494	0.466583306	0.485285598
Standard Deviation	0.006595247	0.006316437	0.005874452	0.004874071	0.004428915	0.004021793	0.004092878	0.004041382	0.003770385	0.0040638	0.004106154	0.004144909
Standard Error	0.0020856	0.001997433	0.001857665	0.001541316	0.001400546	0.001271803	0.001294282	0.001277997	0.0011923	0.001285086	0.00129848	0.001310735
95%CI	0.004087776	0.003914968	0.003641023	0.00302098	0.00274507	0.002492733	0.002536792	0.002504875	0.002336909	0.002518769	0.002545021	0.002569041
95%CI/Average	8.38%	99.02%	5.15%	1.56%	1.09%	0.76%	0.68%	0.61%	0.54%	0.54%	0.55%	0.53%

Speed6

Measured Pressure Value

L/D_{inlet}	0.25	0.5	1	2	2.25	2.5	2.75	3	3.5	4	4.5	4.75
Average	-912.41047	-868.477652	-804.16172	-694.25301	-646.250338	-577.96986	-543.381422	-510.935844	-484.84327	-456.02836	-455.726358	-441.838646
Standard Deviation	4.447885562	4.166273072	3.756007186	3.311003317	3.056630486	2.589736506	2.43000251	2.1907998	2.173085448	2.297878256	2.240291228	2.000799119
Standard Error	1.406544915	1.317491226	1.187753761	1.047031182	0.96659143	0.81894659	0.768434265	0.692791726	0.687189957	0.726652907	0.70844229	0.632708236
95%CI	2.756828033	2.582282803	2.327997372	2.052181117	1.894519203	1.605135316	1.50613116	1.357871784	1.346892315	1.424239699	1.388546889	1.240108142
95%CI/Average	0.30%	0.30%	0.29%	0.30%	0.29%	0.28%	0.28%	0.27%	0.28%	0.31%	0.30%	0.28%

C_p

Average	-0.042853745	0.007359953	0.080870848	0.206492719	0.26135812	0.339400355	0.378933748	0.416017926	0.44584084	0.47877529	0.479120467	0.494993644
Standard Deviation	0.00508378	0.004761907	0.004292987	0.003784363	0.003493623	0.00295998	0.002777409	0.002504009	0.002483762	0.002626396	0.002560576	0.002286844
Standard Error	0.001607632	0.001505847	0.001357562	0.001196721	0.001104781	0.000936028	0.000878294	0.000791837	0.000785434	0.000830539	0.000809725	0.000723164
95%CI	0.00315096	0.00295146	0.002660821	0.002345572	0.00216537	0.001834614	0.001721456	0.001552001	0.001539452	0.001627857	0.001587061	0.001417401
95%CI/Average	7.35%	40.10%	3.29%	1.14%	0.83%	0.54%	0.45%	0.37%	0.35%	0.34%	0.33%	0.29%

Speed8

Measured Pressure Value

L/D_{inlet}	0.25	0.5	1	2	2.25	2.5	2.75	3	3.5	4	4.5	4.75
Average	-1238.78768	-1176.90764	-1088.98698	-939.314434	-874.49818	-780.439872	-734.593736	-689.853392	-653.842448	-612.847946	-612.892822	-594.965812
Standard Deviation	3.949017264	3.942354741	3.65769143	3.14170723	2.93363844	3.098501084	2.693375373	2.867229432	2.612908549	2.686183722	2.655113398	2.54735878
Standard Error	1.248788907	1.246682033	1.15666359	0.993495059	0.92769793	0.979832076	0.851720077	0.906697558	0.826274233	0.849445878	0.839620578	0.805545576
95%CI	2.447626259	2.443496784	2.267060636	1.947250315	1.818287943	1.920470868	1.669371351	1.777127214	1.619497497	1.66491392	1.645656334	1.57886933
95%CI/Average	0.20%	0.21%	0.21%	0.21%	0.21%	0.25%	0.23%	0.26%	0.25%	0.27%	0.27%	0.27%

C_p

Average	-0.052156211	0.000401196	0.075076033	0.202199431	0.257250692	0.337138501	0.376077616	0.414077535	0.444663195	0.479481607	0.479443491	0.49466968
Standard Deviation	0.003354072	0.003348413	0.003106636	0.002668388	0.002491667	0.002631692	0.002287601	0.002435263	0.002219257	0.002281493	0.002255103	0.002163583
Standard Error	0.001060651	0.001058861	0.000982405	0.000843819	0.000787934	0.000832214	0.000723403	0.000770098	0.000701791	0.000721471	0.000713126	0.000684185
95%CI	0.002078875	0.002075368	0.001925513	0.001653884	0.001544351	0.001631139	0.00141787	0.001509391	0.00137551	0.001414084	0.001397727	0.001341002
95%CI/Average	3.99%	517.30%	2.56%	0.82%	0.60%	0.48%	0.38%	0.36%	0.31%	0.29%	0.29%	0.27%

Speed10

Measured Pressure Value

L/D_{inlet}	0.25	0.5	1	2	2.25	2.5	2.75	3	3.5	4	4.5	4.75
Average	-1400.0883	-1328.60842	-1230.00564	-1059.30514	-986.4676	-880.790818	-829.419972	-779.140318	-737.697806	-690.526186	-691.066852	-671.021616
Standard Deviation	2.972028871	2.78447787	2.534298516	3.330999989	2.608683744	2.346140846	1.741670186	1.796986756	1.6755315	2.212009295	2.200865686	2.212904662
Standard Error	0.93983805	0.880529216	0.801415558	1.053354685	0.824938233	0.741914879	0.550764472	0.568257107	0.529849583	0.699498758	0.695974839	0.699781898
95%CI	1.842082579	1.725837264	1.570774494	2.064575183	1.616878936	1.454153162	1.079498365	1.11378393	1.038505183	1.371017565	1.364110685	1.371572519
95%CI/Average	0.13%	0.13%	0.13%	0.19%	0.16%	0.17%	0.13%	0.14%	0.14%	0.20%	0.20%	0.20%

C_p

Average	-0.056112469	-0.002193875	0.072184024	0.200946564	0.255889266	0.335603215	0.374353193	0.412280065	0.443540917	0.479123342	0.478715507	0.493835999
Standard Deviation	0.002241856	0.002100383	0.001911668	0.002512635	0.001967778	0.001769737	0.001313774	0.0013555	0.001263884	0.001668559	0.001660154	0.001669235
Standard Error	0.000708937	0.000664199	0.000604523	0.000794565	0.000622266	0.00055964	0.000415452	0.000428647	0.000399675	0.000527645	0.000524987	0.000527858
95%CI	0.001389517	0.001301831	0.001184864	0.001557347	0.001219642	0.001096895	0.000814286	0.000840148	0.000783364	0.001034184	0.001028974	0.001034602
95%CI/Average	2.48%	59.34%	1.64%	0.78%	0.48%	0.33%	0.22%	0.20%	0.18%	0.22%	0.21%	0.21%

Table 12: Statistical Parameters for Type2 C_p Experimental Data at 180°

180°

Speed2

Measured Pressure Value

L/D_{inlet}	0.25	0.5	1	1.625	2	2.25	2.5	2.75	3	3.25	3.5	4	4.5	4.75
Average	-293.128476	-298.801488	-282.567948	-250.654358	-213.300092	-180.25696	-171.459086	-148.71355	-153.25917	-134.70645	-157.729384	-122.873512	-118.22069	-123.337824
Standard Deviation	3.002796453	1.468722608	1.682373771	1.391281244	1.14833282	0.796830398	1.004511385	0.864362766	1.060189217	1.245335376	1.005867466	0.626484392	0.42209083	0.516538843
Standard Error	0.949567614	0.464450869	0.532013299	0.43996176	0.363134722	0.251979897	0.317654391	0.273335507	0.335261268	0.393809624	0.318083222	0.19811176	0.13347684	0.163343924
95%CI	1.861152524	0.910323704	1.042746066	0.862325049	0.711744056	0.493880597	0.622602607	0.535737593	0.657112085	0.771866863	0.623443115	0.388299049	0.261614607	0.320154092
95%CI/Average	0.63%	0.30%	0.37%	0.34%	0.33%	0.27%	0.36%	0.36%	0.43%	0.57%	0.40%	0.32%	0.22%	0.26%

C_p

Average	-0.184448406	-0.207371426	-0.14177633	-0.012822633	0.138115282	0.271633135	0.30718283	0.399091041	0.38072349	0.45568973	0.362660633	0.503503251	0.522303975	0.501627099
Standard Deviation	0.012133442	0.005934688	0.006797992	0.00562177	0.004640085	0.003219764	0.004058943	0.003492643	0.004283922	0.005032044	0.004064423	0.002531444	0.001705548	0.002087186
Standard Error	0.003836931	0.001876713	0.002149714	0.00177776	0.001467324	0.001018179	0.001283551	0.001104471	0.001354695	0.001591272	0.001285283	0.000800513	0.000539342	0.000660026
95%CI	0.007520385	0.003678358	0.004213439	0.003484409	0.002875954	0.00199563	0.002515759	0.002164763	0.002655202	0.003118893	0.002519155	0.001569005	0.00105711	0.001293651
95%CI/Average	4.08%	1.77%	2.97%	27.17%	2.08%	0.73%	0.82%	0.54%	0.70%	0.68%	0.69%	0.31%	0.20%	0.26%

Speed4

Measured Pressure Value

L/D_{inlet}	0.25	0.5	1	1.625	2	2.25	2.5	2.75	3	3.25	3.5	4	4.5	4.75
Average	-552.200626	-555.596544	-521.246896	-464.682638	-400.10518	-338.871016	-314.893882	-284.653424	-281.099866	-258.640552	-275.15046	-241.73506	-233.909556	-240.581972
Standard Deviation	2.662700097	2.895257271	2.584022088	2.353229149	1.973270497	1.848000366	2.05971791	2.013938862	2.292609818	2.390360856	1.922891888	2.378793615	2.102991533	1.767723537
Standard Error	0.842019703	0.915560739	0.817139532	0.744156397	0.624002921	0.584389027	0.651339993	0.636863387	0.724986881	0.755898473	0.608071806	0.752240591	0.665024314	0.559003265
95%CI	1.650358618	1.794499048	1.601593483	1.458546537	1.223045725	1.145402494	1.276626387	1.248252239	1.420974287	1.481561008	1.19182074	1.474391558	1.303447656	1.095646399
95%CI/Average	0.30%	0.32%	0.31%	0.31%	0.31%	0.34%	0.41%	0.44%	0.51%	0.57%	0.43%	0.61%	0.56%	0.46%

C_p

Average	-0.135976865	-0.142962884	-0.072299427	0.044063513	0.17691106	0.302880844	0.352206158	0.414416267	0.42172658	0.467929463	0.433965587	0.502707127	0.518805609	0.505079239
Standard Deviation	0.005477657	0.005956069	0.005315802	0.004841019	0.004059375	0.003801672	0.004237213	0.004143038	0.004716314	0.004917406	0.003955737	0.00489361	0.004326235	0.003636528
Standard Error	0.001732187	0.001883475	0.001681004	0.001530865	0.001283687	0.001202194	0.001339925	0.001310144	0.00149143	0.00155502	0.001250914	0.001547495	0.001368076	0.001149971
95%CI	0.003395087	0.00369161	0.003294768	0.003000495	0.002516027	0.002356301	0.002626252	0.002567881	0.002923202	0.00304784	0.002451791	0.003033091	0.002681428	0.002253943
95%CI/Average	2.50%	2.58%	4.56%	6.81%	1.42%	0.78%	0.75%	0.62%	0.69%	0.65%	0.56%	0.60%	0.52%	0.45%

Speed6

Measured Pressure Value

L/D_{inlet}	0.25	0.5	1	1.625	2	2.25	2.5	2.75	3	3.25	3.5	4	4.5	4.75
Average	-982.687556	-972.703078	-916.270592	-815.416304	-701.84976	-599.635344	-559.00421	-516.455416	-492.393726	-461.595892	-470.241238	-433.579538	-422.663196	-433.31571
Standard Deviation	7.758413348	7.07905155	5.608023257	3.121837534	3.918389648	5.108890497	11.76572863	11.65566849	12.14891852	11.22718287	8.256849803	26.7387008	26.4991747	27.33366051
Standard Error	2.453425721	2.238592657	1.773412666	0.987211709	1.239103605	1.615573029	3.720650079	3.685846007	3.841825364	3.550346958	2.611045167	8.455519619	8.379774816	8.643662401
95%CI	4.808714413	4.387641608	3.475888826	1.93493495	2.428643065	3.166523136	7.292474155	7.224258175	7.529977713	6.958680037	5.117648528	16.57281845	16.42435864	16.94157831
95%CI/Average	0.49%	0.45%	0.38%	0.24%	0.35%	0.53%	1.30%	1.40%	1.53%	1.51%	1.09%	3.82%	3.89%	3.91%

C_p

Average	-0.123178034	-0.11176612	-0.047265731	0.068007246	0.197809895	0.314637452	0.361077439	0.409709246	0.437210929	0.472411792	0.462530459	0.50443352	0.516910523	0.504735066
Standard Deviation	0.008867599	0.008091112	0.006409777	0.003568153	0.004478584	0.005839286	0.013447823	0.013322028	0.013885795	0.012832283	0.009437295	0.030561414	0.030287644	0.031241433
Standard Error	0.002804181	0.002558634	0.00202695	0.001128349	0.001416253	0.001846544	0.004252575	0.004212795	0.004391074	0.004057924	0.002984335	0.009664368	0.009577794	0.009879408
95%CI	0.005496195	0.005014923	0.003972821	0.002211564	0.002775855	0.003619227	0.008335047	0.008257078	0.008606505	0.007953532	0.005849296	0.018942161	0.018772476	0.019363641
95%CI/Average	4.46%	4.49%	8.41%	3.25%	1.40%	1.15%	2.31%	2.02%	1.97%	1.68%	1.26%	3.76%	3.63%	3.84%

Speed8

Measured Pressure Value

L/D_{inlet}	0.25	0.5	1	1.625	2	2.25	2.5	2.75	3	3.25	3.5	4	4.5	4.75
Average	-1320.8749	-1315.24508	-1239.80322	-1104.78502	-957.629172	-817.211298	-754.230668	-697.472594	-661.934234	-626.833638	-628.585124	-576.540268	-563.165924	-575.895058
Standard Deviation	3.179811085	2.169828557	2.457886574	1.988320644	2.314518223	2.732386889	3.567118287	2.68835576	3.664171422	3.898239386	2.779382677	3.228124086	2.719669603	2.229016045
Standard Error	1.005544556	0.686160037	0.777251981	0.628762195	0.731914927	0.864056602	1.128021847	0.850132736	1.158712743	1.232731532	0.878917975	1.020822468	0.860035043	0.704876764
95%CI	1.970867329	1.344873673	1.523413882	1.232373903	1.434553257	1.69355094	2.21092282	1.666260163	2.271076976	2.416153803	1.722679231	2.000812037	1.685668684	1.381558458
95%CI/Average	0.15%	0.10%	0.12%	0.11%	0.15%	0.21%	0.29%	0.24%	0.34%	0.39%	0.27%	0.35%	0.30%	0.24%

C_p

Average	-0.121876455	-0.117094804	-0.053018754	0.061658071	0.186643928	0.305906931	0.359399117	0.407606215	0.437790489	0.467602951	0.466115337	0.510319295	0.521678707	0.5108673
Standard Deviation	0.002700752	0.00184293	0.00208759	0.001688767	0.001965821	0.002320735	0.003029709	0.002283337	0.00311214	0.003310944	0.00236065	0.002741786	0.002309934	0.0018932
Standard Error	0.000854053	0.000582786	0.000660154	0.000534035	0.000621647	0.000733881	0.000958078	0.000722055	0.000984145	0.001047012	0.000746503	0.000867029	0.000730465	0.000598682
95%CI	0.001673943	0.00114226	0.001293902	0.001046709	0.001218428	0.001438406	0.001877833	0.001415227	0.001928924	0.002052144	0.001463146	0.001699377	0.001431712	0.001173418
95%CI/Average	1.37%	0.98%	2.44%	1.70%	0.65%	0.47%	0.52%	0.35%	0.44%	0.44%	0.31%	0.33%	0.27%	0.23%

Speed10

Measured Pressure Value

L/D_{inlet}	0.25	0.5	1	1.625	2	2.25	2.5	2.75	3	3.25	3.5	4	4.5	4.75
Average	-1410.81698	-1409.21944	-1326.54622	-1181.32996	-1023.78654	-875.173232	-809.278058	-748.808492	-707.840664	-670.762214	-670.712404	-644.250884	-630.620966	-645.232626
Standard Deviation	2.675348362	2.107433803	2.150663185	2.232111084	2.386056848	1.835657469	3.107650201	2.916403492	3.30201815	3.243289584	2.378387292	3.279205899	2.649873584	2.09830233
Standard Error	0.846019436	0.666429084	0.680099415	0.705855502	0.754537427	0.58048586	0.982725281	0.922247761	1.044189823	1.02561822	0.7521121	1.036975956	0.837963604	0.663541458
95%CI	1.658198094	1.306201004	1.332994853	1.383476783	1.478893356	1.137752286	1.926141555	1.807605612	2.046612053	2.01021171	1.474139716	2.032472873	1.642408663	1.300541258
95%CI/Average	0.12%	0.09%	0.10%	0.12%	0.14%	0.13%	0.24%	0.24%	0.29%	0.30%	0.22%	0.32%	0.26%	0.20%

C_p

Average	-0.06420531	-0.063000256	-0.000638319	0.108900988	0.2277389	0.339840664	0.389546611	0.435159922	0.466062711	0.494031671	0.494069243	0.514029657	0.524310956	0.513289111
Standard Deviation	0.002018065	0.001589676	0.001622285	0.001683723	0.001799847	0.00138467	0.002344158	0.002199897	0.002490773	0.002446473	0.001794061	0.002473566	0.001998849	0.001582788
Standard Error	0.000638168	0.0005027	0.000513012	0.00053244	0.000569162	0.000437871	0.000741288	0.000695669	0.000787652	0.000773643	0.000567332	0.00078221	0.000632091	0.000500522
95%CI	0.001250809	0.000985292	0.001005503	0.001043582	0.001115557	0.000858228	0.001452924	0.00136351	0.001543797	0.00151634	0.001111971	0.001533132	0.001238899	0.000981022
95%CI/Average	1.95%	1.56%	157.52%	0.96%	0.49%	0.25%	0.37%	0.31%	0.33%	0.31%	0.23%	0.30%	0.24%	0.19%

Table 13: Statistical Parameters for Type3 C_p Experimental Data at 0°

0°

Speed2

Measured Pressure Value

L/D_{inlet}	0.25	0.5	1	1.625	2	2.25	2.5	2.75	3	3.25	3.5	4	4.5	4.75
Average	-244.947739	-227.786752	-209.226384	-157.332232	-184.931723	-148.982037	-187.772447	-209.124064	-240.329032	-253.818059	-253.962095	-185.98618	-159.011439	-142.421292
Standard Deviation	3.438305993	3.220626915	2.800920977	3.838395019	2.554778199	1.925605907	2.221177548	2.286359107	2.755995217	3.492649957	4.028663201	8.606615071	6.851869255	5.861641182
Standard Error	0.768828593	0.720154071	0.62630497	0.858291219	0.571265772	0.430578571	0.496670399	0.511245438	0.616259265	0.780980273	0.900836478	1.924497636	1.532124543	1.310702814
95%CI	1.506904042	1.411501979	1.227557742	1.682250789	1.119680913	0.843933999	0.973473981	1.002041059	1.20786816	1.530721334	1.765639496	3.772015366	3.002964104	2.568977516
95%CI/Average	0.62%	0.62%	0.59%	1.07%	0.61%	0.57%	0.5C2%	0.48%	0.50%	0.60%	0.70%	2.03%	1.89%	1.80%

C_p

Average	-0.018692797	0.052676606	0.129865778	0.345684055	0.230902825	0.380410987	0.219088774	0.130291308	0.00051556	-0.055582833	-0.056181853	0.226517531	0.33870054	0.407695924
Standard Deviation	0.014299285	0.013393998	0.011648517	0.015963182	0.010624855	0.008008242	0.009237471	0.009508549	0.011461679	0.014525292	0.016754473	0.035793336	0.02849567	0.024377492
Standard Error	0.003197417	0.002994989	0.002604688	0.003569476	0.00237579	0.001790697	0.002065561	0.002126176	0.002562909	0.003247954	0.003746414	0.008003633	0.006371825	0.005450973
95%CI	0.006266938	0.005870178	0.005105188	0.006996173	0.004656548	0.003509767	0.0040485	0.004167305	0.005023303	0.00636599	0.007342971	0.015687121	0.012488778	0.010683907
95%CI/Average	33.53%	11.14%	3.93%	2.02%	2.02%	0.92%	1.85%	3.20%	974.34%	11.45%	13.07%	6.93%	3.69%	2.62%

Speed4

Measured Pressure Value

L/D_{inlet}	0.25	0.5	1	1.625	2	2.25	2.5	2.75	3	3.25	3.5	4	4.5	4.75
Average	-458.920389	-426.484988	-393.989023	-304.127835	-347.12455	-282.76539	-352.457571	-393.867852	-454.290293	-486.951787	-486.560578	-373.615491	-324.423458	-294.111008
Standard Deviation	3.387927045	3.218823465	2.840803322	2.871852766	2.030403607	1.557266311	2.097453899	3.111819812	4.974743076	6.652688403	7.105270583	6.604557628	6.899020107	6.826166944
Standard Error	0.757563518	0.719750808	0.635222934	0.642165801	0.454012049	0.348215333	0.46900495	0.695824063	1.112386369	1.48758635	1.588786802	1.476823982	1.542667794	1.526377331
95%CI	1.484824495	1.410711583	1.245036951	1.258644969	0.889863616	0.682502053	0.919249702	1.363815164	2.180277283	2.915669247	3.114022132	2.894575004	3.023628876	2.991699569
95%CI/Average	0.32%	0.33%	0.32%	0.41%	0.26%	0.24%	0.26%	0.35%	0.48%	0.60%	0.64%	0.77%	0.93%	1.02%

C_p

Average	0.024717004	0.093647685	0.162707075	0.35367721	0.262301961	0.399075998	0.250968394	0.162964584	0.034556737	-0.03485443	-0.034023045	0.206004257	0.310545599	0.374964652
Standard Deviation	0.007199915	0.006840541	0.006037185	0.00610317	0.004314949	0.003309453	0.004457442	0.00661314	0.010572166	0.014138082	0.015099895	0.014035796	0.014661578	0.014506753
Standard Error	0.00160995	0.001529591	0.001349956	0.00136471	0.000964852	0.000740016	0.000996714	0.001478743	0.002364008	0.003161371	0.003376439	0.003138499	0.003278428	0.003243808
95%CI	0.003155502	0.002997999	0.002645913	0.002674832	0.00189111	0.001450432	0.00195356	0.002898337	0.004633456	0.006196287	0.006617821	0.006151459	0.00642572	0.006357865
95%CI/Average	12.77%	3.20%	1.63%	0.76%	0.72%	0.36%	0.78%	1.78%	13.41%	17.78%	19.45%	2.99%	2.07%	1.70%

Speed6

Measured Pressure Value

L/D_{inlet}	0.25	0.5	1	1.625	2	2.25	2.5	2.75	3	3.25	3.5	4	4.5	4.75
Average	-757.0782	-703.26359	-652.646205	-508.646893	-573.856182	-471.581761	-584.225318	-656.047951	-760.830507	-827.904607	-825.695448	-670.785124	-587.548235	-535.906089
Standard Deviation	2.508923546	2.534243719	3.013870029	3.640430824	2.35259927	2.165125796	2.782694959	2.427220834	1.891103422	2.137939197	2.339069724	9.413398964	6.029277286	4.780730612
Standard Error	0.56101236	0.566674123	0.673921826	0.814025079	0.526057189	0.484136846	0.622229509	0.542743078	0.42286358	0.478057738	0.523031891	2.104899998	1.348187387	1.069003863
95%CI	1.099584225	1.110681281	1.320886779	1.595489155	1.031072091	0.948908218	1.219569837	1.063776433	0.828812617	0.936993166	1.025142506	4.125603996	2.642447278	2.095247572
95%CI/Average	0.15%	0.16%	0.20%	0.31%	0.18%	0.20%	0.21%	0.16%	0.11%	0.11%	0.12%	0.62%	0.45%	0.39%

C_p

Average	0.074170937	0.13998069	0.201880566	0.377976969	0.29823269	0.423303828	0.2855523	0.197720579	0.06958225	-0.012442502	-0.009740927	0.179698526	0.281488713	0.344641766
Standard Deviation	0.003068156	0.00309912	0.003685654	0.004451874	0.002876988	0.002647727	0.003402951	0.002968242	0.002312626	0.002614481	0.002860443	0.011511622	0.007373188	0.005846344
Standard Error	0.000686061	0.000692984	0.000824137	0.000995469	0.000643314	0.00059205	0.000760923	0.000663719	0.000517119	0.000584616	0.000639614	0.002574077	0.001648695	0.001307282
95%CI	0.001344679	0.001358249	0.001615309	0.00195112	0.001260896	0.001160418	0.001491409	0.00130089	0.001013553	0.001145847	0.001253644	0.005045191	0.003231442	0.002562273
95%CI/Average	1.81%	0.97%	0.80%	0.52%	0.42%	0.27%	0.52%	0.66%	1.46%	9.21%	12.87%	2.81%	1.15%	0.74%

Speed8

Measured Pressure Value

L/D_{inlet}	0.25	0.5	1	1.625	2	2.25	2.5	2.75	3	3.25	3.5	4	4.5	4.75
Average	-1005.107092	-930.414568	-864.682123	-626.449101	-755.768568	-622.110656	-766.667064	-860.310822	-998.336446	-1087.39817	-1079.73162	-926.237037	-816.029855	-746.406835
Standard Deviation	6.760183816	6.482086507	6.28654549	4.857156113	4.817379589	3.759581955	4.013602794	3.619340453	4.823376853	7.36348592	8.215080368	10.45763629	5.893702115	4.209329313
Standard Error	1.511623055	1.449438607	1.405714306	1.086093124	1.077198823	0.840668082	0.897468868	0.809309129	1.078539852	1.646525507	1.836947814	2.338398562	1.317871857	0.941234648
95%CI	2.962781188	2.840899669	2.75520004	2.128742524	2.111309694	1.64770944	1.759038982	1.586245892	2.113938111	3.227189993	3.600417716	4.583261182	2.58302884	1.844819911
95%CI/Average	0.29%	0.31%	0.32%	0.34%	0.28%	0.26%	0.23%	0.18%	0.21%	0.30%	0.33%	0.49%	0.32%	0.25%

C_p

Average	0.0896874	0.157335461	0.216868493	0.432633085	0.315510103	0.436562359	0.305639475	0.220827525	0.095819487	0.015157427	0.022100923	0.161118997	0.260932228	0.323988904
Standard Deviation	0.006122612	0.005870743	0.005693644	0.004399064	0.004363039	0.003405005	0.003635069	0.00327799	0.004368471	0.006669015	0.007440293	0.009471347	0.00533785	0.003812336
Standard Error	0.001369058	0.001312738	0.001273137	0.000983661	0.000975605	0.000761382	0.000812826	0.000732981	0.00097682	0.001491237	0.0016637	0.002117858	0.00119358	0.000852464
95%CI	0.002683353	0.002572966	0.002495349	0.001927975	0.001912186	0.001492309	0.001593139	0.001436643	0.001914567	0.002922825	0.003260852	0.004151001	0.002339416	0.00167083
95%CI/Average	2.99%	1.64%	1.15%	0.45%	0.61%	0.34%	0.52%	0.65%	2.00%	19.28%	14.75%	2.58%	0.90%	0.52%

Speed10

Measured Pressure Value

L/D_{inlet}	0.25	0.5	1	1.625	2	2.25	2.5	2.75	3	3.25	3.5	4	4.5	4.75
Average	-1118.33764	-1034.17512	-962.591834	-705.392963	-840.478422	-692.429929	-853.474922	-960.391324	-1118.81523	-1223.23863	-1214.59488	-1040.26669	-915.818719	-837.748133
Standard Deviation	6.053447534	5.604481384	6.701103688	5.288921874	3.665890921	2.762129045	2.814663407	2.719910622	3.654710793	4.929611701	4.800096588	8.817107452	6.540314113	5.385281083
Standard Error	1.353592018	1.253200135	1.498412337	1.182638884	0.81971813	0.617630831	0.629377871	0.608190504	0.817218177	1.102294687	1.073334227	1.971565163	1.462458695	1.204185458
95%CI	2.653040356	2.456272265	2.936888181	2.317972212	1.606647534	1.210556428	1.233580628	1.192053388	1.601747627	2.160497586	2.103735085	3.864267719	2.866419042	2.360203498
95%CI/Average	0.24%	0.24%	0.31%	0.33%	0.19%	0.17%	0.14%	0.12%	0.14%	0.18%	0.17%	0.37%	0.31%	0.28%

C_p

Average	0.093732565	0.161935358	0.219944316	0.428370603	0.31890138	0.438875458	0.308369404	0.221727544	0.09334554	0.008723934	0.015728571	0.156998932	0.257847852	0.321113924
Standard Deviation	0.004905533	0.004541704	0.005430374	0.004285984	0.002970729	0.002238347	0.002280919	0.002204134	0.002961669	0.00399481	0.003889855	0.007145121	0.005300075	0.004364071
Standard Error	0.001096911	0.001015556	0.001214269	0.000958375	0.000664275	0.00050051	0.000510029	0.000492859	0.000662249	0.000893267	0.000869798	0.001597698	0.001185133	0.000975836
95%CI	0.002149945	0.00199049	0.002379966	0.001878415	0.001301979	0.000980999	0.000999657	0.000966004	0.001298008	0.001750803	0.001704804	0.003131487	0.00232286	0.001912638
95%CI/Average	2.29%	1.23%	1.08%	0.44%	0.41%	0.22%	0.32%	0.44%	1.39%	20.07%	10.84%	1.99%	0.90%	0.60%

Table 14: Statistical Parameters for Type3 C_p Experimental Data at 60°

60°

Speed2

Measured Pressure Value

L/D_{inlet}	0.25	0.5	1	1.625	2	2.25	2.5	2.75	3	3.5	4	4.5	4.75
Average	-210.21321	-202.629962	-183.916279	-170.967018	-161.02867	-168.91116	-164.09877	-170.469499	-186.136707	-176.774243	-160.123696	-144.301477	-132.727467
Standard Deviation	6.727365084	6.438064351	5.552263199	5.106999763	4.835969337	5.315496652	5.474490774	6.517076718	8.186178393	8.608666502	7.534819215	6.122154533	5.347539758
Standard Error	1.504284564	1.439594953	1.241523794	1.141959863	1.081355618	1.188581185	1.224133351	1.457262655	1.830485136	1.924956349	1.684836796	1.36895537	1.195746241
95%CI	2.948397745	2.821606108	2.433386637	2.238241332	2.11945701	2.329619122	2.399301368	2.856234805	3.587750867	3.772914445	3.302280121	2.683152526	2.343662633
95%CI/Average	1.40%	1.39%	1.32%	1.31%	1.32%	1.38%	1.46%	1.68%	1.93%	2.13%	2.06%	1.86%	1.77%

C_p

Average	0.12576175	0.15729909	0.235125871	0.288979476	0.330311246	0.297529413	0.317543262	0.291048567	0.225891517	0.264828291	0.334074867	0.399876579	0.448010767
Standard Deviation	0.02797788	0.026774731	0.023090846	0.021239077	0.020111911	0.022106177	0.022767405	0.027103329	0.034044817	0.035801868	0.031335933	0.02546092	0.022239439
Standard Error	0.006256044	0.005987012	0.00516327	0.004749202	0.00449716	0.004943092	0.005090946	0.006060489	0.007612653	0.008005541	0.007006928	0.005693235	0.00497289
95%CI	0.012261846	0.011734543	0.010120009	0.009308436	0.008814434	0.009688459	0.009978255	0.011878558	0.014920799	0.01569086	0.013733578	0.01115874	0.009746864
95%CI/Average	9.75%	7.46%	4.30%	3.22%	2.67%	3.26%	3.14%	4.08%	6.61%	5.92%	4.11%	2.79%	2.18%

Speed4

Measured Pressure Value

L/D_{inlet}	0.25	0.5	1	1.625	2	2.25	2.5	2.75	3	3.5	4	4.5	4.75
Average	-424.103615	-407.241883	-369.323522	-346.874729	-328.668602	-343.513564	-334.234221	-349.331487	-378.13109	-360.245419	-328.283563	-293.966287	-272.369737
Standard Deviation	15.2104527	14.67312219	13.67629092	12.67183175	11.75592598	9.90705625	9.375876284	7.768870644	6.419592931	6.016309194	6.175207628	6.704450601	6.920153969
Standard Error	3.401160621	3.281009865	3.058111618	2.833507718	2.628704962	2.215285123	2.096509672	1.737172287	1.435464618	1.345287633	1.380818403	1.499160729	1.547393469
95%CI	6.666274818	6.430779336	5.993898772	5.553675128	5.152261726	4.341958841	4.109158957	3.404857682	2.813510651	2.636763761	2.70640407	2.93835503	3.032891199
95%CI/Average	1.57%	1.58%	1.62%	1.60%	1.57%	1.26%	1.23%	0.97%	0.74%	0.73%	0.82%	1.00%	1.11%

C_p

Average	0.098708503	0.134542519	0.215125413	0.262832873	0.301523954	0.269975913	0.289696078	0.257611849	0.19640785	0.234417908	0.302342226	0.375272209	0.421168509
Standard Deviation	0.03232477	0.031182852	0.029064418	0.026929773	0.02498332	0.02105416	0.019925314	0.016510156	0.013642714	0.012785669	0.013123355	0.014248085	0.014706491
Standard Error	0.007228038	0.006972698	0.006499001	0.00602168	0.00558644	0.004707853	0.004455436	0.003691783	0.003050604	0.002858962	0.002934471	0.003185969	0.003288471
95%CI	0.014166955	0.013666487	0.012738043	0.011802494	0.010949423	0.009227393	0.008732654	0.007235895	0.005979183	0.005603566	0.005751564	0.006244499	0.006445404
95%CI/Average	14.35%	10.16%	5.92%	4.49%	3.63%	3.42%	3.01%	2.81%	3.04%	2.39%	1.90%	1.66%	1.53%

Speed6

Measured Pressure Value

L/D_{inlet}	0.25	0.5	1	1.625	2	2.25	2.5	2.75	3	3.5	4	4.5	4.75
Average	-752.421837	-722.361381	-656.390894	-591.734812	-589.282443	-623.360877	-602.418586	-635.448937	-692.409001	-660.660721	-600.531743	-531.03454	-493.798425
Standard Deviation	6.669218822	6.409549157	5.877854366	10.57471841	3.905099291	3.498403584	3.00323595	6.526682181	12.44075517	13.32408083	8.811891481	4.839177127	3.804093891
Standard Error	1.491282664	1.433218762	1.314328192	2.364578921	0.873206747	0.782266823	0.671543974	1.459410502	2.781837424	2.979355046	1.970398836	1.082072901	0.850621253
95%CI	2.922914022	2.809108774	2.576083257	4.634574685	1.711485225	1.533242972	1.316226188	2.860444585	5.452401352	5.839535891	3.861981719	2.120862886	1.667217657
95%CI/Average	0.39%	0.39%	0.39%	0.78%	0.29%	0.25%	0.22%	0.45%	0.79%	0.88%	0.64%	0.40%	0.34%

C_p

Average	0.079865191	0.116626049	0.197301195	0.276368958	0.279367954	0.237693521	0.263303797	0.222911062	0.153254741	0.192079634	0.265611213	0.350599171	0.396135124
Standard Deviation	0.008155771	0.007838222	0.007188014	0.012931797	0.004775536	0.004278189	0.00367265	0.007981464	0.015213769	0.016293986	0.01077604	0.005917818	0.004652017
Standard Error	0.001823686	0.00175268	0.001607289	0.002891638	0.001067842	0.000956632	0.000821229	0.00178471	0.003401902	0.003643446	0.002409596	0.001323264	0.001040223
95%CI	0.003574424	0.003435252	0.003150286	0.00566761	0.002092971	0.001874999	0.00160961	0.003498031	0.006667728	0.007141154	0.004722808	0.002593598	0.002038836
95%CI/Average	4.48%	2.95%	1.60%	2.05%	0.75%	0.79%	0.61%	1.57%	4.35%	3.72%	1.78%	0.74%	0.51%

Speed8

Measured Pressure Value

L/D_{inlet}	0.25	0.5	1	1.625	2	2.25	2.5	2.75	3	3.5	4	4.5	4.75
Average	-1046.19805	-1004.106648	-912.241531	-805.318341	-820.238017	-876.289359	-837.990022	-884.018686	-965.905572	-919.857472	-836.352511	-735.674638	-684.727944
Standard Deviation	9.34631529	9.059237435	8.429814886	7.975367709	4.338830176	2.877670266	4.154672982	9.607005866	15.62991641	14.96716346	8.994934651	4.747454442	3.583453999
Standard Error	2.089899633	2.025707073	1.884963912	1.783346434	0.970191922	0.643466633	0.929013121	2.148191818	3.494955558	3.346759492	2.011328533	1.061563085	0.801284674
95%CI	4.09620328	3.970385863	3.694529268	3.495359011	1.901576166	1.261194601	1.820865717	4.210455963	6.850112893	6.559648605	3.942203925	2.080663647	1.57051796
95%CI/Average	0.39%	0.40%	0.40%	0.43%	0.23%	0.14%	0.22%	0.48%	0.71%	0.71%	0.47%	0.28%	0.23%

C_p

Average	0.052471847	0.09059349	0.173794548	0.270633509	0.25712095	0.206355969	0.241043187	0.199355616	0.125191714	0.166896888	0.242526259	0.333708918	0.379850685
Standard Deviation	0.008464838	0.008204835	0.007634775	0.007223188	0.003929623	0.002606269	0.003762834	0.008700942	0.014155815	0.013555568	0.008146597	0.004299709	0.003245488
Standard Error	0.001892795	0.001834657	0.001707188	0.001615154	0.00087869	0.000582779	0.000841395	0.00194559	0.003165336	0.003031117	0.001821634	0.000961444	0.000725713
95%CI	0.003709879	0.003595928	0.003346088	0.003165702	0.001722233	0.001142248	0.001649135	0.003813356	0.006204059	0.00594099	0.003570404	0.00188443	0.001422398
95%CI/Average	7.07%	3.97%	1.93%	1.17%	0.67%	0.55%	0.68%	1.91%	4.96%	3.56%	1.47%	0.56%	0.37%

Speed10

Measured Pressure Value

L/D_{inlet}	0.25	0.5	1	1.625	2	2.25	2.5	2.75	3	3.5	4	4.5	4.75
Average	-1165.77134	-1119.09016	-1017.461333	-895.170743	-916.753101	-983.04407	-939.693414	-994.623911	-1090.7417	-1039.67796	-943.121811	-825.713686	-768.289447
Standard Deviation	13.09390946	12.71108979	12.02919458	10.01049598	8.411473723	8.085963672	5.352778492	6.238434084	10.30093931	11.49248307	7.761398576	4.757335317	4.204797583
Standard Error	2.927887164	2.842286085	2.689809679	2.238414951	1.880862703	1.808076443	1.196917658	1.394956268	2.303360054	2.569797337	1.735501482	1.063772516	0.940221323
95%CI	5.738658842	5.570880726	5.272026971	4.387293303	3.686490899	3.543829829	2.345958609	2.734114286	4.514585706	5.03680278	3.401582904	2.084994131	1.842833792
95%CI/Average	0.49%	0.50%	0.52%	0.49%	0.40%	0.36%	0.25%	0.27%	0.41%	0.48%	0.36%	0.25%	0.24%

C_p

Average	0.055293711	0.093122745	0.175479712	0.274580355	0.257090657	0.203370435	0.238500512	0.193986477	0.116095491	0.157476021	0.235722242	0.330866281	0.37740117
Standard Deviation	0.010610913	0.010300688	0.0097481	0.008112207	0.006816407	0.006552624	0.004337732	0.005055441	0.008347574	0.009313165	0.006289606	0.003855203	0.003407442
Standard Error	0.002372672	0.002303304	0.002179741	0.001813945	0.001524195	0.001465211	0.000969946	0.001130431	0.001866574	0.002082487	0.001406399	0.000862049	0.000761927
95%CI	0.004650438	0.004514475	0.004272293	0.003555332	0.002987422	0.002871814	0.001901095	0.002215645	0.003658485	0.004081675	0.002756541	0.001689617	0.001493377
95%CI/Average	8.41%	4.85%	2.43%	1.29%	1.16%	1.41%	0.80%	1.14%	3.15%	2.59%	1.17%	0.51%	0.40%

Table 15: Statistical Parameters for Type3 C_p Experimental Data at 120°

120°

Speed2

Measured Pressure Value

L/D_{inlet}	0.25	0.5	1	2	2.25	2.5	2.75	3	3.5	4	4.5	4.75
Average	-270.693751	-264.297413	-243.763027	-220.374562	-205.354506	-190.331616	-186.610573	-178.163788	-164.743062	-154.214364	-149.002863	-144.924567
Standard Deviation	3.869552049	4.047185231	3.692347105	3.45008117	2.44023411	2.590582839	3.764078186	3.833965823	2.795332353	2.149138844	1.85703827	1.778224915
Standard Error	0.865258142	0.90497813	0.825633912	0.771461602	0.545652935	0.579271933	0.84167347	0.85730082	0.625055316	0.480562055	0.415246381	0.397623179
95%CI	1.695905959	1.773757134	1.618242468	1.512064741	1.069479753	1.135372989	1.649680001	1.680309608	1.225108419	0.941901627	0.813882906	0.779341431
95%CI/Average	0.63%	0.67%	0.66%	0.69%	0.52%	0.60%	0.88%	0.94%	0.74%	0.61%	0.55%	0.54%

C_p

Average	-0.125765746	-0.099164548	-0.013765796	0.083502547	0.14596821	0.208445659	0.223920795	0.259049428	0.31486377	0.358650697	0.380324375	0.397285262
Standard Deviation	0.016092758	0.016831502	0.015355796	0.014348256	0.010148487	0.01077376	0.015654112	0.015944762	0.011625275	0.008937875	0.007723082	0.007395312
Standard Error	0.00359845	0.003763638	0.00343366	0.003208368	0.002269271	0.002409086	0.003500366	0.003565357	0.002599491	0.00199857	0.001726934	0.001653642
95%CI	0.007052962	0.007376731	0.006729974	0.0062884	0.00444777	0.004721808	0.006860717	0.0069881	0.005095002	0.003917196	0.00338479	0.003241138
95%CI/Average	5.61%	7.44%	48.89%	7.53%	3.05%	2.27%	3.06%	2.70%	1.62%	1.09%	0.89%	0.82%

Speed4

Measured Pressure Value

L/D_{inlet}	0.25	0.5	1	2	2.25	2.5	2.75	3	3.5	4	4.5	4.75
Average	-516.997393	-502.477883	-464.473369	-416.503812	-393.974178	-367.567344	-360.136484	-341.924006	-315.8927	-293.230145	-282.894239	-275.496948
Standard Deviation	4.877674437	5.123635591	5.042924039	3.080451381	1.886191024	3.919614979	6.782014713	6.836936495	4.491990853	2.398798198	1.891887394	1.965367866
Standard Error	1.090681161	1.145679747	1.127632096	0.688809869	0.421765135	0.876452554	1.516504592	1.528785476	1.00443969	0.536387584	0.423038882	0.439469615
95%CI	2.137735076	2.245532305	2.210158908	1.350067343	0.826659664	1.717847006	2.972349001	2.996419533	1.968701793	1.051319664	0.829156209	0.861360445
95%CI/Average	0.41%	0.45%	0.48%	0.32%	0.21%	0.47%	0.83%	0.88%	0.62%	0.36%	0.29%	0.31%

C_p

Average	-0.098706395	-0.067849995	0.012915988	0.114859363	0.162738623	0.218857586	0.234649413	0.273353991	0.328674894	0.376836634	0.398802172	0.41452266
Standard Deviation	0.010365878	0.010888587	0.010717062	0.006546477	0.004008473	0.008329841	0.014412922	0.01452964	0.009546236	0.00509785	0.004020579	0.004176737
Standard Error	0.002317881	0.002434762	0.002396408	0.001463837	0.000896322	0.001862609	0.003222827	0.003248926	0.002134603	0.001139914	0.000899029	0.000933947
95%CI	0.004543047	0.004772134	0.004696959	0.00286912	0.001756791	0.003650714	0.006316741	0.006367895	0.004183822	0.002234231	0.001762096	0.001830536
95%CI/Average	4.60%	7.03%	36.37%	2.50%	1.08%	1.67%	2.69%	2.33%	1.27%	0.59%	0.44%	0.44%

Speed6

Measured Pressure Value

L/D_{inlet}	0.25	0.5	1	2	2.25	2.5	2.75	3	3.5	4	4.5	4.75
Average	-883.037704	-856.288133	-792.324385	-706.956387	-671.683304	-626.557175	-610.522882	-577.414082	-535.639886	-496.332096	-479.604557	-465.93916
Standard Deviation	10.03468901	10.4344517	10.34853661	6.315745303	3.583929358	7.323363686	13.36909379	13.44255894	8.017689021	3.84884417	2.947176305	3.11400086
Standard Error	2.243824675	2.333214331	2.314003133	1.412243583	0.801390967	1.637553903	2.989420251	3.005847557	1.792809767	0.86062772	0.659008656	0.69631176
95%CI	4.397896363	4.573100088	4.53544614	2.767997422	1.570726296	3.209605649	5.859263693	5.891461212	3.513907144	1.686830331	1.291656966	1.36477105
95%CI/Average	0.50%	0.53%	0.57%	0.39%	0.23%	0.51%	0.96%	1.02%	0.66%	0.34%	0.27%	0.29%

C_p

Average	-0.07986463	-0.047152646	0.031068464	0.135464778	0.178600144	0.233784776	0.253393074	0.293881743	0.344967305	0.393036704	0.41349277	0.430204151
Standard Deviation	0.012271396	0.012760265	0.0126552	0.007723509	0.004382778	0.008955723	0.016349032	0.016438872	0.009804812	0.004706742	0.003604095	0.003808104
Standard Error	0.002743968	0.002853282	0.002829789	0.001727029	0.000980019	0.002002561	0.003655755	0.003675844	0.002192423	0.00105246	0.0008059	0.000851518
95%CI	0.005378177	0.005592433	0.005546386	0.003384977	0.001920837	0.003925019	0.007165279	0.007204653	0.004297148	0.002062821	0.001579564	0.001668975
95%CI/Average	6.73%	11.86%	17.85%	2.50%	1.08%	1.68%	2.83%	2.45%	1.25%	0.52%	0.38%	0.39%

Speed8

Measured Pressure Value

L/D_{inlet}	0.25	0.5	1	2	2.25	2.5	2.75	3	3.5	4	4.5	4.75
Average	-1162.0692	-1124.34456	-1040.16084	-926.776023	-883.321181	-825.508682	-803.409611	-759.496322	-704.98085	-651.761936	-629.721987	-611.19689
Standard Deviation	7.750267025	7.626996535	7.099941064	5.100450503	3.387571449	7.056404726	11.55279206	11.22288622	6.463392236	3.606436627	2.851232082	2.725292642
Standard Error	1.733012391	1.705448272	1.587595086	1.140495404	0.757484004	1.577860064	2.583282838	2.509513648	1.44525844	0.806423746	0.637554875	0.609393961
95%CI	3.396704286	3.342678612	3.111686368	2.235370992	1.484668648	3.092605726	5.063234362	4.918646751	2.832706543	1.580590541	1.249607556	1.194412163
95%CI/Average	0.29%	0.30%	0.30%	0.24%	0.17%	0.37%	0.63%	0.65%	0.40%	0.24%	0.20%	0.20%

C_p

Average	-0.052471167	-0.018304445	0.05793967	0.160630845	0.199987338	0.252347376	0.272362221	0.312133924	0.361507888	0.409707575	0.429668874	0.446446817
Standard Deviation	0.007019317	0.006907673	0.006430326	0.004619413	0.00306808	0.006390895	0.010463216	0.010164424	0.005853811	0.003266303	0.002582324	0.002468263
Standard Error	0.001569567	0.001544603	0.001437865	0.001032932	0.000686044	0.001429048	0.002339646	0.002272834	0.001308952	0.000730368	0.000577425	0.00055192
95%CI	0.003076351	0.003027421	0.002818214	0.002024547	0.001344645	0.002800933	0.004585706	0.004454755	0.002565546	0.001431521	0.001131754	0.001081764
95%CI/Average	5.86%	16.54%	4.86%	1.26%	0.67%	1.11%	1.68%	1.43%	0.71%	0.35%	0.26%	0.24%

Speed10

Measured Pressure Value

L/D_{inlet}	0.25	0.5	1	2	2.25	2.5	2.75	3	3.5	4	4.5	4.75
Average	-1296.2367	-1252.14805	-1158.11423	-1032.89697	-987.609392	-924.463938	-899.335547	-849.410174	-787.530034	-727.257409	-702.525793	-682.229858
Standard Deviation	11.68219986	11.3100133	10.69093027	6.366725092	3.023094113	9.670610353	18.58884038	18.10460396	11.20824287	5.698646082	3.852212213	3.73787909
Standard Error	2.612219302	2.528995856	2.390564684	1.42364301	0.675984394	2.162414213	4.156591071	4.048312516	2.506239296	1.274256002	0.861380837	0.835815174
95%CI	5.119949832	4.956831879	4.68550678	2.7903403	1.324929412	4.238331858	8.146918499	7.934692531	4.91222902	2.497541764	1.688306441	1.63819774
95%CI/Average	0.39%	0.40%	0.40%	0.27%	0.13%	0.46%	0.91%	0.93%	0.62%	0.34%	0.24%	0.24%

C_p

Average	-0.050431522	-0.014703396	0.061498804	0.162971133	0.199670834	0.250842025	0.271205323	0.311663354	0.361809172	0.410652308	0.430694071	0.447141291
Standard Deviation	0.009466906	0.009165297	0.008663611	0.005159404	0.002449825	0.007836774	0.015063841	0.014671431	0.009082825	0.004618013	0.003121718	0.003029066
Standard Error	0.002116865	0.002049423	0.001937242	0.001153678	0.000547798	0.001752356	0.003368377	0.003280632	0.002030982	0.001032619	0.000698037	0.00067732
95%CI	0.004149054	0.004016869	0.003796995	0.002261208	0.001073683	0.003434618	0.00660202	0.006430038	0.003980724	0.002023933	0.001368153	0.001327547
95%CI/Average	8.23%	27.32%	6.17%	1.39%	0.54%	1.37%	2.43%	2.06%	1.10%	0.49%	0.32%	0.30%

Table 16: Statistical Parameters for Type3 C_p Experimental Data at 180°

180°

Speed2

Measured Pressure Value

L/D_{inlet}	0.25	0.5	1	1.625	2	2.25	2.5	2.75	3	3.25	3.5	4	4.5	4.75
Average	-299.165712	-299.549809	-282.739066	-246.883372	-215.051753	-210.535186	-207.952058	-201.27497	-189.866095	-181.506969	-167.290089	-122.989312	-122.028896	-115.662364
Standard Deviation	4.314175753	4.552932671	4.356371986	4.90824564	2.914389558	2.359065614	3.092568683	4.07096624	4.959469559	5.423849722	4.490807493	6.577596297	5.433253963	4.960124964
Standard Error	0.964679025	1.018066695	0.97411439	1.09751709	0.651677316	0.527503108	0.69151938	0.910295725	1.108971107	1.212809668	1.004175083	1.470795245	1.21491252	1.10911766
95%CI	1.890770889	1.995410722	1.909264204	2.151133497	1.27728754	1.033906091	1.355377985	1.78417962	2.173583369	2.377106949	1.968183162	2.88275868	2.381228539	2.173870613
95%CI/Average	0.63%	0.67%	0.68%	0.87%	0.59%	0.49%	0.65%	0.89%	1.14%	1.31%	1.18%	2.34%	1.95%	1.88%

C_p

Average	-0.244175419	-0.245772808	-0.175860006	-0.02674274	0.105639135	0.12442271	0.135165467	0.162934253	0.210381675	0.24514575	0.304271151	0.488509971	0.492504165	0.518981406
Standard Deviation	0.017941867	0.018934813	0.018117353	0.020412495	0.012120413	0.009810922	0.012861427	0.016930403	0.020625526	0.022556798	0.018676446	0.027355019	0.022595908	0.020628252
Standard Error	0.004011923	0.004233953	0.004051163	0.004564373	0.002710207	0.002193789	0.002875902	0.003785753	0.004612008	0.005043853	0.00417618	0.006116768	0.005052599	0.004612617
95%CI	0.00786337	0.008298548	0.00794028	0.00894617	0.005312005	0.004299826	0.005636769	0.007420076	0.009039535	0.009885953	0.008185313	0.011988866	0.009903093	0.00904073
95%CI/Average	3.22%	3.38%	4.52%	33.45%	5.03%	3.46%	4.17%	4.55%	4.30%	4.03%	2.69%	2.45%	2.01%	1.74%

Speed4

Measured Pressure Value

L/D_{inlet}	0.25	0.5	1	1.625	2	2.25	2.5	2.75	3	3.25	3.5	4	4.5	4.75
Average	-560.271925	-562.252314	-524.608208	-462.156346	-407.09767	-398.533895	-393.268854	-381.881009	-360.54655	-342.885839	-314.815456	-248.666109	-244.76188	-237.391222
Standard Deviation	3.944638099	4.480974255	4.484098698	6.621339971	2.617494302	5.951175735	9.10196356	11.39468376	11.95813833	10.87426411	7.599487857	4.393752424	4.553384129	4.979480331
Standard Error	0.882047894	1.001976304	1.002674951	1.480576628	0.585289519	1.330723349	2.035260925	2.547928748	2.673921018	2.431559375	1.699297144	0.98247291	1.018167644	1.113445651
95%CI	1.728813871	1.963873556	1.965242903	2.90193019	1.147167457	2.608217764	3.989111413	4.993940346	5.240885195	4.765856375	3.330622403	1.925646903	1.995608582	2.182353476
95%CI/Average	0.31%	0.35%	0.37%	0.63%	0.28%	0.65%	1.01%	1.31%	1.45%	1.39%	1.06%	0.77%	0.82%	0.92%

C_p

Average	-0.190672053	-0.194880712	-0.114880657	0.017840051	0.134848996	0.153048458	0.164237556	0.188438641	0.233777954	0.271309935	0.330964219	0.471542704	0.479839847	0.495503735
Standard Deviation	0.008383019	0.009522824	0.009529464	0.014071461	0.005562616	0.012647249	0.019343203	0.024215619	0.025413055	0.02310964	0.01615019	0.009337463	0.009676707	0.010582233
Standard Error	0.0018745	0.002129368	0.002130853	0.003146474	0.001243839	0.002828011	0.004325272	0.005414777	0.005682532	0.005167473	0.003611292	0.00208792	0.002163777	0.002366259
95%CI	0.00367402	0.004173562	0.004176472	0.00616709	0.002437924	0.005542901	0.008477533	0.010612963	0.011137762	0.010128246	0.007078133	0.004092323	0.004241004	0.004637868
95%CI/Average	1.93%	2.14%	3.64%	34.57%	1.81%	3.62%	5.16%	5.63%	4.76%	3.73%	2.14%	0.87%	0.88%	0.94%

Speed6

Measured Pressure Value

L/D_{inlet}	0.25	0.5	1	1.625	2	2.25	2.5	2.75	3	3.25	3.5	4	4.5	4.75
Average	-923.560359	-928.102718	-856.833655	-757.784136	-676.635469	-666.067398	-661.893409	-647.709794	-613.119433	-581.133443	-531.409196	-451.325587	-439.039927	-431.010672
Standard Deviation	3.544711333	3.805827189	3.690764509	4.094572245	2.456396609	3.745332277	3.866695519	3.619976309	4.374100277	4.836549317	3.993877392	9.293263082	6.660242643	5.118526823
Standard Error	0.79262155	0.85100883	0.825280033	0.915574188	0.54926698	0.837481757	0.864619403	0.80945131	0.978078556	1.081485305	0.893058134	2.078036798	1.48927553	1.144537392
95%CI	1.553538238	1.667977308	1.617548865	1.794525408	1.07656328	1.641464244	1.69465403	1.586524568	1.91703397	2.119711197	1.750393943	4.072952125	2.918980038	2.243293288
95%CI/Average	0.17%	0.18%	0.19%	0.24%	0.16%	0.25%	0.26%	0.24%	0.31%	0.36%	0.33%	0.90%	0.66%	0.52%

C_p

Average	-0.129419685	-0.134974525	-0.047819763	0.073307649	0.172544154	0.185467822	0.190572183	0.207917291	0.250217758	0.289333346	0.350141005	0.448075053	0.463099156	0.472918112
Standard Deviation	0.004334819	0.004654137	0.004513427	0.005007242	0.003003921	0.004580158	0.004728572	0.00442686	0.005349076	0.005914604	0.004884103	0.011364709	0.008144794	0.006259434
Standard Error	0.000969295	0.001040697	0.001009233	0.001119653	0.000671697	0.001024154	0.001057341	0.000989876	0.00119609	0.001322546	0.001092119	0.002541226	0.001821231	0.001399652
95%CI	0.001899818	0.002039765	0.001978097	0.002194521	0.001316527	0.002007343	0.002072388	0.001940157	0.002344336	0.00259219	0.002140552	0.004980803	0.003569613	0.002743318
95%CI/Average	1.47%	1.51%	4.14%	2.99%	0.76%	1.08%	1.09%	0.93%	0.94%	0.90%	0.61%	1.11%	0.77%	0.58%

Speed8

Measured Pressure Value

L/D_{inlet}	0.25	0.5	1	1.625	2	2.25	2.5	2.75	3	3.25	3.5	4	4.5	4.75
Average	-1224.99577	-1232.10644	-1135.26797	-1009.840292	-893.050621	-871.87247	-859.103178	-833.065229	-782.79056	-741.858856	-682.273197	-623.285132	-606.605356	-597.80054
Standard Deviation	8.925483345	9.466125668	8.581397998	9.345776153	6.153900984	5.936554592	5.89475911	10.75214781	13.74088727	12.13746813	7.986607873	7.858259073	6.30154576	5.324768952
Standard Error	1.995798749	2.116690048	1.918858927	2.089779078	1.376054093	1.327453962	1.318108208	2.40425334	3.0725558	2.714020381	1.785859811	1.757160147	1.409068468	1.190654534
95%CI	3.911765548	4.148712494	3.760963496	4.095966993	2.697066022	2.601809765	2.583492088	4.712336546	6.022209368	5.319479946	3.50028523	3.444033889	2.761774198	2.333682887
95%CI/Average	0.32%	0.34%	0.33%	0.41%	0.30%	0.30%	0.30%	0.57%	0.77%	0.72%	0.51%	0.55%	0.46%	0.39%

C_p

Average	-0.109462955	-0.115902997	-0.028197637	0.085400602	0.191175509	0.210356288	0.221921272	0.245503509	0.291036631	0.328107951	0.382073918	0.435498651	0.450605311	0.458579719
Standard Deviation	0.008083696	0.008573349	0.007772062	0.00846435	0.005573509	0.005376661	0.005338808	0.009738082	0.012444945	0.010992749	0.007233368	0.007117124	0.005707229	0.004822575
Standard Error	0.001807569	0.001917059	0.001737886	0.001892686	0.001246275	0.001202258	0.001193794	0.002177501	0.002782774	0.002458053	0.00161743	0.001591437	0.001276175	0.001078361
95%CI	0.003542836	0.003757436	0.003406256	0.003709665	0.002442698	0.002356426	0.002339836	0.004267903	0.005454238	0.004817785	0.003170163	0.003119217	0.002501303	0.002113587
95%CI/Average	3.24%	3.24%	12.08%	4.34%	1.28%	1.12%	1.05%	1.74%	1.87%	1.47%	0.83%	0.72%	0.56%	0.46%

Speed10

Measured Pressure Value

L/D_{inlet}	0.25	0.5	1	1.625	2	2.25	2.5	2.75	3	3.25	3.5	4	4.5	4.75
Average	-1363.37057	-1371.3383	-1260.19683	-1121.37008	-994.287932	-971.715493	-960.993384	-937.699133	-883.595089	-836.229041	-763.80238	-701.980496	-678.763516	-669.834742
Standard Deviation	6.791465497	7.682696599	7.373720022	8.889916593	3.653095275	5.964606952	7.69881191	8.749239524	8.466486885	8.269695161	5.867223279	7.501564195	7.096084101	5.904467199
Standard Error	1.518617852	1.717903184	1.648813922	1.987845782	0.816856936	1.33372666	1.721506678	1.956389433	1.893164021	1.849160053	1.311951009	1.677400748	1.586732642	1.320279003
95%CI	2.97649099	3.367090242	3.231675286	3.896177732	1.601039595	2.614104254	3.374153088	3.834523288	3.71060148	3.624353704	2.571423978	3.287705466	3.109995979	2.587746846
95%CI/Average	0.22%	0.25%	0.26%	0.35%	0.16%	0.27%	0.35%	0.41%	0.42%	0.43%	0.34%	0.47%	0.46%	0.39%

C_p

Average	-0.104834806	-0.111291617	-0.021225887	0.091275166	0.194258745	0.212550775	0.221239652	0.240116618	0.28396092	0.322344951	0.381037355	0.431135964	0.449950311	0.457185923
Standard Deviation	0.005503601	0.006225828	0.005975443	0.007204123	0.002960359	0.004833539	0.006238887	0.007090122	0.006860988	0.006701514	0.004754623	0.006079044	0.005750455	0.004784804
Standard Error	0.001230643	0.001392137	0.00133615	0.001610891	0.000661956	0.001080812	0.001395058	0.0015854	0.001534164	0.001498504	0.001063166	0.001359315	0.001285841	0.001069915
95%CI	0.002412059	0.002728589	0.002618853	0.003157346	0.001297435	0.002118392	0.002734313	0.003107383	0.003006961	0.002937068	0.002083805	0.002664258	0.002520248	0.002097033
95%CI/Average	2.30%	2.45%	12.34%	3.46%	0.67%	1.00%	1.24%	1.29%	1.06%	0.91%	0.55%	0.62%	0.56%	0.46%

Table 17: Statistical Parameters for Type4 C_p Experimental Data at 0°

0°

Speed2

Measured Pressure Value

L/D_{inlet}	0.25	0.5	1	1.625	2	2.25	2.5	2.75	3	3.25	3.5	4	4.5	4.75
Average	-221.299047	-207.682953	-192.822539	-166.481329	-168.492454	-166.628605	-170.763074	-189.77616	-218.036673	-233.329483	-234.249798	-209.817694	-184.865413	-171.724948
Standard Deviation	1.788500336	1.757798896	1.660195043	1.434146222	1.456541246	1.366895986	1.308608139	1.489305262	2.394589536	3.187533156	3.418457469	1.774634467	1.348732457	1.196308605
Standard Error	0.399920833	0.393055782	0.371230897	0.320684844	0.325692524	0.305647234	0.292613676	0.33301878	0.535446498	0.712754082	0.764390328	0.39682033	0.301585746	0.267502736
95%CI	0.783844832	0.770389333	0.727612558	0.628542295	0.638357347	0.599068579	0.573522804	0.65271681	1.049475136	1.396998	1.498205042	0.777767847	0.591108062	0.524305363
95%CI/Average	0.35%	0.37%	0.38%	0.38%	0.38%	0.36%	0.34%	0.34%	0.48%	0.60%	0.64%	0.37%	0.32%	0.31%

C_p

Average	0.098034469	0.153530629	0.214098361	0.321459254	0.313262358	0.32085899	0.304007817	0.226514722	0.111331177	0.049001096	0.045250098	0.144829902	0.246529831	0.300087434
Standard Deviation	0.007289528	0.007164396	0.006766585	0.00584526	0.005936537	0.005571163	0.005333595	0.006070076	0.009759813	0.012991674	0.01393287	0.007233014	0.005497133	0.004875887
Standard Error	0.001629988	0.001602008	0.001513054	0.00130704	0.00132745	0.00124575	0.001192628	0.00135731	0.00218236	0.002905027	0.003115484	0.001617351	0.001229196	0.001090281
95%CI	0.003194777	0.003139935	0.002965586	0.002561798	0.002601802	0.00244167	0.002337551	0.002660328	0.004277426	0.005693852	0.006106349	0.003170008	0.002409225	0.002136952
95%CI/Average	3.26%	2.05%	1.39%	0.80%	0.83%	0.76%	0.77%	1.17%	3.84%	11.62%	13.49%	2.19%	0.98%	0.71%

Speed4

Measured Pressure Value

L/D_{inlet}	0.25	0.5	1	1.625	2	2.25	2.5	2.75	3	3.25	3.5	4	4.5	4.75
Average	-412.82932	-386.669015	-360.337473	-314.624516	-314.117334	-310.934855	-319.031186	-355.233826	-410.690071	-444.629307	-445.154669	-421.119438	-372.716668	-345.355931
Standard Deviation	2.629953291	2.574068944	2.272651323	2.167295487	1.996079839	1.86139102	1.742802065	1.602398738	1.943675498	2.388976623	2.415836935	5.357874272	4.634719005	4.10459152
Standard Error	0.588075434	0.575579314	0.508180285	0.484622004	0.446337021	0.416219685	0.389702389	0.35830725	0.434619054	0.534191413	0.540197561	1.198057109	1.036354675	0.917814566
95%CI	1.15262785	1.128135455	0.996033358	0.949859127	0.874820561	0.815790583	0.763816682	0.702282211	0.851853346	1.047015169	1.058787219	2.348191933	2.031255163	1.798916549
95%CI/Average	0.28%	0.29%	0.28%	0.30%	0.28%	0.26%	0.24%	0.20%	0.21%	0.24%	0.24%	0.56%	0.54%	0.52%

C_p

Average	0.121632269	0.177292966	0.233318001	0.330580439	0.331659559	0.338430848	0.321204466	0.244176916	0.126183902	0.053972147	0.052854346	0.10399357	0.206979064	0.265193893
Standard Deviation	0.005595693	0.005476789	0.00483547	0.004611306	0.004247015	0.00396044	0.003708121	0.003409388	0.004135515	0.005082972	0.005140122	0.01139983	0.009861188	0.008733248
Standard Error	0.001251235	0.001224647	0.001081244	0.001031119	0.000949661	0.000885581	0.000829161	0.000762362	0.000924729	0.001136587	0.001149366	0.002549079	0.002205029	0.001952814
95%CI	0.002452421	0.002400309	0.002119238	0.002020994	0.001861336	0.001735739	0.001625156	0.00149423	0.001812469	0.002227711	0.002252758	0.004996196	0.004321856	0.003827515
95%CI/Average	2.02%	1.35%	0.91%	0.61%	0.56%	0.51%	0.51%	0.61%	1.44%	4.13%	4.26%	4.80%	2.09%	1.44%

Speed6

Measured Pressure Value

L/D_{inlet}	0.25	0.5	1	1.625	2	2.25	2.5	2.75	3	3.25	3.5	4	4.5	4.75
Average	-720.995616	-673.86497	-630.286709	-554.598968	-546.785688	-540.40421	-553.814553	-616.28989	-713.845865	-779.4344	-776.38053	-695.469567	-618.079493	-572.036247
Standard Deviation	2.653055272	2.24094358	2.723617217	1.829623621	1.872135424	1.875642159	2.092573428	2.59829107	4.270418538	5.962214985	6.204575086	2.627172386	1.827034173	1.504239121
Standard Error	0.593241194	0.501090218	0.609019324	0.409116279	0.418622207	0.419406337	0.467913643	0.580995546	0.954894614	1.3331918	1.387385166	0.587453604	0.408537261	0.336358093
95%CI	1.162752739	0.982136827	1.193677875	0.801867907	0.820499526	0.82203642	0.917110741	1.13875127	1.871593444	2.613055929	2.719274926	1.151409065	0.800733031	0.659261862
95%CI/Average	0.16%	0.15%	0.19%	0.14%	0.15%	0.15%	0.17%	0.18%	0.26%	0.34%	0.35%	0.17%	0.13%	0.12%

C_p

Average	0.082303476	0.142292231	0.197759446	0.2940962	0.304041087	0.31216355	0.295094618	0.215574856	0.091403811	0.007921513	0.011808535	0.114793502	0.213297016	0.271901709
Standard Deviation	0.003376858	0.002852314	0.00346667	0.002328779	0.002382889	0.002387352	0.002663466	0.003307153	0.005435468	0.007588817	0.007897298	0.003343913	0.002325483	0.001914623
Standard Error	0.000755088	0.000637797	0.000775171	0.000520731	0.00053283	0.000533828	0.000595569	0.000739502	0.001215407	0.001696911	0.001765889	0.000747722	0.000519994	0.000428123
95%CI	0.001479973	0.001250082	0.001519335	0.001020632	0.001044347	0.001046303	0.001167315	0.001449424	0.002382199	0.003325946	0.003461143	0.001465535	0.001019188	0.000839121
95%CI/Average	1.80%	0.88%	0.77%	0.35%	0.34%	0.34%	0.40%	0.67%	2.61%	41.99%	29.31%	1.28%	0.48%	0.31%

Speed8

Measured Pressure Value

L/D_{inlet}	0.25	0.5	1	1.625	2	2.25	2.5	2.75	3	3.25	3.5	4	4.5	4.75
Average	-940.3708	-878.81184	-822.863448	-725.756499	-713.958198	-705.267262	-722.964386	-803.426429	-929.979363	-1017.803228	-1011.613417	-884.072986	-788.096942	-729.367847
Standard Deviation	3.724813265	3.450692032	3.616387181	3.194278672	3.188804555	3.191030532	3.276883744	3.125759204	4.674285744	6.903840994	6.711670146	4.146196341	3.655864369	3.181994133
Standard Error	0.832893566	0.771598195	0.808648757	0.714262425	0.713038375	0.7135361 19	0.732733481	0.698941006	1.045202067	1.543745777	1.500775069	0.927117687	0.817476125	0.711515519
95%CI	1.63247139	1.512332463	1.584951563	1.399954353	1.397555216	1.398530793	1.436157622	1.369924372	2.048596051	3.025741723	2.941519135	1.817150666	1.602253204	1.394570416
95%CI/Average	0.17%	0.17%	0.19%	0.19%	0.20%	0.20%	0.20%	0.17%	0.22%	0.30%	0.29%	0.21%	0.20%	0.19%

C_p

Average	0.086299212	0.146112288	0.200473919	0.294826801	0.306290489	0.31473494	0.297539727	0.219359681	0.096395936	0.011062858	0.017077119	0.141000355	0.234254406	0.291317876
Standard Deviation	0.003619173	0.003352826	0.003513822	0.003103685	0.003098366	0.003100529	0.003183948	0.003037109	0.004541718	0.00670804	0.006521319	0.004028605	0.00355218	0.003091749
Standard Error	0.000809272	0.000749715	0.000785715	0.000694005	0.000692816	0.000693299	0.000711952	0.000679118	0.001015559	0.001499963	0.001458211	0.000900824	0.000794292	0.000691336
95%CI	0.001586173	0.001469441	0.00154	0.00136025	0.001357919	0.001358867	0.001395427	0.001331072	0.001990495	0.002939928	0.002858094	0.001765614	0.001556811	0.001355019
95%CI/Average	1.84%	1.01%	0.77%	0.46%	0.44%	0.43%	0.47%	0.61%	2.06%	26.57%	16.74%	1.25%	0.66%	0.47%

Speed10

Measured Pressure Value

L/D_{inlet}	0.25	0.5	1	1.625	2	2.25	2.5	2.75	3	3.25	3.5	4	4.5	4.75
Average	-1062.96202	-992.243461	-931.24177	-819.376394	-805.533006	-795.122268	-814.8742	-905.980455	-1050.28794	-1151.16542	-1143.17125	-991.765495	-884.090384	-818.01162
Standard Deviation	4.656850958	4.065508406	4.363773264	2.814975602	2.279295021	2.313943073	3.142738615	4.794233998	7.649293272	10.23525265	10.03971042	9.119194089	5.999639488	4.69264529
Standard Error	1.04130353	0.909075316	0.975769366	0.62944768	0.509665861	0.517413401	0.702737718	1.072023312	1.710433974	2.288672068	2.244947498	2.039113788	1.341560173	1.049307386
95%CI	2.040954919	1.781787619	1.912507957	1.233717453	0.998945087	1.014130265	1.377365927	2.101165692	3.352450588	4.485797254	4.400097096	3.996663025	2.62945794	2.056642477
95%CI/Average	0.19%	0.18%	0.21%	0.15%	0.12%	0.13%	0.17%	0.23%	0.32%	0.39%	0.38%	0.40%	0.30%	0.25%

C_p

Average	0.08154415	0.142648755	0.195357467	0.292015116	0.303976541	0.312971974	0.295905251	0.21718459	0.09249523	0.00533171	0.012239099	0.143061743	0.236098779	0.293194353
Standard Deviation	0.004023767	0.003512816	0.003770533	0.002432289	0.001969432	0.00199937	0.002715494	0.004142474	0.006609397	0.008843804	0.008674845	0.00787947	0.005184008	0.004054696
Standard Error	0.000899742	0.00078549	0.000843117	0.000543876	0.000440378	0.000447073	0.000607203	0.000926285	0.001477906	0.001977535	0.001939754	0.001761903	0.00115918	0.000906658
95%CI	0.001763494	0.001539559	0.001652509	0.001065998	0.000863142	0.000876263	0.001190118	0.001815519	0.002896696	0.003875968	0.003801918	0.00345333	0.002271992	0.001777049
95%CI/Average	2.16%	1.08%	0.85%	0.37%	0.28%	0.28%	0.40%	0.84%	3.13%	72.70%	31.06%	2.41%	0.96%	0.61%

Table 18: Statistical Parameters for Type4 C_p Experimental Data at 60°

60°

Speed2

Measured Pressure Value

L/D_{inlet}	0.25	0.5	1	1.625	2	2.25	2.5	2.75	3	3.5	4	4.5	4.75
Average	-231.919462	-220.086121	-198.639015	-190.067673	-183.822028	-191.215263	-188.655932	-200.802158	-212.201452	-201.727536	-185.583513	-169.162623	-156.917905
Standard Deviation	1.602700572	1.552020458	1.385161823	1.23817697	1.102849766	1.261802441	1.124776934	1.519678248	2.119550694	2.176994838	1.654901314	1.195819819	1.084990696
Standard Error	0.358374743	0.347042325	0.3097316	0.276864787	0.246604705	0.282147603	0.251507768	0.339810387	0.473945943	0.486790844	0.370047183	0.26739344	0.242611295
95%CI	0.702414495	0.680202956	0.607073935	0.542654983	0.483345221	0.553009302	0.492955226	0.666028358	0.928934049	0.954110055	0.72529248	0.524091143	0.475518138
95%CI/Average	0.30%	0.31%	0.31%	0.29%	0.26%	0.29%	0.26%	0.33%	0.44%	0.47%	0.39%	0.31%	0.30%

C_p

Average	0.054748027	0.102978085	0.190391703	0.22532658	0.250782435	0.220649259	0.231080521	0.181575214	0.135114236	0.17780358	0.243603015	0.310530898	0.360437637
Standard Deviation	0.00653225	0.006325689	0.00564561	0.005046533	0.00449497	0.005142825	0.00458434	0.006193869	0.008638816	0.008872945	0.006745008	0.004873895	0.00442218
Standard Error	0.001460655	0.001414467	0.001262397	0.001128439	0.001005106	0.001149971	0.00102509	0.001384991	0.001931698	0.001984051	0.00150823	0.001089836	0.000988829
95%CI	0.002862885	0.002772355	0.002474298	0.002211741	0.001970007	0.002253943	0.002009175	0.002714583	0.003786128	0.00388874	0.00295613	0.002136079	0.001938106
95%CI/Average	5.23%	2.69%	1.30%	0.98%	0.79%	1.02%	0.87%	1.50%	2.80%	2.19%	1.21%	0.69%	0.54%

Speed4

Measured Pressure Value

L/D_{inlet}	0.25	0.5	1	1.625	2	2.25	2.5	2.75	3	3.5	4	4.5	4.75
Average	-460.94184	-438.796779	-398.66235	-380.566724	-367.564171	-387.877357	-377.809062	-403.268719	-432.413242	-412.171226	-378.064933	-338.869277	-315.922359
Standard Deviation	5.570869985	5.369656491	4.978882666	4.781253567	4.518954547	5.42174222	4.631889472	5.089025337	5.98038019	5.414366947	4.465668507	3.741364167	3.415687701
Standard Error	1.245684398	1.200691693	1.113312009	1.069120799	1.010468955	1.212338416	1.035721972	1.137940659	1.337253664	1.210689255	0.998553835	0.836594461	0.763770989
95%CI	2.44154142	2.353355718	2.182091538	2.095476767	1.980519153	2.376183295	2.030015066	2.230363692	2.621017181	2.37295094	1.957165516	1.639725143	1.496991138
95%CI/Average	0.53%	0.54%	0.55%	0.55%	0.54%	0.61%	0.54%	0.55%	0.61%	0.58%	0.52%	0.48%	0.47%

C_p

Average	0.019264334	0.066381886	0.151775015	0.190276675	0.217941917	0.174722004	0.196144091	0.141974147	0.079963995	0.123032481	0.19559968	0.278995402	0.327819047
Standard Deviation	0.011853016	0.011424898	0.010593458	0.010172967	0.009614879	0.01153572	0.009855168	0.010827806	0.012724321	0.011520028	0.009501503	0.007960417	0.007267482
Standard Error	0.002650415	0.002554685	0.002368769	0.002274744	0.002149952	0.002579465	0.002203683	0.002421171	0.002845245	0.002575957	0.002124601	0.001780003	0.001625058
95%CI	0.005194813	0.005007182	0.004642787	0.004458499	0.004213906	0.005055752	0.004319218	0.004745495	0.00557668	0.005048875	0.004164217	0.003488807	0.003185115
95%CI/Average	26.97%	7.54%	3.06%	2.34%	1.93%	2.89%	2.20%	3.34%	6.97%	4.10%	2.13%	1.25%	0.97%

Speed6

Measured Pressure Value

L/D_{inlet}	0.25	0.5	1	1.625	2	2.25	2.5	2.75	3	3.5	4	4.5	4.75
Average	-767.535388	-731.56433	-666.189219	-635.102799	-611.300367	-653.291188	-627.330252	-667.701632	-721.100196	-686.309161	-628.903015	-560.198565	-523.089307
Standard Deviation	2.341607903	2.271731681	2.092888298	1.903854963	1.719657034	2.851099686	1.689742359	2.379172379	3.932091376	3.760514864	2.55776356	1.468710268	1.345510828
Standard Error	0.523599445	0.507974647	0.46798405	0.425714912	0.384527003	0.637525271	0.377837878	0.531999117	0.879242361	0.840876687	0.571933319	0.3284136	0.300865368
95%CI	1.026254912	0.995630307	0.917248739	0.834401227	0.753672925	1.249549531	0.740562241	1.042718269	1.723315028	1.648118306	1.120989305	0.643690656	0.58969612
95%CI/Average	0.13%	0.14%	0.14%	0.13%	0.12%	0.19%	0.12%	0.16%	0.24%	0.24%	0.18%	0.11%	0.11%

C_p

Average	0.023066795	0.068851421	0.152062069	0.191629438	0.221925613	0.168478921	0.201522479	0.150137042	0.082170364	0.126453036	0.199520637	0.286968929	0.334202278
Standard Deviation	0.002980442	0.002891502	0.002663867	0.002423262	0.002188811	0.003628932	0.002150735	0.003028255	0.005004838	0.004786453	0.003255569	0.001869402	0.001712591
Standard Error	0.000666447	0.00064656	0.000595659	0.000541858	0.000489433	0.000811454	0.000480919	0.000677138	0.001119116	0.001070283	0.000727967	0.000418011	0.000382947
95%CI	0.001306236	0.001267257	0.001167491	0.001062041	0.000959289	0.00159045	0.000942601	0.001327191	0.002193467	0.002097755	0.001426816	0.000819301	0.000750576
95%CI/Average	5.66%	1.84%	0.77%	0.55%	0.43%	0.94%	0.47%	0.88%	2.67%	1.66%	0.72%	0.29%	0.22%

Speed8

Measured Pressure Value

L/D_{inlet}	0.25	0.5	1	1.625	2	2.25	2.5	2.75	3	3.5	4	4.5	4.75
Average	-981.943453	-936.03288	-853.599818	-812.859777	-781.156413	-840.312362	-800.099616	-849.943051	-921.12022	-876.537309	-803.632256	-713.272177	-666.879965
Standard Deviation	4.219162598	4.116375062	3.855230145	3.651624081	3.465107148	4.731012236	3.346590095	3.856440756	5.818900912	5.455389588	4.274147507	2.824895869	2.614999682
Standard Error	0.943433438	0.920449446	0.862055667	0.816527967	0.774821513	1.057886496	0.748320295	0.862326368	1.301145799	1.219862196	0.955728437	0.631665919	0.584731705
95%CI	1.849129538	1.804080914	1.689629108	1.600394816	1.518650166	2.073457532	1.466707777	1.690159682	2.550245767	2.390929904	1.873227737	1.238065202	1.146074142
95%CI/Average	0.19%	0.19%	0.20%	0.20%	0.19%	0.25%	0.18%	0.20%	0.28%	0.27%	0.23%	0.17%	0.17%

C_p

Average	0.045905608	0.090514104	0.170609268	0.210193874	0.240998094	0.183519876	0.222592142	0.174162325	0.105003823	0.148322311	0.219159692	0.306957054	0.352033528
Standard Deviation	0.004099502	0.00399963	0.003745891	0.00354806	0.003366833	0.004596835	0.003251677	0.003747068	0.00565387	0.005300668	0.004152928	0.002744779	0.002540835
Standard Error	0.000916677	0.000894344	0.000837607	0.00079337	0.000752847	0.001027884	0.000727097	0.00083787	0.001264244	0.001185265	0.000928623	0.000613751	0.000568148
95%CI	0.001796686	0.001752915	0.001641709	0.001555006	0.001475579	0.002014652	0.00142511	0.001642225	0.002477918	0.00232312	0.001820101	0.001202952	0.00111357
95%CI/Average	3.91%	1.94%	0.96%	0.74%	0.61%	1.10%	0.64%	0.94%	2.36%	1.57%	0.83%	0.39%	0.32%

Speed10

Measured Pressure Value

L/D_{inlet}	0.25	0.5	1	1.625	2	2.25	2.5	2.75	3	3.5	4	4.5	4.75
Average	-1101.02033	-1049.42511	-957.656119	-912.008628	-876.583346	-946.837812	-899.359354	-955.836796	-1038.249679	-987.256135	-904.319786	-799.073357	-746.664827
Standard Deviation	3.841011442	3.776669066	3.590256289	3.657386211	4.211786293	4.291054795	6.489608366	8.964688704	12.11207788	12.03967125	8.757634864	5.197793959	4.046114451
Standard Error	0.858876269	0.844488876	0.802805712	0.817816419	0.941784046	0.959509022	1.451120545	2.004565334	2.708342949	2.692152335	1.958266688	1.162262063	0.904738696
95%CI	1.683397486	1.655198197	1.573499195	1.602920181	1.84589673	1.880637682	2.844196269	3.928948055	5.308352181	5.276618576	3.838202708	2.278033643	1.773287844
95%CI/Average	0.15%	0.16%	0.16%	0.18%	0.21%	0.20%	0.32%	0.41%	0.51%	0.53%	0.42%	0.29%	0.24%

C_p

Average	0.048659741	0.093240762	0.172534062	0.211975927	0.24258526	0.181881656	0.222905575	0.174106054	0.10289693	0.14695807	0.218619497	0.309558022	0.354841786
Standard Deviation	0.003318839	0.003263243	0.003102173	0.003160177	0.003639208	0.0037077	0.005607368	0.007745969	0.010465481	0.010402918	0.007567063	0.004491171	0.003496059
Standard Error	0.000742115	0.000729683	0.000693667	0.000706637	0.000813752	0.000829067	0.001253846	0.001732051	0.002340153	0.002326163	0.001692047	0.001004256	0.000781742
95%CI	0.001454545	0.001430179	0.001359587	0.001385008	0.001594953	0.001624971	0.002457537	0.003394821	0.004586699	0.00455928	0.003316412	0.001968343	0.001532215
95%CI/Average	2.99%	1.53%	0.79%	0.65%	0.66%	0.89%	1.10%	1.95%	4.46%	3.10%	1.52%	0.64%	0.43%

Table 19: Statistical Parameters for Type4 C_p Experimental Data at 120°

120°

Speed2

Measured Pressure Value

L/D_{inlet}	0.25	0.5	1	2	2.25	2.5	2.75	3	3.5	4	4.5	4.75
Average	-258.78369	-255.037426	-233.34958	-220.417862	-202.879855	-188.472475	-188.989462	-181.269255	-165.688113	-160.15128	-149.250583	-152.225414
Standard Deviation	1.739810505	1.661600725	1.59865894	1.241069974	1.171415634	1.317459054	1.874343608	2.042323794	1.794921236	1.347049073	1.06552281	0.977884732
Standard Error	0.389033456	0.371545217	0.357471006	0.277511683	0.261936499	0.2945928	0.419115972	0.456677483	0.40135659	0.30120933	0.238258144	0.218661673
95%CI	0.762505573	0.728228626	0.700643172	0.543922898	0.513395538	0.577401889	0.821467305	0.895087868	0.786658916	0.590370286	0.466985961	0.42857688
95%CI/Average	0.29%	0.29%	0.30%	0.25%	0.25%	0.31%	0.43%	0.49%	0.47%	0.37%	0.31%	0.28%

C_p

Average	-0.054744571	-0.039475635	0.048919185	0.101625982	0.173106985	0.231828251	0.229721127	0.261186968	0.324692226	0.347259122	0.39168793	0.379563183
Standard Deviation	0.007091079	0.006772314	0.006515777	0.005058324	0.004774429	0.005369669	0.007639406	0.008324056	0.007315698	0.005490271	0.004342833	0.00398564
Standard Error	0.001585614	0.001514335	0.001456972	0.001131076	0.001067595	0.001200695	0.001708223	0.001861316	0.00163584	0.001227662	0.000971087	0.000891216
95%CI	0.003107803	0.002968097	0.002855665	0.002216908	0.002092486	0.002353361	0.003348117	0.003648178	0.003206246	0.002406218	0.001903331	0.001746784
95%CI/Average	5.68%	7.52%	5.84%	2.18%	1.21%	1.02%	1.46%	1.40%	0.99%	0.69%	0.49%	0.46%

Speed4

Measured Pressure Value

L/D_{inlet}	0.25	0.5	1	2	2.25	2.5	2.75	3	3.5	4	4.5	4.75
Average	-479.049774	-469.0567	-432.65333	-397.754298	-373.516629	-349.857652	-346.868816	-331.654957	-305.170305	-289.315608	-273.346404	-274.235551
Standard Deviation	17.65889334	17.01874712	15.7692413	14.1802395	13.91835985	13.34108044	12.74660718	12.09744695	11.09681066	10.18799341	9.620061203	9.390422727
Standard Error	3.948648592	3.805507545	3.526109549	3.170797946	3.112239877	2.983156276	2.850228013	2.705071373	2.481322296	2.278104581	2.15111108	2.099762355
95%CI	7.73935124	7.458794788	6.911174717	6.214763974	6.099990159	5.846986301	5.586446905	5.301939892	4.863391701	4.465084979	4.216177716	4.115534217
95%CI/Average	1.62%	1.59%	1.60%	1.56%	1.63%	1.67%	1.61%	1.60%	1.59%	1.54%	1.54%	1.50%

C_p

Average	-0.019263513	0.001998528	0.079453166	0.153707057	0.205277004	0.255615682	0.261974961	0.29434515	0.350695953	0.384429638	0.418406957	0.416515138
Standard Deviation	0.037572433	0.036210408	0.033551863	0.030170979	0.029613784	0.028385519	0.027120672	0.025739468	0.023610436	0.021676766	0.02046839	0.019979793
Standard Error	0.008401451	0.008096893	0.007502425	0.006746436	0.006621843	0.006347195	0.006064367	0.00575552	0.005279454	0.004847072	0.004576871	0.004467618
95%CI	0.016466845	0.015869911	0.014704752	0.013223015	0.012978813	0.012440502	0.011886158	0.011280819	0.01034773	0.009500262	0.008970667	0.00875653
95%CI/Average	85.48%	794.08%	18.51%	8.60%	6.32%	4.87%	4.54%	3.83%	2.95%	2.47%	2.14%	2.10%

Speed6

Measured Pressure Value

L/D_{inlet}	0.25	0.5	1	2	2.25	2.5	2.75	3	3.5	4	4.5	4.75
Average	-803.781364	-783.544019	-724.899541	-656.067227	-621.630951	-583.415661	-573.50452	-546.384786	-506.438005	-475.938491	-453.547001	-450.558863
Standard Deviation	3.513686393	3.365943669	3.001741684	2.541740677	2.714913071	3.748434263	4.374178972	4.304309184	3.402884925	2.471358846	1.647717796	1.411603176
Standard Error	0.785684163	0.752647885	0.671209846	0.568350493	0.607073018	0.838175382	0.978096153	0.962472793	0.760908201	0.552612638	0.3684409	0.315644066
95%CI	1.539940959	1.475189855	1.315571298	1.113966967	1.189863115	1.642823749	1.917068459	1.886446675	1.491380074	1.08312077	0.722144164	0.618662369
95%CI/Average	0.19%	0.19%	0.18%	0.17%	0.19%	0.28%	0.33%	0.35%	0.29%	0.23%	0.16%	0.14%

C_p

Average	-0.023067752	0.002690714	0.077334488	0.164945527	0.208776655	0.257417781	0.270032864	0.304551362	0.355396362	0.394216706	0.422717008	0.426520365
Standard Deviation	0.004472285	0.004284235	0.003820672	0.003235174	0.003455591	0.004771076	0.005567536	0.005478604	0.004331255	0.003145591	0.002097246	0.001796715
Standard Error	0.001000033	0.000957984	0.000854328	0.000723407	0.000772694	0.001066845	0.001244939	0.001225053	0.000968498	0.000703376	0.000468958	0.000401758
95%CI	0.001960065	0.001877649	0.001674483	0.001417878	0.00151448	0.002091016	0.00244008	0.002401104	0.001898256	0.001378616	0.000919158	0.000787445
95%CI/Average	8.50%	69.78%	2.17%	0.86%	0.73%	0.81%	0.90%	0.79%	0.53%	0.35%	0.22%	0.18%

Speed8

Measured Pressure Value

L/D_{inlet}	0.25	0.5	1	2	2.25	2.5	2.75	3	3.5	4	4.5	4.75
Average	-1076.43478	-1046.62378	-968.827281	-874.244547	-832.604888	-782.281039	-767.131673	-730.186983	-677.414078	-632.469306	-602.512064	-596.029702
Standard Deviation	3.264953063	2.946318327	2.779082037	6.100260358	8.196537026	10.95927926	11.74550392	11.35123952	9.33874026	6.677270368	4.041740938	2.866921746
Standard Error	0.730065699	0.658816806	0.621421635	1.364059684	1.832801397	2.450569341	2.62637452	2.538214321	2.088205805	1.493083045	0.903760749	0.641063191
95%CI	1.43092877	1.29128094	1.217986405	2.673556981	3.592290738	4.803115908	5.147694059	4.974900068	4.092883377	2.926442767	1.771371067	1.256483854
95%CI/Average	0.13%	0.12%	0.13%	0.31%	0.43%	0.61%	0.67%	0.68%	0.60%	0.46%	0.29%	0.21%

C_p

Average	-0.045905835	-0.016940309	0.05864979	0.150550048	0.191008757	0.239905363	0.254625076	0.290521971	0.341798175	0.385468261	0.414575881	0.420874395
Standard Deviation	0.003172355	0.002862757	0.002700264	0.00592725	0.007964074	0.010648461	0.011412388	0.011029305	0.009073883	0.006487895	0.003927112	0.002785613
Standard Error	0.00070936	0.000640132	0.000603797	0.001325373	0.001780821	0.002381068	0.002551887	0.002466228	0.002028982	0.001450737	0.000878129	0.000622882
95%CI	0.001390346	0.001254659	0.001183443	0.002597732	0.003490409	0.004666894	0.005001699	0.004833806	0.003976804	0.002843445	0.001721133	0.001220849
95%CI/Average	3.03%	7.41%	2.02%	1.73%	1.83%	1.95%	1.96%	1.66%	1.16%	0.74%	0.42%	0.29%

Speed10

Measured Pressure Value

L/D_{inlet}	0.25	0.5	1	2	2.25	2.5	2.75	3	3.5	4	4.5	4.75
Average	-1213.65087	-1179.46112	-1092.83108	-980.653226	-934.205316	-875.792693	-856.237246	-814.308602	-757.156544	-707.382378	-675.723221	-668.448595
Standard Deviation	3.363968333	3.661138443	3.644098033	3.51013972	5.463874852	7.78014046	9.956998348	10.17342933	8.359184579	5.402570787	3.048998611	2.390585484
Standard Error	0.752206187	0.818655443	0.814845092	0.784891102	1.221759559	1.739692294	2.226452516	2.274847955	1.869170496	1.208051553	0.681776816	0.534551165
95%CI	1.474324126	1.604564669	1.59709638	1.538386561	2.394648736	3.409796897	4.363846931	4.458701991	3.663574171	2.367781044	1.336282559	1.047720283
95%CI/Average	0.12%	0.14%	0.15%	0.16%	0.26%	0.39%	0.51%	0.55%	0.48%	0.33%	0.20%	0.16%

C_p

Average	-0.04865905	-0.019117283	0.05573569	0.152663335	0.192796806	0.243268426	0.260165375	0.296393958	0.345776383	0.388783916	0.416139115	0.42242478
Standard Deviation	0.002906648	0.003163419	0.003148695	0.003032948	0.004721079	0.006722456	0.008603377	0.008790385	0.007222781	0.004668109	0.002634497	0.002065593
Standard Error	0.000649946	0.000707362	0.00070407	0.000678188	0.001055665	0.001503187	0.001923774	0.00196559	0.001615063	0.001043821	0.000589092	0.000461881
95%CI	0.001273895	0.001386429	0.001379976	0.001329248	0.002069104	0.002946246	0.003770596	0.003852556	0.003165523	0.002045889	0.001154619	0.000905286
95%CI/Average	2.62%	7.25%	2.48%	0.87%	1.07%	1.21%	1.45%	1.30%	0.92%	0.53%	0.28%	0.21%

Table 20: Statistical Parameters for Type4 C_p Experimental Data at 180°

180°

Speed2

Measured Pressure Value

L/D_{inlet}	0.25	0.5	1	1.625	2	2.25	2.5	2.75	3	3.25	3.5	4	4.5	4.75
Average	-268.20118	-270.215346	-253.113132	-223.495021	-198.231199	-194.258821	-193.22766	-186.898409	-176.33539	-167.651211	-158.352605	-144.417549	-139.158334	-140.070811
Standard Deviation	2.010142519	2.192003261	2.078411506	2.358144453	1.610136086	2.624048022	3.381998315	4.044932467	4.049198907	3.581382534	2.609777803	1.316872106	1.166600956	1.189991697
Standard Error	0.449481532	0.49014683	0.464746941	0.52729713	0.360037374	0.586754975	0.756237813	0.904474396	0.905428401	0.80082148	0.583564057	0.294461555	0.260859904	0.266090233
95%CI	0.880983802	0.960687786	0.910904005	1.033502374	0.705673253	1.150039752	1.482226114	1.772769816	1.774639666	1.569610101	1.143785553	0.577144647	0.511285412	0.521536856
95%CI/Average	0.33%	0.36%	0.36%	0.46%	0.36%	0.59%	0.77%	0.95%	1.01%	0.94%	0.72%	0.40%	0.37%	0.37%

C_p

Average	-0.114300633	-0.123776148	-0.052651171	0.07052513	0.17559274	0.192113132	0.196401542	0.222723738	0.2666534	0.30276931	0.34144051	0.399393857	0.421265969	0.417471144
Standard Deviation	0.011308749	0.00911614	0.008643733	0.009807091	0.006696261	0.010912935	0.014065112	0.016822134	0.016839877	0.014894314	0.010853588	0.00547663	0.00485168	0.004948958
Standard Error	0.002528713	0.002038431	0.001932797	0.002192932	0.00149733	0.002440207	0.003145055	0.003761543	0.003765511	0.00333047	0.002426936	0.001224612	0.001084869	0.001106621
95%CI	0.004956278	0.003995325	0.003788283	0.004298147	0.002934766	0.004782805	0.006164307	0.007372625	0.007380401	0.006527721	0.004756795	0.002400239	0.002126342	0.002168976
95%CI/Average	4.34%	3.23%	7.20%	6.09%	1.67%	2.49%	3.14%	3.31%	2.77%	2.16%	1.39%	0.60%	0.50%	0.52%

Speed4

Measured Pressure Value

L/D_{inlet}	0.25	0.5	1	1.625	2	2.25	2.5	2.75	3	3.25	3.5	4	4.5	4.75
Average	-500.126653	-502.675978	-467.75036	-414.441128	-370.002571	-364.401241	-362.702645	-352.892022	-333.483257	-314.777138	-294.770647	-292.407905	-281.006863	-281.431786
Standard Deviation	3.041786354	3.208010071	3.304899135	3.42573119	1.546261758	1.909705166	2.171707344	2.539388285	2.568165521	2.290942841	1.810312631	3.418793104	3.228899072	3.192946035
Standard Error	0.680164106	0.717332859	0.738997912	0.766016781	0.34575464	0.427023057	0.485608525	0.567824483	0.574259268	0.512270393	0.40479821	0.764465378	0.722003782	0.713964438
95%CI	1.333121648	1.405972404	1.448435908	1.501392891	0.677679095	0.836965191	0.951792708	1.112935986	1.125548166	1.004049969	0.793404492	1.498352141	1.415127412	1.399370299
95%CI/Average	0.27%	0.28%	0.31%	0.36%	0.18%	0.23%	0.26%	0.32%	0.34%	0.32%	0.27%	0.51%	0.50%	0.50%

C_p

Average	-0.064108318	-0.06953246	0.004777998	0.118202861	0.212753787	0.224671612	0.228285677	0.249159521	0.290455117	0.330255709	0.372823073	0.377850226	0.402107969	0.40120387
Standard Deviation	0.006471941	0.006825611	0.00703176	0.007288852	0.003289947	0.004063237	0.004620693	0.005403	0.005464228	0.004874388	0.003851762	0.00727409	0.006870056	0.00679356
Standard Error	0.00144717	0.001526253	0.001572349	0.001629837	0.000735654	0.000908567	0.001033218	0.001208147	0.001221839	0.001089946	0.00086128	0.001626536	0.001536191	0.001519086
95%CI	0.002836453	0.002991456	0.003081805	0.00319448	0.001441883	0.001780792	0.002025108	0.002367969	0.002394804	0.002136295	0.001688109	0.00318801	0.003010935	0.002977409
95%CI/Average	4.42%	4.30%	64.50%	2.70%	0.68%	0.79%	0.89%	0.95%	0.82%	0.65%	0.45%	0.84%	0.75%	0.74%

Speed6

Measured Pressure Value

L/D_{inlet}	0.25	0.5	1	1.625	2	2.25	2.5	2.75	3	3.25	3.5	4	4.5	4.75
Average	-871.5071	-874.92559	-810.563713	-722.420259	-643.048015	-630.580799	-625.564294	-607.556394	-571.733427	-540.806188	-506.398918	-483.806041	-465.415499	-466.262479
Standard Deviation	2.872041538	3.072023155	3.100889055	3.519465434	2.251956591	4.646524504	5.248460571	6.201779908	6.349110422	5.487336427	3.864837069	1.678908985	1.586267103	1.759292403
Standard Error	0.642208011	0.68692526	0.693379872	0.786976395	0.503552802	1.038994465	1.173591461	1.386760146	1.41970425	1.227005727	0.864203841	0.375415462	0.354700107	0.393389741
95%CI	1.258727702	1.34637351	1.359024549	1.542473735	0.986963492	2.036429152	2.300239264	2.718049885	2.78262033	2.404931224	1.693839528	0.735814305	0.69521221	0.771043892
95%CI/Average	0.14%	0.15%	0.17%	0.21%	0.15%	0.32%	0.37%	0.45%	0.49%	0.44%	0.33%	0.15%	0.15%	0.17%

C_p

Average	-0.109270319	-0.113621436	-0.031700451	0.080490164	0.18151662	0.197385123	0.203770223	0.226691011	0.272287144	0.311651905	0.355446113	0.384202743	0.407610565	0.406532513
Standard Deviation	0.003655587	0.003910128	0.003946869	0.004479641	0.002866332	0.005914182	0.006680337	0.00789374	0.008081265	0.006984383	0.004919236	0.002136946	0.00201903	0.00223926
Standard Error	0.000817414	0.000874331	0.000882547	0.001001678	0.000640931	0.001322451	0.001493769	0.001765094	0.001807026	0.001561756	0.001099975	0.000477836	0.000451469	0.000500714
95%CI	0.001602132	0.001713689	0.001729792	0.001963289	0.001256225	0.002592005	0.002927787	0.003459584	0.003541771	0.003061041	0.00215595	0.000936558	0.000884879	0.000981399
95%CI/Average	1.47%	1.51%	5.46%	2.44%	0.69%	1.31%	1.44%	1.53%	1.30%	0.98%	0.61%	0.24%	0.22%	0.24%

Speed8

Measured Pressure Value

L/D_{inlet}	0.25	0.5	1	1.625	2	2.25	2.5	2.75	3	3.25	3.5	4	4.5	4.75
Average	-1136.73046	-1140.83972	-1053.8419	-941.342765	-838.078693	-820.261331	-812.665143	-789.145133	-741.610405	-700.64631	-655.401227	-616.168826	-593.671841	-594.768789
Standard Deviation	4.245292037	4.407342766	4.209979222	4.192775862	3.379866003	6.148098968	6.378360008	5.418595525	4.319361224	3.209050949	2.576457081	2.6309595	2.751684519	2.807296156
Standard Error	0.949276158	0.985511803	0.941379972	0.937533184	0.755761014	1.374756723	1.426244656	1.211634794	0.965838532	0.717565606	0.576113318	0.588300429	0.615295364	0.627730504
95%CI	1.860581269	1.931603133	1.845104746	1.837565041	1.481291587	2.694523176	2.795439526	2.374804196	1.893043522	1.406428589	1.129182102	1.153068841	1.205978913	1.230351787
95%CI/Average	0.16%	0.17%	0.18%	0.20%	0.18%	0.33%	0.34%	0.30%	0.26%	0.20%	0.17%	0.19%	0.20%	0.21%

C_p

Average	-0.104491459	-0.108484175	-0.023953715	0.085354813	0.185690196	0.203002237	0.210382988	0.233235943	0.279422531	0.319224836	0.363186716	0.40130644	0.423165385	0.422099547
Standard Deviation	0.004124891	0.004282345	0.004090579	0.004073864	0.003284009	0.005973732	0.006197462	0.005264918	0.004196859	0.003118039	0.002503386	0.002556342	0.002673644	0.002727678
Standard Error	0.000922354	0.000957562	0.000914681	0.000910944	0.000734327	0.001335767	0.001385795	0.001177271	0.000938446	0.000697215	0.000559774	0.000571616	0.000597845	0.000609927
95%CI	0.001807813	0.001876821	0.001792775	0.00178545	0.00143928	0.002618103	0.002716158	0.002307452	0.001839355	0.001366541	0.001097157	0.001120366	0.001171776	0.001195458
95%CI/Average	1.73%	1.73%	7.48%	2.09%	0.78%	1.29%	1.29%	0.99%	0.66%	0.43%	0.30%	0.28%	0.28%	0.28%

Speed10

Measured Pressure Value

L/D_{inlet}	0.25	0.5	1	1.625	2	2.25	2.5	2.75	3	3.25	3.5	4	4.5	4.75
Average	-1283.37147	-1289.63027	-1187.23522	-1063.59915	-947.962271	-926.588784	-916.074228	-887.044741	-831.983481	-787.404241	-736.643007	-689.988433	-663.051484	-662.782422
Standard Deviation	4.954662669	5.617394206	5.072006583	6.500832725	5.025627418	8.93491501	11.10899481	13.56473576	14.16401555	12.18581522	8.006702173	5.103468584	2.480273763	2.455765481
Standard Error	1.107896253	1.25608753	1.13413515	1.453603388	1.123764454	1.997907734	2.484046756	3.033167125	3.16717016	2.724831119	1.790353034	1.141170267	0.554606074	0.549125855
95%CI	2.171476657	2.461931559	2.222904895	2.849115561	2.202578329	3.915899158	4.868731641	5.945007564	6.207653514	5.340668994	3.509091946	2.236693724	1.087027904	1.076286676
95%CI/Average	0.17%	0.19%	0.19%	0.27%	0.23%	0.42%	0.53%	0.67%	0.75%	0.68%	0.48%	0.32%	0.16%	0.16%

C_p

Average	-0.108901365	-0.114309302	-0.02583452	0.080993635	0.180910063	0.199377895	0.208463032	0.233546057	0.281121921	0.31964076	0.363501173	0.403813212	0.427088171	0.427320655
Standard Deviation	0.004281093	0.004853728	0.004382484	0.005617066	0.00434241	0.007720243	0.009598764	0.011720655	0.012238464	0.010529194	0.006918218	0.004409669	0.002143089	0.002121912
Standard Error	0.000957281	0.001085327	0.000979953	0.001256014	0.000970992	0.001726299	0.002146349	0.002620818	0.002736604	0.002354399	0.00154696	0.000986032	0.000479209	0.000474474
95%CI	0.001876272	0.00212724	0.001920708	0.002461788	0.001903145	0.003383546	0.004206844	0.005136803	0.005363744	0.004614623	0.003032043	0.001932623	0.00093925	0.000929969
95%CI/Average	1.72%	1.86%	7.43%	3.04%	1.05%	1.70%	2.02%	2.20%	1.91%	1.44%	0.83%	0.48%	0.22%	0.22%